

Engineering Materials

Amirhossein Pakseresht

Kamalan Kirubaharan Amirtharaj Mosas *Editors*

Ceramic Coatings for High-Temperature Environments

From Thermal Barrier to Environmental
Barrier Applications

 Springer

Engineering Materials

This series provides topical information on innovative, structural and functional materials and composites with applications in optical, electrical, mechanical, civil, aeronautical, medical, bio- and nano-engineering. The individual volumes are complete, comprehensive monographs covering the structure, properties, manufacturing process and applications of these materials. This multidisciplinary series is devoted to professionals, students and all those interested in the latest developments in the Materials Science field, that look for a carefully selected collection of high quality review articles on their respective field of expertise.

Indexed at Compendex (2021) and Scopus (2022)

Amirhossein Pakseresht ·
Kamalan Kirubaharan Amirtharaj Mosas
Editors

Ceramic Coatings for High-Temperature Environments

From Thermal Barrier to Environmental
Barrier Applications

 Springer

Editors

Amirhossein Pakseresht
FunGlass—Centre for Functional
and Surface Functionalized Glass
Alexander Dubček University of Trenčín
Trenčín, Slovakia

Kamalan Kirubakaran Amirtharaj Mosas
FunGlass—Centre for Functional
and Surface Functionalized Glass
Alexander Dubček University of Trenčín
Trenčín, Slovakia

ISSN 1612-1317

Engineering Materials

ISBN 978-3-031-40808-3

<https://doi.org/10.1007/978-3-031-40809-0>

ISSN 1868-1212 (electronic)

ISBN 978-3-031-40809-0 (eBook)

© The Editor(s) (if applicable) and The Author(s), under exclusive license to Springer Nature Switzerland AG 2024

This work is subject to copyright. All rights are solely and exclusively licensed by the Publisher, whether the whole or part of the material is concerned, specifically the rights of translation, reprinting, reuse of illustrations, recitation, broadcasting, reproduction on microfilms or in any other physical way, and transmission or information storage and retrieval, electronic adaptation, computer software, or by similar or dissimilar methodology now known or hereafter developed.

The use of general descriptive names, registered names, trademarks, service marks, etc. in this publication does not imply, even in the absence of a specific statement, that such names are exempt from the relevant protective laws and regulations and therefore free for general use.

The publisher, the authors, and the editors are safe to assume that the advice and information in this book are believed to be true and accurate at the date of publication. Neither the publisher nor the authors or the editors give a warranty, expressed or implied, with respect to the material contained herein or for any errors or omissions that may have been made. The publisher remains neutral with regard to jurisdictional claims in published maps and institutional affiliations.

This Springer imprint is published by the registered company Springer Nature Switzerland AG
The registered company address is: Gewerbestrasse 11, 6330 Cham, Switzerland

Paper in this product is recyclable.

Preface

Many industrial processes run in harsh environmental conditions with high pressure, a significant temperature gradient, and the presence of corrosion and oxidation atmospheres. Materials are exposed to temperatures that change their physical and chemical properties due to environmental reactions with the material and its surface. The science and technology of surface modification of materials have become more important over the past few decades. The best way to protect materials from oxidation and hot corrosion is through the application of coatings. Researchers thought that applying a suitable coating can be a good strategy to protect the underlying material by acting as a potential barrier between the material and the environment, so it has been constantly improved and developed.

Over the past few decades, coatings have come a long way and are now used for many different things. High-temperature coatings are a technologically significant, cost-effective, and rapidly expanding field. These coatings are designed for use at temperatures more than 2000 °C. High-temperature coatings include thermal barriers, environmental barriers, anti-corrosion, hard, and anti-wear coatings. These coatings are commonly used in power generation, petrochemical, aerospace, and manufacturing industries.

There is much useful information available regarding coatings for high-temperature environments and how they perform. However, this knowledge is spread through conference proceedings, book chapters, monographs, journals, and published industrial reports. The authors decided to put this collective information together under the theme of coatings for high-temperature environments. This book covers different parts of coatings used for high-temperature environments. In addition, this book also addresses the basic understanding of materials and their selection, basic principles of physical and chemical metallurgy, design considerations, manufacturing methods, performance upgrades, and different methods for evaluating the coating microstructure and application. This book covers thermal barrier coatings (TBCs), environmental barrier coatings (EBCs), and ultra-high temperature coatings. It also includes fundamental studies, including simulation, creating coating architecture, methods of preparation, and coating performances for the temperature range of applications. Phase stability, thermal properties, adhesion, defects, crystal

structure, and mechanical properties of coatings at high-temperature exposures are also covered in this book.

Organization of the Chapter

For a better organization of chapters, this book is physically separated into three parts, beginning with thermal barrier coatings for aerospace applications, environmental barrier coatings, and ending with ultra-high-temperature ceramic coatings for high-temperature environments.

Thermal barrier coatings (TBCs) are designed to protect the surface of metallic components of turbine engines exposed to extreme temperatures as well as to environmental attack promoted by oxygen and molten deposits. Chapter 1 discusses the design of TBC systems and the common coating methods for employing TBCs through plasma spraying and electron beam physical vapor deposition methods. A variety of ceramic materials used for TBC applications are also discussed in this chapter. In Chap. 2, the preparation of TBCs through suspension plasma spray and their damage mechanisms of calcium-magnesium-aluminosilicate (CMAS) through isothermal cycling and thermal gradient cycling tests were explored. The current potential solutions against CMAS attack through material and coating strategies are also discussed. The choice of selecting TBC materials is essential to protect against CMAS and hot corrosion, including considering the high melting point, low thermal conductivity, corrosion resistance, thermal expansion coefficient, lattice mismatch, and phase transformation during exposure at high temperatures. Chapter 3 presents an overview of oxide TBC materials, focusing on rare earth zirconate TBCs and the influence of ion doping, as well as the crystal structures and thermodynamic properties of niobates and tantalates.

Chapter 4 covers the topic of applying TBCs based on alumina. Various aspects related to the production methods of alumina-based TBCs and their failure mechanisms are discussed in this chapter. Interestingly, the laser surface modification process of alumina-based TBCs provides significant improvements in CMAS and hot corrosion failure mechanisms. Chapters 5 and 6 deal with ceramic composite coatings used as thermal barriers for industrial hot structural components, their latest advances in fabrication and performance, and recommendations for their use in harsh high-temperature environments.

Environmental barrier coatings enable ceramic matrix composites to operate under harsh environments. The material systems, preparation technologies, mechanical properties, and high-temperature failure behaviors of EBCs are systematically discussed in Chap. 7. The evolution of first-, second-, and third-generation EBC materials, fabrication methods, properties, and their main failure mechanisms are discussed in Chap. 8. Chapter 9 comprehensively evaluates the selection of silicates (mullite and BSAS), properties and corrosion behavior, and spraying techniques for EBCs and discusses their prospects. The research status of 1D micro/nanomaterials (SiC, ZrC, and HfC)-reinforced ceramic coatings and their fabrication methods for C/

C composites are discussed in Chap. 10. Chapter 11 explores the design of modified bi-layer and tri-layer EBCs based on mullite ceramic coatings with long service life in high-temperature and complex environments. An overview of the experimental activity developed during recent years on C/C materials for protecting aerospace structures from thermal shock in re-entry missions is discussed in Chap. 12.

The third part of Chaps. 13–15 discusses ultra-high temperature ceramic coatings. Chapters 13 and 14 cover a wide range of ultra-high temperature ceramic (UHTC) materials and provide a brief overview of the synthesis method, densification processes, and coating methods along with a description of the properties and applications of emerging high-entropy UHTCs. The use of W/ZrC composites using reactive sintering and infiltration methods for coating applications at ultra-high temperatures is discussed in Chap. 15.

Conclusion

The main aim of the book, *Ceramic Coatings for High-Temperature Environments: From Thermal Barrier to Environmental Barrier Applications*, is to offer a comprehensive overview of the advancements, potential challenges, and applications of a wide variety of materials in the field of high-temperature coatings. By the contribution of leading researchers, engineers, and industrial experts in this book, we hope that this book will serve as a valuable resource for academicians, students, researchers, and industrial experts seeking to improve their knowledge in the field of high-temperature coatings.

Trenčín, Slovakia

Amirhossein Pakseresht
Kamalan Kirubaharan Amirtharaj Mosas

Acknowledgements

We would like to extend our heartfelt thanks and appreciation to all the contributing authors who have shared their knowledge and expertise in this book. This book would not be possible without their dedication and excellent contributions in their respective disciplines. The editors would like to thank the reviewers for their helpful contributions in improving the chapter contents, cohesion, and narrative of each chapter. The majority of the contributing authors also worked as reviewers, and we would like to thank them for their tireless efforts in completing the reviewing process in such a short period of time. The editors would like to thank the readers of the high-temperature coating community for providing inspiration for this work. We feel this book will be extremely beneficial to their studies and research. Finally, we would like to thank the Springer Nature publisher personnel for their assistance from the beginning of the book proposal submission process. This would not have been feasible without their prompt assistance. We would also like to thank the editorial and production teams for their dedicated efforts and for making the publication possible.

Finally, the editors would like to express their gratitude to the FunGlass Centre at Alexander Dubcek University in Trenčín, Slovakia, for providing us with a dynamic environment in which to complete this book. This work is a part of dissemination activities of project FunGlass. This project has received funding from the European Union's Horizon 2020 research and innovation program under grant agreement No. 739566. Also, this work was supported by the VEGA grant no. 1/0171/21 and APVV grant no. APVV-22-0070.

Trenčín, Slovakia

Amirhossein Pakseresht
Kamalan Kirubaharan Amirtharaj Mosas

About This Book

This book addresses the recent trends in thermal and environmental barrier coatings and their applications in extreme environments. It introduces the state of the art in coating materials and processes for high- and ultra-high temperature environments and identifies areas for improvement in materials selection, performance upgrades, design considerations, and manufacturing methods. This book also covers fundamental studies involving modeling, creating coating architectures, coating preparation methods, and coating capability throughout a wide temperature range. The book examines a variety of high-temperature coatings prepared through various synthesis processes such as thermal spraying, electron beam evaporation, and sol-gel methods. This book also covers ultra-high temperature ceramic (UHTC) materials and provides a brief overview of the synthesis method, densification processes, and coating methods along with the properties and applications of emerging high-entropy UHTCs.

With contributions from international researchers active in the field, this edited book features the most recent and up-to-date literature references for a broad readership consisting of academic and industrial professionals. It is suitable for graduate students as well as materials scientists and engineers working in the area of high and ultra-high temperature ceramic materials.

Contents

Thermal Barrier Coatings	
New Materials for Thermal Barrier Coatings: Design, Manufacturing and Performance	3
Giovanni Di Girolamo	
Trends and Perspectives in Mitigating CMAS Infiltration in Thermal Barrier Coating	37
Maxime Gaudin, Lucille Despres, Alice Dolmaire, Emilie Béchade, Alan Kéromnès, Simon Goutier, Alain Denoirjean, Aurélien Joulia, Vincent Rat, and Armelle Vardelle	
New Materials for Thermal Barrier Coatings	87
Feifei Zhou and Shun Wang	
Recent Developments on Al₂O₃-Based Thermal Barrier Coatings	125
Fatih Kirbiyik, Mustafa Guven Gok, and Gultekin Goller	
Zirconia-Based Thermal Barrier Coatings Systems for Aero-Industry	151
Adriana Stefan, Victor Manoliu, and George Catalin Cristea	
Multilayered Coatings by Thermal Spray for High-Temperature Applications	179
John Henao, Marco A. Rivera-Gil, Carlos A. Poblano-Salas, Diego G. Espinosa-Arbelaez, Luis G. Trapaga-Martinez, Oscar Sotelo Mazon, and Jorge Corona Castuera	
Environmental Barrier Coatings	
Environmental Barrier Coatings (EBCs) for Ceramic Matrix Composites	215
Feifei Zhou and Donghui Guo	

Environmental Barrier Coatings (EBCs) for Silicon-Based Ceramics and Composites	243
Jia-Hu Ouyang, Gui Cao, and Shu-Qi Wang	
Development of Silicates and Spraying Techniques for Environmental Barrier Coatings	283
Ayahisa Okawa, Son Thanh Nguyen, Tadachika Nakayama, Hisayuki Suematsu, Takashi Goto, and Koichi Niihara	
1D Micro/Nanomaterial Toughened Ceramic Coatings for Carbon/Carbon Composites	313
Xuemin Yin, Huimin Liu, Xin Zhang, and Hejun Li	
Oxidation and Thermal Cycle Behavior of $\text{Yb}_2\text{Si}_2\text{O}_7$-$c$-$\text{AlPO}_4$-$\text{SiC}_w$-Mullite Multilayer Coatings	339
Pengju Chen, Peng Xiao, and Yang Li	
Space Environment Effects on Advanced Ceramic Coating for Aerospace Thermal-Proof Re-entry Systems	385
Roberto Pastore, Andrea Delfini, Marta Albano, Fabio Santoni, Fabrizio Piergentili, and Mario Marchetti	
Ultra High Temperature and High Temperature Coatings	
Recent Advances in Ultra-High-Temperature Ceramic Coatings for Various Applications	409
K. Deepthi Jayan	
Ultra-High-Temperature Ceramic Coatings ZrC, ZrB_2, HfC, and HfB_2	441
Suprabha Das, Md. Shariful Islam Sozal, Wenhao Li, and Denny John	
High-Temperature W/ZrC Composite Coatings	471
Aliasghar Najafzadehkhoe, Maryam Vakhshouri, Pavol Hvizdoš, and Dušan Galusek	

Thermal Barrier Coatings

New Materials for Thermal Barrier Coatings: Design, Manufacturing and Performance



Giovanni Di Girolamo

Abstract Ceramic thermal barrier coatings (TBCs) are aimed to protect the surface of metallic components of turbine engines exposed to extreme temperature as well as to environmental attack promoted by oxygen and molten deposits. Their application allows to extend component life and can improve thermal capability and efficiency of next-generation engines. TBC design includes detailed analysis of materials' composition and TBC architecture. Basic requirements are demanded in terms of low thermal conductivity and high phase stability, whereas the porous and stress compliant microstructure should preserve high-temperature performance, since thermal cycling typically promotes partial sintering and thermal expansion mismatch between coating and substrate, thus assisting typical detrimental effects such as cracking, delamination and spallation. Yttria stabilized zirconia is the most common ceramic for industrial TBC manufacturing, under a large variety of operating environments. During the last decades, many ceramic oxides with potential enhanced properties were investigated and fabricated TBCs were tested at laboratory scale. However, prolonged high-temperature service requires further validation steps to successfully apply novel systems in real engines. This chapter explores state-of-the-art and recent developments in the matter of TBCs, focusing on the properties of novel compositions and TBC architectures, taking in account the main mechanisms inducing their in-service failure.

Keywords Thermal barrier coating · Extreme temperature · Thermal spraying · EB-PVD · Zirconia · Ceramics

List of Abbreviations

3D 3 Dimension
APS Air Plasma Spraying

G. Di Girolamo (✉)

Territorial and Production Systems Sustainability Department, ENEA, Palermo, Italy
e-mail: giovanni.digirolamo@enea.it

© The Author(s), under exclusive license to Springer Nature Switzerland AG 2024
A. Pakseresht and K. K. Amirtharaj Mosas (eds.), *Ceramic Coatings for High-Temperature Environments*, Engineering Materials,
https://doi.org/10.1007/978-3-031-40809-0_1

CMAS	Calcium Magnesium Aluminum Silicate
CTE	Coefficient of Thermal Expansion
CYSZ	Ceria Yttria co-Stabilized Zirconia
DED	Direct Energy Deposition
DySZ	Dysprosia Stabilized Zirconia
EB-PVD	Electron Beam Physical Vapor Deposition
FGM	Functionally Graded Material
GZ	Gadolinium Zirconate
NdCSZ	Neodymia Ceria Stabilized Zirconia
LaYSZ	Lanthana Yttria Stabilized Zirconia
LC	Lanthanum Cerate
LPPS	Low Pressure Plasma Spraying
LZ	Lanthanum Zirconate
PECs	Pockets of energy concentration
PS-PVD	Plasma Spraying Physical Vapor Deposition
ScYSZ	Scandia Yttria Stabilized Zirconia
SPS	Suspension Plasma Spraying
SPPS	Solution Precursor Plasma Spraying
SZ	Samarium Zirconate
TBC	Thermal Barrier Coating
TGO	Thermally Grown Oxide
YSZ	Yttria Stabilized Zirconia

1 Introduction

Thermal barrier coatings (TBCs) are suitable to protect the surface of Ni-based superalloy turbine engine parts operating at extreme temperature and under oxidative and corrosive environments, such as air seals, stationary guide vanes, blades, shrouds in high-pressure sections, after-burners in tail section. The application of a thick coating (from 120 to 400 μm) is able to lower surface temperature from 100 to 300 $^{\circ}\text{C}$. TBCs are usually deposited on internally air-cooled components, such as combustor parts or transition ducts of stationary and rotating airfoils, with the purpose to reduce cooling air flow and energy consumption, thus increasing the turbine efficiency [1, 2]. The surface temperature of turbine blades can reach 1450 $^{\circ}\text{C}$, so that these components are air-cooled to reduce the temperature of about 300–400 $^{\circ}\text{C}$ [3].

The actual technical challenges are oriented to improve the capability of industrial TBC systems, usually restricted to temperatures of about 1100–1200 $^{\circ}\text{C}$, by developing materials with enhanced performance as well as by developing optimized coating technologies allowing the deposition of materials with fine microstructure, that being associated with improved functional properties.

Based on that, this chapter is aimed to fill the existing knowledge gap in the design of TBC materials and related systems, manufactured using various processing

technologies, on the basis of detailed analysis of the required key properties as well as on the high-temperature behavior under harsh environments and operating cycles typically experienced by industrial turbines.

In the last decades, the literature has been enriched by a multitude of researches and operative reports, but the data provided appeared frequently dispersed and a comparative analysis taking into account all the major mechanisms and effects conditioning the durability of these complex articles was rarely presented.

The increasing request for improved in-service performance requires the employment of materials with better capability as well as more efficient processing technologies in order to manufacture well-tailored morphologies and microstructures. Many validation steps are then requested to promote market uptake of novel materials and TBC architectures.

Following this approach, this review will present a detailed summary of recent studies, focused on the design of TBC materials, their architecture and their performance at conditions simulating the real working environment or close to that, thus offering to producers clear practical recommendations for manufacturing of materials and components matching specific characteristics.

As an example, the experience of end users has demonstrated that sintering and CMAS are major issues for current TBCs, those being main drivers for unexpected failure, heavily impacting on engine efficiency as well as on safety issues.

The latest enhancements in materials' design, manufacturing and performance of TBC systems are then addressed to draw major trends of future industrial developments.

2 Design of TBC Systems

Ni-based super-alloys could operate at the high temperature experienced by turbine engines, but their surface and microstructure would be irremediably subjected to progressive and extensive damage because of environmental attack promoted by highly oxidative and corrosive media. Therefore, their protection represents an incoming technological challenge in order to prevent fast damage of the component and to extend its durability.

Figure 1 shows a representation of aircraft engine, turbine blade and related TBC system, respectively. It is globally ascertained that a common TBC can be designed as a layered system, where the outer layer is the ceramic top coat. In line of principle, a conventional TBC is composed of an underlying Ni-based super-alloy component, coated by an intermediate metallic layer, commonly named bond coat, and an upper thermally insulating ceramic layer [4–7].

The bond coating provides high resistance to oxygen and molten salts infiltration as well as slightly increases the temperature capability of the substrate thanks to the presence of alloying elements like Cr, Al and Y. In addition, its application is beneficial to increase the adhesion of the ceramic TBC to the substrate surface, balancing the mismatch in their related chemical and thermal properties. MCrAlY

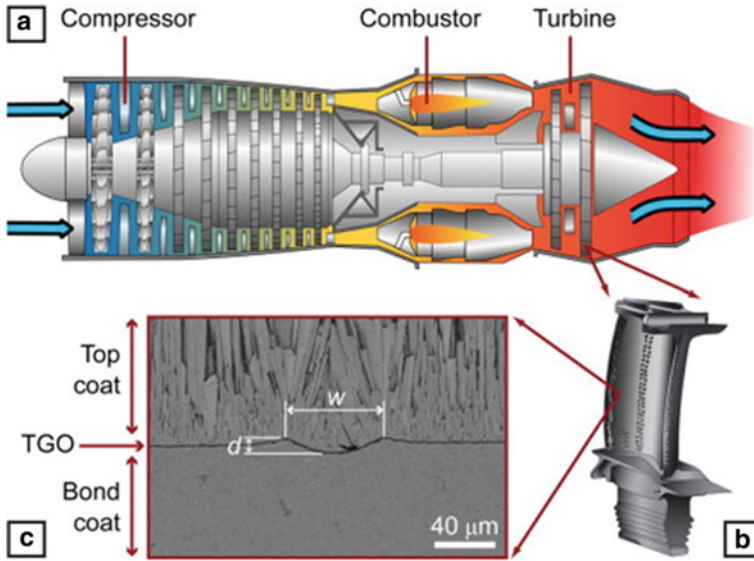


Fig. 1 **a** A schematization of a jet engine (reprinted with the kind permission of Jeff Dahl). **b** A turbine blade. **c** A cross-section of a specific TBC system used in the present study (note the predefined irregularity at the TC–BC interface. Reprinted from Hille, T.S., Njidam, T.J., Sujker, A.S.J., et al.: Damage growth triggered by interface irregularities in thermal barrier coatings. *Acta Mater.* 57(9), 2624–2630 (2009), with permission from Elsevier [19]. The image from Jeff Dahl is licensed under CC BY 4.0

alloys ($M = \text{Ni}$ and/or Co) are then applied as overlay coatings to protect the surface of metallic components; the alloying of small amount of reactive elements (Y , Re , Zr , Ir) is considered useful to improve surface adhesion and resistance to high-temperature oxidation [8–11]. Intermetallic $\beta\text{-NiAl}$ or $\beta\text{-PtNiAl}$ layers are alternative bond coating compositions able to provide high-temperature oxidation resistance, by inhibiting the oxygen diffusion to the metal substrate, so that they can be applied as intermediate coatings before depositing the upper thermally insulating ceramic layer counteracting the heat transfer to the metallic surface [12–14].

Technical design should take in account any key aspects, such as material selection, manufacturing for producing tailored microstructure, TBC architecture and so on.

TBC architecture should be properly designed depending on the basic properties of all its elements as well as on the expected operating environments it is addressed to.

Focusing on the top coat insulating layer, it could be designed as a single ceramic layer. On the other hand, the investigators use to identify as multilayered system a TBC composed of two or more ceramic top coats, where an intermediate layer, deposited on bond coat surface, is assigned to partially inhibit heat transfer to the substrate, whereas the outer sacrificial layer is expected to maximize resistance to hot corrosion in specific hostile engine environments.

Therefore, multilayered TBC systems put together the basic characteristics of different ceramic materials with the purpose to increase the temperature capability of the whole system and/or to improve the environmental resistance under well-defined operating conditions, e.g., the prevalence of one effect on another.

Recently, the application of functionally graded materials (FGM) has been presented as a promising technical solution for TBC manufacturing [15], especially in conjunction with the diffusion of additive manufacturing technologies. FGM-based TBC systems combine the basic characteristics of both metallic and ceramic high-temperature materials, by gradually changing the chemical composition of the related manufactured coatings along coating thickness, e.g., by depositing mixtures with different contents of metallic and ceramic compounds during processing, starting from bond coat composition and gradually reducing the content of the metal alloy in favor of the related content of the ceramic, up to achieve the total content of ceramic material on the upper surface. Based on its intrinsic property, a graded microstructure is particularly suitable to reduce the thermal expansion mismatch between overlapped layers and the thermal stresses typically arising during service and evolving in TBC spallation during long-term exposure [16–18].

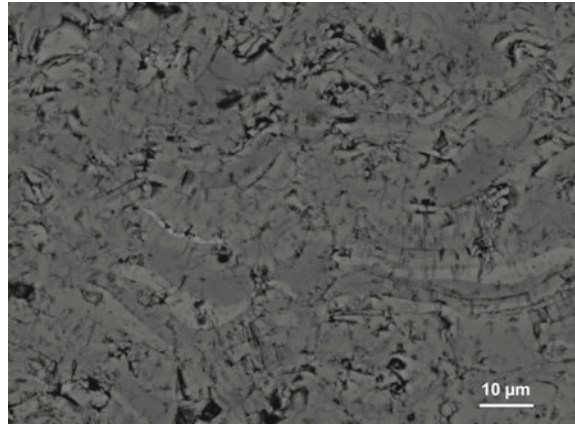
3 Common Technologies Employed for TBC Manufacturing

Manufacturing process is a key factor for producing TBC systems with well-determined microstructure and functional characteristics. Thermal spraying and electron beam physical vapor deposition (EB-PVD) are recognized as the best available industrial technologies suitable for fabrication of porous and strain-tolerant thermal barrier coatings. They are able to process different categories of materials, giving to fabricated TBC systems tailored functional properties, matching the specific operating conditions expected in the working environment.

3.1 Thermal Spraying Processing Technologies

Thermal spraying includes different processes and, among them, the most suitable ones for TBC fabrication commonly use a gas plasma as energy source for melting feedstock materials employed. An inert gas is superheated and ionized to generate a high-temperature plasma ($T > 10,000$ K, speeds of about 600–2300 m/s) [20]. Feedstock particles with typical size of 10–100 μm , fed by a carrier gas, are injected in the plasma jet and overheated. Molten droplets are then accelerated by the gas stream toward the substrate top surface. Upon impact at speed of 30–500 m/s, molten particles are subjected to flattening and quenching to room temperature, assisting the formation of typical splatted particles. Overlapped deposited splats gradually

Fig. 2 Lamellar microstructure of plasma sprayed ceria–yttria co-stabilized zirconia coating (CYSZ)



generate thick coating with typical porous and lamellar microstructure, as observable in Fig. 2.

Air plasma spraying (APS) is suitable to deposit relatively thick coatings on complex components. It is a well-established manufacturing technology, quick and cost-efficient, characterized by high deposition rate, low processing times and low preparation costs [21]; in the last decade, the interest in grain size reduction and processing of finer microstructures with tailored properties led to the diffusion of optimized spraying technologies, such as suspension plasma spraying (SPS) and solution precursor plasma spraying (SPPS). The as-produced microstructures and their basic properties, first of all the thermal conductivity, are positively affected by smaller size and in-flight fragmentation of sprayed molten ceramic particles within the plasma jet [22].

The suspensions typically constituted of fine particulates dispersed in liquid suspension are pressurized, injected in the plasma jet and atomized in a stream of fine molten particles, following a mechanism dealing with particle breaking up, liquid evaporation, sintering and melting. The agglomeration of fine particles impacting substrate top surface leads to the buildup of the final coating [23, 24].

Otherwise, the solutions are composed of inorganic salts dissolved in a solvent, pressurized, melted and deposited on the substrate as molten and un-pyrolized particles, thus forming a porous coating [25, 26].

SPS method allows to manufacture coatings with optimized and sub-micrometer porosity with the aim to reduce the thermal conductivity at values lower than $1 \text{ Wm}^{-1} \text{ K}^{-1}$ [27, 28]. In summary, these last processes are characterized by different in-flight precipitation mechanism of sprayed particles and are able to produce well-tailored microstructures.

3.2 EB-PVD Deposition Method

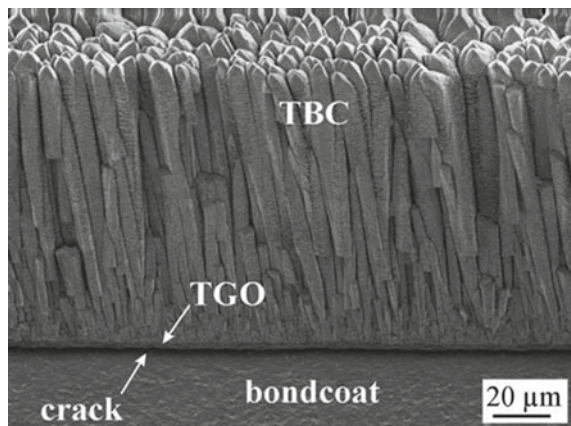
In EB-PVD technology a target anode is bombarded with an electron beam generated by a charged tungsten filament under high-vacuum conditions. The highly energized triggered atoms are vaporized and then accelerated toward a substrate, where they are gradually deposited, thus forming a thin coating [29].

Based on the intrinsic characteristics of the deposition process, EB-PVD coatings exhibit good adhesion to the substrate and a typical segmented columnar structure (see Fig. 3), composed of columns growing along the cooling direction, particularly suitable to accommodate thermal expansion of overlapped layers. Indeed, their typical own segmentation cracks increase the strain tolerance of the whole system, accompanying the release of residual stresses. However, at the same time, the typical gaps between adjacent columns act as preferential paths for heat transfer as well as for infiltration of oxygen and molten salts along coating thickness, facilitating the gradual loss of thermal insulation and the oxidation of underneath metal surface [30–32].

On the other hand, as reported in the previous section, APS coatings exhibit a lamellar microstructure produced by the deposition of molten splats and embedding a network of globular pores and microcracks, produced by rapid cooling of molten particles at room temperature, so that APS TBCs are generally marked by lower thermal conductivity and higher porosity than EB-PVD ones; indeed their thermal conductivity is generally lower than $1.2 \text{ Wm}^{-1} \text{ K}^{-1}$, whereas it is slightly higher in the case of EB-PVD produced counterparts ($1.2\text{--}2.2 \text{ Wm}^{-1} \text{ K}^{-1}$). However, values comparable to those measured on APS coatings have been achieved in any recent works [29, 31].

Some economic aspects related to processing should be also taken in account when referred to industrial applications. In EB-PVD, the preheating of the substrate is mandatory and the deposition rate is quite low in comparison with APS processing. The process is time-consuming and more expensive, so that is generally adopted to

Fig. 3 YPSZ thermal barrier coating with strain-tolerant columnar microstructure fabricated by EB-PVD. Reproduced from Schulz, U., Leyens, C., Fritscher, K., et al.: Some recent trends in research and technology of advanced thermal barrier coatings. *Aerospace Science and Technology* 7(1) 73–80 (2003), Copyright © 2003 Elsevier Masson SAS. All rights reserved [29]



functionalize the surface of more critical and expensive components such as rotor parts. Otherwise, plasma sprayed TBCs are usually deposited on industrial components such as first-stage blades, stator vanes and after-burner holders, since the process is cheaper and less time-consuming, then more suitable for mass production.

A few recent works have also mentioned a hybrid technique for coating deposition, called plasma spraying-physical vapor deposition (PS-PVD). Like-PVD TBCs are fabricated using a LPPS (low pressure plasma spraying) apparatus equipped with high-energy plasma gun working at pressure of 0.1 kPa. Based on that, the powder feedstock is partly melted and vaporized, originating a unique microstructure out of the vapor phase, that combines the advantaged of both the single techniques [33].

3.3 Additive Manufacturing

Additive manufacturing is one of the key driver of green and digital industrial transition and a processing technology suitable to fabricate various categories of materials and three-dimensional (3D) printed components.

It has recently emerged as a potential technology for manufacturing of TBC systems, especially when they are designed as functionally graded material (FGM) systems, whose composition gradually changes along the thickness, starting from the bond coat surface up to the external TBC surface. Indeed, 3D printing processes allow to produce unique coating microstructure by gradually modifying the chemical composition and the porosity of the materials employed along the same coating thickness [34, 35].

To this regard, promising additive manufacturing techniques can include direct energy deposition (DED), stereo-lithography and powder bed melting.

However, many technical issues have to be properly faced to manufacture components with acceptable microstructure and functional characteristics. In particular, it has been reported that the growth of microcrack networks during fabrication and the presence of any un-melted particles as well as the formation of unwanted inter-metallic phases in the final microstructure play key role in high-temperature performance of these systems, their cracking mechanisms and their resulting environmental resistance [18].

4 TBC Materials

Jet engine components typically experience extreme temperature during service and are subjected to thermal cycles between peak and low temperatures during take-off, landing and on-ground operations. The presence of severe oxidizing and corrosive environment, as well as of high working pressure (close to 10 atm) and maximum gas speed ($> \text{Mach}1$), impose stringent requirements, in terms of functional design and use of high-temperature resistant materials for their manufacturing, in order to

ensure life-long service as well as security and safety for vehicles and passengers, respectively.

It is widely known that the properties of yttria stabilized zirconia (YSZ)—zirconia is partially stabilized with 8 wt.% Y_2O_3 to prevent typical high-temperature phase changes—have been investigated for a lot of decades. YSZ actually represents the state-of-the-art TBC material: based on testing at laboratory scale and in various real environments, YSZ has commonly ensured a good combination of many basic properties demanded to TBC materials, *e.g.*, good thermal conductivity (approximately in the range from 0.8 to 1.1 $Wm^{-1} K^{-1}$ for as-sprayed YSZ, increasing up to 1.5–1.7 after high-temperature exposure), good fracture toughness ($\sim 3.4 MPam^{1/2}$), good phase stability up to 1200 °C, relatively high CTE ($\sim 11 \times 10^{-6} K^{-1}$), high microhardness (~ 14 GPa), low elastic modulus (~ 40 GPa). It has been reported that the application of YSZ TBC with thickness of 100–200 μm can decrease the temperature on the metallic surface of about 170 °C [36–42].

However, various researches conducted in the last two decades highlighted that YSZ TBCs can suffer common and remarkable damaging effects after long-term exposure at temperature above 1200 °C, because of any sintering mechanisms and phase transitions, typically producing an increase of thermal conductivity as well as some detrimental effects, such as cracking and spallation. Particularly, the sintering occurs via closure of fine pores and microcracks, as well as via the development of sintering necks between the lamellae, thus affecting the elastic properties of the same TBC [39].

Generally speaking, TBC materials should exhibit high phase stability, thermal conductivity lower than 2 $Wm^{-1} K^{-1}$ [43, 44], relatively high CTE (>10 – $11 \times 10^{-6} K^{-1}$) to withstand the thermal expansion mismatch with the bond coat (CTE $\sim 17.5 \times 10^{-6} K^{-1}$, in the range from RT to 1000 °C), low sintering activity, low Young's modulus, high fracture toughness, high chemical compatibility with TGO (thermally grown oxide) growing at the interface between ceramic and metallic layers due to high-temperature oxygen infiltration and propagation.

The different CTE values of overlapped layers can generate a mismatch in their thermal expansion during thermal cycling, thus producing high thermal stresses at their interface, those being responsible for coating delamination and spallation. In turn, Young's modulus affects the strain compliance of the whole TBC and the amount of thermal stresses.

In turn, coating porosity is a basic property to tailor mechanical and thermal properties of a TBC system, provided that splat boundaries and globular pores embedded in plasma sprayed TBC microstructure play a significant role in reducing stiffness and increasing strain tolerance, as well as in lowering thermal conductivity value.

It is widely accepted that finer microstructures can provide better functional properties. As an example, the thermal conductivity of SPS YSZ coatings was found to be of about 0.5–1.0 $Wm^{-1} K^{-1}$, by means of larger amount of fine pores and strain-compliant vertical microcracks running through coating thickness. Their measured Young's modulus, equal to 3.3 GPa, was quite low with respect to APS coatings (15–20 GPa) at room temperature [45]. Highly segmented SPS TBCs survived up to 660 cycles at 1400 °C, until partial spallation took place, due to growth and propagation

of delamination cracks [46, 47], even if it has been highlighted anytime that, under thermal cycling conditions, these microstructures have shown high sintering rate of overspray fine particles and neck formation between lamellae.

Nanostructured YSZ TBCs characterized by low thermal conductivity ($0.55\text{--}0.65 \text{ Wm}^{-1} \text{ K}^{-1}$) have been also fabricated using SPPS method. Again the retention of smaller porosities and the growth of segmented cracks during processing, running along coating thickness, allowed to maximize the strain tolerance and to reduce stiffness, then contributing to increase the thermal cycling resistance by a factor of 2.5 in comparison with conventional air plasma sprayed TBCs.

Therefore, the search for alternative and more performant TBC materials should start from primary selection and detailed analysis of any basic characteristics, such as mechanical, microstructural and thermal properties, up to focus on high-temperature behavior under the action of surrounding oxidizing and/or corrosive media, typically promoting any damaging and failure mechanism affecting the durability of the related covered components during operation life.

Based on the last advancements in the field, as it will be discussed in detail in the next sections, the most promising ceramic materials for manufacturing of advanced TBCs can be categorized as follows:

- Zirconia-based materials, obtained by doping ZrO_2 with metallic and/or rare-earth oxides.
- Alternative compositions including:
 - (a) Zirconates with general formula $\text{Re}_2\text{Zr}_2\text{O}_7$ ($\text{RE} = \text{Gd}, \text{La}, \text{Nd}, \text{Sm}$) and pyrochlore structure;
 - (b) Perovskites (*e.g.*, SrZrO_3)
 - (c) Rare-earth cerates such as $\text{La}_2\text{Ce}_2\text{O}_7$ and $\text{Nd}_2\text{Ce}_2\text{O}_7$;
 - (d) Rare-earth tantalates and similar mixed compositions obtained by substituting Ta with alternative chemical elements.

4.1 Zirconia-Based Materials

Different oxide stabilizers can be employed to induce dislocation effects and lattice defects in the structure of zirconia, thus improving both phase stability and thermal expansion coefficient as well as reducing the thermal conductivity. As an example, doping of YSZ with oxides as CeO_2 , Yb_2O_3 , Gd_2O_3 induces more oxygen vacancies and high concentration of lattice defects, promoting enhanced phonon scattering and thus decreasing the value of thermal conductivity [48–51].

The use of different amounts of CeO_2 is able to stabilize YSZ in tetragonal or cubic phase. Ceria–yttria co-stabilized zirconia (CYSZ) TBCs showed decreased thermal conductivity, higher CTE (12.6 against $10.7 \times 10^{-6} \text{ K}^{-1}$ for YSZ, with temperature ranging from between 50 and 900 °C), higher phase stability, better sintering resistance and, finally, higher durability when isothermally exposed at temperature above 1200 °C [52–54]. The thermal diffusivity of nanostructured SPS CYSZ deposits was

found to be lower than that of YSZ ones ($0.33\text{--}0.55 \times 10^{-6} \text{ m}^2\text{s}^{-1}$ against $0.51\text{--}0.75 \times 10^{-6} \text{ m}^2\text{s}^{-1}$) [55, 56].

Doping with rare-earth elements is an effective option for improving the thermal insulation property of YSZ, that being affected by intrinsic properties and by boundary convection, thermal radiation and gas pressure of the surrounding environment [57].

Plasma sprayed Dy_2O_3 -doped zirconia (DySZ) TBCs have shown higher phase stability at temperature of $1300 \text{ }^\circ\text{C}$ and a thermal conductivity lower than $0.7 \text{ Wm}^{-1} \text{ K}^{-1}$ in as-sprayed condition, increased to $1.1 \text{ Wm}^{-1} \text{ K}^{-1}$ after heat treatment at $1050 \text{ }^\circ\text{C}$ [58]. Higher CTE value has been also measured for Dy_2O_3 -doped zirconia (DySZ) and Yb_2O_3 -doped zirconia [59–61].

Lanthana (La_2O_3) can be also employed as zirconia stabilizer. LaYSZ (lanthana yttria stabilized zirconia), exhibited similar conductivity and CTE, but better sintering resistance than YSZ. The main drawback was represented by the fact that LaYSZ partially decomposes at $1300 \text{ }^\circ\text{C}$ [62–64].

It is worth noting that, when using two rare-earth oxides as dopants, e.g., Nd_2O_3 or Gd_2O_3 or Sm_2O_3 as first dopant and Sc_2O_3 or Yb_2O_3 as second dopant, the thermal conductivity decreases to $0.5\text{--}0.7 \text{ Wm}^{-1} \text{ K}^{-1}$. At the same time, the resulting compositions are characterized by higher CTE value ($11.5\text{--}13.5 \times 10^{-6} \text{ K}^{-1}$) and higher thermal stability. For example $\text{CeO}_2\text{-Nd}_2\text{O}_3$ doped zirconia (NdCSZ) has exhibited promising high CTE ($12.8 \times 10^{-6} \text{ K}^{-1}$) up to $1250 \text{ }^\circ\text{C}$ [65, 66], whereas the addition of scandia to YSZ (ScYSZ, scandia yttria stabilized zirconia) seemed to be particularly suitable for improving high-temperature corrosion resistance [67, 68].

Table 1 shows the values of thermal conductivity and thermal expansion coefficient measured on a large variety of TBC materials produced by plasma spraying and EB-PVD processes.

4.2 Alternative Compositions

Seeking for further advanced materials matching the requirements for turbine engine TBCs, $\text{RE}_2\text{Zr}_2\text{O}_7$ compounds have emerged as well. Rare-earth zirconates with pyrochlore structure, a complex ordered structure with more oxygen vacancies within the crystal, exhibited excellent thermal stability. They provide good thermal insulating property ($\lambda \sim 1.1\text{--}1.5 \text{ Wm}^{-1} \text{ K}^{-1}$), because of increased phonon scattering, and relatively high CTE (between 8 and $11 \times 10^{-6} \text{ K}^{-1}$, measured between 700 and $1200 \text{ }^\circ\text{C}$) [40, 69]. Among them, lanthanum zirconate ($\text{La}_2\text{Zr}_2\text{O}_7$), samarium zirconate ($\text{Sm}_2\text{Zr}_2\text{O}_7$) and gadolinium zirconate ($\text{Gd}_2\text{Zr}_2\text{O}_7$) were investigated as alternative TBC materials since ‘2000. In particular, lanthanum zirconate (LZ) has been one of the first pyrochlore structure-based materials investigated as potential TBC candidate because of its high-temperature thermal conductivity ($\sim 20\%$ lower than that of YSZ) and low Young’s modulus [70, 71]. Above $1200 \text{ }^\circ\text{C}$, LZ coatings have shown inelastic deformation and non-linear mechanical behavior, related to their peculiar microstructure, as well as a toughening effect [72].

Table 1 Thermo-physical properties of different TBC ceramic materials. * sintered or EB-PVD coating

	Thermal conductivity ($\text{Wm}^{-1} \text{K}^{-1}$)	CTE (10^{-6}K^{-1})	Reference number
YSZ	0.8–1.2	10.5–11	[36–42]
CYSZ	0.5	12.6	[52–54]
DySZ	0.6–1.2	9.5–12.5	[58–60]
YbSZ	1.6	12.5	[60, 61]
(Gd/Nd/Sm) (Sc/Yb) YSZ	0.5–0.7	11.5–13.5	[61]
LaYSZ	0.6	9–10.5	[61–64]
NdCSZ	–	12.8	[65, 66]
$\text{La}_2\text{Zr}_2\text{O}_7$	0.7–0.8	9.5	[69–74]
$\text{Gd}_2\text{Zr}_2\text{O}_7$	1–1.7*	10.5	[80]
$\text{Nd}_2\text{Zr}_2\text{O}_7$	0.6–1*	10.1–10.6	[80]
$\text{Sm}_2\text{Zr}_2\text{O}_7$	0.25–0.45	10.8	[78, 79, 81]
$\text{Nd}_2\text{Ce}_2\text{O}_7$ ($\text{Nd}_2\text{Ce}_{3.25}\text{O}_{9.5}$)	~ 1.57–3.4 (700–20 °C)	11.57–12.14	[78]
SrZrO_3	2.3*	10.9	[69, 83, 84]
$\text{La}_2\text{Ce}_2\text{O}_7$	0.6–1.3 0.5–0.75	10.3 (up to 14 at 1200 °C)	[89–91]
$(\text{Nd}_{1-x}\text{Yb}_x)_2\text{AlTaO}_7$	0.8	8.82–9.93 (1200 °C)	[96]
$(\text{Sm/Gd})_3\text{Ce}_7\text{Ta}_2\text{O}_{23.5}$	0.67/1.07	>12	[99]
$\text{Ca}_3(\text{Dy/Nd})_3\text{Ce}_7\text{Ta}_2\text{O}_{26.5}$	1.09/1.73	11.92/12.1	[100]
$\text{Y}(\text{Ta}_{1-x}\text{Nb}_x)\text{O}_4$	1.5	10 (1200 °C)	[101]
$\text{Yb}(\text{Ta}_{1-x}\text{Nb}_x)\text{O}_4$	1.49 (min at 1200 °C)	10.6 (max 1200 °C)	[102]

Another interesting and intrinsic property of lanthanum zirconate is its low ionic conductivity ($9.2 \pm 0.3 \times 10^{-4} \Omega^{-1} \text{cm}^{-1}$ versus $0.1 \Omega^{-1} \text{cm}^{-1}$ measured on YSZ) at 1000 °C, that reducing oxygen ionic diffusion mechanism along TBC crystalline structure; the formation and gradual growth of TGO at the interface with the bond coating is hence mainly affected by gas penetration mechanism through the network of pores and microcracks (see Fig. 4), while the permeation across the ceramic microstructure is reduced to very low extent. The growth rate of TGO is then restricted by decreasing the oxygen partial pressure and the oxygen activity at the interface.

Plasma sprayed lanthanum zirconate TBCs have exhibited excellent thermal shock resistance at 1200 °C and slow sintering kinetics. However, their relatively low toughness and CTE value (slightly lower than that of YSZ, *e.g.*, $9.45 \times 10^{-6} \text{K}^{-1}$ vs. $10.7 \times 10^{-6} \text{K}^{-1}$) played a negative effect on their thermal cycling lifetime, by promoting formation and propagation of lateral cracks at the interface and coating spallation at

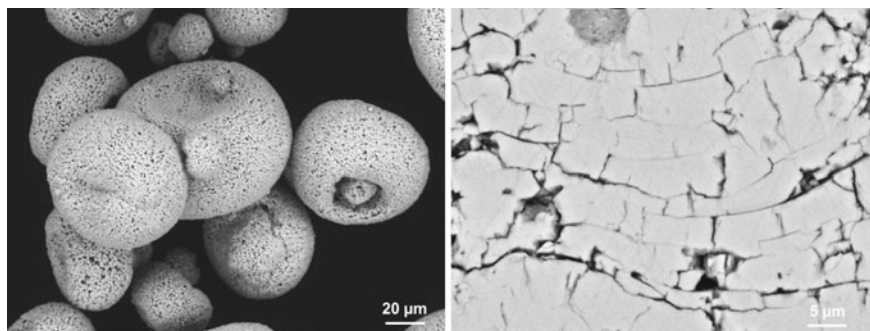


Fig. 4 LZ particle morphology particles and lamellar microstructure of as-sprayed LZ coating

temperature close to 1300 °C [72–74]. Therefore, its application as single TBC layer seems to be somehow restricted.

On the other hand, when used as outer layer applied on traditional YSZ TBC, zirconate-based coating is able to enhance the temperature capability of the whole system as well as to reduce the CTE mismatch between the overlapped layers, thus reducing the content of interfacial thermal stresses and increasing the final durability [75–77].

Further improvements have been achieved when nanostructured lanthanum zirconate TBCs have been fabricated using SPS method: their thermal conductivity was found to be lower than that of YSZ ones ($0.73 < \lambda < 0.79 \text{ Wm}^{-1} \text{ K}^{-1}$ versus $0.8\text{--}1.2 \text{ Wm}^{-1} \text{ K}^{-1}$, in the range from 200 °C to 1200 °C). After thermal treatment at 1300 °C and 1400 °C, the related increase in thermal conductivity was of about 0.3 and $0.6 \text{ Wm}^{-1} \text{ K}^{-1}$, respectively [73].

Further rare-earth zirconates can be successfully employed to overcome the limitations of $\text{La}_2\text{Zr}_2\text{O}_7$. In line of principle, it is widely demonstrated that the addition of rare-earth oxides as Gd_2O_3 , Nd_2O_3 , and Sm_2O_3 to zirconia allows to synthesize rare-earth zirconates with enhanced thermal properties in terms of decreased thermal conductivity and higher CTE [78–80]. After thermal aging at 1200 and 1300 °C, $\text{Sm}_2\text{Zr}_2\text{O}_7$ TBCs were found to be affected by sintering effect, but their related insulating properties were not influenced at large extent. As an example, the thermal conductivity of $\text{Sm}_{1-x}\text{La}_x\text{Zr}_2\text{O}_7$ coatings slightly increased, but remained below $1 \text{ Wm}^{-1} \text{ K}^{-1}$ [81].

EB-PVD $\text{Gd}_2\text{Zr}_2\text{O}_7$ TBCs have shown better resistance in comparison with YSZ ones when exposed at 1100 °C, even if it should be underlined that this temperature is rather low looking at next-generation turbines. Moreover, $\text{Gd}_2\text{Zr}_2\text{O}_7$ revealed high tendency for cracking and its CTE was found to be lightly lower than that of YSZ. Nanostructured $\text{Gd}_2\text{O}_3\text{-Y}_2\text{O}_3\text{-ZrO}_2$ TBCs sprayed by APS were characterized by thermal conductivity lower than that of both conventional and nanostructured YSZ ones (0.9 and $1.05 \text{ Wm}^{-1} \text{ K}^{-1}$, against $1.1\text{--}1.2$ for nanostructured YSZ and $1.3\text{--}1.45$ for conventional YSZ, from room temperature to 1200 °C): indeed, the presence of finer porosities positively affected the heat transfer along TBC microstructure [82].

In turn perovskites with cubic structure showed promising thermal properties for TBC fabrication, even if the thermal conductivity of plasma sprayed SrZrO₃ coatings ($< 2.2 \text{ Wm}^{-1} \text{ K}^{-1}$) was generally high, while their CTE and thermal cycling lifetime at 1250 °C were comparable to those measured on YSZ, or sometimes slightly lower (higher than $8.5 \times 10^{-6} \text{ K}^{-1}$) [70, 83, 84]. In addition, the retention of tetragonal zirconia in the phase composition of as-produced coatings can restrict their operating temperature, as well as their relatively low fracture toughness and sintering resistance.

By adding Yb₂O₃ and Gd₂O₃ as dopants a further decrease in thermal conductivity and Young's modulus can be achieved, in conjunction with enhanced thermal stability and fracture toughness, as observed in the case of any specific compositions like Sr(Zr_{0.9}Yb_{0.1})O_{2.95} and Sr(Zr_{0.8}Gd_{0.2})O_{2.9}. The measured CTE value of Sr(Zr_{0.9}Yb_{0.1})O_{2.95} coating was $9.2\text{--}10.6 \times 10^{-6} \text{ K}^{-1}$ (in the range 200–1100 °C), higher than that found for Sr(Zr_{0.8}Gd_{0.2})O_{2.9}, that falling in the range between 8.7 and $10.8 \times 10^{-6} \text{ K}^{-1}$. In addition, the thermal conductivity of Sr(Zr_{0.9}Yb_{0.1})O_{2.95} was $\sim 20\%$ lower than that of SrZrO₃, in the temperature range from 200 to 1200 °C, and the Young's modulus was lower as well. Finally, the fracture toughness of the optimized SrZrO₃ was found to be comparable to that of plasma sprayed YSZ, since it was found to be close to $1.1 \text{ MPa m}^{1/2}$ for Sr(Zr_{0.9}Yb_{0.1})O_{2.95} and $1.6 \text{ MPa m}^{1/2}$ for Sr(Zr_{0.8}Gd_{0.2})O_{2.9}, respectively [85–88].

In the recent years, the discussion about alternative TBC materials has been enlarged to further more complex compositions.

For example, many investigators focused their attention on lanthanum cerate (La₂Ce₂O₇, LC), provided that the substitution of Zr⁴⁺ with Ce⁴⁺ ions allowed to reduce the order degree of crystal structure and the overall bond energy, producing a positive response on the thermal and mechanical characteristics of these compound [89]. Plasma sprayed cerate TBCs have exhibited thermal conductivity of about $0.5\text{--}0.75 \text{ Wm}^{-1} \text{ K}^{-1}$ [90] and enhanced durability up to 1400 °C. However, it has been also observed that the high-temperature formation of LaAlO₃ at the interface with the TGO induced any detrimental delamination mechanisms. Moreover, although a maximum CTE of $14 \times 10^{-6} \text{ K}^{-1}$ was measured on La₂Ce₂O₇ samples with fluorite structure, their thermal expansion drastically dropped in low-temperature range ($200 < T < 400 \text{ °C}$), that having the potential for producing noticeable mechanical interfacial stresses [91]. Segmented coatings were then produced to increase the strain tolerance and to counteract thermal expansion mismatch and high-temperature sintering effects, in conjunction with the fabrication of multilayered TBC system. Therefore, the thermal shock durability of segmented doubled LC/YSZ TBC was 50% higher than that of unsegmented one; in this system, the failure was finally produced by chipping spallation and internal delamination cracking [92, 93].

Nd₂Ce₂O₇ has also emerged in a few investigations as a material with relatively high CTE, although further investigations and measurement of its thermal insulation properties are required to explore its full potential for TBC manufacturing.

However, the main novelty, presented in very recent works, deals with the use of rare-earth tantalates (RETaO₄, RE = Dy, Gd, Lu, Nd, Sc, Yb) as promising TBC materials; based on their high thermal stability, low thermal conductivity, low elastic

modulus and enhanced fracture toughness, they could potentially operate at temperature higher than 1600 °C. Moreover, their intrinsic ionic conductivity can be beneficial to reduce the propagation of oxygen along coating thickness, preventing, retarding or reducing TGO growth, that being negligible in comparison with what found in the case of YSZ TBC, and thus prolonging the lifetime of the whole TBC system [94–96].

The composition of these compounds is susceptible to be modified to the purpose, as observed in the case of $(\text{Nd}_{1-x}\text{Yb}_x)_2\text{AlTaO}_7$: the addition of an electronegative element as Yb_2O_3 was suitable to decrease the thermal conductivity as well as to moderately enhance the CTE value, even if that was generally lower than $10 \times 10^{-6} \text{ K}^{-1}$ [97].

In addition, single-fluorite-type lattice $(\text{La/Nd})_3\text{Ce}_7\text{Ta}_2\text{O}_{23.5}$ and $(\text{Sm/Gd})_3\text{Ce}_7\text{Ta}_2\text{O}_{23.5}$ ceramics were manufactured through a solid-state fritting method using La_2O_3 or Nd_2O_3 , Ta_2O_5 and CeO_2 as raw materials. These compounds, characterized by large atomic weight and high level of oxygen vacancies, have shown better thermal properties than YSZ. In particular, their CTE was close to $12 \times 10^{-6} \text{ K}^{-1}$ [98, 99]. Pyrochlore-type $\text{Ca}_3(\text{Dy/Nd})_3\text{Ce}_7\text{Ta}_2\text{O}_{26.5}$ samples, prepared using high-temperature solid-state sintering at 1600 °C, have also exhibited a thermal conductivity between 1.09 and 1.73 $\text{W m}^{-1} \text{ K}^{-1}$, whereas their CTE was close to $12 \times 10^{-6} \text{ K}^{-1}$ [100].

Finally, Ta substitution with Nb was found to be a viable solution for reducing thermal conductivity as well for improving CTE value of YTao_4 -based ceramics, typically synthesized via solid-state reaction. Indeed, the minimum thermal conductivity measured on $\text{Yb}(\text{Ta}_x\text{Nb}_{1-x})\text{O}_4$ ceramic samples was 1.49 $\text{W m}^{-1} \cdot \text{K}^{-1}$. The maximum CTE was found to be $10.6 \times 10^{-6} \text{ K}^{-1}$ (measured at 1200 °C). These compounds have interestingly exhibited lower elastic modulus and higher hardness as well [101, 102].

In line of principle, most of these last compounds are characterized by lower thermal conductivity and higher CTE in comparison with conventional YSZ and zirconates. The synthesis of micron-sized sprayable particles or ingots for manufacturing of TBCs with well-determined microstructural, thermal and mechanical characteristics represents a current challenge. Indeed, it is should be noted that these properties have been measured on sintered samples, so that they should be validated in the case of porous APS or EB-PVD coatings, where the optimization of the microstructure could reasonably produce further benefits.

Further investigations are then expected to demonstrate their performance in terms of thermal cycling behavior and resistance to environmental attack promoted by corrosive agents as calcium–magnesium–aluminum–silicate (CMAS), taking in account that TBC failure in turbine environment is a very complex mechanism affected by many factors and the comprehension of the basic properties of raw materials and as-produced coatings could not to be enough to validate their real performance.

Moreover, all these alternative compositions generally imply the use of critical raw materials for the European industry, including heavy and light rare-earth oxides

and elements such as niobium, tantalum, strontium, so that the aspects referring to sustainable and secure global industry sourcing should be properly pointed out.

5 Multilayered TBCs

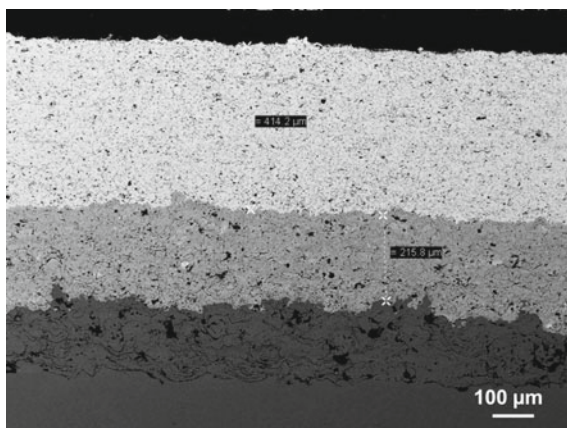
Previous discussion has highlighted that YSZ TBCs are consolidated systems for various industrial applications, since their functional performance has been extensively studied and validated under real working conditions of jet turbines. However, the need for increasing working temperature and component lifetime has revealed any critical restrictions, based on the fact that the failure of YSZ TBC is commonly affected by complex degradation and damaging effects.

As discussed above, any alternative materials seem to possess interesting basic characteristics, but there is no common consensus for substituting YSZ in many key industrial applications. The old-fashioned concept for substituting material with another material has revealed its clear weakness, thus suggesting to follow an alternative approach, based on different TBC design.

To this purpose, high attention has been focused on multilayered TBC systems, where the ceramic TBC can be designed by applying two overlapped layers; YSZ is usually applied as an insulating layer on bond coat and furtherly covered by an upper ceramic layer with higher temperature stability and resistance to infiltration of oxygen and corrosive agents [103–105]. The design of doubled TBC system (see Fig. 5) allows to reduce the thermal stresses arising at the interface between metal and ceramic due to their different thermal expansion during high-temperature exposure. Plasma sprayed doubled TBCs have shown improved durability during high-temperature thermal cycling at different surface temperatures (1250 °C, 1350 °C and 1450 °C). When exposed at temperature of 1250 °C plasma sprayed doubled TBCs survived up to 4000 cycles, that being comparable to the resistance of single YSZ TBC. Otherwise, a graded TBC, composed of a mixture of YSZ and $\text{La}_2\text{Zr}_2\text{O}_7$, survived 2000–2800 cycles. The investigators remarked that with increasing the temperature of testing to 1350 °C, doubled YSZ/ $\text{La}_2\text{Zr}_2\text{O}_7$ TBC became the more performant system, followed by a YSZ/ $\text{Nd}_2\text{Zr}_2\text{O}_7$ TBC system. At the highest temperature (1450 °C), YSZ/ $\text{La}_2\text{Zr}_2\text{O}_7$ TBC lasted more than 1200 cycles. In these last cases, the thermal cycling lifetime was largely higher than that of standard YSZ TBC [106, 107].

Functionally graded EB-PVD $(\text{GdYb})_2\text{Zr}_2\text{O}_7/8\text{YSZ}$ TBCs exhibited better high-temperature sintering resistance and thermal cycling lifetime with respect to doubled coatings (1346 versus 942 cycles at 1350 °C), and their better performance was ascribed to different failure mechanism experienced. Indeed, the failure of doubled TBC was mainly characterized by inter-lamellar delamination, because of propagation of cracks generated by concentration of internal stresses: during cooling, when the stresses exceeded the adhesive–cohesive strength of the splats, cracking and delamination took place. Otherwise, the damaging of functionally graded ceramic TBC was mainly promoted by TGO interfacial growth and CTE mismatch between

Fig. 5 Multilayered TBC system, composed of metal bond coat, intermediate ceria–yttria co-stabilized zirconia layer and upper lanthanum zirconate layer



overlapped layers, whose main effect was the final TBC spallation [108]. At moderate heat fluxes and high temperature, the failure was mainly affected by TGO growth and inelastic behavior, whereas fracture occurred at the interface. With increasing ceramic surface temperature and thermal gradient, thermal expansion mismatch played a key role on internal TBC delamination.

Further multilayered TBCs have taken into consideration the application of $Gd_2Zr_2O_7$ as outer layer directly facing the surrounding and harsh environment. However, the use of gadolinium zirconate ($Gd_2Zr_2O_7$) in aircraft engine components could be somehow restricted by its relatively low toughness (1.02 against $2 \text{ MPam}^{1/2}$ for YSZ) and high tendency to form $GdAlO_3$ phase when directly applied on the outer surface of a $MCrAlY$ coating [109–111]. However, multilayered $Gd_2Zr_2O_7$ /YSZ TBC has exhibited extremely longer thermal cyclic lifetime at $1300 \text{ }^\circ\text{C}$ in comparison with the performance of single YSZ one, that was more prone to internal splat delamination, whereas the multilayered TBC failed because of horizontal cracking within the GZ layer, near the interface with YSZ [112].

The design of doubled TBCs with different high-temperature materials could also include the use of perovskites and cerates as outer sacrificial TBC layers. For example, it has been reported that the durability of doubled $Sr(Zr_{0.9}Yb_{0.1})O_{2.95}$ /YSZ and $Sr(Zr_{0.8}Gd_{0.2})O_{2.9}$ /YSZ coatings during thermal cycling at a surface temperature of $\sim 1250 \text{ }^\circ\text{C}$ was higher than that of $Sr(Zr_{0.9}Yb_{0.1})O_{2.95}$ and $Sr(Zr_{0.8}Gd_{0.2})O_{2.9}$ coatings, that being equivalent to that of single YSZ TBC system. However, as temperature reached $1350 \text{ }^\circ\text{C}$, the durability of doubled $Sr(Zr_{0.9}Yb_{0.1})O_{2.95}$ /YSZ TBC system under thermal cycling conditions revealed to be interestingly higher, *e.g.*, ~ 25 higher than that shown by YSZ TBC [84–86].

6 High-Temperature Behavior and Common TBC Failure Mechanisms

As anticipated in the previous sections, many high-temperature effects typically affect the performance of TBC systems, modifying mechanical, microstructural and physical properties of the same ones through common degradation phenomena [113].

First of all, the phase and thermal stability of the TBC materials should be high enough to prevent or reduce the content of phase transition typically occurring during cooling to room temperature, since these transformations, as observed in the case of YSZ, are usually accompanied by volume change promoting microcracks' growth and propagation, facilitating delamination and creating a preferential path for infiltration of both oxygen and molten salts.

In line of principle, TBC degradation is the synthesis of different effects, such as mechanical damaging, compaction, oxidation, environmental attack, sintering of the porous microstructure and erosion [114, 115]. Among them, testing of components at laboratory scale and during service in real environment suggests to take in high consideration TGO growth mechanism at the interface between the ceramic TBC and the metallic coating and the related thermal stresses, in conjunction with the thermal stresses arisen by thermal expansion mismatch between overlapped layers. The development of stresses in the whole TBC system is responsible for extended cracking, delamination and spallation, produced by TGO swelling, typically occurring during the cooling engine cycle [116].

Moreover, TBC failure is strongly affected by high-temperature sintering of the porous microstructure, evolving in partial densification and reduced stress compliance.

Finally, the environmental attack promoted by molten salts and CMAS is able to strongly affect the lifetime of TBC systems. In a special manner, the microstructural changes promoted by CMAS infiltration have become a key challenge for current TBCs used in aircraft engines. It should be noted that the durability of turbine engine articles is also affected by hot corrosion promoted by molten salts, like sodium sulfate and vanadium pentoxide.

In synthesis, all these TBC degradation phenomena are recognized to be sources of thermal stresses, typically assisting cracking, delamination and final TBC spallation.

6.1 TGO Growth and Delamination

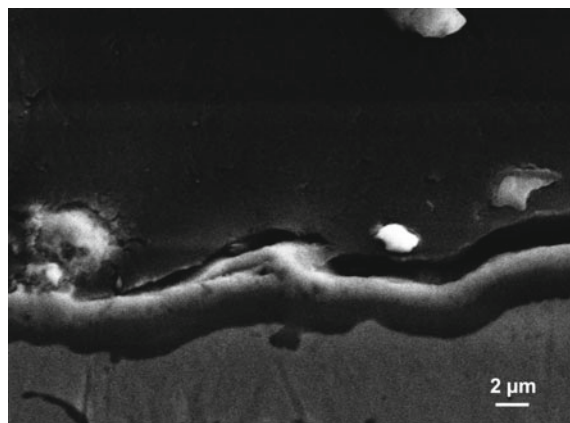
The oxidation of metallic bond coat surface is governed by two transfer mechanisms, such as the ionic diffusion through the ceramic TBC and the penetration through coating porosities and microcracks. The diffusion and the propagation of oxygen along coating thickness during high-temperature exposure typically assists formation and growth of a thermally grown oxide at the interconnection between ceramic and metallic layers [117, 118].

The amount of Al contained in the composition of the bond coat alloy drivers selective oxidation, assisting the formation of this TGO (Fig. 6). A thin, continuous and dense α -Al₂O₃ TGO ($\sim 2 \mu\text{m}$) with low oxygen permeability can act as further barrier against oxidation. However, the extended Al depletion occurring during repeated thermal cycles leads to the interfacial growth of undesired brittle mixed oxides like spinels and Ni/Co oxides, characterized by the presence of surface protrusions and discontinuities, so that the fast growth of mixed TGO on the surface of alumina layer is accompanied by mechanical stresses, evolving in extended crack tips, propagation of vertical cracks and lose of adherence [119–121]. As the critical thickness (5–6 μm) of TGO is achieved, delamination commonly takes place [122]. A brittle TGO is more prone to volumetric expansion, propagation of microcracks and delamination. TGO should keep its elasticity to the highest temperature and should not creep, to prevent cavitation or rumpling under thermal cycling, since rumpling can cause local growing separations [123, 124]. Summarizing, mechanical stresses within the TGO scale arise from TGO lateral expansion, volume expansion and gradual thickening, but from thermal mismatch between overlapped ceramic and metallic layers as well. Tensile stresses promote deformation, horizontal cracking and delamination of the oxide scale; as the size of lateral cracks rises above its critical value spallation at the interface takes place [125], leaving the bulk component uncovered and subjected to extreme temperature, above its typical temperature capability.

The authors of a recent work observed and described in detail a new spallation mechanism: they have found that local strain energy concentrations, there called pockets of energy concentration (PECs), occurred around the interface between the TGO and the bond coat, arising from local phase changes as well as from uneven creep and plastic relaxation effects. As a consequence, PECs and buckling facilitated TBC spallation mechanism [126].

In conclusion, failure generated by TGO formation and growth is a complex mechanism, where any chemical incompatibilities between overlapped layers, associated

Fig. 6 TGO growth on the top of bond coating



to high-temperature formation of any phases, play a significant role, as observed in $\text{Gd}_2\text{Zr}_2\text{O}_7$ TBC directly deposited on the metallic layer [110].

6.2 Sintering of Porous TBC Microstructure

As earlier reported, as temperature arises above 1200 °C some sintering effects on the TBC porous microstructure can become noticeably. They are accompanied by the partial densification of globular pores, closure of vertical microcracks and formation of sintering necks at splat boundary, that increasing the inter-lamellar bonding and the coating density. The evolution of coating microstructure is responsible for the increase of thermal insulation property, facilitating heat transfer to the metallic substrate and TGO growth. Moreover, stiffness concomitantly increases, negatively conditioning the strain tolerance and the compliance of the whole TBC, mitigating stress accommodation properties, facilitating growth of thermal stresses and propagation of microcracks, and thus increasing the risk for coating delamination. In particular, the formation of sintering necks between the lamellae increases the viscosity by raising the threshold load for the onset of splat sliding and can involve propagation mechanism of cracks, despite high-temperature sintering causes the healing of any finer cracks [127–130].

As detectable in Fig. 7, after exposure at 1200 and 1350 °C, the mechanical properties and the thermal conductivity of LZ coatings increased, because of the fast healing of inter-lamellar bonded interfaces, e.g., the formation of grain bridging and sintering necks between the lamellae, whose typical morphology changes to more dense microstructure with globally reduced porosity [131, 132].

It has been widely accepted that pore distribution and size in as-produced coating play a major role on the sintering resistance of TBCs. Indeed, the anti-sintering performance can be enhanced by optimizing the manufacturing process of powder feedstocks' employed, e.g., by embedding particles with micron-scale pores in the microstructure; high-temperature exposure (1300 °C) of properly designed TBCs, with finer porosity, did not produce significant changes in thermal conductivity and Young's modulus with respect to YSZ TBCs sprayed using conventional powder particles. The presence of extended vertical microcracks can also retard sintering effects, prolonging the lifetime of TBC system [133].

In line of principle, the current TBC designers are focusing their attention on alternative compositions and TBC architectures, less prone to suffer remarkable high-temperature sintering phenomena.

6.3 Microstructural Damage Promoted by CMAS Infiltration

The intake of air during flight and land operation of aircrafts is responsible for the ingestion of silica-based solid mineral particulates, like airborne dust, fly ash, debris

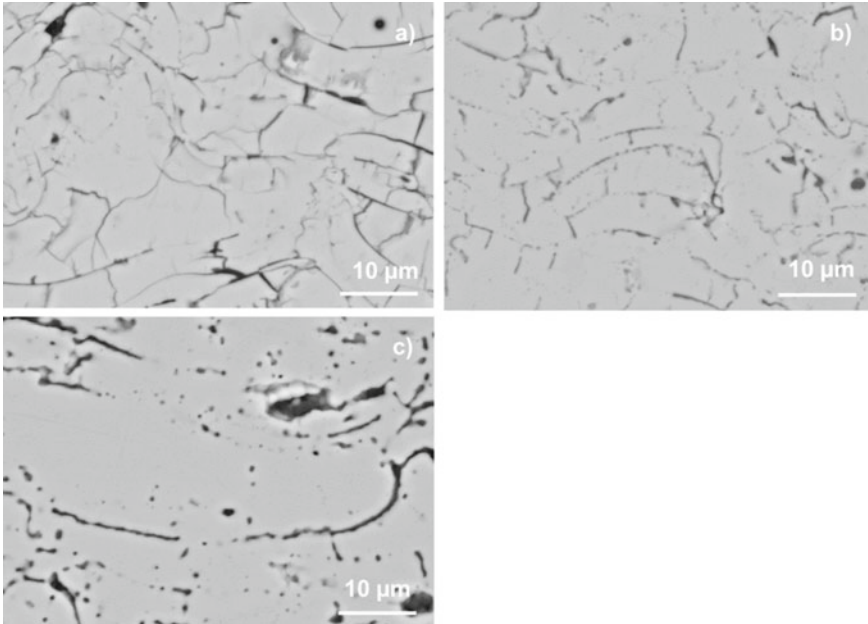


Fig. 7 Evolution of $\text{La}_2\text{Zr}_2\text{O}_7$ TBC microstructure due to high-temperature sintering effects: **a** as-sprayed, **b** aged at 1200 °C and **c** aged at 1350 °C for 50 h

and sand, able to deposit and adhere on the top surface of hot jet engine components, combustor parts, airfoils and shrouds, usually covered by a TBC system [134]. The partial or fully melting of these particulates typically evolves in glassy melts based on calcium–magnesium–aluminum–silicate (CMAS) oxides [135]. In-flight melting of siliceous particles can occur through the combustor or, more frequently, during the hottest stages of the engine cycle—typically at peak temperature close to 1250 °C—particularly during take-off or landing operations. This last circumstance has been clearly confirmed by the presence of these agglomerates on the surface of airfoils. The rate of accumulation is higher on the hottest regions of high-pressure section, whereas small deposits are generally detectable at the leading edge. Otherwise, no deposits are observed on the suction side. Most silicate deposits melt at temperature close to 1200 °C, so that an increase of the operating temperature can make CMAS issue a big challenge for future and more efficient turbine engines.

This molten glassy material wets the top surface and penetrates into TBC microstructure by capillarity action, reacting with and chemically dissolving the surrounding material. As the temperature drops, the glassy materials crystallizes [136]. This fast degradation process supports sintering and related stiffening of the microstructure as well as partial loss of related thermal insulation characteristics. Thermal mismatch between layers characterized by variable chemical compositions accelerates delamination mechanisms and extended TBC degradation. The penetration of CMAS can also reach the interface between top coat and bond coat, promoting

delamination along the TGO or creep cavitation effects within the metal, wherein the delamination paths can furtherly propagate [137].

Obviously the microstructure of the ceramic TBC has a major role in the mechanism of degradation. For example, it has been reported that the columnar microstructure of EB-PVD YSZ coating is affected by sudden CMAS permeation after short exposure at a temperature close to 1250 °C. The mechanism is quite fast. In the first hours of exposure, CMAS glass seeped through the ceramic microstructure along inter-columnar gaps, attacking and deforming the column tips. Its rapid reaction with surrounding YSZ originated an interaction mixed area (~20 μm thicker) composed of existing CMAS and YSZ with equiaxial grains, followed by an area characterized by relatively lower degradation, wherein the column were somehow retained and the amount of globular particles gradually decreased. Ytria depletion, associated with its migration toward the upper molten CMAS and dissolution, assisted detrimental monoclinic zirconia transition [138, 139].

The changes in microstructure, producing areas with different morphological features and composition, inevitably altered all the thermal and mechanical characteristics of the un-aged TBC. Indeed, pore healing and intra-columnar sintering, promoted by CMAS infiltration and subsequent solidification upon cooling, produced noticeable stiffening, loss of thermal insulation characteristic and thermal mismatch between adjacent areas, susceptible to promote formation and propagation of cracks during next thermal cycles [140, 141]. Indeed, as the time of thermal exposure was increased to 8 h, a network of vertical and transverse cracks was observed within YSZ TBC; as microcracks propagated to the edge of vertical cracks delamination and partial spallation occurred at the interface between the modified mixed area and the unaffected YSZ-rich region, although the TBC appeared well-adherent to the TGO yet, that being probably ascribed to the good adhesion of EB-PVD TBC to the metallic substrate. In addition, vertical cracks were preferential paths for further CMAS attack.

These results make clear the typical operating limitations of YSZ, subjected to persistence of dissolution and re-precipitation phenomena, whereas substantial enhancements have been achieved by using alternative TBC compositions.

For example, the addition of rare-earth elements can mitigate the CMAS attack, as observed in the case of Er₂O₃-doped YSZ TBC, since its higher reactivity with CMAS allowed to block or reduce the penetration of CMAS with respect to YSZ, partially retaining the starting thermal insulation property. As observed in Figs. 8 and 9, the columnar microstructure of YSZ was attacked by infiltration of melted CMAS and partial dissolution occurred. CMAS infiltration assisted inter-lamellar and intra-lamellar sintering and formation of TGO at the interface [142]. Upon cooling the residual CMAS and the precipitated new phases recrystallized. In turn, visible cracks were detected in the case of Er-doped TBC, where very fast precipitation and crystallization of stable apatite and fluorite phases produced a dense layer hindering further penetration and, at the same time, prevented the increase of thermal conductivity.

Further investigations were carried out on Ga₂Zr₂O₇ TBCs exposed at 1300 °C. The molten glassy phase suddenly wet the inner surface of columns, whose tips suffered moderate attack, and filled the voids. The inter-columnar gaps were early

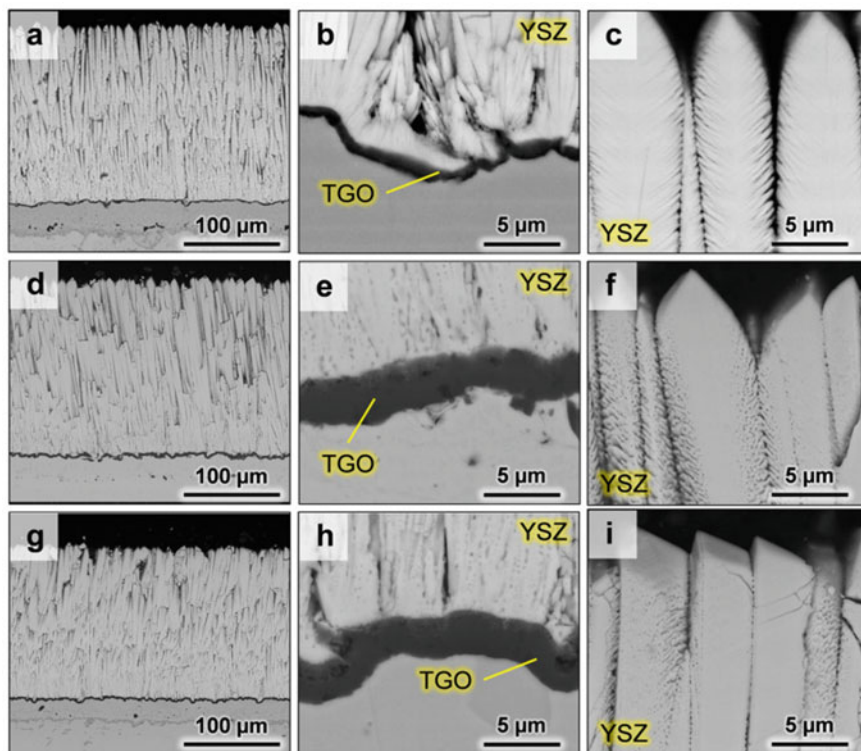


Fig. 8 SEM micrographs of the electron beam physical vapor deposition (EB-PVD) standard yttria stabilized zirconia (8YSZ) coatings in the as-deposited conditions with **a–c** (similar for both standard and Er_2O_3 -doped coatings) and after aging in air at $1250\text{ }^\circ\text{C}$ for 1 h with **d–f** for the standard 8YSZ coating and **g–i** for the ErYSZ coating. Reprinted from Boissonet, G., Chalk, C., Nicholls, J.R.: Thermal insulation of YSZ and Erbium-Doped Yttria-Stabilised Zirconia EB-PVD Thermal Barrier Coating Systems after CMAS Attack. *Mater.* 13(19), 4382 (2020), Copyright © 2020 MDPI, CC BY 4.0 [142]

sealed by crystalline reaction products, while the molten CMAS spread laterally covering the column surface. The precipitation process assisted the formation of dense and fine-grained reaction layer acting as a diffusion barrier against further infiltration and penetration of molten CMAS. This layer was composed of $\text{Gd}_8\text{Ca}_2(\text{SiO}_4)_6\text{O}_2$ apatite and cubic fluorite ZrO_2 grains. The column tips were then subjected to slow attack and dissolution from bulk CMAS, producing a graded microstructure, followed by further re-precipitation of crystalline phases during cooling. As a consequence, the resistance of $\text{Gd}_2\text{Zr}_2\text{O}_7$ (GZ) was substantially better than that of YSZ; indeed, after short thermal exposure at $1300\text{ }^\circ\text{C}$, the CMAS melt infiltrated until $30\text{ }\mu\text{m}$, causing rapid dissolution of GZ into the melt and precipitation of stable crystalline Gd-apatite, fluorite and small traces of spinel phase from the GZ/CMAS melt, mitigating the environmental attack and prolonging TBC lifetime [143, 144].

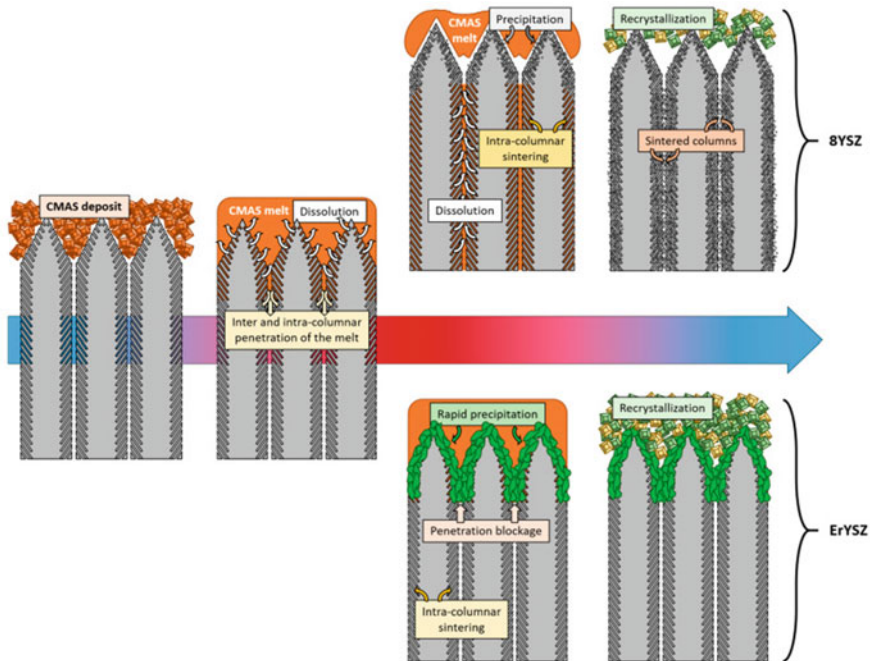


Fig. 9 Schematic drawing of the CMAS interaction with the 8YSZ and ErYSZ columnar coatings during the annealing at 1250 °C (1 h) and final cooling. Reprinted from Boissonet, G., Chalk, C., Nicholls, J.R.: Thermal insulation of YSZ and Erbium-Doped Ytria-Stabilised Zirconia EB-PVD Thermal Barrier Coating Systems after CMAS Attack. *Mater.* 13(19), 4382 (2020), Copyright © 2020 MDPI, CC BY 4.0 [142]

The mechanism observed in the case of TBCs deposited by APS and containing extended segmented cracks was quite similar, apart some small changes associated with different microstructures produced by different coating deposition technologies. The barrier layer, composed of Gd-apatite and Gd depleted fluorite, blocked further interaction, without arresting the infiltration of molten CMAS through microcracks. As a consequence, the grain boundary dissolution observed in YSZ, was not detected [134].

All the mentioned works have demonstrated that rare-earth zirconates are potentially able to counteract the environmental attack from CMAS, mitigating the detrimental microstructural changes induced by their fast infiltration, via the rapid crystallization of stable apatite and fluorite phases, preventing deep penetration of the molten silicates, thus avoiding extended sintering of the whole TBC layer and the propagation of the environmental attack up to the TGO [144–149].

The high-temperature behavior of the applied TBCs is also affected by the composition as well as by the amount of molten glass deposited on their surface. To this purpose, some authors have focused their attention on the high-temperature behavior

of NdYbZr₂O₇ TBCs under the attack of CMAS, volcanic or fly ashes. These compositions were characterized by dissimilar temperature viscosities, and thus different tendency for wetting and infiltration. Indeed, CMAS deposits exhibited the highest dynamic wettability because of their lower viscosity, whereas the largest infiltration depth was achieved in the case of volcanic ash, probably because of the relatively high solubility of RE₂O₃ in the same molten ash.

In summary, the investigators have found that NdYbZr₂O₇ TBCs exhibited better resistance than YSZ ones; fast precipitation of (Nd,Yb)-apatite and cubic zirconia phases promoted the growth of an usual dense reaction layer, as previously reported for GZ TBC, inhibiting further penetration of molten CMAS through coating thickness [150].

The same mechanism was finally observed in ScTaO₄ exposed to 1300 °C, when a discontinuous layer rich of CaTa₂O₆ and Sc₂SiO₅ was formed by dissolution re-precipitation. ScTaO₄ showed satisfactory phase stability, due to low solubility of Sc³⁺ in CMAS. However, it should be pointed out that the thermal properties of (Sc/Yb/Lu) TaO₄ can limit their performance under thermal cycling conditions, since their thermal conductivity at 900 °C reached 1.6 W m⁻¹ K⁻¹, whereas their CTE was quite low in comparison with YSZ (measured from 200 to 1200 °C) [151, 152].

In conclusion, based on the high variety of case studies herein discussed, the application of multilayered TBCs seems to be the most effective solution to be adopted when severe environmental attack is expected during service. Following this concept, in samarium zirconate/YSZ doubled TBCs aged at 1250 °C, the penetration of CMAS was reduced by about a factor of five, even if the whole TBC seemed to be totally soaked after four hours of exposure, and CMAS totally filled the interface between SZ and YSZ layers. Dissolution and precipitation of faceted apatite and fluorite phases took place too. It was accompanied by interfacial debonding between SZ and YSZ layers. Faceted and globular particles replaced the column tips and co-existed with large volume fraction of CMAS. The penetration of apatite was less effective in comparison with single GZ TBC and the rate of CMAS penetration was slower than that found in YSZ. At the end of the story, these TBCs have exhibited excellent properties in terms of delamination resistance, decreased thermal conductivity, reinforced thermal and sintering resistance [153, 154].

7 Drawing Next Perspectives

High-temperature performance of TBC systems substantially depends on manufacturing technology, since that influences the intrinsic characteristics of as-produced microstructure and the related mechanical and thermal properties. For many years, APS and EB-PVD have been recognized as the most common techniques aimed to TBC fabrication. The manufacturing of finer microstructures with high strain compliance and better sintering resistance, e.g., employing more recent SPS and SPPS methods, allows to enhance any of the key functional properties demanded to TBC systems.

Additive manufacturing methods have also recently emerged with the purpose to produce functionally graded TBCs, composed of a mixture of metallic and ceramic materials, less prone to be subjected to thermal and mechanical stresses during exposure at extreme temperature.

Up to now, YSZ has represented the material industrially adopted for TBC manufacturing, but its applications can be somehow restricted, since the highest temperatures expected for next-generation turbines are able to promote thermal degradation and sintering of the porous microstructure, as well as any damaging mechanisms induced by penetration of CMAS typically ingested into jet engines.

The study of novel TBC materials is at the core of TBC designers. Identification and selection of innovative ceramic compositions should be based on key properties, including reduced high-temperature thermal conductivity ($\sim 0.5\text{--}1 \text{ Wm}^{-1} \text{ K}^{-1}$ in as-sprayed condition) and a thermal expansion coefficient as much as possible close to that of the metal bond coat, and typically above $11\text{--}12 \times 10^{-6} \text{ K}^{-1}$ or higher. Rare-earth dopants can be successfully employed to synthesize more stable zirconia-based compounds or zirconates with pyrochlore structure, to manufacture microstructures characterized by low Young's modulus and low thermal conductivity at extreme temperature. The current limitations of zirconates are related to the mismatch with the CTE value of the bond coat material as well as to their relatively low fracture toughness in comparison with YSZ, so that they are generally applied as upper coatings on the surface of YSZ. Therefore, multilayered TBC systems seem to be the best technical viable option for restricting TGO growth and thermal stresses arising from CTE mismatch, those being recognized as main drivers for TBC spallation.

TBC failure is a very complex mechanism based on various degradation interconnected effects that should be carefully analyzed to evaluate the durability of TBC systems operating in real environment. A better comprehension of these major effects is then required; to this purpose, sintering kinetics and damaging promoted by CMAS infiltration are two key factors to be investigated in detail. The adhesion and the penetration of molten deposits can furtherly promote sintering and cracking effects, leading to TBC delamination and spallation. One more rare-earth elements are able to partially mitigate the penetration of CMAS deposits and their detrimental interaction with the surrounding TBC microstructure, by assisting the crystallization of stable apatite and fluorite phases forming a stable barrier layer, able to prevent or retard deep penetration of molten silicates, partially suppressing the sintering of the whole TBC and the propagation of the environmental attack until metallic surface.

In conclusion, based on the current investigations in the field, these seem to be the right directions for manufacturing of highly durable TBC systems for jet engines, combining high-temperature durability and enhanced resistance in harsh operating environments.

References

1. Clarke, D.R., Oechsner, M., Pature, N.: Thermal-barrier coatings for more efficient gas-turbine engines. *MRS Bull.* **37**(10), 891–898 (2012)
2. Lakiza, S.M., Grechanyuk, M.I., Ruban, O.K., et al.: Thermal barrier coatings: current status, search, and analysis. *Powder Metall. Met. Ceram.* **57**, 82–113 (2018)
3. Xu, L., Sun, Z., Ruan, Q., et al.: Development trend of cooling technology for the turbine blades at super-high temperature of above 2000 K. *Energies* **16**, 668 (2023)
4. Szczepankowski, A., Przysowa, R., Perczyński, J., et al.: Health and durability of protective and thermal barrier coatings monitored in service by visual inspection. *Coatings* **12**, 624 (2022)
5. Pature, N.P., Gell, M., Jordan, E.H.: Thermal barrier coatings for gas-turbine engine applications. *Science* **296**, 280–284 (2022)
6. Wee, S., Do, J., Kim, K., et al.: Review on mechanical thermal properties of superalloys and thermal barrier coating used in gas turbines. *Appl. Sci.* **10**(16), 5476 (2020)
7. Mehta, A., Vasudev, H., Singh, S., et al.: Processing and advancements in the development of thermal barrier coatings: a review. *Coatings* **12**, 1318 (2022)
8. Ghadami, F., Aghdam, A.S.R., Ghadami, S.: A comprehensive study on the microstructure evolution and oxidation resistance of conventional and nanocrystalline MCrAlY coatings. *Sci. Rep.* **11**, 875 (2021)
9. Meng, G.H., Liu, H., Liu, M.J.: Highly oxidation resistant MCrAlY bond coats prepared by heat treatment under low oxygen contents. *Surf. Coat. Technol.* **368**, 192–201 (2019)
10. Chen, Y., Zhao, X., Xiao, P.: Effect of microstructure on early oxidation of MCrAlY coatings. *Acta Mater.* **159**, 150–162 (2018)
11. Weng, W.X., Wang, Y.M., Liao, Y.M., et al.: Comparison of microstructural evolution and oxidation behavior of NiCoCrAlY and CoNiCrAlY as bond coats used for thermal barrier coatings. *Surf. Coat. Technol.* **352**, 285–294 (2018)
12. Li, H.F., Zhou, Z.H., Hesnawi, A., et al.: A comparative study of two-layer NiAl bond coat TBC and its failure mechanism. *Key Eng. Mater.* **336–338**, 1770–1772 (2007)
13. Fan, X., Zhu, L., Huang, W.: Investigation of NiAl intermetallic compounds as bond coats for thermal barrier coatings on Mg alloy. *J. Alloys Compd.* **729**(30), 617–626 (2017)
14. Zhao, C., Luo, L., Xiao, C., et al.: The oxidation performance of plasma-sprayed NiAl bond coat: effect of Hf addition in bond coat and substrate. *Surf. Coat. Technol.* **352**, 49–58 (2018)
15. Chen, Y., Zhao, X., Xiao, P.: Effect of surface curvature on oxidation of a MCrAlY coating. *Corrosion Sci.* **163**, 108256 (2020)
16. Heydari, P.: A review on functionally graded-thermal barrier coatings (FG-TBC) fabrication methods in gas turbines. *Am. J. Mech. Mater. Eng.* **6**(2), 18–26 (2022)
17. Latka, L., Pawlowski, L., Winnicki, M., et al.: Review of functionally graded thermal sprayed coatings. *Appl. Sci.* **10**, 5153 (2020)
18. Pakseresht, A.H., Rahimpour, M.R., Alizadeh, M., et al.: Concept of advanced thermal barrier functional coatings in high temperature engineering components. In: Zuzuarregui, A., Morant-Minana, M.C. (eds.) *Research Perspectives on Functional Micro- and Nanoscale Coatings*, pp. 396–419. IGI Global, Hershey PA (2016)
19. Hille, T.S., Njidad, T.J., Sujker, A.S.J., et al.: Damage growth triggered by interface irregularities in thermal barrier coatings. *Acta Mater.* **57**(9), 2624–2630 (2009)
20. Yang, G.J., Suo, X.K., Li, R.G.: Introduction to advanced micro-nanocoating materials and thermal spray. In: Yang, G.J., Suo, X.K. (eds.) *Micro and Nano Technologies, Advanced Nanomaterials and Coatings by Thermal Spray*, pp. 1–11. Elsevier (2019)
21. Pawlowski, L.: *The Science and Engineering of Thermal Spray Coatings*, 2nd edn. Wiley, New York (2009)
22. Uczak de Goes, W., Somhorst, J., Maroksan, M., et al.: Suspension plasma-sprayed thermal barrier coatings for light-duty diesel engines. **28**, 1674–1687 (2019)

23. Arhens, M., Lampenscherf, S., Vassen, R.: Deposition and characteristics of submicrometer-structured thermal barrier coatings by suspension plasma spraying. *J. Therm. Spray Technol.* **21**(3–4), 432–442 (2012)
24. Mahade, S., Curry, N., Bjorklund, S., et al.: Engineered thermal barrier coatings deposited by suspension plasma spray. *Mater. Lett.* **209**, 517–521 (2017)
25. Jordan, E.H., Jiang, C., Gell, M.: The solution precursor plasma spray (SPS) process: a review with energy considerations. *J. Therm. Spray Technol.* **24**, 1153–1165 (2015)
26. Fauchais, P., Joulia, A., Goutier, S., et al.: Suspension and solution plasma spraying. *J. Phys. D Appl. Phys.* **46**(22), 224015 (2013)
27. Zhao, Y., Wen, J., Peyraut, F., et al.: Porous architecture and thermal properties of thermal barrier coatings deposited by suspension plasma spray. *Surf. Coat. Technol.* **386**, 125462 (2020)
28. Curry, N., Van Every, K., Snyder, T., et al.: Thermal conductivity analysis and lifetime testing of suspension plasma-sprayed thermal barrier coatings. *Coatings* **4**, 630–650 (2014)
29. Schulz, U., Leyens, C., Fritscher, K., et al.: Some recent trends in research and technology of advanced thermal barrier coatings. *Aerosp. Sci. Technol.* **7**(1), 73–80 (2003)
30. Mauer, G., Vassen, R.: Coatings with columnar microstructures for thermal barrier applications. *Adv. Eng. Mater.* **22**, 1–9 (2020)
31. Shen, Z., Liu, Z., Mu, R., et al.: LaGdZrO/YSZ thermal barrier coatings by EB-PVD: microstructure, thermal properties and failure mechanism. *Chem. Eng. J. Adv.* **5**(15), 100073 (2021)
32. Hu, X., Liu, G., Liu, Q., et al.: Failure mechanisms of EB-PVD thermal barrier coatings under the synergistic effect of thermal shock and CMAS corrosion. *Coatings* **12**(9), 1290 (2022)
33. Cheng, Z., Yang, J., Shao, F., et al.: Thermal stability of PS-PVD YSZ coatings with typical dense layered and columnar structures. *Crystals* **10**(9), 826 (2020)
34. Zhang, C., Chen, F., Huang, Z., et al.: Additive manufacturing of functionally graded materials: a review. *Mater. Sci. Eng. A* **764**, 138209 (2019)
35. Yan, L., Chen, Y., Liou, F.: Additive manufacturing of functionally graded metallic materials using laser metal deposition. *Addit. Manuf.* **31**, 100901 (2020)
36. Rao, H., Oleksak, R.P., Favara, K., et al.: Behavior of yttria-stabilised zirconia (YSZ) during laser direct energy deposition of an Inconel 625-YSZ cermet. *Addit. Manuf.* **31**, 100932 (2020)
37. Bakan, E., Mack, D.E., Mauer, G., et al.: High temperature materials for power generation in gas turbines. In: Guillon, O. (ed) Elsevier Series on Advanced Ceramic Materials, *Advanced Ceramics for Energy Conversion and Storage*, pp. 3–62. Elsevier (2020)
38. Trice, R.W., Su, Y.J., Mawdsley, J.R., et al.: Effect of heat treatment on phase stability, microstructure, and thermal conductivity of plasma-sprayed YSZ. *J. Mater. Sci.* **37**(11), 2359–2365 (2002)
39. Di Girolamo, G., Blasi, C., Pagnotta, L., et al.: Phase evolution and thermophysical properties of plasma sprayed thick zirconia coatings after annealing. *Ceram. Int.* **36**(8), 2273–2280 (2010)
40. Evans, A.G., Clarke, D.R., Levi, C.G.: The influence of oxides on the performance of advanced gas turbines. *J. Eur. Ceram. Soc.* **28**, 1405–1419 (2008)
41. Vassen, R., Jarligo, M.O., Steinke, T., et al.: Overview on advanced thermal barrier coatings. *Surf. Coat. Technol.* **205**, 938–942 (2010)
42. Huang, Y., Hu, N., Zeng, Y., et al.: Effect of different types of pores on thermal conductivity of YSZ thermal barrier coatings. *Coatings* **9**, 138 (2019)
43. Clarke, D.R., Levi, C.G.: Material design for the next generation thermal barrier coatings. *Ann. Rev. Mater. Res.* **33**(1), 383–417 (2003)
44. Gandhi, A.S.: Materials aspects of thermal barrier coatings. In: Mahajan, Y.R., Johnson, R. (eds.) *Handbook of Advanced Ceramics and Composites*, pp. 1443–1463. Springer, Cham (2020)
45. Jadhav, A.D., Padture, N.P.: Mechanical properties of solution-precursor plasma sprayed thermal barrier coatings. *Surf. Coat. Technol.* **202**, 4976–4979 (2008)

46. Chen, X., Honda, H., Kuroda, S., et al.: Highly segmented thermal barrier coatings deposited by suspension plasma spray: effects of spray process on microstructure. *J. Therm. Spray Technol.* **25**, 1638–1649 (2016)
47. Guignard, A., Mauer, G., Vassen, R., et al.: Deposition and Characteristics of submicrometer structured thermal barrier coatings by suspension plasma spraying. *J. Therm. Spray Technol.* **21**(3–4), 416–424 (2012)
48. Jiang, K., Liu, S., Wang, X.: Low-thermal conductivity and high-toughness CeO₂-Gd₂O₃ co-stabilised zirconia ceramic for potential thermal barrier coating applications. *J. Eur. Ceram. Soc.* **38**, 3986–39993 (2018)
49. Tabatabaiean, M.R., Rahmanifard, R., Seyed Jalili, Y.: The study of phase stability and thermal shock resistance of Scandia-ceria stabilized zirconia as a new TBC material. *Surf. Coat. Technol.* **374**, 752–762 (2019)
50. Bobzin, K., Zhao, L., Ote, M., et al.: A highly porous thermal barrier coating based on Gd₂O₃-Yb₂O₃ co-doped YSZ. *Surf. Coat. Technol.* **366**, 349–354 (2019)
51. Khan, M., Zeng, Y., Lan, Z., et al.: Reduced thermal conductivity of solid solution of 20% CeO₂ + ZrO₂ and 8% Y₂O₃ + ZrO₂ prepared by atmospheric plasma spray technique. *Ceram. Int.* **45**, 839–842 (2019)
52. Di Girolamo, G., Blasi, C., Schioppa, M., et al.: Structure and thermal properties, of heat-treated plasma sprayed ceria-yttria co-stabilized zirconia coatings. *Ceram. Int.* **36**, 961–968 (2010)
53. Sodeoka, S., Suzuki, M., Ueno, K.: Thermal and mechanical properties of ZrO₂-CeO₂ plasma-sprayed coatings. *J. Therm. Spray Technol.* **6**, 361–367 (1997)
54. Alfano, M., Di Girolamo, G., Pagnotta, L., et al.: The influence of high temperature sintering on microstructure and mechanical properties of APS CeO₂-Y₂O₃-ZrO₂ coatings. *J. Mater. Sci.* **45**(10), 2662–2669 (2010)
55. Jin, L., Yu, Q., Ni, L., et al.: Microstructure and thermal properties of nanostructured 8 wt.% CeO₂ doped YSZ coatings prepared by atmospheric plasma spraying. *J. Therm. Spray Technol.* **21**(5), 928–934 (2012)
56. Latka, L., Cattini, A., Chicot, D., et al.: Mechanical properties of yttria-and ceria-stabilized zirconia coatings obtained by suspension plasma spraying. *J. Therm. Spray Technol.* **22**(2–3), 125–130 (2013)
57. Wu, S., Zhao, Y., Li, W., et al.: Research progresses on ceramic materials of thermal barrier coatings on gas turbine. *Coatings* **11**(1) 79, 1–18 (2021)
58. Curry, N., Markocsan, N., Ostergren, L.G., et al.: Evaluation of the Lifetime and thermal conductivity of dysprosia-stabilized thermal barrier coating systems. *J. Therm. Spray Technol.* **22**(6), 864–872 (2013)
59. Qu, L., Choy, K.L., Wheatley, R.: Enhanced doping effects of multielement on anisotropic thermal expansion in ZrO₂ with new compositions. *J. Am. Ceram. Soc.* **103**, 5881–5890 (2020)
60. Paul, S., Cipitria, A., Tsipas, S.A., et al.: Sintering characteristics of plasma-sprayed zirconia coatings containing different stabilisers. *Surf. Coat. Technol.* **203**(8), 1069–1074 (2009)
61. Shi, Q., Yuan, W., Chao, X., et al.: Phase stability, thermal conductivity and crystal growth behavior of RE₂O₃ (RE = La, Yb, Ce, Gd) co-doped Y₂O₃ stabilized ZrO₂ powder. *J. Sol-Gel Technol.* **84**, 341–348 (2017)
62. Guo, X., Lin, C., Zhang, J., et al.: Effect of La₂O₃ on microstructure and thermal conductivity of La₂O₃-doped YSZ coatings. *Materials* **12**(18), 2966 (2019)
63. Zhang, J., Guo, X., Jung, Y.G., et al.: Lanthanum zirconate based thermal barrier coatings: a review. *Surf. Coat. Technol.* **323**, 18–29 (2017)
64. Rauf, A., Yu, Q.H., Jin, L., et al.: Microstructure and thermal properties of nanostructured lanthana-doped yttria-stabilized zirconia thermal barrier coatings by air plasma spraying. *Scri. Mater.* **66**(2), 109–112 (2012)
65. Dai, H., Li, J., Cao, X., et al.: Thermal barrier coating material. US Patent US20097597971B2 (2009)

66. Dai, H., Zhong, X., Li, J., et al.: Neodymium-cerium oxide as new thermal barrier coating material. *Surf. Coat. Technol.* **201**(6), 2527–2533 (2006)
67. Fan, W., Bai, Y., Liu, Y.F., et al.: Corrosion behavior of $\text{Sc}_2\text{O}_3\text{-Y}_2\text{O}_3$ co-stabilized ZrO_2 thermal barrier coatings with CMAS attack. *Ceram. Int.* **45**, 15763–15767 (2019)
68. Fan, W., Wang, Z.Z., Bai, Y., et al.: Improved properties of Scandia and yttria co-doped zirconia as a potential thermal barrier material for high temperature applications. *J. Eur. Ceram. Soc.* **38**, 4502–4511 (2018)
69. Cao, X.Q., Vassen, R., Stover, D.: Ceramic materials for thermal barrier coatings. *J. Eur. Ceram. Soc.* **24**(1), 1–10 (2004)
70. Zhang, J., Guo, X., Jung, J.G., et al.: Lanthanum zirconate based thermal barrier coatings: a review. *Surf. Coat. Technol.* **323**, 18–29 (2017)
71. Vassen, R., Cao, X., Tietz, F., et al.: Zirconates as new materials for thermal barrier coatings. *J. Am. Ceram. Soc.* **83**(8), 2023–2028 (2000)
72. Di Girolamo, G., Marra, F., Blasi, C., et al.: High-temperature mechanical behavior of plasma sprayed lanthanum zirconate coatings. *Ceram. Int.* **40**, 11433–11436 (2014)
73. Wang, C., Wang, J., Wang, L., et al.: Nanocomposite lanthanum zirconate thermal barrier coating deposited by suspension plasma spray process. *J. Therm. Spray Technol.* **23**(7), 1030–1036 (2014)
74. Wu, J., Wei, X., Padture, N.P., et al.: Low-thermal conductivity rare-earth zirconates for potential thermal-barrier-coating applications. *J. Eur. Ceram. Soc.* **85**, 3031–3035 (2002)
75. Guo, X., Lu, Z., Park, H.Y., et al.: Thermal properties of $\text{La}_2\text{Zr}_2\text{O}_7$ double-layer thermal barrier coatings. *Adv. Appl. Ceram.* **118**(3), 91–97 (2019)
76. Doleker, K.M., Karaoglanli, A.: Comparison of oxidation behavior of YSZ and $\text{Gd}_2\text{Zr}_2\text{O}_7$ thermal barrier coatings (TBCs). *Surf. Coat. Technol.* **318**, 198–207 (2017)
77. Doleker, K.M., Karaoglanli, A., Ozgurluk, Y., et al.: Performance of single YSZ, $\text{Gd}_2\text{Zr}_2\text{O}_7$ and double-layered YSZ/ $\text{Gd}_2\text{Zr}_2\text{O}_7$ thermal barrier coatings in isothermal oxidation test conditions. *Vacuum* **177**, 109401 (2020)
78. Ejaz, N., Ali, L., Ahmad, A., et al.: Thermo-physical properties measurement of advanced TBC materials with pyrochlore and perovskite structures. *Key Eng. Mater.* **778**, 236–244 (2018)
79. Subramanian, R.: Thermal barrier coatings having high phase stability. US Patent 6387539 (2002)
80. Lehmann, H., Pitzer, D., Pracht, G., et al.: Thermal conductivity and thermal expansion coefficients of the lanthanum rare-earth-element zirconate system. *J. Am. Ceram. Soc.* **86**(8), 1338–1344 (2003)
81. Zhang, H., Sun, K., Xu, Q., et al.: Thermal conductivity of $(\text{Sm}_{1-x}\text{La}_x)\text{Zr}_2\text{O}_7$ ($x=0, 0.25, 0.5, 0.75$ and 1) oxides for advanced thermal barrier coatings. *J. Rare Earths* **27**, 222–226 (2009)
82. Wang, Y., Zhou, C.: Microstructure and thermal properties of nanostructured gadolinia doped yttria-stabilized zirconia thermal barrier coatings produced by air plasma spraying. *Ceram. Int.* **42**, 13047–13052 (2016)
83. Li, X., Ma, W., Wen, J., et al.: Preparation of SrZrO_3 thermal barrier coating by solution precursor plasma spray. *J. Therm. Spray Technol.* **26**, 371–377 (2017)
84. Ma, W., Li, X., Meng, X., et al.: Microstructure and thermophysical properties of SrZrO_3 thermal barrier coating prepared by solution precursor plasma spray. *J. Therm. Spray Technol.* **27**, 1056–1063 (2018)
85. Ma, W., Jarligo, M.O., Mack, D.E., et al.: New generation perovskite thermal barrier coating materials. *J. Therm. Spray Technol.* **17**, 831–837 (2008)
86. Gao, Y., Ma, W., Meng, X., et al.: Phase composition and thermal properties of Yb-Gd codoped SrZrO_3 coating prepared by the solution precursor plasma spray. *J. Therm. Spray Technol.* **30**, 1174–1182 (2021)
87. Zhang, J., Bai, Y., Li, E., et al.: $\text{Yb}_2\text{O}_3\text{-Gd}_2\text{O}_3$ codoped strontium zirconate composite ceramics for potential thermal barrier coating applications. *Int. J. Appl. Ceram. Technol.* **17**, 1608–1618 (2020)

88. Khan, M. Zeng, Y.: Achieving low thermal conductivity in $\text{Sr}(\text{Zr}_{0.9}\text{Yb}_{0.05}\text{Gd}_{0.05})\text{O}_{2.95}$: a suitable material for high temperature applications. *Ceram. Int.* **46**, 28778–28784 (2020)
89. Zhang, H., Yuan, J., Song, W., et al.: Composition, mechanical properties and thermal cycling performance of YSZ toughened $\text{La}_2\text{Ce}_2\text{O}_7$ composite thermal barrier coatings. *Ceram. Int.* **46**, 6641–6651 (2020)
90. Feng, B.B., Wang, Y., Jia, Q., et al.: Thermophysical properties of solution precursor plasma-sprayed $\text{La}_2\text{Ce}_2\text{O}_7$ thermal barrier coatings. *Rare Met.* **38**, 689–694 (2019)
91. Liu, X.Y., Yi, H., Che, J.W., et al.: Phase, compositional, structural, and chemical stability of $\text{La}_2\text{Ce}_2\text{O}_7$ after high temperature heat treatment. *Ceram. Int.* **45**, 5030–5035 (2019)
92. Ma, W., Dong, H., Guo, H., et al.: Thermal cycling behavior of $\text{La}_2\text{Ce}_2\text{O}_7/8\text{YSZ}$ double-ceramic-layer thermal barrier coatings prepared by atmospheric plasma spraying. *Surf. Coat. Technol.* **204**, 3336–3370 (2010)
93. Guo, H., Wang, Y., Wang, L., et al.: Thermal physical properties and thermal shock resistance of $\text{La}_2\text{Ce}_2\text{O}_7/\text{YSZ}$ thermal barrier coating. *J. Therm. Spray Technol.* **18**(4), 665–671 (2009)
94. Wu, P., Chong, X., Wu, F., et al.: Investigation of the thermophysical properties of $(\text{Y}_{1-x}\text{Yb}_x)\text{TaO}_4$ ceramics. *J. Eur. Ceram. Soc.* **40**, 3111–3121 (2020)
95. Wu, S., Zhao, Y., Li, W., et al.: Research progresses on ceramic materials of thermal barrier coatings on gas turbine. *Coatings* **11**(79), 1–18 (2021)
96. Zhang, Q., Lu, K., Wang, S.H., et al.: Synthesis and thermophysical performances of $(\text{Nd}_{1-x}\text{Yb}_x)_2\text{AlTaO}_7$ oxides for heat-insulation coating applications. *Ceram. Int.* **46**, 26754–26759 (2020)
97. Chen, X., Li, H., Zhang, H., et al.: Influence of Yb substitution for La on thermophysical property of $\text{La}_2\text{AlTaO}_7$ ceramics. *Ceram. Int.* **43**(10), 7537–7542 (2017)
98. Chen, X.G., Zhang, H.S., Tong, Y.P., et al.: Thermophysical properties of $\text{Ln}_3\text{Ce}_7\text{Ta}_2\text{O}_{23.5}$ ($\text{Ln} = \text{Nd}$ and La) composite oxides. *Ceram. Int.* **46**, 8903–8909 (2020)
99. Chen, X.G., Yang, S.S., Song, Y., et al.: Phase structures, thermophysical properties of $\text{Sm}_3\text{Ce}_7\text{Ta}_2\text{O}_{23.5}$ and $\text{Gd}_3\text{Ce}_7\text{Ta}_2\text{O}_{23.5}$ oxides for thermal barrier coating applications. *Ceram. Int.* **46**, 8238–8243 (2020)
100. Zhang, S., Feng, Y., Tong, Y.P., et al.: Thermal-physical performance of novel pyrochlore-type $\text{Ca}_3\text{Ln}_3\text{Ce}_7\text{Ta}_2\text{O}_{26.5}$ ($\text{Ln} = \text{Nd}$ and Dy) oxides. *Ceram. Int.* **46**, 11416–11420 (2020).
101. Yang, K., Chen, L., Wu, F., et al.: Thermophysical properties of $\text{Yb}(\text{Ta}_x\text{Nb}_{1-x})\text{O}_4$ ceramics with different crystal structures. *Ceram. Int.* **40**(8), 3111–3121 (2020)
102. Zheng, Q., Wu, F., Chen, L., et al.: Thermophysical and mechanical properties of YTaO_4 ceramic by niobium substitution tantalum. *Mater. Lett.* **268**, 127586 (2020)
103. Cao, X.Q., Vassen, R., Tietz, F., et al.: New double-ceramic-layer thermal barrier coatings based on zirconia-rare earth composite oxides. *J. Eur. Ceram. Soc.* **26**, 247–251 (2006)
104. Amer, M., Curry, N., Hayat, Q., et al.: Cracking behavior of $\text{Gd}_2\text{Zr}_2\text{O}_7/\text{YSZ}$ multi-layered thermal barrier coatings deposited by suspension plasma spray. *Coatings* **13**(1), 107 (2023)
105. Di Girolamo, G., Blasi, C., Brentari, A., et al.: Microstructural, mechanical and thermal characteristics of zirconia-based thermal barrier coatings deposited by plasma spraying. *Ceram. Int.* **41**(9), 11776–11785 (2015)
106. Liu, Z.G., Zhang, W.H., Ouyang, J.H., et al.: Novel thermal barrier coatings based on rare-earth zirconates/YSZ double-ceramic-layer system deposited by plasma spraying. *J. Alloys Compd.* **647**, 438–444 (2015)
107. Vassen, R., Traeger, F., Stoeber, D.: New thermal barrier coatings based on pyrochlore/YSZ double-layer systems. *Int. J. Appl. Ceram. Technol.* **1**, 351–361 (2004)
108. Zhang, H., Guo, L., Ma, Y., et al.: Thermal cycling behavior of $(\text{Gd}_{0.9}\text{Yb}_{0.1})_2\text{Zr}_2\text{O}_7/8\text{YSZ}$ gradient thermal barrier coatings deposited on Hf-doped NiAl bond coat by EB-PVD. *Surf. Coat. Technol.* **258**, 950–955 (2014)
109. Bakan, E., Mack, D.E., Mauer, G., et al.: Gadolinium zirconate/YSZ thermal barrier coatings: plasma spraying, microstructure and thermal cycling behavior. *J. Am. Ceram. Soc.* **97**, 4045–4051 (2014)
110. Frommherz, M., Scholz, A., Oechsner, M., et al.: Gadolinium zirconate/YSZ thermal barrier coatings: mixed-mode interfacial fracture toughness and sintering behavior. *Surf. Coat. Technol.* **286**, 119–128 (2016)

111. Zhong, X., Zhao, H., Zhou, X., et al.: Thermal shock behavior of toughened gadolinium zirconate/YSZ double-ceramic-layered thermal barrier coating. *J. Alloys Compd.* **593**, 50–55 (2014)
112. Mahade, S., Curry, N., Bjorklund, S., et al.: Functional performance of Gd₂Zr₂O₇/YSZ multi-layered thermal barrier coatings deposited by suspension plasma spray. *Surf. Coat. Technol.* **318**, 208–216 (2016)
113. Karaoglanli, A.C., Doleker, K.M., Ozgurluk, Y.: State of the art thermal barrier coating (TBC) materials and TBC failure mechanisms. In: Öchsner, A., Altenbach, H. (eds) *Properties and Characterization of Modern Materials . Advanced Structured Materials*, vol. 33. Springer, Singapore 441–452 (2017)
114. Mondal, K., Nunez, L., Downey, C.M., et al.: Thermal barrier coatings overview: design, manufacturing, and applications in high-temperature industries. *Ind. Eng. Chem. Res.* **60**, 6061–6077 (2021)
115. Pakseresht, A., Sharifianjazi, F., Esmailkhainian, A., et al.: Failure mechanisms and structure tailoring of YSZ and new candidates for thermal barrier coatings: A systematic review. *Mater. Des.* **222**, 111044 (2022)
116. Hutchinson, J.W., Evans, A.G.: On the delamination of thermal barrier coatings in a thermal gradient. *Surf. Coat. Technol.* **149**(2–3), 179–184 (2002)
117. Essa, S.K., Chen, K., Liu, R., et al.: Failure Mechanisms of APS-YSZ-CoNiCrAlY Thermal Barrier Coating Under Isothermal Oxidation and Solid Particle Erosion. *J. Therm. Spray Technol.* **30**(1–2), 424–441 (2021)
118. Takahashi, R.J., Assis, J.M.K., Piorino Neto, F., et al: Heat treatment for TGO growth on NiCrAlY for TBC application. *Mater. Res. Express* **6**, 126442 (2019)
119. Shi, J., Zhang, T., Sun, B., et al.: Isothermal oxidation and TGO growth behavior of NiCoCrAlY-YSZ thermal barrier coatings on a Ni-based superalloy. *J. Alloys Compd.* **844**, 156093 (2020)
120. Di Girolamo, G., Brentari, A., Blasi, C., et al.: High-temperature oxidation and oxide scale formation in plasma-sprayed CoNiCrAlYRe coatings. *Metall. Mater. Trans. A Phys. Metall. Mater. Sci.* **45**(12), 5362–5370 (2014)
121. Di Girolamo, G., Alfano, M., Pagnotta, L., et al.: On the early stage isothermal oxidation of APS CoNiCrAlY coatings. *J. Mater. Eng. Perf.* **21**(9), 1989–1997 (2012)
122. Dong, H., Yang, G.J., Li, C.X., et al.: Effect of TGO thickness on thermal cyclic lifetime and failure mode of plasma-sprayed TBCs. *J. Am. Ceram. Soc.* **97**, 1226–1232 (2014)
123. Liu, P., Jiang, P., Sun, Y., et al.: Numerical Analysis of stress evolution in thermal barrier coating system during two-stage growth of heterogeneous oxide. *Ceram. Int.* **47**, 14311–14319 (2021)
124. Jing, F., Yang, J., Tang, S., et al.: Quantitative characterization of the interfacial damage in EB-PVD thermal barrier coating. *Coat.* **12**(984), 1–18 (2022)
125. Saremi, M., Afrasiabi, A., Kobayashi, A.: Microstructural analysis of YSZ and YSZ/Al₂O₃ plasma sprayed thermal barrier coatings after high temperature oxidation. *Surf. Coat. Technol.* **202**, 3233–3238 (2008)
126. Yuan, B., Harvey, C.M., Thomson, R.C., et al.: A new spallation mechanism of thermal barrier coatings and a generalized mechanical model. *Compos. Struct.* **227**, 111314 (2019)
127. Yan, J., Wang, X., Chen, K., et al.: Sintering modeling of thermal barrier coatings at elevated temperatures: a review of recent advances. *Coatings* **11**(10), 1214 (2021)
128. Wang, L.S., Song, J.B., Dong, H., et al.: Sintering-induced failure mechanism of thermal barrier coatings and sintering-resistant design. *Coatings* **12**, 1083 (2022)
129. Lv, B., Fan, X., Li, D., et al.: Towards enhanced sintering resistance: air-plasma-sprayed thermal barrier coating system with porosity gradient. *J. Eur. Ceram. Soc.* **38**(4), 1946–1956 (2018)
130. Kim, K., Kim, W.: Effect of heat treatment on microstructure and thermal conductivity of thermal barrier coating. *Materials* **14**(24), 7801 (2021)
131. Di Girolamo, G., Marra, F., Schioppa, M., et al.: Evolution of microstructural and mechanical properties of lanthanum zirconate thermal barrier coatings at high temperature. *Surf. Coat. Technol.* **268**, 298–302 (2015)

132. Liu, T., Chen, X., Yang, G.J., et al.: Properties evolution of plasma-sprayed $\text{La}_2\text{Zr}_2\text{O}_7$ coating induced by pore structure evolution during thermal exposure. *Ceram. Int.* **42**, 15485–15492 (2016)
133. Huang, J., Chu, X., Yang, T., et al.: Achieving high anti-sintering performance of plasma-sprayed YSZ thermal barrier coatings through pores structure design. *Surf. Coat. Technol.* **435**, 128259 (2022)
134. Morelli, S., Bursich, S., Testa, V., et al.: CMAS corrosion and thermal cyclign fatigue resistance of alternative thermal barrier coating materials and architectures: a comparative evaluation. *Surf. Coat. Technol.* **439**, 128433 (2022)
135. Nieto, A., Agrawal, R., Bravo, L., et al.: Calcia-magnesia-alumina-silicate (CMAS) attack mechanisms and roadmap towards sandphobic thermal and environmental barrier coatings. *Int. Mater. Rev.* **66**, 451–492 (2021)
136. Drexler, J.M., Shinoda, K., Ortiz, A.L., et al.: Air-plasma-sprayed thermal barrier coatings that are resistant to high-temperature attack by glass deposits. *Acta Mater.* **58**, 6835–6844 (2010)
137. Levi, C.G., Hutchinson, J.W., Vidal-Setif, M.H., et al.: Environmental degradation of thermal barrier coatings by molten deposits. *MRS Bull.* **37**, 932–941 (2012)
138. Peng, H., Wang, L., Guo, L., et al.: Degradation of EB-PVD thermal barrier coatings caused by CMAS deposits. *Prog. Nat. Sci.: Mater. Int.* **22**, 461–467 (2012)
139. Zhao, H., Levi, C.G., Wadley, H.N.G.: Molten silicate interactions with thermal barrier coatings. *Surf. Coat. Technol.* **251**, 74–86 (2014)
140. Kramer, S., Yang, J., Levi, C.G., et al.: Thermochemical interaction of thermal barrier coatings with molten $\text{CaO-MgO-Al}_2\text{O}_3\text{-SiO}_2$ (CMAS) deposits. *J. Am. Ceram. Soc.* **89**, 3167–3175 (2006)
141. Wu, J., Guo, H.B., Gao, Y.Z., et al.: Microstructure and thermophysical properties of yttria stabilized zirconia coatings with CMAS deposits. *J. Eur. Ceram. Soc.* **31**(10), 1881–1888 (2011)
142. Boissonet, G., Chalk, C., Nicholls, J.R.: Thermal insulation of YSZ and Erbium-Doped Yttria-Stabilised Zirconia EB-PVD Thermal Barrier Coating Systems after CMAS Attack. *Mater.* **13**(19), 4382 (2020)
143. Kramer, S., Yang, J., Levi, C.G.: Infiltration-Inhibiting Reaction of Gadolinium Zirconate Thermal Barrier Coatings with CMAS Melts. *J. Am. Ceram. Soc.* **91**, 576–583 (2008)
144. Deng, W., Fergus, J.W.: Effect of CMAS composition on hot corrosion behavior of gadolinium zirconate thermal barrier coatings materials. *J. Electrochem. Soc.* **164**, C526–C531 (2017)
145. Zhou, X., Wang, J., Yuan, J., et al.: Calcium-magnesium-alumino-silicate induced degradation and failure of $\text{La}_2(\text{Zr}_{0.7}\text{Ce}_{0.3})_2\text{O}_7$ /YSZ double-ceramic-layer thermal barrier coatings prepared by electron-beam-physical vapor deposition. *J. Eur. Ceram. Soc.* **38**, 1897–1907 (2018)
146. Perrudin, F., Vidal-Setif, M.H., Rio, C., et al.: Influence of rare earth oxides on kinetics and reaction mechanisms in CMAS silicate melts. *J. Eur. Ceram. Soc.* **39**, 4223–4232 (2019)
147. Xia, J., Yang, L., Wu, R.T., et al.: On the resistance of rare-earth oxide-doped YSZ to high temperature volcanic ash attack. *Surf. Coat. Technol.* **307**, 534–541 (2016)
148. Kandasamy, P., Govindarajan, S., Gurusmay, S.: Volcanic ash infiltration resistance of new-generation thermal barrier coatings at 1150 °C. *Surf. Coat. Technol.* **401**, 126226 (2020)
149. Zhou, X., He, L., Cao, X., et al.: $\text{La}_2(\text{Zr}_{0.7}\text{Ce}_{0.3})_2\text{O}_7$ thermal barrier coatings prepared by electron beam-physical vapor deposition that are resistant to high temperature attack by molten silicate. *Corros. Sci.* **115**, 143–151 (2017)
150. Wu, Y., Song, W., Dingwell, D.B., et al.: Silicate ash-resistant novel thermal barrier coatings in gas turbines. *Corros. Sci.* **194**, 109929 (2022)
151. Ye, F., Yuan, Y., Yan, S., et al.: High-temperature corrosion mechanism of a promising scandium tantalate ceramic for next generation thermal barrier coating under molten calcium-magnesium-aluminosilicate (CMAS). *Mater. Chem. Phys.* **256**, 123679 (2020)
152. Chen, L., Hu, M., Guo, J., et al.: Mechanical and thermal properties of RETaO_4 (RE=Yb, Lu, Sc) ceramics with monoclinic-prime phase. *J. Mater. Sci. technol.* **52**, 20–28 (2020)

153. Zhao, H., Begley, M.R., Heuer, A., et al.: Reaction, transformation and delamination of samarium zirconate thermal barrier coatings. *Surf. Coat. Technol.* **205**, 4355–4365 (2011)
154. Cai, L., Ma, W., Ma, B., et al.: Air plasma-sprayed $\text{La}_2\text{Zr}_2\text{O}_7\text{-SrZrO}_3$ composite thermal barrier coating subjected to $\text{CaO-MgO-Al}_2\text{O}_3\text{-SiO}_2$ (CMAS). *J. Therm. Spray Technol.* **26**, 1076–1083 (2017)

Trends and Perspectives in Mitigating CMAS Infiltration in Thermal Barrier Coating



Maxime Gaudin, Lucille Despres, Alice Dolmaire, Emilie Béchade, Alan Kéromnès, Simon Goutier, Alain Denoirjean, Aurélien Joulia, Vincent Rat, and Armelle Vardelle

Abstract The aerospace industry is facing challenges in meeting environmental and energy demands, which require a reduction in fuel consumption, emissions and production costs while improving the efficiency of aero-engines. One way to achieve this is by developing a thermal barrier coating (TBC) on the hottest components of the turbine to increase its inlet temperature. Different methods are used to deposit TBC, including air plasma spray (APS) and electron beam physical vapor deposition (EB-PVD), with each having its advantages and disadvantages. Current process developments are constantly trying to find a good compromise between intrinsic material properties, production cost and feasibility. With this in mind, suspension plasma spraying (SPS) has emerged as a viable option that can replace some applications. However, in service, complex loadings and environmental contaminants such as calcium-magnesium-aluminosilicate (CMAS) damage the TBC and reduce its durability. After presenting the SPS process, its application to thermal barrier coatings and industrialization challenges of the process, the chapter discusses the effects of CMAS infiltration on TBC and the methodologies used to characterize the damage during engine operation. Then, it explores potential solutions to mitigate CMAS attack, including modifying the coating composition, introducing additional layers, using SPS coatings and developing “CMAS-superphobic” surfaces.

Keywords Aero engines · Thermal barrier coating · Suspension plasma spray · Yttria-partially stabilized zirconia · CMAS infiltration

M. Gaudin · L. Despres (✉) · E. Béchade · A. Kéromnès · S. Goutier · A. Denoirjean · V. Rat · A. Vardelle

University of Limoges, CNRS, IRCER, UMR 7315, 87000 Limoges, France

e-mail: lucille.despres@unilim.fr

M. Gaudin · A. Joulia

SAFRAN TECH, 78772 Magny Les Hameaux, France

A. Dolmaire

DMAS, ONERA, Université Paris Saclay, 91123 Palaiseau, France

© The Author(s), under exclusive license to Springer Nature Switzerland AG 2024

A. Pakseresht and K. K. Amirtharaj Mosas (eds.), *Ceramic Coatings*

for *High-Temperature Environments*, Engineering Materials,

https://doi.org/10.1007/978-3-031-40809-0_2

1 Introduction

Climate change, caused by the release of greenhouse gases from human activities such as burning fossil fuels, is having a significant impact on the planet and is increasingly becoming a major concern for society [1, 2]. As a result, there is growing pressure on industries to reduce their greenhouse gas emissions and transition to more sustainable practices. This pressure is coming from a variety of sources, including governments, investors, consumers and activists. Many industries, such as the power, transportation and manufacturing sectors, are facing increasing regulations and incentives to reduce their emissions, as well as growing demand for sustainable products and services [3]. Some companies are also taking voluntary actions to address their climate impacts, such as setting emissions reduction targets and investing in renewable energy [4].

Aviation is one of the fastest-growing sources of greenhouse gas emissions. In 2021, aviation accounted for over 2% of global energy-related CO₂ emission due to the burning of fossil fuels and this percentage is projected to grow in the future as air traffic increases. The International Air Transport Association (IATA) predicts that the number of air passengers will triple by 2050, to about 8.2 billion per year [5], considering the emergence of the tourism, the demographic and economic development, especially in Asian countries. The aeronautical designers anticipate a clear high demand for passenger and cargo aircrafts (see Fig. 1). Airbus foresees 39,500 new passenger and freighter aircraft deliveries over 2022–2041 [6], while Boeing plans forecasts demand for more than 41,000 new airplanes by 2041 [7].

Additionally, the high altitudes at which aircraft fly can result in the formation of contrails, which can also contribute to warming [8]. Therefore, there is a growing

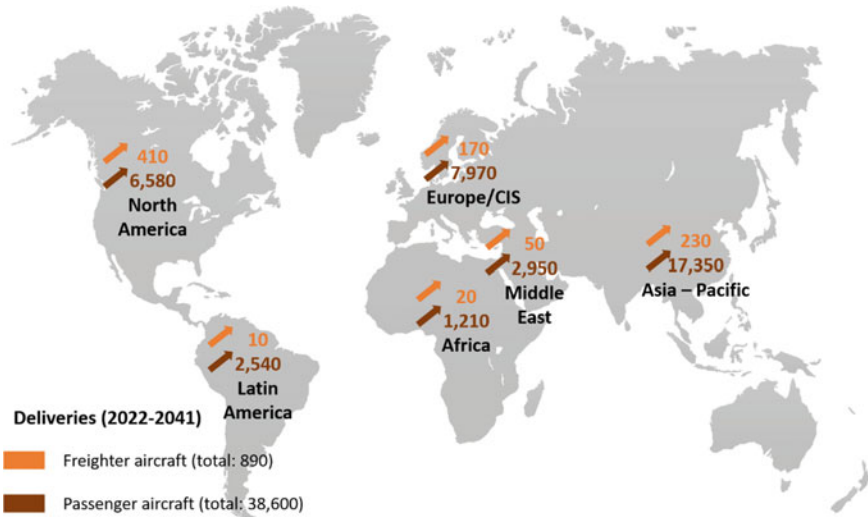


Fig. 1 Airbus freighter and passenger aircraft delivery forecasts for the period 2022–2041, data collected from [6]

interest in developing more sustainable aviation technologies and practices to reduce the environmental impact of the aerospace industry.

In 2008, leaders from across the industry came together at Air Transport Action Group (ATAG's) Aviation and Environment Summit to present a strategic vision for sustainable aviation, signing the Climate Change Action Commitment [9]. In October 2021, the global aviation industry took its climate commitment a step further by declaring that it will achieve net zero carbon emissions by 2050, supported by accelerated efficiency measures, energy transition and innovation across the aviation sector and in partnership with governments worldwide [10].

There are several ways to reduce emissions from current aircraft engines. One of them is to improve engine efficiency to generate more power while using less fuel. This is accomplished by increasing the inlet temperature of the turbines, allowing the fuel to burn at higher temperatures and pressures [11, 12]. The result is more thrust per unit of fuel consumed, resulting in a more fuel-efficient aircraft. An internal cooling network and the use of a thermal barrier coating can allow an aircraft engine's operating temperature to be increased by effectively dissipating heat from the hottest components [13–15]. A commonly used thermal barrier coating for high-pressure turbine blades is a multilayer system consisting of a bondcoat, a thermally grown oxide and a ceramic topcoat that are deposited on a single crystal nickel-based superalloy [15, 16]. The bondcoat bonds the other layers to the substrate and protects it from oxidation by forming a stable, slow-growing and adherent alumina layer. The topcoat provides insulation to protect the blade from the high temperatures encountered during operation. It is usually made of yttria-partially stabilized zirconia (ZrO_2 -6 at 8% wt. Y_2O_3). This material was chosen because of its high coefficient of expansion for a ceramic, its low thermal conductivity, its high toughness, its structural stability at high temperatures, its chemical stability against the oxidizing environment of fuel gases, its compatibility with the underlying alumina layer and its compatibility with a deposition process. Its intrinsic properties are largely controlled by its microstructure, which depends on the deposition process.

Currently, two deposition techniques are commonly used to deposit the ceramic topcoat [17]. In systems with low mechanical stress as engine's combustion chambers, it is deposited by atmospheric plasma spraying (APS). The coating has a lamellar microstructure that reduces its thermal conductivity. For more stressed systems, such as aeronautical turbine blades, the topcoat is deposited by evaporation (EB-PVD: Electron Beam Physical Vapor Deposition) and has a columnar structure, which is advantageous for mechanical properties (better strain tolerance and thermal shock resistance) but detrimental for thermal properties. In addition, EB-PVD has several other drawbacks: high cost, complexity of operation and maintenance, low deposition rate, high-energy consumption and limitation of deposition to small areas [16].

Today, coating processes based on the simpler principle of APS are being developed; they aim to replicate in some way the microstructure of EB-PVD coatings but with lower thermal conductivity [11, 17–20]. They include plasma spray physical vapor deposition (PS-PVD), solution precursor plasma spray (SPPS) and suspension plasma spray (SPS). It is expected that they will be used for both the combustion

chamber and the high-pressure turbine components. Suspension plasma spray process is now emerging at an industrial level and will be the focus of this chapter.

In service, high-pressure turbine blades are subjected to damage mechanisms that are classified into intrinsic and extrinsic mechanisms [21]. The latter are related to particle ingestion and severe environment and will be described in detail in Sect. 2 of this chapter.

The intrinsic mechanisms are induced by the differences in thermomechanical properties of the different layers of the system. Indeed, the operation of the engine at high temperature (1200 °C) leads to the dissociation of the metastable phase of the yttria-partially stabilized zirconia (noted “YSZ” in the chapter) into a cubic phase, richer in yttrium and a quadratic phase, poorer in yttria, which is likely to be transformed into a monoclinic phase (<200 °C) during the cooling of the engine [22]. These phase changes induce localized volumetric variations of the thermal barrier, creating residual stresses, which can lead to delamination of the TBC [23]. In addition, TBC is subject to thermal aging. Repeated flight cycles above 1200 °C lead to its sintering, i.e., densification of the thermal barrier, which induces additional residual stresses during engine cooling and reduces the thermal insulation capacity of the TBC. Finally, the thermomechanical fatigue at high temperature (>1100 °C) leads to an evolution of the interface between the underlayer and the ceramic. This evolution depends on the morphology and the nature of the bonding layer, but also on the thermal conditions surrounding the system (isothermal or not). This interface zone, called thermally grown oxide (TGO), is an alumina (α -Al₂O₃) oxide, which is necessary to limit the corrosion phenomena. However, the progressive oxidation of the bonding layer will increase the thickness of this layer during engine thermal cycles and induces high residual compressive stresses during cooling (3–6 GPa at room temperature [24]). The stress relaxation then deforms the surface of the TGO (“rumpling” or “ratcheting” phenomenon), causes localized separation zones at the TGO/ceramic interface and promotes the nucleation of cracks [21, 24]. These defects grow as the thermal cycles are repeated, until they cause spalling of the TBC.

The increase in temperature inside the engine leads to additional extrinsic damage mechanisms as dust, sand and volcanic ash, commonly referred to as calcium-magnesium-alumino-silicates (CMAS), which are ingested by aircraft engines, melt at a temperature close to 1240 °C [24] and infiltrate the topcoat. This infiltration leads to chemical reactions with the partially yttria-stabilized zirconia and induced mechanical stresses during engine cooling, which can be very detrimental to the lifespan of the thermal barrier coating system [21]. Therefore, new thermal barrier coating systems need to prove their thermomechanical performance and durability in a harsh environment where they can be subjected to the CMAS problem.

This chapter mainly addresses this issue and focuses on CMAS infiltration mitigation strategies using suspension plasma spray (SPS) coatings. It first describes the SPS process and its current challenges, keeping in mind an objective view of economic, industrial and technological realities. It then describes the thermomechanical degradation and chemical reaction between the TBC and molten CMAS. Next, it presents some methodologies used to evaluate the behavior of thermal barrier coating systems during engine operation and their resistance to CMAS attack. Finally, it presents the

current potential solutions against CMAS attack including the use of SPS coatings. The conclusion provides some perspectives on potential solutions.

2 Suspension Plasma Spray

2.1 Process Description

Thermal spraying belongs to the family of dry deposition techniques and refers to ballistic processes. It consists in accelerating and spraying solid particles on a prepared surface to form a coating resulting from the accumulation of flattened particles (splats). The deposition mechanism is based on the deformation of particles at impact and it can be achieved at low temperature only for metallic particles due to their plastic deformation [25]. However, in the case of micron-sized ceramic particles and owing to their brittle property, they have to be in molten or semi-molten state to form splats upon impact. A thermal plasma jet, generated by a non-transferred arc plasma torch, is usually used as a relevant heat and momentum source for high-melting point materials like ceramics [26].

A plasma forming gas mixture (e.g., Ar, H₂, N₂, or He) is injected into the torch body, while an electric arc is generated between the electrodes with a particular design including the inter-electrode space, the gas injection ring and eventual neutrode stack arrangement [27]. Plasma jet's core temperatures at the nozzle exit can reach up to 13,000 K [28, 29]. The velocities of the plasma jet are between 900 and 2000 m·s⁻¹ depending on plasma conditions, torch design and electrical power [30]. In atmospheric plasma spraying (APS), the powders, processed at atmospheric pressure, have diameters generally between approximately 5 and 50 μm. They enter the plasma core and move with a velocity on the order of 150–300 m·s⁻¹ [31–33], resulting in the formation of lamellar coatings with a porosity on the order of 5–20% [31].

At the beginning of the 2000s, the needs of new generation thermal barrier coatings used in harsher environment, prompted research into improving the thermal insulation and thermomechanical performance of TBCs. This has led to the development of thermal spray processes that take advantage of nanometer and submicron materials [34–36].

The submicron-sized particles must have enough momentum to penetrate the plasma jet. The technological choice was therefore to trap them in a liquid phase to efficiently inject them in the plasma core. This injection method has highlighted some major issues related to plasma interactions with the liquid phase and to the subsequent particles' treatment. The liquid phase is composed of submicron particles dispersed by means of chemical additives within an aqueous or alcoholic solvent forming a suspension. The key properties of the suspension, such as density, viscosity, surface tension, vaporization latent heat of the liquid depend on particle size distribution, solvent, and powder loading rate. The suspension properties associated with the

injection direction (axially or radially to the plasma jet) have a predominant influence on the deposit microstructure due to plasma/suspension interactions [37, 38].

Suspension plasma spraying (SPS) process has succeeded in attracting the interest of researchers and manufacturers due to the easy obtention of a relatively large range of microstructures. SPS has become a competitive deposition process of thermal barrier coatings not only in terms of improvement of coating properties but also in terms of cost-effectiveness [16], compared to the EB-PVD process. However, plasma-related process parameters must be considered and require specific optimization for each type of desired microstructure.

2.2 *Process Parameters Influencing the Coating Formation*

Empirical models obtained from the observations of the first layers of SPS coatings suggest that particle size, direction and impact velocity have a dominant influence on the resulting coating morphology [19, 39–45]. The surface preparation of substrates is also a significant parameter, especially the surface roughness (mainly Ra and Rsm) [40, 46, 47]. The size of impacting particles and their directions upon impact combined with the surface roughness leads to a “shadow effect”, particularly accentuated by the smallest particles [41]. Indeed, for low Stokes numbers (<1), particles tend to follow the streamlines of the plasma flow which means that their velocity component parallel to the substrate surface is increased. Larger particles, less subjected to plasma jet streamlines, form large splats onto the substrate surface, giving rise to more homogenous and larger columns and/or homogeneous lamellar structures. A critical impact velocity between 50 and 70 $\text{m}\cdot\text{s}^{-1}$ is required to ensure particle spreading of a YSZ suspension of median diameter 0.7 μm [48, 49]. Below this critical velocity, fine particles do not spread on the target surface, even when the target is preheated to high temperatures (approximately 500 °C). These particles with low Stokes numbers and low impact velocities form stacking defects (porosities, encapsulated particles, ...) in the coating microstructure, promoting columnar structures.

The formation of SPS coatings and their microstructures depends on the heat and momentum transfers from plasma species to particles that govern their trajectories in the plasma jet. Submicron and nanometric-sized particles will be more strongly subjected to the lesser hydrodynamic fluctuations of the plasma flow [50] and to all velocity and temperature gradients encountered during their flight [51–53].

Three main categories of first-order operating parameters are important to control: (1) suspension properties and injection method, (2) plasma torch parameters (torch design, arc current, electrical power, plasma forming gases, their mass flow rates), (3) bench conditions (spraying distance, scan velocity, substrate surface condition) [19, 39, 45, 53–57].

The torch parameters should be optimized according to the suspension properties to promote the suspension fragmentation and solvent evaporation into the plasma jet [37]. A high electrical power of the torch and a high total mass flow rate of the

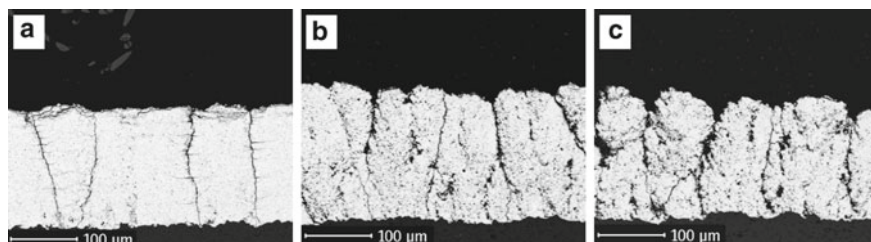


Fig. 2 Examples of microstructures obtained by suspension plasma spraying: A dense vertically cracked (DVC), B compact columnar and C columnar microstructures

plasma forming gases promote, respectively, the degree of solvent evaporation and particle melting on the one hand, and the efficiency of fragmentation and the low residence time of particles in the plasma on the other hand [54]. The average plasma specific enthalpy and the average plasma velocity are the derived physical properties from these torch parameters. They can be used as generalized measures to study the evolution of coating morphologies. For instance, a study showed the impact of these measures on the width and densification controls of columns in SPS coatings [53]. The hydrogen content of the plasma forming gases specifically increases the plasma enthalpy significantly and leads to better heat transfers. It turns out that a balance must be struck between fragmentation/evaporation efficiency that provide small particle size distributions and the need to generate particle streams with high Stokes number to achieve higher deposition rate efficiency and fewer stacking defects (fewer particles flowing around the target or not sticking to the surface).

The spraying distance and the scanning speed, respectively, modify the residence time of the particles and the stacking area of the splats on the target. In fact, these two easily controllable parameters have a significant effect on the direction and velocity gradients of the plasma jet as well as on the coating morphology [59–63].

A wide variety of coating morphologies is thus possible to achieve due to the sensitivity of the fine particles to each process parameter, resulting in coatings that are more or less dense, comprising of narrow to flared columns or forming a more homogeneous lamellar layer [55, 64, 65]. The versatility of the microstructures (see Fig. 2) that can be obtained by the SPS process is one of its main advantages, compared to the APS process.

2.3 Challenges of SPS Coatings: The Case of High-Turbine Blade TBCs

Due to the specific columnar microstructures provided by SPS, several comparative studies have shown that, in isothermal thermo-cyclic fatigue tests at 1100 °C, SPS TBCs have a longer lifetime than APS coatings (up to 450 cycles for SPS coatings

versus 300 for APS coatings for instance) [66, 67]. There are three major reasons for this difference:

- The internal porosity of the coating that relaxes thermomechanical stresses at the interface with the thermally grown oxide (TGO), one of the main places of damaging with this test (further details in Sect. 4).
- The roughness state of the bondcoat surface which affects the crack propagation energy in the coating [68].
- The oxidation rate of the bondcoat depending on its chemical nature which will then affect the state of stress at the TGO-coating interface.

In these comparative studies, measured porosity levels and the columnar microstructure generated by the SPS process allow to relax more efficiently the thermomechanical stresses at the interface with the TGO, which is a targeted feature for high-turbine blades TBCs.

The erosion resistance of SPS coatings can also be improved to APS and EB-PVD coatings [69, 70]. Crack propagation caused by projectile impacts is limited by the column width in the case of columnar SPS coatings compared to APS lamellar coatings, where cracks propagate more easily between the lamellae as hypothesized by Mahade et al. [69]. The depth of erosion within these lamellar coatings also gets higher with the same amount of erosive projectiles, meaning more coating material is delaminated compared to SPS coatings [69].

Another technical advantage of SPS columnar deposits is their low thermal conductivity. Indeed, it has been shown that SPS coating morphology (porosity, column widths and inter-column spaces) influences the type of thermal diffusivity mechanisms in yttria-stabilized zirconia coatings [55, 64, 71]. In the case of a coating with “compact” columns (very narrow inter-columnar spaces to none), there are no possible direct air conducts down to the metallic substrate and therefore no contribution of radiation in the thermal diffusivity [46, 71]. Heat diffusion in this coating is significantly reduced compared to coatings with more spread out columns (diffusivity of $3.0 \cdot 10^{-7} \text{ m}^2 \cdot \text{s}^{-1}$ versus $6.0 \cdot 10^{-7} \text{ m}^2 \cdot \text{s}^{-1}$ for the most “open” structure) and is close to the dense APS coatings (diffusivity of $3.5 \cdot 10^{-7} \text{ m}^2 \cdot \text{s}^{-1}$). Some of the columnar coatings tested in these studies also exhibit lower thermal conductivity than the EB-PVD coatings currently used on turbine blades [64]. These results can be explained by the presence of more tortuous air conducts or even the absence of such conducts in columnar coatings produced by SPS compared to the numerous straight air conducts between the columns of EB-PVD coatings. The tortuosity and width of these conducts can be controlled by changing only the scanning velocity of the torch in front of the substrate, according to Bernard et al. [19, 71]

The greater thermal insulation of SPS coatings compared to EB-PVD coatings may also be related to the multiscale nature of the porosity of SPS coatings (micro-, submicro- and nano-porosity). This multiscale porosity makes thermal conduction pathways more difficult within the coating material compared to EB-PVD coatings with dense columns. All of this data and assumptions are summarized in Fig. 3.

Lower thermal conductivity values were also found when comparing several SPS conditions leading to different YSZ coating morphologies compared to a dense,

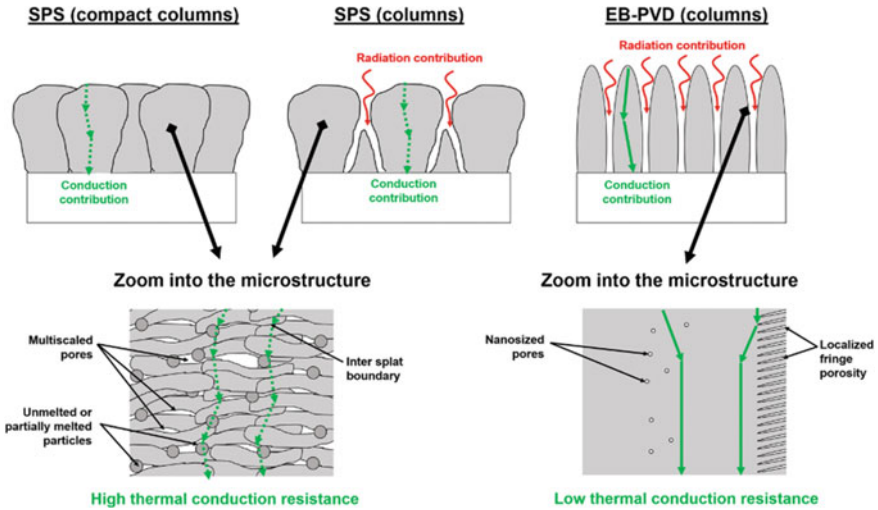


Fig. 3 Summary of thermal conduction paths in coatings for different deposition methods [46]

vertically cracked APS-sprayed YSZ coating (thermal conductivities between 0.8 and $1 \text{ W}\cdot\text{m}^{-1}\cdot\text{K}^{-1}$ at 25°C for SPS coatings versus $2 \text{ W}\cdot\text{m}^{-1}\cdot\text{K}^{-1}$ for APS coating) [67, 72]. All these studies show the advantage of the multiscale porosity obtained by the SPS process compared to coatings from currently used technologies presenting a less varied porosity.

Nevertheless, the industrialization of this process is still encountering some “lock” regarding the reproducibility of the coating morphology and thickness along complex surfaces such as high-turbine blades. The morphology of the coating can vary with the curves, hollows and hills of the blades (see Fig. 4) [40, 46, 49]. In-depth knowledge is currently necessary to better assess particles’ dynamics at impact upon these complex surfaces and to find ways to mitigate effectively these morphological differences.

The evolution of the thermal and chemical environment applied to TBCs must also be taken into account during the development of these coating processes. Indeed, as the operating temperatures of aeronautical turbines increase, thermal barrier coatings

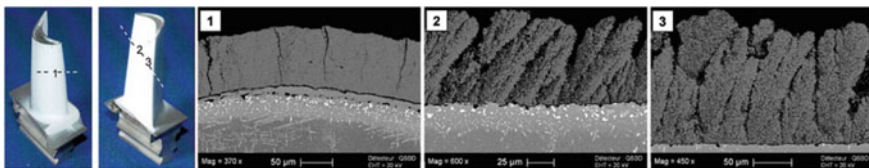


Fig. 4 Photograph of a coated high-pressure turbine blade covered after SPS (far left) and then micrographs of the obtained coating morphologies obtained as a function of the covered surface [46]

are facing more severe and increasingly corrosive environments. Three types of hot corrosion encountered can be listed:

- Corrosion initiated by sodium sulfates (Na_2SO_4) formed during fuel combustion and by sulfur in the fuel.
- The double thermochemical and thermomechanical attack of silicate particles, named CMAS (for CaO , MgO , Al_2O_3 , SiO_2 -rich particles), which are ingested by the engine during all phases of use. These particles are usually sand or volcanic ashes.
- Corrosion initiated by the combustion of so-called sustainable aviation fuels (SAF) developed by the aviation industry to reduce their fuel consumption [73–75].

The degradation mechanisms related to CMAS environment seem to be predominant for the new generations of TBCs and their complexity requires further explanations, given in the following sections, keeping in mind the development of SPS coatings.

3 Damage Mechanisms of CMAS Infiltration

The air ingested by aircraft engines contains various siliceous particles (CMAS), the nature and size of which depend on their geological origins and the regions of the world over which the aircraft fly (desert, volcano, urban environment, ocean...) [76]. These airborne particles are being studied by various laboratories around the world, not for their direct effect on TBCs, but on human health [77–79]. In the Earth's atmosphere, the concentration of small diameter particles ($\leq 2.5 \mu\text{m}$: $\text{PM}_{2.5}$) is naturally relatively low: between 5 and $35 \mu\text{g}\cdot\text{m}^{-3}$ [80, 81]. However, in highly urbanized or industrialized areas such as airports, this value can increase up to tenfold [81, 82]. Aviation safety authorities have set the maximum particulate matter threshold for air travel, at $2 \text{mg}\cdot\text{m}^{-3}$. Particle concentration reaches maximum values during volcanic eruptions or sandstorms. Therefore, desert regions and areas close to volcanoes are the places with the highest concentrations. In the deserts regions of Iran, e.g., the concentration of PM_{10} particles (diameter less than $10 \mu\text{m}$) reaches an average of $5479 \mu\text{g}\cdot\text{m}^{-3}$ on sandstorm days, [83, 84], whereas during routine days (without sandstorms), the daily PM_{10} concentration averages less than $200 \mu\text{g}\cdot\text{m}^{-3}$ in most desert regions [85–90]. In 2010, during the eruption of the Icelandic volcano Eyjafjallajökull, the PM_{10} concentration reached a maximum value of $13,000 \mu\text{g}\cdot\text{m}^{-3}$. As a result of this eruption, air travel had to be suspended (108,000 flights canceled [91]), resulting in an estimated loss of between US\$ 1.7 and US\$ 3.3 billion to the aviation industry [92–94].

Take-off, landing and cruise periods are all phases when particles are likely to enter aircraft engines. The airflow ingested by the engine guides these particles to the high-pressure turbine blades, where the thermal environment is severe ($>1600 \text{ }^\circ\text{C}$). However, only a portion of the particles in the secondary air stream is deposited on the blades and initiates a chemical and mechanical reaction on them. Several models

have shown that depending on the generalized values of the Stokes number, a particle tends to follow the airflow or to deposit on the surface of the blade [95–98]. This Stokes number depends on the morphology and chemical composition of the particle, as well as the characteristics of the air flow (namely velocity and dynamic viscosity) [99]. The higher the generalized Stokes number is, the greater is the probability of a particle impacting a turbine blade.

It has been shown that it is primarily particles between 4 and 10 μm in diameter that are deposited on the turbine blades [80, 97, 100, 101]. The next sections are going to focus solely on CMAS infiltration within TBCs and the damage mechanisms therein, letting aside other aspects of CMAS attack on TBCs such as erosion or clogging effects into the leading air ducts.

3.1 Chemical Mechanisms of CMAS Infiltration Attack

Silica (SiO_2) is the main component of CMAS particles, seconded by lime (CaO). Depending on the content of complementary oxides contained in these CMAS particles contain (MgO , Al_2O_3 , Fe_2O_3 , TiO_2 , etc.), the thermochemistry of the particle changes. In particular, the melting point of silica (1730 $^\circ\text{C}$) is strongly impacted by these chemical variations. In flight in such hot environments, CMAS particles present a significant risk of glass formation, whose reactivity with TBC is conditioned by various interdependent physico-chemical characteristics of CMAS, such as: particle size, basicity index, glass transition point T_g and rheological properties (viscosity, wettability).

Table 1 classifies the main oxides constituting CMAS according to their thermochemical characteristics [102–104] and their modes of action on the formation of a glassy network [105].

The addition of lattice modifying oxides, mainly composed of alkali or alkaline-earth oxides (such as CaO , MgO , ...), has the effect of depolymerizing the glass lattice by breaking the bridges of the forming oxide, Si-O-Si in the case of CMAS. The alkali or alkaline-earth cation is positioned in close proximity to one or two “non-bridging” oxygens created, to ensure electrical neutrality. The ionic field strengths ($\text{FS} \sim 0.13\text{--}0.44 \text{ \AA}^{-2}$) are weak because of the small size and charge of the cations. They become highly mobile in the CMAS glass, but also ultimately have a strong polarizing effect on the chemical bonds at the interface with the TBC.

The basicity index (BI) of CMAS (Eq. 1) is used to classify CMAS into three categories, according to their formulation [106–109]:

$$\text{BI}(\text{Basicity Index}) = \frac{\sum \text{Basic oxides}(\text{mol.}\%) }{\sum \text{Acidic oxides}(\text{mol.}\%) } \quad (1)$$

Intermediate oxides such as Al_2O_3 , TiO_2 or ZrO_2 participate in the BI equilibrium in two ways:

Table 1 Thermochemical characteristics of the various oxides involved in the composition of glassy networks

	Metal oxidation state	Coordination number CN	% ionicity (Stanworth's criterion)	Cationic radius (Å)	Melting point T_F (K)	Bond strength F_{M-O} (kcal.mol ⁻¹)	Cation field strength FS^1 (Å ⁻²)	Rawson's criterion $F_{M,O}/T_F$ (kcal.mol ⁻¹ .K ⁻¹)
Acidic oxides/ Lattice former	SiO ₂	4	51	0.4	1993	106	1.23	0.053
	P ₂ O ₅	4	39	0.38	843	88–117	1.58	0.104–0.131
Basic oxide/ Lattice modifier	CaO	8	79	1	2773	32	0.35	0.011
	MgO	6	73	0.72	2913	37	0.44	0.013
	Na ₂ O	6	82	1.02	1132	20	0.17	0.018
	K ₂ O	9	84	1.38	646	13	0.13	0.02
Amphoteric oxides / Intermediate oxides	Al ₂ O ₃	4	63	0.39	2072	101–79	0.94	0.038–0.049
	ZrO ₂	6		0.54		53–67	0.8	0.032–0.026
		7–8	67	0.8	2923	81	0.83	0.023

The cation field strength is defined as $FS = Z/((Rc + Ra)^2)$, where Z is the charge, Rc and Ra are the radius of cation and anion, respectively, with the appropriate coordination number (CN)

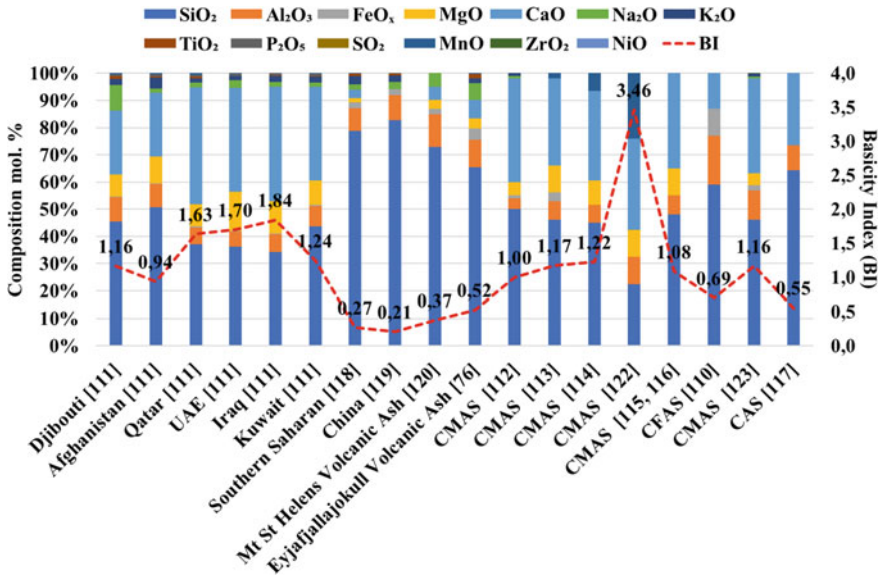


Fig. 5 Composition of different CMAS used in the laboratory and naturally occurring particles (PM₁₀) in different regions of the world—with basicity index for each composition, data collected from [76, 110–123]

- If they act as nucleating agents (for low BIs), they result in promoting the germination/growth of microcrystals within the glass (e.g., anorthite formation),
- If they act as a stabilizing agent of the glass network (high basicity index > 2.2), they are found in high concentrations in the melt (as amorphous phases) via the introduction of new eutectics [103].

The composition of CMAS particles is a variable data and strongly depends on the geographical factor. Figure 5 compares different compositions of natural and artificial CMAS.

The majority of CMAS studied in the literature have a basicity index below 2.2 [103, 124] (Fig. 5) and glass transition temperatures below 1300 °C. Upon slow cooling, they can therefore form relatively stable crystalline phases, in the polymorph range of CaSiO₃ pseudo-wollastine and anorthite (Ca,Mg)Al₂Si₂O₈ for CAS and diopside CaMgSi₂O₆ or merwinite Ca₃ Mg(SiO₄)₂ mixed with akermanite Ca₂MgSi₂O₇ in CMAS depending on the CaO/SiO ratio [112, 113, 125]. For high basicity index (BI > 2.2), the addition of lime, normally used in small amounts to increase the chemical resistance and decrease the solubility of the glass, conversely causes devitrification and an increase in the melting temperature of the mixture formed [126, 127]. The intermediate oxides act as network-forming agents to compensate for this effect. The precipitated and crystallized phases must then contain a significant amount of calcium in their structure. The CaO-Al₂O₃-SiO₂ ternary phase diagrams give a very complete description of these equilibria. The implementation

of these databases, for more complex systems, combined with thermal and XRD analyses, gives a complete description and characterization of the phase equilibria and liquidus layers (viscosity calculation) for multiple CMAS [128–130].

Chemical degradations caused by sands from different regions of the world or over different service times have thus resulted in a large number of studies that show a relatively similar degradation mechanism for the most widely used YSZ TBCs [113, 114, 131–134]. CMAS particles (less than 30 μm in diameter [135, 136]), which enter the hot section of the aircraft engine, undergo a rapid change of state and become molten, due to the very high temperatures in the combustion chamber (1400–1800 $^{\circ}\text{C}$) as well as in the turbine inlet (around 1600 $^{\circ}\text{C}$). This now viscous CMAS, totally or partially transformed in the combustor, sticks to the surface of the TBCs on which the temperature of the CMAS can quickly reach the glass transition point. There, the melt seeps into the inter-columnar spaces or into open porosities of the TBC. At the (liquid)_{CMAS}/(YSZ)_{TBC} interface, new amorphous or crystalline oxides precipitate by thermochemical exchanges [113, 117, 126, 128, 129, 131, 137].

The infiltration of molten particles is facilitated by their low viscosity and good wettability toward the zirconia lattice [114, 138]. Y^{3+} cations (FS $\sim 0.46 \text{ \AA}^{-2}$, close to the well-known modifier Mg^{2+}) diffuse progressively into the infiltrated glassy phase, and act on the non-bridging oxygens of the glassy lattice. Zr^{4+} cations also diffuse into the glass and act as nucleating agents similar to Al^{3+} due to their similar field strength (FS $\sim 0.62 \text{ \AA}^{-2}$). They form precipitates such as $\text{Ca}_2\text{Zr}(\text{Y})\text{Si}_4\text{O}_{12}$, for low- or mid-range BI (<2) [114, 117]. These diffusion mechanisms lead in parallel to the formation/re-precipitation of nanometric zirconia nodules at the (liquid)_{CMAS}/(YSZ)_{TBC} interface (see Fig. 6), weakly stabilized in yttria Y_2O_3 (t phase) [21, 117, 137, 139]. These globular particles or nodules are not stable, creating potentially mechanically brittle areas over the temperature changes, due to the polymorphic nature of zirconia over the operating temperature range of aircraft engines [23, 64, 113, 126, 140, 141]. For high BI (>2.2), the high concentration of lime results in favored precipitation of various cubic calcium zirconates (such as CaZrO_3) [103]. The proportion of acidic cations (Si^{4+} , Al^{3+}) is low, or non-existent, in these precipitated areas ensuring the cross-linking of the infiltrated glass. All these thermochemical damages lead to a very fast degradation and infiltration (<1 min at 1240 $^{\circ}\text{C}$ in EB-PVD coatings) of the TBC [114]. Only the nature of the re-precipitated phases varies depending on the role that the intermediate oxides take, i.e., depending on the basicity index of the melt [113, 115, 126, 142–144].

The degree of intensity of CMAS melt attack on the TBC also increases with the concentration ([CMAS]) and exposure time (Δt) of CMAS particles inside the aircraft engine [145, 146]. To characterize this intensity, the “particle dose” was introduced by Clarkson et al. as follows (Eq. 2):

$$\delta = [\text{CMAS}] \times \Delta t \quad (2)$$

Using this tool, they were able to generate a diagram predicting the damages ensured by a Rolls Royce aircraft engine as a function of exposure time and airborne concentration of different types of CMAS [147, 148] (Fig. 7).

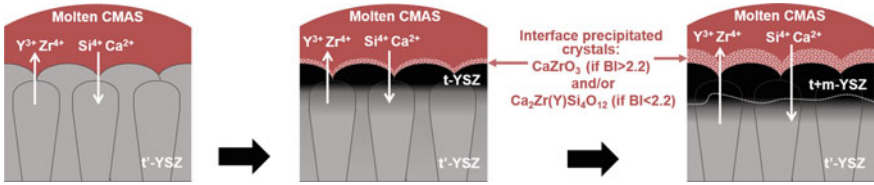


Fig. 6 Schematic of the dissolution–precipitation mechanism leading to the destabilization of YSZ upon contact with glass melt. Upon exposure to the CMAS molten, the tetragonal phase dissolves more rapidly. The chemical potential gradients between the layers lead to the formation of an intermediate phase enriched in Ca, Zr, Y, Si (such as CaZrO_3 or $\text{Ca}_2\text{Zr}(\text{Y})\text{Si}_4\text{O}_{12}$ phases). Below this zone, the Y-depleted zirconia phases precipitate epitaxially (black area) forming a shell on the remaining undissolved YSZ core (gray area). The shell transforms into a monoclinic phase upon cooling, and the ensuing stresses trigger transformation of the marginally stabilized core

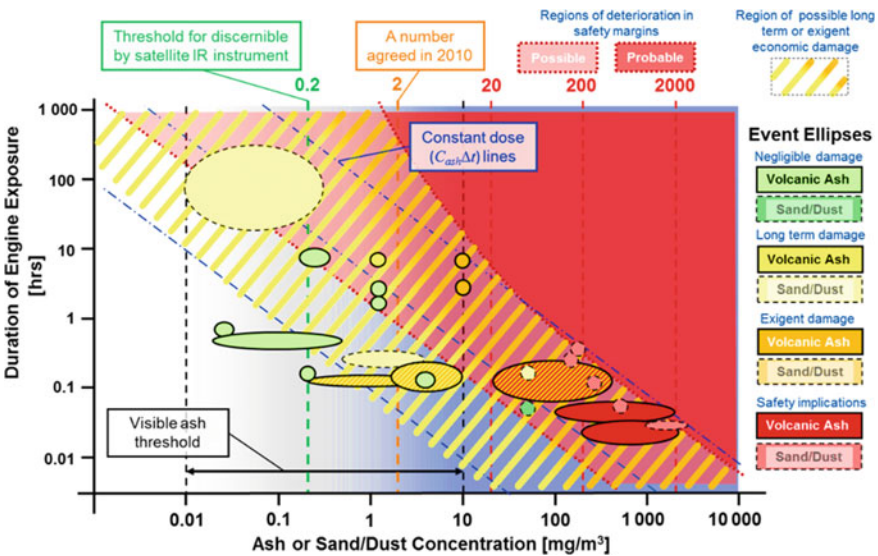


Fig. 7 Diagram illustrating the duration of exposure of an engine to a concentration of particles (sand or ash), indicating safe areas of use [147]

3.2 Mechanical Damages Induced by CMAS Infiltration Attack

Molten particle infiltration (CMAS) not only causes thermochemical degradations but also generates significant mechanical stresses in the topcoat, leading to its spalling. These stresses are dependent on the microstructure of the coating and evolve with the thickness of the coating, which is probably due to the thermal gradient experienced in service [133, 140].

In the case of a dense lamellar microstructure, it appears that CMAS particles infiltrate into pre-existing cracks and pores in the thermal barrier coating due to capillary forces that cause the separation of the inter- or intrasplat boundaries, resulting in expansion of the coating volume. This expansion induces compressive stresses due to the physical constraint of the substrate on the topcoat, which can lead to buckling to release the stress. This buckling process occurs at elevated temperatures. As the CMAS gradually solidifies during the cooling process, it sets the buckling shape, but the thermal expansion coefficient mismatches between the metallic part, the corroded topcoat and the non-penetrated topcoat can still cause an increase in bending [132, 149–151].

In the case of a columnar coating, it appears that during cooling, solidification of the infiltrated CMAS stiffens the topcoat (higher Young's modulus) and reduces its ability to resist accommodative deformation. Rapid cooling appears to initiate high in-plane tensile stresses in the topcoat, leading to the opening of vertical cracks from the top surface downward in the thermal barrier coating. In addition, stress accumulation, probably due to thermal expansion coefficient mismatch, promotes horizontal cracking in three main areas: just below the top surface of the topcoat, at the interface between the CMAS-penetrated and non-penetrated areas, and near the topcoat/bondcoat interfaces [152]. The various authors working on the subject seem to agree on the delamination mechanisms but not necessarily on the nature of the stresses induced during the cooling phases [140, 151, 152].

It is, therefore, necessary to provide additional answers on the mechanical stresses induced by the infiltration and solidification of these molten particles, especially as they seem to depend on the microstructure of the coating. It appears that these stresses are the main factor leading to the spalling of thermal barrier coatings. This type of degradation affects all types of TBC, regardless of the microstructure or the deposition process [113, 140, 141, 153].

In summary, the intensity and mechanisms of CMAS infiltration in TBCs vary depending on the following parameters:

- The amount of CMAS particles deposited on the TBC surface. It is proportional, at constant temperature, to the concentration of CMAS particles in the air and to time. It is directly related to the Stokes number of CMAS particles in the aircraft engine.
- Temperature at the surface of the TBC. It determines the melting state of the deposited CMAS particles. As a result, CMAS melts exhibit changing viscosity and surface tension, increasing or decreasing contact on the TBC and the degree of the chemical attack intensity.
- The quantity and size of open porosities, cracks, inter-columnar spaces... on the TBC surface. They influence the number of entry points for molten CMAS into the coating and the volume of interaction with the TBC [105, 154].
- The chemical composition of the molten CMAS. It influences the infiltration rate of molten CMAS into the TBC as well as the nature of the phases formed at this interface with respect to thermochemical reactivities and kinetics [103, 124, 155].

- Engine temperature cycles. They cause repeated thermal shocks and vitrification upon cooling of CMAS infiltrated into TBCs, leading to the accumulation of residual stresses and eventual delamination of the attacked TBC.

Since CMAS-induced degradation of thermal barrier coatings is a complex phenomenon, it is crucial to consider the multifactorial nature of these effects when testing the durability of TBCs. To do so, the characterization method employed must be both appropriate and rigorously controlled to provide the most accurate diagnosis possible.

4 Methodologies for Characterizing Damage to SPS Coatings, Including CMAS

It is essential to consider the environment surrounding the aircraft engine parts during the heating and cooling cycles as accurately as possible if the durability of TBC under CMAS attack is to be realistically characterized. In the case of high-pressure turbine blades, the surface of the TBC is naturally coated with molten CMAS particles less than 30 μm in diameter and is exposed to temperatures typically above 1200 $^{\circ}\text{C}$ in a corrosive atmosphere. The underlying metal turbine blade has multiple air-cooling channels leading to the TBC surface. These opening channels also allow the formation of an air film on the TBC surface that simultaneously reduces its surface temperature. At the end of the engine thermal cycle, a sharp temperature drop is observed within 3–4 min. Thus, in order to evaluate the thermal barrier resistance to the environment in which it evolves, the means of characterization must be able to simulate as well as possible these thermal, mechanical and chemical constraints.

Two main tests are currently used to characterize the durability of TBCs at high temperature: the isothermal cycling test and the thermal gradient cycling test. In both cases, the durability of TBCs is evaluated by the number of cycles performed before the spallation of the ceramic layer at atmospheric pressure. The major difference lies in the thermal loads which are more or less representative of the thermal history experienced by the parts in service. It is also important to note that on the most common test benches reported below, the degradation mechanisms induced by the corrosive atmosphere of the engine are not yet well considered or well recreated. This section will, therefore, not focus extensively on this aspect.

4.1 Isothermal Cycling Test

The most common test in industry and laboratories is the isothermal cycling test. This test is relatively simple to implement and requires little equipment (furnace). It consists of three main steps (see Fig. 8):

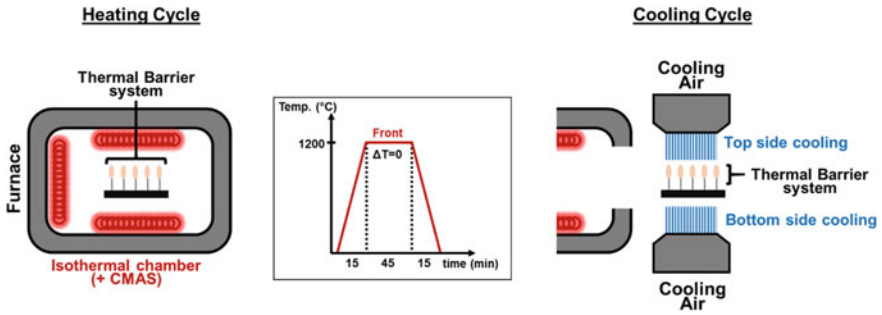


Fig. 8 Schematic diagram illustrating the principle of the isothermal cycling test

1. Introduction of the samples into the oven at the targeted temperature (usually 1200 °C), inducing a rapid temperature rise of the samples (<15 min).
2. Stabilization at high temperature for 45 min (thermal stabilization, depending on the test conditions).
3. Removal of the samples from the oven, resulting in rapid cooling under compressed air to temperature values below 100 °C (<15 min).

With appropriate instrumentation, this test can be automated. Cycles are repeated until 10–20% of the coating which is spalled [156]. Because the deposit and substrate are heated to the same temperature, the primary damage mechanisms without CMAS infiltration are controlled by growth of the TGO [115], and deformation of TGO/bondcoat interface by ratcheting [157] or rumpling [158], in order to release accumulated stresses [157, 159–166].

CMAS particle deposition is typically performed by hand using a powder or paste on the samples before they are introduced into the oven [64, 115]. However, the amount deposited, about $30 \pm 10 \text{ mg}\cdot\text{cm}^{-2}$, saturates the TBC system and is not representative of real-world CMAS etching, where deposition is done discontinuously over time.

In summary, this test is particularly accessible and easy to implement but is not sufficiently representative, in terms of thermal and mechanical stresses, to correctly predict the behavior of TBC systems in service. This is why engine manufacturers, in collaboration with laboratories, have developed thermal gradient cycling tests with different CMAS deposition processes.

4.2 Thermal Gradient Cycling Test

The considerable difference between the temperature at the outlet of the combustion chamber and the temperature used for internal cooling of the high-pressure turbine blades results in a significant thermal gradient in the TBC system. A.G. Evans and J.W. Hutchinson were the first, using a mechanical approach, to demonstrate the influence of this thermal gradient on the damage mechanisms of the TBC, with and

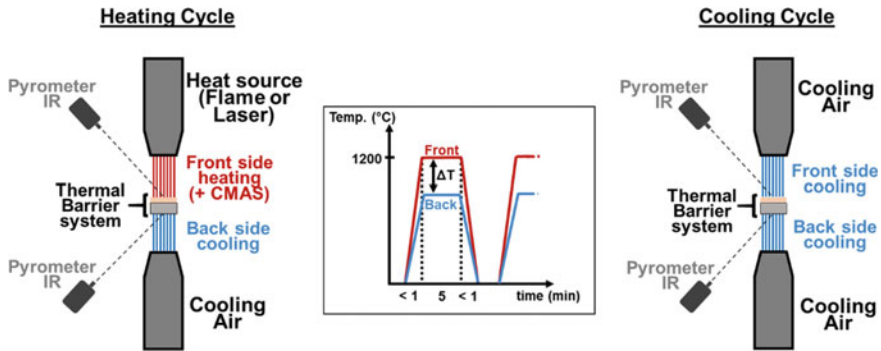


Fig. 9 Schematic diagram illustrating the principle of the thermal gradient cycling test

without CMAS [134, 157]. Based on flight return parts, they were able to show, by modeling with realistic turbojet conditions, that the engine cooling phase is the most detrimental for the life of the coatings. There is also a clear correlation between the cooling kinetics and the delamination depth related to different damage mechanisms. The need to generate a thermal gradient in the TBC system to simulate realistic damage mechanisms under service conditions is the main conclusion of this study [167].

There is not a single standard thermal gradient test bench. However, the common goal seems to be the generation of a thermal gradient in the topcoat that tends to $1\text{ }^{\circ}\text{C}\cdot\mu\text{m}^{-1}$. The main idea is to use, at the same time, a heat source and a cooling system, respectively, in front of the topcoat and at the back of the substrate (see Fig. 9).

These test benches can be commonly classified (except in rare cases) into two groups according to the heat source used: laser or flame. On the one hand, the use of a CO_2 laser heat source [168–174] allows homogeneous heating on the top surface of the TBC by surface scanning [110, 175]. To ensure a thermal gradient inside the TBC, the back side of the sample is usually cooled with compressed air. This low-noise technology is particularly suitable for acoustic damage characterization [176–178]. On the other hand, the flame derived from an oxygen/fuel mixture (commonly gas [179] or kerosene [180]) is the most commonly used heat source, often coupled with compressed air cooling on the backside of the sample [181–183]. One of the most interesting advantages of these test benches is the ability to inject a controlled amount of liquid or solid CMAS directly into the heat source, creating a corrosive environment similar to service conditions and simulating more realistic damage mechanisms.

In both cases, the surface temperature of the coating is determined by means of pyrometric measurements or of infrared thermal cameras. In addition, a thermocouple is usually placed in the sample substrate. Knowing the thicknesses and conductivities of the different materials, it is thus possible to determine an interface temperature and deduce the thermal gradient induced across the TBC. While thermal gradient

tests are more representative of flight conditions [184] and thus degradation mechanisms [185], they are also more complex to implement and require greater accuracy in temperature measurements. Infrared temperature measurements are particularly sensitive to the emissivity of the TBC material (typically YSZ). The maximum radiative emission area (>90%) for YSZ has been determined to be between 8 and 12.5 μm [186]. These wavelength ranges favor the use of pyrometric devices to have the most accurate temperature measurements possible. In addition, a variation of 55 $^{\circ}\text{C}$ on the surface of the TBC can reduce the lifetime of the TBC by approximately 60% [187]. Therefore, an error in thermal measurement or a small thermal variation can have a relatively large impact on TBC damage [188]. Because the reaction kinetics between TBC and CMAS are strongly influenced by temperature, the surface temperature measurement should be as accurate as possible.

Table 2 gives an example of several test rigs developed by laboratories to study the behavior of TBC systems [179, 189], with or without CMAS infiltration. As observed, the heat sources, the cooling means, temperature ranges achieved, the type of loading considered and the possibility of implementing CMAS infiltration differ significantly from one rig to another [183].

In summary, thermal gradient tests require sophisticated facilities and accurate temperature measurements (± 20 $^{\circ}\text{C}$) of the surface but they can be more representative of flight conditions for TBC systems. The CMAS solicitations implemented during the cycles may vary according to the test rig (CMAS paste deposition, liquid or solid CMAS injection, etc....) but the dose of CMAS tested is often higher than in real service conditions [147]. The corrosive environment of the aircraft engine can also be more or less re-simulated depending on the nature of the heat source (see Table 2).

Finally, a thermal barrier coating must also allow the highest thermal gradient within it to effectively protect the underlying metal parts from the surrounding high temperatures (above 1200 $^{\circ}\text{C}$). Table 3 compares the temperature differences between the TBC surface and the TBC/substrate interface (ΔT), and the thermal gradient (grad T) within different types of thermal barrier coatings (APS, EB-PVD, SPS, SPPS and PS-PVD) obtained in the thermal gradient test. The thermal gradients obtained with the SPS coatings appear comparable to those obtained with the APS coatings. Nevertheless, the three values of thermal gradients given, in Table 3, for SPS are relatively different (between 0.61 and 0.98 $^{\circ}\text{C}\cdot\mu\text{m}^{-1}$) contrary to the thermal gradient obtained by APS. This can be explained by the differences in microstructure (column density and porosity) on the studied TBCs [58] that can be obtained in SPS.

However, it is interesting to note that the solution precursor plasma spray (SPPS) deposit referenced here has a gradient comparable to that of the APS deposits. The SPS process offers comparable or superior thermal properties to the other processes.

Ultimately, the choice of the type of durability tests depends only on what one primarily wants to study. For example, for characterizing chemical damage on the surface TBC with CMAS, the isothermal cycling test may be sufficient and is simpler to implement. It should be kept in mind that this test is only partially representative of in-service chemical degradation because the dose of CMAS deposited at one time is

Table 2 Non-exhaustive inventory list of gradient rig tests currently present in laboratories around the world

Laboratory/ institution	Country	Heat source	Heat source details	Sample temperature range	Sample shape	Cooling system	CMAS solicitation	Details of CMAS solicitation	Main solicitation
NASA [190]	USA	Flame	Natural gas/O ₂	Up to 1650 °C	Multi-shapes (bar and flat)	Ambient air (backside)	Not reported	–	High thermal flow + water vapor created by combustion
Stony Brook University [191]	USA	Flame	C ₃ H ₈ /O ₂	Use 1250 °C	Flat disk	Oil pump vacuum system (backside)	Yes	CMAS solid —ash, radial injection through the flame with powder feed system	CMAS + Thermal solicitation
Forschungszentrum Jülich GmbH [181, 192]	Germany	Flame	CH ₄ /O ₂	1150 °C to 1550 °C	Flat disk	Compressed air (backside)	Yes	CMAS liquid —liquid solution (0.1 wt.%) axial injection within the flame	CMAS + Thermal solicitation
Pprime [193, 194]	France	Flame	CH ₄ /O ₂	300 to 1600 °C	Multi-shapes (tubular, flat and blade)	Compressed air (backside/ internal)	Not reported	–	Mechanical (tensile/ compressive) solicitation + High thermal flow

(continued)

Table 2 (continued)

Laboratory/ institution	Country	Heat source	Heat source details	Sample temperature range	Sample shape	Cooling system	CMAS solicitation	Details of CMAS solicitation	Main solicitation
Marine new materials and related technology [123]	China	Flame	C ₃ H ₈ /O ₂	Use 1300 °C	Flat disk	Compressed air (backside)	Yes	CMAS Paste —CMAS paste (2 wt.%—mixture of CMAS powder + ethanol) brushed every 2 cycles	CMAS + Thermal solicitation
Shanghai Institute of Ceramics [195]	China	Flame	C ₃ H ₈ /O ₂	Use 1350 ± 20 °C	Flat disk	Compressed air (backside)	Yes	CMAS suspension —CMAS suspension at 25 wt.% deposited by atomization at 7 mg·cm ⁻² before each test	CMAS + Thermal solicitation
India institute of technology [196]	India	Flame	Liquefied petroleum gas/O ₂	Use 1400 °C	Flat disk	Compressed air (backside)	Not reported	–	Thermal solicitation
University of California [110]	USA	Laser	2 kW CO ₂	Use 1300 °C	Flat disk	Compressed air (backside)	Yes	CMAS Paste —Powder + ethanol suspended mixture (CM(F)/AS) (5 mg·cm ⁻²)	CMAS + Thermal solicitation

(continued)

Table 2 (continued)

Laboratory/ institution	Country	Heat source details	Sample temperature range	Sample shape	Cooling system	CMAS solicitation	Details of CMAS solicitation	Main solicitation
National Research Council of Canada [170]	Canada	3 kW CO ₂ laser	Up to 1530 °C	Flat disk	Compressed air (backside)	No	–	High thermal flow
Institute of Materials Research [197]	Germany	Kerosene Micro engine	Up to 1600 °C	Blade (simple form)	Conduction between blade to shaft which is internally cooled by air	Yes	CMAS solid —Volcanic ash particle disperser (2 mg·m ⁻³ - 4 mg·m ⁻³)	CMAS + Erosion solicitation + Rotation

Table 3 Comparison of the thermal gradient obtained by gradient testing with different spraying process

Top coat (process, μm)	ΔT (Top coat) ($^{\circ}\text{C}$)	grad T (Top coat) ($^{\circ}\text{C}\cdot\mu\text{m}^{-1}$)	Refs
7YSZ (APS, 600 μm)	466	0.78	[198]
YSZ (APS, 283 μm)	226	0.80	[199]
YSZ (APS, 272 μm)	286	1.05	[199]
YSZ (SPS, 245 μm)	241	0.98	[58]
YSZ (SPS, 257 μm)	227	0.88	[58]
YSZ (SPS, 317 μm)	194	0.61	[58]
YSZ + Al + Ti (SPPS, 200 μm)	177	0.88	[200]
YSZ porous (PS-PVD, 300 μm)	208	0.69	[201]
YSZ dense (PS-PVD, 330 μm)	200	0.61	[201]
7YSZ (EB-PVD, 350 μm)	247	0.71	[110]

often too high, but it provides a good understanding of the underlying chemical mechanisms by placing the test conditions in the most severe scenario. For more realistic stresses of in-service engine operating conditions with CMAS attacks, the thermal gradient test is preferable because the thermomechanical stresses are better simulated on such benches. With this test, residual stresses and a slower TGO growth are obtained, which brings the characterizations to a more realistic state of the operating conditions.

Nevertheless, there are few comparisons between isothermal and thermal gradient tests on the durability of TBCs under CMAS attack, especially for SPS coatings. The lifetime of SPS coatings in thermal gradient tests with CMAS stresses appears to be lower than the results obtained in isothermal tests [202]. The multiple degradation mechanisms (mainly CMAS) are not yet sufficiently well characterized to allow predictive optimizations of SPS coatings yet.

5 Current Potential Solutions Against the CMAS Attack

Currently, two development axes are studied by academic and industrial actors. They focus, respectively, on strategies related to materials or coatings, with possibility of interlocking. Both strategies have the same objectives: to radically improve the thermochemical and thermomechanical properties of TBCs in order to increase their resistance to the more difficult engine environments, including CMAS.

5.1 Material Strategies

As previously mentioned, starting around 2000, many topcoat materials were investigated to overcome the limitations of yttria-stabilized zirconia in new generations of TBCs [140, 203, 204]. The mapping shown Fig. 10 illustrates, in a non-exhaustive manner, the families of materials studied so far, to help identify potential materials with thermophysical properties equivalent to YSZ [205–207].

The co-doped zirconia $\text{RE}_2\text{O}_3\text{-ZrO}_2$ or $\text{Y}_2\text{O}_3(\text{RE}_1)_2\text{O}_3\text{-(RE}_2)_2\text{O}_3\text{-...-ZrO}_2$ with a fluorite/fluorine structure (“RE” stands for rare earth other than yttrium) as well as the pyrochlore family $\text{RE}_2\text{Zr}_2\text{O}_7$ has been identified as the materials offering the best compromise in thermal conductivity and coefficient of thermal expansion (CTE) [212, 213]. The thermal conductivity values are significantly lower than those of yttria-stabilized zirconia, with similar CTE. These materials may also exhibit sufficient resistance to high-temperature cyclic oxidation as well as good erosion resistance (for co-doped zirconia with several rare earths) to TBCs containing YSZ [212, 214, 215].

Coatings specifically containing $\text{RE}_2\text{Zr}_2\text{O}_7$ pyrochlores have been extensively studied in the literature, which means that there is a large data available on these coatings subjected to infiltration tests with different CMAS. This family of materials will be the subject of the following paragraphs.

The dissolution/precipitation mechanisms observed with $\text{RE}_2\text{Zr}_2\text{O}_7$ are close to those of YSZ in CMAS, i.e., RE^{3+} cations (RE: La \rightarrow Yb) have a marked basic

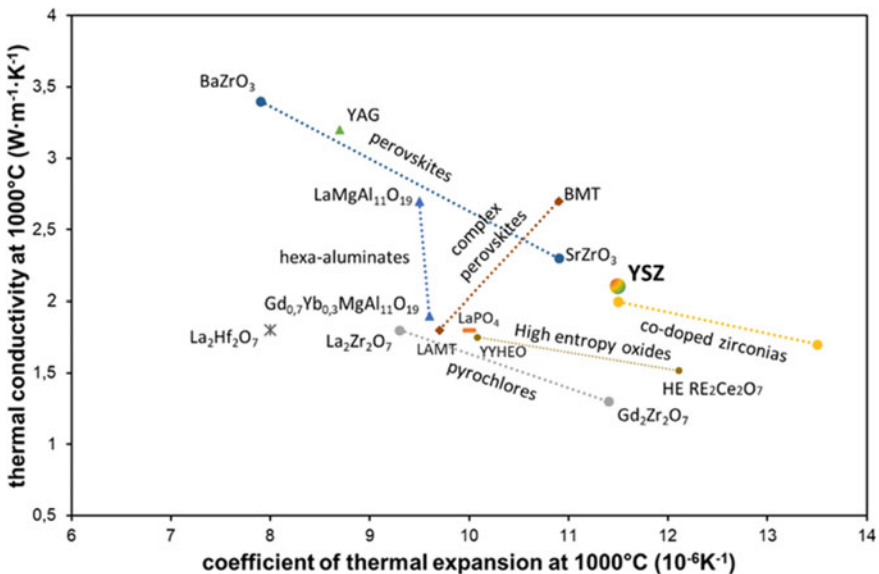


Fig. 10 Thermal conductivity of materials in each identified family as a function of their coefficient of thermal expansion, graph adapted and values taken from [205–211]

role and act preferentially as lattice modifying oxides. The larger their radius, the more basic the cations are, the more soluble they are in acidic media, such as fused silicates. They facilitate depolymerization of this medium and initiate the formation of crystalline silicate phases, which equilibrate and stabilize in temperature, such as the cyclosilicates $\text{Ca}_3\text{RE}_2(\text{Si}_3\text{O}_9)_2$, orthosilicate apatite phases $\text{Ca}_2\text{RE}_8(\text{SiO}_4)_6\text{O}_2$ or the disilicate pyrochlores $\text{RE}_2\text{Si}_2\text{O}_7$ [125, 216–222]. Significant distortions can appear in the crystal structure of these new compounds. They are strongly correlated with the ionic radius of the rare earth, which has an impact its coordination number in the crystal structure.

The smallest cations, such as Yb^{3+} and Dy^{3+} , behave similarly to Y^{3+} , and stabilize a mixture of the three silicate phases mentioned above, with preferential formation and stability of cyclosilicates. Perrudin et al. [130] showed that these cyclosilicates have a lower solubility in silicate glasses than other types of silicate by-products, meaning that less RE^{3+} is dissolved in the melt to form this phase (RE:Si ratio = 0.33). This results in less recession of the coating containing these rare earths when exposed to CMAS, due to the lower solubility of the cations, as has been observed in other studies [129, 216, 223]. Compounds rich in Gd^{3+} , Sm^{3+} and Nd^{3+} form the apatite phase predominantly (RE:Si ratio = 1.33), with coating recession increasing with the size of the rare earth ionic radius, due to the higher solubility of these cations in CMAS [129, 223]. Perrudin et al. [130] also noted a discontinuity in the relationship between cation field strength and solubility/basicity behavior for the smaller cations Yb^{3+} and Dy^{3+} , for short periods of exposure with CMAS (<4 h at 1200 °C), compared to compounds with the larger cations.

This could be due to the concomitant formation and stability during this time period of the RE:Si equilibrium phase $\text{Yb}_2\text{Si}_2\text{O}_7$ in the latter case. Therefore, the “anti-CMAS” chemical potential of RE-doped zirconia is highly dependent on the stability of the crystallized silicate phases and the solubility of the RE^{3+} cations in the glass.

In addition, all studies on the interaction between RE-zirconia and CMAS lead to the conclusion that the rate of sealing of coatings’ porosities must be a main factor for the development of an effective “anti-CMAS” coating. The introduction of Gd species into the CMAS-TBC environment, especially through $\text{Gd}_2\text{Zr}_2\text{O}_7$ (“GZ”) coatings, presents the best compromise among RE-zirconias for the reactivity with CMAS (cation field strength and solubility/basicity) and for the sealing mechanism in this respect. In this case, an interface layer between the TBC and CMAS is formed within one min of CMAS infiltration into the coating, between 1150 and 1200 °C [131, 224]. This layer effectively seals the porosities with a surface opening of less than 1 μm [225] and typically consists of a “dense” layer composed of weakly Gd-doped zirconia nodules and needle-like Gd-apatite crystals [140, 226]. Dolmaire et al. [227] also observed the presence of a thin layer of Gd-disilicate species at this interface, the formation and stability of which is concomitant in temperature with the formation and stability of Gd-apatites and depends on the Si:Ca ratio of the starting mixtures of oxides derived from CMAS. This concomitant precipitation of Gd-disilicates and Gd-apatites could be due to the intermediate basic character of Gd^{3+} in CMAS melts. Dolmaire et al. established a diffusion model similar to that

one proposed in Fig. 6 of this chapter, in which the presence of a thin layer of Gd-disilicate at the (liquid)_{CMAS}/(Gd-apatite)_{crystals} interface appears to slow down the interdiffusion of ionic species at the interface and may explain why Gd-based coatings exhibit such a good compromise. This specificity of GZ reactivity leads to both a lower level of coating surface recession, compared to RE-zirconia containing larger RE cations, and a shallower depth of infiltration into the coating volume compared to RE-zirconia containing smaller RE cations [129].

5.2 Coating Strategies

The choice of materials is of paramount importance in the “anti-CMAS” strategy, but the coating morphology should not be neglected either. Indeed, depending on the coating treatment, variable porosity levels and/or controlled macro-defects such as columns or wide cracks will be obtained. These process-dependent features influence the degree of degradation of CMAS infiltration, as open coating structures favor the flowability of identical CMAS into the coating compared to denser structures [115, 191, 225, 228].

Yang et al. [228] compared the spreading of volcanic ashes on YSZ coatings produced by APS (highly porous lamellar structure) and EB-PVD (columnar structure with interconnected inter-columnar spaces) at different temperatures (from 1200 to 1600 °C). They showed that the dynamic spreading rate of spherical volcanic ashes on TBC is strongly influenced by the melt viscosity, concentration gradient and coating morphology. When the melt reaches the target temperatures (i.e., 1200, 1400 or 1600 °C), the low viscosity (> 362 Pa·s at 1200 °C, 80.7 Pa·s at 1400 °C, 10.3 Pa·s at 1600 °C) favors interactions with the surface and microstructure of the coating. According to their observations, the coating morphology then becomes the dominant factor in controlling the spreading of volcanic ashes. Surface spreading is more extensive on the APS coating surface because the surface roughness is higher. This factor increases the wettability of the melt due to the large capillary forces. Comparatively, the vertical and lateral subsurface infiltration depths of the CMAS melt are higher in EB-PVD coatings at the same melting stage due to the higher pore connectivity (inter-column spaces), while the spreading front on the surface is less extensive due to the lower surface roughness. Therefore, they propose that producing YSZ coatings with minimal surface roughness (promoting non-wetting behavior) and low-connected porosity (attenuating infiltration depths) is more likely to withstand CMAS degradation in temperature and for a longer period of time.

This proposal is in line with the overall development trends of TBCs that attempt to trade-off thermomechanical requirements for the coating with mitigation of CMAS degradation. Two main architectural strategies can be distinguished among these: the development of multilayer topcoats or the texturing of coating surfaces [191, 209, 229].

Specifically, attempts have been made to combine the thermomechanical properties of yttria-stabilized zirconia with the “anti-CMAS” behavior of other materials,

either through reactivity to CMAS and associated chemical sealing mechanisms or through a non-wetting effect on CMAS [23, 208].

As previously reported, the $\text{RE}_2\text{Zr}_2\text{O}_7$ pyrochlore materials have been identified as excellent candidates to replace YSZ in TBCs, particularly GZ which exhibits the best reactivity to CMAS infiltration among them. However, in a traditional TBC system, GZ reacts at temperature with the alumina that forms between the ceramic coating and the (Ni, Pt)-Al bondcoat, resulting in the formation of GdAlO_3 phases detrimental to the oxidation protection of the bondcoat [230, 231]. GZ coatings also exhibit poor thermomechanical properties compared to YSZ coatings in isothermal cyclic oxidation and erosion resistance tests [69, 215, 232, 233]. Therefore, efforts have been made to develop multilayer YSZ/GZ coatings to combine the beneficial properties from both materials and counteract the mechanical weaknesses of GZ [191, 234–236]. In these architectures, YSZ is always the first ceramic layer above the bondcoat to prevent reactions between GZ and the TGO.

The work of Mahade et al. [69, 156, 233–235] can be particularly highlighted with respect to the study of thermomechanical properties of SPS coatings with multilayer YSZ/GZ architectures. Their experiments using isothermal furnaces or a burner rig show that higher oxidation resistance and thermal shock resistance can be achieved with double or triple-layer YSZ/GZ SPS coatings compared to SPS coatings comprising only a single layer of YSZ [156, 234, 235]. Notably, the thickness of the YSZ layer in the double-layer coatings is almost inversely proportional to the TBC lifetime in their burner rig test conditions (thermal gradient of 200 °C in the samples with the TBC surface exposed to 1350 °C during the heating stage). Thicker layers of GZ in double-layer coatings have a beneficial impact on oxidation resistance. Mahade et al. hypothesize this is likely due to the lower thermal conductivity of GZ compared to YSZ, which results in slower growth of the TGO film between the topcoat and the metal bondcoat, which is a known factor in TBC failure. The lower fracture toughness of GZ would be the primary factor in the faster failure of the coating with the thickest YSZ, they hypothesize. In this case, the GZ layer crumbles early in the test, resulting in higher thermomechanical stresses in the rest of the YSZ coating and to lower thermal shock resistance.

YSZ/GZ multilayer coatings have also been tested against CMAS attack in thermal shock or infiltration tests under isothermal or thermal gradient conditions [191, 228, 237]. For example, the results of Gildersleeve et al. [191] show that double-layer YSZ/GZ APS coatings effectively resist a single exposure to lignite ash (35 $\text{mg}\cdot\text{cm}^{-2}$ of CMAS) during thermal shock tests featuring a thermal gradient of 250 °C in the samples during the heating phase (TBC surface held at 1250 °C in a burner rig). Other attacks lead to the complete spallation of the APS GZ layer during cooling and the mechanical degradation (cracks) of the underlying YSZ layer. To counteract this phenomenon, they developed a multilayer YSZ/GZ APS coating with alternate layers of each, keeping a GZ layer on top (Fig. 11). The spray parameters were adapted to produce porous layers of each material in order to control the thermomechanical stresses after each CMAS attack. Indeed, they noticed with single and double-layer coatings that sufficiently high porosity forced delamination between each layer and reduced the thickness of CMAS infiltration, compared to denser coatings with vertical

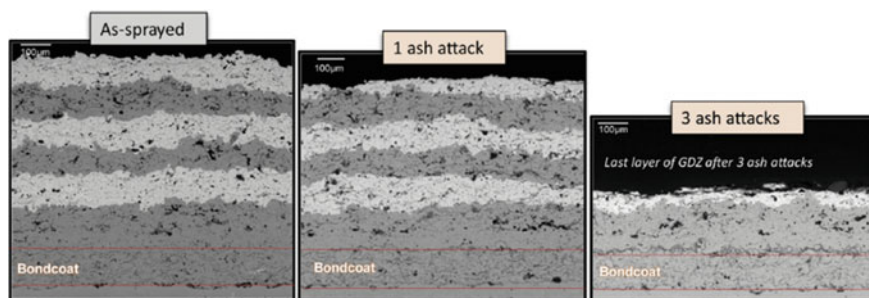


Fig. 11 Multilayer coating consisting of GZ (light layer) and YSZ (dark layer) subjected to successive attacks of lignite ash in a thermal gradient test (burner rig) [191]

cracks. These two microstructural observations were also highlighted by Morelli et al. in their studies of CMAS infiltration at 1250 °C and thermal shocks resistance of YSZ/GZ APS coatings at 1100 °C in isothermal furnaces [236]. The results obtained after several CMAS attacks under a thermal gradient show that the porous multilayer YSZ/GZ system is effective in withstanding several attacks while preserving the advantages of the double-layer system (i.e., retaining the combination of an anti-CMAS layer with a thermomechanical compliant underlayer), although the inevitable delamination of the infiltrated top layers (Fig. 11).

Zhou et al. [237] studied the same phenomena with YSZ/GZ multilayer coatings comprising a porous APS YSZ layer and columnar or dense SPS GZ top layers (Fig. 12). Their results highlight a significantly higher thermal shock resistance under thermal gradients of the APS/SPS multilayer coatings compared to single APS YSZ TBCs (TBC surfaces held at 1400 °C with a thermal gradient of 300 °C during the heating stage). They infer this is due to the greater strain tolerance improved by the SPS columns and the lower thermal conductivity of GZ. The addition of CMAS attacks during these thermal shocks shows that the best thermal resistance to thermal shock and infiltration comes from the triple-layer coating containing a densified SPS GZ topcoat with vertical as-sprayed cracks (Fig. 12 b and d). The CMAS infiltration depth remains the same in the YSZ/GZ coatings tested independently of the microstructures of the GZ top layers under their test conditions (TBC surfaces held at 1250 °C with a thermal gradient of 250 °C within the samples). All APS/SPS multilayer coatings failed under cold shocks (spallation of the GZ layers from cracks within the GZ layers). The differences in thermal shock resistance between the multilayer YSZ/GZ coatings tested could be due to the better thermomechanical properties of the triple-layer YSZ/GZ coating. In the latter case, it has a higher fracture toughness and elastic modulus than the other type of multilayer coating tested which could allow the coatings to withstand longer.

Ultimately, this strategy capitalizes on the sacrificial effect of GZ reactivity to CMAS. The TBC will ineluctably delaminate, whether as a result of successive CMAS attacks or other extrinsic degradations. Such multilayer TBCs are interesting because they should allow for a longer service lifetime before inevitable maintenance.

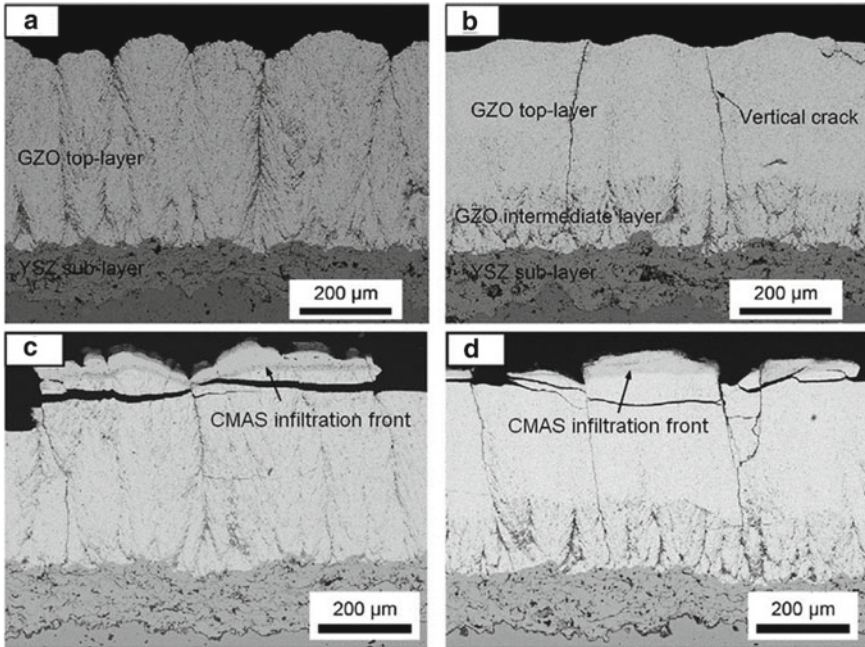


Fig. 12 Multilayer coating consisting of SPS GZ (light layers) and APS YSZ (dark, porous layers) subjected to CMAS attacks in a thermal gradient test (burner rig). **A** and **B** show the as-sprayed coatings, **C** and **D** show the SPS GZ/APS YSZ double-layer (**C**) and the triple-layer SPS-dense GZ/SPS GZ/APS YSZ (**D**) coatings after CMAS infiltration and delamination [237]

Several patents mention the non-wetting behavior to CMAS of topcoats including noble metals, carbides, borides, ... [238, 239] but very few studies have been published on these materials to corroborate these claims [121, 240]. However, recent studies have emphasized on the prominent role of surface texturing and geometry in promoting a non-wetting behavior to CMAS. Strategies used lie in optimizing deposition processes or in post-process modifications such as polishing or laser-texturing TBCs [154, 241–247].

Qu et al. [248] tested the wettability of CMAS on single cubic crystals of YSZ with three different orientations. Their study shows that, during CMAS attack, the YSZ nodules forming at the $(\text{liquid})_{\text{CMAS}}/(\text{YSZ})_{\text{crystal}}$ interface into inverted trapezoids are favorable for maintaining a higher contact angle and limiting the spreading rate of CMAS below 1230 °C in air. This microgeometry of the re-precipitated zirconia nodules was a characteristic of YSZ crystals oriented in the $\{1\ 0\ 0\}$ direction. As they report, this experimental result is contrary to first-principle descriptions of Young wetting model predicting that the $\{1\ 1\ 1\}$ cubic crystal should lead to the lowest CMAS spreading velocity and higher contact angle, due to the limited surface energy of the crystal relative to the $\{1\ 0\ 0\}$ plane ($65\ \text{meV}\cdot\text{\AA}^{-2}$ and $109\ \text{meV}\cdot\text{\AA}^{-2}$, respectively). They conclude that the microgeometry formed at the $(\text{liquid})_{\text{CMAS}}/$

(YSZ)_{crystals} interface during infiltration is the main factor in the wetting behavior of CMAS with YSZ. This microgeometry significantly weakens the action of surface energy. They deduced that the interface composed of inverted trapezoids of YSZ could promote a composite contact between the molten CMAS melt, the YSZ nodules and the air trapped at the interface (Cassie wetting model, Fig. 13). This hypothesis would explain the unexpected wetting behavior, due to the lower surface energy between the melt and the gas. Contact angle calculations using the Cassie model seem to confirm this experimental result.

Other studies have reported similar effects of surface geometry on the non-wetting behavior to CMAS for several surface structural scales [154, 241–247]. Some of the experimental data described below have been summarized in Fig. 14.

For example, Yang et al. [243] compared several CMAS spreading rates on APS YSZ coatings with increasing surface roughness using a temperature wettability test (in unknown atmosphere). They observed on all samples and with all types of

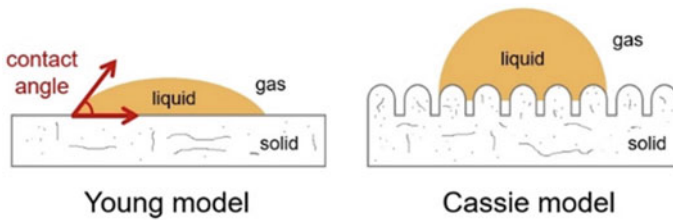


Fig. 13 Wetting models

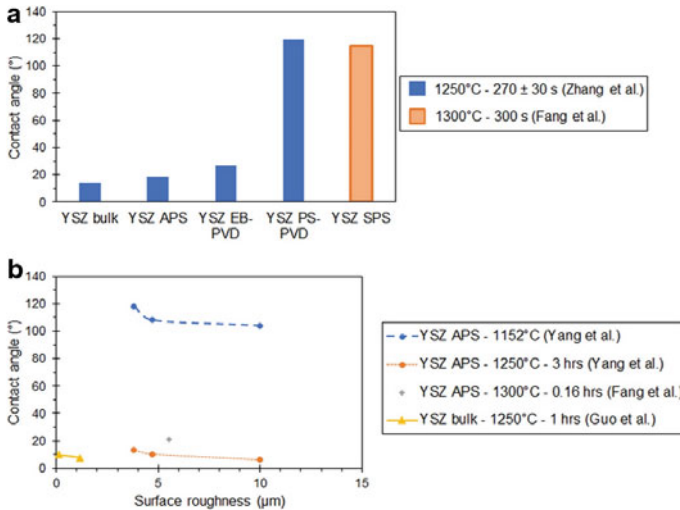


Fig. 14 Contact angles between YSZ coatings and CMAS as a function of a coating processes and b surface roughness, data collected from [154, 242, 243, 249]

CMAS (natural volcanic ash, industrial by-product fly ash, synthetic CMAS) a short period of non-wetting behavior (contact angles greater than 120° between coating and melt) before the viscosity of the CMAS melt reaches a value low enough to initiate spreading on all YSZ coatings (between 1200 and 1250°C). Furthermore, as the coating roughness decreases, this non-wetting behavior extends over time, regardless of the chemical composition of the CMAS. The wetting area of the melts also decreases with the reduction in surface roughness over the same time. This has an impact on the lasting spreading area of the melts at higher temperatures. Yang et al. observed the smallest spreading zones for YSZ coatings with the highest contact angle with the melts during the previous non-wetting step. Guo et al. [154] demonstrated the same phenomena in their study comparing the wetting behavior of CMAS on YSZ, GdPO_4 and LaPO_4 coatings with different surface roughnesses. They also noted advantages related to the initial coating chemistry for similar surface roughnesses, with REPO_4 coatings retaining higher contact angles with CMAS than YSZ coatings (nearly 70° for GdPO_4 vs. to 11° for YSZ polished bulks after 1 h at 1250°C in air). They attribute these differences to lower surface energies of REPO_4 . The precipitation of Gd or La-compounds at the (liquid)_{CMAS}/(solid)_{coating} interface could also play a role into this non-wetting behavior by modifying the topography of the interface, in a similar fashion than Qu et al. experiments reported previously, but this aspect was not investigated by the authors.

Zhang et al. [242] investigated the potential effect of multiscale roughness on the wettability of CMAS by comparing the spreading of CMAS at 1250°C (unknown atmosphere) on YSZ coatings produced by different techniques (i.e., EB-PVD, APS and PS-PVD). They found out that PS-PVD dual-scale surface roughness, comprising of round-shaped micro-protuberances (diameter between 1 and $7\ \mu\text{m}$) on which branch-like nano-scale tips are observed (tip diameter between 50 and 100 nm), is beneficial for the promotion of a “CMAS-superphobic” surface in the first minutes of CMAS melting (Fig. 14). The gas, trapped between the multiscale tips of the coating and the molten CMAS, could be the main driver of the observed superphobic surface behavior (contact angle of about 120°), based on surface energy calculations.

Such surface texturing, achieved through the characteristics of the PS-PVD process, can also be achieved by SPS, using the right set of spraying parameters. Fang et al. [249] investigated this, examining the infiltration of CMAS on a YSZ coating consisting of a columnar layer produced by SPS on an APS layer. After 5 min at 1300°C , they measured a contact angle of 115° between CMAS and the YSZ surface, which they attribute to the micro and nano-scale morphology of the coating surface, analogous to PS-PVD coatings. However, the melt eventually wets the surface of YSZ coating surface in all cases.

Other studies focusing on laser-glazed or laser-ablated TBCs report similar results to either CMAS wetting behavior or infiltration into TBCs thanks to a significant decrease in surface roughness and entry points [250, 251] or a promotion of a three-phase contact angle (liquid CMAS, solid TBC and gases) [246, 247]. Study by Guo et al. [246] especially insists on a lasting non-wetting behavior of laser-ablated coatings (contact angle around 105° at 1200°C) after thermal aging (10 h at 1300°C), which is a critical variable considering the TBC environment. They explain this

lasting effect by the higher concentration of nanoparticles covering the coating tips after coating re-melting during laser-ablation, compared to as-deposited PS-PVD coatings (which retain a contact angle of 90° at 1200°C after thermal aging). Therefore, they achieved this result thanks to an enhanced micro and nano-scale surface morphology as underlined before.

In summary, an ideal TBC exhibiting anti-CMAS behavior and conformal thermomechanical properties should have the following characteristics:

- A textured surface containing micro and nano-scale tips to promote “CMAS-superphobic” behavior to slow down CMAS wetting over time and temperature through gas entrapment at the (liquid)_{CMAS}/(solid)_{coating} interface.
- A low surface roughness at the macroscopic scale to inhibit capillary forces that drive molten CMAS into the porosities of the coating.
- A multilayer architecture comprising at least:
 - A GZ top layer to limit the depth of CMAS infiltration into the TBC and limit coating recession, due to the high reactivity at the (liquid)_{CMAS}/(GZ)_{coating} interface.
 - A GZ top layer dense enough to limit CMAS entry points during infiltration and to reduce the thermal conductivity of the coating.
 - A lower YSZ layer composed of porous columns to effectively accommodate thermomechanical stresses and further lower the thermal conductivity.

This architecture and properties can be achieved by SPS (Fig. 15) by optimizing all the parameters. The multiscale microstructure and diversity of coating morphologies offered by the SPS process should allow coatings to be tailored to fulfill the anti-CMAS strategies described: a “CMAS-superphobic” surface behavior to limit CMAS attack with an underlying multilayer coating with conformal thermochemical (high reactivity to CMAS) and thermomechanical properties. Further studies are needed to test these hypotheses under realistic service conditions and compare the available data.

In particular, research on CMAS infiltration in YSZ/GZ multilayer coatings has not yet been performed using coating architectures comprising only of SPS layers, as far as we know. This research would provide new insights into the wetting behavior of CMAS during infiltration and the thermomechanical behavior of SPS multilayer coatings.

6 Conclusion

As the challenges of climate change continue to mount, it becomes increasingly crucial to reduce the polluting emissions of air transportation. To this end, engine manufacturers are exploring various solutions, and one of them involves increasing the efficiency of aircraft engines by raising the temperature at the outlet of the combustion chamber. However, this poses challenges for the lifespan of thermal

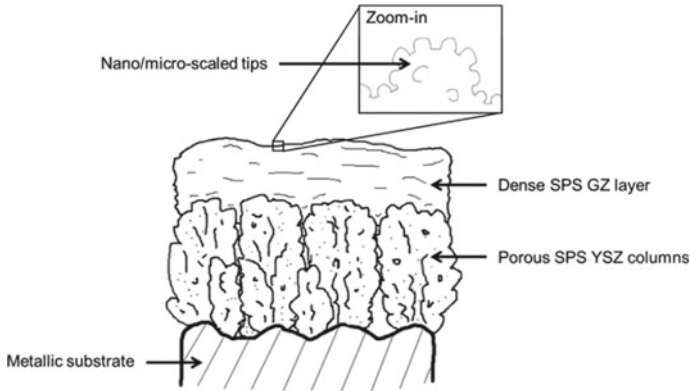


Fig. 15 Proposed coating architecture and materials to improve the anti-CMAS and thermomechanical properties of future TBCs, using only the SPS process

barrier coatings. During flight, engines ingest sand and volcanic ash particles known as CMAS, which can accumulate on the thermal barrier coating among other possibilities (erosion, clogging). The thermochemical properties of these particles, such as flowability and basicity, determine the extent to which they infiltrate the coating's porosity, leading to chemical degradation of the yttria-stabilized zirconia. During engine cooling phases, these particles vitrify, causing mechanical stresses in the coating and promoting the initiation of cracks parallel to the interface, ultimately leading to spalling of the thermal barrier.

To address these premature flaking issues, various strategies are proposed in the literature, such as using materials that slow down the infiltration of particles (e.g., gadolinium zirconate) or modifying the surface roughness to make the coating "CMAS-superphobic". However, it is necessary not to degrade the main properties of the topcoat, which are low thermal conductivity and the ability to accommodate thermal stresses. It has been widely demonstrated that these properties are controlled by the microstructure of the yttria-stabilized zirconia topcoat. In this chapter, the authors explored how the suspension plasma spray (SPS) process can address these challenges while remaining economically viable.

Indeed, the SPS process allows great versatility in microstructure and could be used to coat both components of the combustion chamber and high-pressure turbines, while being less expensive than the EB-PVD process. That is why many engine manufacturers are interested in developing these SPS thermal barrier coatings.

However, properly characterizing the in-service behavior of these new thermal barrier coatings is necessary to consider their future industrialization. To date, two main tests are used: the isothermal test and the thermal gradient test. The latter is more representative but more complex to implement, especially regarding temperature control. For both tests, the CMAS sollicitation is not very representative of what happens in service because the topcoat is saturated with CMAS while infiltration should occur over time. Moreover, each test bench is developed separately,

and the results cannot be correctly compared. The question then arises of how to properly characterize these thermal barriers. By refining the characterization, it will be easier to determine which composition, microstructure and architecture are the best adapted to the conditions the TBC is subjected in service. The SPS process parameters could then be optimized to achieve the desired coating characteristics. However, this requires an understanding of the interactions between the materials and process parameters, which are generally closely related to each other. This understanding is aided by the use of sensors to study in-flight material processing and coating growth and/or numerical process models. Sensors and digital models, along with massive data collection, also form the basis for developing digital twins to mimic the SPS process. Digital process twins will enable much faster coating development for parts with complex geometry and prediction of coating characteristics. Digital twins and big data can also be used to predict the life of different parts of an aircraft engine operated with different fuels in different environments allowing for rapid screening and selection of promising material configurations. Ultimately, this integration of SPS, big data and digital twins could enable the development of TBCs with increased performance and durability and reduce the development time and cost of TBC systems.

Acknowledgements This work received no specific grant from any funding agency in the public or commercial sectors but M.G. would like to thank SAFRAN for the funding of his thesis. The authors of IRCER and ONERA would also like to thank the New Aquitaine region and SAFRAN for their support to the development of new generation coatings for aeronautics.

References

1. Pörtner, H.-O. et al., (eds.). (2022). Climate change 2022: Impacts, adaptation and vulnerability. Contribution of Working Group II to the Sixth Assessment Report of the Intergovernmental Panel on Climate Change
2. Atwoli, L., et al.: Call for emergency action to limit global temperature increases, restore biodiversity, and protect health. *N. Engl. J. Med.* **385**(12), 1134–1137 (2021). <https://doi.org/10.1056/NEJMe2113200>
3. Airbus, The Boeing Company, Dassault Aviation, GE Aviation, Rolls-Royce, Safran and United Technologies Corporation, 'The Sustainability of Aviation', NVI Joint statement
4. 'Air France-KLM CO₂ emissions reduction targets for 2030 approved by the Science Based Targets initiative (SBTi)*|AIR FRANCE KLM'. <https://www.airfranceklm.com/en/newsroom/air-france-klm-co2-emissions-reduction-targets-2030-approved-science-based-targets-0> (Accessed 12 Feb 2023)
5. 'Aviation—Analysis', IEA. <https://www.iea.org/reports/aviation> (Accessed 12 Feb 2023)
6. Stan Shparberg and Bob Lange, 'Global Market Forecast 2022'. Airbus presentation
7. Mosely, 'As air travel rebounds, boeing forecasts demand for more than 41,000 new airplanes by 2041', MediaRoom (2022). <https://boeing.mediaroom.com/2022-07-16-As-Air-Tra-vel-Rebounds,-Boeing-Forecasts-Demand-for-More-than-41,000-New-Airplanes-by-2041> (Accessed 12 Feb 2023)
8. Fred Pearce, 'How airplane contrails are helping make the planet warmer', Yale E360. <https://e360.yale.edu/features/how-airplane-contrails-are-helping-make-the-planet-warmer> (Accessed 12 Feb 2023)

9. 'ATAG'. <https://www.atag.org/our-activities/climate-change.html> (Accessed Feb. 12, 2023).
10. IATA (77th IATA Annual General Meeting). (2021). 'Resolution on the industry's commitment to reach net zero carbon emissions by 2050'
11. Advisory Group for Aerospace Research and Development (AGARD), Advanced Aero-Engine Concepts and Controls (1996). Accessed: 12 Feb 2023. [Online]. Available: http://archive.org/details/DTIC_ADA311466
12. Dorfman, M.R., Dwivedi, G., Dambra, C., Wilson, S.: Perspective: Challenges in the aerospace marketplace and growth opportunities for thermal spray. *J. Therm. Spray Technol.* **31**(4), 672–684 (2022). <https://doi.org/10.1007/s11666-022-01351-x>
13. Paquin, S., Cariou, R.P., Flamme, T.M., Rollinger, A.B.V.: Turbine blade having an improved structure. WO2018189434A3 (2018)
14. Rollinger, A.B.V., Cariou, R.P., Flamme, T.M., Paquin, S.: Turbine blade comprising a cooling circuit. US10844733B2 (2020)
15. Vagge, S.T., Ghogare, S.: Thermal barrier coatings: review. *Mater. Today: Proc.* **56**, 1201–1216 (2022). <https://doi.org/10.1016/j.matpr.2021.11.170>
16. Feuerstein, A., Knapp, J., Taylor, T., Ashary, A., Bolcavage, A., Hitchman, N.: Technical and economical aspects of current thermal barrier coating systems for gas turbine engines by thermal spray and EBPVD: a review. *J. Therm. Spray Technol.* **17**(2), Art. no. 2 (2008). <https://doi.org/10.1007/s11666-007-9148-y>
17. Vardelle, A., Moreau, C., Themelis, N.J., Chazelas, C.: A perspective on plasma spray technology. *Plasma Chem. Plasma Process.* (2015). <https://doi.org/10.1007/s11090-014-9600-y>
18. Kumar, N., Gupta, M., Mack, D.E., Mauer, G., Vaßen, R.: Columnar thermal barrier coatings produced by different thermal spray processes. *J. Therm. Spray Technol.* **30**(6), 1437–1452 (2021). <https://doi.org/10.1007/s11666-021-01228-5>
19. Bernard, B., Bianchi, L., Malié, A., Joulia, A., Rémy, B.: Columnar suspension plasma sprayed coating microstructural control for thermal barrier coating application. *J. Euro. Ceram. Soc.* **36**(4), Art. no. 4 (2016). <https://doi.org/10.1016/j.jeurceramsoc.2015.11.018>
20. Kebriyaei, A., Rahimipour, M.R., Razavi, M., Alizade Herfati, A.: Effect of solution precursor on microstructure and high-temperature properties of the thermal barrier coating made by solution precursor plasma spray (SPPS) process. *J. Therm. Spray Technol.* (2022) <https://doi.org/10.1007/s11666-022-01470-5>
21. Pujol, G., Ansart, F., Bonino, J.-P., Malié, A., Hamadi, S.: Step-by-step investigation of degradation mechanisms induced by CMAS attack on YSZ materials for TBC applications. *Surf. Coat. Technol.* **237**, 71–78 (2013). <https://doi.org/10.1016/j.surfcoat.2013.08.055>
22. Wellman, R.G., Nicholls, J.R.: A review of the erosion of thermal barrier coatings. *J. Phys. D Appl. Phys.* **40**(16), R293 (2007). <https://doi.org/10.1088/0022-3727/40/16/R01>
23. Bacos, M.P. et al.: 10 Years-activities at Onera on advanced thermal barrier coatings. *AerospaceLab*, no. 3, Art. no. 3 (2011)
24. Darolia, R.: Thermal barrier coatings technology: critical review, progress update, remaining challenges and prospects. *Int. Mater. Rev.* **58**(6), 315–348 (2013). <https://doi.org/10.1179/1743280413Y.0000000019>
25. Fauchais, P.L., Heberlein, J.V.R., Boulos, M.I.: *Thermal spray fundamentals*. Springer US (2014). <https://doi.org/10.1007/978-0-387-68991-3>
26. Vardelle, A. et al.: The 2016 thermal spray roadmap. *J. Therm. Spray Technol.* **25**(8), Art. no. 8 (2016). <https://doi.org/10.1007/s11666-016-0473-x>
27. Ruelle, C., Goutier, S., Rat, V., Keromnes, A., Chazelas, C., Meillot, E.: Study of the electric arc dynamics in a cascaded-anode plasma torch. *Surface Coatings Technol.* (2023)
28. Pfender, E.: Fundamental studies associated with the plasma spray process. *Surf. Coat. Technol.* **34**(1), 1–14 (1988). [https://doi.org/10.1016/0257-8972\(88\)90083-7](https://doi.org/10.1016/0257-8972(88)90083-7)
29. Zhukovskii, R., Chazelas, C., Vardelle, A., Rat, V.: Control of the arc motion in DC plasma spray torch with a cascaded anode. *J. Therm. Spray Technol.* **29**(1), 3–12 (2020). <https://doi.org/10.1007/s11666-019-00969-8>

30. Fauchais, P., Coudert, J.F., Vardelle, M., Vardelle, A., Denoirjean, A.: Diagnostics of thermal spraying plasma jets. *JTST* **1**(2), 117–128 (1992). <https://doi.org/10.1007/BF02659011>
31. Vardelle, M., Vardelle, A., Leger, A.C., Fauchais, P., Gobin, D.: Influence of particle parameters at impact on splat formation and solidification in plasma spraying processes. *JTST* **4**(1), 50–58 (1995). <https://doi.org/10.1007/BF02648528>
32. Blanchi, L., Grimaud, A., Blein, F., Lucchèse, P., Fauchais, P.: Comparison of plasma-sprayed alumina coatings by RF and DC plasma spraying. *JTST* **4**(1), 59–66 (1995). <https://doi.org/10.1007/BF02648529>
33. Mauer, G., Vaßen, R., Stöver, D.: Comparison and Applications of DPV-2000 and accuraspray-g3 diagnostic systems. *J. Therm. Spray Technol.* **16**(3), 414–424 (2007). <https://doi.org/10.1007/s11666-007-9047-2>
34. Hui, R., et al.: Thermal plasma spraying for SOFCs: applications, potential advantages, and challenges. *J. Power. Sources* **17**(2), 308–323 (2007). <https://doi.org/10.1016/j.jpowsour.2007.03.075>
35. Clarke, D.R., Oechsner, M., Padtare, N.P.: Thermal-barrier coatings for more efficient gas-turbine engines. *MRS Bull.* **37**(10), Art. no. 10 (2012) <https://doi.org/10.1557/mrs.2012.232>
36. Padtare, N.P.: Thermal barrier coatings for gas-turbine engine applications. *Science* **296**(5566), Art. no. 5566 (2002). <https://doi.org/10.1126/science.1068609>
37. Rat, V., Chazelas, C., Goutier, S., Keromnes, A., Mariaux, G., Vardelle, A.: In-flight mechanisms in suspension plasma spraying: Issues and perspectives. *J. Therm. Spray Technol.* **31**(4), 699–715 (2022). <https://doi.org/10.1007/s11666-022-01376-2>
38. Łatka, L.: Thermal barrier coatings manufactured by suspension plasma spraying—a review. *Adv. Mater. Sci.* **18**(3), 95–117 (2018). <https://doi.org/10.1515/adms-2017-0044>
39. Sokołowski, P., Kozerski, S., Pawłowski, L., Ambroziak, A.: The key process parameters influencing formation of columnar microstructure in suspension plasma sprayed zirconia coatings. *Surf. Coat. Technol.* **260**, 97–106 (2014). <https://doi.org/10.1016/j.surfcoat.2014.08.078>
40. Caio, F., Moreau, C.: Influence of substrate shape and roughness on coating microstructure in suspension plasma spray. *Coatings* **9**(11), 746 (2019). <https://doi.org/10.3390/coatings9110746>
41. VanEvery, K., et al.: Column formation in suspension plasma-sprayed coatings and resultant thermal properties. *J. Therm. Spray Technol.* **20**(4), 817–828 (2011). <https://doi.org/10.1007/s11666-011-9632-2>
42. Aubignat, E., et al.: Optimization of the injection with a twin-fluid atomizer for suspension plasma spray process using three non-intrusive diagnostic tools. *J. Vis.* **19**(1), 21–36 (2016). <https://doi.org/10.1007/s12650-015-0281-2>
43. Zhao, Y., et al.: Influence of substrate properties on the formation of suspension plasma sprayed coatings. *J. Therm. Spray Technol.* **27**(1), 73–83 (2018). <https://doi.org/10.1007/s11666-017-0671-1>
44. Ganvir, A., Calinas, R.F., Markocsan, N., Curry, N., Joshi, S.: Experimental visualization of microstructure evolution during suspension plasma spraying of thermal barrier coatings. *J. Eur. Ceram. Soc.* **39**(2), 470–481 (2019). <https://doi.org/10.1016/j.jeurceramsoc.2018.09.023>
45. Joulia, A., Duarte, W., Goutier, S., Vardelle, M., Vardelle, A., Rossignol, S.: Tailoring the spray conditions for suspension plasma spraying. *J. Therm. Spray Technol.*, **24**(1), Art. no. 1 (2015) <https://doi.org/10.1007/s11666-014-0184-0>
46. Bernard, B., et al.: Effect of suspension plasma-sprayed YSZ columnar microstructure and bond coat surface preparation on thermal barrier coating properties. *J. Therm. Spray Technol.* **26**(6), 1025–1037 (2017). <https://doi.org/10.1007/s11666-017-0584-z>
47. Curry, N., Tang, Z., Markocsan, N., Nylén, P.: Influence of bond coat surface roughness on the structure of axial suspension plasma spray thermal barrier coatings—thermal and lifetime performance. *Surf. Coat. Technol.* **268**, 15–23 (2015). <https://doi.org/10.1016/j.surfcoat.2014.08.067>
48. Bidron, G., Goutier, S., Vardelle, M., Denoirjean, P., Fauchais, P.: Flattening behavior of micro- and nano-sized yttria-stabilized zirconia particles plasma-sprayed on smooth preheated (610

- K) nickel substrate: part I. *J. Phys. D Appl. Phys.* **52**(16), 165201 (2019). <https://doi.org/10.1088/1361-6463/aafd81>
49. Dolmaire, A., Goutier, S., Vardelle, M., Geffroy, P.-M., Joulia, A.: Investigations on particle behavior at the stagnation zone for a suspension particle jet in plasma spray conditions. *J. Therm. Spray Technol.* **30**(4), 1001–1014 (2021). <https://doi.org/10.1007/s11666-021-01174-2>
 50. Delbos, C., Fazilleau, J., Rat, V., Coudert, J.F., Fauchais, P., Pateyron, B.: Phenomena involved in suspension plasma spraying part 2: Zirconia particle treatment and coating formation. *Plasma Chem. Plasma Process.* **26**(4), 393–414 (2006). <https://doi.org/10.1007/s11090-006-9020-8>
 51. Oberste-Berghaus, J., Bouaricha, S., Legoux, J.-G., Moreau, C.: Injection conditions and in-flight particle states in suspension plasma spraying of alumina and zirconia nano-ceramics. In: Presented at the Proceedings of the International Thermal Spray Conference, pp. 2–4. Basel (2005)
 52. Etchart-Salas, R., et al.: Influence of plasma instabilities in ceramic suspension plasma spraying. *J. Therm. Spray Technol.* **16**(5), 857–865 (2007). <https://doi.org/10.1007/s11666-007-9084-x>
 53. Dolmaire, A., et al.: Benefits of hydrogen in a segmented-anode plasma torch in suspension plasma spraying. *J. Therm. Spray Technol.* **30**(1), 236–250 (2021). <https://doi.org/10.1007/s11666-020-01134-2>
 54. Seshadri, R.C., Dwivedi, G., Viswanathan, V., Sampath, S.: Characterizing suspension plasma spray coating formation dynamics through curvature measurements. *J. Therm. Spray Technol.* **25**(8), 1666–1683 (2016). <https://doi.org/10.1007/s11666-016-0460-2>
 55. Ganvir, A., Curry, N., Björklund, S., Markocsan, N., Nylén, P.: Characterization of microstructure and thermal properties of YSZ coatings obtained by axial suspension plasma spraying (ASPS). *J. Therm. Spray Technol.* **24**(7), 1195–1204 (2015). <https://doi.org/10.1007/s11666-015-0263-x>
 56. Chen, X., Kuroda, S., Ohnuki, T., Araki, H., Watanabe, M., Sakka, Y.: Effects of Processing parameters on the deposition of yttria partially stabilized zirconia coating during suspension plasma spray. *J. Am. Ceram. Soc.* **99**(11), 3546–3555 (2016). <https://doi.org/10.1111/jace.14393>
 57. Chen, X., et al.: Highly segmented thermal barrier coatings deposited by suspension plasma spray: effects of spray process on microstructure. *J. Therm. Spray Technol.* **25**(8), 1638–1649 (2016). <https://doi.org/10.1007/s11666-016-0469-6>
 58. Zhou, D., Guillon, O., Vaßen, R.: Development of YSZ thermal barrier coatings using axial suspension plasma spraying. *Coatings* **7**(8), 120 (2017). <https://doi.org/10.3390/coatings7080120>
 59. Fauchais, P., Etchart-Salas, R., Rat, V., Coudert, J.F., Caron, N., Wittmann-Ténèze, K.: Parameters controlling liquid plasma spraying: solutions, sols, or suspensions. *J. Therm. Spray Technol.* **17**(1), 31–59 (2008). <https://doi.org/10.1007/s11666-007-9152-2>
 60. Jadidi, M., Mousavi, M., Moghtadernejad, S., Dolatabadi, A.: A three-dimensional analysis of the suspension plasma spray impinging on a flat substrate. *J. Therm. Spray Tech.* **24**(1), 11–23 (2015). <https://doi.org/10.1007/s11666-014-0166-2>
 61. Phillips, C.G., Kaye, S.R.: The influence of the viscous boundary layer on the critical stokes number for particle impaction near a stagnation point. *J. Aerosol Sci.* **30**(6), 709–718 (1999). [https://doi.org/10.1016/S0021-8502\(98\)00766-6](https://doi.org/10.1016/S0021-8502(98)00766-6)
 62. Farrokhpahan, A., Coyle, T.W., Mostaghimi, J.: Numerical study of suspension plasma spraying. *J. Therm. Spray Tech.* **26**(1), 12–36 (2017). <https://doi.org/10.1007/s11666-016-0502-9>
 63. Pourang, K., Moreau, C., Dolatabadi, A.: Effect of substrate and its shape on in-flight particle characteristics in suspension plasma spraying. *J. Therm. Spray Technol.*, **25**(1), Art. no. 1 (2016). <https://doi.org/10.1007/s11666-015-0342-z>
 64. Bernard, B.: Barrières thermiques par projection plasma de suspensions : développement et caractérisation de microstructures à faible conductivité thermique. Université de Lorraine (2016)

65. Joeris, J., Tiwari, A., Brinckmann, S., Kurze, F., Guillon, O., Vaßen, R.: Evaluation of major factors influencing the TBC topcoat formation in axial suspension plasma spraying (SPS). *Int. J. Appl. Ceram. Technol.* <https://doi.org/10.1111/ijac.14288>.
66. Zhao, Y., et al.: Thermal shock behaviors of YSZ thick thermal barrier coatings fabricated by suspension and atmospheric plasma spraying. *Surf. Coat. Technol.* **249**, 48–55 (2014). <https://doi.org/10.1016/j.surfcoat.2014.03.046>
67. Curry, N., VanEvery, K., Snyder, T., Markocsan, N.: Thermal conductivity analysis and lifetime testing of suspension plasma-sprayed thermal barrier coatings. *Coatings* **4**(3), 630–650 (2014). <https://doi.org/10.3390/coatings4030630>
68. Gupta, M., Markocsan, N., Li, X.-H., Kjellman, B.: Development of bondcoats for high lifetime suspension plasma sprayed thermal barrier coatings. *Surf. Coat. Technol.* **371**, 366–377 (2019). <https://doi.org/10.1016/j.surfcoat.2018.11.013>
69. Mahade, S., et al.: Understanding the effect of material composition and microstructural design on the erosion behavior of plasma sprayed thermal barrier coatings. *Appl. Surf. Sci.* **488**, 170–184 (2019). <https://doi.org/10.1016/j.apsusc.2019.05.245>
70. Lima, R.S., Guerreiro, B.M.H., Aghasibeig, M.: Microstructural characterization and room-temperature erosion behavior of as-deposited SPS, EB-PVD and APS YSZ-based TBCs. *J. Therm. Spray Technol.* **28**(1), 223–232 (2019). <https://doi.org/10.1007/s11666-018-0763-6>
71. Bernard, B. et al.: Thermal insulation properties of YSZ coatings: Suspension Plasma Spraying (SPS) versus Electron Beam Physical Vapor Deposition (EB-PVD) and Atmospheric Plasma Spraying (APS). *Surface Coatings Technol.* (2016) <https://doi.org/10.1016/j.surfcoat.2016.06.010>
72. Ganvir, A., Curry, N., Govindarajan, S., Markocsan, N.: Characterization of Thermal barrier coatings produced by various thermal spray techniques using solid powder, suspension, and solution precursor feedstock material. *Int. J. Appl. Ceram. Technol.* **13**(2), 324–332 (2016). <https://doi.org/10.1111/ijac.12472>
73. Su-ungkavatin, P., Tiruta-Barna, L., Hamelin, L.: Biofuels, electrofuels, electric or hydrogen?: a review of current and emerging sustainable aviation systems. *Prog. Energy Combust. Sci.* **96**, 101073 (2023). <https://doi.org/10.1016/j.peccs.2023.101073>
74. Cabrera, E., de Sousa, J.M.M.: Use of sustainable fuels in aviation—a review. *Energies* **15**(7), Art. no. 7 (2022). <https://doi.org/10.3390/en15072440>
75. Irimiea, C. et al.: ALTERNATE: Experimental and modeling study of soot formation in high-pressure kerosene and SAF combustion. In: Presented at the Towards Sustainable Aviation Summit 2022 (TSAS 2022) (2022). Accessed: 01 Mar 2023. [Online]. Available: <https://hal.science/hal-03943930>
76. Chen, W.R., Zhao, L.R.: Review—volcanic ash and its influence on aircraft engine components. *Proc. Eng.* **99**, 795–803 (2015). <https://doi.org/10.1016/j.proeng.2014.12.604>
77. Martin, R.V.: Satellite remote sensing of surface air quality. *Atmos. Environ.* **42**(34), 7823–7843 (2008). <https://doi.org/10.1016/j.atmosenv.2008.07.018>
78. Hoff, R.M., Christopher, S.A.: Remote sensing of particulate pollution from space: have we reached the promised land? *J. Air Waste Manag. Assoc.* **59**(6), 645–675 (2009). <https://doi.org/10.3155/1047-3289.59.6.645>
79. ‘Ambient (outdoor) air pollution’. [https://www.who.int/news-room/fact-sheets/detail/ambient-\(outdoor\)-air-quality-and-health](https://www.who.int/news-room/fact-sheets/detail/ambient-(outdoor)-air-quality-and-health) (Accessed 22 Feb 2023)
80. Nieto, A., Agrawal, R., Bravo, L., Hofmeister-Mock, C., Pepi, M., Ghoshal, A.: Calcium-magnesia-alumina-silicate (CMAS) attack mechanisms and roadmap towards Sandphobic thermal and environmental barrier coatings. *Int. Mater. Rev.* **66**(7), 451–492 (2021). <https://doi.org/10.1080/09506608.2020.1824414>
81. Donkelaar van, A., et al.: Global estimates of ambient fine particulate matter concentrations from satellite-based aerosol optical depth: development and application. *Environ. Health Perspect.* **118**(6), 847–855 (2010). <https://doi.org/10.1289/ehp.0901623>
82. Amato, F., et al.: Concentrations, sources and geochemistry of airborne particulate matter at a major European airport. *J. Environ. Monit.* **12**(4), 854–862 (2010). <https://doi.org/10.1039/B925439K>

83. Shahsavani, A., et al.: The evaluation of PM₁₀, PM_{2.5}, and PM₁ concentrations during the Middle Eastern Dust (MED) events in Ahvaz, Iran, from april through september 2010. *J. Arid Environ.* **77**, 72–83 (2012). <https://doi.org/10.1016/j.jaridenv.2011.09.007>
84. Amanollahi, J., Kaboodvandpour, S., Abdullah, A.M., Ramli, M.F.: Accuracy assessment of moderate resolution image spectroradiometer products for dust storms in semiarid environment. *Int. J. Environ. Sci. Technol.* **8**(2), 373–380 (2011). <https://doi.org/10.1007/BF03326224>
85. Altuwajjiri, A., Pirhadi, M., Kalafy, M., Alharbi, B., Sioutas, C.: Impact of different sources on the oxidative potential of ambient particulate matter PM₁₀ in Riyadh, Saudi Arabia: A focus on dust emissions. *Sci. Total Environ.* (2022). <https://doi.org/10.1016/j.scitotenv.2021.150590>
86. Amarloei, A., Fazlzadeh, M., Jafari, A.J., Zarei, A., Mazloomi, S.: Particulate matters and bioaerosols during Middle East dust storms events in Ilam, Iran. *Microchem. J.* **152**, 104280 (2020). <https://doi.org/10.1016/j.microc.2019.104280>
87. Tsiouri, V., Kakosimos, K.E., Kumar, P.: Concentrations, sources and exposure risks associated with particulate matter in the Middle East Area—A review. *Air Qual. Atmos. Health* **8**(1), 67–80 (2015). <https://doi.org/10.1007/s11869-014-0277-4>
88. Saliba, N.A., El Jam, F., El Tayar, G., Obeid, W., Roumie, M.: Origin and variability of particulate matter (PM₁₀ and PM_{2.5}) mass concentrations over an Eastern Mediterranean city. *Atmos. Res.* **97**(1), 106–114 (2010). <https://doi.org/10.1016/j.atmosres.2010.03.011>
89. Al-Zu'bi, A.: Evaluation of the Jordanian environmental legislations. *World Appl. Sci. J.* **14**(10), 1438–1444 (2011)
90. Al Katheri, E., Al Jallad, F., Al Omar, M.: Assessment of gaseous and particulate pollutants in the ambient air in Al Mirfa City, United Arab Emirates. *J. Environ. Protect.* **3**(7), 640–647 (2012)
91. Alexander, D.: Volcanic ash in the atmosphere and risks for civil aviation: a study in European crisis management. *Int. J. Disaster Risk Sci.* **4**(1), 9–19 (2013). <https://doi.org/10.1007/s13753-013-0003-0>
92. Bolić, T., Sivčev, Ž.: Eruption of Eyjafjallajökull in Iceland: experience of European air traffic management. *Transp. Res. Record* **2214**(1), 136–143 (2011). <https://doi.org/10.3141/2214-17>
93. Mazzocchi, M., Hansstein, F., Ragona, M.: The 2010 volcanic ash cloud and its financial impact on the European airline industry. In *CESifo Forum: IFO Institut für Wirtschaftsforschung an der Universität München* (pp. 92–100) (2010)
94. Ragona, M., Hannstein, F., Mazzocchi, M.: The financial impact of the volcanic ash crisis on the European airline industry. *Governing Disasters: The Challenges of Emergency Risk Regulation*, pp. 27–50 (2011)
95. Elghobashi, S.: An updated classification map of particle-laden turbulent flows. In *IUTAM Symposium on Computational Approaches to Multiphase Flow* (pp. 3–10). Springer (2006)
96. Elghobashi, S.: On predicting particle-laden turbulent flows. *Appl. Sci. Res.* **52**(4), 309–329 (1994). <https://doi.org/10.1007/BF00936835>
97. Bojdo, N., Filippone, A., Parkes, B., Clarkson, R.: Aircraft engine dust ingestion following sand storms. *Aeros. Sci. Technol.* **106**, 106072 (2020). <https://doi.org/10.1016/j.ast.2020.106072>
98. Bojdo, N.: *Rotorcraft Engine Air Particle Separation*. University of Manchester (2013)
99. Bojdo, N., Ellis, M., Filippone, A., Jones, M., Pawley, A.: Particle-vane interaction probability in gas turbine engines. *J. Turbomachinery* **141**(9) (2019). <https://doi.org/10.1115/1.4043953>
100. Bojdo, N., Filippone, A.: A simple model to assess the role of dust composition and size on deposition in rotorcraft engines. *Aerospace* **6**(4), Art. no. 4 (2019) <https://doi.org/10.3390/aerospace6040044>
101. Ellis, M., Bojdo, N., Filippone, A., Clarkson, R.: Monte Carlo predictions of aero-engine performance degradation due to particle ingestion. *Aerospace* **8**(6), Art. no. 6 (2021) <https://doi.org/10.3390/aerospace8060146>
102. Abdelouhab, S., Podor, R., Rapin, C., Toplis, M.J., Berthod, P., Vilasi, M.: Determination of Na₂O activities in silicate melts by EMF measurements. *J. Non-Crystalline Solids* **354**(26), Art. no. 26 (2008) <https://doi.org/10.1016/j.jnoncrysol.2007.12.003>

103. Craig, M., Ndamka, N.L., Wellman, R.G., Nicholls, J.R.: CMAS degradation of EB-PVD TBCs: the effect of basicity. *Surface Coatings Technol.* **270**, 145–153 (2015). <https://doi.org/10.1016/j.surfcoat.2015.03.009>
104. Phalippou, J.: Verres: aspects théoriques. *Techniques de l'ingénieur. Sci. Fondamentales* **7**(AF3600), AF3600–1 (2001)
105. Wu, Y., et al.: Comparison of CMAS corrosion and sintering induced microstructural characteristics of APS thermal barrier coatings. *J. Mater. Sci. Technol.* **35**(3), 440–447 (2019). <https://doi.org/10.1016/j.jmst.2018.09.046>
106. Ghosh, D., Chatterjee, A.: *Iron Making and Steelmaking: Theory and PRACTICE*. PHI Learning Pvt. Ltd (2008)
107. Petitjean, C., Panteix, P.-J., Rapin, C., Vilasi, M., Podor, R.: Electrochemical behavior of glass melts: application to corrosion processes. In: 2nd International summer school on nuclear glass wasteform: structure, Properties, and long-term behavior (SUMGLASS 2013), Angeli, F., Delaye, J.M., Schuller, S., Pinet, O., Rebiscoul, D., Gin, S., Peugeot, S., (eds.). *Procedia Materials Science*, vol. 7. pp. 101–110 (2014). <https://doi.org/10.1016/j.mspro.2014.10.014>
108. Chellah, N., Vidal-Setif, M.H., Petitjean, C., Panteix, P.J., Rapin, C., Vilasi, M.: Calcium-Magnesium-Alumino-Silicate (CMAS) degradation of thermal barrier coatings: solubility of different oxides from ZrO₂-Nd₂O₃ system in a model CMAS. Presented at the HTCPM8, Les Embiez (2012)
109. Bodsworth, C.: *HBB. Physical Chemistry of Iron and Steel Manufacture* (1972)
110. Jackson, R.W., Zaleski, E.M., Poerschke, D.L., Hazel, B.T., Begley, M.R., Levi, C.G.: Interaction of molten silicates with thermal barrier coatings under temperature gradients. *Acta Mater.* **89**, 396–407 (2015). <https://doi.org/10.1016/j.actamat.2015.01.038>
111. Engelbrecht, J.P., McDonald, E.V., Gillies, J.A., Jayanty, R.K.M., Casuccio, G., Gertler, A.W.: Characterizing mineral dusts and other aerosols from the middle east—part 1: ambient sampling. *Inhalation Toxicol.* **21**(4), 297–326 (2009). <https://doi.org/10.1080/08958370802464273>
112. Aygun, A., Vasiliev, A.L., Pature, N.P., Ma, X.: Novel thermal barrier coatings that are resistant to high-temperature attack by glassy deposits. *Acta Materialia* **55**(20), Art. no. 20 (2007) <https://doi.org/10.1016/j.actamat.2007.08.028>
113. Borom, M.P., Johnson, C.A., Peluso, L.A.: Role of environment deposits and operating surface temperature in spallation of air plasma sprayed thermal barrier coatings. *Surface Coatings Technol.* **86**, 116–126 (1996)
114. Krämer, S., Yang, J., Levi, C.G., Johnson, C.A.: Thermochemical interaction of thermal barrier coatings with molten CaO-MgO-Al₂O₃-SiO₂ (CMAS) deposits. *J. Am. Ceram. Soc.*, **89**(10), Art. no. 10 (2006) <https://doi.org/10.1111/j.1551-2916.2006.01209.x>
115. Morelli, S., et al.: CMAS corrosion of YSZ thermal barrier coatings obtained by different thermal spray processes. *J. Euro. Ceram. Soc.* **40**(12), 4084–4100 (2020). <https://doi.org/10.1016/j.jeurceramsoc.2020.04.058>
116. Wellman, R., Whitman, G., Nicholls, J.R.: CMAS corrosion of EB PVD TBCs: Identifying the minimum level to initiate damage. *Int. J. Refractory Metals Hard Mater.* **28**(1), Art. no. 1 (2010) <https://doi.org/10.1016/j.ijrmhm.2009.07.005>
117. Vidal-Sétif, M.H., Rio, C., Boivin, D., Lavigne, O.: Microstructural characterization of the interaction between 8YPSZ (EB-PVD) thermal barrier coatings and a synthetic CAS. *Surface Coatings Technol.* **239**, 41–48 (2014). <https://doi.org/10.1016/j.surfcoat.2013.11.014>
118. Wilke, B.M., Duke, B.J., Jimoh, W.L.O.: Mineralogy and chemistry of harmattan dust in Northern Nigeria. *CATENA* **11**(1), 91–96 (1984). [https://doi.org/10.1016/S0341-8162\(84\)80009-0](https://doi.org/10.1016/S0341-8162(84)80009-0)
119. Goudie, A.S.: Dust storms and their geomorphological implications. *J. Arid Environ.* **1**(4), 291–311 (1978). [https://doi.org/10.1016/S0140-1963\(18\)31712-9](https://doi.org/10.1016/S0140-1963(18)31712-9)
120. Taylor, H.E., Lichte, F.E.: Chemical composition of Mount St. Helens volcanic ash. *Geophys. Res. Lett.* **7**(11), 949–952 (1980). <https://doi.org/10.1029/GL007i011p00949>
121. Rai, A.K., Bhattacharya, R.S., Wolfe, D.E., Eden, T.J.: CMAS-resistant thermal barrier coatings (TBC): CMAS-resistant thermal barrier coatings. *Int. J. Appl. Ceram. Technol.* **7**(5), Art. no. 5 (2009) <https://doi.org/10.1111/j.1744-7402.2009.02373.x>

122. Braue, W.: Environmental stability of the YSZ layer and the YSZ/TGO interface of an in-service EB-PVD coated high-pressure turbine blade. *J. Mater. Sci.* **44**(7), 1664–1675 (2009). <https://doi.org/10.1007/s10853-008-3215-8>
123. Fang, H. et al.: Comparative study on failure behavior of promising CMAS-resistant plasma-sprayed thermal barrier coatings in burner rig test with/without CMAS deposition. *Ceram. Int.* (2022) <https://doi.org/10.1016/j.ceramint.2022.12.099>
124. Ndamka, N.L., Wellman, R.G., Nicholls, J.R.: The degradation of thermal barrier coatings by molten deposits: introducing the concept of basicity. *Mater. High Temp.* **33**(1), Art. no. 1 (2016) <https://doi.org/10.1179/1878641315Y.0000000017>
125. Perrudin, F.: Étude de la dissolution de diverses terres rares dans des liquides silicatés (CMAS) de composition variable: contribution au développement des barrières thermiques en ZRO₂-RE₂O₃ (RE=La-Lu). Université de Lorraine (2018)
126. Stott, F.H., De Wet, D.J., Taylor, R.: Degradation of thermal-barrier coatings at very high temperatures. *MRS Bull.* **19**(10), Art. no. 10 (1994)
127. Svancarek, P., et al.: A comparison of the microstructure and mechanical properties of two liquid phase sintered aluminas containing different molar ratios of calcia–silica sintering additives. *J. Euro. Ceram. Soc.* **24**(12), 3453–3463 (2004). <https://doi.org/10.1016/j.jeurceramsoc.2003.10.032>
128. Poerschke, D.L., Barth, T.L., Levi, C.G.: Equilibrium relationships between thermal barrier oxides and silicate melts. *Acta Mater.* **120**, 302–314 (2016). <https://doi.org/10.1016/j.actamat.2016.08.077>
129. Poerschke, D.L., Jackson, R.W., Levi, C.G.: Silicate deposit degradation of engineered coatings in gas turbines: progress toward models and materials solutions. *Annu. Rev. Mater. Res.*, **47**(1), Art. no. 1 (2017) <https://doi.org/10.1146/annurev-matsci-010917-105000>
130. Perrudin, F., Vidal-Sétif, M.H., Rio, C., Petitjean, C., Panteix, P.J., Vilasi, M.: Influence of rare earth oxides on kinetics and reaction mechanisms in CMAS silicate melts. *J. Euro. Ceram. Soc.* **39**(14), Art. no. 14 (2019) <https://doi.org/10.1016/j.jeurceramsoc.2019.06.036>
131. Levi, C.G., Hutchinson, J.W., Vidal-Sétif, M.-H., Johnson, C.A.: Environmental degradation of thermal-barrier coatings by molten deposits. *MRS Bull.* **37**(10), Art. no. 10 (2012) <https://doi.org/10.1557/mrs.2012.230>
132. Mercer, C., Faulhaber, S., Evans, A.G., Darolia, R.: A delamination mechanism for thermal barrier coatings subject to calcium–magnesium–alumino–silicate (CMAS) infiltration. *Acta Materialia* **53**(4), Art. no. 4 (2005) <https://doi.org/10.1016/j.actamat.2004.11.028>
133. Chen, X.: Calcium–magnesium–alumina–silicate (CMAS) delamination mechanisms in EB-PVD thermal barrier coatings. *Surface Coatings Technol.* **200**(11), 3418–3427 (2006). <https://doi.org/10.1016/j.surfcoat.2004.12.029>
134. Evans, A.G., Hutchinson, J.W.: The mechanics of coating delamination in thermal gradients. *Surface Coatings Technol.* **201**(18), 7905–7916 (2007). <https://doi.org/10.1016/j.surfcoat.2007.03.029>
135. Vogel, A., Clarkson, R., Durant, A., Cassiani, M., Stohl, A.: Volcanic ash ingestion by a large gas turbine aeroengine: fan-particle interaction, EPSC2016–15419 (2016)
136. Taltavull, C., Dean, J., Clyne, T.W.: Adhesion of volcanic ash particles under controlled conditions and implications for their deposition in gas turbines. *Adv. Eng. Mater.* **18**(5), 803–813 (2016). <https://doi.org/10.1002/adem.201500371>
137. Holgate, C.S., Seward, G.G.E., Ericks, A.R., Poerschke, D.L., Levi, C.G.: Dissolution and diffusion kinetics of yttria-stabilized zirconia into molten silicates. *J. Euro. Ceram. Soc.* **41**(3), 1984–1994 (2021). <https://doi.org/10.1016/j.jeurceramsoc.2020.10.056>
138. Strangman, T., Raybould, D., Jameel, A., Baker, W.: Damage mechanisms, life prediction, and development of EB-PVD thermal barrier coatings for turbine airfoils. *Surface Coatings Technol.*, **202**(4–7), Art. no. 4–7 (2007) <https://doi.org/10.1016/j.surfcoat.2007.06.067>
139. VanValzah, J.R., Eaton, H.E.: Cooling rate effects on the tetragonal to monoclinic phase transformation in aged plasma-sprayed yttria partially stabilized zirconia. *Surface Coatings Technol.*, **46**(3), Art. no. 3 (1991) [https://doi.org/10.1016/0257-8972\(91\)90171-R](https://doi.org/10.1016/0257-8972(91)90171-R)

140. Krämer, S. et al.: Mechanisms of cracking and delamination within thick thermal barrier systems in aero-engines subject to calcium-magnesium-alumino-silicate (CMAS) penetration. *Mater. Sci. Eng.: A* **490**(1–2), Art. no. 1–2 (2008) <https://doi.org/10.1016/j.msea.2008.01.006>
141. Vidal-Setif, M.H., Chellah, N., Rio, C., Sanchez, C., Lavigne, O.: Calcium–magnesium–alumino-silicate (CMAS) degradation of EB-PVD thermal barrier coatings: characterization of CMAS damage on ex-service high pressure blade TBCs. *Surface Coatings Technol.* **208**, 39–45 (2012). <https://doi.org/10.1016/j.surfcoat.2012.07.074>
142. A. D. Gledhill, K. M. Reddy, J. M. Drexler, K. Shinoda, S. Sampath, and N. P. Padture, ‘Mitigation of damage from molten fly ash to air-plasma-sprayed thermal barrier coatings’, *Materials Science and Engineering: A*, vol. 528, no. 24, Art. no. 24, Sep. 2011, doi: <https://doi.org/10.1016/j.msea.2011.06.041>.
143. Stott, F.H., Taylor, R., de Wet, D.J.: The effects of molten silicate deposits on the stability of thermal barrier coatings for turbine applications at very high temperatures. In: *Proceedings of Advanced Materials* (1992)
144. Krause, A.R., Garces, H.F., Dwivedi, G., Ortiz, A.L., Sampath, S., Padture, N.P.: Calcium-magnesia-alumino-silicate (CMAS)-induced degradation and failure of air plasma sprayed yttria-stabilized zirconia thermal barrier coatings. *Acta Mater.* **105**, 355–366 (2016). <https://doi.org/10.1016/j.actamat.2015.12.044>
145. Kim, J., Dunn, M.G., Baran, A.J., Wade, D.P., Tremba, E.L.: Deposition of volcanic materials in the hot sections of two gas turbine engines. *J. Eng. Gas Turbines Power* **115**(3), 641–651 (1993). <https://doi.org/10.1115/1.2906754>
146. Döring, F., Staudacher, S., Koch, C., Weißschuh, M.: Modeling particle deposition effects in aircraft engine compressors. *J. Turbomachinery* **139**(5) (2017). <https://doi.org/10.1115/1.4035072>
147. Clarkson, R., Simpson, H.: Maximising airspace use during volcanic eruptions: matching engine durability against ash cloud occurrence. In: *Proceedings of the NATO STO AVT-272 Specialists Meeting on: Impact of Volcanic Ash Clouds on Military Operations*, pp. 15–17. Vilnius, Lithuania (2017)
148. Clarkson, R.J., Majewicz, E.J., Mack, P.: A re-evaluation of the 2010 quantitative understanding of the effects volcanic ash has on gas turbine engines. *Proc. Inst. Mech. Eng. Part G: J. Aero. Eng.* **230**(12), 2274–2291 (2016). <https://doi.org/10.1177/0954410015623372>
149. Li, D., Jiang, P., Gao, R., Sun, F., Jin, X., Fan, X.: Experimental and numerical investigation on the thermal and mechanical behaviours of thermal barrier coatings exposed to CMAS corrosion. *J. Adv. Ceram.* **10**(3), 551–564 (2021). <https://doi.org/10.1007/s40145-021-0457-2>
150. Shan, X., et al.: Buckling failure in air-plasma sprayed thermal barrier coatings induced by molten silicate attack. *Scripta Mater.* **113**, 71–74 (2016). <https://doi.org/10.1016/j.scriptamat.2015.09.029>
151. Chen, X., Wang, R., Yao, N., Evans, A.G., Hutchinson, J.W., Bruce, R.W.: Foreign object damage in a thermal barrier system: mechanisms and simulations. *Mater. Sci. Eng.: A* **352**(1–2), Art. no. 1–2 (2003) [https://doi.org/10.1016/S0921-5093\(02\)00905-X](https://doi.org/10.1016/S0921-5093(02)00905-X)
152. Zhang, G., Fan, X., Xu, R., Su, L., Wang, T.J.: Transient thermal stress due to the penetration of calcium-magnesium-alumino-silicate in EB-PVD thermal barrier coating system. *Ceram. Int.* **44**(11), 12655–12663 (2018). <https://doi.org/10.1016/j.ceramint.2018.04.065>
153. Peng, H., Wang, L., Guo, L., Miao, W., Guo, H., Gong, S.: Degradation of EB-PVD thermal barrier coatings caused by CMAS deposits. *Progress Natl. Sci.: Mater. Int.* **22**(5), Art. no. 5 (2012) <https://doi.org/10.1016/j.pnsc.2012.06.007>
154. Guo, L., Li, G., Gan, Z.: Effects of surface roughness on CMAS corrosion behavior for thermal barrier coating applications. *J. Adv. Ceram.* **10**(3), 472–481 (2021). <https://doi.org/10.1007/s40145-020-0449-7>
155. Ndamka, N.L.: *Microstructural damage of thermal barrier coatings due to CMAS*. Cranfield University (2013)
156. Mahade, S., Curry, N., Björklund, S., Markocsan, N., Nylén, P.: Failure analysis of Gd2Zr2O7/YSZ multi-layered thermal barrier coatings subjected to thermal cyclic fatigue. *J. Alloys Compounds* **689**, 1011–1019 (2016). <https://doi.org/10.1016/j.jallcom.2016.07.333>

157. Evans, A.G., Mumm, D.R., Hutchinson, J.W., Meier, G.H., Pettit, F.S.: Mechanisms controlling the durability of thermal barrier coatings. *Progress Mater. Sci.* **46**(5), Art. no. 5 (2001)
158. Dryepondt, S., Porter, J.R., Clarke, D.R.: On the initiation of cyclic oxidation-induced rumpling of platinum-modified nickel aluminide coatings. *Acta Mater.* **57**(6), 1717–1723 (2009). <https://doi.org/10.1016/j.actamat.2008.12.015>
159. Spitsberg, I.T., Mumm, D.R., Evans, A.G.: On the failure mechanisms of thermal barrier coatings with diffusion aluminide bond coatings. *Mater. Sci. Eng. A* **394**(1), 176–191 (2005). <https://doi.org/10.1016/j.msea.2004.11.038>
160. Tolpygo, V.K., Clarke, D.R.: Surface rumpling of a (Ni, Pt)Al bond coat induced by cyclic oxidation. *Acta Mater.* **48**(13), 3283–3293 (2000). [https://doi.org/10.1016/S1359-6454\(00\)00156-7](https://doi.org/10.1016/S1359-6454(00)00156-7)
161. Ruud, J.A., Bartz, A., Borom, M.P., Johnson, C.A.: Strength degradation and failure mechanisms of electron-beam physical-vapor-deposited thermal barrier coatings. *J. Am. Ceramic Soc.* **84**(7), 1545–1552 (2001). <https://doi.org/10.1111/j.1151-2916.2001.tb00875.x>
162. Giggins, C.S., Kear, B.H., Pettit, F.S., Tien, J.K.: Factors affecting adhesion of oxide scales on alloys. *Metall. Trans. B* **5**(7), 1685–1688 (1974). <https://doi.org/10.1007/BF02646343>
163. Evans, H.E.: Modelling oxide spallation. *Mater. High Temperatures* **12**(2–3), 219–227 (1994). <https://doi.org/10.1080/09603409.1994.11689489>
164. Tolpygo, V.K., Clarke, D.R.: On the rumpling mechanism in nickel-aluminide coatings: part II: characterization of surface undulations and bond coat swelling. *Acta Mater.* **52**(17), 5129–5141 (2004). <https://doi.org/10.1016/j.actamat.2004.07.023>
165. Tolpygo, V.K., Clarke, D.R., Murphy, K.S.: Oxidation-induced failure of EB-PVD thermal barrier coatings. *Surface Coatings Technol* **146–147**, 124–131 (2001). [https://doi.org/10.1016/S0257-8972\(01\)01482-7](https://doi.org/10.1016/S0257-8972(01)01482-7)
166. Zhao, H., Yu, Z., Wadley, H.N.G.: The influence of coating compliance on the delamination of thermal barrier coatings. *Surface Coatings Technol* **204**(15), 2432–2441 (2010). <https://doi.org/10.1016/j.surfcoat.2010.01.018>
167. Dong, H., Yang, G.-J., Cai, H.-N., Ding, H., Li, C.-X., Li, C.-J.: The influence of temperature gradient across YSZ on thermal cyclic lifetime of plasma-sprayed thermal barrier coatings. *Ceramics Int., Part A* **41**(9), 11046–11056 (2015) <https://doi.org/10.1016/j.ceramint.2015.05.049>
168. Zhu, D., Miller, R.A.: Determination of creep behavior of thermal barrier coatings under laser imposed high thermal and stress gradient conditions. *J. Mater. Res.* **14**(1), 146–161 (1999). <https://doi.org/10.1557/JMR.1999.0023>
169. Vaßen, R., Kagawa, Y., Subramanian, R., Zombo, P., Zhu, D.: Testing and evaluation of thermal-barrier coatings. *MRS Bull.* **37**(10), 911–916 (2012). <https://doi.org/10.1557/mrs.2012.235>
170. Musalek, R., Tesar, T., Medricky, J., Lukac, F., Lima, R.S.: High-temperature cycling of plasma sprayed multilayered NiCrAlY/YSZ/GZO/YAG thermal barrier coatings prepared from liquid feedstocks. *J. Therm. Spray Tech.* **30**(1), 81–96 (2021). <https://doi.org/10.1007/s11666-020-01107-5>
171. Zhu, D., Miller, R.A.: Thermal conductivity and elastic modulus evolution of thermal barrier coatings under high heat flux conditions. *J. Therm. Spray Tech.* **9**(2), 175–180 (2000). <https://doi.org/10.1361/105996300770349890>
172. Nies, D., Pulz, R., Glaubitz, S., Finn, M., Rehmer, B., Skrotzki, B.: Testing of thermal barrier coatings by laser excitation. *Adv. Eng. Mater.* **12**(12), 1224–1229 (2010). <https://doi.org/10.1002/adem.201000212>
173. Wu, Y., et al.: Laser thermal gradient testing and fracture mechanics study of a thermal barrier coating. *J. Therm. Spray Tech.* **28**(6), 1239–1251 (2019). <https://doi.org/10.1007/s11666-019-00879-9>
174. Gentleman, M.M., Eldridge, J.I., Zhu, D.M., Murphy, K.S., Clarke, D.R.: Non-contact sensing of TBC/BC interface temperature in a thermal gradient. *Surface Coatings Technol.* **201**(7), 3937–3941 (2006). <https://doi.org/10.1016/j.surfcoat.2006.08.102>

175. Jackson, R.W., Zaleski, E.M., Hazel, B.T., Begley, M.R., Levi, C.G.: Response of molten silicate infiltrated Gd₂Zr₂O₇ thermal barrier coatings to temperature gradients. *Acta Mater.* **132**, 538–549 (2017). <https://doi.org/10.1016/j.actamat.2017.03.081>
176. Yang, L., Zhou, Y.C., Mao, W.G., Lu, C.: Real-time acoustic emission testing based on wavelet transform for the failure process of thermal barrier coatings. *Appl. Phys. Lett.* **93**(23), 231906 (2008). <https://doi.org/10.1063/1.3043458>
177. Wang, H., Dinwiddie, R.B.: Characterization of thermal barrier coatings using thermal methods. *Adv. Eng. Mater.* **3**(7), 465–468 (2001). [https://doi.org/10.1002/1527-2648\(200107\)3:7%3c465::AID-ADEM465%3e3.0.CO;2-G](https://doi.org/10.1002/1527-2648(200107)3:7%3c465::AID-ADEM465%3e3.0.CO;2-G)
178. Voyer, J., Gitzhofer, F., Boulos, M.I.: Study of the performance of TBC under thermal cycling conditions using an acoustic emission rig. *J. Therm. Spray Tech.* **7**(2), 181–190 (1998). <https://doi.org/10.1361/105996398770350909>
179. Traeger, F., Vaßen, R., Rauwald, K.-H., Stöver, D.: Thermal cycling setup for testing thermal barrier coatings. *Adv. Eng. Mater.* **5**(6), 429–432 (2003). <https://doi.org/10.1002/adem.200300337>
180. Zhu, W., Li, Z.Y., Yang, L., Zhou, Y.C., Wei, J.F.: Real-time detection of CMAS corrosion failure in aps thermal barrier coatings under thermal shock. *Exp. Mech.* **60**(6), 775–785 (2020). <https://doi.org/10.1007/s11340-020-00603-7>
181. Steinke, T., Sebold, D., Mack, D.E., Vaßen, R., Stöver, D.: A novel test approach for plasma-sprayed coatings tested simultaneously under CMAS and thermal gradient cycling conditions. *Surface Coatings Technol.* **205**(7), 2287–2295 (2010). <https://doi.org/10.1016/j.surfcoat.2010.09.008>
182. Fox, D.S., Miller, R.A., Zhu, D., Perez, M., Cuy, M.D., Robinson, R.C.: Mach 0.3 Burner Rig Facility at the NASA Glenn Materials Research Laboratory. E-17628 (2011)
183. Vaßen, R. et al.: Recent activities in the field of thermal barrier coatings including burner rig testing in the European Union. *Adv. Eng. Mater.*, **10**(10), Art. no. 10 (2008) <https://doi.org/10.1002/adem.200800015>
184. Maurel, V. et al.: Recent Progress in local characterization of damage evolution in thermal barrier coating under thermal cycling. In: Superalloys 2020, Tin, S., Hardy, M., Clews, J., Cormier, J., Feng, Q., Marcin, J., O'Brien, C., Suzuki, A. (eds.) *The Minerals, Metals and Materials Series*, pp. 813–823. Cham, Springer International Publishing (2020) https://doi.org/10.1007/978-3-030-51834-9_80
185. Mumm, D.R., Watanabe, M., Evans, A.G., Pfaendtner, J.A.: The influence of test method on failure mechanisms and durability of a thermal barrier system. *Acta Mater.* **52**(5), 1123–1131 (2004). <https://doi.org/10.1016/j.actamat.2003.10.045>
186. Eldridge, J.I., Spuckler, C.M., Street, K.W., Markham, J.R.: Infrared radiative properties of yttria-stabilized zirconia thermal barrier coatings. In 26th Annual Conference on Composites, Advanced Ceramics, Materials, and Structures: Ceramic Engineering and Science Proceedings, pp. 417–430. Wiley (2002)
187. Demasi, J.T., Ortiz, M.: Thermal barrier coating life prediction model development, phase 1', NASA-CR-182230 (1989). Accessed 15 Sep 2022. [Online]. Available: <https://ntrs.nasa.gov/citations/19900004072>
188. Berndt, C.C., et al.: Current problems in plasma spray processing. *JTST* **1**(4), 341–356 (1992). <https://doi.org/10.1007/BF02647162>
189. Shinozaki, M., Roberts, K.A., van de Goor, B., Clyne, T.W.: Deposition of ingested volcanic ash on surfaces in the turbine of a small jet engine. *Adv. Eng. Mater.* **15**(10), 986–994 (2013). <https://doi.org/10.1002/adem.201200357>
190. Fox, D.S. et al.: Natural gas/oxygen burner rig at the NASA glenn materials research laboratory. E-20020 (2022)
191. Gildersleeve, E., Viswanathan, V., Sampath, S.: Molten silicate interactions with plasma sprayed thermal barrier coatings: Role of materials and microstructure. *J. Euro. Ceramic Soc.* **39**(6), 2122–2131 (2019). <https://doi.org/10.1016/j.jeurceramsoc.2019.01.023>
192. Mack, D.E., Wobst, T., Jarligo, M.O.D., Sebold, D., Vaßen, R.: Lifetime and failure modes of plasma sprayed thermal barrier coatings in thermal gradient rig tests with simultaneous

- CMAS injection. *Surface Coatings Technol.* **324**, 36–47 (2017). <https://doi.org/10.1016/j.surfcoat.2017.04.071>
193. Mauget, F., Hamon, F., Morisset, M., Cormier, J., Riallant, F., Mendez, J.: Damage mechanisms in an EB-PVD thermal barrier coating system during TMF and TGMF testing conditions under combustion environment. *Int. J. Fatigue* **99**, 225–234 (2017). <https://doi.org/10.1016/j.ijfatigue.2016.08.001>
 194. Despres, L.: Comportement en fatigue thermomécanique à haute température d'un système barrière thermique texturé par laser. Université Bourgogne Franche-Comté (2020)
 195. Wang, T. et al.: Corrosion behavior of air plasma spraying zirconia-based thermal barrier coatings subject to Calcium–Magnesium–Aluminum–Silicate (CMAS) via burner rig test. *Ceramics Int. Part B*, **46**(11), 18698–18706 (2020) <https://doi.org/10.1016/j.ceramint.2020.04.184>
 196. Jana, P., Jayan, P.S., Mandal, S., Biswas, K.: Thermal cycling life and failure analysis of rare earth magnesium hexaaluminate based advanced thermal barrier coatings at 1400°C. *Surface Coatings Technol.* **328**, 398–409 (2017). <https://doi.org/10.1016/j.surfcoat.2017.09.019>
 197. Naraparaju, R., et al.: Integrated testing approach using a customized micro turbine for a volcanic ash and CMAS related degradation study of thermal barrier coatings. *Surface Coatings Technol.* **337**, 198–208 (2018). <https://doi.org/10.1016/j.surfcoat.2018.01.030>
 198. Vaßen, R., et al.: Performance of YSZ and Gd₂Zr₂O₇/YSZ double layer thermal barrier coatings in burner rig tests. *J. Euro. Ceramic Soc.* **40**(2), 480–490 (2020). <https://doi.org/10.1016/j.jeurceramsoc.2019.10.021>
 199. Vaßen, R.: Entwicklung neuer oxidischer Wärmedämmschichten für Anwendungen in stationären und Flug-Gasturbinen. Forschungszentrum Jülich GmbH (2004)
 200. Drexler, J.M., Aygun, A., Li, D., Vaßen, R., Steinke, T., Pature, N.P.: Thermal-gradient testing of thermal barrier coatings under simultaneous attack by molten glassy deposits and its mitigation. *Surface Coatings Technol.* **204**(16), 2683–2688 (2010). <https://doi.org/10.1016/j.surfcoat.2010.02.026>
 201. Kumar, N., Mahade, S., Ganvir, A., Joshi, S.: Understanding the influence of microstructure on hot corrosion and erosion behavior of suspension plasma sprayed thermal barrier coatings. *Surface Coatings Technol.* **419**, 127306 (2021). <https://doi.org/10.1016/j.surfcoat.2021.127306>
 202. Mahade, S.: Functional Performance of Gadolinium Zirconate/Yttria Stabilized Zirconia Multi-Layered Thermal Barrier Coatings (2018)
 203. Levi, C.G.: Emerging materials and processes for thermal barrier systems. *Curr. Opinion Solid State Mater. Sci.*, **8**(1), Art. no. 1 (2004) <https://doi.org/10.1016/j.cossms.2004.03.009>
 204. Mauer, G., Jarligo, M.O., Mack, D.E., Vaßen, R.: Plasma-sprayed thermal barrier coatings: new materials, processing issues, and solutions. *J. Therm. Spray Technol.*, **22**(5), Art. no. 5 (2013) <https://doi.org/10.1007/s11666-013-9889-8s>
 205. Vaßen, R., Jarligo, M.O., Steinke, T., Mack, D.E., Stöver, D.: Overview on advanced thermal barrier coatings. *Surface Coatings Technol.* **205**(4), 938–942 (2010). <https://doi.org/10.1016/j.surfcoat.2010.08.151>
 206. Winter, M.R., Clarke, D.R.: Oxide materials with low thermal conductivity. *J. Am. Ceramic Soc.*, **90**(2), Art. no. 2 (2007) <https://doi.org/10.1111/j.1551-2916.2006.01410.x>
 207. Pragatheeswaran, A., et al.: Plasma spray-deposited lanthanum phosphate coatings for protection against molten uranium corrosion. *Surface Coatings Technol.* **265**, 166–173 (2015). <https://doi.org/10.1016/j.surfcoat.2015.01.040>
 208. Vaßen, R., Bakan, E., Mack, D.E., Guillon, O.: A perspective on thermally sprayed thermal barrier coatings: current status and trends. *J. Therm. Spray Tech.* **31**(4), 685–698 (2022). <https://doi.org/10.1007/s11666-022-01330-2>
 209. Bakan, E., Vaßen, R.: Ceramic top coats of plasma-sprayed thermal barrier coatings: materials, processes, and properties. *J. Therm. Spray Tech.* **26**(6), Art. no. 6 (2017) <https://doi.org/10.1007/s11666-017-0597-7>
 210. Xu, L., Wang, H., Su, L., Lu, D., Peng, K., Gao, H.: A new class of high-entropy fluorite oxides with tunable expansion coefficients, low thermal conductivity and exceptional sintering

- resistance. *J. Euro. Ceramic Soc.* **41**(13), 6670–6676 (2021). <https://doi.org/10.1016/j.jeurceramsoc.2021.05.043>
211. Song, D., et al.: Glass-like thermal conductivity in mass-disordered high-entropy (Y, Yb)₂(Ti, Zr, Hf)₂O₇ for thermal barrier material. *Mater. Des.* **210**, 110059 (2021). <https://doi.org/10.1016/j.matdes.2021.110059>
212. Zhu, D.: Design and performance optimizations of advanced erosion-resistant low conductivity thermal barrier coatings for rotorcraft engines (2012)
213. Schlegel, N., Sebold, D., Sohn, Y.J., Mauer, G., Vaßen, R.: Cycling performance of a columnar-structured complex perovskite in a temperature gradient test. *J. Therm. Spray Technol.* **24**(7), Art. no. 7 (2015). <https://doi.org/10.1007/s11666-015-0254-y>
214. Zhu, D., Nesbitt, J.A., Mccue, T.R., Barrett, C.A., Miller, R.A.: Furnace cyclic behavior of plasma-sprayed zirconia–yttria and multi-component rare earth oxide doped thermal barrier coatings. In 26th Annual Conference on Composites, Advanced Ceramics, Materials, and Structures: B: Ceramic Engineering and Science Proceedings, pp. 533–545. Wiley (2002). <https://doi.org/10.1002/9780470294758.ch59>
215. Vassen, R., Traeger, F., Stöver, D.: New thermal barrier coatings based on Pyrochlore/YSZ double-layer systems. *Int. J. Appl. Ceramic Technol.* **1**(4), 351–361 (2004)
216. Schulz, U., Braue, W.: Degradation of La₂Zr₂O₇ and other novel EB-PVD thermal barrier coatings by CMAS (CaO–MgO–Al₂O₃–SiO₂) and volcanic ash deposits. *Surface Coatings Technol.* **235**, 165–173 (2013). <https://doi.org/10.1016/j.surfcoat.2013.07.029>
217. Drexler, J.M., Ortiz, A.L., Padture, N.P.: Composition effects of thermal barrier coating ceramics on their interaction with molten Ca–Mg–Al–silicate (CMAS) glass. *Acta Mater.* **60**(15), 5437–5447 (2012). <https://doi.org/10.1016/j.actamat.2012.06.053>
218. Ahlborg, N.L., Zhu, D.: Calcium–magnesium aluminosilicate (CMAS) reactions and degradation mechanisms of advanced environmental barrier coatings. *Surface Coatings Technol.* **237**, 79–87 (2013). <https://doi.org/10.1016/j.surfcoat.2013.08.036>
219. Xia, J., et al.: On the resistance of rare earth oxide-doped YSZ to high temperature volcanic ash attack. *Surface Coatings Technol.* **307**, 534–541 (2016). <https://doi.org/10.1016/j.surfcoat.2016.09.033>
220. Gok, M.G., Goller, G.: Microstructural characterization of GZ/CYSZ thermal barrier coatings after thermal shock and CMAS+hot corrosion test. *J. Euro. Ceramic Soc.*, (2017) <https://doi.org/10.1016/j.jeurceramsoc.2017.02.004>
221. Nieto, A., et al.: Layered, composite, and doped thermal barrier coatings exposed to sand laden flows within a gas turbine engine: Microstructural evolution, mechanical properties, and CMAS deposition. *Surface Coatings Technol.* **349**, 1107–1116 (2018). <https://doi.org/10.1016/j.surfcoat.2018.05.089>
222. Lashmi, P.G. et al.: Solution combustion synthesis of calcia-magnesia-aluminosilicate powder and its interaction with yttria-stabilized zirconia and co-doped yttria-stabilized zirconia. *Ceramics Int.*, **45**(15), Art. no. 15 (2019) <https://doi.org/10.1016/j.ceramint.2019.06.036>
223. Poerschke, D.L., Levi, C.G.: Effects of cation substitution and temperature on the interaction between thermal barrier oxides and molten CMAS. *J. Euro. Ceramic Soc.* **35**(2), 681–691 (2015). <https://doi.org/10.1016/j.jeurceramsoc.2014.09.006>
224. Mechnich, P., Braue, W.: Volcanic ash-induced decomposition of EB-PVD Gd₂Zr₂O₇ thermal barrier coatings to Gd-oxyapatite, zircon, and Gd, Fe-zirconolite. *J. Am. Ceramic Soc.* **96**(6), 1958–1965 (2013). <https://doi.org/10.1111/jace.12251>
225. Kumar, R., Cietek, D., Jiang, C., Roth, J., Gell, M., Jordan, E.H.: Influence of microstructure on the durability of gadolinium zirconate thermal barrier coatings using APS and SPSS processes. *Surface Coatings Technol.* **337**, 117–125 (2018). <https://doi.org/10.1016/j.surfcoat.2018.01.004>
226. Levi, C.G.: Science underpinning TBC design for durability in aggressive environments. DTIC (2008)
227. Dolmaire, A., et al.: Reaction mechanisms of Gd₂Zr₂O₇ in silicate melts derived from CAS. *J. Euro. Ceramic Soc.* **42**(15), 7247–7257 (2022). <https://doi.org/10.1016/j.jeurceramsoc.2022.08.051>

228. Yang, S., Song, W., Lavallee, Y., Zhou, X., Dingwell, D.B., Guo, H.: Dynamic spreading of re-melted volcanic ash bead on thermal barrier coatings. *Corrosion Sci.* **170**, 108659 (2020). <https://doi.org/10.1016/j.corsci.2020.108659>
229. Song, W., Guo, H.: CMAS dilemma in jet engines: beginning or ending? *matlab*, pp. 220042–4 (2022) <https://doi.org/10.54227/mlab.20220042>
230. Leckie, R.M., Krämer, S., Rühle, M., Levi, C.G.: Thermochemical compatibility between alumina and ZrO₂–GdO₃/2 thermal barrier coatings. *Acta Mater.* **53**(11), 3281–3292 (2005). <https://doi.org/10.1016/j.actamat.2005.03.035>
231. Munawar, A.U., Schulz, U., Cerri, G., Lau, H.: Microstructure and cyclic lifetime of Gd and Dy-containing EB-PVD TBCs deposited as single and double-layer on various bond coats. *Surface Coatings Technol.* **245**, 92–101 (2014). <https://doi.org/10.1016/j.surfcoat.2014.02.047>
232. Schmitt, M.P., Rai, A.K., Bhattacharya, R., Zhu, D., Wolfe, D.E.: Multilayer thermal barrier coating (TBC) architectures utilizing rare earth doped YSZ and rare earth pyrochlores. *Surface Coatings Technol.* **251**, 56–63 (2014). <https://doi.org/10.1016/j.surfcoat.2014.03.049>
233. Mahade, S., Curry, N., Björklund, S., Markocsan, N., Nylén, P., Vaßen, R.: Erosion performance of gadolinium zirconate-based thermal barrier coatings processed by suspension plasma spray. *J. Therm. Spray Technol.* **26**(1–2), 108–115 (2017). <https://doi.org/10.1007/s11666-016-0479-4>
234. Mahade, S., Curry, N., Björklund, S., Markocsan, N., Nylén, P., Vaßen, R.: Functional performance of Gd₂Zr₂O₇/YSZ multi-layered thermal barrier coatings deposited by suspension plasma spray. *Surface Coatings Technol.* (2016) <https://doi.org/10.1016/j.surfcoat.2016.12.062>
235. Mahade, S., Curry, N., Jonnalagadda, K.P., Peng, R.L., Markocsan, N., Nylén, P.: Influence of YSZ layer thickness on the durability of gadolinium zirconate/YSZ double-layered thermal barrier coatings produced by suspension plasma spray. *Surface Coatings Technol.* **357**, 456–465 (2019). <https://doi.org/10.1016/j.surfcoat.2018.10.046>
236. Morelli, S., Bursich, S., Testa, V., Bolelli, G., Miccichè, A., Lusvardi, L.: CMAS corrosion and thermal cycling fatigue resistance of alternative thermal barrier coating materials and architectures: a comparative evaluation. *Surface Coatings Technol.* **439**, 128433 (2022). <https://doi.org/10.1016/j.surfcoat.2022.128433>
237. Zhou, D., et al.: Thermal cycling performances of multilayered yttria-stabilized zirconia/gadolinium zirconate thermal barrier coatings. *J. Am. Ceramic Soc.* **103**(3), 2048–2061 (2020). <https://doi.org/10.1111/jace.16862>
238. Hasz, W.C., Borom, M.P., Johnson, C.A.: Protected thermal barrier coating composite with multiple coatings. US6261643B1, Jul. 17, 2001 Accessed 26 Jun 2018. [Online]. Available: <https://patents.google.com/patent/US6261643B1/en>
239. Bianchi, L., Joulia, A., Bernard, B.D.R.J.: Revêtement anti-cmas a efficace renforcee. FR3067391A1, Dec. 14, 2018 Accessed 12 Jan 2020. [Online]. Available: <https://patents.google.com/patent/FR3067391A1/en?q=non-wetting&q=CMAS&q=thermal&q=barrier&q=coatings&oq=non-wetting+CMAS+thermal+barrier+coatings>
240. Lokachari, S., et al.: Novel thermal barrier coatings with hexagonal boron nitride additives resistant to molten volcanic ash wetting. *Corrosion Sci.* **168**, 108587 (2020). <https://doi.org/10.1016/j.corsci.2020.108587>
241. Kang, Y.X., et al.: High temperature wettability between CMAS and YSZ coating with tailored surface microstructures. *Mater. Lett.* **229**, 40–43 (2018). <https://doi.org/10.1016/j.matlet.2018.06.066>
242. Zhang, B., et al.: Novel thermal barrier coatings repel and resist molten silicate deposits. *Scripta Mater.* **163**, 71–76 (2019). <https://doi.org/10.1016/j.scriptamat.2018.12.028>
243. Yang, S.-J., Song, W.-J., Dingwell, D.B., He, J., Guo, H.-B.: Surface roughness affects metastable non-wetting behavior of silicate melts on thermal barrier coatings. *Rare Met.* **41**(2), 469–481 (2022). <https://doi.org/10.1007/s12598-021-01773-6>
244. Song, W., et al.: Biomimetic super “Silicate” phobicity and superhydrophobicity of ceramic material. *Adv. Mater. Interfaces* **9**(32), 2201267 (2022). <https://doi.org/10.1002/admi.202201267>

245. Wang, Y. et al.: Preparation and CMAS wettability investigation of CMAS corrosion resistant protective layer with micro-nano double scale structure. *Coatings* **12**(5), Art. no. 5 (2022). <https://doi.org/10.3390/coatings12050648>
246. Guo, Y., et al.: Ultrafast laser reconstructed PS-PVD thermal barrier coatings with superior silicophobic triple-scale micro/nano structure. *Mater. Des.* **228**, 111846 (2023). <https://doi.org/10.1016/j.matdes.2023.111846>
247. Wu, H., Huo, K., Ye, F., Hua, Y., Dai, F.: Wetting and spreading behavior of molten CMAS on the laser textured thermal barrier coatings with the assistance of Pt-modification. *Appl. Surface Sci.* **622**, 156887 (2023). <https://doi.org/10.1016/j.apsusc.2023.156887>
248. Qu, W., Li, S., Jing, J., Pei, Y., Gong, S.: The spreading behavior of CMAS melt on YSZ single crystal with low index orientation. *Appl. Surface Sci.* **527**, 146846 (2020). <https://doi.org/10.1016/j.apsusc.2020.146846>
249. Huanjie, F., Weize, W., Zexin, Y.U.: Preparation of micro-nano hierarchical microstructure and its performance against CMAS wetting of thermal barrier coatings. *HDLGDXXBZRKXB* **48**, 1–8 (2022). <https://doi.org/10.14135/j.cnki.1006-3080.20220331001>
250. Ushmaev, D., Norton, A., Kell, J.: Thermally sprayed coatings resistant to environmental degradation: columnar-like coatings through laser ablation and surface melting approach. *Surface Coatings Technol.* **460**, 129394 (2023). <https://doi.org/10.1016/j.surfcoat.2023.129394>
251. Guo, L., Gao, Y., Cheng, Y., Sun, J., Ye, F., Wang, L.: Microstructure design of the laser glazed layer on thermal barrier coatings and its effect on the CMAS corrosion. *Corrosion Sci.* **192**, 109847 (2021). <https://doi.org/10.1016/j.corsci.2021.109847>

New Materials for Thermal Barrier Coatings



Feifei Zhou and Shun Wang

Abstract Thermal barrier coatings (TBCs) are essential for protecting hot-end components of aero-engine and gas turbine against thermal and corrosion damage, thereby improving thermal efficiency and extending its service life. The selection of TBCs materials is crucial including high melting point, low thermal conductivity, corrosion resistance, thermal expansion coefficient, substrate matching, and no phase transformation or sintering during service. Yttrium-stabilized zirconia (YSZ) is a typical material with desirable properties, but it cannot withstand temperatures above 1200 °C for prolonged service. Novel TBCs materials have been developed, including rare earth zirconate, hexaluminate, niobates, and tantalates. This chapter presents an overview of oxide TBCs materials, focusing on rare earth zirconate TBCs and the influence of ion doping, as well as the crystal structures and thermodynamic properties of niobates and tantalates. Finally, this summary work provides insight into the development of TBCs materials.

Keywords Thermal barrier coatings · Novel materials · Rare earth doping

1 Metal Oxide and Their Doped Materials

Among the metal oxides, zirconia (ZrO_2)-based materials are the most widely used in thermal barrier coatings. In order to improve the performance of ZrO_2 -based coatings, doping modification is usually carried out on materials, among which rare

F. Zhou (✉)

School of Materials Science and Engineering, Harbin Institute of Technology, Harbin 150001, People's Republic of China
e-mail: snowy_hit@163.com

Zhengzhou Research Institute, Harbin Institute of Technology, Zhengzhou 450000, People's Republic of China

S. Wang

Institute of Advanced Structure Technology, Beijing Institute of Technology, Beijing, People's Republic of China

earth oxides are widely used in the modification of thermal barrier coatings. This section introduces ZrO_2 -based materials as the main object.

1.1 Crystal Structure and Thermal Properties of Materials

Zirconia (ZrO_2) is an excellent functional and structural integration material [1–5] which is highly abundant and inexpensive. As a high-temperature structural ceramic material, ZrO_2 has the reputation of “ceramic steel” and has been widely used in many industrial fields in recent years. ZrO_2 exhibits high melting point, strength, hardness, toughness, friction resistance, low thermal conductivity, and chemical stability, making it resistant to high-temperature corrosion. However, pure phase ZrO_2 undergoes a temperature-dependent phase transition from monoclinic (m) \rightarrow tetragonal (t) \rightarrow cubic (c), with the reverse process taking place upon cooling. This non-diffusion martensite phase transition process occurs rapidly during cooling, causing approximately 3.5% volume expansion, equivalent to a reduction in theoretical density from 6.1 to 5.9 g/cm^3 . Therefore, pure phase ZrO_2 is not suitable for thermal barrier coating applications [6–10] (Fig. 1).

To enhance the comprehensive properties of ZrO_2 ceramics and mitigate phase transition defects, stabilizers such as magnesium oxide (MgO), calcium oxide (CaO), yttrium oxide (Y_2O_3), cerium oxide (CeO_2), and others are used [12–14]. The addition of tetravalent oxides, such as MgO, generates oxygen vacancies through charge balance, while cation substitution defects in the ZrO_2 ceramic lattice play a secondary role. 7–8 wt% yttria-stabilized zirconia (7YSZ) is widely used for thermal barrier coatings due to its intrinsic low thermal conductivity (about 2.5 W/(m k)), high thermal expansion coefficient (about $10\text{--}11 \times 10^{-6} \text{ K}^{-1}$), high hardness (about 10 GPa), and low elastic modulus (about 220 GPa), exhibiting improved comprehensive performance at high temperatures up to 900 °C [15].

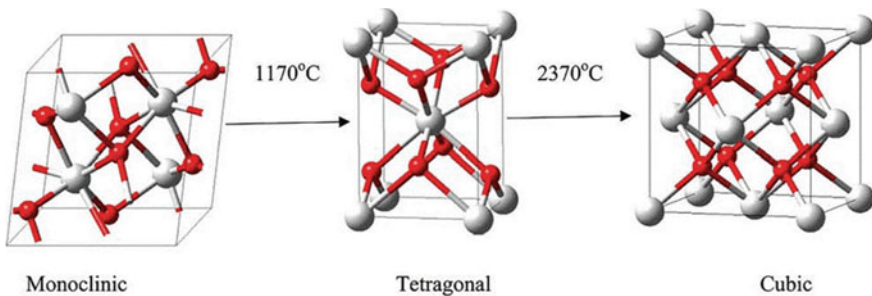


Fig. 1 Zirconia allotropes and the phase transformation temperature [11]

1.2 Effect of Doping Modification on Materials

The incorporation of Y_2O_3 in zirconia has been found to prevent the $t' \rightarrow m$ phase transition in zirconia. When the mass fraction of Y_2O_3 exceeds 22%, zirconia is fully stabilized into the cubic phase at room temperature, which is referred to as yttria completely stabilized zirconia [16]. Alternatively, when the mass fraction of Y_2O_3 is less than 22%, zirconia can be partially stabilized into the tetragonal phase (8–22% mass fraction) or the metastable tetragonal phase (6–8% mass fraction) depending on the stabilizer used, and this is referred to as yttria partially stabilized zirconia. At present, stable ZrO_2 with a Y_2O_3 mass fraction ranging from 6 to 8%, denoted as 6–8YSZ, is the most commonly used material for various applications including thermal barrier coatings. Metastable tetragonal 6–8YSZ exhibits excellent fracture toughness ($1.85\text{--}2.23 \text{ MPa m}^{1/2}$), good thermal insulation properties ($2.1 \text{ W m}^{-1} \text{ K}^{-1}$), a thermal expansion coefficient ($10.5\text{--}11.5 \times 10^{-6} \text{ K}^{-1}$) that is similar to that of metal bonding layers, and good corrosion resistance [16, 17]. Coatings prepared using the air plasma Spraying (APS) method by Zhang et al. did not exhibit any phase transitions after oxygenation at $900 \text{ }^\circ\text{C}$ for 100 h, and the coatings retained their metastable tetragonal and cubic phases. To investigate the effect of the thickness of the ceramic layer on the thermal shock performance of the YSZ coating, researchers prepared three thermal barrier coating systems using the APS method with a top thickness of 8YSZ on an Inconel 718 superalloy matrix. The thermal shock life of the coatings at $1000 \text{ }^\circ\text{C}$ was analyzed, and it was found that the coating life decreased with increasing thickness of the top ceramic layer. This is likely due to an increase in the deposition time of the coating with increasing thickness, leading to the accumulation of residual stress, microcracks, and pores in the coating, which reduce its thermal shock performance. Thick coatings tend to accumulate more residual stress during the deposition process, leading to the presence of more microcracks and pores in the prepared coating. During thermal shock tests, such residual stress may be released through crack expansion, causing thick coatings to experience cracked connections, which eventually leads to their detachment. While YSZ has excellent thermophysical properties and is widely used in thermal barrier coatings, high temperatures above $1200 \text{ }^\circ\text{C}$ can cause t' phase zirconia to transform into m phase, along with a volume expansion that creates significant internal stress and cracks within the coating. This situation provides an entry point for oxygen and molten corrosion, speeding up the internal corrosion of the coating and shortening its service life. Additionally, the sintering rate of YSZ increases at high temperatures, resulting in reduced porosity of the coating and decreased thermal insulation performance, while also weakening phonon scattering. Moreover, sintering increases the elastic modulus of the coating, reduces its crack stability, and accelerates crack propagation [18]. As a replacement material for YSZ, YGYZ refers to YSZ doped with Yb_2O_3 and Gd_2O_3 as stabilizers. Compared to YSZ, YGYZ exhibits improved oxidation resistance, sintering resistance, higher corrosion resistance, better high-temperature phase stability, and lower thermal conductivity, particularly at high temperatures where the thermal conductivity of YGYZ is only 1.24 W/(m K) . Researchers conducted an analysis of the

$\text{Na}_2\text{SO}_4 + \text{V}_2\text{O}_5$ corrosion behavior of APS-prepared YGYZ coating at 1100 °C and found that the coating exhibited good corrosion resistance and phase stability, retaining a high tetragonal phase even after 20 h of corrosion, with a degraded coating 40% less than that of YSZ. However, YGYZ has a low thermal expansion coefficient of only $9\text{--}10 \times 10^{-6} \text{ K}^{-1}$, which is much lower than the thermal expansion coefficient of nickel-based bonding layers ($15.0 \times 10^{-6} \text{ K}^{-1}$). The significant difference in thermal expansion coefficient makes it unsuitable to directly prepare YGYZ on the bonding layer as the top ceramic layer, and its fracture toughness is quite low, ranging from only 0.95–1.25 MPa m^{1/2}, making the coating susceptible to cracking easily in high-temperature working environments. To enhance the feasibility of YGYZ as an optimal ceramic layer material, Jung et al. [19] devised a high-purity YSZ buffer layer situated between the nickel-based bonding layer and the superior YGYZ ceramic layer to mitigate thermal expansion discrepancies and alleviate mismatch stress. The findings demonstrate that the YGYZ coating with high-purity YSZ buffer layer exhibited 2000 cycles in the jet engine test, which is significantly higher than those without buffer layer, ranging from 350 to 678 cycles, and higher than those with conventionally purified YSZ buffer layer, which ranged from 1127 to 1130 cycles. ScYSZ denotes YSZ doped with Sc₂O₃ as a stabilizer. Given that doping zirconia with Sc does not cause notable lattice distortion owing to its small ionic radius, the researchers opted to alter the Sc₂O₃ doping content to modify the performance of ScYSZ coating. Liu et al. [20] analyzed the phase composition of the ScYSZ coating with 8.0 mol% Sc₂O₃ after heat treatment at 1500 °C for 10 h, and the results showed that the ScYSZ coating after heat treatment was still a single non-transformable tetragonal phase. Under the same conditions, the content fraction of monoclinic phase in YSZ coating reaches 49.4 mol%, and its excellent high-temperature phase stability enables it to be applied in higher temperature environments. Fan et al. [21] studied the thermal shock life of ScYSZ coating at 1300 °C when the content fraction of Sc₂O₃ is 7 mol%. Although the doping of Sc element slightly reduces its fracture toughness ($(4.3 \pm 0.3) \text{ MPa m}^{1/2}$), its good t' phase stability and high comprehensive performance. As a result, it still has an extremely high thermal cycle life, up to 2.6 times that of YSZ coating. Although numerous studies have reported on zirconia or YSZ doped with rare earth elements, few have investigated the doping mechanism, the effect of doping content on coating properties, or the impact of different preparation methods on doped powder. With the development of nano-sized powders, the properties of nanostructured doped coatings are one of the important research directions (Fig. 2).

1.3 Preparation and Properties of YSZ TBCs

There are many preparation processes for thermal barrier coatings, mainly including thermal spraying [22], electron beam physical vapor deposition (EB-PVD) [23], chemical vapor deposition (CVD) [24], etc. Thermal spraying technologies include supersonic flame spraying (HVOF) [25], atmospheric plasma spraying (APS) [26],

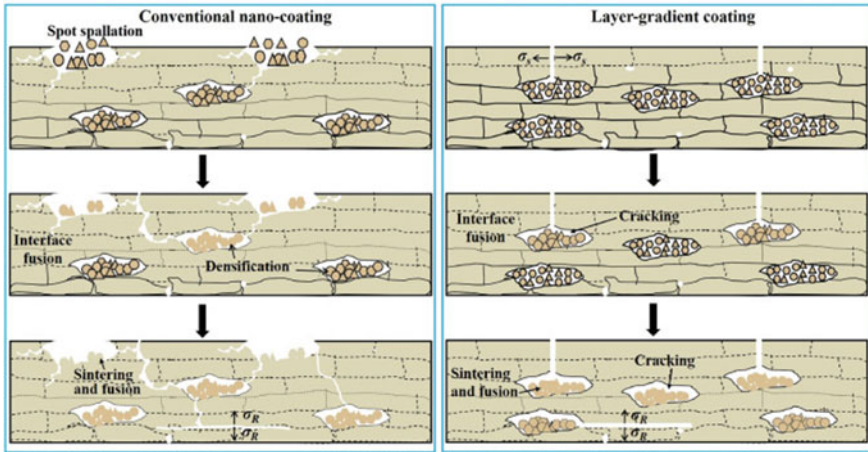


Fig. 2 Failure mechanisms of different coatings during the thermal cycling test [21]

low-pressure plasma spraying (LPPS), and the latest plasmon sprayed physical vapor deposition (PS PVD), which combines the advantages of both plasma spraying (PS) and EB-PVD [27, 28]. APS and EB-PVD spraying technologies are mainly introduced here.

Atmospheric plasma spraying is a prevalent method for preparing ceramic thermal barrier coatings due to its rapid deposition rate and cost-effectiveness [29]. Because the plasma flame flow temperature is very high, can melt most materials including metals and ceramics, atmospheric plasma spraying has a wide range of applications. Since plasma spraying involves rapid heating and cooling processes, it has a small heat-affected zone on the substrate, and some amorphous and nanocrystals may be produced in the sprayed coating [30, 31]. Figure 3 illustrates the atmospheric plasma spraying process [29]. The working gas, usually Ar and H₂/N₂, creates an arc between the cathode and anode, and the working gas is ionized to produce a plasma arc. Plasma arc has the characteristics of high temperature and high speed. In atmospheric plasma spraying, carrier gas transports the spraying powder into the plasma flame flow, where it is heated to a melting or semi-melting state. The high-speed plasma flame flow impacts the substrate surface, forming a coating. Spraying parameters such as power, plasma gas composition, and spraying distance affect the powder’s melting state, particle speed, and coating microstructure. The resulting coating has a layered structure with pores and cracks. While pores reduce thermal conductivity, cracks decrease thermal cycle life.

Advancements in nanotechnology have enabled the preparation of nanostructured thermal barrier coatings through atmospheric plasma spraying. Plasma spraying of nanostructured thermal barrier coatings has become a significant method for producing high-performance thermal barrier coatings [24, 32, 33]. By controlling spraying parameters, part of the nanostructured feed is retained in the coating without melting or partially melting to form the nanostructured coating.

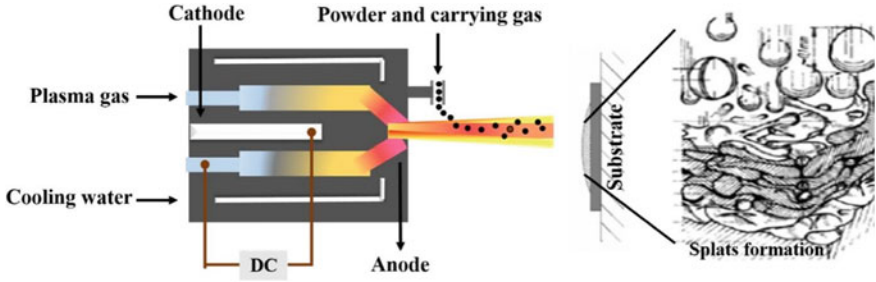


Fig. 3 Schematic diagram of atmospheric plasma spraying [29]

EB-PVD heats the target with a high-energy electron beam to vaporize it, then deposits gas-phase atoms on the substrate surface to form a coating, as illustrated in Fig. 4 [34]. The microstructure of thermal barrier coating prepared by EB-PVD is columnar crystal. Compared with APS coating, EB-PVD coatings exhibit greater strain tolerance, compactness, and bonding strength. However, its thermal conductivity is relatively high, deposition rate is slow, and cost is high.

PS-PVD is a recently developed technology for preparing thermal barrier coatings that challenges traditional understanding of plasma spraying. In an ultra-low-pressure environment (pressure of about 50–200 Pa), a large power (up to 130 kW) spray gun is used to generate a plasma flame with a length of 2 m and a diameter of 0.2–0.4 m, as shown in Fig. 5 [35]. PS-PVD enables solid, liquid, and gas multiphase deposition as well as non-line-of-sight deposition. By adjusting spraying

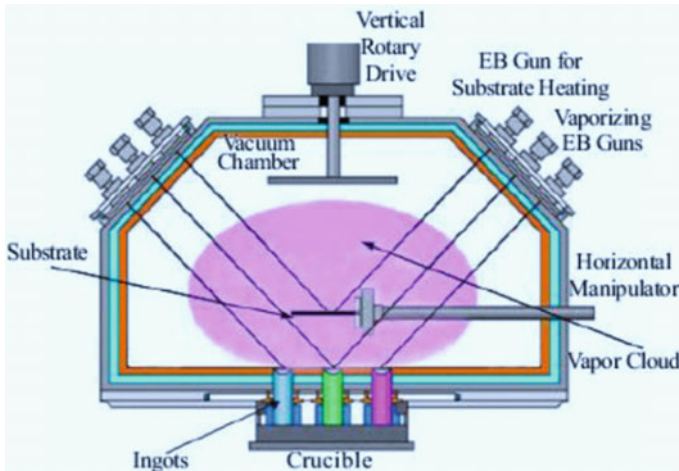


Fig. 4 Schematic diagram of EB-PVD [34]

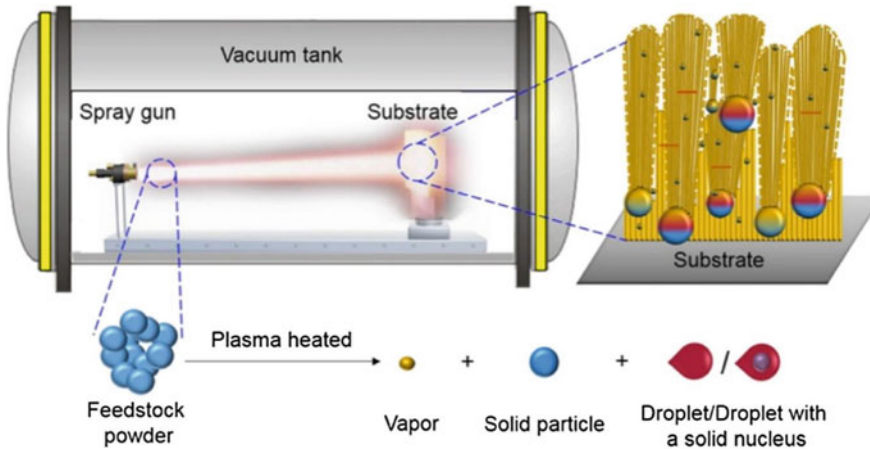


Fig. 5 Plasma jet of PS-PVD [35]

parameters, thermal barrier coatings with layered, columnar, and layered structures can be obtained. Therefore, as an advanced thermal barrier coating preparation technology, PS-PVD holds significant potential for future preparation of high-performance high-temperature and ultra-high-temperature thermal barrier coatings [36, 37].

Yttrium oxide-stabilized zirconia (6–8YSZ) with a mass fraction of 6–8% is the most excellent and widely used thermal barrier coating material at present. YSZ has advantages such as high melting point ($\sim 2700\text{ }^{\circ}\text{C}$), low thermal conductivity ($2\text{--}3\text{ W m}^{-1}\text{ K}^{-1}$), high thermal expansion coefficient ($\sim 11.0 \times 10^{-6}\text{ K}^{-1}$), excellent chemical stability at high temperature and comprehensive mechanical properties. In particular, its excellent toughness at high temperature is incomparable to other thermal barrier coating materials. The fracture toughness of YSZ can reach $3\text{ MPa m}^{1/2}$, which is related to the ferroelastic toughening mechanism existing in t, the metastable tetragonal phase of YSZ. t phase usually only exists in YSZ coating prepared by atmospheric plasma spraying or electron beams-physical gas deposition.

The T' phase is a metastable phase between the T and C phases. Unlike the T phase, the T' phase does not undergo a transformation to the M phase, enhancing YSZ's phase stability and preventing volume expansion caused by martensitic transition. In addition, t-phase YSZ is also a kind of ferroelastic material with excellent fracture toughness at high temperature. Under the action of stress, long strip domain structure, called ferroelastic domain, will be formed in the grain. In the t' phase, the ferroelastic domain structure will be deflected under the action of stress, from the original along $\langle 111 \rangle$ superlattice crystal faces stacked in the direction and containing only a single orientation are transformed into superlattice faces containing three orientations parallel to axes a, b, and c, respectively. The steering process is shown in 1.6 (a) 34. The nucleation and steering of ferroelastic domains will absorb part of the energy

of crack growth, slow down the rate of crack growth, cause stress–strain hysteresis effect, and thus, improve the fracture toughness of YSZ.

As engine service temperatures increase, the corrosion of thermal barrier coatings by CMAS ($\text{CaO-MgO-Al}_2\text{O}_3\text{-SiO}_2$) becomes more severe. Shan et al. [38] studied the buckling of plasma-sprayed YSZ thermal barrier coatings under CMAS erosion and its induced effects. At high temperature, the liquid CMAS permeates the weakened interface into the YSZ due to capillary force and makes the YSZ expand significantly by about 32%, resulting in a wide range of YSZ buckling. To demonstrate the process, baseless APS TBC coated with CMAS were prepared and heated to 1250 °C in a tubular furnace. Figure 6a shows the buckling process of TBC under different heat treatment times. With the increase of holding time, the penetration depth of CMAS increases, and the buckling becomes more obvious. Based on the discussion, the buckling failure mechanism of TBC under the action of CMAS is proposed, as shown in Fig. 6b. Thornton et al. [39] found that molten CMAS increased mass transport in YSZ coatings prepared by APS and EB-PVD, leading to densification and peeling during cooling. Increased mass transport can destabilize the YSZ coating by incorporating stabilizers and precipitating the zircon phase. Finally, the corrosion failure mechanism of CMAS coating is proposed, namely “penetration, dissolution, densification, precipitation, and spalling”.

Despite its advantages as a thermal barrier coating material, YSZ has limitations. As aero-engine technology advances, YSZ’s shortcomings become more apparent. When the service temperature exceeds 1200 °C, the T phase dissolves into the C and T’ phases, reducing the coating’s fracture toughness. Increased T phase content

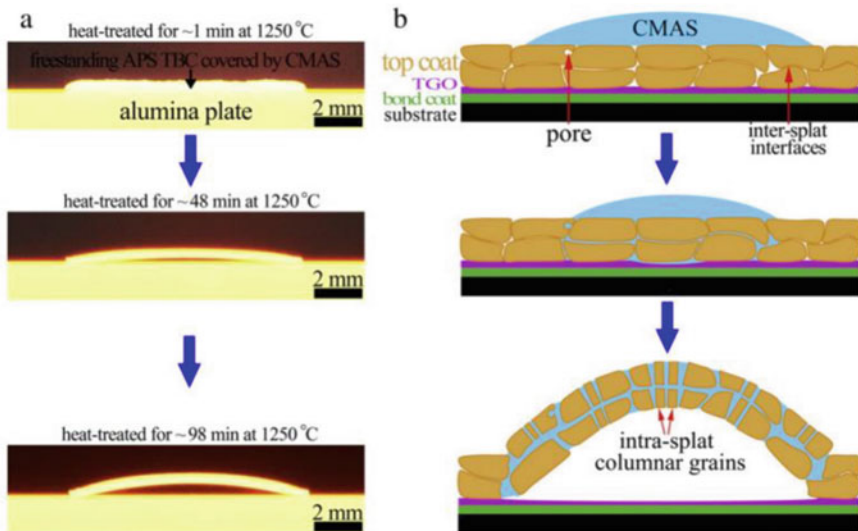


Fig. 6 a Buckling failure processes of APS TBC with CMAS at 1250 °C and b schematic illustration of buckling failure mechanism of APS TBC after CMAS attack

exacerbates volume expansion caused by the $T \rightarrow M$ phase transition, leading to cracking and coating detachment. Thus, YSZ's working temperature is limited to below 1200 °C. In addition, as an excellent conductor of oxygen ions, YSZ is usually used as electrode material for solid batteries. In particular, YSZ has a very high permeability of oxygen ions at high temperature, which will accelerate the oxidation of metal bonding layer to form TGO. Problems such as poor sintering resistance, high thermal conductivity, and poor corrosion resistance also greatly limit the application of YSZ thermal barrier coating on high-performance aero-engines. Therefore, to find a new thermal barrier coating material that can replace YSZ has become the focus of research.

1.4 Application of Hafnium Oxide in TBCs

In the top thermal barrier layer, hafnium exists as HfO_2 , stabilized by yttrium or other rare earth oxides. Alternatively, hafnium dioxide can be used as an additive to conventional coatings that stabilize ZrO_2 . Common techniques for applying hafnium dioxide thermal barrier coatings include electron beam physical vapor deposition (EB-PVD), air plasma spray (APS), and magnetron sputtering. When HfO_2 is stabilized with 27 wt% Y_2O_3 , it exhibits reduced Young's modulus and thermal conductivity (by 30% to 0.5–1 W/(m K)) at high temperatures, resulting in higher sintering resistance and heat resistance compared to 8YSZ coating. Doping ZrO_2 and HfO_2 with a mixture of trivalent ions larger and smaller than Y^{3+} maintains the metastable t' phase structure. Phase diagrams are crucial for selecting surface components and doping elements of the adhesive coating. Adding up to 1 wt% hafnium to the bonded coating improves its cyclic oxidation resistance and increases the adhesion and strength of the hot-growing oxide layer to the bonded coating.

2 Rare Earth Zirconate

2.1 Crystal Structure of Rare Earth Zirconate in TBCs

Rare earth zirconates ($Ln_2Zr_2O_7$) include ordered pyrochloitic structures and disordered defect fluorite structures. The transformation of two structures under normal temperature and pressure is dependent on the Ln^{3+}/Zr^{4+} cation radius ratio. An ordered pyrochloitic structure of $Ln_2Zr_2O_7$ occurs when the Ln^{3+}/Zr^{4+} radius ratio is between 1.46 and 1.78. A disordered defective fluorite structure occurs when the ratio is less than 1.46. The general formula for the pyrochloitic structure of rare earth zirconate is $Ln_2Zr_2O_6O'$, which belongs to the $Fd\bar{3}m$ space group with ordered Ln^{3+}/Zr^{4+} cations. Its single cell structure is shown in Fig. 7a. This structure has four crystallographic inequivalent atomic positions, namely Ln^{3+} occupying the 16d

space position and Ln^{3+} occupying the 16d space position. It can coordinate with the surrounding eight oxygen ions to form a cube. Zr^{4+} at position 16c, together with six surrounding oxygen ions, forms an octahedral structure. The oxygen ion O at position 48f, and the oxygen ion O' at position ④8b. In addition, the oxygen vacancy at position 8a in Fig. 7a, which is in the tetrahedron formed by Zr^{4+} , also shows ordering. The general formula of the disorder defect fluorite type rare earth zirconate is $(\text{Ln}, \text{Zr})_4\text{O}_7$ and belongs to the $\text{Fm}\bar{3}\text{m}$ space group, as shown in Fig. 7b. The Ln^{3+} , Zr^{4+} cations share a crystallographic position 4a, and the oxygen ions only have a crystallographic position 8c. The structure also has 1/8 oxygen ion vacancies. It is caused by the random distribution of equivalent crystallographic positions, and the position of oxygen vacancies is also randomly distributed. Rare earth zirconate has an oxygen vacancy in each molecular unit, so its lattice has a high oxygen vacancy concentration. Ln^{3+} and Zr^{4+} can be substituted by various cations with similar atomic radii. The material's complex unit cell structure and large rare earth atoms result in a high melting point, low thermal conductivity, and high chemical stability. It has been extensively studied in the field of TBCs and is expected to become a candidate for new TBCs.

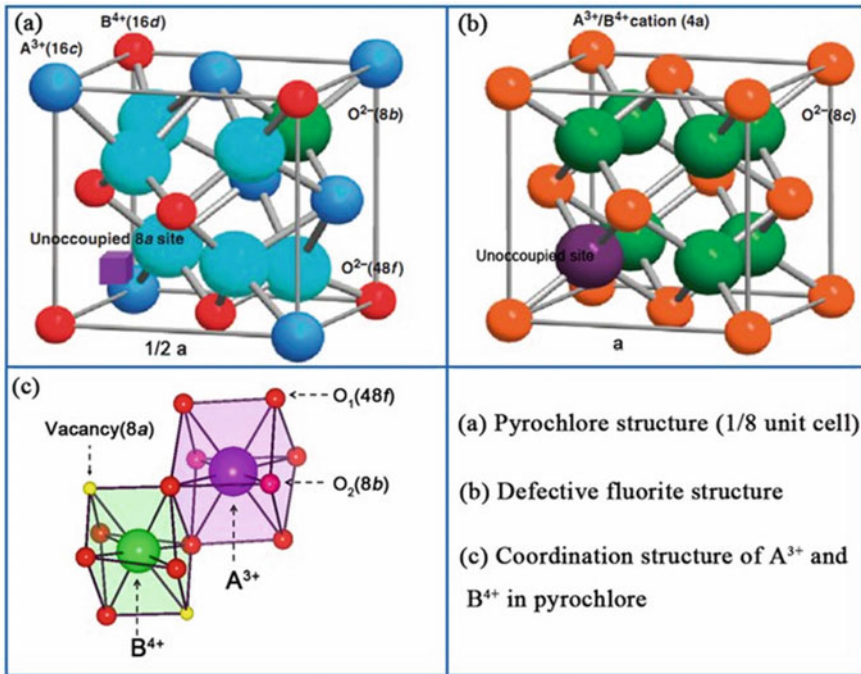


Fig. 7 Crystal structures of pyrochlore and defective fluorite: **a** one-eighth of unit cell of pyrochlore structure; **b** defective fluorite structure; **c** coordination structure of A^{3+} and B^{4+} in pyrochlore [40]

2.2 Properties of Rare Earth Zirconate TBCs

Rare earth zirconate is a promising thermal barrier coating (TBC) material due to its high phase stability, low thermal conductivity, anti-sintering properties, and low oxygen transmittance. It is particularly resistant to CMAS corrosion.

Rare earth zirconate materials have intrinsic oxygen vacancies in each crystal structure unit, whether it is a pyrochlore or defect fluorite structure. The high concentration of oxygen vacancies and the presence of large rare earth atoms in the unit cell enhance phonon scattering and decrease the mean free path, resulting in low thermal conductivity. While there are variations in thermal conductivity due to differences in preparation processes, material porosity, and testing conditions, these materials generally have lower thermal conductivity than conventional YSZ under the same conditions. Their thermal expansion coefficient is equivalent to or slightly lower than that of YSZ.

As a potential new type of thermal barrier coating, rare earth zirconate thermal barrier coating, its high-temperature corrosion resistance in $\text{Na}_2\text{SO}_4\text{-V}_2\text{O}_5$ environment, and the ability to resist the corrosion of $\text{CaO-MgO-Al}_2\text{O}_3\text{-SiO}_2$ (CMAS) are also the main goals of TBCs development. Kramer et al. [41] used the electron beam physical vapor deposition method to prepare $\text{Gd}_2\text{Zr}_2\text{O}_7$ coating. After coating the surface of $\text{Gd}_2\text{Zr}_2\text{O}_7$ with CMAS molten salt ($33\text{CaO-9MgO-13AlO}_{3/2}\text{-45SiO}_2$) at a concentration of 8 mg/cm^2 and holding it at 1573 K for 4 h , a dense fine-grained reaction layer with a thickness of about $6\text{ }\mu\text{m}$ was formed at the interface between the $\text{Gd}_2\text{Zr}_2\text{O}_7$ coating and CMAS. The reaction layer is mainly composed of $\text{Gd}_2\text{Ca}_2(\text{SiO}_4)_6\text{O}_2$ apatite phase and ZrO_2 fluorite phase with solid solution of Gd and Ca. This study shows that the depth of the CMAS molten salt penetrating into the cylindrical crystal gap of the ceramic layer is about $30\text{ }\mu\text{m}$. When the cylindrical crystal gap is filled with the generated product and molten salt, the molten salt infiltration will stop, and then, the top of the cylindrical crystal will be slowly eroded.

Our research group used EB PVD to deposit YSZ and LZ7C3 coatings on ceramic substrates and studied their high-temperature CMAS behavior at $1250\text{ }^\circ\text{C}$. It was found that the LZ7C3 coating was highly resistant to CMAS penetration within 24 h , while the conventional YSZ was completely permeated by the CMAS melt within 30 min . This resistance is mainly due to the high-temperature chemical interaction between the LZ7C3 coating and CMAS glass, which crystallizes to form a protective layer. The crystallization product is primarily composed of La Ce apatite and cubic phase ZrO_2 , which can form a closed layer that effectively prevents further CMAS penetration. This is mainly due to the high-temperature chemical interaction between the LZ7C3 coating and the CMAS glass, which crystallizes to form this resistance. The crystallization product is mainly composed of La Ce apatite and cubic phase ZrO_2 , which is easy to form a closed layer and can effectively prevent further penetration of CMAS.

2.3 Modification of Rare Earth Zirconate

Rare earth zirconate $\text{La}_2\text{Zr}_2\text{O}_7$ is used in thermal barrier coatings (TBCs) due to its thermal expansion coefficient being close to that of the currently used TBC material YSZ, its lower thermal conductivity, and higher phase stability. However, $\text{La}_2\text{Zr}_2\text{O}_7$ has some shortcomings, such as insufficient sintering activity, poor thermal cycle performance, and high-temperature thermal radiation that increases thermal conductivity. To reduce the thermal conductivity of TBC ceramics, researchers have doped them with different rare earth elements or other stabilizers to improve their performance. In recent years, a series of complex rare earth zirconates with varying thermal and mechanical properties have been obtained by doping zirconates with rare earth elements, such as $(\text{La}_x\text{Gd}_{1-x})_2\text{Zr}_2\text{O}_7$, $(\text{Sm}_x\text{Yb}_{1-x})_2\text{Zr}_2\text{O}_7$, $(\text{La}_x\text{Yb}_{1-x})_2\text{Zr}_2\text{O}_7$, and $(\text{La}_x\text{Gd}_{1-x})_2\text{Zr}_2\text{O}_7$, $\text{Gd}_2(\text{Zr}_x\text{Ti}_{1-x})_2\text{O}_7$, $(\text{Sm}_{2-x}\text{Mg}_x)_2\text{Zr}_2\text{O}_{7-x/2}$, $\text{La}_2(\text{Zr}_x\text{Ce}_{1-x})_2\text{O}_7$ and further reduce the thermal conductivity of the system, while obtaining a higher thermal expansion coefficient. The following are some studies on the doping of $\text{La}_2\text{Zr}_2\text{O}_7$.

(1) Single doping of rare earth elements forms rare earth zirconate

Wang et al. [42] doped $\text{La}_2\text{Zr}_2\text{O}_7$ with Nd oxide (Nd_2O_3) to form $\text{La}_{2-x}\text{Nd}_x\text{Zr}_2\text{O}_7$ ceramic materials, and $\text{La}_{1.4}\text{Nd}_{0.6}\text{Zr}_2\text{O}_7$ has the lowest coefficient of thermal expansion ($8.928 \times 10^{-6} \text{ K}^{-1}$) and the best anti-sintering performance. Good anti-sintering ability reduces the thermal effect force between the ceramic coating and metal substrate, which is crucial for thermal barrier coating (TBC) materials. Lehmann et al. [43] Nd_2O_3 , Eu_2O_3 , Gd_2O_3 , Dy_2O_3 doped $\text{La}_2\text{Zr}_2\text{O}_7$ formed $\text{La}_{1.4}\text{Nd}_{0.6}\text{Zr}_2\text{O}_7$, $\text{La}_{1.4}\text{Eu}_{0.6}\text{Zr}_2\text{O}_7$. The thermal conductivity of $\text{La}_{1.4}\text{Gd}_{0.6}\text{Zr}_2\text{O}_7$ and $\text{La}_{1.7}\text{Dy}_{0.3}\text{Zr}_2\text{O}_7$ is lower than that of $\text{La}_2\text{Zr}_2\text{O}_7$, which is $1.55 \text{ W}/(\text{m K})$. Therefore, the doping of rare earth oxide can improve the performance of thermal barrier coating materials. The thermal conductivity of $\text{La}_{1.4}\text{Gd}_{0.6}\text{Zr}_2\text{O}_7$ and $\text{La}_{1.7}\text{Dy}_{0.3}\text{Zr}_2\text{O}_7$ is lower than that of $\text{La}_2\text{Zr}_2\text{O}_7$ ($1.55 \text{ W}/(\text{m K})$), indicating that doping with rare earth oxide can improve the performance of thermal barrier coating materials. Wan et al. [44] found that $\text{La}_{1.4}\text{Gd}_{0.6}\text{Zr}_2\text{O}_7$ had lower thermal diffusivity and conductivity than undoped rare earth misate ceramic material. Replacing La with other rare earth ions weakens the La–O bond and facilitates its expansion, improving the thermal expansion coefficient of zirconate. Studies on Gd_2O_3 -doped $\text{La}_2\text{Zr}_2\text{O}_7$ ($\text{La}_{1.7}\text{Dy}_{0.3}\text{Zr}_2\text{O}_7$, $\text{La}_{1.7}\text{Yb}_{0.3}\text{Zr}_2\text{O}_7$, and $\text{La}_{1.7}\text{Yb}_{0.15}\text{Gd}_{0.15}\text{Zr}_2\text{O}_7$) showed lower thermal conductivity than undoped $\text{La}_2\text{Zr}_2\text{O}_7$ due to strong phonon scattering caused by the vibration of 3-valent rare earth ions with smaller ion radius and larger mass in the original lattice. Thus, doping $\text{La}_2\text{Zr}_2\text{O}_7$ with active ions with small ion radius and large mass can achieve lower thermal conductivity.

Wan et al. [45] studied Yb_2O_3 doped with $\text{La}_2\text{Zr}_2\text{O}_7$, and in the system of $(\text{La}_x\text{Yb}_{1-x})_2\text{Zr}_2\text{O}_7$, Yb^{3+} with smaller radius was doped instead of La^{3+} with larger radius, which caused strong vibration of atoms at this position and reduced the phonon mean free path equals the level of nearest neighbor atomic spacing during heat conduction, which significantly decreased low material thermal conductivity,

different from the traditional YSZ thermal barrier coating phase transition aging, the phase transition process of $\text{LaYb}_2\text{Zr}_2\text{O}_7$ is relatively slow, and there is no huge mismatch between components or the generation of new phases that can induce catastrophic consequences. The phases involved in the phase transition have a high similarity, and the two new phases can coexist stably at high temperature for a long time. These characteristics make $\text{LaYb}_2\text{Zr}_2\text{O}_7$ a promising candidate for use as a thermal barrier coating material.

(2) Zr position in rare earth element doped zirconate ($\text{La}_2\text{Zr}_2\text{O}_7$)

In thermal insulation materials such as ceramics, the thermal conductivity is mainly affected by phonons, so if the elements with large ionic radius and large relative atomic mass are doped in the material, the thermal conductivity will naturally decrease. The ease of doping and the decrease in thermal conductivity of a system are influenced by the difference between the ionic radius and average atomic mass of doped and raw material atoms. Ce^{4+} has a larger ionic radius and relative atomic mass than Zr^{4+} , making it beneficial to replace Zr^{4+} with Ce^{4+} in lanthanum zirconate to improve its thermal expansion coefficient and reduce its thermal conductivity. Cao et al. [46] studied the thermal properties of $\text{La}_2(\text{Zr}_{1-x}\text{Ce}_x)_2\text{O}_7$ thermal barrier coating material and found that the addition of CeO_2 significantly increased the thermal expansion coefficient of $\text{La}_2\text{Zr}_2\text{O}_7$ due to the large ionic radius of Ce^{4+} and weak Ce–O bond energy. The thermal conductivity also decreased significantly due to the complex crystal structure reducing the mean free path of phonons. At 1000 °C, $\text{La}_2(\text{Zr}_{0.7}\text{Ce}_{0.3})_2\text{O}_7$ ceramic material had the lowest thermal conductivity ($0.87 \text{ W m}^{-1} \text{ K}^{-1}$) and best sintering resistance, improving its thermal stability. No phase transition occurred below 1200 °C, and at 1200 °C its thermal conductivity and thermal expansion coefficient were $0.79 \text{ W m}^{-1} \text{ K}^{-1}$ and $11.6 \times 10^{-6} \text{ K}^{-1}$, respectively, representing a 50% reduction and 20% increase compared to $\text{La}_2\text{Zr}_2\text{O}_7$.

(3) Double doped rare earth element modified $\text{La}_2\text{Zr}_2\text{O}_7$ ceramic material

Cao et al. [46, 47], to enhance the material's chemical and phase stability, completely or partially replaced La_2O_3 with Y_2O_3 , and the products after substitution included $\text{Y}_2\text{Ce}_2\text{O}_7$, $\text{Y}_2(\text{Zr}_{0.7}\text{Ce}_{0.3})_2\text{O}_7$, and $\text{Yb}_2(\text{Zr}_{0.7}\text{Ce}_{0.3})_2\text{O}_7$, among all the components, $\text{Y}_2\text{Ce}_2\text{O}_7$ is monophasic, and the other components are mixtures with different structures. The complete or partial substitution of Y_2O_3 for La_2O_3 resulted in a linear decrease in the unit cell parameters of the product, indicating that Y^{3+} replaced the lattice site of La^{3+} or Ce^{4+} . Of these products, LZC3 has the lowest thermal conductivity. It is also the most resistant to sintering, so it has an important application in high-temperature thermal barrier coating. The $\text{La}_{1.7}\text{Dy}_{0.3}(\text{Zr}_{0.8}\text{Ce}_{0.2})_2\text{O}_7$ and $\text{La}_{1.7}(\text{DyNd})_{0.15}(\text{Zr}_{0.8}\text{Ce}_{0.2})_2\text{O}_7$ ceramic materials studied by Zhou have good phase stability at high temperature, and no phase occurred. Consequently, there is an increase in the thermal expansion coefficient and a decrease in thermal conductivity. In comparison with non-doped $\text{La}_2\text{Zr}_2\text{O}_7$, these doped products exhibit greater suitability as high-temperature thermal barrier coating materials. Despite the fact that ion substitution can enhance its performance to a certain degree, it remains challenging

to improve the thermal expansion coefficient of $\text{La}_2\text{Zr}_2\text{O}_7$ to match that of the current thermal barrier coating 7–8YSZ. The reason is that, except for the substitution of La by light rare earth elements, the substitution of other ions is not conducive to the stability of the structure and forms a heterophase. In other words, the doped ions do not enter the Gd site of La or Zr and generate impurities; ion substitution has little effect on the specific heat capacity.

Overall, rare earth zirconate is considered the most comparable thermal barrier coating material system to yttria-stabilized zirconia due to its lower thermal conductivity, similar thermal expansion coefficient to yttria-stabilized zirconia (YSZ), and high phase stability. However, rare earth zirconate still has insufficient comprehensive mechanical properties, poor thermal cycling performance, and radiation at extremely high temperature. Thermal conductivity results in an increase in thermal conductivity and numerous other issues. Extensive research is required prior to the realization of industrial application.

2.4 Properties of Nanostructured Rare Earth Zirconate Coatings

With the development of nanotechnology, the combination of nanomaterials and plasma spraying technology makes it possible to fabricate nanostructured thermal barrier coatings by plasma spraying. By controlling the spraying parameters, the nanostructured granulating powder only partially melts before colliding and depositing with the matrix, forming a structure in which the internal solid nanoparticles are wrapped by the fully melted liquid phase, so that the final coating contains both the fully melted region and the nano-region with the morphology similar to the microscopic nanoparticles of the granulating powder. Over the past 20 years, many researchers at home and abroad have conducted a lot of research on the nanostructure YSZ thermal barrier coating. Research has demonstrated that the properties of YSZ thermal barrier coatings, when incorporating nano-regions, exhibit significant improvements compared to traditional thermal barrier coatings. These improvements include high bond strength, robust thermal shock resistance, high thermal insulation, and strong corrosion resistance. Currently, several major aviation and development enterprises in China have implemented nanostructured YSZ ceramic thermal barrier coatings.

(1) Effect on thermal conductivity

For crystalline materials, phonon heat conduction can be understood as the result of phonon–phonon, phonon–impurity, defect, and grain boundary collisions according to the phonon theory of lattice waves. The elevated concentration of oxygen vacancies in rare earth zirconate crystals results in strong phonon scattering, reducing its thermal conductivity by nearly 30% compared to YSZ. Furthermore, doping of rare earth zirconate at the Ln and Zr sites leads to an increase in oxygen vacancies and a

decrease in the mean free path of phonons, further scattering phonons and reducing the thermal conductivity of materials. As grain size decreases to the nanometer level, grain boundaries increase dramatically in nanostructured coatings. Generally, grain boundaries act as barriers to thermal conductivity, resulting in lower thermal conductivity for nano-polycrystalline materials compared to their single-crystalline counterparts and decreasing with decreasing grain size. Additionally, the uniform distribution of pores in nanostructured coatings is a significant factor contributing to low thermal conductivity.

Taleghani et al. [48] synthesized LZ7C3 nano-powder via the chemical precipitation method and subsequently fabricated a nanostructured LZ7C3/YSZ double-ceramic layer thermal barrier coating using the plasma spraying process after granulation. Results indicate that the thermal insulation capability of the nanostructured bi-ceramic barrier coating is 58.8% greater than that of traditional YSZ coatings. This enhancement in thermal insulation capability is attributed to the extensive presence of nano-regions in the top microstructure of the coated ceramic, with the existence of nanoparticles and nanopores contributing to a significant reduction in thermal conductivity.

(2) Effect on the coefficient of thermal expansion

The thermal expansion of crystalline materials arises from the non-harmonic vibration of atoms. As temperature increases, the average atomic spacing within the crystal expands, resulting in crystal expansion. The coefficient of thermal expansion is proportional to the average distance between lattice particles, with lower bond energy corresponding to larger average lattice distances and higher coefficients of thermal expansion. Kutty et al. [49] and Shimamura et al. [50] investigated the thermal expansion coefficient of rare earth zirconia $\text{Ln}_2\text{Zr}_2\text{O}_7$ ($\text{Ln} = \text{La}, \text{Nd}, \text{Sm}, \text{Eu}, \text{Gd}$) over a temperature range from room temperature to 1500 °C and discovered that the thermal expansion coefficient increased gradually with decreasing ion radius. Schelling et al. [30, 51] also summarized the thermal expansion coefficients of $\text{La}_2\text{Zr}_2\text{O}_7$, $\text{Sm}_2\text{Zr}_2\text{O}_7$ and $\text{Gd}_2\text{Zr}_2\text{O}_7$ as 9.1×10^{-6} , 10.8×10^{-6} and $11.6 \times 10^{-6} \text{ K}^{-1}$ (20–1000 °C), respectively. In the crystal structure of rare earth zirconate, the primary determinant of material expansion is the thermal expansion of Ln–O and Zr–O bonds upon heating. Fan et al. [21] found from theoretical calculations that Zr–O bond had the greatest influence on thermal expansion, followed by Ln–O bond. Research also showed that Zr-site doping was more effective than Ln site doping in improving thermal expansion coefficient. Simultaneously, doping introduces point defects into the lattice, relaxing the lattice, reducing crystal bond energy, and increasing the expansion coefficient.

Li et al. [52] synthesized $\text{La}_2\text{Zr}_2\text{O}_7$ nano-powder with an average particle size of approximately 20 nm via the sol–gel method and evaluated its thermophysical properties after high-pressure sintering into a ceramic block. Results indicated that the thermal expansion coefficient of the ceramic block prepared from $\text{La}_2\text{Zr}_2\text{O}_7$ nano-powder was $(9.6 \pm 0.4) \times 10^{-6} \text{ K}^{-1}$ (20–1000 °C), significantly higher than that of the non-nano-powder sample $(9.1 \pm 0.4) \times 10^{-6} \text{ K}^{-1}$. It was also noted that powder nanometerization is an effective means of improving the performance of

thermal barrier coatings, demonstrating the potential of nanostructured coatings in enhancing the thermal expansion coefficient of thermal barrier coatings.

The fracture toughness index of thermal barrier coatings indicates their ability to resist crack instability propagation or fracture. The nanostructure of nano-thermal barrier coatings can enhance the coating's toughness. According to Hall–Petch's equation, reducing the grain size from micrometers to nanometers can improve the material's mechanical properties. In addition, increasing grain boundaries is a method that can slow down crack propagation. In nanostructured coatings, crack propagation is easily blocked, tortuified, and deflected by the nano-regions in the coating, so that the crack propagation path in nano-thermal barrier coatings has no obvious direction. For conventional coatings with a dominant melting region, the crack propagation is clearly directional, usually along the direction of the lamellae interface. As a result, the fracture toughness of nano-coatings is higher than that of conventional coatings.

Li et al. [53] prepared $\text{La}_2\text{Zr}_2\text{O}_7$ micro and nano-powders using solid-phase and sol–gel methods and found that the fracture toughness of bulk materials prepared from nano-powder ($1.98 \pm 0.07 \text{ MPa m}^{1/2}$) was significantly higher than that of micro powder samples ($1.40 \pm 0.23 \text{ MPa m}^{1/2}$). Researchers pointed out that compared with the traditional $\text{Gd}_2\text{Zr}_2\text{O}_7$ coating that failed after 40 h oxidation at $1100 \text{ }^\circ\text{C}$ in previous studies the oxidation life of $\text{Gd}_2\text{Zr}_2\text{O}_7$ coating with nanostructure increased by more than 2 times to 100 h at $1100 \text{ }^\circ\text{C}$. The increase of the grain boundaries of the nanostructured coating leads to slower crack propagation, which has a significant effect on improving the fracture toughness and the life of the coating.

3 Rare Earth Cerate

3.1 Crystal Structure of Rare Earth Cerate in TBCs

The crystal structure of rare earth cerite $\text{RE}_2\text{Ce}_2\text{O}_7$ is similar to that of rare earth zirconate. However, due to the large ionic radius of Ce^{4+} , the ratio of the ionic radius of the A site to the B site is typically less than 1.46, resulting in a defect fluorite structure with a 1/8 oxygen vacancy. Rare earth cerates are solid solutions formed by solid solution of other kinds of rare earth oxides into the CeO_2 lattice. Therefore, they have the same cubic fluorite structure as CeO_2 . Taking lanthanum cerate (LC) as an example, it is a solid solution with La_2O_3 as the solute and CeO_2 as the solvent. In this structure, La^{3+} and Ce^{4+} occupy the 4a site together, with oxygen vacancies randomly distributed in the oxygen ion sublattice. Figure 8 shows the distribution of anions and cations in the unit cell of the ideal cubic fluorite structure (MO_2), where cations form a face-centered cubic arrangement and anions are placed in the tetrahedral center formed by cations. This special configuration endows $\text{La}_2\text{Ce}_2\text{O}_7$ with many excellent characteristics, showing good chemical stability and ionic conductivity.

Praveen [55] comparative analysis of rare earth cerate coatings of doped systems prepared by APS and SPPS. Figure 9 shows no obvious phase transition before or

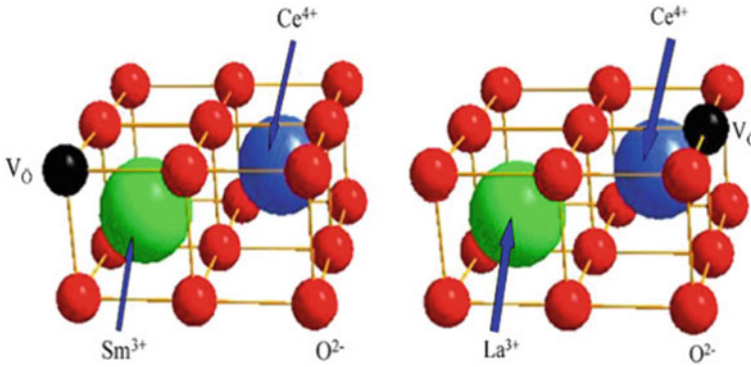
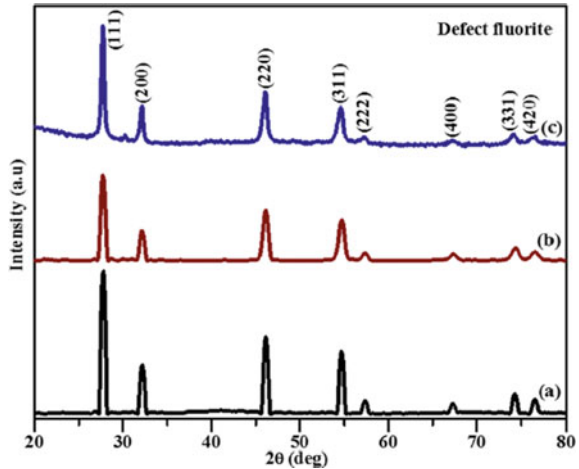


Fig. 8 Distribution of cations and anions in a fluorite cell [54]

Fig. 9 XRD pattern of a Gd-LC powder, b APS, and c SPPS coatings [55]



after APS deposition, indicating a single-phase defect fluorite structure. The SPPS coating has a prominent high peak and lower XRD intensity than synthetic powder, possibly due to the high solidification rate during plasma spraying.

3.2 Properties of Rare Earth Cerate TBCs

The rare earth cerate with fluorite structure can be understood as a solid solution generated by the dissolution of rare earth oxides in the CeO_2 lattice. CeO_2 has a low thermal conductivity and the fluorite structure's oxygen vacancies can optimize the thermal insulation performance of rare earth cerate. The large ionic radius of Ce^{4+} and weak Ce–O bond result in a high thermal expansion coefficient at high temperatures. These

properties make it a candidate for thermal barrier coatings. Researchers prepared $\text{Dy}_2\text{Ce}_2\text{O}_7$ and $\text{Y}_2\text{Ce}_2\text{O}_7$ by solid-phase reaction and measured their thermal conductivity at 800 °C to be 1.78 W/(m K) and 1.82 W/(m K), respectively, much lower than that of 8YSZ (2.15 W/(m K)) at the same temperature.

Guo et al. [56] prepared $\text{La}_2\text{Ce}_2\text{O}_7$ (LC)/yttria-stabilized zirconia (YSZ) thermal barrier coating (TBC) with a segmented crack structure using plasma spraying technology. They studied the thermal–physical properties and thermal cycling properties, such as thermal diffusivity and conductivity, of the segmented LC/YSZ TBC. The thermal conductivity of segmented coatings measured at 1200 °C was about 1.02 W/(m K), lower than that of non-segmented coatings. The thermal cycle life of segmented LC/YSZ TBC is approximately 2100 cycles, which is nearly 50% more durable than unsegmented TBC. The failure of segmented coatings is mainly due to peeling and delamination cracking inside the coating.

Researchers used $\text{La}_2\text{Ce}_{2.5}\text{O}_8$ as raw material powder to obtain $\text{La}_2\text{Ce}_2\text{O}_7$ (LC) coating close to 1 by optimizing the spraying parameters. The spraying distance significantly influences the phase composition, stability, and porosity of LC coating while keeping other spray parameters unchanged. A plasma spray coating was prepared and evaluated for thermal cycle life using a gas burner test. The thermal cycle life of LC/YSZ double-layer coatings was more than 3 times that of single-layer LC coatings and comparable to YSZ coatings at 1230 °C. At 1320 °C, the LC/YSZ coating had a thermal cycle life approximately 40% that of optimized YSZ coating but significantly lower at 1350 °C. The thermal cycling failure mechanism of LC and LC/YSZ coatings under different conditions was also established.

Researchers studied the microstructure evolution of $\text{La}_2\text{Ce}_2\text{O}_7$ (LC) and YSZ thermal barrier coatings sprayed at 1250 °C plasma. After heat treatment at 1250 °C for 12 h, the YSZ coating was severely impacted by CMAS glass-like deposition with a penetration depth exceeding 250 μm . CMAS deposition chemically reacted with LC coatings to form an interactive layer consisting mainly of $\text{Ca}_2(\text{La}_x\text{Ce}_{1-x})_8(\text{SiO}_4)_6\text{O}_{6-4x}$ and CeO_2 . The size of the interaction layer increased after 40 h of thermal exposure at 1250 °C and then remained unchanged with a thickness of <50 μm . The micro-hardness of the interaction layer after 100 h of heat exposure was about 10–12 GPa, harder than that of LC coating.

3.3 Modification of Rare Earth Cerate

Doping rare earth cerite with one or more rare earth elements can enhance the coating's performance by reducing its thermal conductivity and increasing its thermal expansion coefficient. However, in this brief introduction, the doping of Ce and Zr positions in zirconate mostly coincide.

Researchers doped Nd and La elements as dopant in $\text{Sm}_2\text{Ce}_2\text{O}_7$ and prepared $(\text{Sm}_{0.5}\text{La}_{0.1}\text{Nd}_{0.4})_2\text{Ce}_2\text{O}_7$ coating with pure fluorite structure. At 1000 °C, the thermal conductivity of the coating ranges from 1.32 to 1.58 W/(m K), while that of $\text{Sm}_2\text{Ce}_2\text{O}_7$ is 1.69 W/(m K). Doping increases the thermal expansion coefficient by

$2-3 \times 10^{-6} \text{ K}^{-1}$. According to the phonon thermal conductivity mechanism, the ion radius and relative atomic mass of the doping rare earth elements differ significantly from those in the matrix. This increases defects in rare earth cerite unit cells and reduces the coating's thermal conductivity through extra phonon scattering space.

Rare earth cerium salt exhibits excellent thermal insulation and a high thermal expansion coefficient. However, preparing lanthanum cerium coating with the rated stoichiometric ratio presents a significant challenge in its application. During plasma spraying, 30–40% of CeO_2 in rare earth lanthanum cerate is lost, resulting in a lower deposition rate for the coating. Therefore, it is necessary to increase the content of CeO_2 to obtain a prepared rare earths lanthanum cerate coating with a standard stoichiometric ratio, and the slight composition shift of CeO_2 will have a significant impact on the performance of the coating. Thermal cycling tests were carried out on the coatings with three powder doping ratios of $\text{La}_2\text{O}_3 \cdot 3.0\text{CeO}_2$ (LC3), $\text{La}_2\text{O}_3 \cdot 3.25\text{CeO}_2$ (LC3.25), and $\text{La}_2\text{O}_3 \cdot 3.5\text{CeO}_2$ (LC3.5). It was found that the composition deviation seriously affected the high-temperature life of the rare earth cerate coating. The lifetime of LC3.25 was 3238, while that of LC3 and LC3.5 was 847 and 50, respectively.

4 Rare Earth Hexaluminate

4.1 *Synthesis and Crystal Structure of Hexaluminate* *Materials*

Yttrium-stabilized zirconia (YSZ) is currently the most widely used TBC material, with 8% Y_2O_3 -stabilized ZrO_2 exhibiting the best thermophysical properties. However, when operating temperatures exceed 1200°C , ZrO_2 undergoes a transformation from monoclinic to tetragonal to cubic phase. This causes grain growth, microporosity shrinkage, and secondary sintering, ultimately leading to coating failure and an inability to meet the higher performance requirements of new-generation aero-engines. Therefore, it is the general trend to improve and develop new TBCs materials, so that they can work at higher temperatures for a long time, so as to meet the increasing service requirements of engines. In recent years, new TBCs materials have been emerging, and magnetic leadstone hexaluminate compounds have attracted great interest from researchers as relatively potential materials.

Hexaaluminates have a hierarchical structure consisting of alumina blocks with a spinel-like structure, separated by a single layer of symmetrical mirror planes containing large cations [57]. The crystal structure can be either β -alumina or magnetoplumbite (MP), depending on the ion radius and valence state of the metal ion. Certain metal ions can partially or completely replace aluminum. The ionic radius and charge magnitude of the metal ion determine the crystal structure. Replacement hexaaluminates may not follow the same rules as pure hexaaluminates (Fig. 10).

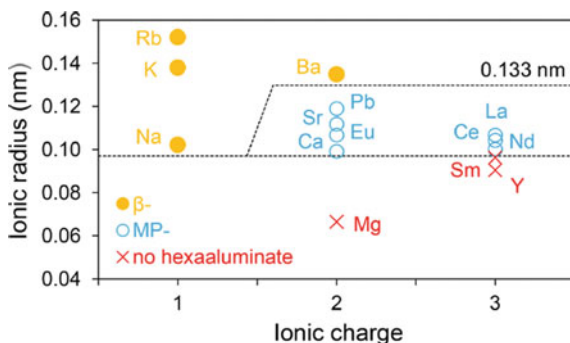


Fig. 10 Effect of charge and radius of large cation M on the formation of unsubstituted hexaaluminate [57]

The main difference between β and MP hexaaluminates is the composition and occupation of the mirror plane. In MP, the mirror plane is tightly packed, while in β it is not. The separation of spinel blocks by mirror surfaces hinders three-dimensional crystal growth, resulting in slow sintering and high stability at extreme temperatures. Crystal growth is inhibited along the C-axis to obtain a plate-like morphology with a relatively high surface area. In hexaaluminates, oxygen binds less strongly in the mirror plane than in rigid spinel blocks, making it a favorable pathway for oxide ion diffusion. This is important in catalytic applications such as combustion and selective oxidation. Alkali-containing β -HAs decompose above ~ 1000 °C in open systems due to alkali oxide vaporization, while MP-HAs with alkaline earth or rare earth cations in the mirror plane do not have this issue (Fig. 11).

In order to enhance the stability of crystal structure, some Al^{3+} ions in the crystal structure of magnetite lanthanum hexaaluminate ($LaAl_{12}O_{19}$) are usually replaced by divalent or trivalent metal cations to form $LaM_xAl_{12-x}O_{19}$ compound. When M is replaced by Mg, a magnesium-based lanthanum hexaluminate compound is formed, with the formula $LaMgAl_{11}O_{19}$ (LMA for short), which follows the principle of electric neutrality. The cell structure diagram of the material is shown in Fig. 12, which is composed of LaO_{12} decahedron containing La^{3+} ions and $(MgAl)O_4$ and AlO_6 spinel blocks separated by the mirror plane of the decahedron alternately stacked. The structural integrity of the LMA material is mainly due to the presence of orderly arranged spinel blocks reducing the $LaAl_{12}O_{19}$ cell. The cell structure diagram of the material is shown in Fig. 12. It consists of LaO_{12} decahedra containing La^{3+} ions and $(MgAl)O_4$ and AlO_6 spinel blocks separated by the mirror plane of the decahedron, stacked alternately. The structural integrity of LMA material is mainly due to the presence of orderly arranged spinel blocks reducing the $LaAl_{12}O_{19}$ cell. The void in LaO_{12} can be perfectly combined with the LaO_{12} decahedron to form stable and compact crystal structure.

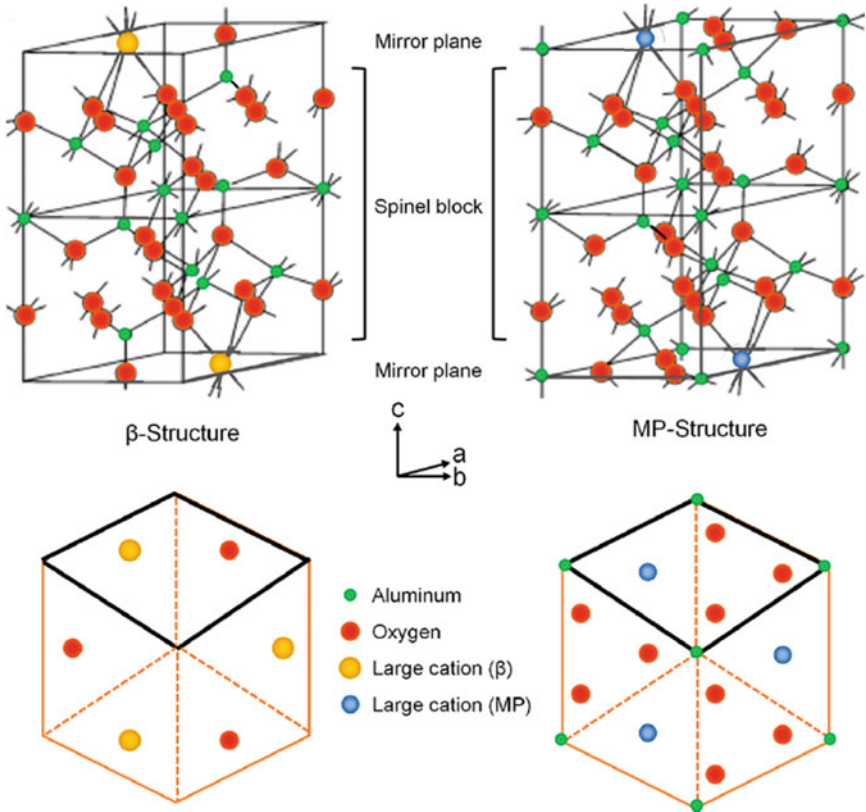
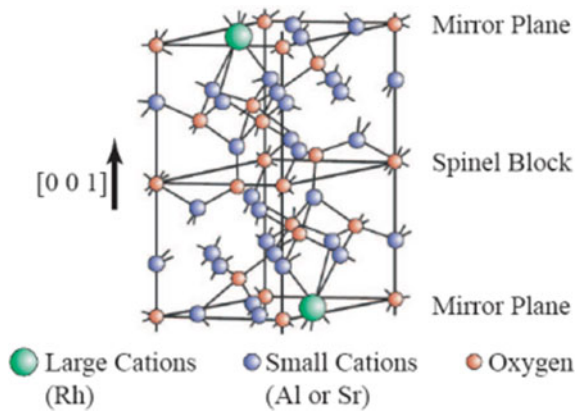


Fig. 11 Two groups of large cations depicted in Fig. 10 have an ideal hexaaluminate cell structure. The mirror plane, viewed along the C-axis, is shown below each structure. It is tightly packed in MP structures but not in β structures. In each mirror plane, the portion belonging to a cell is highlighted in bold/black [57]

Fig. 12 Schematic diagram of hexaluminate structure



The commonly used preparation methods for magnetic leadstone hexaluminate series materials mainly include solid-phase sintering method, sol-gel method, coprecipitation method, and hydrothermal method. Among them, the preparation temperature of solid-phase sintering method is high, and the calcination temperature is generally higher than 1500 °C, which has strict requirements on sintering equipment. The sol-gel method involves the hydrolysis of precursors such as alcohol salts and nitrates to generate a uniform sol, which is then converted into a gel with the assistance of an organic complexing agent. Compared to solid-phase sintering, this method reduces the crystallization temperature and produces nano-level powder material with uniform particle size and a large specific surface area. This results in improved thermal performance of the material. The material prepared by chemical coprecipitation method has the advantages of nanometer size and high purity. However, the precipitation method is more demanding on the selection of precipitant, dropping method, and dropping acceleration rate, and the aging process after precipitation takes a long time. The centrifugal filtration and cleaning process is complex, tedious, time-consuming, and labor consuming. However, the application of hydrothermal method is limited due to higher experimental conditions, greater risk coefficient, and less output.

Sol-gel method and coprecipitation method are the most commonly used methods to prepare hexaaluminate materials. The preparation process is described in detail here.

The process of preparing powder materials by sol-gel method mainly includes: the first step of metal brine hydrolysis process: the raw materials such as alkoxide and nitrate that meet the stoichiometric ratio are dissolved in the appropriate solvent, and the uniform solution is obtained by stirring and mixing for a period of time. Then there is the sol-formation process: the solution in the previous step is mixed with the appropriate and appropriate complexing agent solution, and the mixture is fully stirred to obtain a uniform mixture. Then there is the gel-forming process: the above sol is heated to obtain a thick, highly adhesive gel. It is then thoroughly dried to produce a fluffy, porous dry gel that can be easily ground into a powder. Finally, the target product was obtained after high-temperature calcination and annealing.

Coprecipitation method is to drop precipitant solution into metal salt solution, and reverse coprecipitation is to drop metal salt solution into precipitant solution. The main process of precipitation method is roughly as follows: the first is the solution preparation process: the raw materials such as carbonate and nitrate that meet the stoichiometric ratio are dissolved in the solvent together, and the salt solution is stirred evenly. Similarly, the appropriate and appropriate amount of precipitant is dissolved in the solvent, and the precipitant solution is obtained by stirring fully. Then there is the precipitation reaction process: the salt solution and the precipitant solution are titrated according to the selected method. In order to ensure the thorough reaction and obtain the fully reacted precipitate, it is required to stir while titrating, and the titration rate is as slow as possible. Then comes the aging process: after the suspension is obtained, in order to ensure that the salt ions and the precipitant are fully combined and settled, it is allowed to stand for a period of time (the standing time is related to the reaction of the material and the degree of settlement). This is followed

by the filtration process: a number of centrifugal filtrations with the appropriate cleaning solvent are carried out until the resulting filtrate has a pH value close to neutral. Finally, drying and high-temperature calcination: the cleaned precipitate is fully dried and then calcined at high temperature and annealed to obtain the target product.

4.2 Preparation and Properties of Hexaluminate TBCs

The microstructure of a material determines its performance, with variations in mechanical and thermal properties resulting from differences in microstructure. This affects the application of thermal barrier coatings (TBCs). The development of advanced coating preparation technology, which can alter the microstructure of materials, has garnered significant attention. Common TBC preparation technologies include atmospheric plasma spray (APS) and electron beam physical vapor deposition (EB-PVD), among others such as chemical vapor deposition (CVD) and high-speed flame spraying (HVOF).

Atmospheric plasma spraying (APS) is a thermal spray technology that uses plasma heating to melt powder and deposit it onto a substrate to form a thermal protective coating. APS improves the corrosion, wear, high temperature, oxidation, and fatigue resistance of the substrate. Advantages include low equipment cost, relaxed raw material requirements, fast coating preparation, and simple production. Ceramic powder is injected into the plasma flame stream and heated rapidly. Molten or partially molten particles impact the substrate at high speed. Typical APS coatings have pores and microcracks with adjustable porosity. Pores may result from non-molten particle deformation, while microcracks are related to quenching stress from rapid cooling and insufficient density of the pancake coating stack. Porosity can be adjusted by changing spraying parameters such as distance, power, and matrix temperature.

Electron beam physical vapor deposition (EB-PVD) uses electron beam energy to heat and process target material in a vacuum. The material is heated and vaporized, then deposited onto a substrate to form a protective coating. The process is environmentally friendly and produces coatings with low impurity content and consistent phase and element content. EB-PVD coatings have a columnar crystal structure with longitudinal cracks that reduce stress concentration during high-temperature service. Compared to APS coatings, EB-PVD coatings have better mechanical properties due to chemical bonding and lack of layered structure. The microstructure has higher strain tolerance and can alleviate thermal shock stress, resulting in better fatigue resistance and service life. However, EB-PVD has limitations including high cost, limited working space, inability to prepare coatings for large workpieces or complex compositions, and high pretreatment temperature for alloy matrices. Impurity elements can penetrate longitudinal cracks and erode the alloy matrix during thermal shock. Therefore, atmospheric plasma spraying is used for LMA coating preparation.

In recent decades, the research work of this material used as TBCs have been reported one after another. Its special crystal structure endows it with high-temperature phase stability and excellent electrical insulation properties, making it a promising new TBCs material for the next generation. The research progress of hexaluminate used as TBCs materials in recent years is summarized, mainly divided into the following aspects:

In addition, according to reference the intrinsic thermal conductivity of $\text{LaMgAl}_{11}\text{O}_{19}$ is lower than that of 7YSZ. The synthesized $\text{LaMgAl}_{11}\text{O}_{19}$ has no change in phase structure after heat treatment at 1600–1700 °C, indicating that the $\text{LaMgAl}_{11}\text{O}_{19}$ phase is stable below 1700 °C, which is very important for thermal barrier coatings (TBCs) at high temperature. Through SEM detection, $\text{LaMgAl}_{11}\text{O}_{19}$ has a better plate and strip structure, which improves the heat insulation and temperature resistance [58].

Phase, microstructure and thermodynamic properties of LMA pure phase materials; Sun et al. [59, 60] studied the microstructure, thermal/mechanical properties, thermal cycling and aging process at high temperatures, and crystallization mechanism of amorphous phase of LMA materials. The former found LMA ceramics from 200 to 1200 °C The linear thermal expansion coefficient at 1000 °C is $9.17 \times 10 \text{ K}^{-1}$, and the thermal conductivity at 1000 °C is 2.55 W/(m K). The latter found that the content of the amorphous phase of the LMA coating would increase with the increase of spraying power, thereby reducing the porosity of the coating, making the volume shrinkage of the coating larger and the thermal expansion coefficient lower. Sun also studied the thermal cycling behavior of the LMA coating at 1100 °C and found that the spallation of TBCs was mainly related to the formation of thermally grown oxide (TGO) and the mismatch of the thermal expansion coefficient between the coating and the matrix. It was proved that the lower the amorphous phase content of the LMA coating, the higher the bond strength with the adhesive layer, thus prolonging the service life and further crystallization of the amorphous phase The mechanism was investigated, and it was found that the highly charged La^{3+} ions in the LMA magnetite structure controlled the crystallization rate of the material, that is, the higher the La^{3+} content in the material, the more difficult the crystallization transition from multiphase to monophasic is to proceed.

Study on the erosion and high-temperature degradation mechanism of LMA materials by molten $\text{CaO-MgO-Al}_2\text{O}_3\text{-SiO}_2$ (CMAS) deposits and $\text{Na}_2\text{SO}_4 + \text{V}_2\text{O}_5$ molten salts had been carried out. Chen et al. [61] found that the microstructure and thermal properties of LMA coating are very similar to those of LMA block obtained by sintering, and the LMA coating and ceramic green body can withstand thermal corrosion for 60 h at 950 °C in the high-temperature molten salt of 50 wt% $\text{Na}_2\text{SO}_4 + 50 \text{ wt}\% \text{V}_2\text{O}_5$ without falling off. The mechanism by which molten CMAS deposits corrode thermal barrier coatings and promote their degradation at high temperature was studied and be found that a dissolution–reprecipitation reaction process would occur between LMA ceramic coatings and molten CMAS, in which $\text{CaAl}_2\text{Si}_2\text{O}_8$ and $\text{Ca}(\text{Mg, Al})(\text{Al, Si})_2\text{O}_6$ mixture, which is highly corrosive and will severely corrode the LMA coating and cause cracking and exfoliation of the coating.

LMA was synthesized with YSZ, $(\text{Yb}, \text{Er})_2\text{SiO}_5$, and $\text{Yb}_3\text{Al}_5\text{O}_{12}$. The study of the novel functional gradient TBCs of the LMA/YSZ series found that LMA and YSZ coatings are chemically compatible at high temperatures, and the LMA flake grains appearing in the recrystallizing process of the LMA material make the composite coating better sintered resistance and can reduce the density, hardness, and residual stress to 1372 °C has a cycle life of up to 11,749 cycles. Researchers used atmospheric plasma spraying to deposit a new coating with Er_2SiO_5 as the inner layer and LMA material as the top layer on a C/SiC composite. The coating improved high-temperature oxidation resistance but was prone to liquid sintering and bubble formation between the matrix and coating, leading to failure. The LMA/ $\text{Yb}_3\text{Al}_5\text{O}_{12}$ ceramic composite composed of magnetite and garnet structure showed little improvement in LMA material performance. Its thermal conductivity and thermal expansion coefficient at 1200 °C were 3.9 W/(m K) and $8.41 \times 10^{-6} \text{ K}^{-1}$, respectively.

4.3 Other Rare Earth Hexaluminate TBCs Materials

In order to further improve the performance of LMA, the modification of LMA materials with ion doping was studied. The La, Al, and Mg sites of LMA materials were replaced or co-doped. At present, the doped ions of La site mainly include Sr^{2+} , Nd^{3+} , Sm^{3+} , Gd^{3+} , Dy^{3+} , and Yb^{3+} . The doped ions of Al site include Ti^{2+} and Sc^{3+} ions, while the Mg site doping is rarely reported. The incorporation of metal cations can cause point defects and high-density grain boundaries in the crystal structure, which to some extent enhances phonon scattering and thus reduces the thermal conductivity of the material. Sr^{2+} , Zn^{2+} , and Ti^{4+} codoped with LMA material can obtain a lower thermal conductivity of 1.16 W/(m K) at 800 °C. Lu et al. [62] optimized the thermophysical properties of LMA materials by simultaneously replacing La3t and Al ions with Nd3t and Sc3t ions. The results showed that co-substitution had a significant effect on improving the thermal expansion coefficient and reducing the thermal conductivity, which gradually decreased with the increase of ion doping concentration, the lowest thermal conductivity could reach 2.04 W/(m K) at 1000 °C, and the thermal expansion coefficient can reach up to $8.53 \times 10^{-6} \text{ K}^{-1}$. At the same time, the compound doping of Nd^{3+} and Sc^{3+} can also improve the mechanical properties of the material and reduce the conductivity of the material. Li et al. [63] believed that the difference in the negativity between La^{3+} and O^{2-} ions had a negative impact on the increase of the thermal expansion coefficient of the material, so Sm^{3+} and Gd^{3+} ions were selected to partially replace La^{3+} ions to study its thermal properties, and a thermal expansion coefficient of $10.84 \times 10^{-6} \text{ K}^{-1}$ and 1.6 W/(m K) was obtained at 950 °C. The thermal conductivity of and the thermal conductivity coefficient of Dy^{3+} ion doped LMA material at 1200 °C is between 2.52 and 2.89 W/(m K). Wang et al. [64] revealed that the root cause of poor water resistance of LMA materials was the easy position migration of Mg^{2+} ions in the wet environment and proposed that Mg^{2+} ions in the crystal structure of LMA should be completely replaced by

Zn^{2+} ions to improve its delamination resistance, analyzed the root cause of improved delamination resistance, and reduced thermal conductivity of $LaZnAl_{11}O_{19}$ materials in depth.

Rare earth titanium-aluminum oxide ($LnTi_2Al_9O_{19}$) is a potential thermal barrier coating (TBC) material with excellent phase stability and ideal thermophysical properties from room temperature to 1600 °C. However, its thermal cycling performance is poor, and its fracture toughness is low. Researchers prepared $LaTi = Al_9O_{19}$ (LTA)/yttrium oxide-stabilized zirconia (YSZ) bilayer TBCs and evaluated their thermal cycle life at a coating surface temperature of 1300 ± 50 °C. Unlike conventional plasma sprayed TBCs, the LTA layer ruptured in the central part of the TBC after approximately 3000 cycles (equivalent to 500 h at 1300 ± 50 °C). Failure was due to decomposition and sintering of LTA exposed to high-temperature gas flame. After another 1000 cycles, the YSZ layer also broke along its interface with the bond layer.

5 Other TBCs Materials

In addition to YSZ, rare earth zirconate, rare earth cerate, and rare earth hexaluminate, other materials with low thermal conductivity are being explored. Each of these materials has advantages and disadvantages. Considering the factors such as thermal expansion coefficient, thermal conductivity, and chemical compatibility of these materials, only a small part of the materials have the potential to be used as a new thermal barrier ceramic layer system.

5.1 Titanate

In recent years, $BaLn_2Ti_3O_{10}$ ($Ln = La, Sm, Nd$) ceramic materials have also attracted attention, which are potential thermal barrier coating materials due to their lower thermal conductivity, comparable thermal expansion coefficient to YSZ, and good high-temperature phase stability. However, due to the relatively large number of elements in these materials, technological issues such as vapor pressure matching in the spraying process need to be further explored.

$BaLn_2Ti_3O_{10}$ ($Ln: Sm, Nd, Pr, \text{ and } La$) can be synthesized by high-temperature solid-phase reaction and sol-gel methods. Its crystal structure is a layered perovskite with BaO layers inserted into the perovskite block every third layer along the [001] direction. This structure reduces thermal conductivity due to weak bonding between planes containing rigid polyhedra. Lamellar perovskites also show good sintering resistance up to 1773 K and lower thermal conductivity than YSZ. Further studies using plasma spraying (PS) or electron beam physical vapor deposition (EB-PVD) are needed to prepare BLT coatings. Researchers [56] have studied the thermophysical and high-temperature properties of $BaLn_2Ti_3O_{10}$ coatings as a potential TBC material. Guo et al. synthesized $BaLn_2Ti_3O_{10}$ (BLT) by sintering $BaCO_3$, TiO_2 , and La_2O_3

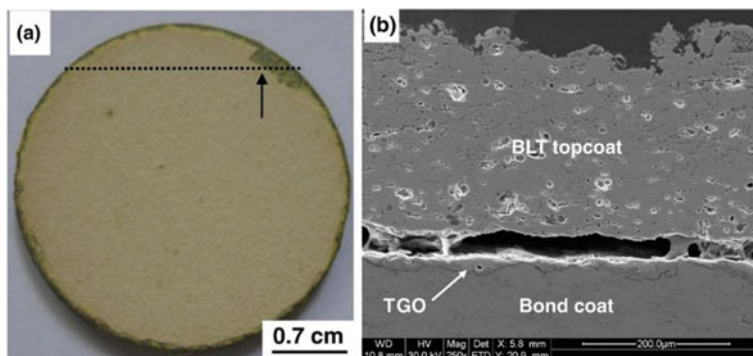


Fig. 13 Photograph (a) and SEM micrograph of cross-section (b) of BLT coating after 1195 thermal cycles. The dashed line and arrow direction of a show the cutting direction and analysis section of the coating [56]

at 1500 °C for 48 h. After sintering at 1500 °C for 110 h, BLT remained phase stable from room temperature to 1400 °C with no decomposition. Its coefficients of thermal expansion (CTEs) are comparable to 7YSZ. BLT coatings prepared by atmospheric pressure plasma spraying have a segmented crack structure and 13% porosity. The micro-hardness is 3.9–4.5 GPa, and thermal conductivity at 1200 °C is about 0.7 W/mK, reduced by about 30% compared to 7YSZ TBCs. Thermal cycling tests show a life exceeding 1100 cycles at 1100 °C. Coating failure occurs due to cracking of the thermal growth oxide (TGO) layer from severe oxidation of the bond layer (Fig. 13).

5.2 Perovskite Structure

The structural atomic composition of perovskite is ABO_3 , and the typical component is $CaTiO_3$. The crystal structure of perovskite is composed of octahedrons with common vertices, which can accommodate various solid ions including large atoms. The most common A-site elements are +2 valent metal ions (Ca^{2+} , Sr^{2+} , Ba^{2+} , Zn^{2+} , Fe^{2+} , Co^{2+} , Ni^{2+} , etc.). The most common B-site elements are +4 valent metal ions (Ti^{4+} , Zr^{4+} , Hf^{4+} , Ru^{4+} , Ce^{4+} , Mo^{4+} , Th^{4+} , U^{4+} , etc.). Most perovskites are stable at high temperature, so they can be used as TBC materials. Alkaline earth zirconate is the most common TBC material in perovskite. $BaZrO_3$ is one of the earliest applications on TBC. Although $BaZrO_3$ has a melting point of up to 2600 °C, its poor thermochemical stability results in poor thermal cycling performance at 1200 °C. In contrast, $SrZrO_3$ has excellent thermal cycling performance when the coating surface temperature exceeds 1250 °C, either as a single layer or as a double ceramic layer deposited on the YSZ surface. The stability of $SrZrO_3$ phase is poor, and it will change from orthogonal to tetragonal phase at 730 °C, which affects the performance of the coating. However, doping Gd and Yb can effectively inhibit this phase transition

and improve the thermal–physical properties of SrZrO₃ coating under extreme high-temperature conditions. As a perovskite-type alkaline earth zirconate, CaZrO₃ has been applied to TBC relatively late. Although its melting point is lower than YSZ, its low thermal conductivity (2 W/m K) makes it a promising new perovskite-type TBC material.

In addition to the high melting point of perovskite, another characteristic is that the B-site atoms are interchangeable, allowing the material's properties to be regulated according to the type of B-site atom. For example, Ba(Mg_{1/3}Ta_{2/3})O₃ has disordered cubic system and ordered tripartite system structure, which is more conducive to the formation of tripartite system structure, especially when the synthesis temperature rises to 1650 °C. The disordered cubic structure of Ba(Mg_{1/3}Ta_{2/3})O₃ coating prepared by APS often exists, and the structure of Ba(Mg_{1/3}Ta_{2/3})O₃ coating is characterized by high temperature (>1250 °C) gradually transformed into an orderly structure during heat treatment. Thermal expansion studies have shown that although this order–disorder transition has some effect on the use of materials, it is not disastrous for the structure of materials. The same B-site arrangement effect also appears in La(Al_{1/4}Mg_{1/2}Ta_{1/4})O₃ material, but this does not affect its use as TBC material. A large number of longitudinal crack networks exist in the coating deposited by APS technology, which is beneficial to reduce the thermal conductivity of the coating and increase the strain tolerance. The microstructure of La(Al_{1/4}Mg_{1/2}Ta_{1/4})O₃ coating applied in the double ceramic layer is shown in Fig. 15. Other properties of this kind of perovskite material are excellent, but the fracture toughness is not as good as YSZ. Due to the high saturated vapor pressure of the oxides in the components, these non-zirconia-based perovskite materials are volatile in the spraying process. The chemical composition of the deposited coating deviates from the standard stoichiometric ratio, which brings serious impact on the performance of the coating. The research shows that by adjusting the spraying parameters to reduce the residence time of the powder particles in the flame, the spraying can be reduced to the greatest extent influence of component volatilization on coating properties during coating. Interestingly, for BaLa₂Ti₃O₁₀, there is no volatilization during the spray process, and no impurity phase deviating from the standard stoichiometric ratio is present in the prepared coating. In addition, because the layered perovskite contains many rigid polyhedrons, the bonding strength between the polyhedrons is weak, which helps to reduce the thermal conductivity, plus the cracking caused by the APS process. The thermal cycling performance of BaLa₂Ti₃O₁₀ coating at 1200 °C is better than YSZ coating due to the effect of the grain. However, due to the low melting point of the material, whether the material can be widely used as TBC at 1200 °C remains to be further investigated.

5.3 Rare Earth Niobate

Rare earth niobate (M₃NbO₇) has two crystal structures: pyrochlore for M = La–Gd and defect fluorite for M = Dy, Lu, Y. The disordered distribution of oxygen vacancies

and large chemical heterogeneity in these structures result in low thermal conductivity with low correlation to temperature. At 25–1000 °C, thermal conductivity is only 1.18–1.26 W/(m K). Research on rare earth niobate TBCs includes introducing rare earth cations to improve mechanical and thermal properties and studying non-standard stoichiometric rare earth niobate by changing elemental composition. Zhu et al. [65] prepared $(\text{Dy}_{0.2}\text{Ho}_{0.2}\text{Er}_{0.2}\text{Y}_{0.2}\text{Yb}_{0.2})_3\text{NbO}_7$ high-entropy rare earth niobate by solid-phase reaction and compared it to single rare earth niobate. The high-entropy rare earth niobate has uniformly distributed rare earth elements forming a single-phase solid solution with increased configuration entropy, resulting in higher Vickers hardness (9.51 HV), fracture toughness ($2.13 \text{ MPa m}^{1/2}$), and thermal expansion coefficient ($10.2 \times 10^{-6} \text{ K}^{-1}$). Due to cation disorder and thermodynamic high-entropy effect, its thermal conductivity is only 0.724 W/(m K), far lower than single rare earth niobate.

In terms of elemental composition, studies on thermal barrier coatings of non-standard stoichiometry are more extensive than those of gadolinium zirconate, while there are few studies on rare earth niobate in this area. Huang et al. [66] analyzed the structure and performance of the coating with non-standard stoichiometric ratio $\text{Y}_{1-x}\text{Nb}_x\text{O}_{1.5+x}$ and found that when the amount ratio of Y/Nb material changes around 3:1, the cationic conductivity of the coating will increase anomalously. In addition, the elastic modulus of the coating will increase with the increase of Nb content. However, due to the inefficient effect of grain size and porosity changes, the Vickers hardness and fracture toughness did not change significantly, and Y_3NbO_7 was found to have the lowest thermal conductivity, the best mechanical properties, and the slowest sintering rate.

Niobate has a ferroelastic toughening mechanism similar to YSZ, with high fracture toughness, and the volume expansion caused by ferroelastic phase transition is basically negligible; that is, it has good high-temperature phase stability. However, the niobate crystal structure lacks intrinsic oxygen vacancies, and the thermal conductivity is higher than other new thermal barrier coating materials, so the performance needs to be further improved.

5.4 Rare Earth Tantalate

Relevant studies show that $\text{ZrO}_2\text{--Y}_2\text{O}_3\text{--Ta}_2\text{O}_5$ terpolymer system has special corrosion resistance (1500 °C), high fracture toughness (equivalent to YSZ fracture toughness), low thermal conductivity, and other advantages, so it has attracted much attention. However, previous studies mainly focused on ZrO_2 rich areas, as shown in Fig. 16, and ZrO_2 material has some bottleneck problems that are difficult to solve at high temperature, so it is a research hot spot to find low thermal conductivity materials from $\text{ZrO}_2\text{--Y}_2\text{O}_3\text{--Ta}_2\text{O}_5$ terpolymer system. Clarke et al. [67] predicted the thermal conductivity of materials in the ternary system of $\text{ZrO}_2\text{--Y}_2\text{O}_3\text{--Ta}_2\text{O}_5$ by using molecular dynamics method. Low thermal conductivity was mainly concentrated in the solid solution region of ZrO_2 and YTao_4 . Figure 16 shows the thermal

conductivity distribution of ZrO_2 - Y_2O_3 - Ta_2O_5 ternary system at 100 and 1000 °C. Thermal conductivity is as low as 1.5 W/(m K) at 1000 °C, which is about 40% lower than YSZ. When the temperature exceeds 1426 ± 7 °C, $YTaO_4$ ceramic will undergo a ferroelastic transition from monoclinic phase to tequartet phase ($M \rightarrow T$), and the volume change is small before and after the phase transition process, thus avoiding martensitic phase transition similar to YSZ, which overcomes the defect of coating failure caused by volume change of YSZ. Therefore, $YTaO_4$ ceramic was considered as a potential ceramic layer material by Clarke et al. (Fig. 14).

In addition, Clarke et al. demonstrated that $YTaO_4$ ceramic had iron-bullet phase transition phenomenon by using the method of first-principles calculation combined with experiment, and ZrO_2 could effectively reduce the iron-bullet phase transition temperature of $YTaO_4$ ceramic. In Fig. 16, the “domain” structure can be clearly observed. SEM results show that twin structures (vertical domain structures within a grain) appear on the grain surface, and the vertical intersections are amplified in the high-resolution transmission electron microscopy images, clearly demonstrating the existence of twin structures (Fig. 15).

Researchers successfully prepared $RETaO_4$ (RE-Nd, Eu, Gd, Dy, Er, Yb, and Lu) ceramics by solid-phase reaction method and systematically studied the thermal and physical properties, as shown in Fig. 17. The thermal conductivity of $RETaO_4$ ceramic is 1.38–1.94 W/(m K) at 800 °C, while that of 8YSZ ceramic is 2.47 W/(m K) at 800 °C, which is reduced by 21–45%. Moreover, this ceramic system has a high coefficient of thermal expansion, which is about $(10\text{--}11) \times 10^{-6} \text{ K}^{-1}$. Some people further reduced the thermal conductivity of $RETaO_4$ by doping, alloying, and other methods and obtained good results. The stability of the crystal structure

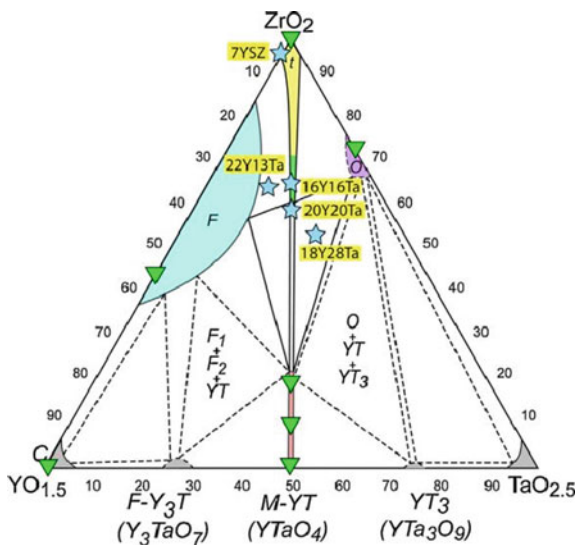


Fig. 14 Isothermal section of the ZrO_2 - Y_2O_3 - Ta_2O_5 phase diagram at 1500 °C [68]

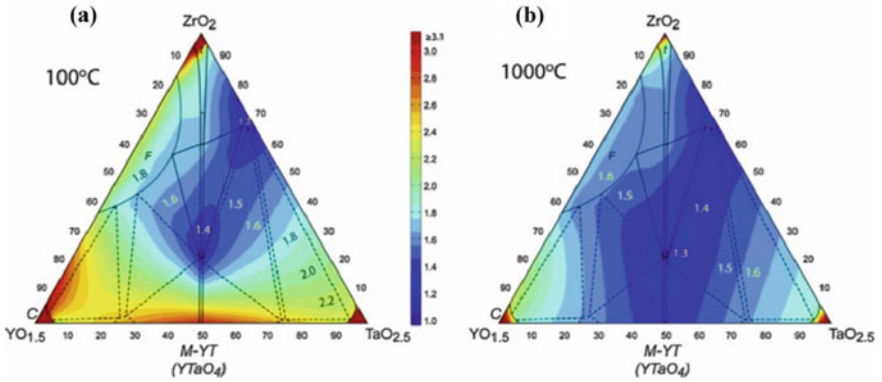


Fig. 15 Thermal conductivity simulation diagram of different components in ZrO₂-Y₂O₃-Ta₂O₅ ternary system, **a** 100 °C and **b** 1000 °C [68]

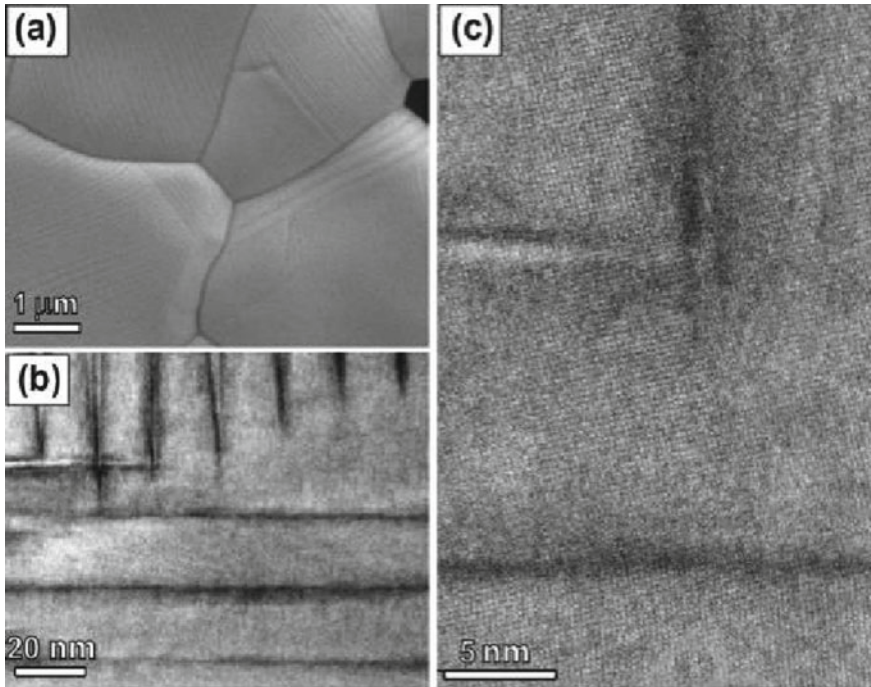


Fig. 16 **a** The SEM of YTaO₄ ceramic, **b** the TEM of domain structure for YTaO₄ ceramic, and **c** the HRTEM of YTaO₄ ceramic [68]

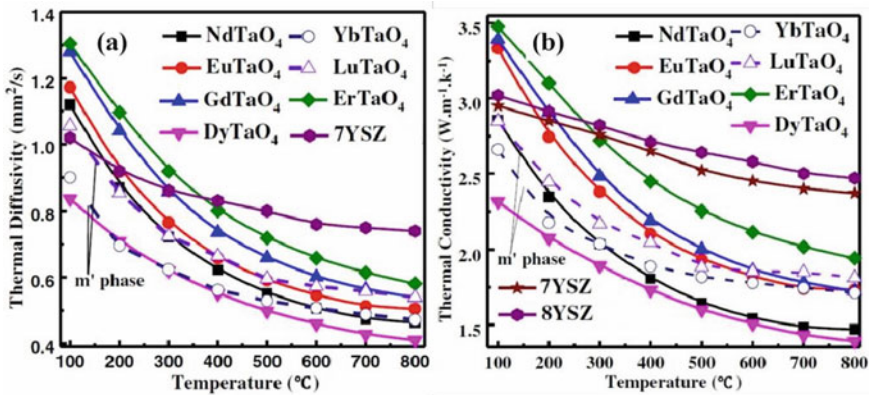


Fig. 17 a Thermal diffusion coefficient and b thermal conductivity of RETaO_4 ceramic [69]

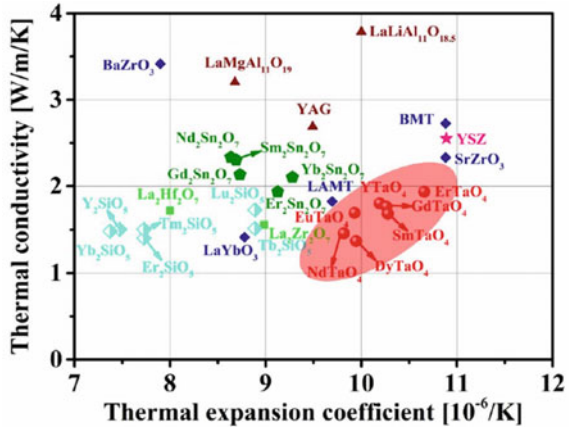
of the system depends on the degree of distortion of Ta–O tetrahedron. There is a certain relationship between Young’s modulus and low Windebye temperature. The reason for the improvement of thermal conductivity at high temperature is attributed to thermal radiation effect.

Figure 18 shows the comparison of thermal conductivity and thermal expansion coefficient between RETaO_4 ceramic and other potential ceramic layer materials. RETaO_4 has relatively low thermal conductivity (1.38–1.94 $\text{W}/(\text{m K})$) and high thermal expansion coefficient ($10\text{--}11 \times 10 \text{ K}^{-1}$). Compared with YSZ, RETaO_4 ’s high-temperature thermal conductivity is only half that of YSZ, and its service temperature can reach 1600 $^\circ\text{C}$, which has obvious advantages. In addition, it is found that RETaO_4 has iron domain structure similar to YSZ, excellent thermal and physical properties and mechanical properties, which further proves that RETaO_4 is a ceramic layer material with great potential. However, at present, there are few researches on the binding mechanism and thermo physical property matching theory of RETaO_4 ceramic and bond layer material, and there is a lack of necessary systematic theoretical analysis and experimental verification.

6 Trend of TBCs Development

As engine technology advances and thrust–weight ratio increases, the working environment of hot-end engine components becomes more severe. High-temperature oxidation, wear, and corrosion can cause irreversible damage to blades. Thermal barrier coatings (TBCs) are necessary to protect their normal operation. Common TBC materials include rare earth doped zirconia, rare earth zirconate, rare earth cerate, rare earth tantalite, and rare earth hexaluminat. Here provides a brief outlook on future TBC materials.

Fig. 18 Schematic diagram of thermal conductivity and thermal expansion of $RETaO_4$ and potential ceramic layer [69]



- (1) To develop nano-thermal barrier coating material preparation technology. Nanoparticles exhibit a series of properties that make nanomaterials a research hot spot. It is an important development direction of thermal barrier coating to introduce nanostructure into thermal barrier coating, which is the advantage of nano-thermal barrier coating. Considering the urgent need of high-performance thermal barrier coating technology for advanced gas turbine engines, the preparation of nano-thermal barrier coating materials and the scientific problems in high-temperature failure were focused to provide theoretical basis for the development of high-performance thermal barrier coating materials, so as to promote the further development of aero-engines and gas turbines.
- (2) To develop related high-entropy rare earth ceramic materials based on potential thermal barrier coating materials and further improve the performance of materials through the unique effects of high-entropy materials. In view of the uncertainty of high-entropy material components, the related concepts of material genetic engineering can be appropriately introduced, and the combination of high-entropy rare earth elements with lower theoretical thermal conductivity better match between CTEs and alloy matrix, and better mechanical properties can be screened through theoretical calculation. Of course, the work on high entropy cannot be limited to rare earth oxides with five components and equimolar components. The research on high-entropy rare earth oxides can be extended to rare earth oxides with more complex components, including medium entropy and non-equimolar components, in order to obtain better coating performance.
- (3) To develop self-healing thermal barrier coating materials. As an important technology, self-healing technology has important applications in the field of corrosion resistance. In terms of thermal barrier coating, self-healing materials can be developed to repair the cracks and voids of the coating, which can effectively reduce the penetration path of oxygen and prevent the formation of TGO, thereby improving the thermal cycling performance of the coating and improving the

thermal shock life of the coating system. At the same time, the self-healing material prevents the penetration of molten corrosion into the coating while repairing cracks and voids. In addition, the closed pores reduce the oxygen diffusivity, further slowing the erosion of the coating system by external impurities, and prolonging the service life of the coating. The time control required for self-healing materials to generate repair oxides is a difficulty in the development of self-healing coatings. The oxide generated under too little oxidation time cannot completely repair the cracks appearing in the coating, and the cracks will still expand in the subsequent high-temperature environment, which also limits the development of self-healing materials.

References

1. Yang, J., Shahid, M., Wan, C., Jing, F., Pan, W.: Anisotropy in elasticity, sound velocities and minimum thermal conductivity of zirconia from first-principles calculations. *J. Eur. Ceram. Soc.* **37**(2), 689–695 (2017)
2. Khattab, E.-S.R., Abd El Rehim, S.S., Hassan, W.M., El-Shazly, T.S.: Band Structure Engineering and Optical Properties of Pristine and Doped Monoclinic Zirconia (m-ZrO₂): density functional theory theoretical prospective. *ACS Omega* **6**(44), 30061–30068 (2021)
3. Lombardo, S., Nelson, C., Chae, K., et al.: Atomic-scale imaging of polarization switching in an (anti-) ferroelectric memory material: Zirconia (ZrO₂). In: 2020 IEEE Symposium on VLSI Technology, pp. 1–2. IEEE (2020)
4. Jose, J., Vigneshwaran, J., Baby, A., Viswanathan, R., Jose, S.P., Sreeja, P.: Dimensionally engineered ternary nanocomposite of reduced graphene oxide/multiwalled carbon nanotubes/zirconium oxide for supercapacitors. *J. Alloy. Compd.* **896**, 163067 (2022)
5. Selvi, S., Nataraj, N., Chen, T.-W., et al.: In-situ formation of 2H phase MoS₂/cerium-zirconium oxide nanohybrid for potential electrochemical detection of an anticancer drug flutamide. *Mater Today Chem* **23**, 100749 (2022)
6. Padture, N.P.: Advanced structural ceramics in aerospace propulsion. *Nat. Mater.* **15**(8), 804–809 (2016)
7. Pan, W., Phillpot, S.R., Wan, C., Chernatynskiy, A., Qu, Z.: Low thermal conductivity oxides. *MRS Bull.* **37**(10), 917–922 (2012)
8. Raghavan, S., Wang, H., Porter, W., Dinwiddie, R., Mayo, M.: Thermal properties of zirconia co-doped with trivalent and pentavalent oxides. *Acta Mater. Mater.* **49**(1), 169–179 (2001)
9. Shen, Z., Liu, Z., Mu, R., He, L., Liu, G.: Y–Er–ZrO₂ thermal barrier coatings by EB-PVD: thermal conductivity, thermal shock life and failure mechanism. *Appl. Surf. Sci. Adv.* (2021)
10. Wei, X., Hou, G., An, Y., Yang, P., Chen, J.: Effect of doping CeO₂ and Sc₂O₃ on structure, thermal properties and sintering resistance of YSZ. *Ceram. Int.* **47**(5) (2020)
11. Khodaii, J., Barazandeh, F., Rezaei, M., Hamed, A., Ahmed, A.D.S.: Influence of grinding parameters on phase transformation, surface roughness, and grinding cost of bioceramic partially stabilized zirconia (PSZ) using diamond grinding wheel. *Int. J. Adv. Manuf. Technol.* **105**(11) (2019)
12. Fan, W., Wang, Z., Bai, Y., et al.: Improved properties of scandia and yttria co-doped zirconia as a potential thermal barrier material for high temperature applications. *J. Eur. Ceram. Soc.* **38**(13), 4502–4511 (2018)
13. Zhao, P., Zheng, H., Li, G., et al.: CMAS corrosion resistant of La³⁺-Yb³⁺-Ce⁴⁺ co-doped ZrO₂ based TBCs: experimental and theoretical research. *Ceram. Int.* **49**(11), 19402–19411 (2023)

14. Rebollo, N.R., Fabrichnaya, O., Levi, C.G.: Phase stability of Y+ Gd co-doped zirconia. *Int. J. Mater. Res.* **94**(3), 163–170 (2022)
15. Liu, Q., Huang, S., He, A.: Composite ceramics thermal barrier coatings of yttria stabilized zirconia for aero-engines. *J. Mater. Sci. Technol.* **35**(12), 2814–2823 (2019)
16. Feng, Y., Dong, T.-s., Li, G.-l., et al.: The roles of stress in the thermal shock failure of YSZ TBCs before and after laser remelting. *J. Alloys Compd.* **828**, 154417 (2020)
17. Lavasani, H.Q., Valefi, Z., Ehsani, N., Masoule, S.T.: Studying the effect of spraying parameters on the sintering of YSZ TBC using APS method. *Surf. Coat. Technol.* **360**, 238–246 (2019)
18. Zhang, H., Liu, Z., Yang, X., Xie, H.: Interface failure behavior of YSZ thermal barrier coatings during thermal shock. *J. Alloy. Compd.* **779**, 686–697 (2019)
19. Jung, S.-H., Lu, Z., Jung, Y.-G., et al.: Thermal durability and fracture behavior of layered Yb-Gd-Y-based thermal barrier coatings in thermal cyclic exposure. *Surf. Coat. Technol.* **323**, 39–48 (2017)
20. Liu, H., Li, S., Li, Q., Li, Y.: Investigation on the phase stability, sintering and thermal conductivity of $\text{Sc}_2\text{O}_3\text{-Y}_2\text{O}_3\text{-ZrO}_2$ for thermal barrier coating application. *Mater. Des.* **31**(6), 2972–2977 (2010)
21. Fan, W., Bai, Y., Wang, Y., et al.: Microstructural design and thermal cycling performance of a novel layer-gradient nanostructured $\text{Sc}_2\text{O}_3\text{-Y}_2\text{O}_3$ co-stabilized ZrO_2 thermal barrier coating. *J. Alloy. Compd.* **829**, 154525 (2020)
22. Wei, Z.-Y., Meng, G.-H., Chen, L., et al.: Progress in ceramic materials and structure design toward advanced thermal barrier coatings. *J. Adv. Ceram.* **11**(7), 985–1068 (2022)
23. Vardelle, A., Moreau, C., Akedo, J., et al.: The 2016 thermal spray roadmap. *J. Therm. Spray Technol.* **25**, 1376–1440 (2016)
24. Goto, T.: Thermal barrier coatings deposited by laser CVD. *Surf. Coat. Technol.* **198**(1–3), 367–371 (2005)
25. Kiilakoski, J., Puranen, J., Heinonen, E., Koivuluoto, H., Vuoristo, P.: Characterization of powder-precursor HVOF-sprayed $\text{Al}_2\text{O}_3\text{-YSZ/ZrO}_2$ coatings. *J. Therm. Spray Technol.* **28**, 98–107 (2019)
26. Lima, R.S., Porous, A.P.S.: YSZ TBC manufactured at high powder feed rate (100 g/min) and deposition efficiency (70%): microstructure, bond strength and thermal gradients. *J. Therm. Spray Technol.* **31**(3), 396–414 (2022)
27. Mauer, G., Jarligo, M.O., Rezanka, S., Hospach, A., VaßEn, R.: Novel opportunities for thermal spray by PS-PVD. *Surf. Coat. Technol.* **268**, 52–57 (2015)
28. Yang, J., Zhao, H., Zhong, X., et al.: Thermal cycling behavior of quasi-columnar YSZ coatings deposited by PS-PVD. *J. Therm. Spray Technol.* (2016)
29. Lashmi, P.G., Ananthapadmanabhan, P.V., Unnikrishnan, G., Aruna, S.T.: Present status and future prospects of plasma sprayed multilayered thermal barrier coating systems. *J. Eur. Ceram. Soc.* **40**(8), 2731–2745 (2020)
30. Schlichting, K.W., Padture, N.P., Jordan, E.H., Gell, M.: Failure modes in plasma-sprayed thermal barrier coatings. *Mater. Sci. Eng. A* **342**(1–2), 120–130 (2003)
31. Soltani, R., Coyle, T.W., Mostaghimi, J.: Creep behavior of plasma-sprayed zirconia thermal barrier coatings. *J. Am. Ceram. Soc.* **90**(9), 2873–2878 (2010)
32. Lima, R.S., Kucuk, A., Berndt, C.C.: Integrity of nanostructured partially stabilized zirconia after plasma spray processing. *Mater. Sci. Eng. A* **313**(1–2), 75–82 (2001)
33. Lima, R.S., Kucuk, A., Berndt, C.C.: Bimodal distribution of mechanical properties on plasma sprayed nanostructured partially stabilized zirconia. *Mater. Sci. Eng. A* **327**(2), 224–232 (2002)
34. Bernier, J.S.: Evolution and characterization of partially stabilized zirconia (7wt% Y_2O_3) thermal barrier coatings deposited by electron beam physical vapor deposition (2002)
35. Zhang, B., Song, W., Wei, L., et al.: Novel thermal barrier coatings repel and resist molten silicate deposits. *Scripta Mater. Mater.* **163**, 71–76 (2019)
36. Gao, L., Guo, H., Wei, L., Li, C., Xu, H.: Microstructure, thermal conductivity and thermal cycling behavior of thermal barrier coatings prepared by plasma spray physical vapor deposition. *Surf. Coat. Technol.*, 424–430 (2015)

37. Li, C., Guo, H., Gao, L., Wei, L., Gong, S., Xu, H.: Microstructures of yttria-stabilized zirconia coatings by plasma spray-physical vapor deposition. *J. Therm. Spray Technol.* **24**, 534–541 (2015)
38. Shan, X., Zou, Z., Gu, L., et al.: Buckling failure in air-plasma sprayed thermal barrier coatings induced by molten silicate attack. *Scripta Mater. Mater.* **113**, 71–74 (2016)
39. Thornton, J., Wood, C., Kimpton, J.A., Sesso, M., Zonneveldt, M., Armstrong, N.: Failure mechanisms of calcium magnesium aluminum silicate affected thermal barrier coatings. *J. Am. Ceram. Soc.* **100**(6), 2679–2689 (2017)
40. Wang, Z., Zhou, G., Jiang, D., Wang, S.: Recent development of $A_2B_2O_7$ system transparent ceramics. *J. Adv. Ceram.* **7**(4), 289–306 (2018)
41. KräMer, S., Yang, J., Levi, C.G.: Infiltration-inhibiting reaction of gadolinium zirconate thermal barrier coatings with CMAS melts. *J. Am. Ceram. Soc.* **91**(2), 576–583 (2010)
42. Wang, C., Huang, W., Wang, Y., et al.: Synthesis of monodispersed $La_2Ce_2O_7$ nanocrystals via hydrothermal method: a study of crystal growth and sintering behavior. *Int. J. Refract Metal Hard Mater.* **31**, 242–246 (2012)
43. Lehmann, H., Pitzer, D., Pracht, G., Vassen, R., Stöver, D.: Thermal conductivity and thermal expansion coefficients of the lanthanum rare-earth-element zirconate system. *J. Am. Ceram. Soc.* **86** (2010)
44. Wan, C.L., Pan, W., Xu, Q., Qin, Y.X., Fang, M.H.: Effect of point defects on the thermal transport properties of $(La_xGd_{1-x})_2Zr_2O_7$: experiment and theoretical model. *Physrevb* **74**(14), 144109 (2006)
45. Wan, C., Wei, Z., Wang, Y., et al.: Glass-like thermal conductivity in ytterbium-doped lanthanum zirconate pyrochlore. *Acta Mater. Mater.* **58**(18), 6166–6172 (2010)
46. Cao, X., Li, J., Zhong, X., et al.: $La_2(Zr_{0.7}Ce_{0.3})_2O_7$ —a new oxide ceramic material with high sintering-resistance. *Mater. Lett.* **62**(17–18), 2667–2669 (2008)
47. Cao, X., Vassen, R., Stöver, D.: Ceramic materials for thermal barrier coatings. *J. Eur. Ceram. Soc.* **24**(1), 1–10 (2004)
48. Taleghani, P.R., Valefi, Z., Ehsani, N.: Synthesis of $La_2(Zr_{0.7}Ce_{0.3})_2O_7$ nanopowder using a simple chemical precipitation method and heat treatment at high temperature. *Int. J. Mater. Res.* **110**(8), 757–764 (2019)
49. Kutty, K., Rajagopalan, S., Mathews, C.K., Varadaraju, U.V.: Thermal expansion behaviour of some rare earth oxide pyrochlores. *Mater. Res. Bull.* **29**(7), 759–766 (1994)
50. Shimamura, K., Arima, T., Idemitsu, K., Inagaki, Y.: Thermophysical properties of rare-earth-stabilized zirconia and zirconate pyrochlores as surrogates for actinide-doped zirconia. *Int. J. Thermophys. Thermophys.* **28**, 1074–1084 (2007)
51. Schelling, P., Phillpot, S., Grimes, R.: Optimum pyrochlore compositions for low thermal conductivity. *Philos. Mag. Lett.* **84**(2), 127–137 (2004)
52. Li, J.Y., Dai, H., Li, Q., Zhong, X.H., Cao, X.Q.: Improvement of fracture toughness lanthanum zirconate. *Mater. Eng.* **2006**(5) (2006)
53. Li, J., Dai, H., Li, Q., Zhong, X., Cao, X.: Improvement of fracture toughness lanthanum zirconate. *Cailiao Gongcheng* **5**, 51–56 (2006)
54. Zhu, Z., Liu, B., Shen, J., Lou, Y., Ji, Y.: $La_2Ce_2O_7$: a promising proton ceramic conductor in hydrogen economy. *J. Alloy. Compd.* **659**, 232–239 (2016)
55. Praveen, K., Sravani, N., Alroy, R.J., Shanmugavelayutham, G., Sivakumar, G.: Hot corrosion behaviour of atmospheric and solution precursor plasma sprayed $(La_{0.9}Gd_{0.1})_2Ce_2O_7$ coatings in sulfate and vanadate environments. *J. Eur. Ceram. Soc.* **39**(14), 4233–4244 (2019)
56. Guo, H., Gong, S., Xu, H.: Evaluation of hot-fatigue behaviors of EB-PVD gradient thermal barrier coatings. *Mater. Sci. Eng. A* **325**(1–2), 261–269 (2002)
57. Heveling, J.: La-doped alumina, lanthanum aluminate, lanthanum hexaaluminate, and related compounds: a review covering synthesis, structure, and practical importance. *Ind. Eng. Chem. Res.* **62**(6), 2353–2386 (2023)
58. Pan, W., Xu, Q., Qi, L., et al.: Novel low thermal conductivity ceramic materials for thermal barrier coatings. In: *China International Conference on High-Performance Ceramics* (2005)

59. Machida, M., Kawasaki, H., Eguchi, K., Arai, H.: Surface areas and catalytic activities of Mn-substituted hexaaluminates with various cation compositions in the mirror plane. *Chem. Lett.* **17**(9), 1461–1464 (1988)
60. Sun, J., Hui, Y., Jiang, J., Deng, L., Cao, X.: Crystallization mechanism of plasma-sprayed LaMgAl₁₁O₁₉ coating. *Appl. Surf. Sci.* **504**, 144509 (2019)
61. Chen, X., Zhao, Y., Fan, X., et al.: Thermal cycling failure of new LaMgAl₁₁O₁₉/YSZ double ceramic top coat thermal barrier coating systems. *Surf. Coat. Technol.* **205**(10), 3293–3300 (2011)
62. Lu, H., Wang, C.-A., Zhang, C.: Low thermal conductivity Sr²⁺, Zn²⁺ and Ti⁴⁺ ions co-doped LaMgAl₁₁O₁₉ for potential thermal barrier coating applications. *Ceram. Int.* **40**(10), 16273–16279 (2014)
63. Li, W., Zhou, X., Lei, Q., Wang, S.: Heat and moisture resistance of divalent metals substituted La-Hexaaluminates prepared by reverse microemulsion. *Ceram. Int.* (2020)
64. Wang, Y.-H., Ouyang, J.-H., Liu, Z.-G.: Influence of dysprosium oxide doping on thermophysical properties of LaMgAl₁₁O₁₉ ceramics. *Mater. Des.* **31**(7), 3353–3357 (2010)
65. Zhu, Y., Wang, X., Wang, A., Wu, G., Wang, J., Zhang, T.: Identification of the chemical state of Fe in barium hexaaluminate using Rietveld refinement and 57Fe Mössbauer spectroscopy. *J. Catal. Catal.* **283**(2), 149–160 (2011)
66. Huang, C., Zhou, X., Ding, C.: Investigation of the thermomechanical properties of a plasma-sprayed nanostructured zirconia coating. *J. Eur. Ceram. Soc.* **23**(9), 1449–1455 (2003)
67. Clarke, D., Levi, C.: Materials design for the next generation thermal barrier coatings. *Annu. Rev. Mater. Res.* *Rev. Mater. Res.* **33**(1), 383–417 (2003)
68. Limarga, A.M., Shian, S., Leckie, R.M., Levi, C.G., Clarke, D.R.: Thermal conductivity of single-and multi-phase compositions in the ZrO₂-Y₂O₃-Ta₂O₅ system. *J. Eur. Ceram. Soc. Ceram. Soc.* **34**(12), 3085–3094 (2014)
69. Wang, J., Chong, X.Y., Zhou, R., Feng, J.: Microstructure and thermal properties of RETaO₄ (RE = Nd, Eu, Gd, Dy, Er, Yb, Lu) as promising thermal barrier coating materials. *Scripta Materialia* **126**(Complete), 24–28 (2017)

Recent Developments on Al₂O₃-Based Thermal Barrier Coatings



Fatih Kirbiyik, Mustafa Guven Gok, and Gultekin Goller 

Abstract The rising demand for increasing the operating temperature of gas turbine engines has generated many technological inventions. With the high-performance expectation of gas turbine engines for an economical and environmental aspect, researchers focus on the development of materials which can tolerate high temperatures, high stress, and the evolution of ceramic coatings. In this respect, thermal barrier coatings (TBC) play a major role in protecting hot sections of modern gas turbine systems. Yttria-stabilized zirconia (YSZ) is widely used commercially on metal superalloy parts to provide insulation for high temperatures. However, some disadvantages of YSZ such as high-temperature phase transformation (~1200 °C) and high oxygen ions permeability enable researchers to search for alternative thermal barrier coatings materials and designs. One of the TBC materials alumina (Al₂O₃) is not viable alone for TBC top coat because of its low coefficient of thermal elongation compared with bond coat and substrate. However, Al₂O₃ coating together with other TBC materials on the metal substrate using different methods and designs can improve the mechanical and thermal properties of TBC while providing better protection to the metal substrate from oxidation. This chapter discusses the Al₂O₃-based TBC systems, the production of different complex designs, laser surface modification, comparison with YSZ and ceria-yttria-stabilized zirconia (CYSZ), and testing methodology.

Keywords Thermal barrier coating · Alumina · Zirconia · Thermal tests · CMAS · Hot corrosion · Laser surface modification

F. Kirbiyik · G. Goller (✉)

Department of Metallurgical and Materials Engineering, Istanbul Technical University, 34469
Istanbul, Turkey
e-mail: goller@itu.edu.tr

M. G. Gok

Department of Metallurgical and Materials Engineering, Gaziantep University, 27310 Gaziantep,
Turkey

Abbreviations

APS	Atmospheric plasma spray
BC	Bond coat
CMAS	Calcium-magnesia-alumina-silica
CTE	Thermal elongation coefficient
EB-PVD	Electron-beam physical vapor deposition
HVOF	High-velocity oxygen fuel
SEM	Scanning electron microscope
SPS	Suspension plasma spray
TC	Top coat
TGO	Thermally grown oxide
α	Alfa
γ	Gamma
δ	Delta

1 Introduction

Thermal barrier coatings (TBCs) are sophisticated material systems that are employed in extreme high-temperature environment, such as in aircraft and industrial engines. The primary function of TBCs is to safeguard the metallic components of gas turbine engines' hot sections from the detrimental effects of elevated temperatures. These coatings consist of a porous ceramic top coat (TC) (generally yttria (Y_2O_3) stabilized zirconia (Zr_2O_3) (YSZ)), a thermally grown oxide layer (TGO) ($\alpha-Al_2O_3$) and bond coat (BC) (MCrAlY (M = Ni, Co or Fe) on a nickel-based super-alloy metallic substrate. The most used producing methods are air plasma spraying (APS) and electron beam physical vapor deposition (EB-PVD) for TBCs. They are usually selected depending on changing structure and properties of coatings and are widely used to produce isolating ceramic top coats. Although the ceramic top coat has a porous structure to insulate the heat from the surface, the bond coat structure is designed as a dense structure to improve the adhesion capability inter the ceramic top coat and substrate. Therefore, high-velocity oxygen fuel (HVOF) spraying that provides high dense structure is commonly used to produce metallic bond coat. Alumina TGO layer forms between TC/BC interface under operating conditions to protect the bond coat and substrate from oxidation. Forming oxide layer thickness can be adjusted on the aluminum proportion of the composition bond coat [1–3] (Fig. 1).

The components responsible for the operation of airplane jet engines undergo severe mechanical, chemical, and thermal strains. On account of some property requirements of TBC, ceramic top coats must adhere to some limitations for design and material selection. These requirements can be listed as follows.

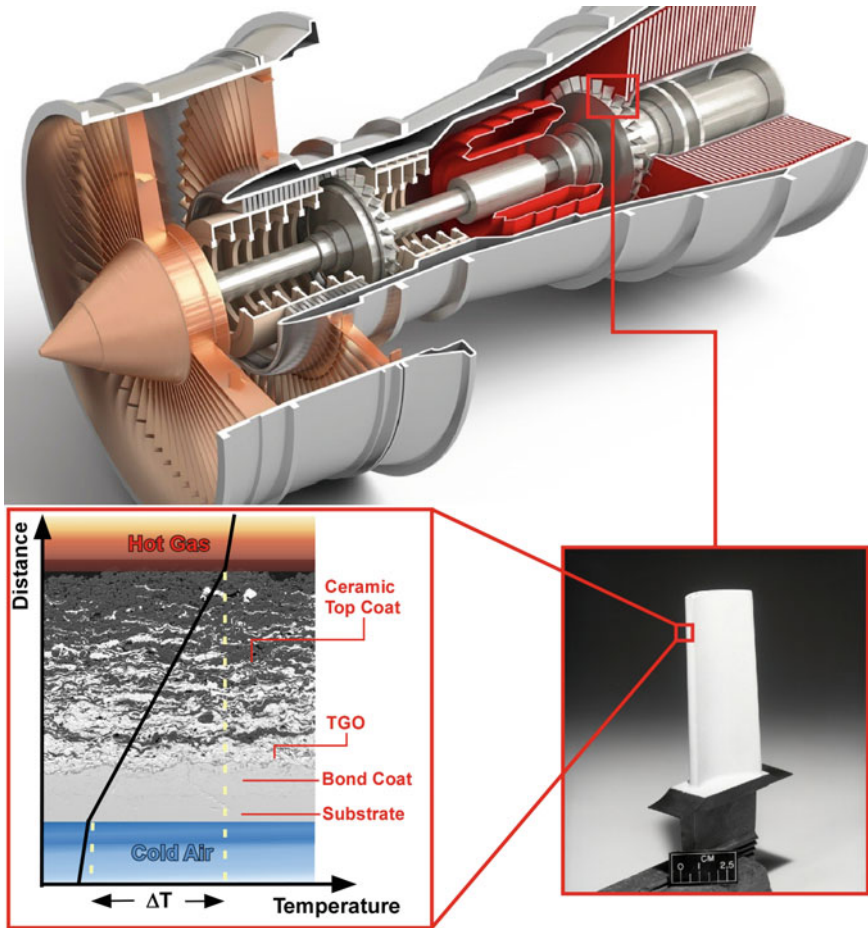


Fig. 1 Cross-section microstructure of APS functionally graded TBC

1. High melting points provide resistance at elevated temperatures experienced by gas turbine engines.
2. Inhibiting phase transformation to not have volume changing between room and operating temperatures.
3. Low thermal conductivity to provide thermal insulation for metallic parts.
4. Chemical inertness against to engine environment (fuel impurities and corrosive particles that enter to engine).
5. Thermal expansion compatibility with the metallic substrate.
6. Strong adhesion to the metallic substrate.
7. Low sintering rate of the porous microstructure.

These requirements cannot be met by most of the materials. Researchers have studied many TBC materials such as Al₂O₃, TiO₂, mullite, CaO/MgO + ZrO₂, YSZ,

$\text{CeO}_2 + \text{YSZ}$, zircon $\text{La}_2\text{Zr}_2\text{O}_7$, $\text{La}_2\text{Ce}_2\text{O}_7$, $\text{LaMgAl}_{11}\text{O}_{19}$, SrZrO_3 , and $\text{Gd}_2\text{Zr}_2\text{O}_7$ because of their different properties. Until now, only a limited number of materials have met these requirements. Especially, most satisfying material is zirconia because of its high thermal expansion coefficient that matches mostly with metallic materials. However, zirconia is restricted to use alone because of tetragonal-monoclinic phase transformation around 1170°C . Phase transformation is accompanied by a volume expansion, which causes large stresses and leads to the spallation of coating [4–8]. Therefore, zirconia can be used with only stabilizing alloying. Stabilization of pure zirconia can be achieved by using other oxides such as calcium oxide (CaO), magnesium oxide (MgO), cerium (II) oxide (CeO_2 , ceria), and yttrium oxide (Y_2O_3 , yttria) for prolonging high-temperature resistance and volume stabilization. In literature, the most effective stabilizers are accepted as yttria (Y_2O_3) and ceria (CeO_2) for transformation toughening. The tetragonal phase can be stabilized by using these two agents and form tetragonal zirconia polycrystals (TZP). The primary distinction between the two forms lies in the average grain dimensions. Ce-TZP grains are larger (ca. 2.0 μm) than Y-TZP (ca. 0.5–0.8 μm). In general, the best proportion of YSZ for stabilization tetragonal phase and improved thermal shock resistance is 7–8% Y_2O_3 addition to ZrO_2 (7–8YSZ) [9].

To the high-performance requirement of TBC materials, even tetragonal zirconia stabilization is not enough to withstand a gas turbine engine environment. Although YSZ has advantages for use as TBC material, it has plenty of disadvantages such as sintering above 1200°C that leads to lower thermal isolation, high oxygen transparency, and low corrosion resistance. This leads researchers to search for new designs and ceramic top coat materials. As a summary, the limitation of YSZ can be listed below:

1. Above 1200°C , YSZ has tetragonal to monoclinic phase transformation for the long-term operation which leads to volume change and stress inter-coating structure and exhibits the spallation of coating.
2. YSZ is sensitive to hot corrosion. If fuel does not exist impurities like S, Na, and V ions, YSZ can exhibit higher performance. However, in particular, the deposit salts of Na_2O , SO_3 , or V_2O_5 react with Y_2O_3 and produce corrosion product VYO_4 in elevated temperatures and depletion of Y_2O_3 in zirconia coating cause to the monoclinic transformation of zirconia.
3. Another degradation of YSZ can be brief as SiO_2 segregates at the grain boundaries of YSZ. Segregation of YSZ grains leads to localized degradation and an increase in sintering.
4. YSZ coating possesses a high concentration of oxygen ion vacancies. These vacancies allow oxygen transport and the oxidation of bond coat at high temperatures. Thermally grown oxide layer (TGO) forms and grows between ceramic top coat and bond coat. TGO causes the stress and spallation of ceramic top coat [10].

Recent studies continue to be investigated to complement the above-listed shortcomings of YSZ. Another ceramic top layer material used as an alternative in the

studies carried out is alumina (Al₂O₃). However, its relatively high thermal conductivity and low thermal elongation coefficient (CTE) compared with YSZ make alumina limited for single usage as TBC. The plasma-sprayed alumina contains mainly unstable phases such as γ -Al₂O₃ and δ -Al₂O₃. At elevated temperatures of gas turbine engines, these unstable phases transform into stable α -Al₂O₃ which results in volume change ($\gamma \rightarrow \alpha \sim 15\%$). Therefore, alumina is generally preferred as second material in addition to YSZ or CYSZ to improve high-temperature oxidation and corrosion resistance [10].

In literature, recent studies which investigate alumina as a TBC top coat material show that the addition of alumina as bulk or layered improves the oxidation and corrosion resistance of TBCs noticeably. Keyvani et al. [11, 12] have studied Al₂O₃/YSZ-layered composite coatings. Al₂O₃ layers decrease the O₂ diffusion and reduce TGO growth rate. This decrease leads thermal cycle resistance of TBC. Saremi et al. [13] reported that the addition Al₂O₃ layer on YSZ top coat reduced the oxygen permeation toward the bond coat which could improve the lifetime of TBCs during thermal cycling. Zhang et al. [14] produced different proportions of alumina layered on zirconia by using air plasma spraying and investigating oxidation and corrosion of TBCs. ZrO₂ + Al₂O₃ composite coatings showed improved oxidation resistance of the bond coat and corrosion resistance of the top coat. According to the studies, TBC development was achieved with a composite structure formed with alumina-YSZ and CYSZ, multilayered (MLed) or functionally graded (FGed) designs.

The objective of this chapter is to provide a summary of the characteristics of thermal barrier coatings based on alumina. The sections that follow will cover the techniques used in their production, the design of the coatings, their thermal conductivity, mechanical properties, performance during thermal cycling, and resistance to hot corrosion and CMAS. The chapter will also address the process of laser surface modification and the performance of TBCs that have undergone this process in thermal cycling and gradient condition.

2 Coating Process and Design

2.1 Production of Alumina-Based Thermal Barrier Coatings

The production method of producing TBC is important for controlling the microstructure of the coating. Different types of production methods are used for producing alumina-based TBC such as air plasma spraying (APS) [12, 13, 15, 16], electron beam physical vapor deposition (EB-PVD) [17, 18], and suspension plasma sputtering [19]. When comparing these different deposition methods, it is evident that they provide varying morphologies. However, these morphologies may have certain defects. For instance, the air plasma spraying method, which involves high-temperature melting, can result in defects that effectively reduce thermal conductivity throughout the coating. Similarly, the suspension plasma spraying (SPS) method tends to provide

coatings with higher porosity due to rapid solidification. However, this can lead to lower mechanical properties due to the increased porosities. On the other hand, TBCs produced by the EB-PVD method exhibit columnar structures. These structures can reduce the oxidation resistance of the bond coat. In contrast, the magnetron sputter method has been utilized in some studies as an oxidation barrier to enhance oxidation resistance by creating a denser layer. In summary, the most used two methods are APS and EB-PVD to produce alumina composite coatings.

In a study, alumina/CYSZ functionally layered 8-layered (FG8) TBC was produced by using the APS process on a NiCoCrYAl bond coat. The cross-section microstructure is given in Fig. 2. Typical morphologic properties (such as cracks, porosities, and unmelted particles) of APS-produced FGed $\text{Al}_2\text{O}_3/\text{CYSZ}$ can be seen on the cross-section image of TBC [20]. The interface between ceramic and bond coat seems continuous and permanent.

Powder alumina has the structure of a rhombohedral $\alpha\text{-Al}_2\text{O}_3$ phase (JCPDS 71-1683). While the process of air plasma spraying, alumina powders transform to cubic $\gamma\text{-Al}_2\text{O}_3$ phase because of effective high temperature (JCPDS 10-0425). This phase transformation prevents the use of alumina alone as TBC. The volume change ($\sim 15\%$) that occurs because of phase transformation, however, can be ignored with a TBC material whose thermal expansion (8YSZ CTE $a = 10.7 \times 10^{-6} \text{ K}^{-1}$ 1000 °C [4]) is higher than that of alumina (CTE $a = 9.6 \times 10^{-6} \text{ K}^{-1}$ at 1000 °C [4]) [20] (Fig. 3).

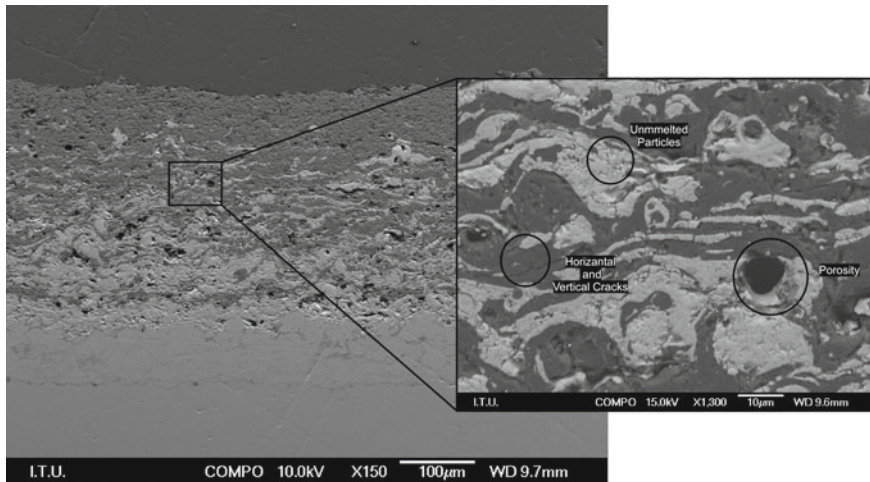
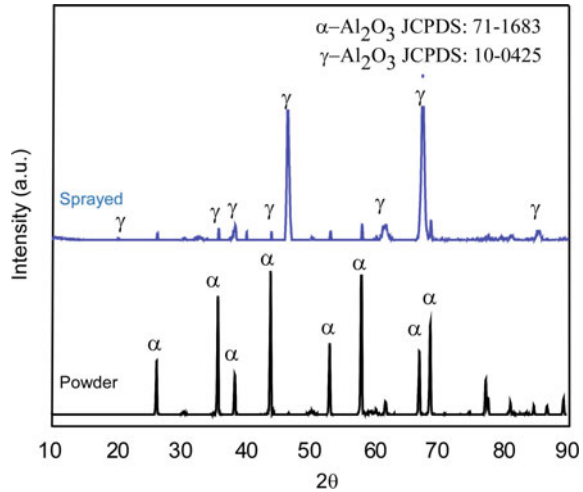


Fig. 2 Cross-section SEM image of air plasma sprayed functionally graded alumina/CYSZ 8-layered TBC

Fig. 3 Phase analysis of powder and air plasma-sprayed alumina/CYSZ coating



2.2 Design of Alumina-Based Thermal Barrier Coatings

The importance of typical morphological properties such as cracks and horizontal pores plays a vital role in lowering the thermal conductivity of the TBCs. Individual defects and horizontal cracks that are vertical to the spray direction act a role in lowering the thermal conductivity. Specifically, the presence of parallel cracks among the splats results in a decrease in thermal conductivity. The parallel cracks can be produced by using a multilayered (MLed) or functionally graded (FGed) structure. Another feature mentioned in the previous section is that alumina has phase transformation while spraying from α -Al₂O₃ to γ -Al₂O₃. Under operating temperatures, γ -Al₂O₃ phase transforms back to stable α -Al₂O₃. Thanks to the layering structure that is provided by MLed (Fig. 4a–c) or FGed design (Fig. 4d–e), thermal elongation mismatch of zirconia and alumina caused by alumina phase transformation can be tolerated.

In our previous studies [20, 21], MLed (Type I–II) and FGed (Type III) designs were investigated (Fig. 5). Type I consists CYSZ and Al₂O₃ coatings with multilayered 4, 8 and 12 layers. Type II consists CYSZ and Al₂O₃ + YSZ (1:1) multilayered 4, 8, and 12 layers. Type III consists CYSZ and Al₂O₃ with functionally graded 4, 8, and 12 layers. The top coating of powders was produced by the APS system. The total layered top coat was sprayed around 400 μ m by the thickness. The porosity level of ceramic top coat layers prepared in 4, 8, and 12 layers were 13, 11, and 7% for Type I, 10, 8, and 6% for Type II coatings and 6, 7, and 8% for Type III, respectively. While the alumina proportion of coatings was increased, the porosity level of coatings was decreasing. Because of the lower melting temperature of alumina, the densification of alumina while the spraying process was higher than YSZ and CYSZ. Thermal and mechanical properties will be discussed in the following sections.

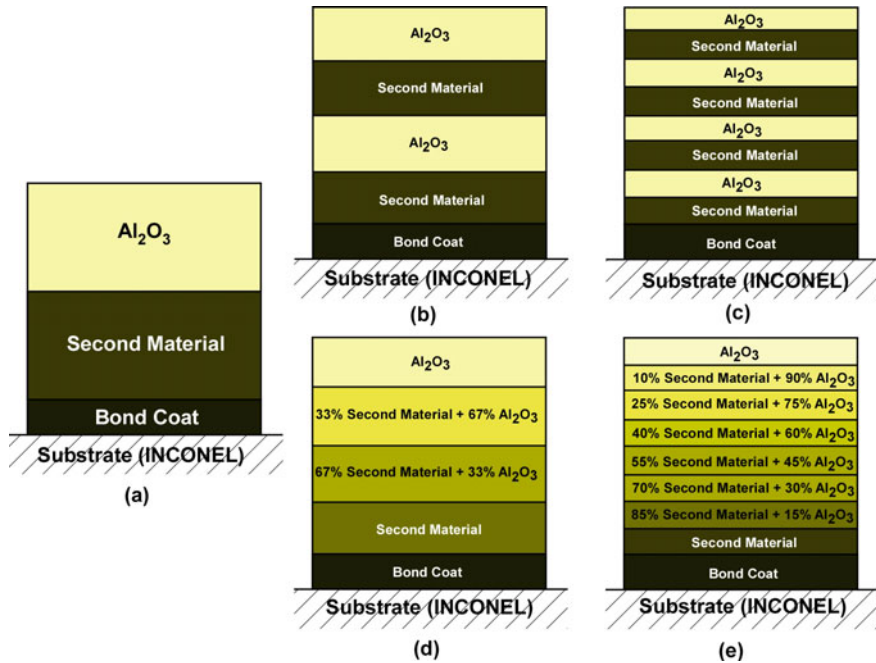


Fig. 4 Schematic view of DL (a) MLED (b, c) and FGed (d, e) coating design

3 Thermal Properties and Thermal Tests

3.1 Thermal Conductivity

TBC aims to insulate the substrate from high operating temperatures. Therefore, TBC should decrease the effective temperature of metallic parts of turbines. Phonons play a crucial role in the heat conduction of ceramics. The ability of ceramic materials to conduct heat is influenced by how easily phonons are scattered. Factors such as the presence of various atoms within the unit cell, porosities, grain boundaries, and impurities can all scatter phonons within the material's structure. As a result, these structural features can lower the material's thermal conductivity [22]. Depending on the microstructure of the most used TBC-producing method (APS, EB-PVD), thermal conductivity can vary. The coating produced with air plasma spray for YSZ has 0.8–1.0 W/mK thermal conductivity at room temperature. These values are much higher with EB-PVD coatings, and the thermal conductivity of YSZ is 1.5–1.9 W/mK for the same coating materials [23].

Alumina TBC is a type of ceramic coating that is applied to high-temperature components such as turbine blades and exhaust systems to improve their thermal insulation properties. The thermal conductivity of alumina TBC can vary depending on the specific formulation and manufacturing process used. However, in general,

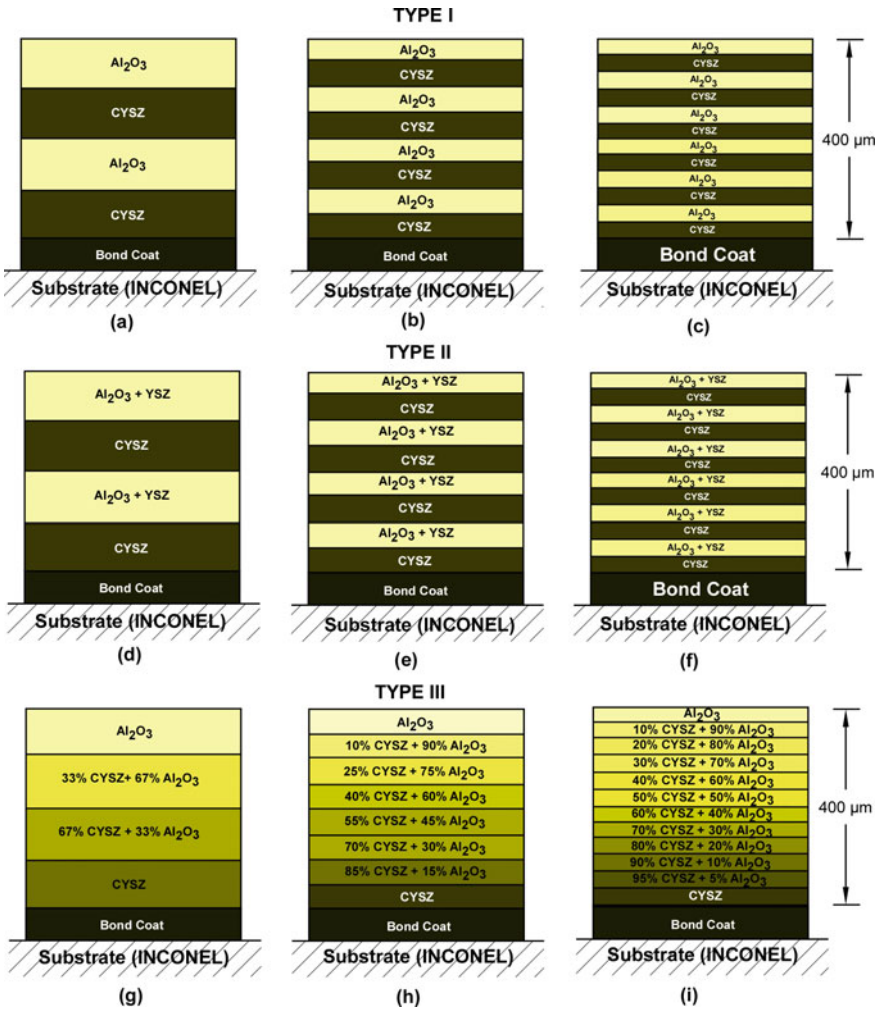


Fig. 5 Schematic view of 4, 8, and 12 MLed (a–c), Al₂O₃/CYSZ (d–f) and Al₂O₃ + YSZ/CYSZ FGed (g–i) Al₂O₃/CYSZ coatings

alumina TBC has a low thermal conductivity, typically in the range of 0.5 to 2.0 W/mK. This low thermal conductivity is due to the unique microstructure of the coating, which consists of a layered structure of ceramic materials that trap air in between the layers. This trapped air acts as an insulating layer, reducing the amount of heat that can be transferred through the coating.

Even if, as reported in a study [4] thermal conductivities of CYSZ, Al₂O₃, and YSZ ceramic TBC materials are 2.77, 5.8, and 2.12 W/mK, respectively. Thermal conductivities of type-I and type-II multilayered designs (MLed) were lower than single-layer (SL) coatings, because of unique porosities. Thermal conductivities of

Table 1 Thermal conductivity of APS-produced alumina-based TBCs

Design	Composition	Production technique	Thermal conductivity (W/mK)	Temperature (°C)	Reference
Single layered	Al ₂ O ₃	APS	3.8–12	25–1200	[24, 25]
Multilayered	Al ₂ O ₃ /CYSZ	APS	1.07–1.50	25	[21]
	Al ₂ O ₃ + YSZ/ CYSZ	APS	0.99–1.07	25	[21]
	20%Al ₂ O ₃ + 80%YSZ/YSZ	APS	0.92–1.19	25–1000	[26]
	Al ₂ O ₃ /YSZ	APS	2.2–2.8	25–1000	[24]
Functionally graded	Al ₂ O ₃ /CYSZ	APS	0.81–1.05	25–835	[20]

type-I 4-, 8-, and 12-layered structures were 1.07, 1.28, and 1.50 W/mK, respectively. Thermal conductivities of type-II 4-, 8-, and 12-layered structures were 1.07, 0.99, and 1.00 W/mK at room temperature [21]. Thermal conductivities of FGED design were measured at 4 ramps between room temperature to 835 °C. The lowest thermal conductivity could be measured by FGED 4-layered design as 0.81 W/mK at 595 °C. There are not many studies in the literature that measure the thermal conductivity of alumina-based thermal barrier coatings. The measurement temperatures and production techniques of some studies that measured thermal conductivity are listed in Table 1.

3.2 Thermal Cycling Tests

Gas turbines are subject to harsh environments that can cause damage to their components. One way to protect them is by using thermal barrier coatings (TBC) that reduce the surface temperature of the substrate. However, accurately predicting the temperature gradient (or temperature drop) in TBC is crucial to determine the life expectancy of the components. The problem is that bulk ceramic materials, which are commonly used for analysis, have different properties than thin ceramic layers due to processing and microstructure differences. Furthermore, ceramic sprayed on different materials with high conductivity results in different interfacial properties. Therefore, developing a thermal barrier performance test method using TBC applied to real gas turbines is necessary.

Recent studies show that multilayered (MLed) and functionally graded (FGed) structures rather than single layers improve the thermal cycling properties TBCs without depending on the material selection, considerably [22, 26–29]. As it is discussed in previous parts alumina is not compatible to use single-layered TBCs. Therefore, multilayered and functionally graded designed alumina-based TBCs will be investigated for thermal cycling performance. The thermal cycling performance of

MLED Al₂O₃/CYSZ (Type I), MLED Al₂O₃ + YSZ/CYSZ (Type II) and FGED Al₂O₃/CYSZ (Type III) were measured by using the gas burner method (oxy-propane flame) [20, 21]. To simulate the gas turbine engine environment for operating temperature while taking off and landing, TBC samples were heated up to 1250 °C for one min by an oxy-propane gun and cooled down to room temperature for one min. by using a compressed air gun. 2 min. of heating and cooling represented one cycle of test. Single-layered CYSZ was used for comparison of MLED and FGED design. There was no failure after thermal cycling tests on macro examination for three types of TBCs (Fig. 6). After the macro examination, samples were prepared for cross-section microstructure examination. Field emission-scanning electron microscope (FE-SEM) was used to understand the failure of TBC samples. Although there is no failure for MLED (type I) macro-observation, the cross-section microstructure showed us the separation of the bond coat and top coat interface (Fig. 7a–b). The ceramic top coat materials comprised CYSZ and Al₂O₃. It was anticipated that interface stresses would arise during the cooling of the thermal barrier coating due to differences in the coefficient of thermal expansion (CTE) values among the bond coat, CYSZ ($13 \times 10^{-6} \text{ K}^{-1}$) and Al₂O₃ ($9.6 \times 10^{-6} \text{ K}^{-1}$). These stresses could result in the formation of cracks, which could eventually lead to spallation at the layer interfaces as cracks nucleated. Consequently, the primary factor contributing to the failure of Type I coatings was the thermal stresses arising from the mismatch in thermal expansion coefficients between the layers. As it is explained in the introduction part, after alumina spraying, it transformed into the metastable γ -Al₂O₃ phase and then reverts to the α -Al₂O₃ phase under the high-temperature effect after thermal cycling. This phase transformation caused a 15% change in the volume of alumina. It is understood that the cracks formed between the alumina layers on the top surface of the ceramic layer, marked by arrows in Fig. 7a, have been damaged due to the volume change of the alumina. Figure 7c and d show the microstructure of the functionally graded design. In Fig. 7d, it is observed that the 12-layer design with functional grading has separated from the ceramic layer at a 45° angle due to coefficient of thermal expansion (CTE) mismatches. However, the 8-layer design shown in Fig. 7c did not exhibit any damage after the thermal cycling test [21, 22]. Therefore, the FGED 8-layer design was chosen for CMAS and hot corrosion testing due to its superior thermal cycling resistance. In Sect. 5, CMAS and hot corrosion performance of TBCs will be discussed.

4 Mechanical Properties

The process of adhesive bonding can involve multiple mechanisms that occur simultaneously, with varying degrees of intensity. In the case of air plasma spraying (APS), the most crucial mechanism is the joint formed due to the roughness of the substrate surface. The success of the coating's adhesion depends on several factors such as the substrate surface cleaning, grit blasting techniques, coating parameters, and the environment. The most important one is the grit blasting of the substrate surface.

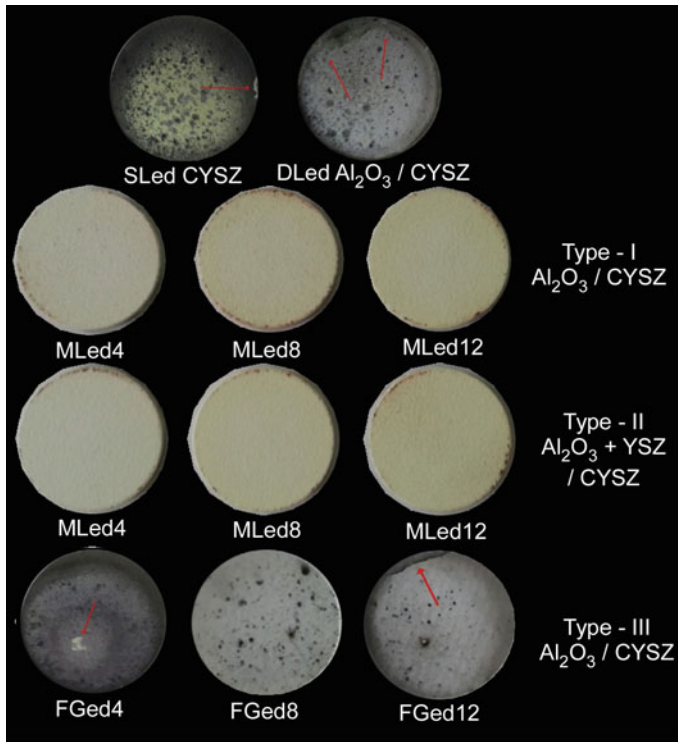


Fig. 6 Surface macroscopic images of TBCs after thermal cycling tests (MLed (Type I), MLed $\text{Al}_2\text{O}_3 + \text{YSZ}/\text{CYSZ}$ (Type II), and FGed (Type III) $\text{Al}_2\text{O}_3/\text{CYSZ}$)

The preparation of the substrate surface by using grit blasting (45° to the surface and 10 cm away) affects increasing the adhesion interface of the bond coat to the substrate. In a previous study, researchers showed that roughness of grit blasted surface increased to 2.3 mm from 0.5 mm. This provides higher wetting of bond coat. The higher wetting of the substrate results in higher mechanical bonding of the bond coat and substrate interface [20, 30].

The tensile adhesion strength test based on the ASTM-C633 standard is commonly used to determine the adhesion strength of APS coatings. This test involves coating the pull rods and measuring the load required to cause separation of the parts under tensile loading. The separation of the pull rods may occur at either the interface between the substrate, bond coat, and top coat (adhesive) or within the top coat layers (cohesive) during the test [30].

Some bonding strength properties and porosity levels of alumina-based TBCs produced by APS are given in Table 2. The majority of the fracture occurs at the interface between the bond coat and the top coat. To understand this phenomenon, it is important to know the bonding mechanism of coatings. Three types of bonding occur

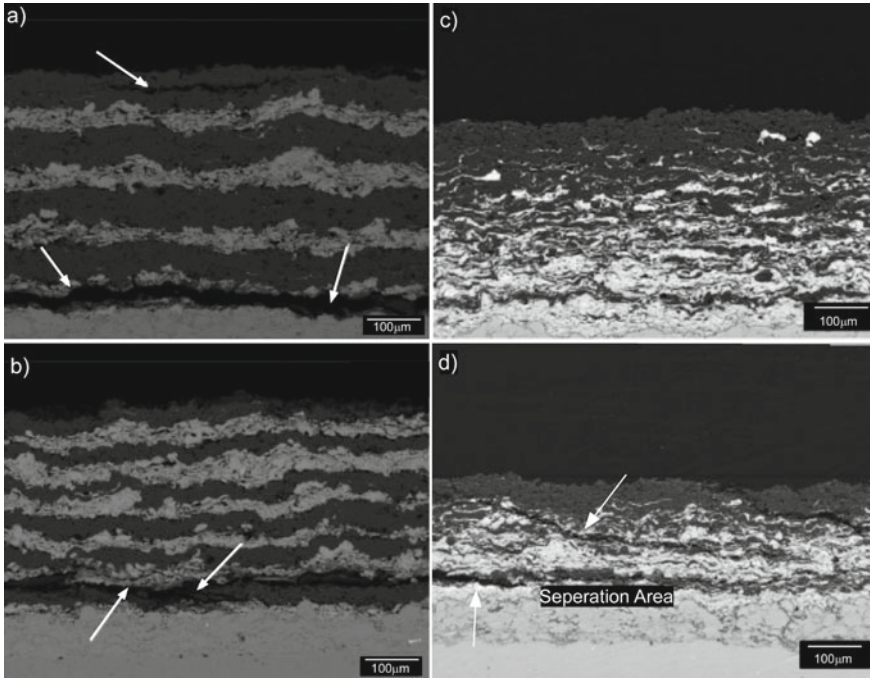


Fig. 7 Cross-section microscopic images of TBCs after thermal cycling tests, **a, b** MLED Al₂O₃/CYSZ (Type I) and **c, d** FGed (Type III) Al₂O₃/CYSZ

during plasma spraying between the powder and substrate due to the solidification of the sprayed powder when it cools with the substrate. These include

1. Mechanical bonding, which involves the interlocking of splats to the substrate's irregularities;
2. Metallurgical bonding, which is a chemical reaction between the lamella and substrate, or diffusion; and
3. Weak Vander Waals bonding, which is the result of atomic attraction between the lamella and the substrate [31].

As can be seen in Table 2, FGed alumina-based TBCs have higher tensile strength and adhesion. This is generally because of the metallurgical and mechanical bonding of the interface of the top coat. The graded structure of alumina or zirconia results in the diffusion of similar coating powders that leads to strong interlocking of layers. The lower porosity level of a functionally graded structure, as compared to a single or multilayer structure, could help to explain these differences [20]. In a study, Dong et al., have fabricated NiCoCrAlY/7YSZ by FGed 5 layer and double-layered coating. The result has showed that FGed design was higher tensile strength over double-layered design. This is attributed because functionally graded design has reduced the strain mismatch within the coating and substrate. While dublex coating has 9 MPa, FGed coating has 18 MPa bond strength [32]. In another study, Saremi et al. have

Table 2 Bonding strength and porosity of alumina-based TBCs

Design		Composition	Production technique	Bonding strength (MPa)	Porosity (%)	Reference
Single layer		YSZ	APS	8.46 ± 2.01	17	[34]
		Nano-YSZ	APS	41.0 ± 8.0	21	[33]
		CYSZ	APS	13.4	12	[20]
Multilayered	Type-I	$Al_2O_3/CYSZ$	APS	8.7 ± 1.9	7–13	[21]
	Type-II	$Al_2O_3 + YSZ/CYSZ$	APS	9.9 ± 1.16	6–10	[21]
		$Al_2O_3/CYSZ$	APS	8.5 ± 1.0	12	[33]
Functionally graded	Type-III	$Al_2O_3/CYSZ$	APS	22.84 ± 0.5	6–8	[20]
		Al_2O_3/YSZ	APS	19.0 ± 2.5	9	[33]

produced nano agglomerated powders by using APS. Three types (YSZ, double-layered YSZ–alumina, and FGed YSZ/alumina) have been compared for mechanical properties. Tensile strength measurement results have showed as FGed coating design has superior properties than double-layered structure [33].

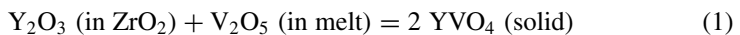
5 Calcia-Magnesia-Alumina-Silica (CMAS) and Hot Corrosion Resistance Performance

Hot corrosion and calcium-magnesium-alumino-silicates (CMAS) attacks are two major factors that can cause TBCs to fail in gas turbine engines. Hot corrosion is caused by the reaction between molten salts (such as Na_2SO_4 and V_2O_5) and the coating materials at high temperatures, which can lead to the formation of corrosive compounds and the depletion of protective oxide layers. On the other hand, a CMAS attack occurs when molten deposits of calcium, magnesium, and other impurities from the combustion gases infiltrate the coating and react with the ceramic materials, leading to the formation of low-melting eutectics that can cause cracking, spalling, and erosion of the coating [35].

In turbine engines, impurities like sodium (Na), vanadium (V), and sulfide (SO_4) are present in liquid fuels. When combusted, these impurities convert into oxides or salts, leading to the creation of vanadium pentoxide (V_2O_5) and sodium sulfate (Na_2SO_4). These substances react with yttria-stabilized zirconia coatings, thereby accelerating the transformation of zirconia. However, ceria (Ce_2O_3) alloying in zirconia as a stabilizer slows the reaction to molten salts. This material exhibits higher thermal expansion, lower thermal conductivity, and higher thermal cycling resistance than yttria (Y_2O_3) alloying in zirconia. While ceria and yttria addition provides less reaction of yttria with vanadium pentoxide (hot corrosion salt). The reaction of yttria and vanadium oxide will be discussed following paragraphs.

The coating of turbine engines can be impacted by various environmental factors, such as the presence of dust, sand, or volcanic ash, which lead to the formation of a substance known as calcium-magnesium-alumina-silicate (CMAS). When CMAS enters the engine inlet, it melts and sticks to the surface of the ceramic layer and penetrates into the coating and altering the material's characteristics at high temperatures. Consequently, the coating may fail prematurely, before the anticipated maintenance period. Alumina is a key material used as a TBC to increase resistance to CMAS and hot corrosion. Due to its high melting point and good wear resistance, it provides higher erosion resistance. The stabilization of zirconia decreases with the reduction of yttria, which causes the transformation of zirconia and results in the occurrence of stresses that damage the coatings [11, 17, 36–41]. Alumina has great chemically inert features against impurities. Many studies indicate that using alumina as a second material for zirconia-based coating materials improves the CMAS and hot corrosion resistance of the TBC system.

In a study, researchers conducted hot corrosion tests in which they deposit an alumina layer by using EB-PVD on a YSZ coating to serve as a protective layer. This technique resulted in less infiltration of hot corrosion salts into the lower layer YSZ and significantly reduced the degradation of zirconia [42]. As it is mentioned in previous parts, yttria usage in YSZ powder tends to exhibit the tetragonal-monoclinic transformation of zirconia at elevated temperatures of gas turbines. Hot corrosion powders penetrate the coating surface and react with yttria. This reaction leads to the production of VYO₄ oxides and the depletion of yttria in the coating structure. Either, newly formed VYO₄ existence results to stress through the TBC and depletion of yttria cause the breaking of zirconia phase stabilization. Tetragonal-monoclinic transformation of zirconia takes place and results in the volume exchange of TBCs (Reaction 1). Keyvani et al. [11] found that the YSZ + Al₂O₃ composite coatings had better resistance to hot corrosion compared to single-layer YSZ coatings. This was attributed to the higher oxide barrier of alumina, which reduced the depletion of Y₂O₃, resulting in less transformation of the tetragonal phase of zirconia to the monoclinic phase. This transformation can be calculated by using Rietveld refinement of XRD patterns. So far, the monoclinic transformation ratio of zirconia can help us to understand the stabilization resistance of the coating. The researchers determined the monoclinic transformations of YSZ, Al₂O₃/YSZ, Al₂O₃ + YSZ, and YSZ/Al₂O₃ TBCs by analyzing their phase intensity. The results showed that the proportion of monoclinic transformations was 55% for YSZ, 55% for Al₂O₃/YSZ, 42% for Al₂O₃ + YSZ, and 25% for YSZ/Al₂O₃. The findings indicated that when alumina is on the upper surface of cross-section TBCs, there is a decrease in the monoclinic transformation of zirconia in differently structured TBCs.



In literature, a study [1] investigates the effect of Al₂O₃ modification on the properties of YSZ for corrosion resistance, wetting, and thermal–mechanical properties. The addition of Al₂O₃ concentrations of YSZ was 0, 1, 22.5, 30, 40, 45, and 50. CMAS and Al₂O₃–Yttria–Zirconia were exposed to 1300 °C for 4 h. When Al₂O₃

is added to the CMAS/YSZ system, the melting point can increase due to the formation of anorthite, which has a high melting point. However, if the Al_2O_3 content exceeds 40%, the melting point decreases. Wetting testing has shown that when 40% of Al_2O_3 is added to the system, an anorthite layer forms at the CMAS/plate interface, and the system exhibits the highest apparent contact angle. As more Al_2O_3 is added, the anorthite layer gradually disappears, and the contact angle decreases.

Both hot corrosion and CMAS attack can occur simultaneously in the same engine, and their effects can be exacerbated by thermal cycling and thermal gradients that cause mechanical stresses and thermal shock in the coating. Therefore, it is important to develop thermal barrier coatings that can withstand both types of attack and provide long-term protection under the harsh operating conditions of gas turbine engines [35].

A study aimed at improving the resistance of thermal barrier coatings (TBCs) against CMAS and hot corrosion, and researchers used a laser heater to calculate the monoclinic transformation of zirconia after thermal cycling and thermal gradient tests. To prevent the penetration of CMAS and hot corrosion powder and salts mixture, as well as monoclinic transformation caused by the penetration of hot corrosion salts, the researchers produced an $\text{Al}_2\text{O}_3/\text{CYSZ}$ FGed design using APS. They also applied the same tests to a single-layered CYSZ produced by APS to compare the alumina-based structure with the single-layered CYSZ structure.

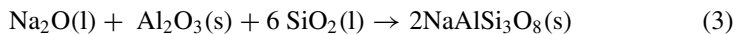
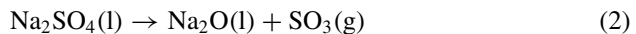
After subjecting the coatings to thermal cycling tests under dynamic conditions, the researchers observed no observable damage on the coatings even after 100 cycles. According to the Rietveld analysis, it was discovered that the surface coating was composed of 64.1% monoclinic and 35.9% tetragonal phases. Furthermore, the interface between the bond coat ceramic top coat of the single-layer CYSZ coating was examined to determine the effects of penetration by CMAS dust and hot corrosion salt during thermal cycling. The analysis revealed that the interface between the bond and ceramic coating consisted of 66.4% tetragonal and 33.6% monoclinic phases in the single-layer CYSZ.

To investigate the transformation of $\gamma\text{-Al}_2\text{O}_3$ on the coating surface under thermal cycling conditions with hot corrosion and CMAS, the Rietveld analysis was employed on the $\text{Al}_2\text{O}_3/\text{CYSZ}$ functionally graded coating after 100 cycles. The findings indicated that 82.6% of the transformation involved $\gamma\text{-Al}_2\text{O}_3$. In comparison, the sprayed coating had $\gamma\text{-Al}_2\text{O}_3$ present at a lower rate of 54.6%, implying that the amount of $\gamma\text{-Al}_2\text{O}_3$ on the surface increased during the dynamic thermal cycling test conducted with hot corrosion and CMAS salts. According to the analysis of the bond-ceramic coating interface, it was found that the zirconia remained in the tetragonal phase and did not undergo any transformation to the monoclinic phase during the spraying process. These results indicate that when alumina is used in near-surface areas in thermal barrier coatings, it inhibits the reaction that causes zirconia phase transformation as it prevents CMAS and hot corrosion penetration. The study investigated the performance of an $\text{Al}_2\text{O}_3/\text{CYSZ}$ functionally graded thermal barrier coating (FGed TBC) at a constant temperature of 1200 °C. The coating was subjected to one hour of heating with a laser and simultaneous cooling with a copper plate that passed cooling water. The Rietveld analysis using the High Score X'pert program was conducted to determine the transformation rate of the material. The analysis

showed that 93.5% of the material was tetragonal ZrO₂, and 6.5% was monoclinic ZrO₂, indicating a similar transformation rate for both measurements. To further analyze the coating, phase analysis was conducted on bond coat and ceramic coat interface of the single-layer CYSZ to examine the lower temperature effect at the CYSZ-bond coat interface and the more intense interface cracks in the cross-section microstructure. The analysis revealed that 87.7% of the zirconia on the bond-ceramic coating interface was tetragonal, and 12.3% was monoclinic.

The proportion of monoclinic phase was greater on the back surface of the coating separation zone in comparison with the upper surface. This difference may be attributed to the temperature gradient that occurs during the thermal cycling test. The single-layer CYSZ coating exhibited a *t-m* phase transformation of 66.4% following thermal cycling, whereas no transformation was observed in the FGED alumina-based TBC. The transformation was observed on the surface of the single-layer CYSZ coating.

Figure 8 provides a phase analysis of the FGED Al₂O₃/CYSZ TBC and shows that the NaAlSi₃O₈ albite phase was detected on the surface of the coating. It has been reported that albite phase formation occurs as a result of the sequential reactions of CMAS and hot corrosion powder + salt composition placed on the surface (Reactions 2 and 3). The Rietveld method was used to perform alumina phase ratios, which revealed that 81.6% of the γ -Al₂O₃ phase was present on the surface. The sprayed coating had a γ -Al₂O₃ phase ratio of 54.6%. The amount of γ -Al₂O₃ phase increased with increasing temperature generated by the laser beam. However, no new reaction took place, and the Y₂O₃ phase from CYSZ did not decompose in the phase analysis conducted from the bond-ceramic coating interface. As shown in Fig. 9b, the zirconia remained in a 100% tetragonal phase on the bond-ceramic coating interface, and the *t-m* phase transformation did not occur. Thus, the alumina prevented hot corrosion penetration by protecting the CYSZ layers. In 1-h thermal gradient tests, the rate of failure was assessed for both SL and FGED coatings using the *t-m* zirconia transformation. In the single-layer CYSZ TBC, the transformation of monoclinic zirconia was 12.3%, while no such transformation was detected in the FGED alumina-based TBC [35].



Cross-section micro examination of TBCs was important to carry out. As seen in Fig. 10, no interaction was observed between CMAS and hot components in the alumina-based surface structure (Fig. 10b). On the other hand, when the single-layer CYSZ TBC was examined, it was observed that CMAS and hot corrosion components reacted with the CYSZ surface to exhibit yttria depletion (Fig. 10a). While no TGO formation is observed on the bond layer in the FGED alumina CYSZ TBC structure, an oxidation zone in the range of 0.5–2 mm is observed on the bond layer in the single-layer CYSZ structure. It is observed that there are separations between CYSZ

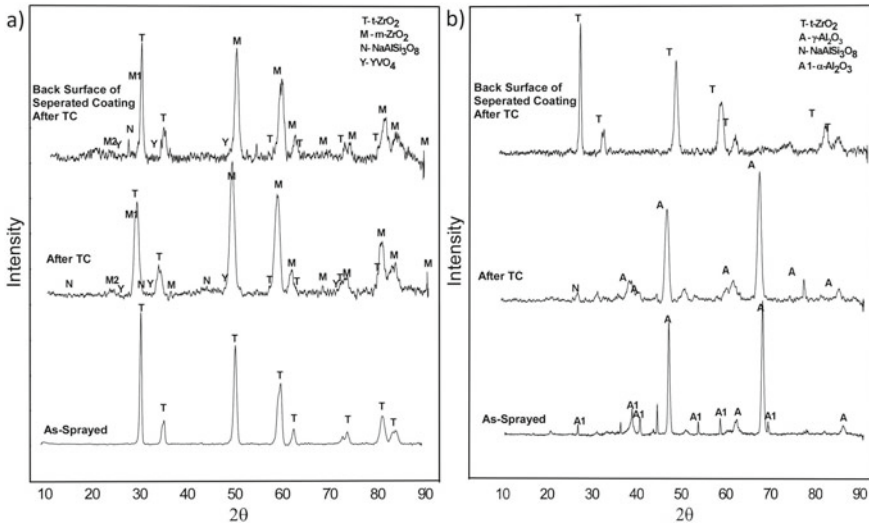


Fig. 8 Phase analysis of **a** SL CYSZ and **b** FGed Al₂O₃/CYSZ TBC (as-sprayed surface, laser threated surface, and bond coat ceramic coat interface after thermal cycling test)

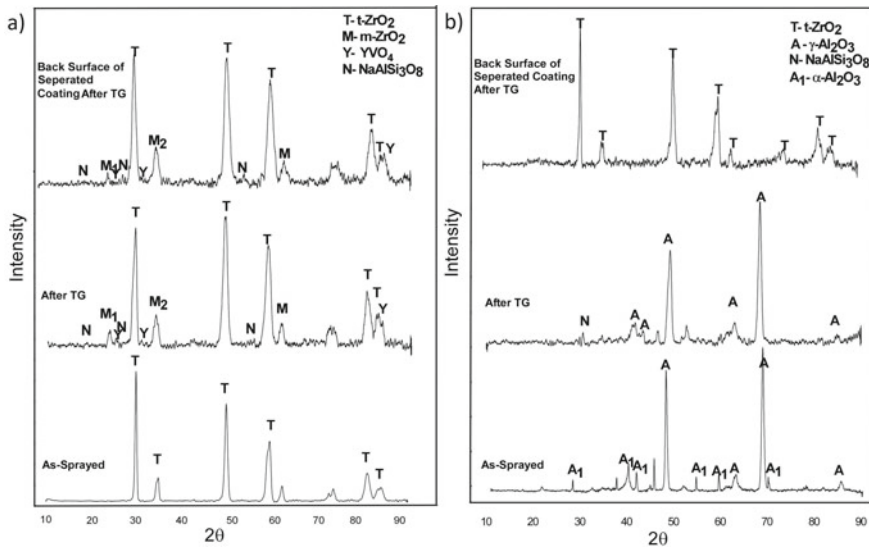


Fig. 9 Phase analysis of **a** SL CYSZ and **b** FGed Al₂O₃/CYSZ TBC (as-sprayed surface, laser threated surface, and bond coat ceramic coat interface after thermal gradient test)

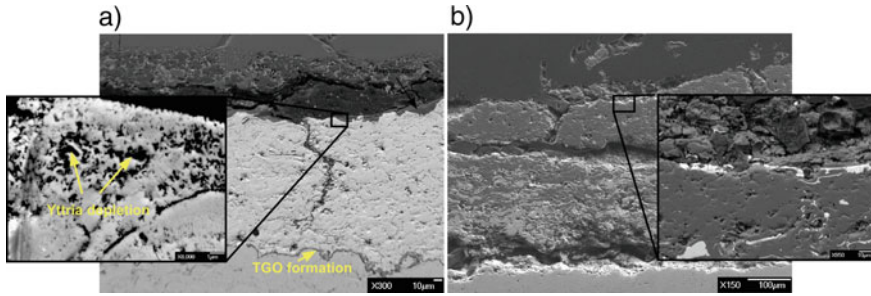


Fig. 10 Cross-section FE-SEM images of **a** SL CYSZ, **b** FGed Al₂O₃/CYSZ TBC after a 1-h thermal gradient test

and Al₂O₃ in FGed Al₂O₃/CYSZ TBC due to thermal expansion mismatches and Al₂O₃ phase transformation [34].

6 Laser Surface Modification

6.1 Laser Surface Modification of Al₂O₃-Based Thermal Barrier Coatings

The use of laser beams for surface modification is a promising new technique for enhancing certain characteristics of plasma-sprayed TBCs. Laser surface melting refers to a method of modifying a surface where the substrate's surface is melted and quickly solidified to create a refined microstructure. This process enhances the mechanical properties of the surface without affecting the bulk properties [43]. Different laser parameters are used depending on the melting degrees of the surface used by the laser. As it is known, the laser used may be pulse or continuous modes. It is better to use continuous mode instead of pulsed mode during laser treatment to prevent thermal shock. Additionally, continuous mode results in a smoother surface with a topology that is preferred in coating technology [44]. Based on researches [5, 44–49], the laser remelting solidification process has led to a decrease in surface roughness and specific surface area. Additionally, laser parameters can be adjusted to achieve a segmented crack network perpendicular to the surface, along with sealed porosities, and a columnar cross-sectional structure. As a result, properties such as hardness, resistance to hot corrosion, CMAS, erosion, and thermal cycle lifetime of TBCs can be further enhanced through laser surface modification.

1. The surface roughness and specific surface area reduction achieved through laser surface modification can enhance the TBC's erosion, CMAS, and hot corrosion resistance.

2. The generation of segment cracks on the TBC's surface through laser surface modification can improve its thermal shock resistance.
3. The TBC's thermal cycle life can be extended by improving its strain accommodation capability through segmented cracks.
4. Grain size alteration can increase the TBC's hardness.

Some studies on surface hardness have shown that the hardness increased by remelting and lower grains of the surface. Morks et al. [50] investigated the surface microstructure influence of laser-glazed YSZ TBCs. Samples had a small grain size of 2–3 μm , which exhibited high hardness values greater than 22.56 GPa. On the other hand, samples with bigger grain sizes ($>5 \mu\text{m}$) showed lower hardness values, less than 12.75 GPa. These results suggest that small grains have a higher resistance to deformation caused by the Vickers indenter during loading. Antou et al. [51] conducted a study to examine the mechanical properties of YSZ TBC surfaces that were either as-sprayed or treated with a laser. The study found that the laser-treated surface had a higher hardness of 20.5 GPa, compared to the as-sprayed surface with a hardness of 17.4 GPa. Similarly, the young modulus of the laser-treated surface was measured at 274 GPa, while the as-sprayed surface had a lower young modulus of 259 GPa. In another study [52], plasma-sprayed YSZ and containing 8% Al_2O_3 (YSZAl) TBC was examined to understand the difference of mechanical properties before and after laser treatment such as hardness and fracture toughness. The addition of alumina to YSZ increased the hardness results of the surface from ~ 5.69 – 7.36 GPa to ~ 7.36 – 8.83 GPa. The hardness of sealed layers YSZAl and YSZ TBC was compared, and results showed while YSZAl has 16.67 GPa hardness, YSZ has 14.22 GPa. The fracture toughness of YSZAl and YSZ was $\sim 4 \text{ MPa}\sqrt{\text{m}}$ and $\sim 3.5 \text{ MPa}\sqrt{\text{m}}$, respectively.

After laser surface modification, the TBC's surface should meet the following criteria:

1. Possess a remelted layer with a melting depth of 20–50 μm .
2. Remain intact with the as-sprayed layer.
3. Have a smooth surface, with a surface roughness value (R_a) of less than 5 μm .
4. Display an equiaxed distribution of the crack network [53].

In a new study on laser surface modification, the laser surface parameters of the alumina surface were determined (Fig. 11). According to the SEM images of FGeD $\text{Al}_2\text{O}_3/\text{CYSZ}$ from the surface (Fig. 11a) and cross-section (Fig. 11b), the desired properties such as dense surface regions, equiaxed distributed crack network, lower surface roughness (Fig. 10c), and non-separation in the coating after modification were successfully achieved. Laser parameters for alumina surface to achieve these morphological properties were determined as 380 W laser power, 100 W/cm^2 laser power density, 5.5 cm laser distance, 2.2 mm laser spot size, and 170 mm/s laser tracking speed. Surface roughness (R_a) before and after laser surface modification were 4.69 mm and 3.81 mm, respectively (Fig. 11c).

In the research, we encountered certain issues that have yet to be resolved. Specifically, we observed the presence of open channels (Fig. 11a), predominantly consisting

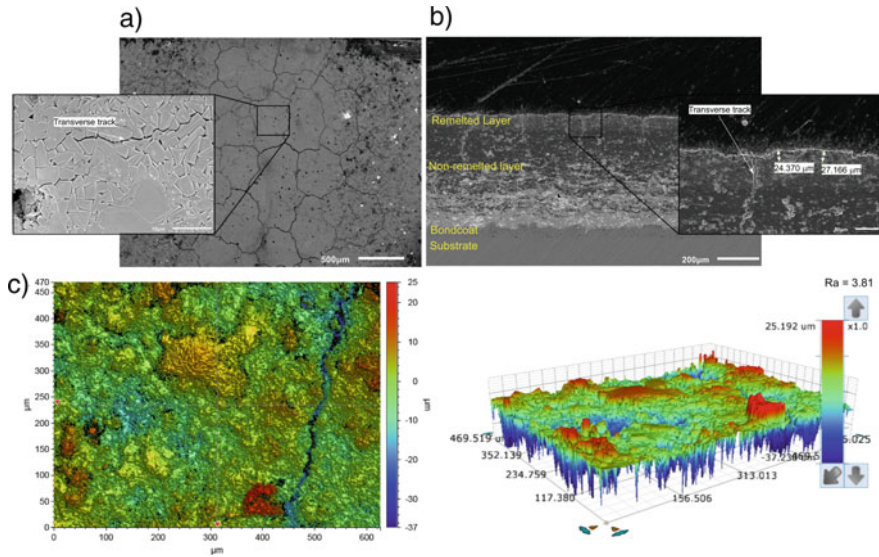


Fig. 11 Surface-modified FGed Al₂O₃/CYSZ TBC: **a** surface, **b** cross-section SEM images, **c** surface roughness

of vertical cracks and columnar gaps, within the laser-glazed layer that extends to the unmodified coating. These transverse tracks could allow CMAS to permeate and react with the coating, ultimately resulting in the degradation of the coating's microstructure during extended periods of heat treatment. However, the existence of these cracks and gaps could also enhance the coating's strain tolerance and improve its thermal shock performance. In a study [54], the thermal shock resistance of multilayered laser surface-modified Al₂O₃/YSZ TBC was investigated. The results indicate that the lifetime of the coatings improved with laser glazing. Specifically, the number of cycles required to cause 20% destruction of the top surface of the coatings increased from 232 cycles in the sprayed coating to 325 cycles in the laser-glazed Al₂O₃/YSZ coating, indicating a 40% increase in thermal shock resistance due to the laser glazing process. The increase in strain adaptability through the creation of segmented cracks perpendicular to the top surface, resulting from laser glazing, led to an increase in the lifetime of the sprayed TBCs.

Laser surface modification of TBCs is new and evolving and still needs to be improved process. However, in light of the studies, it has been demonstrated that surface modification improves the surface and environmental effects of TBCs. In particular, segment cracks on the surface provide weak properties against CMAS and hot corrosion. In this respect, Fan et al. used femtosecond laser polishing to improve the hot corrosion properties of YSZ TBCs. The findings showed the surface of femtosecond laser polishing provided the lower roughness and uncracked surface that occurred on laser remelting. In this context, laser remelting has shown that the desired non-porous surface can be obtained depending on the melting properties [55].

7 Conclusion

The current chapter covers the topic of applying thermal barrier coatings (TBC) based on alumina. The chapter discusses various aspects related to the production methods of alumina-based TBCs, including APS, EB-PVD, and SPS, as well as the coating process, thermal and mechanical properties, thermal tests, and failure mechanisms. In addition, the chapter evaluates the resistance of these TBCs to CMAS and hot corrosion and also examines the laser surface modification process of alumina-based TBCs.

Alumina's chemical inertness and densification mechanism make it unique for use as second material for TBCs. Although single usage of alumina has low points for thermal conductivity of TBC, multilayer and functionally graded designs make alumina-based TBCs improved insulation and lower thermal conductivity even comparingly YSZ. Alumina-based TBCs have a significant improvement in CMAS and hot corrosion failure mechanisms. After laser surface modification of alumina-based TBC, great improvement is achieved for thermal shock and CMAS and hot corrosion attacks. As a result, in the light of research, alumina is an important and promising alternative TBC material.

8 Suggestions

In the future works:

1. It is necessary to conduct research on the mechanical properties of alumina-based thermal barrier coatings (TBCs) made through electron beam physical vapor deposition (EB-PVD) and suspension plasma spraying (SPS) techniques.
2. The stability of the alumina phase could be enhanced by employing various alloying methods suitable for the high temperatures in gas turbine engines. Alumina-based TBCs need to be tested under in-situ conditions, using new testing approaches and harsh environments.
3. It is advisable to explore different mechanisms for sealing and laser surface modification of alumina-based TBCs, in order to evaluate their effectiveness against the mechanisms of CMAS and hot corrosion.
4. The bonding strength, thermal conductivity, and thermal shock resistance of alumina-based TBCs should be assessed after performing laser surface modification.

Acknowledgements The authors thank Prof. Dr. Dermot Brabazon, Prof. Dr. Yılmaz Taptik, Assist. Prof. Dr Nuri Solak, and Hasan Huseyin Sezer for their contributions. Special thanks to my beloved daughter Asya.

References

1. Yin, B., Zhang, F., Zhu, W., Yang, L., Zhou, Y.: Effect of Al₂O₃ modification on the properties of YSZ: corrosion resistant, wetting and thermal-mechanical properties. *Surf. Coat. Technol.* **357**, 161–171 (2019). <https://doi.org/10.1016/j.surfcoat.2018.09.048>
2. Chen, W.R., Wu, X., Marple, B.R., Nagy, D.R., Patnaik, P.C.: TGO growth behaviour in TBCs with APS and HVOF bond coats. *Surf. Coat. Technol.* **202**, 2677–2683 (2008). <https://doi.org/10.1016/j.surfcoat.2007.09.042>
3. Fang, X., Zhang, G., Feng, X.: Performance of TBCs system due to the different thicknesses of top ceramic layer. *Ceram. Int.* **41**, 2840–2846 (2015). <https://doi.org/10.1016/j.ceramint.2014.10.105>
4. Cao, X.Q., Vassen, R., Stoeber, D.: Ceramic materials for thermal barrier coatings. *J. Eur. Ceram. Soc.* **24**, 1–10 (2004). [https://doi.org/10.1016/S0955-2219\(03\)00129-8](https://doi.org/10.1016/S0955-2219(03)00129-8)
5. Gok, M.G., Goller, G.: Microstructural evaluation of laser remelted gadolinium zirconate thermal barrier coatings. *Surf. Coat. Technol.* **276**, 202–209 (2015). <https://doi.org/10.1016/j.surfcoat.2015.06.074>
6. Liu, Z.G., Ouyang, J.H., Zhou, Y., Li, S.: High-temperature hot corrosion behavior of gadolinium zirconate by vanadium pentoxide and sodium sulfate in air. *J. Eur. Ceram. Soc.* **30**, 2707–2713 (2010). <https://doi.org/10.1016/j.jeurceramsoc.2010.05.002>
7. Afrasiabi, A., Saremi, M., Kobayashi, A.: A comparative study on hot corrosion resistance of three types of thermal barrier coatings: YSZ, YSZ + Al₂O₃ and YSZ/Al₂O₃. *Mater. Sci. Eng. A* **478**, 264–269 (2008). <https://doi.org/10.1016/j.msea.2007.06.001>
8. Keyvani, A., Saremi, M., Sohi, M.H.: Oxidation resistance of YSZ-alumina composites compared to normal YSZ TBC coatings at 1100 °C. *J. Alloys Compd.* **509**, 8370–8377 (2011). <https://doi.org/10.1016/j.jallcom.2011.05.029>
9. Chevalier, J., Gremillard, L., Virkar, A.v., Clarke, D.R.: The tetragonal-monoclinic transformation in zirconia: lessons learned and future trends. *J. Am. Ceram. Soc.* **92**, 1901–1920 (2009). <https://doi.org/10.1111/j.1551-2916.2009.03278.x>
10. Ma, W., Dong, H.: Ceramic thermal barrier coating materials. *Thermal Barrier Coat.*, 25–52 (2011). <https://doi.org/10.1016/B978-1-84569-658-0.50002-8>
11. Keyvani, A., Saremi, M., Sohi, M.H.: Microstructural stability of zirconia-alumina composite coatings during hot corrosion test at 1050 °C. *J. Alloys Compd.* **506**, 103–108 (2010). <https://doi.org/10.1016/j.jallcom.2010.06.110>
12. Keyvani, A.: Microstructural stability oxidation and hot corrosion resistance of nanostructured Al₂O₃/YSZ composite compared to conventional YSZ TBC coatings. *J. Alloys Compd.* **623**, 229–237 (2015). <https://doi.org/10.1016/j.jallcom.2014.10.088>
13. Saremi, M., Afrasiabi, A., Kobayashi, A.: Microstructural analysis of YSZ and YSZ/Al₂O₃ plasma sprayed thermal barrier coatings after high temperature oxidation. *Surf. Coat. Technol.* **202**, 3233–3238 (2008). <https://doi.org/10.1016/j.surfcoat.2007.11.029>
14. Zhang, J., Kobayashi, A.: Corrosion resistance of the Al₂O₃+ZrO₂ thermal barrier coatings on stainless steel substrates. *Vacuum* **83**, 92–97 (2008). <https://doi.org/10.1016/j.vacuum.2008.03.090>
15. Keyvani, A., Saremi, M., Sohi, M.H.: Oxidation resistance of YSZ-alumina composites compared to normal YSZ TBC coatings at 1100 °C. *J. Alloys Compd.* **509**, 8370–8377 (2011). <https://doi.org/10.1016/j.jallcom.2011.05.029>
16. Karaoglanli, A.C., Altuncu, E., Ozdemir, I., Turk, A., Ustel, F.: Structure and durability evaluation of YSZ+Al₂O₃ composite TBCs with APS and HVOF bond coats under thermal cycling conditions. *Surf. Coat. Technol.* **205** (2011). <https://doi.org/10.1016/j.surfcoat.2011.04.081>
17. Naraparaju, R., Pubbysetty, R.P., Mechnich, P., Schulz, U.: EB-PVD alumina (Al₂O₃) as a top coat on 7YSZ TBCs against CMAS/VA infiltration: deposition and reaction mechanisms. *J. Eur. Ceram. Soc.* **38**, 3333–3346 (2018). <https://doi.org/10.1016/j.jeurceramsoc.2018.03.027>
18. Li, Y., Xie, Y., Huang, L., Liu, X., Zheng, X.: Effect of physical vapor deposited Al₂O₃ film on TGO growth in YSZ/CoNiCrAlY coatings. *Ceram. Int.* **38**, 5113–5121 (2012). <https://doi.org/10.1016/j.ceramint.2012.03.014>

19. Steinberg, L., Mikulla, C., Naraparaju, R., Toma, F.L., Großmann, H., Schulz, U., Leyens, C.: Erosion resistance of CMAS infiltrated sacrificial suspension sprayed alumina top layer on EB-PVD 7YSZ coatings. *Wear*, 438–439 (2019). <https://doi.org/10.1016/j.wear.2019.203064>
20. Kirbiyik, F., Gok, M.G., Goller, G.: Microstructural, mechanical and thermal properties of Al₂O₃/CYSZ functionally graded thermal barrier coatings. *Surf. Coat. Technol.* **329**, 193–201 (2017). <https://doi.org/10.1016/j.surfcoat.2017.08.025>
21. Dokur, M.M., Goller, G.: Processing and characterization of CYSZ/Al₂O₃ and CYSZ/Al₂O₃+YSZ multilayered thermal barrier coatings. *Surf. Coat. Technol.* **258**, 804–813 (2014). <https://doi.org/10.1016/j.surfcoat.2014.07.077>
22. Gok, M.G., Goller, G.: State of the Art of Gadolinium Zirconate Based Thermal Barrier Coatings: Design, Processing and Characterization
23. Cahit, A., Ogawa, K., Turk, A., Ozdemir, I.: Thermal shock and cycling behavior of thermal barrier coatings (TBCs) used in gas turbines. In: *Progress in Gas Turbine Performance*. InTech (2013)
24. Taylor, R.E.: Thermal conductivity determinations of thermal barrier coatings. *Mater. Sci. Eng. A* **245**, 160–167 (1998). [https://doi.org/10.1016/S0921-5093\(97\)00847-2](https://doi.org/10.1016/S0921-5093(97)00847-2)
25. Jankowiak, A.: *Potential and Perspectives for Oxide/Oxide Composites* (2017)
26. Han, J., Zou, Y., Wu, D., Zhang, Y.: Investigating the thermal, mechanical and thermal cyclic properties of plasma-sprayed Al₂O₃-7YSZ/7YSZ double ceramic layer TBCs. *J. Eur. Ceram. Soc.* (2023). <https://doi.org/10.1016/j.jeurceramsoc.2023.03.004>
27. Han, M., Huang, J., Chen, S.: Behavior and mechanism of the stress buffer effect of the inside ceramic layer to the top ceramic layer in a double-ceramic-layer thermal barrier coating. *Ceram. Int.* **40**, 2901–2914 (2014). <https://doi.org/10.1016/j.ceramint.2013.10.021>
28. Wang, L., Wang, Y., Sun, X.G., He, J.Q., Pan, Z.Y., Wang, C.H.: Finite element simulation of residual stress of double-ceramic-layer La₂Zr₂O₇/8YSZ thermal barrier coatings using birth and death element technique. *Comput. Mater. Sci.* **53**, 117–127 (2012). <https://doi.org/10.1016/j.commatsci.2011.09.028>
29. Doleker, K.M., Ozgurluk, Y., Karaoglanli, A.C.: TGO growth and kinetic study of single and double layered TBC systems. *Surf. Coat. Technol.* **415** (2021). <https://doi.org/10.1016/j.surfcoat.2021.127135>
30. Pasupuleti, K.T., Prasad, G.V., Prabhu Akhil, M., Ramaswamy, P., Narayana Murty, S.V.S.: Adhesion strength studies on zirconia based pyrochlore and functionally gradient thermal barrier coatings. In: *Materials Today: Proceedings*, pp. 568–574. Elsevier Ltd. (2019)
31. Ghasemi, R., Vakili, H.: Plasma-sprayed nanostructured YSZ thermal barrier coatings: thermal insulation capability and adhesion strength. *Ceram. Int.* **43**, 8556–8563 (2017). <https://doi.org/10.1016/j.ceramint.2017.03.074>
32. Dong, Z.L., Khor, K.A., Gu, Y.W.: Microstructure formation in plasma-sprayed functionally graded NiCoCrAlY/yttria-stabilized zirconia coatings (1999)
33. Saremi, M., Valefi, Z.: Thermal and mechanical properties of nano-YSZ-Alumina functionally graded coatings deposited by nano-agglomerated powder plasma spraying. *Ceram. Int.* **40**, 13453–13459 (2014). <https://doi.org/10.1016/j.ceramint.2014.05.068>
34. Ang, A.S.M., Berndt, C.C.: Investigating the anisotropic mechanical properties of plasma sprayed yttria-stabilised zirconia coatings. *Surf. Coat. Technol.* **259**, 551–559 (2014). <https://doi.org/10.1016/j.surfcoat.2014.10.031>
35. Kirbiyik, F., Gok, M.G., Goller, G.: Application of thermal gradient and thermal cycling tests to Al₂O₃/CYSZ functionally graded TBC in the presence of simultaneous hot corrosion and CMAS effects. *Surf. Coat. Technol.* **444** (2022). <https://doi.org/10.1016/j.surfcoat.2022.128688>
36. Ben-Nissan, B., Vasile, I.: Elsevier Editorial System (tm) for Surface and Coatings Technology Manuscript Draft Title: CMAS and Hot Corrosion Resistance Behavior of High-Temperature Resistant Functionally Graded CYSZ/Al₂O₃ Thermal Barrier Coatings

37. Göller, G., Author, F., Kirbiyik, F., Guven Gok Gültekin Göller, M., Goto, T., Ben Nissan, B., Vasile, I.: Surface & Coatings Technology Application of thermal gradient and thermal cycling tests to Al₂O₃/CYSZ functionally graded TBC in the presence of simultaneous hot corrosion and CMAS effects-Manuscript Draft-Powered by Editorial Manager® and ProduXion Manager® from Aries Systems Corporation
38. Gok, M.G., Goller, G.: Microstructural characterization of GZ/CYSZ thermal barrier coatings after thermal shock and CMAS+hot corrosion test. *J. Eur. Ceram. Soc.* **37**, 2501–2508 (2017). <https://doi.org/10.1016/j.jeurceramsoc.2017.02.004>
39. Bakkar, S., Pantawane, M.V., Gu, J.J., Ghoshal, A., Walock, M., Murugan, M., Young, M.L., Dahotre, N., Berman, D., Aouadi, S.M.: Laser surface modification of porous yttria stabilized zirconia against CMAS degradation. *Ceram. Int.* (2019). <https://doi.org/10.1016/J.CERAMINT.2019.11.061>
40. Rai, A.K., Bhattacharya, R.S., Wolfe, D.E., Eden, T.J., Jin, Z., Su, Y., Alamos, L., Anions, D., Gas, O., Of, S., Polypyr, C., Cited, R., Zhang, X. feng, Zhou, K. song, Xu, W., Chen, B. yu, Song, J. bing, Liu, M., Mohan, P., Yao, B., Patterson, T., Sohn, Y.H., Yao, B., Sohn, Y.H., Wellman, R., Whitman, G., Nicholls, J.R.: Electrophoretically deposited alumina as protective overlay for thermal barrier coatings against CMAS degradation. *Surf. Coat. Technol.* **28**, 156–167 (2010). <https://doi.org/10.1016/j.surfcoat.2009.09.055>
41. Habibi, M.H.: Hot Corrosion Behaviour of New Candidates for Thermal Barrier Coatings Application in Turbine Simulated Environments (2014)
42. Wu, N., Chen, Z., Mao, S.X.: Hot corrosion mechanism of composite alumina/yttria-stabilized zirconia coating in molten sulfate-vanadate salt. *J. Am. Ceram. Soc.* **88**, 675–682 (2005). <https://doi.org/10.1111/j.1551-2916.2005.00120.x>
43. Jeyaprakash, N., Yang, C.-H., Raj Kumar, D.: Laser surface modification of materials. In: Practical Applications of Laser Ablation. IntechOpen (2021)
44. Al Harbi, N., Benyounis, K.Y., Looney, L., Stokes, J.: Laser surface modification of ceramic coating materials. In: Encyclopedia of Smart Materials, pp. 445–461. Elsevier (2021)
45. Batista, C., Portinha, A., Ribeiro, R.M., Teixeira, V., Costa, M.F., Oliveira, C.R.: Morphological and microstructural characterization of laser-glazed plasma-sprayed thermal barrier coatings. *Surf. Coat. Technol.* **200**, 2929–2937 (2006). <https://doi.org/10.1016/j.surfcoat.2004.10.134>
46. Lee, J.H., Tsai, P.C., Chang, C.L.: Microstructure and thermal cyclic performance of laser-glazed plasma-sprayed ceria-yttria-stabilized zirconia thermal barrier coatings. *Surf. Coat. Technol.* **202**, 5607–5612 (2008). <https://doi.org/10.1016/j.surfcoat.2008.06.118>
47. Moncayo, M.A., Santhanakrishnan, S., Vora, H.D., Paital, S.R., Dahotre, N.B.: Laser surface modification of alumina: integrated computational and experimental analysis. *Ceram. Int.* **39**, 6207–6213 (2013). <https://doi.org/10.1016/j.ceramint.2013.01.040>
48. Ahmadi-Pidani, R., Shoja-Razavi, R., Mozafarinia, R., Jamali, H.: Laser surface modification of plasma sprayed CYSZ thermal barrier coatings. *Ceram. Int.* **39**, 2473–2480 (2013). <https://doi.org/10.1016/j.ceramint.2012.09.005>
49. Arshad, A., Yajid, M.A.M., Idris, M.H.: Microstructural characterization of modified plasma spray LZ/YSZ thermal barrier coating by laser glazing. In: Materials Today: Proceedings, pp. 941–946. Elsevier Ltd (2019)
50. Morks, M.F., Berndt, C.C., Durandet, Y., Brandt, M., Wang, J.: Microscopic observation of laser glazed yttria-stabilized zirconia coatings. *Appl. Surf. Sci.* **256**, 6213–6218 (2010). <https://doi.org/10.1016/j.apsusc.2010.03.143>
51. Antou, G., Montavon, G., Hlawka, F., Cornet, A., Coddet, C., Machi, F.: Modification of thermal barrier coating architecture by in situ laser remelting. *J. Eur. Ceram. Soc.* **26**, 3583–3597 (2006). <https://doi.org/10.1016/j.jeurceramsoc.2006.01.003>
52. Mohammed Jasim, K.: Laser sealing of zirconia–yttria–alumina plasma sprayed coating. *J. King Saud Univ. Eng. Sci.* **25**, 11–20 (2013). <https://doi.org/10.1016/j.jksues.2011.10.004>
53. Guo, L., Gao, Y., Cheng, Y., Sun, J., Ye, F., Wang, L.: Microstructure design of the laser glazed layer on thermal barrier coatings and its effect on the CMAS corrosion. *Corros. Sci.* **192** (2021). <https://doi.org/10.1016/j.corsci.2021.109847>

54. Ahmadi, M.S., Shoja-Razavi, R., Valefi, Z., Jamali, H.: The effect of laser surface treatment on the thermal shock behavior of plasma sprayed $\text{Al}_2\text{O}_3/\text{YSZ}$ multilayer thermal barrier coatings. *Surf. Coat. Technol.* **366**, 62–69 (2019). <https://doi.org/10.1016/j.surfcoat.2019.03.024>
55. Fan, Z., Sun, X., Zhuo, X., Mei, X., Cui, J., Duan, W., Wang, W., Zhang, X., Yang, L.: Femtosecond laser polishing yttria-stabilized zirconia coatings for improving molten salts corrosion resistance. *Corros. Sci.* **184** (2021). <https://doi.org/10.1016/j.corsci.2021.109367>

Zirconia-Based Thermal Barrier Coatings Systems for Aero-Industry



Adriana Stefan, Victor Manoliu, and George Catalin Cristea

Abstract Intelligent thermal spray processing is vital in many fields with high-temperature applicability for efficient production. For aircraft turbo engines in the aeronautical industry, temperatures above 1000 °C are demanded, as well as thermal shock, erosive and corrosive wear, sliding friction. All of those hard conditions indicate the need for the development of protective solutions with optimal properties of interface and volume to which is added the appropriate chemical and mechanical stability. Two of the benefits of thermal protection layers are low diffusivity and low expansion coefficient. However, at the interface between the bonding layer and the ceramic layer, an intermediate oxide layer, named TGO (Thermally Grown Oxide), is formed, which is a weak spot in the system. The monitoring of thermo-physical properties together with morphostructural investigations allowed the evaluation of the structure characteristics of obtained ceramic materials, emphasizing the need for reduced thermal conductivity as well as the critical need to predict the life span. This chapter will provide a short review on the present status of the research of ceramics composites coatings used as thermal barrier for industrial hot structural components, their latest advanced in fabrication and performance, as well as recommendation of their use in harsh high-temperature environments.

Keywords TBC · TGO · Deposition methods · YSZ · QTS

Abbreviations

AC-HVAF Activated combustion high-velocity air fuel
APS Air plasma spray
ASTM American society for testing and materials

A. Stefan (✉) · G. C. Cristea
National Institute for Aerospace Research “Elie Carafoli”, Bucharest, Romania
e-mail: stefan.adriana@incas.ro

V. Manoliu
Aerospace Services, Bucharest, Romania

© The Author(s), under exclusive license to Springer Nature Switzerland AG 2024
A. Pakseresht and K. K. Amirtharaj Mosas (eds.), *Ceramic Coatings for High-Temperature Environments*, Engineering Materials,
https://doi.org/10.1007/978-3-031-40809-0_5

CVD	Chemical vapor deposition
D-Gun	Detonation gun
EB-PVD	Electron beam physical vapor deposition
FGM	Functionally gradient material
HVAF	High-velocity air fuel
HVOF	High-velocity oxygen fuel
LPG	Liquefied petroleum gas
PTA	Plasma-transferred arc
PVD	Physical vapor deposition
QTS	Quick thermal shock
TBC	Thermal barrier coating
TGO	Thermally grown oxide
TIG	Tungsten inert gas
YSZ	Yttrium-stabilized zirconia

1 Introduction

1.1 *Current Trends in Ceramic Materials—Thermal Barrier Coatings as Protection Systems*

Conventional Thermal Barrier Coating (TBC) systems are defined as a duplex or triplex structure with a metallic bonding layer and a heat-insulating ceramic surface layer [1]. Basically, a thermal barrier layer system consists of multilayer coatings composed of a porous, insulating, YSZ (Yttrium-Stabilized Zirconia) outer layer that provides thermal protection, an oxide layer—TGO (Thermally Grown Oxide) that provides hot oxidation and corrosion protection, and a base aluminide bonding layer that is used to form the TGO layer [2, 3]. In most applications, the bonding layer is MeCrAlY (where Me=Ni or NiCo) or a modified Pt aluminate layer. It is necessary that the bonding layer is dense to provide protection of the substrate, against hot corrosion and oxidation, by forming a TGO layer, on the surface of the substrate [4].

The first generation of TBC layers consists of $\text{ZrO}_2\text{7\%Y}_2\text{O}_3$ with a typical thickness of 100–300 μm . The $\text{ZrO}_2\text{7\%Y}_2\text{O}_3$ layer is used as an insulating layer due to its low coefficient of conductivity (approximately 2.6 W/mK for a dense material), a relatively high-thermal expansion coefficient, and good thermal stability. Current research aims to improve the properties of the bond coat by adding Pt or small amounts of reactive elements such as Hf, Y, Gd or La to the layer [4]. Zr-based ceramic materials withstand lower temperatures, up to 600–700 °C and can be used to execute parts of the adiabatic ceramic engine that do not operate at very high temperatures, such as the combustion chambers. Ceramics are used in thermodynamic processes that use combustion gases, in the chemical industry, railways, in

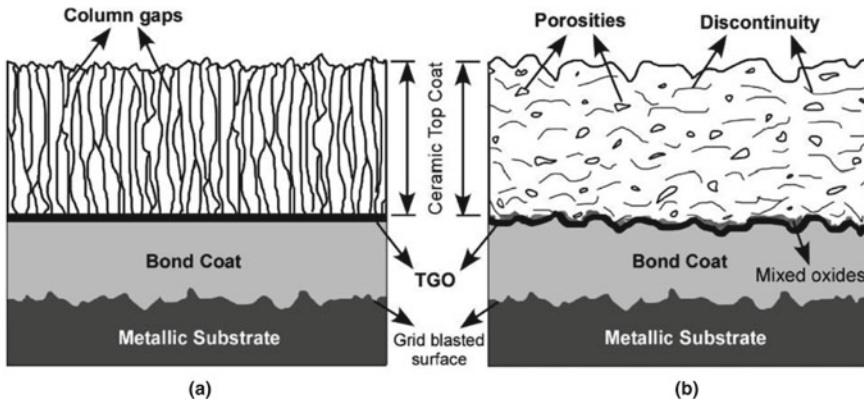


Fig. 1 General schematic structures of TBC produced by **a** EB-PVD method; **b** APS method [11]

the cellulose and paper industry, in heat exchangers, in furnaces, mining and mineral processes, in the nuclear and space engineering industries.

For superior protection, required for certain applications, the upper layer can be composed of several ceramic layers, each with different properties. These modern systems in which the ceramic layer is composed of multiple layers have demonstrated improved temperature capability compared to standard YSZ. The YSZ layer should have low-thermal conductivity and be able to sustain thermal expansion mismatch with the substrate. By creating a porous, columnar morphology the mismatched thermal expansion stresses that would otherwise develop in service can be minimized. This layer is currently deposited using Electron Beam Physical Vapor Deposition (EB-PVD) technology (Fig. 1a).

In aerospace applications, such as jet engines, gas turbines and rocket propulsion systems, components are subjected to extremely high temperatures generated by the combustion of fuel and the compression of air. These temperatures can exceed the melting point of the materials used to construct these components, leading to their degradation and failure. Over time, TBCs have evolved from simple insulating layers to intricate designs [5]. This progress has been achieved through the optimization of geometries and the careful selection of materials, resulting in higher thermal efficiency. Researchers are currently exploring new materials [6, 7], structures, and manufacturing processes [8, 9] for TBCs in order to enhance future aircraft engines. The improved TBC materials contribute to the efficiency enhancement of engines, leading to better thrust-to-weight ratios and energy savings. For instance, advancements in TBC materials and advanced manufacturing technologies have significantly increased the take-off thrust of Pratt and Whitney PW4000 series aircraft engines [10]. The PW4000-94 engine, which powers the Boeing 747, has witnessed an increase from 222–276 KN to 408–441 KN in the PW4000-112 engine for the Boeing 777. Presently, turbine engine heat components, based on nickel-based superalloys, have reached their temperature limits. Consequently, alternative materials

such as silicon carbide (SiC) fiber/SiC ceramic matrix composites (CMCs) are being investigated as the next generation of turbine engine heat components.

In the EB-PVD process, the material to be deposited is heated with an electron beam; following the process, vapors are produced, and the evaporated atoms condense on the substrate. Crystal nuclei form at favored locations and grow laterally and in thickness to form individual columns that provide in-plane alignment [11–13]. However, such approaches provide only limited control over the morphology of the coatings result in sub-optimal thermal conductivity of 1.6 W/mK. Therefore, new YSZ deposition techniques with a high degree of control over the coating and pore morphology are desirable to optimize thermal protection [3, 14, 15].

Depending on the targeted field, the deposition technology as well as the ceramic materials are selected based on the specific characteristics of the application. The working environment and the geometry of the part, which define the field of application, constitute the basic factor in the choice of the thermal barrier system. Mechanical, physical and chemical properties and last but not least the type of microstructure, are essential factors in the choice of the substrate type for the ceramic protection system. For example, in modern gas turbines, increased gas temperatures and pressures lead to an increased fraction of radiative heat flux [16]. Coatings with increased reflectivity can be used to avoid direct heating of metal substrates by this radiation. An effective method of producing such coatings is plasma jet spraying at atmospheric pressure (Air Plasma Spray—APS—Fig. 1b). These coatings will lower the temperatures of the elements exposed to the heat flux by approximately $170\text{ }^{\circ}\text{C} \div 200\text{ }^{\circ}\text{C}$ and thus allow the system to operate for a longer period. TBCs can extend the operating time of the covered elements up to 4 times, having as a side effect the reduction of fuel consumption.

While TBCs provide significant benefits, they are also susceptible to several failure mechanisms. Understanding and addressing these failure mechanisms is crucial to ensure the reliability and longevity of TBC systems. Some of the common failure mechanisms and the methods used to address them include: delamination, spallation, erosion and Foreign Object Damage (FOD), oxidation and corrosion.

Delamination refers to the separation or detachment of the TBC layers from each other or from the underlying substrate. It can occur due to thermal cycling, mechanical stresses, or interfacial oxidation. To address delamination, improved coating deposition techniques, such as electron-beam physical vapor deposition (EB-PVD), can be used to enhance coating adherence. Additionally, optimizing the composition and microstructure of the bond coat can improve the bond strength between the coating layers and the substrate.

Spallation refers to the complete loss or cracking of the TBC system. It can occur when the stresses exceed the strength of the coating or when the coating is subjected to thermal shock. To address spallation, researchers are continuously working on developing advanced ceramic materials with higher toughness and improved resistance to thermal shock. Novel deposition techniques and optimized coating architectures, such as graded or functionally graded coatings, can also enhance the resistance to spallation.

TBCs can be subjected to erosion and damage from foreign objects, such as dust, sand, or ice particles, in the engine's operating environment. Erosion can result in the loss of coating material and degradation of the coating's thermal insulation properties. To address erosion and FOD, researchers are exploring the use of more erosion-resistant ceramic materials and developing surface modifications, such as microstructures or coatings that can mitigate erosion effects.

Corrosion and oxidation resistance are also added to these factors [11] when choosing the type of outer layer for the complete definition of the thermal barrier system. They are important in choosing the protection system and play a defining role in characterizing thermal barrier coatings as durable, and resistant to high temperatures with long exposure times to corrosive environments. For example, in the cutting tool industry, ceramic materials such as: $\text{Al}_2\text{O}_3 + \text{ZrO}_2$, $\text{Al}_2\text{O}_3 + \text{TiC}$, $\text{Al}_2\text{O}_3 + \text{Si}_3\text{N}_4$, etc. are used in the manufacture of sintered plates, or as reinforcement layer for the active areas of drills, milling cutters and abrasive discs, made of materials with low physical and chemical properties. In the civil engineering industry, ceramic materials are used as tiles, bricks, stoneware, earthenware, pipes and sanitary ware, dishes and kitchenware, heat insulators, installations for chemical processes, etc. In automobile construction, ceramic materials such as aluminum oxide (Al_2O_3) or zirconium oxide (ZrO_2) are used to make the body of spark plugs and to clad oscillating levers. Ceramic materials such as Si_3N_4 are used for spark plug electrodes and aluminum titanate (Al_2TiO_5) for cylinders, pistons and piston rings, as well as for exhaust gas galleries. In the aerospace field, ceramic materials are used both for protecting turbine engines and, more particularly, for jet engines. The efficiency of jet propulsion is directly dependent on the temperature of the combustion gases, which has led to the emergence of practical realizations of materials capable of ensuring low thermal levels.

One study showed that over 83% of high-performance ceramics made in Japan are used for ceramic electronic components such as capacitors, substrates for micro-electronic chips, etc. In fact, ceramics have expanded from electronics, to applications in heat engines. The hardness of ceramics is close to that of diamond, it is resistant to wear and high temperatures and does not rust. However, strength and hardness, and in particular resistance to thermal shock and high-temperature gradients, still pose major problems for engine manufacturers today, and these will surely be solved soon. High technology is required to produce a ceramic of a certain purity for its intended purpose, composed of ultrafine particles of Al, Ti, SiO_2 , as well as other minerals. Chemicals are added to form a paste that is mixed and formed into mold at high pressures and temperatures. This process is called calcination and it is obtained in furnaces with a rigorously controlled atmosphere. The main difficulties in the development of ceramics are their fragility and the tendency to crack at high temperatures. Under the influence of stress factors, the brittleness of ceramics allows the appearance of fine cracks invisible to the naked eye that grow rapidly. Several methods are used to improve quality, including obtaining a highly uniform microscopic structure and using several means of quality control (ultrasound, X-rays, etc.) in order to detect manufacturing cracks before they begin to enlarge. Some companies from America have succeeded in making ceramic composite materials, in which

the thermal resistance was superior to Ni-based superalloys. These are used in gas tubes.

In 2019, Mustafa Guven Gok and Gultekin Goller studied the behaviour of Gadolinium Zirconate at high temperatures by analysing the morpho structural changes during testing. The research carried out by the two concluded that Gadolinium zirconate ($\text{Gd}_2\text{Zr}_2\text{O}_7$ or GZ) with pyrochlore or defect fluorite-type structure is a new and promising alternative ceramic top coating material to YSZ [11].

Promising physical and thermal properties of pyrochlore and perovskite type materials, used as a complementary top layer of YSZ in TBC FGM (Functionally Gradient Material) systems, have been demonstrated by several researchers [11, 17, 18]. However, when applied as isolated ceramic layers, these materials tend to show lower resistance to thermal shock due to cracks occurring in the TBC system, since both the substrate and the bond coat have relatively higher values of thermal expansion coefficients. Consequently, the TGO layer is very detrimental to the performance of TBCs [19].

The composition of the current exterior ceramic layers is limited by changes in phase and thermal stability at extreme temperatures leading to layer fragmentation due to erosion at high temperatures. In a TBC system, an internal metallic bond coat layer is used for anchoring the TBC to the substrate. The bond coat layer must show resistance to oxidation, high temperatures and high creep resistance. The main purpose of the bonding layer is to ensure the adhesion of the ceramic layer and to protect the substrate from the formation of the TGO layer [4]. Normally, this layer is formed during thermal cycling or thermal shock test. TGO induces additional stress near the interface within the TBC and leads to crack propagation [17].

1.2 The Development Process of TGO by Thermal Treatment

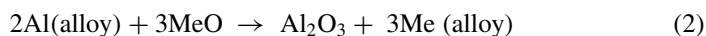
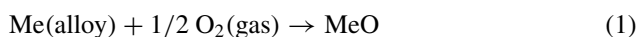
Degradation of the layers occurs through the appearance of two important factors: TGO growth and TGO adhesion to the bonding layer and the ceramic layer. In the literature, it is mentioned that the $\alpha\text{-Al}_2\text{O}_3$ layer that forms exclusively on the surface of the ceramic layer after pre-oxidation is a good protection against corrosion at high temperatures [20–22]. Normally, the initial oxidation stage of NiCoCrAlY alloy starts with the simultaneous formation of $\alpha\text{-Al}_2\text{O}_3$ and one or more transient oxides grown on the layer surface and in the layer, such as $\theta\text{-Al}_2\text{O}_3$, Cr_2O_3 , NiO, NiCr_2O_4 or NiAl_2O_4 . The development of transient oxides depends on the composition, microstructure, bonding layer surface conditions and pre-oxidation parameters. After heat treatment, TGO has a double-layered microstructure consisting of small grains. The constitution of the outer layer strongly depends on the type of transient oxides present at the surface of the oxide layer after pre-oxidation.

Some studies have shown that during heat treatment, a dispersed NiAl_2O_4 layer rich in Zr particles occurs at the TBC/TGO interface. This layer developed during thermal cycling is explained by Ni transport through TGO. The oxide layer growing

on the surface of bonding layer deposited by EB-PVD or APS at the interface of the TBC/ceramic layer plays a critical role in the interface detachment of the ceramic layer [23–25]. It is obvious that this debonding problem has a negative impact on the performance of the layer by reducing the efficiency. The phase transformation of the ceramic layer from tetragonal to monoclinic, with the increase in volume and oxidation of the cross-talk, has been identified as the primary factor influencing TBC performance.

The formation of the TGO layer involves the diffusion of Al from the NiCrAlY bond coat and the formation of γ' Ni₃Al phases. The ability of the bond coat layer to continue oxidation favours the growth of Al₂O₃. When the concentration of Al in the layer falls below the level at which Al₂O₃ can form, other oxides form with elements in the bonding layer and a state called chemical degradation occurs. During the formation of Al₂O₃, other oxides are chromium-formed by secondary reactions, a process called transient oxidation. After long-term heat treatment at the same temperature, the formation of transient oxide layers occurs on the surface of the initially formed TGO. It is assumed that the formation of these oxide layers occurs by outward diffusion of Ni and Cr through the α -Al₂O₃ layer or by microcracks. After a 24-h treatment, Al and O are concentrated on the surface of the TGO layer and Ni and Cr is uniformly distributed in the bond coat layer. After a longer thermal treatment (50–95 h) Ni and Cr diffuse from the bonding layer to the TGO surface forming simple oxides with Ni and Cr or complex compounds such as spinel phases.

The morphology and composition of the TGO layer are important for the ceramic layer. Oxidation of Y, Al, and Cr causes the bond layer to increase in volume. The growth of NiO and spinel phases (NiCr₂O₄ or NiAl₂O₄) are destructive for the layer because they develop a high growth rate, which favors the volume growth of the bond coat layer. The transport of reactants such as Ni, Cr, Al, and O through α -Al₂O₃ is slow compared to transport through other oxides. Typically, Al₂O₃ is formed by reactions such as:



During plasma sputtering, elements such as Y, and Al show an increased affinity for oxygen, and in a molten particle projected onto the substrate by the plasma jet the metal atom reacts with the dissociated oxygen atom during plasma jet transport. During thermal treatments, at temperatures of 1000 °C, a density of NiO and Cr₂O₃ occurs very near the oxide layer. The presence of α -Al₂O₃ results from the internal diffusion of oxygen anions and external diffusion of cations forming compounds. At temperatures of 1100 °C, the oxidation rate is higher. The transition from NiO to NiAl₂O₄ occurs at this temperature. At 50 h, at this temperature, α -Al₂O₃ constitutes most of the oxide phase. The existence of NiAl₂O₄, NiO, and Cr₂O₃ is also recorded.

The uneven distribution of the elements and discontinuities in the microstructure (lineages of oxides and improper flat areas) lead to an increase in the oxidation

rate. Due to the instability of the elements at high temperatures, it shows a gradual transition from the initial unstable phases of NiO and Cr₂O₃ to more stable NiAl₂O₄ and CrO₃ phases. The increase in the oxidation time involves: the oxidation stage → the formation of the Al₂O₃ protective layer → Al depletion → Ni diffusion outside and the solid-state reaction with Al₂O₃ to form spinel phases → the formation of Cr₂O₃ at the oxide/metal interface, these processes depend on the temperature of oxidation and microstructure of the deposited layer.

2 Materials and Methods

2.1 Suitable Deposition Methods for Hot Structural Components

A wide range of deposition methods may be suitable for selected deposition solutions associated with real parts. As there is no procedural method to classify these techniques, each deposition method depends on the criteria imposed by the mode and operating conditions of the parts selected for deposition and the resources available. In some cases, depending on the type of protective coating, one or more deposition methods may be used. The deposition technique can be chosen depending on the need for protection and the thickness of the layer, but also depending on the material of the substrate and the deposition alloy. Figure 2 shows the graph of the thicknesses of the coating layer for different deposition techniques.

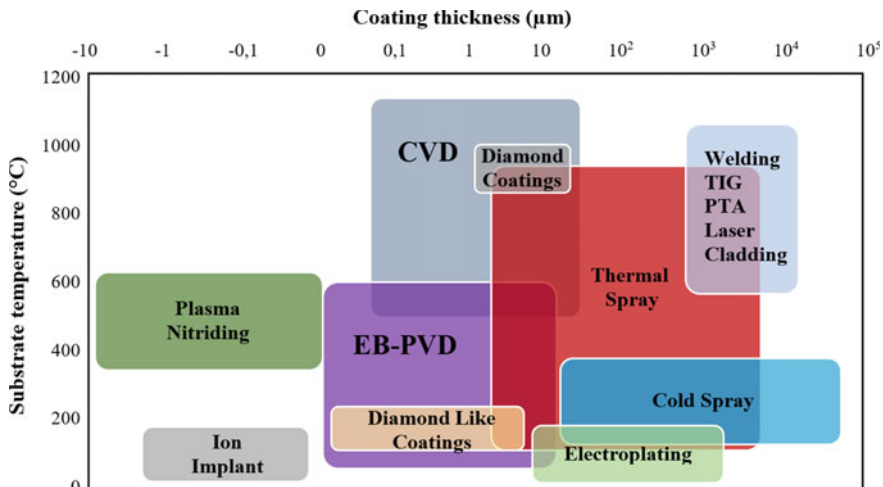


Fig. 2 Graph of coating thicknesses for different deposition techniques

For an easier understanding of modern deposition techniques, we will start by presenting some classical and somewhat known deposition methods. Generally, to obtain high-performance thermal barrier layers, which are particularly required by the demands of the operation of real turbo-engine parts, micronized powders made of ceramic oxides, generally materials with a high melting point, are used.

Regardless of the procedure selected to be used, three stages in the deposition process are identified [4]:

- Heating of sputtering material in order to form molten or semi-molten droplets;
- Designing these high-speed patches on the coated substrate;
- The collision of glowing particles on the substrate which adhere forming coating layers.

In the case of the *Plasma Deposition method*, the spray material used for deposition on real models is in the form of powders.

The plasmatron uses a controlled electric arc between two electrodes to ionize a carrier gas. The high temperatures of around $10,000 \div 20,000$ K created in the arc ensure the melting of all particles thus providing good characteristics to the protective coatings. In order to eliminate the oxidation process of highly reactive oxygen elements, neutral carrier gases are used, leading to powdery, loosely adhering layers that can be compacted by heating.

The choice of the plasma deposition process (Fig. 3) for the deposition of thermal protective coatings can be supported by the following pros:

- The need to achieve very high temperatures for the fusion of ceramic oxides or even metal carbides. The required temperature can reach 3000°C ;
- Relatively short distance between the surface and the nozzle of the metallization gun ($60 \div 200$ mm) which ensures the fusion of ceramic oxides;

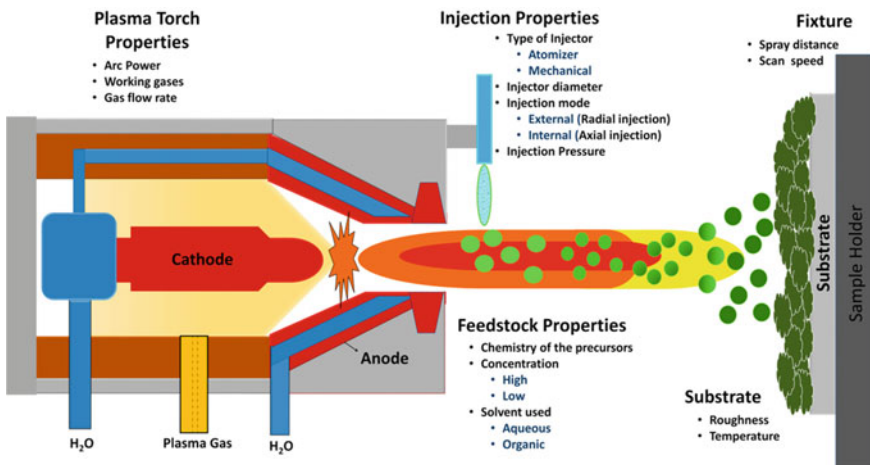


Fig. 3 Schematic diagram of the plasma spray process [26]

- Uses argon as an inert gas forming a protective environment that limits the formation of oxide;
- Achieves optimum adhesion of the ceramic layer and complete fusion at low temperatures (up to $150 \div 200$ °C) without changing the geometry and structure of the material;
- Has a speed of $500 \div 600$ m/s of the plasma jet that favors optimal adhesion.

The process of plasma deposition of a molten material on a surface can be described by a sequence of steps:

1. Fine particles of material are injected into a plasma jet;
2. The particles are rapidly heated to a molten or semi-molten state and projected at high velocity onto the metal substrate;
3. The material is deposited on the surface of the substrate and rapidly cools to form a layer.

The plasma deposition process is an efficient and economical method used to obtain coatings with superior properties and performance.

The structural bond, formed between the ceramic layer and the metal substrate, in the case of plasma jet metallization, allows to obtain adherent deposits with a thin and smooth structure and a thickness between $0.2 \div 2.3$ mm depending on the application requirements.

The layers resulting from powder deposition have the following important properties:

- Resistance to atmospheric oxidation;
- Resistance to corrosive gases;
- Resistance to abrasion.

This diversity is associated with both the rheological properties of the powders, the non-uniform grain size and the objective deposition conditions.

Another known deposition method with thermal spraying is the *High-Velocity Oxygen fuel (HVOF) deposition method* (Fig. 4).

This process was developed for very high spray velocities by the axial injection of a metal powder into an oxygen jet, such as propane, LPG (Liquefied Petroleum Gas), propylene. The gas velocity can reach up to 2700 m/s, the jet having a temperature of about 2750°C. In the deposition process, the metal powder melts and the particles are projected at speeds of up to 800 m/s on the selected area. The result is a compact layer with porosity below 1% and very high adhesion. This method allows to obtain layers twice as thick as those obtained in plasma jet [27].

HVOF guns use different methods to achieve very high coating speeds. One method is based on a high-pressure, water-cooled combustion chamber and a long nozzle. Fuel mixed with oxygen is introduced into the chamber where combustion takes place. The powder is fed axially into the combustion chamber. The coatings obtained with the HVOF system are like those obtained in detonation (D-Gun) and AC-HVAF (Activated Combustion High-Velocity Air-Fuel) systems, that is, they are very dense with very good adhesion, with low residual stresses that allow thicker

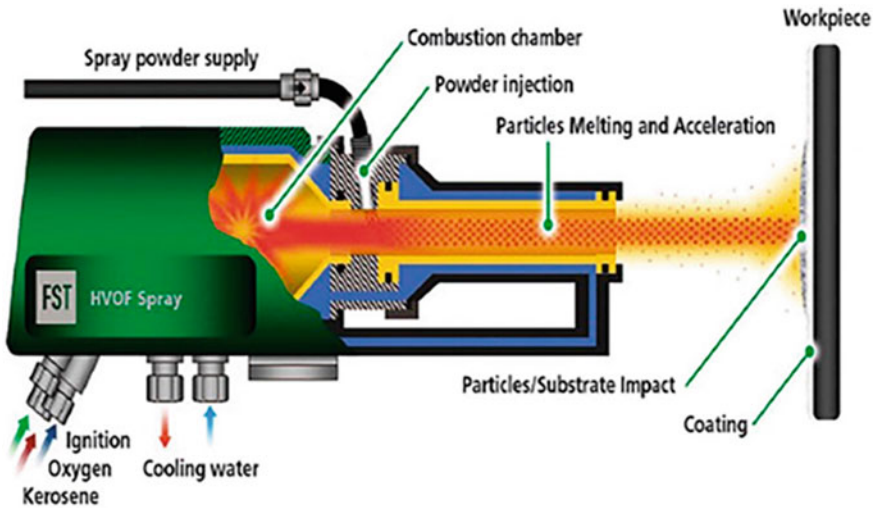


Fig. 4 Schematic diagram of the High-Velocity Oxygen Fuel spray process (HVOF) [28]

coatings to be obtained than with other processes. Even if during the HVOF process, the melting temperature of the powders is not reached, the extremely high speed of the particles leads to a very good quality coating.

In the same category is the *High-Velocity Air–Fuel (HVOF) thermal deposition method*. This is intended for the same applications as HVOF, the jet registering speeds of approximately 2600 m/s. Through this method, very dense coatings can be obtained with no thickness limit. The deposition gun uses hydrogen microinjection to increase the deposition efficiency by 15 ÷ 25% and improve the quality of the coating, the powder jet being extremely concentrated. Width of the powder jet can be controlled, depending on the needs, from the configuration of the powder injector.

Modern coating methods include *PVD—Physical Vapor Deposition* and *CVD—Chemical vapor deposition*. These processes are used to significantly increase the thermal and mechanical performances of the protective coatings used [29]. Although improvements have been made in terms of optimizing the coating parameters, PVD deposition exfoliates due to insufficient substrate surface properties. Thus, the influence of surface properties on the adhesive film of PVD coatings with carbides, for example, is investigated.

Advantages of CVD method are:

- The capability of producing highly dense and pure materials;
- Produces uniform films with good reproducibility and adhesion at reasonably high deposition rates;
- Is a nonline-of-sight process with an efficient spraying power. Therefore, it can be used to uniformly coat complex shaped components and deposit films with good conformal coverage;

- It can control crystal structure, surface morphology and orientation of the CVD products by controlling the process parameters;
- Deposit rate can be easily adjusted;
- Low deposition rate is favored for the growth of epitaxial thin films for micro-electronic applications. However, for the deposition of thick protective coatings, a high deposition rate is preferred and it can be greater than tens of mm per hour.

This is substantially exceeded only by techniques such as plasma spraying [30].

In the case of *Sputtering Deposition* (Fig. 5), the process consists in moving the material from the target to the support, while its surface is attacked with ion gas, accelerated by a high potential difference. In this case, under conditions of abnormal electrical discharge at high voltage such as 100 eV and $p = 10^{-2}$ torr, the entire cathode is covered by plasma [31]. Thus, a space is formed between the cathode and the plasma in which no important ionization or excitation processes take place. This phenomenon is explained by the fact that the space charge in the gap between anode and cathode is so distributed that the entire externally applied potential difference is in the cathode domain; the cathode drop being of the order of hundreds of volts. Thus, upon the impact of the positive ions with the cathode, the pulverization and heating of the cathode takes place, because part of the impact energy of the positive ions is transformed into heat.

In general, the deposition technology has in mind several stages that must be followed in order to obtain multilayer protections.

Degreasing is the first step in the technological process of obtaining the protective coatings and it aims at preparing the metal layer over which the deposition will be made. The recommended solution is chloride-perchloroethylene solvent for 2–3 min to remove any impurities and then the samples are washed with distilled water. After this process, the metal support is sandblasted, a mandatory operation both for additional cleaning and for the creation of a rough surface to facilitate optimal mechanical anchoring of the deposited layer. It is recommended to use corundum

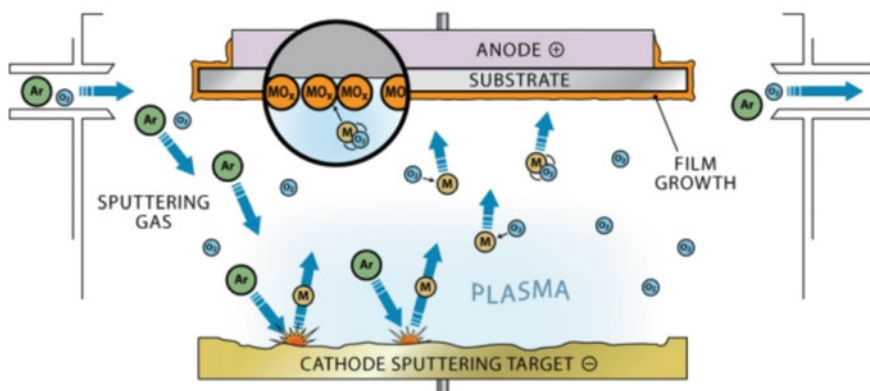


Fig. 5 Schematic of the sputtering process [32]

as blasting material using a design angle of up to 30° [33]. Metallization will take place no later than 2 h after sandblasting to prevent oxidation of the surface. After these stages of preparation of the substrate material, the actual deposition is carried out, starting with the water-repellent layer and then the outer ceramic protective layer. These steps must be followed according to the requirements in order to obtain adherent protective coatings with higher properties than the values of the imposed parameters, which are associated with the composition and grain size of each powder used.

The science and technology of deposition of protective structures has progressed rapidly towards designed coatings and surface engineering. Thus, it appears from the literature that hybrid methods are becoming more and more widely used, facilitating the development of dedicated deposition equipment.

Validation of the performance of the deposited coatings can be supported by thermal tests as close as possible to real conditions. The most conclusive test may be the thermal shock resistance test, which proves to be a high-quality test method for validating the performance of thermal barrier structures.

2.2 High-Quality Testing Methods—Thermal Shock Resistance Test

The ever-increasing needs for obtaining the best performing materials, with superior physical and chemical characteristics, require new testing methods and facilities. Considering this, researchers need dedicated equipment to meet the needs of testing materials and coatings, especially in the aerospace field.

To better understand the Quick Thermal Shock (QTS) method, we begin by describing the installation, designed and developed by the National Institute for Aerospace Research “Elie Carafoli” (Fig. 6) to meet the requirements imposed by the performance of the thermal barrier layers used in the aviation industry. The QTS facility consists of modules, each with specific function and upgradability to increase test quality. The heating enclosure consists of an insulating outer jacket made of several layers of refractory material of the appropriate thickness, with a content of more than 90% Al_2O_3 , which ensures that the outside temperature does not exceed 30 °C. The other layers can be 90% refractory concrete, lightweight concrete, and mineral fiber. Special heating elements such as Kanthal Super 1800 °C are used to ensure a high temperature in the enclosure.

The temperature inside the oven is measured and adjusted using a Pt6%Rh/Pt30%Rh thermocouple. The temperature on the surface of the sample is measured with an optical pyrometer, equipped with cooling jacket and special lens to withstand high temperatures. The facility is equipped with a controller that positions a cover that also serves as a support for the specimen, ensuring the repeatability of the test with an accuracy of ± 0.02 mm. At the same time, the cover serves to close and open the heating enclosure with programmable speeds and to limit the shock at the stroke



Fig. 6 The quick thermal shock installation within the National Institute for Aerospace Research “Elie Carafoli”—INCAS Bucharest [34]

ends by using a linear robot element with an electromagnetic brake. The specimen can have different geometric shapes, such as parallelepiped or cylinder.

The sample is moved vertically with the help of a robot with linear movement. After heating the sample to the desired temperature, it is removed from the oven with the help of the linear robot and brought to a cooling area. Here, compressed air or CO_2 is used to cool the specimen. The cooling gas comes from the side through two nozzles with the possibility of adjusting the flow rate and pressure. The facility is connected to a PC where you can see in real time the temperature of the cooling gas, the flow rate, as well as the temperature of the sample. After cooling, the test cycle can be adjusted as many times as it is considered necessary, respectively until the exfoliation, cracks, detachments are observed on the surface of the sample. The programmable automation system ensures the test cycles. The automation system with programmer ensures the test cycles. Its repeatability, measurement and recording of parameters during the thermal shock test operation are in automatic mode, and the operation can be performed in a manual or programmable cycle [32].

2.3 Classical Thermal Testing of Materials in the Defence and Security Industry. Limitations of the Process

The testing of ceramic coated specimens is more complex than the testing of solid materials because not only the combined properties of the coating and the substrate are involved, but also the bonding conditions between them and the internal stresses resulting from the difference in the physical properties of the materials from which the component parts of the specimen are made. In general, there are three broad categories of test methods:

- I. fundamental evaluations;
- II. tests for fundamental physical properties;
- III. usability tests.

Preliminary tests are especially necessary to check a large number of samples resulting from a change in deposition technology. For example, consider the most important variables in plasma-spray deposition technology.

First, there are several different substrate preparation methods that produce different degrees of layer-substrate adhesion.

Secondly, with a single powder different phases or allotropic shapes, different particle shapes, different particle sizes, variable particle surfaces affecting the flow properties of the powder and the rate of heat transfer from the arc to the powder are obtained.

Third is the influence of deposition technique, that is, type of equipment, powder feed rate, balance gas, flame speed, traverse rate, distance from nozzle to specimen holder and temperature of the holder during deposition. These variables can be combined in order to obtain coatings with superior properties, suitable for the intended purpose.

Tests for fundamental physical properties are those that highlight certain properties such as micro hardness, hardness, porosity, density, etc., which from an engineering point of view represent the fundamental physical properties of the specimen.

Usability tests are those tests that aim to make final judgements on the usability performance of the materials studied. Thus, these tests tend to mimic as closely as possible the conditions under which the test material is used. For ceramic coatings these tests consist of thermal shock resistance tests, corrosion, refractoriness tests, etc.

The purpose of the tests carried out with the specimens obtained by plasma deposition technologies is to obtain the necessary data for the preliminary evaluation of their properties and as far as possible to predict the performance of the coatings in actual use. The following samples were made: MeCrAlY, MeCrAlY/ZrO₂Y₂O₃, MeCrAlY/MeCrAlY + Al₂O₃ and MeCrAlY/MeCrAlY + Al₂O₃ /ZrO₂Y₂O₃ were deposited on Nimonic 80 superalloy support.

3 Results and Discussion

3.1 Thermal Shock Resistance Test

The thermal shock is the heating of the samples to temperatures of hundreds of degrees or even thousands of degrees Celsius in a very short time (approx. 4–5 min) and their sudden cooling down to ambient temperature or even negative temperatures. The thermal shock resistance test aims to record microstructural changes in the shocked specimens; loss of mechanical strength of the coating as well as the number of shocks the specimen can withstand without suffering major cracks or peeling. A specimen is considered to have failed in thermal shock when cracking or peeling is evident.

The test cycles were carried out as follows: heating in the oven for 5 min at the working temperature and cooling for about five minutes under a jet of cold air, by sweeping the jet on the surface of the sample. The dynamics of cooling the samples is very fast and at the end of the 5 min of cooling the samples have a temperature of approx. 40–50 °C. This temperature is due to the relatively large mass of the support compared to the mass of the samples, and therefore the support plays the role of a residual heat source for the samples.

The temperatures at which the thermal cycles were performed were: 900, 950, 1000, 1050C, 1100, 1150 and 1200 °C. All samples were tested for 25 cycles for each temperature. The specimens subjected to thermal shock with forced cooling were visually examined after each cycle. A specimen was considered to have yield to thermal shock when obvious cracks or exfoliation appeared on its surface. The results of the thermal shock resistance tests for the coatings studied in this paper are presented in Table 1.

Table 1 Thermal shock resistance of samples on Nimonic 80 superalloy support

Temperature (°C)	1200	175	175	175	175	175	Total number of cycles
	1150	150	150	150	150	150	
	1100	125	125	125	125	125	
	1050	100	100	100	100	100	
	1000	75	75	75	75	75	
	950	50	50	50	50	50	
	900	25	25	25	25	25	
Coating	MeCrAlY	MeCrAlY/ ZrO ₂ Y ₂ O ₃	MeCrAlY/ MeCrAlY + Al ₂ O ₃	MeCrAlY/ MeCrAlY + Al ₂ O ₃ / ZrO ₂ Y ₂ O ₃			
Substrate	Nimonic 80	Nimonic 80	Nimonic 80	Nimonic 80			

An immediate remark was the fact that the deposits on the copper support lasted very little, compared to those on the Nimonic 80 superalloy support. All the samples changed their colour to a gray-black.

In all samples on Nimonic support, no exfoliation was found after all the test cycles, respectively 175, were performed.

3.2 Thermal Barrier Coating's Structure—Composition and Microstructural Evaluation

Morphstructural and compositional evaluation of thermal barrier structures obtained by conventional or non-conventional deposition technologies provides valuable information on their behavior defining their performance in the actual exploitation process. In this sense, the conditions that the tests to which the specimens deposited with ceramic coatings are subjected must be as close as possible to the real operating conditions. The similarity between the test and the way in which the thermal barrier coatings are used becomes an essential condition for the success of a more accurate evaluation. To this condition is added the reproducibility of the data and their validity for predicting the maximum performance of the coatings.

Electron microscopy is a modern method of studying very fine aspects by using the propagation and focusing properties of electron beams under the action of magnetic or electric fields.

The images formed in this way contain information about the chemical composition, surface topography of the sample or other information, depending on the type of signal used to obtain the micrographs.

The signals generated in the electron-sample interaction zone used in most electron-optical instruments are: backscattered electrons, secondary electrons, Auger electrons, X-rays characteristic of the chemical elements contained in the micro volume of irradiated sample.

It can be said that the morphstructural evaluation of protective structures is the descriptive analysis of the dynamics of changes occurring during thermal tests. Thus, the mechanism of failure of the coatings during thermal shock tests is associated with the residual stresses produced by the growth and shrinkage of the TGO coatings during thermal shock, namely extremely rapid heating/cooling [12].

The NiCoCrAlY interlayer (Figs. 7 and 8) is the source of formation of the Al_2O_3 layer. Yttrium, like other rare elements (Zr, Hf), increases the adhesion of the layer as well as the resistance to oxidation, and Cr accelerates the formation of the Al_2O_3 compound and increases corrosion resistance.

Consequently, oxidation occurring on the surface of the outer layer during thermal shock causes a decrease in the thickness of the layer. From the analysis of the results obtained in the case of the bonding layer, it is revealed that the thickness of the layer (Fig. 8) is non-uniform, the diameter of the micro zones decreases with increasing

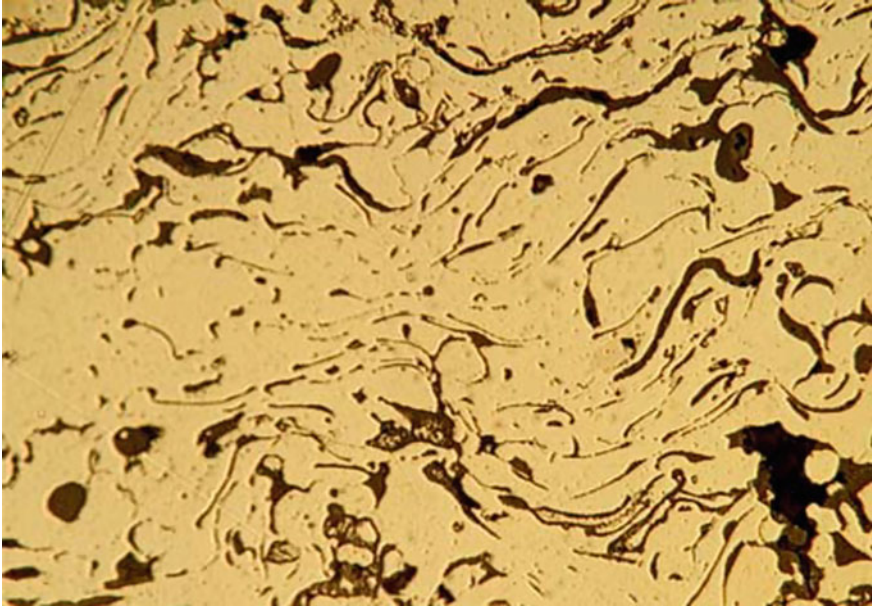


Fig. 7 Porosity of NiCoCrAlY layer thermal shocked at 1200 °C

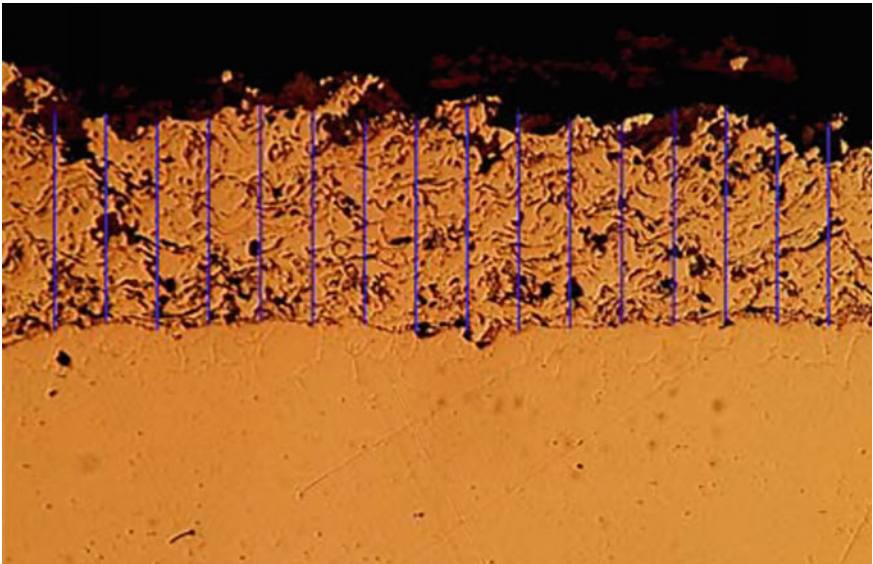


Fig. 8 Thickness of NiCoCrAlY layer thermal shocked at 1200 °C

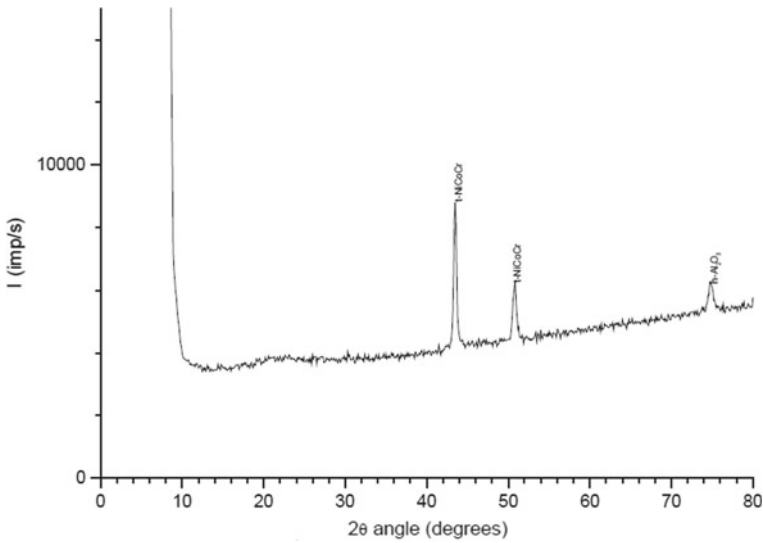


Fig. 9 Diffractogram of the intermediate NiCoCrAlY + Al₂O₃ layer

temperature and thus the porosity decreases with increasing temperature. The qualitative images show that the layers are adherent. Porosity decreases (Fig. 7) with increasing temperature. Porosity influences the thermo-physical properties of the layer. The decrease in porosity from 39% at 1000 °C to 22% at 1100 °C leads to an increase in high-temperature resistance and wear characteristics, but also shows a decrease in thermal conductivity.

Figure 9 shows the diffraction plot for the mixed NiCoCrAlY + Al₂O₃ layer after thermal shock. The diffractogram shows the formation of a tetragonal phase of Cr₃O₄ at high temperatures through an oxidation reaction of the elements in the metal matrix and the surface diffusion of Cr. The formation of a α -Al₂O₃ metastable intermediate phase is highlighted. This phase occurs at temperatures of 1100 °C.

The peak is reflected at 4450 imp/s with lattice plan (200) of maximum intensity of 29,448 imp/s. A recrystallization of α -Al₂O₃ results in well-defined peaks reflected at lattice plan (104) and (122) and (208), respectively, after increasing the temperature up to 1000 °C of the porous sample. The characteristic peak (208) for α -Al₂O₃ at 0.12889 nm is more intense compared to the peak observed at 0.1284 nm in the diffractogram of the thermally unshocked sample. The peak of the tetragonal structure NiCoCr (312) lattice plan is found in the diffractogram of the thermal shocked sample and differs in intensity. The characteristic peak of the tetragonal NiCoCr with lattice plan (112) structure at 0.2143 nm with an intensity of 10,622 imp/s for the thermal shocked sample is comparatively higher than that at 0.2078 nm with an intensity of 8256 imp/s recorded for the porous nonheat shocked sample.

As can be seen from the diffractograms above (Figs. 9, 10 and 11), through oxidation changes occur in the layer through the formation of the hexagonal phase of

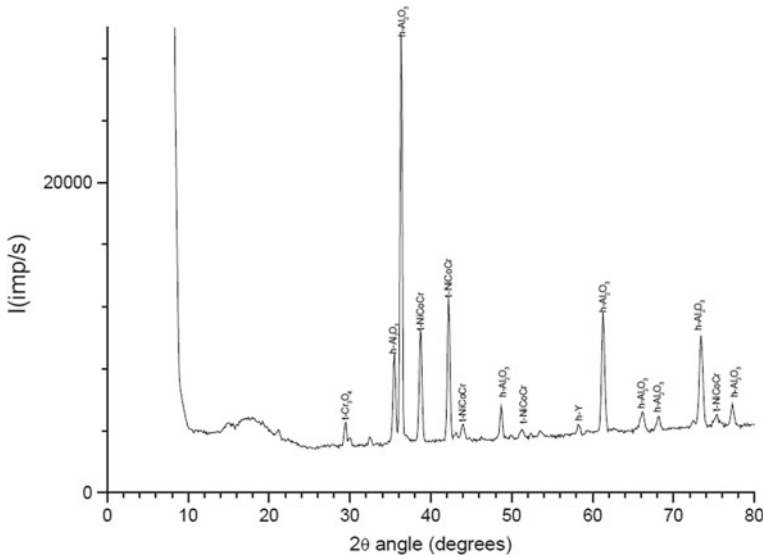


Fig. 10 Diffractogram of the thermal shocked NiCrAlY + Al₂O₃ layer

[α -Al₂O₃(104)]. The presence of the α -Al₂O₃ hexagonal structure reflected in (208) is highlighted. Figure 11 shows the diffraction graph for the ZrO₂Y₂O₃ layer after thermal shock. A maximum peak of the [k-Al₂O₃ (206)] phase resulting from Al diffusion and its oxidation is highlighted. The prominent peak of the cubic Y₂O₃ phase reflected at (431) lattice plan has an intensity of 7885 imp/s. As an exception, the peak (006) in lattice plan at 0.2196 nm has a deviation of 0.031 nm from the one observed in ASTM, from which the existence of a distortion of the α -Al₂O₃ matrix can be deduced.

The structural changes occurring as a result of the oxidation process of the elements, especially Al and Cr, diffusing from the bond coat outwards are produced by the thermal shock (Fig. 11). At 1100 °C a metastable intermediate phase k-Al₂O₃ occurs, which helps the deterioration of the layer.

Thermal shock induces changes in the microstructure of the layers and the formation of new phases by oxidation of existing elements in the matrix [1, 35]. Thus, in Fig. 12, the bond coat is cracked and the adhesion between substrate and bond coat is weak. At the surface of the bond coat the porosity is high. The Zr and Y distribution (Fig. 13) did not induce major changes, the presence of ceramic layer remains in isolated areas (Fig. 15). The distribution of Al, shown in Fig. 15, as well as of oxygen, reveals that Al₂O₃ is slightly segregated in bands (it is also highlighted in the Al variation profile, Fig. 16), in contrast to the situation before testing. From the distribution images (Fig. 15) and the variation profile (Fig. 18), Fe diffusion at the interface between bond coat and ceramic layer is observed.

The Cr distribution (Fig. 15) and the variation profile (Fig. 17) indicates the formation of a barrier at the interface between substrate and bond coat and the Ni

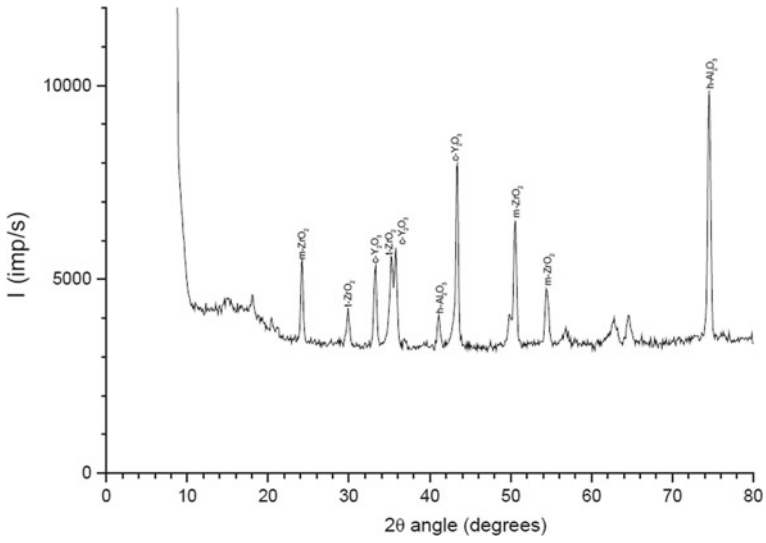


Fig. 11 Diffractogram of the thermal-shocked $\text{ZrO}_2\text{Y}_2\text{O}_3$ layer

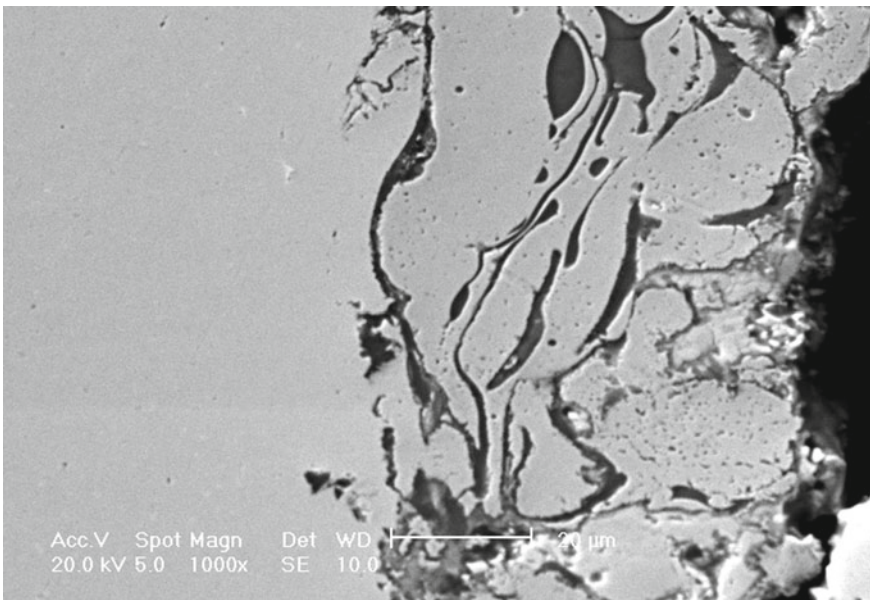


Fig. 12 Micrograph of the thermal barrier coating after thermal shock test

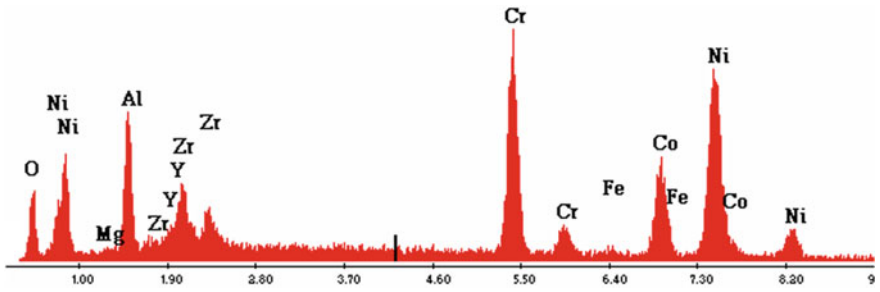


Fig. 13 Spectrum of elements in the X-ray range over a selected area

variation (Fig. 14) indicate a diffusion of the element at the interface between the bond coat and ceramic layer. Adhesion is good at the interface between substrate and bond coat, except for the areas where there are large porosities and detachments. There are very large reticular cracks in the bonding layer.

As can be seen from the micrographs above (Figs. 16, 17 and 18), the bond coat generally has a good adhesion with the substrate material due to the compositional similarity and the ceramic layers show a mechanical anchoring at the level of the microgeometry of the bond coat. Due to the thermal test, the ceramic layer degrades in most areas, while the bonding layer remains adherent. In some isolated areas, there are detachments of the adhesion layer due to reticular cracks and porosity. In the ceramic layers based on $ZrO_2 Y_2O_3$, Cr barriers are highlighted at the interfaces

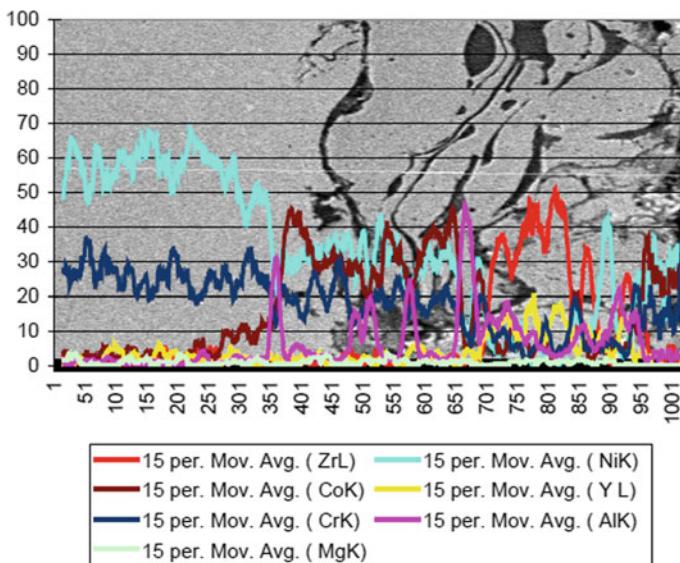


Fig. 14 Variation profile of elements

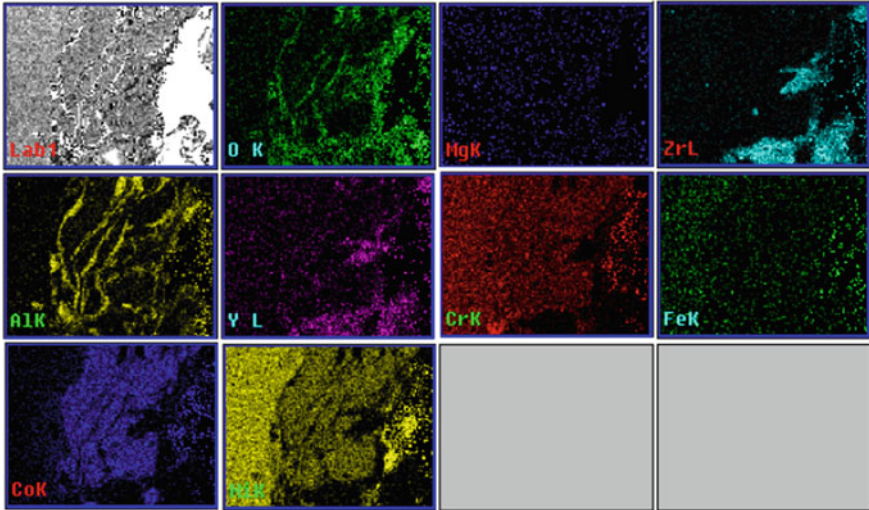


Fig. 15 Distribution of elements per selected area

that could cause the degradation of the layers at high temperatures. The appearance of the κ - Al_2O_3 metastable intermediate phase at temperatures of 1100 °C helps to damage the thermal barrier layer.

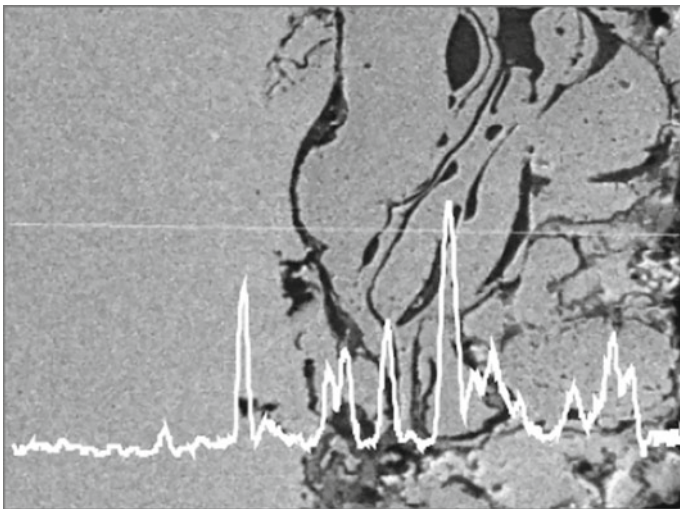


Fig. 16 Variation profile of Al

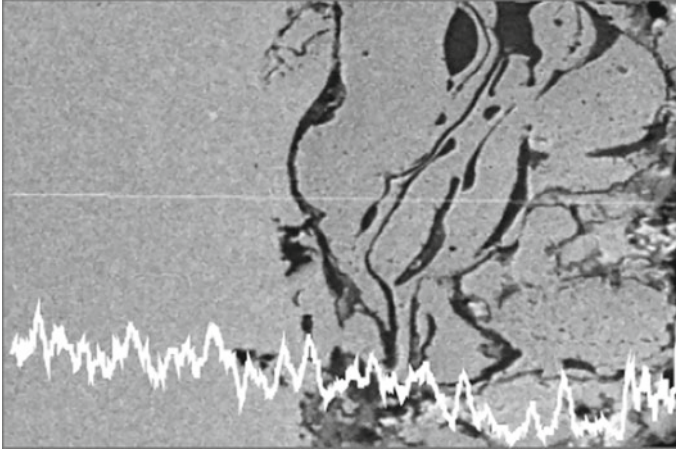


Fig. 17 Variation profile of Cr

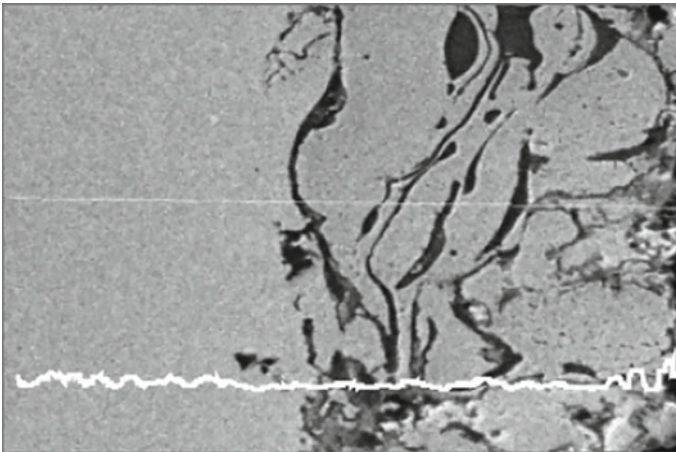


Fig. 18 Variation profile of Fe

4 Conclusions

The properties of ceramic protective layers are determined by a multitude of factors:

- the composition, structure and granulation of the ceramic powder;
- the number of deposited layers, their sequence, the thickness of each layer and assemblies;
- the composition, structure and microgeometry of the metal support on which the ceramic layer is deposited;

- the deposition method and the installation parameters (deposition distance, shape rotation speed, access nozzle size, deposition rate, plasma parameters, etc.)

The studies have shown that, in TBC, the problems appear at the interface between the metallic bond coat and the thermally grown oxide layer (TGO). The oxide scales consist mainly of alumina, grown at the interface between the deposited layers. The observed cracks, appearing in the FGM system at high temperature, are supposed to be due to the phase transformation in the Al_2O_3 layer, more precisely the transformation from γ alumina to α alumina, leading to premature damage of the layer by inducing additional residual stresses.

At the interface between the bond coat and the ceramic layer, the Al_2O_3 -based TGO oxide layer formed during the deposition through the oxidation of Al existing in the bond coat can be identified. The thermal shock favors the development of this TGO oxide layer and the formation of new oxides, thus leading to the damage of the protection system by cracking and detachment of the ceramic protection layer. The stresses that appear due to dilation differences during the thermal shock in the $\text{ZrO}_2\text{Y}_2\text{O}_3$ layers produce their exfoliation. The causes of layer exfoliation are the stresses that appear in the layer, also due to the distortions of the atomic structures of the constituent phases.

Following thermal shock tests, the degradation of Y_2O_3 -stabilized zirconia layers can also be caused by the formation of Cr barriers between bond coat and metal substrate interface. The formation of the respective oxides and especially of NiO (at $1100\text{ }^\circ\text{C}$, with a growth rate 1000 times higher than in the case of Al_2O_3) causes the volume of the bond coat to increase, and the stresses created are added to the stresses induced in the ceramic layer. Together they can determine the cause of exfoliation at the interface between the bond coat and the ceramic layer. Oxidation of the constituent elements of the bonding layer during the deposition process and cyclic heating take place in the following order: Y, Al, Cr, Ni.

References

1. Stefan, A., Bojin, D., Manoliu, V.: Ceramic layers as thermal barrier. *Bull., Series B.* **69** (2007)
2. Jamnapara, N.I., Frangini, S., Alphonsa, J., Chauhan, N.L., Mukherjee, S.: Comparative analysis of insulating properties of plasma and thermally grown alumina films on electrospark aluminate coated 9Cr steels. *Surf. Coat. Technol.* **266**, 146–150 (2015). <https://doi.org/10.1016/j.surfcoat.2015.02.028>
3. Lima, R.S.: Perspectives on thermal gradients in porous ZrO_2 -7-8 wt.% Y_2O_3 (YSZ) thermal barrier coatings (TBCs) manufactured by air plasma spray (APS). *Coatings* **10** (2020). <https://doi.org/10.3390/coatings10090812>
4. Stefan, A.: Contribuții privind realizarea și caracterizarea microstructurală a unor protecții multistrat ceramice pe bază de ZrO_2 rezistente la temperatură și șoc termic (2007)
5. Khor, K.A., Yu, L.G.: Revealing key topics shifts in thermal barrier coatings (TBC) as indicators of technological developments for aerospace engines. *Scientometrics* **125**, 1763–1781 (2020). <https://doi.org/10.1007/s11192-020-03667-3>

6. Wang, C.A., Lu, H., Huang, Z., Xie, H.: Enhanced anti-deliquestent property and ultralow thermal conductivity of magnetoplumbite-type LnMeAl₁₁O₁₉ materials for thermal barrier coating. *J. Am. Ceram. Soc.* **101**, 1095–1104 (2018). <https://doi.org/10.1111/jace.15285>
7. Gurak, M., Flamant, Q., Laversenne, L., Clarke, D.R.: On the Yttrium Tantalate–Zirconia phase diagram. *J. Eur. Ceram. Soc.* **38**, 3317–3324 (2018). <https://doi.org/10.1016/j.jeurceram.soc.2018.03.012>
8. Bakan, E., Vaßen, R.: *Ceramic Top Coats of Plasma-Sprayed Thermal Barrier Coatings: Materials, Processes, and Properties* (2017)
9. Markocsan, N., Gupta, M., Joshi, S., Nylén, P., Li, X.H., Wigren, J.: *Liquid Feedstock Plasma Spraying: An Emerging Process for Advanced Thermal Barrier Coatings* (2017)
10. Bose, S., Demasi-Marcin, J.: Thermal Barrier Coating Experience in Gas Turbine Engines at Pratt & Whitney.
11. Wu, L.T., Wu, R.T., Zhao, X., Xiao, P.: Microstructure parameters affecting interfacial adhesion of thermal barrier coatings by the EB-PVD method. *Mater. Sci. Eng. A* **594**, 193–202 (2014). <https://doi.org/10.1016/j.msea.2013.11.054>
12. Vassen, R., Kassner, H., Stuke, A., Mack, D.E., Jarligo, M.O., Stöver, D.: Functionally graded thermal barrier coatings with improved reflectivity and high-temperature capability. In: *Materials Science Forum*, pp. 73–78. Trans Tech Publications Ltd (2010)
13. Liu, S.H., Li, C.X., Zhang, H.Y., Zhang, S.L., Li, L., Xu, P., Yang, G.J., Li, C.J.: A novel structure of YSZ coatings by atmospheric laminar plasma spraying technology. *Scr. Mater.* **153**, 73–76 (2018). <https://doi.org/10.1016/j.scriptamat.2018.04.022>
14. Gok, M.G., Goller, G.: *State of the Art of Gadolinium Zirconate Based Thermal Barrier Coatings: Design, Processing and Characterization*.
15. B.A. Pint, I.G. Wright, W.J. Brindley: Evaluation of thermal barrier coating systems on novel substrates. *J. Therm. Spray Technol.* **9** (2000)
16. Manning Meier, S., Gupta, D.K.: *The Evolution of Thermal Barrier Coatings in Gas Turbine Engine Applications* (1992)
17. Ma, W., MacK, D.E., Vaßen, R., Stöver, D.: Perovskite-type strontium zirconate as a new material for thermal barrier coatings. *J. Am. Ceram. Soc.* **91**, 2630–2635 (2008). <https://doi.org/10.1111/j.1551-2916.2008.02472.x>
18. Durejko, T., Zietala, M., Polkowski, W., Czujko, T.: Thin wall tubes with Fe3Al/SS316L graded structure obtained by using laser engineered net shaping technology. *Mater. Des.* **63**, 766–774 (2014). <https://doi.org/10.1016/j.matdes.2014.07.011>
19. Evans, H.E.: Oxidation failure of TBC systems: an assessment of mechanisms. *Surf. Coat. Technol.* **206**, 1512–1521 (2011). <https://doi.org/10.1016/j.surfcoat.2011.05.053>
20. Chen, W.R., Irissou, E., Wu, X., Legoux, J.G., Marple, B.R.: The oxidation behavior of TBC with cold spray CoNiCrAlY bond coat. *J. Therm. Spray Technol.* **20**, 132–138 (2011)
21. Ali, I., Sokołowski, P., Grund, T., Pawłowski, L., Lampke, T.: Oxidation behavior of thermal barrier coating systems with Al interlayer under isothermal loading. In: *IOP Conference Series: Materials Science and Engineering*. Institute of Physics Publishing (2018)
22. Ali, I., Sokołowski, P., Pawłowski, L., Wett, D., Grund, T., Lampke, T.: Study on the characteristics of a TBC system containing a PVD-Al interlayer under isothermal loading. *Coatings* **11** (2021). <https://doi.org/10.3390/coatings11080887>
23. Kumar, V., Kandasubramanian, B.: *Processing and Design Methodologies for Advanced and Novel Thermal Barrier Coatings for Engineering Applications* (2016)
24. Chen, W.R., Archer, R., Huang, X., Marple, B.R.: TGO growth and crack propagation in a thermal barrier coating. *J. Therm. Spray Technol.* **17**, 858–864 (2008)
25. Movchan, B.A., Yakovchuk, K.Y.: Graded thermal barrier coatings, deposited by EB-PVD. *Surf. Coat. Technol.* **188–189**, 85–92 (2004). <https://doi.org/10.1016/j.surfcoat.2004.08.006>
26. Unabia, R., Candidato, R., Pawłowski, L.: *Current Progress in Solution Precursor Plasma Spraying of Cermets: A Review* (2018)
27. Oerlikon Metco: *An Introduction to Thermal Spray* (2016)
28. Raza, A., Ahmad, F., Badri, T.M., Raza, M.R., Malik, K.: An Influence of Oxygen Flow Rate and Spray Distance on the Porosity of HVOF Coating and Its Effects on Corrosion—A Review (2022)

29. He, J.L., Yu, C.H., Leyland, A., Wilson, A.D., Matthews, A.: A Comparative Study of the Cyclic Thermal Oxidation of PVD Nickel Aluminide Coatings (2002)
30. Shibe, V., Chawla, V.: An Overview of Research Work in Surface Coating.
31. Liu, Z., Gao, W., Wang, F.: Oxidation Resistance of Magnetron Sputter Deposited β -FeAl+Zr Coatings
32. Alca Technology: Magnetron Sputtering
33. R., J., Vite-Torres, M., Gallardo-Hernandez, E.A., Vera-Crdenas, E.E.: Solid Particle Erosion on Different Metallic Materials. In: Tribology in Engineering. InTech (2013)
34. Manoliu Victor, G.I.: Instalatie de testare la soc termic rapid al materialelor (2010)
35. Manoliu, V., Alexandrescu, E., Stefan, A., Ionescu, G., Mihailescu, A.: Duplex Structures, Ceramic, Microstucturated, on the Basis of Partially Stabilized Zirconia with Cerium Oxide (2013)

Multilayered Coatings by Thermal Spray for High-Temperature Applications



John Henao, Marco A. Rivera-Gil, Carlos A. Poblano-Salas,
Diego G. Espinosa-Arbelaez, Luis G. Trapaga-Martinez,
Oscar Sotelo Mazon, and Jorge Corona Castuera

Abstract Thermal Barrier Coatings (TBCs) play an increasingly vital role in improving efficiency and performance of high-temperature components in energy and aerospace industries. In recent years, materials such as Gadolinium Zirconate (GDZ)-based TBCs have become emerging contenders for conventional TBCs (based on Zr-stabilized systems) since these materials have low-thermal conductivity and excellent ability to withstand extreme chemical environments at high temperature. Another approach to increasing efficiency, performance, and lifetime is related to the development of Ceramic Matrix Composites (CMC) for the fabrication of components. In recent years, several efforts have been put into basic research with the aim of identifying strategies to enhance the performance of current high-temperature engine protective coatings. Notably, multilayered TBCs and the emergent EBCs have been the focus of attention on three aspects for the enhancement of protective

J. Henao

CONACYT-CIATEQ A.C., National Council of Humanities, Science and Technology,
Querétaro, México
e-mail: jhenao@conacyt.mx

M. A. Rivera-Gil (✉) · C. A. Poblano-Salas · J. C. Castuera
CIATEQ A.C., Centro de Tecnología Avanzada, Querétaro, México
e-mail: marco.rivera@me.com

C. A. Poblano-Salas
e-mail: carlos.poblano@ciateq.mx

J. C. Castuera
e-mail: jcorona@ciateq.mx

D. G. Espinosa-Arbelaez
CIDESI, Centro de Ingeniería y Desarrollo Industrial, Querétaro, México
e-mail: diego.espinosa@cidesi.edu.mx

L. G. Trapaga-Martinez
CINVESTAV, Instituto Politécnico Nacional Campus Juriquilla, Querétaro, México
e-mail: gerardo.trapaga@cinvestav.mx

O. S. Mazon
Universidad Autónoma del Estado de Morelos, Cuernavaca, México
e-mail: oscars@uaem.mx

© The Author(s), under exclusive license to Springer Nature Switzerland AG 2024
A. Pakseresht and K. K. Amirtharaj Mosas (eds.), *Ceramic Coatings for High-Temperature Environments*, Engineering Materials,
https://doi.org/10.1007/978-3-031-40809-0_6

coatings: i) the optimization of multilayered TBC/EBC architecture, ii) assessment of the damage of TBC/EBC subjected to thermal cycling and molten silicates attack, and iii) exploration of candidate materials for the fabrication of novel coatings. This chapter has the goal of illustrating new engineering professionals seeking to explore this topic and providing a compilation of key information about recent advances in this coating technology.

Keywords Multilayer coating · Thermal barrier · Environmental barrier · Thermal spray

1 Introduction: Role of a Thermal Barrier and an Environmental Barrier

The aeronautical industry has relentlessly pursued to increase operational safety, cargo capacity, thrust, and time between scheduled maintenance and overhauling. These efforts have also positively impacted on the performance and lifetime of land-based power generation plants [1–4]. All enhancements are related to efficiency increases achieved through the continuously developing materials and processes. The first commercial airplanes were based on internal combustion engines, where engine blocks were constructed mainly from steel and ferrous alloys. Given the intrinsic limitations of these materials, engines were designed to work at temperatures around 850 °C [1]. In the early 1930s, a Whittle's design for a new engine significantly increased thrust, cargo capacity, and efficiency. This new design was later known as a reaction engine, turbofan, or turbine engine. This new design required operating temperatures higher than ferrous alloys could withstand. It took several years until the introduction of nickel-based alloys as materials that were apt for the working conditions set by the new turbine engine design [5]. With the introduction of such alloys, known as superalloys (SAs), and due to their exceptional performance and mechanical stability at high temperatures, turbine engines gained popularity until they became the industry standard. Since adopting this technology, materials used in turbine engines have been subjected to intense research. Great efforts have been made in the aviation industry to increase engine efficiency by increasing the Turbine Entry Temperature (TET). In order to further increase TET, cooling systems for SAs were developed. However, the first cooling systems were based on convective principles, which allowed heat extraction by the action of air flowing through internal paths within the metallic components [6, 7]. Further developments led to complex and intricate flow passages to maximize heat extraction [7]. Nevertheless, to further increase working temperature, while withstanding high mechanical loads and oxidative/corrosive and erosive environments, state-of-the-art materials capable of overcoming these working conditions were further developed and are still employed nowadays.

For instance, Thermal Barrier Coatings (TBCs) were implemented for such purposes allowing turbines to operate in environments with temperatures near or above the melting point of structural metals [4, 8]. This fact is achieved by TBCs acting as thermochemical insulators, thus creating a thermal gradient between the harsh operation conditions of the engine at the surface and the metal inner surface [9]. Overall, it is accepted that TBCs can provide a thermal gradient of around $1\text{ }^{\circ}\text{C}/\mu\text{m}$ for thicknesses from 100 to 350 μm [10]. However, this gradient is not linear with increasing thickness due to microstructural defects in the coatings. Furthermore, an increase in the thickness of the ceramic coating can increase thermal-related stresses that can accumulate within the coating material because of the manufacturing conditions, which must be avoided to prevent premature mechanical failure during service.

TBCs are multilayer and multimaterial systems used in components in the hot zone of turbine engines. Their basic architecture consists of an SA base metal, a Bond Coat (BC), a Thermally Grown Oxide (TGO), and a ceramic TopCoat (TC) [9]. In these systems, each layer fulfills different roles and requires specific characteristics. Let us talk firstly about the structural materials of turbine engines. As mentioned, SAs were introduced to response to the need for a turbine engine material that could work at temperatures near their melting point with small or negligible detrimental changes concerning their mechanical properties. SAs can work at temperatures around 75–90% of their melting point with excellent performance [3]. SAs exhibit outstanding mechanical properties and corrosion/oxidation resistance at high temperatures compared to other alloys. These materials are widely used to fabricate high-temperature components of turbine engines. Their base crystalline structure is γ -FCC that is derived from the Ni–Al phase diagram. Changes to their stoichiometry promote the formation of γ' -Ni₃Al intermetallic [11]. Further changes in the chemical composition, for instance, the addition of reactive elements as Hf and Zr, influence the grain size and physicochemical properties [12]. The content of C and other carbide-forming elements play an important role on the SAs properties as they can form M₂₃C, M₆C, and M₇C₃ along grain boundaries which, if properly controlled, may serve as reinforcement mechanisms against sliding defects and creep. However, when this is not controlled, they may lead to detrimental effects on mechanical properties due to precipitation in grain boundaries [13]. Thermomechanical properties are directly related to the manufacturing process. The most widely used methods for the fabrication include casting, directional solidification, and single crystal growth [11]. Studying processing conditions and chemical compositions has led to the development of advanced state-of-the-art SAs, such as single crystal alloys and two-phase γ , γ' -NiAl-reinforced alloys [13], allowing further temperature and performance increases.

In a TBC architecture, a bonding layer between the ceramic TC and the underlying SA is necessary. This requirement is mainly attributed to a significant difference in Coefficient of Thermal Expansion (CTE) between the ceramic and the base metal, which can promote premature failure of the TBC due to elevated accumulation of thermal stresses. The BC layer acts as a buffer helping to reduce CTE differences between the SA and the ceramic material and, consequently, to reduce the final residual stress accumulation in the TBC. The BC layer is then helpful to keep

mechanical integrity of a TBC. Additionally, oxidation resistance becomes a concern when dealing with SAs. On one side, elements present in Ni-based alloys such as Al and Cr increase their oxidation resistance. Nevertheless, they are also known to increase brittleness and reduce creep resistance. Since one crucial characteristic of SAs is their creep resistance, preference is given to the use of reactive elements (W, Co, Ta, Re, etc.) to benefit creep resistance over oxidation resistance [11, 13]. In order to compensate for this creep resistance-oxidation compromise, the use of an oxidation protective layer is required. BCs containing Al and Cr are effective oxidation protectors thanks to the time/temperature dependent growth of Al_2O_3 or Cr_2O_3 on their surface. The control of BC and their respective oxide layers has been adopted as a strategy to overcome emerging intrinsic oxidation issues.

BCs, with common thickness between 30 and 100 μm [14, 15] are fabricated either by diffusive or overlay processes [16, 17]. Diffusive coatings are mainly fabricated via Chemical Vapor Deposition (CVD) and are based on nickel–platinum aluminides (Ni–Pt)Al which can be doped with elements such as Cr, Hf, Zr, etc. in order to increase oxidation resistance and refractory properties. BCs can also be processed by thermal spraying techniques. The most common being atmospheric plasma spraying, APS, and high-velocity oxy-fuel, HVOF. Thermally sprayed BCs are based on the family of the so-called MCrAlY materials. Where M stands for Ni and/or Co. MCrAlYs are often mixed with refractory elements such as Hf, Zr, Ta, etc. [17, 18]. In thermally sprayed coatings, the final stress state results from a combination of a so-called “quenching” stress and thermal mismatch. The former arises during fabrication from the contraction of liquid particles while they are solidifying on the substrate after impact, while the latter results during cooling due to the difference of CTEs between the substrate and the coating [19]. The quenching stress leads to the accumulation of tensile stresses, whereas thermal mismatch may result in compressive or tensile stresses depending on the difference of CTE between the substrate and the material employed to fabricate the TBC. Thus, the use of a BC is a must in thermally sprayed TBCs not only as an intermediate layer for reducing thermal expansion differences of materials during operation but also to modulate the generation of residual stresses during the fabrication of a TBC.

Under working conditions, BCs containing aluminum, grow a superficial scale of aluminum oxide, known as TGO. This scale grows by the chemical reaction of aluminum from the BC with incoming permeated oxygen from the working environment. TGO is predominantly formed of aluminum and chromium oxides, depending on the BC. The $\alpha\text{-Al}_2\text{O}_3$ is preferred due to its thermomechanical properties [20, 21]. The TGO works as an oxygen diffusion barrier thus preventing extensive damage of the BC and the SA, providing resistance against type-I corrosion [22]. Oxide formation is determined by thermodynamic conditions which include the chemical composition of the BC from which it is grown. As such, the alumina phase, and the growth rate of the TGO can be controlled to some extent by an appropriate design and fabrication of the BC. TGO has its own mechanical and thermomechanical properties, different from BC and TC. Typical thickness of TGO is expected to be below 10 μm [20, 23]. As this thickness is formed, thermomechanical stresses related to the growth of the interphase and expansion–contraction stresses accumulate in the

system and may cause separation of the oxide scale. This is especially seen at the pre-existing superficial crests and valleys of the BC where, according to some laboratory studies, debonding becomes clear as early as 400 h of operation [23]. Separation or debonding, is commonly followed by spallation of the TBC by the formation and propagation of cracks. Phenomena occurring in the proximity of the TGO interfaces are the most common failure mechanisms of TBCs. For this reason, to prevent premature failure, chemical composition of the BC should promote the formation of an α -Al₂O₃ at a controlled rate.

Ceramic TC is the outermost layer of the TBC with thickness values between 100 and 500 μm [9, 24, 25]. It is directly exposed to aggressive conditions in the turbine engines and provides thermal, chemical, and foreign object damage (FOD) protection to the underlying components. Consequently, the TC layer must exhibit characteristics such as high-temperature phase stability, low thermal conductivity, high strain compliance, resistance to sintering, etc. [26–28]. Overall, ceramics exhibit lower thermal conductivity than other materials such as metals. Additionally, even when thermal conductivity is temperature-dependent for most materials, such dependence in ceramics is lower and almost invariant for some specific ones [29–31] Zirconia-based, fluorite-like oxides, and rare-earth pyrochlores are regarded as great materials for TBC applications due to their excellent phase stability at high temperatures [32–36]. Non-transformable tetragonal zirconia stabilized with 6–8% wt. of yttria, also known as yttria-stabilized zirconia or YSZ, has been the main ceramic for TBC applications for several decades. YSZ exhibits a thermal conductivity of around 1 W/(m²K) as well as excellent performance in thermal cycling below 1200 °C. However, above this temperature, YSZ is susceptible to the loss of the non-transformable characteristic of the tetragonal phase, leading to the *t'*-YSZ/*m*-YSZ reaction with a corresponding volume change of about 4% upon cooling. Such volume change can occur through thermal cycling, leading the system to fail [37]. Moreover, above 1200 °C, sintering of the ceramic layer can also occur and increase stiffness, making the system prone to cracking and failing.

As working temperature increases, an emerging issue jeopardizing the integrity of TBCs arises. This issue is related to the corrosion that molten Calcium-Magnesium-Iron-Aluminum Silicates (CMAS) inflict on YSZ TBCs. This damage occurs when ingested airborne CMAS particles melt at temperatures above 1100 °C. Once molten, they stick, infiltrate, and fill the open porosity of the coatings generating additional thermal stresses during thermal cycling. Additionally, at such temperature, CMAS reacts with *t'*-YSZ and produces recrystallized *m*-ZrO₂ and zircon (ZrSiO₄) with extreme microstructural and mechanical changes [38–44].

For these reasons, it is reasonable to state that the operational temperature limits of YSZ have been, or are soon to be, reached, and new materials with enhanced thermal conductivity, phase stability, sintering resistance, and CMAS resistance are currently sought. Among them, rare-earth pyrochlores such as lanthanum zirconate (La₂Zr₂O₇) and gadolinium zirconate (Gd₂Zr₂O₇) are emerging as potential candidates [32, 34, 35, 45–47]. Nevertheless, it has been seen that even when all the above-mentioned characteristics are met with such systems, their thermal cycling durability shows lower performance than YSZ. This impasse is addressed through

different approaches including the study of TC with multilayer architectures and vertically cracked structures [48], development of complex rare-earth ceramics, and the use of advanced dopants [31, 48]. Parallely, systems based on Si rather than SA are being developed.

The observed thermal, chemical, and mechanical limitations of Ni-based alloys and their respective protective systems, led to the development of Mo-based alloys and SiC-based materials. Among them, SiC-fiber-reinforced SiC matrix (SiC/SiC) ceramic matrix composite, CMC, is the most promising candidate to substitute SAs as structural material for high-temperature components [49, 50] CMCs are formed by SiC fibers transversely and longitudinally arranged embedded in a SiC matrix. They are considerably lighter than SAs while exhibiting higher creep resistance, higher resistance to corrosion, and higher resistance to CMAS attack. Also, in addition to the improvement in the mechanical properties, their fiber-reinforced microstructure serves as a self-inhibiting mechanism to crack propagation and failure, thus extending the lifetime of the system. Even when CMCs show exceptional properties compared to SAs, they are very susceptible to recession and degradation when in contact with water vapor, which is unavoidably found in turbine operating conditions. Fabrication of CMC protective EBCs is usually carried out through APS [51–53]. However, as seen with other materials, plasma spraying processing is accompanied with experimental challenges. One of the greatest is the chemical instability of some compounds, which can undergo decomposition and formation of other spurious phases which reduce the performance of EBCs. Consequently, multiple challenges are yet to be addressed for both systems to keep increasing the efficiency and reliability of turbine engines [49, 54]. In the following sections, a deeper explanation about manufacturing, materials, and architectures of thermally sprayed TBCs and EBCs will be presented.

2 Thermal Barrier Coatings by Thermal Spray

TBCs were developed as an improvement for cooling systems of high temperature components. Since their introduction, TBCs have been essential in the design of turbine engines. TBCs are multilayered systems designed to provide thermochemical protection to the underlying SA, working under thermal, chemical and mechanical conditions beyond their safe operation limits. TBCs' architecture can be summarized as (a) a SA, which provides the structural and mechanical integrity (b) a BC, which acts as a CTE buffer between the SA and the TC, (c) a TGO grown at the BC/TC as a physical barrier for oxygen diffusion; and (d) a ceramic topcoat, which is the outermost material of the system [9].

The BC and TC are often manufactured on the SAs surface via different processing techniques. These techniques include physical diffusive coating methods such as electron-beam physical vapor deposition, EB-PVD, and CVD, or through overlaying methods such as thermal spraying techniques [16–18]. Prior to the introduction of TBCs, working temperatures were considerably lower than in today's turbine

engines. Metallic components were protected by the use of Ni–Al-based coatings. Among them, diffusive coatings were made mainly from β -NiAl/ β -(NiAl)Pt whereas overlay coatings were based on γ , β -MCrAlX alloys (M = Ni, Co and X = Y, Hf, Si). Currently, the selection of the fabrication process is based on the final application of the component to be coated. For instance, the microstructure of the overlay TBCs consists of the so-called brick-like structures which is obtained by the subsequent solidification on the substrate of individual molten droplets generated in thermal spraying techniques [55].

Thermal spraying is a family of processes used to produce overlay coatings. In them, a feedstock material, normally powder, is fed into a gas stream. The gas can possess either high temperature, high velocity or both. Kinetic energy from the gas stream is used for propelling the powder material toward the component to be coated by momentum transfer. During the process, the gas also transfers heat to the injected particles, thus increasing their temperature near or beyond their melting point. High-velocity/high-temperature particles then reach and solidify onto the substrate generating a coating [56]. The microstructure obtained by thermal spray exhibits lower thermal conductivity than diffusive coating and possesses a certain degree of porosity, from 2 to 20%. Thermal spray is used to produce TBCs with up to 500 μm thickness for stationary components. On the other hand, diffusive EB-PVD coatings having thicknesses between 100 and 200 μm , consist of the so-called columnar growth, which provide increased compliance and mechanical resistance and are therefore preferred for rotating components [57, 58]. However, these coatings show overall higher thermal conductivity and higher production costs than those thermally sprayed. As mentioned, except for cold spraying techniques, thermal spraying requires the feedstock to acquire temperatures above the melting point to produce an effective coating [56, 59]. Taking this into consideration, the choice of a manufacturing method shall consider, among others, the melting point of the feedstock. In the case of BCs, most widely used processing techniques include atmospheric plasma spray, APS, and high velocity oxy-fuel, HVOF. In the case of TC, APS is preferred.

APS is a spraying technique in which the heat source is a high-energy plasma generated by a nontransferred DC discharge in a chamber where the anode and cathode are surrounded by a gas mixture which ionizes forming the plasma. The gas mixture contains one or two plasma-forming gas such as Ar, H₂, He, and N₂, where one of them, known as primary gas, provides stability to the torch. Normally the role of primary gas relies on heavier gas (Ar, N₂) to provide higher momentum transfer to the feedstock. The other gas, known as secondary gas, is a lighter gas with lower ionization energy and higher enthalpy. This gas provides an increased heat transfer to the feedstock particles. The maximum temperature that can be reached in the plasma is related to the composition of the gas mixture (type and flow) and the discharge DC current. Typical plasma torch temperatures can be found between 8000 and 14,000 K with velocities of 500–2800 m/s. Given the temperatures that can be achieved within the torch, APS is a versatile technique capable of processing materials with very high melting points, including ceramics [55, 56, 59], and materials with relatively high melting points such as Ni-alloys. However, since the velocity of the injected feedstock is relatively low, some metallic materials prone to oxidation are not recommended for

this technique. On the other hand, processing materials with low melting points will cause overheating of the particles which will produce an “exploded” microstructure of the solidified particles called splashing, with excessive cracking, poor adherence and overall undesirable mechanical properties.

The acronym APS comes from atmospheric plasma spray, which indicates that the equipment is operated at room conditions. However, in addition to APS, other plasma spraying techniques have been developed such as Low-Pressure Plasma Spray (LPPS), Very Low-Pressure Plasma Spray (VLPPS), Vacuum Plasma Spray (VPS), among others. However, given the operational and infrastructural costs of such techniques, APS remains as the to-go plasma-spraying technique [60–63].

Another important plasma-spraying variant can be found in the Suspension Plasma Spray (SPS). In SPS, powders with considerably lower particle sizes (from nm to $< 10 \mu\text{m}$) are fed to the plasma system. Given the size of particles, characteristics of gas needed to carry powders to plasma torch will affect the plume. Therefore, the carrier is set in the form of an ethanol/water powder suspension. The lower the mass and size of particles, the higher velocities that can be attained. This reduces the heat transfer and in-flight time of particles. However, an appropriate control of process parameters leads to more homogeneous heating [25, 64]. As such, with SPS, it is possible to produce strain tolerant coatings with low-thermal conductivity. As discussed by Vaßen et al. [25], this fact is related to the energy release and crack formation mechanisms within small-sized splats. Also, as one may expect, lamellas, splats height, and size, are smaller [65]. In addition, cauliflower and semi columnar growth of coatings, which are not possible to produce with conventional APS, can be developed with SPS.

HVOF is a thermal spraying technique where the energy is provided by the combustion reaction between oxygen and a fuel such as methane, propane, etc. The maximum temperature achieved by the system is given by the energy released by the stoichiometric reaction between oxygen and a specific fuel. However, particles' temperatures are most often below this maximum temperature due to their relatively low residence time within the flame. One of the greatest benefits of HVOF is the low residence and low in-flight times due to the high-flux and the high-pressure of combustion gasses, which reach supersonic speeds at the Laval nozzle exit [59]. This translates into coatings with low oxidized particles, high adhesion strength, and high density. Given that the temperature is limited by the combustion, it is not suitable for processing materials with high melting points. Nevertheless, although in HVOF a gas fuel is generally used, there are other variants where liquid fuels such as kerosene, ethanol, or methanol are used. This versatility helps to increase the heat capacity of the flame. Also, a technique called high-velocity air–fuel, HVAF can be used for the preparation of BCs. In HVAF, highly pressurized air and a high flux of fuel is used. This fact reduces further the residence and in-flight time, thus reducing the oxidation of particles [59, 66, 67]. Given the higher costs of liquid fuels and the infrastructure required for HVAF, HVOF is still the preferred combustion technique for TBC applications.

BCs are normally fabricated with Ni/Co-rich CoCrAlY, NiCoCrAlY, or NiCrAlY alloys. Ni-alloys show oxidation resistance and have melting points which are low

enough to be processed through HVOF and high enough to be processed via APS. For these reasons, commercially available BCs feedstock powder can be processed by both processing techniques [17, 68]. The election of HVOF or APS depends sometimes on the available infrastructure (e.g. if only APS is available). However, pertinent considerations such as residual stresses, oxidation, porosity level, etc., should be considered depending on the selected technique and expected performance of the final specimen [69, 70].

The properties of the thermally sprayed coatings depend on the concurrent inter-relationship of dozens of parameters governing the processes. Among those, there are some key factors accessible to the operator which can be modified to exert reasonably good control over the spraying activities. In the case of HVOF, such parameters include the stand-off distance (SOD), the fuel flow, oxygen flow, fuel/oxygen ratio, feeding rate (PFR), particle size distribution (PSD), raster speed, number of coating cycles, preheating of the substrate, among others [59]. The SOD directly influences the in-flight time, the velocity, and temperature of the particles at impact, and thus, is partially responsible for the microstructural features, including oxidized particles, size and shape of lamellar structure, nonmelted particles, over heated particles, intra splat cracking, porosity, thickness, etc. Gas flow influences the velocity of particles and the in-flight time, which is related to the microstructural features mentioned earlier. Fuel/oxygen ratio (F/O_R) determines the stoichiometry of the combustion reaction and therefore impacts the temperature of the flame and its oxidative or reductive characteristics. In some cases where feedstock is prone to oxidation, a reductive flame may help reduce oxidation ($F/O_R > 1$). On the contrary, for coatings for which a reductive flame is not desired, an oxidative flame may be helpful ($F/O_R < 1$). Nevertheless, for both cases, when $F/O_R \neq 1$, flame temperature will be less than the maximum temperature achievable for a given set of other parameters. PFR affects the momentum and heat transfer of the flame to the particles. Low PFR will result in stable velocity and temperature, which translates into controlled porosity and homogeneous microstructure of the coating. However, very high PFR values may create chaotic motion of the particles within the flame creating inhomogeneous and porous coatings. However, the PFR effect is modified when PSD is not monomodal and/or if the width distribution peaks are too wide. Uneven particle size distribution will increase chaotic velocity distribution and heat transfer causing that, when attempting to heat big particles, small ones suffer overheating and cause splashing. In the same way, avoiding overheating of small particles may cause bigger ones to underheat, which may cause them to bounce off the substrate, causing erosion or poor adherence as nonmelted particles. Raster speed can be related to the coating thickness, porosity, thermal stresses, adherence, and overall quality of the coating [71–75]. In the case of APS, arc current, secondary gas flow (voltage), SOD, PFR, raster speed, number of coating cycles, preheating of the substrate, PSD, among others, should be considered. Arc current along with primary and secondary gas flow and pressures can be related to the stability of the plasma torch, the turbulence and swirling of the plume, the trajectory of injected particles, and the heat transfer to the feedstock. Temperature and trajectory are also related to the particle size distribution of the powder. These are influenced by the effects discussed earlier in a similar way for APS and HVOF.

The effect of processing parameters in thermal spraying has been the focus of intense research to understand their influence on the microstructural features, quality, and performance of BCs produced by HVOF and APS, and TCs produced via APS. The development of first and second order process maps which relate the energy/momentum transfer from the source (flame or plasma) to the feedstock, and the relationship of in-flight characteristics of the particles with the coating properties, have been key methods for the analysis of the coatings [45, 55, 56, 59, 76, 77].

In summary, thermal spraying is a set of flexible techniques that can be employed to process BC and TC for TBCs. The quality and performance of the produced coatings is associated with a considerable number of processing parameters. It is of great importance to understand thermal spraying, in particular HVOF and APS, in order to properly produce, develop, and characterize TBCs. Here, only few generalities about parameters and considerations of TBCs were mentioned. Monitoring systems such as DPV-eVOLUTION, Accura Spray, Spray watch, In-situ Coating Properties (ICP), Ex-situ Coating Properties (ECP), etc. as well as dedicated performance measurement techniques such as thermal cycling and thermal gradient testing, were not discussed but should be under the radar of the reader to gather better understanding of advanced characterization of TBCs [78–80].

3 Environmental Barrier Coating by Thermal Spray

Despite many years of constant evolution, gas turbine engines have not reached their full potential as their thermal efficiency is far away from its thermodynamic limits. Therefore, improvements in gas turbine operation have been focused on fuel efficiency and power output. In order to achieve such improvements, the development of advanced materials to increase the gas turbine inlet temperature has been foreseen as a mandatory requirement. Possibly, the most important challenge will be the development of materials for the engine's hot core section in which different components are subjected to harsh temperature conditions. Maximum temperatures reaching, or close to, 2000 °C are expected to be achieved at 1 MPa combustor pressure [81].

An increase in the operating temperatures in modern gas turbines has been possible due to the development of air-cooled components fabricated from SAs and the use of TBCs on those components to minimize the effects of hot corrosion and oxidation. However, a further increase in turbine operating temperatures will adversely affect the performance of these components due to increased susceptibility to sintering [82], severe damage from CMAS melting and infiltration [83, 84], erosion caused by fine particles [85] or superficial damage by Foreign Objects (FOD) [86].

As the use of SA components in advanced gas turbines has reached a limit, the development of materials with better mechanical and chemical stability at high temperatures has become crucial. The high-temperature chemical stability, and lower density of ceramics has been widely recognized for a long time; however, the mechanical properties of single-phase ceramics are not enough for the demanding requirements present at the hot sections in advanced gas turbines. Hence, the development

of fiber-reinforced CMCs has been established as a common practice to produce components for the hot section in advanced gas turbines. These materials are formed by the combination of tolerant damage fibers immersed in a ceramic matrix with weak fiber-matrix interfaces. The most successful systems employ a SiC matrix reinforced with Boron Bitride (BN)-coated SiC fibers. This CMC is fabricated via chemical vapor infiltration of SiC into a preform conformed of BN-coated SiC fibers; the residual porosity of the component is filled out with a silicon slurry followed by a carburization step [87–89].

EBCs were developed primarily by NASA in the late 1990s, as at that time CMCs started to be considered as substitute materials for high-temperature metals to increase the operating temperature and efficiency of gas turbines. Both the first and second generations of EBCs were processed by APS [90–92]. Due to the formation of undesired amorphous phases in rare earth silicates processed by APS, NASA suggested a modification to the fabrication process. Amorphous phases promoted the occurrence of EBCs shrinkage at high temperature leading to crack formation and spallation of the coatings. The proposed modification consisted in spraying at high temperatures (up to 1000 °C), above the glass transformation temperature of silicates, to guarantee nucleation and growth of crystal nuclei, ensuring a highly crystalline microstructure in the EBCs TC [93]. Despite considerable efforts have been performed to obtain fully crystalline EBC coatings by different processes (EB-PVD, APS, RF magnetron sputtering, sol–gel) the formation of amorphous phases remains; therefore, different alternative thermal spray techniques such as high-velocity oxygen fuel (HVOF), suspension plasma spray (SPS), and very low-pressure plasma (VLPPS) have been explored [51]. Bakan et al., reported that the coatings produced by APS and SPS were highly amorphous and showed vertical cracking [51]. Pronounced evaporation of Si-based compounds was also noticed in coatings produced employing both spraying methods leading to the formation of Yb₂O₃. Conversely, highly crystalline and dense Yb₂Si₂O₇ coatings were produced by VLPPS (~98%). The high deposition temperature and post-deposition plasma heating present in the VLPPS process were thought to be responsible for preventing the formation of vertical cracks in the coatings. Finally, HVOF coatings showed contents of crystalline phases between 45 and 50% and no vertical cracking. The specific features of each process (heating/cooling cycles among others) had a strong influence on the final stress state of the coatings, which ultimately controlled the occurrence of cracking. In a recent study, Guo et al. [94] produced high-density Yb₂Si₂O₇ -based EBCs by a plasma spray-physical vapor deposition process. The authors varied the substrate temperature and evaluated its effect on the formation of amorphous Si-based phase. When coatings were deposited on substrates heated up to 700 °C a large amount of silicon-rich amorphous phase was obtained, whereas when substrates were heated up to 1100 °C a coating with high crystallinity and low porosity was formed, that is, 77% and 2%, respectively. Although APS has been the most employed process to produce EBCs, the use of other conventional thermal spray processes and hybrid techniques seems to be promising in order to span the possibilities to produce coatings with controlled architectures able to tackle the challenges associated with the stability of EBCs operating at extreme conditions.

In terms of EBCs materials, different options have been developed since the mid-1990s to protect SiC substrates. Lee et al. [90] developed a mullite coating ($\text{Al}_6\text{Si}_2\text{O}_{13}$) by atmospheric plasma spray (APS) on SiC substrates. The authors found cracking and delamination of the coatings after thermal cycling; this behavior was attributed to the presence of amorphous phase in the as-sprayed condition. In another study, APS mullite coatings were subjected to prolonged thermal exposure; coating volatilization was observed leaving an alumina residual scale over the substrate resulting in limited protection to the SiC substrate [95]. Another effort to develop EBCs by APS was performed by Lee and Miller [96]. This time, the approach was to develop a bi-layer coating formed by YSZ and mullite, the former being the top layer. The coating showed good resistance to cracking and debonding under thermal cycling in air at 1200–1300 °C. However, the presence of a silica-based scale found in the coatings promoted their oxidation and occurrence of porosity, in fact, this issue affected the coating's long-term stability. Cracking and delamination of this type of coatings have been attributed to a large difference in CTE between the materials employed [97]. Later in the early 2000s, different rare earth-based silicates were employed to produce EBCs, having similar CTE values to that of CMC substrates, namely Y_2SiO_5 , Er_2SiO_5 , Yb_2SiO_5 , $\text{Lu}_2\text{Si}_2\text{O}_7$, YB_2O_3 , and $\text{Yb}_2\text{Si}_2\text{O}_7$ [92]. Also, monoclinic and hexagonal barium-strontium aluminosilicate (BSAS) was selected as a promising material to build EBCs by APS. However, BSAS reacted with thermally grown silica during thermal cycling promoting failure at the substrate-coatings interface. The use of an intermediate $\text{Al}_6\text{Si}_2\text{O}_{13}$ layer solved the problem by increasing the EBC service life [91]. At that time, it was also identified that the use of a silicon bond coat between CMC substrate and $\text{Al}_6\text{Si}_2\text{O}_{13}$ resulted in improved coating adhesion because of the precipitation of a SiO_2 dense layer, avoiding the carbon monoxide permeation through the coating (formed from the CMC substrate) at high temperature [91]. Although EBCs based on BSAS and mullite had showed good crack resistance at high temperature (over 1000 h at 1300–1400 °C), these can still suffer volatilization of the BSAS TC and formation of a low-melting glass phase due to the BSAS–silica reaction, which simultaneously promotes the formation of interfacial pores at temperatures as low as 1200 °C. Yb- and Lu-based silicates show interesting properties for applications in EBCs, namely similar CTE values to that of SiC and low volatility under water vapor atmospheres. These materials showed poor performance at high temperatures as single layers. As a result, these silicates are recommended in a Si/mullite/rare earth silicate tri-layered configuration. During the first decade of this century, different studies showed that these EBCs can withstand temperatures exceeding 1300 °C in steam-cycling conditions [98].

To summarize, although the mechanical and chemical properties at high temperature of SiC–SiC CMCs is remarkable, they suffer embrittlement and peeling at 700–900 °C. When the CMC is exposed at high temperature, a SiO_2 protective layer is formed; however, this layer reacts with water vapor during combustion, leading to the formation of volatile $\text{Si}(\text{OH})_4$ [99]. Hence, CMCs also require the use of protective coatings when they operate at high temperatures under combustion gaseous atmospheres. Specifically, for CMCs employed to fabricate components for advanced gas turbines, stringent requirements of thousands of safe operational hours must be met.

The most important requirements for EBCs employed in engine environments are: (i) to show a low recession rate, (ii) to provide complete protection of substrate from oxidizing species penetration (solid-state diffusion through the coating or gas permeation), (iii) to preserve adherence during long-term thermal cycling exposure, and (iv) to be thermochemically stable [100]. EBCs are exposed to the well-identified damage mechanisms in conventional TBCs such as CMAS attack and FOD and, when employed in rotating components, static and cyclic loads which can cause creep and fracture on these [101, 102].

4 Multilayer Coating Architectures

The architecture of a traditional TBC consists of a SA substrate, a bonding (BC) layer, a TGO layer, and a ceramic layer (TC) at the top. A schematic representation of a TBC is shown in Fig. 1a. The BC layer is located between the TC and the substrate material, and its main role is the reduction of thermal mismatch between the SA and the TC layer, then it must have a thermal expansion coefficient between that of the SA and TC. The BC layer contributes to the enhancement of the TC adhesion and provides corrosion and oxidation resistance to the substrate. The thickness of the BC is usually reported in the range of 100 and 200 μm and is mainly composed of MCrAlY-based materials, where M stands for Ni or Co [103]. On the other hand, the TC is at the top of the whole TBC and its main role is the thermal isolation of the system. Then, it must have low thermal conductivity, high melting point, and elevated thermal shock resistance. The TC thickness is often in the range of 100 and 400 μm . The fixing of thickness of each layer in multi-layered coating plays a major impact on selection and performance of multi layered coatings. There are some literature reports about TBCs thicknesses above 1 mm [104, 105]. Such thick TBCs can allow the reduction of cooling air required for the hot section and increase the efficiency of the engine. The use of thick coatings can cause thermal gradients within the TBC and, consequently, thermal stresses can appear. In particular, the elastic strain energy of the coatings increases with the thickness, then the energy release rate for cracking also increases, leading the coating to be prone to mechanical failures. It is important to remark that TGO thickness is very crucial for the whole architecture and mechanical stability of the TBC since it might induce mechanical stresses as it is formed during heating and cooling. A thick TGO can also decrease adhesion. Previous studies suggest a TGO thickness about 2–3 μm as ideal to chemically protect the SA and to avoid excessive mechanical stresses that can affect the mechanical stability of the whole TBC [106].

The most used ceramic TC material is yttria-stabilized zirconia, YSZ, this material possesses suitable thermal expansion and insulation properties, and crack resistance for high-temperature applications [107]. The TGO is formed at the BC/TC interface as a result of the oxidation experienced by the whole TBC system at elevated temperatures. An ideal TGO layer must suppress diffusion and formation of detrimental oxides in service. The chemical composition of TGO is usually reported as

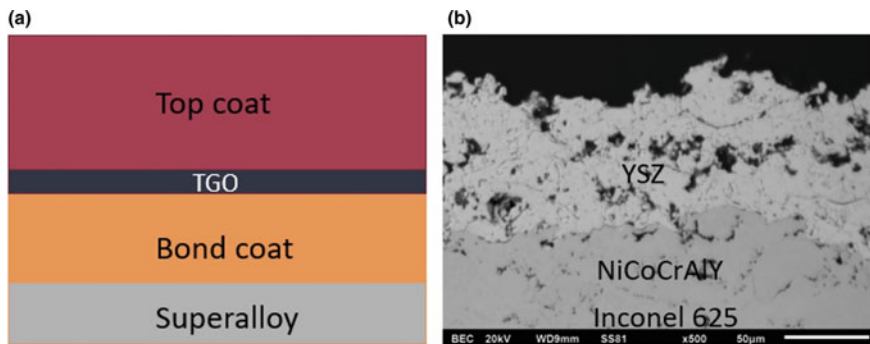


Fig. 1 **a** Schematic representation of a TBC coating; **b** SEM image from the cross-section of a TBC coating sprayed by APS

α -alumina (Al_2O_3) [20]. Figure 1b shows a SEM image of a TBC, YSZ 8%, deposited by APS on an Inconel 625 substrate.

One of the factors that put at risk the stability of TBCs is the composition of the TC layer. For instance, the operating temperature of YSZ is limited to below 1200 °C, presenting a reduced thermal shock lifetime under experimental conditions above 1100 °C. This fact is related to the precipitation of undesired phases and sintering of the YSZ. Some works have recognized the formation of detrimental oxides at the TGO such as chromia, nickel oxide, and spinels [108]. The formation of these oxides promotes premature failure of the TBCs since they act as active sites for crack nucleation and propagation. Currently, there are different methods of thermal shock testing in TBCs fabricated with YSZ to simulate the thermal conditions in an aircraft or an industrial gas turbine engine; such methods are based on the operation temperature with values ranging from 1000 to 1200 °C [109–112]. Bolcavage et al. [113] made a comparison between two different thermal shock tests, that is, the Jet Engine Thermal Shock test (JETS) and the Furnace Cycle Test (FCT) (cyclic oxidation), being both derivatives of the burner ring test. The tests were carried out at temperatures around 1000, 1200, and 1400 °C. In particular, the FCT test is carried out between room temperature and temperatures ranging from 1100 to 1200 °C. Specifically, test cycles for aircraft engine parts consist of periods of 1 h at 1080 °C and cooling at room temperature. Alternatively, the tests can also be performed at 1135 °C and cooling at room temperature. On the other hand, JETS test can be performed at 1400 °C; this temperature test is applied for having the test results faster, *i.e.* in a reduced number of cycles. Finally, the fluidized bed test is operated at 1000 °C [113]. However, modern gas turbines, demanding high efficiency and temperatures above 1200 °C, also involve some associated issues. For instance, a critical aspect in the ongoing development of new TBC systems is the integrity of the ceramic layers against CMAS attack (sand or volcanic ash particles). Another aspect is erosion promoted by solid particles in the working environment that contribute to mass loss and spallation of TBC coating in service.

Due to the increasing demand for service life and working temperature of modern gas turbines, new strategies are being introduced in the architecture and materials involved in the fabrication of TBC coatings. These new coatings should be designed to better adapt to service environments with improved thermal insulation performance, and higher mechanical and chemical resistance at high temperature. Multilayered-multiphase functional coatings are a new tendency in TBCs [32, 114]. These coatings are manufactured by depositing either a gradient material at a controlled amount layer by layer or a different composition of materials layer by layer at a controlled gradient of properties, where each layer has a specific function for the operation of the whole TBC. The gradient of material/composition is focused on reducing the thermomechanical stresses generated in the TBC while in service. The multilayered coating can also be designed to have a gradient of thermal conductivity and diffusivity and should have high chemical resistance at high temperature. Figure 2 shows a schematic representation of a multilayered/multiphase functional coating and includes the main functionality of possible material layers in the TBC.

In terms of materials, some scientific efforts are focused on the development of ceramic materials with better thermal stability, lower thermal diffusivity, and higher chemical stability than current TC materials. These new materials can be used for thermal and environmental protection at temperatures above 1200 °C. For instance, some authors have explored coating architectures taking advantage of the properties of different phases of the same material. For example, a cubic/tetragonal ZrO₂-multilayered coating benefits from the CMAS resistance, thermal conductivity, and

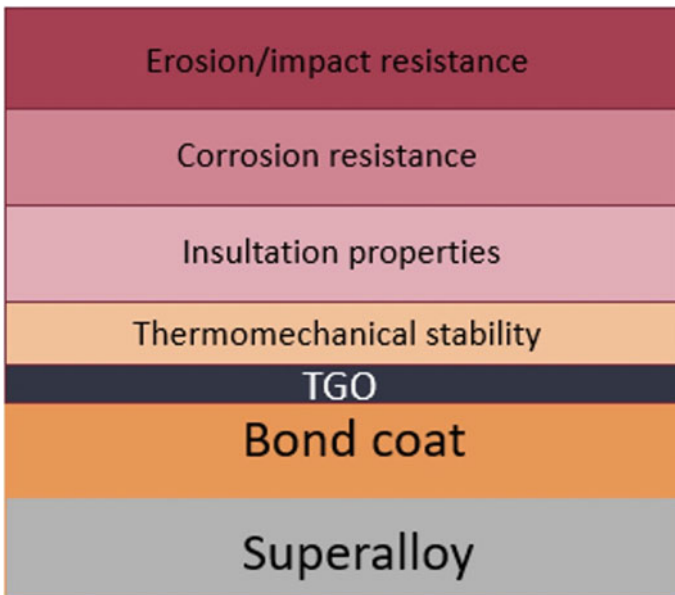


Fig. 2 Schematic representation of a multilayered/multiphase TBC/EBC coating

thermal stability of cubic ZrO_2 outer layer, and the good thermal cycling performance and erosion resistance of an inner tetragonal ZrO_2 coating.

Yttrium garnet YAG was also considered as a third component of the TBC, using the traditional TGO and the MCrAlY BC layers as the four and fifth components, respectively [115]. Overall, this kind of solution has an improved result when comparing against a conventional YSZ-based TBC since the TC increases the operation temperature while the degradation of the TBC is inhibited because the presence of YAG helps to slow down the CMAS infiltration process. Yang et al. [116] reported the fabrication of a similar multilayer coating architecture; they deposited an Al_2O_3 -GdAlO₃ (AGAP) amorphous coating layer, having high-temperature erosion resistance. They also employed an intermediate layer composed of a gadolinium-doped zirconate (GSZC), a third layer using YSZ, and NiCrAlY as bond coat. Interestingly, thanks to the enhanced fracture toughness and low thermal conductivity of the gadolinium-doped zirconate, the multilayer TBC showed good thermal shock resistance. The results also suggested that the Al_2O_3 -GAP coating has a superior erosion-resistant property under severe erosion conditions than the conventional YSZ TC.

Given the promising performance of new multilayered TBCs, a key point in the development of new coating architectures is the identification of ceramic materials and composites that can reasonably work under severe thermal and chemical environments of gas turbines. In this sense, rare-earth zirconates ($RE_2Zr_2O_7$, RE = rare earth element) are the focus of attention since they present phase stability at high temperatures, low thermal conductivity, and high-thermal expansion coefficient. In particular, the $Gd_2Zr_2O_7$ (GDZ) that has two crystal structures, namely pyrochlore structure and defect fluorite structure, both of which are face centered cubic space lattice, has risen as a good candidate for TBCs. This material also has low-oxygen permeability which improves its protection against deterioration of the inner layers and SA substrate [117].

Some other interesting rare-earth oxides for TBC application are niobates (RE_3NbO_7 and $RENbO_4$) and tantalates ($RETaO_4$) since these materials show high-temperature stability without unexpected phase transformation and low thermal conductivity, while the fracture toughness and thermal expansion coefficient are remarkably better than conventional YSZ, providing better stability and strain tolerance during service [118]. Despite the development of new ceramic compositions, there is still work ahead because these new materials present low fracture toughness, which restricts their application in TBCs. Therefore, up to today, no single material aside from YSZ has the entire attributes required for an application in TBCs, and scientific research is currently focused on new materials combinations to balance mechanical and thermal properties for enabling these new materials in new TBCs approaches.

Research of novel materials also includes the performance assessment of MCrAlX with different chemical composition at the BC layer [119–121], including the addition of reactive elements such as Hf or Ta [18]. In terms of the TC, pure and complex rare earth pyrochlores such as $La_2Zr_2O_7$, $(La_xGd_{1-x})_2Zr_2O_7$, yttrium-rich Y_2O_3 - ZrO_2 , and others have been studied [33–35, 46, 47, 117]. These materials have

shown important benefits compared to YSZ such as lower thermal conductivities, phase stability along wider ranges of temperature, intrinsic CMAS recession mechanisms, etc. However, such systems have not shown significant increases in lifetime compared to YSZ. For this reason, research has also been dedicated to the study of new architectures which include multilayered $\text{RE}_2\text{Zr}_2\text{O}_7/\text{YSZ}$ and microstructures with induced vertical cracking [32, 78, 114, 122, 123].

During the last 10 years, different efforts have been performed to produce EBCs conformed by alternative materials and architectures to the well-established silicate-based system. According to Zhu [50], durable and reliable EBCs are very important to emerging SiC/SiC CMCs component technologies. The author mentions that EBC systems have been made on a solid foundation from experience and new EBC coatings have been improved with the current state of the art chemical compositions of higher temperature capabilities, such as multicomponent EBC oxide/silicates. These systems present higher stabilities and improved strength and toughness. Some good examples are the HfO_2 -Si and RE-Si bond coats that have been employed for realizing $1482\text{ }^\circ\text{C} + (2700\text{ }^\circ\text{F} +)$ temperature capabilities and potentially prime-reliant EBC-designs, and also new EBC compositions which have shown improved combustion steam and resistance to CMAS attack.

Richards et al. [100] produced $\text{Yb}_2\text{SiO}_5/\text{Al}_6\text{Si}_2\text{O}_{13}/\text{Si}$ EBCs deposited on α -SiC substrates using low power APS. The coatings were cycled under a 90% $\text{H}_2\text{O}/10\%$ O_2 steam atmosphere to failure, with a 60 min heating stage up to $1316\text{ }^\circ\text{C}$ and cooling down to $110\text{ }^\circ\text{C}$ in a 10 min lapse time. The authors reported the formation of bifurcated mud cracks in the coatings and the penetration of oxidizing species causing oxidation of the Si bond coat. Also, it was reported that a modification of the deposition process, to achieve higher density and increased layer adherence in the coatings, did not overcome the fundamental thermomechanical limitations of the $\text{Yb}_2\text{SiO}_5/\text{Al}_6\text{Si}_2\text{O}_{13}/\text{Si}$ EBC system. Furthermore, the intrinsically high strain energy release rates (ERRs) of this coating system that result from mismatched CTEs, were not overcome by increasing the coating layer density and interface adhesion. An important conclusion of this research was that the examination of the coating cracking/spallation criteria will be critical in the design of future EBCs.

Zhong et al. [124] produced a Si-HfO₂/Yb₂Si₂O₇/Yb₂SiO₅/Gd₂Zr₂O₇ composite multilayered EBC on CMC substrates by a plasma spray-physical vapor deposition hybrid process. The aim of the study was to develop a coating which mechanically performed well under chemical attack and high-temperature conditions. The authors performed thermal cycling by water quenching to evaluate the behavior of the coatings. They reported a structure change in the EBC caused by the formation of point type defects and dislocations in the Yb₂SiO₅ and Gd₂Zr₂O₇ layers. The failure mechanism of coatings under thermal cycling was spalling due to cracking at the Si-HfO₂/Yb₂Si₂O₇ interface. Another exercise performed to develop EBCs employing novel materials was presented by Pan et al. [125]. The authors reported the fabrication of Ca₃ZrSi₂O₉ (CZSO) coatings by atmospheric plasma spray. A complete structural, chemical, and mechanical evaluation of the coatings was performed. A coating containing amorphous phase and microcracking was obtained in the as-sprayed condition; a crystalline transformation was observed between 900 and 960 °C

in the coating and no mass change was registered up to 1300 °C during thermal characterization. Aging heat treatments were performed on the coatings and after 30–200 h heat treatment at 1100 °C, the original lamellar structure in the coatings faded and the density of microcracks sharply decreased. The observed properties of the CZSO coating suggest that it can be regarded as a potential material for the fabrication of EBCs.

5 Mechanical and Chemical Considerations

Mechanical properties of conventional TBCs are crucial for their optimal service and lifetime. There are some factors such as operating temperature that can affect the mechanical response of TBCs. In conventional YSZ TBC coatings, temperature can promote phase changes; in particular, service temperatures above 1200 °C, can induce the transformation from tetragonal (t-ZrO₂) to monoclinic (m-ZrO₂) crystalline phase. This transformation results in lower mechanical properties than those of the t-ZrO₂ leading to the mechanical failure of the TBC.

Another important factor to account for is the growth of an oxide layer formation at the BC-TC interface, TGO. This oxide grows due to aluminum depletion from the bond coat. The TGO is often formed at temperatures below 1200 °C [126]. TBCs can also experience sintering effect due to high temperatures, which can lead to decrease the porosity and increase the Young's modulus decreasing the thermal insulation of the coating. It is worth mentioning that high sintering rates of YSZ promote coating densification and the loss of strain tolerance resulting in spallation [127].

On the other hand, the microstructure of the TBC has a strong influence on its mechanical properties; it depends on factors such as powder characteristics, size, and morphology of particles, and spraying parameters, both having an impact on porosity, microcracks, and presence of partially molten zones. Thus, microcracking and porosity decreases TBC microhardness. Carpio et al. [128] evaluated microhardness and fracture toughness of YSZ coatings fabricated by APS using nano-sized and submicron-sized powders and compared with a commercial microstructured powder. They found that the TBC prepared from commercial powder exhibits lower values of microhardness than that obtained from the TBC prepared from nanostructured powder, which was associated with the high value of porosity in the TBC prepared from the commercial powder. The formation of a bimodal microstructure, conformed by two zones, that is, partially molten zones surrounded by a fully molten matrix, obtained when the TBC is prepared from nanostructured coatings, can behave as a barrier for crack propagation. However, they concluded that, in terms of fracture toughness, the nanostructured coating did not show not large changes with respect to conventional microstructured YSZ coatings [128].

Vassen et al. [126] carried out a study on the evaluation of mechanical properties of two TBCs (BaZrO₃ and La₂Zr₂O₇) and compared the results obtained against the conventional YSZ coating; all TBCs were sprayed by APS. Hardness, fracture toughness, and Young's modulus were the properties evaluated (Table 1). The YSZ

coating had the highest Young's modulus among the coatings studied; the lower elastic modulus obtained in the BaZrO_3 and $\text{La}_2\text{Zr}_2\text{O}_7$ with respect to YSZ has its own benefits since it can help to reduce thermal stresses at high temperature. On the other hand, fracture toughness of the $\text{La}_2\text{Zr}_2\text{O}_7$ coating (measured by indentation) showed a similar value ($1.1 \text{ Mpa} \cdot \text{m}^{1/2}$) than that obtained from the YSZ coating ($1\text{--}2 \text{ Mpa} \cdot \text{m}^{1/2}$). Fracture toughness of the BaZrO_3 coating was not measured due to the uncertainty caused by the porosity that created stress concentration points, leading to the formation of cracks around the indentations [126]. The study of Vassen et al. [126] remarks on the effect of ceramics mechanical properties and microstructural features of the coatings on the performance of a TBC. Both ceramic properties and microstructural defects must be controlled to get the best benefits.

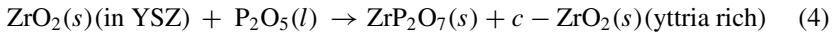
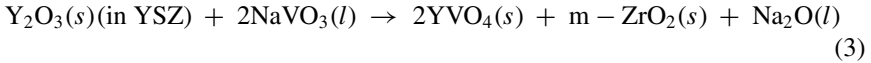
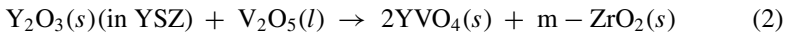
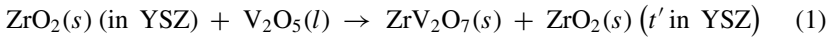
It is well known that TBCs are employed in hot sections of aero and land gas-turbine engines and provide protection against hot corrosion, CMAS attack, and erosion. TBC systems face some challenges under engine working conditions; specifically, these can be erosion, oxidation, foreign objects damage (dust, sand, volcanic ashes, etc.), which can put the mechanical integrity of the whole system at risk. Environmental dust is usually melted above 1200°C what is known as CMAS ($\text{CaO-MgO-Al}_2\text{O}_3\text{-SiO}_2$) attack [129–132]. A dissolution/precipitation mechanism can take place in a TBC due to the infiltration of CMAS within the TC; diffusion of yttrium ions destabilizes the metastable tetragonal phase in the YSZ layer, leading to the transformation of the original tetragonal YSZ into globular particles of monoclinic phase, accompanied by a 2–5% volumetric expansion. This fact causes spallation of the TBC [129]. In addition, molten CMAS can infiltrate the internal porosity of TBCs, leading also to coating spallation. This failure can occur during the turbine engine shutdown, when the molten CMAS solidifies, causing high thermomechanical stresses within the TBC.

On the other hand, the degradation of TBCs is also present in land gas-turbine engines; for instance, gas-turbine engines from integrated gasification combined cycle plants present TBC degradation, which is associated with the use of petroleum coke (petcoke) and coal/petcoke blends as fuels, which contains impurities such as vanadium, phosphorus, sulfur, and sodium. During the TBC operation, the following species: V_2O_5 , P_2O_5 , NaVO_3 and Na_2SO_4 are molten and often deposited on the outer surface of the TBC. The chemical attack of these compounds is known as hot corrosion, and can be described by the reaction between molten V_2O_5 with solid YSZ to produce zirconium pyrovanadate (ZrV_2O_7) below 747°C (Eq. 1). Nevertheless, molten V_2O_5 reacts with YSZ to produce yttrium vanadate (YVO_4) above 747°C (see Eq. 2). Thus, the degradation of the TBC is accelerated because of the precipitation

Table 1 Mechanical properties for different materials [126]

Material	Young's modulus (GPa)	Hardness (GPa)	Fracture toughness ($\text{MPa} \cdot \text{m}^{1/2}$)
BaZrO_3	181	11.1	–
$\text{La}_2\text{Zr}_2\text{O}_7$	175	9.9	1.1
YSZ	210	13	1–2

of YVO_4 that leads to a reduced Y_2O_3 volume fraction and to a detrimental phase change to monoclinic ZrO_2 . Moreover, at high temperatures, the $Na_2SO_4 + V_2O_5$ mixture produces vanadate precipitates that are characterized by their low melting temperature. For instance, the $NaVO_3$ (610 °C) promotes degradation of YSZ by precipitation of YVO_4 at temperatures around 700 °C (Eq. 3). On the other hand, P_2O_5 is also found to react with YSZ in TBCs, leading to the emergence of zirconium pyrophosphate (ZrP_2O_7) at different temperatures, that is, from 200 to 1200 °C. This reaction promotes the formation of the fluorite-cubic ZrO_2 phase (Eq. 4). Molten Na_2SO_4 is chemically inert by itself, but it can infiltrate within interlamellar gaps and pores of TBCs and its solidification during engine cooling can result in thermo-mechanical damage of the coating [133].



There are two ways for the mitigation of CMAS chemical attack; firstly, “immobilizing the melt” by capturing its main constituents into crystalline phases (often silicates); secondly, “generating enough volume of precipitated products” to fill the pores spaces and block access of any residual melt into the remaining TBC.

In the first option, melt immobilization is based on the reactivity of alumina, which is combined with CaO and SiO_2 to form anorthite, $CaAl_2Si_2O_8$. In this way, the incorporation of Al_2O_3 (in the form of a metastable solid solution) into the YSZ with small amounts of TiO_2 can be performed by solution precursor plasma spray (SPPS) or APS to favor this reaction. Basically, YSZ serves as a reservoir of Al and Ti solutes, which are incorporated into the molten CMAS glass in contact with the YSZ ceramic layer. An increase of Al concentration in the molten CMAS, as it infiltrates into the YSZ layer, can change the glass composition from pseudo-wollastonite to anorthite, which is an easy-to-crystallize phase. The incorporated Ti serves as a nucleating agent, promoting CMAS glass crystallization [134]. The second option is chiefly associated with the use of new TBC systems, such as rare-earth zirconates. Specifically, gadolinium zirconate can help to mitigate CMAS attack avoiding its penetration into the TBC; this process happens by dissolution of the zirconate into the CMAS melt, which in turn produces a conversion of CMAS into a mixture of crystalline phases. Such phases fill the channels in which the CMAS flows within the TBC architecture avoiding further penetration. This mechanism is carried out by the formation of a highly stable apatite phase by incorporating Ca, Gd, Si, and Zr. Once the aforementioned channels have been sealed the reaction continues quite slowly, which is beneficial for the survivability of the reaction layer under thermal cycling.

It has been mentioned in the literature that other alternatives to delay or halt CMAS attack in TBCs are the use of alternating layers of YSZ and oxides based on different chemical elements (La, Ce, Pr, Nd, Pm, Sm, Eu, Gd, Tb, Dy, Ho, Er, Tm, Yb, Lu, Sc, In, Zr, Hf, and Ti) or by using gadolinia-stabilized zirconia as a top coat layer [135].

The mechanical behavior in EBCs depends on the tolerance of the coatings to external mechanical damage, the fabrication conditions followed, as well as the service temperature. For example, elastic modulus and hardness values of a plasma-sprayed Yb_2SiO_5 coating increases 49.4% and 42.2%, respectively, after 1500 °C heat-treatment for 50 h [136]. Table 2 displays the Vickers hardness (Hv), elastic modulus (E), and fracture toughness of three EBCs applied by APS. Previous studies [137] have mentioned that Yb_2SiO_5 and $\text{Yb}_2\text{SiO}_2\text{O}_7$ show high fracture toughness due to crack deflection, bridging mechanism, and branching. Thus, this crack extension mode dissipates the fracture energy and stops crack propagation in a local zone; this fact suggests that Yb_2SiO_5 and $\text{Yb}_2\text{SiO}_2\text{O}_7$ are both good damage-tolerant ceramics.

Hu et al. studied the effect of electrical power on the microstructure of Yb_2SiO_5 coatings produced by APS. The authors performed an increment from 40 to 55 kW and found that the Yb_2SiO_5 particles were completely molten when deposited at 55 kW, resulting in a TC with pores and cracks caused by volatilization of SiO_2 (melting point 1723 °C). This fact also promoted the formation of Y_2O_3 rich areas due to dissimilar melting points between SiO_2 and Y_2O_3 (2439 °C). They also reported the formation of cracks in the SiC ceramic composite substrate due to the penetration of oxygen through the EBC, which can lead to accelerated mechanical failure of the entire coating system [140, 141].

On the other hand, CMCs can present stability problems related to the presence of water vapor since, throughout the operation of a combustion power unit, the flame produced can contain from 8 to 10% humidity. This fact can cause a reaction between the TGO and water vapor to form gaseous silicon hydroxides such as $\text{Si}(\text{OH})_4$, resulting in its rapid volatilization [49, 142]. For CMCs, the EBCs consist of a Si bond coat, which has high corrosion resistance at high temperature in a water vapor environment; the main target of the bond coat is preventing the oxygen diffusion and improving the bond strength of the coating. There are many plasma sprayed TC available for EBC systems such as mullite, BSAS ($(1-x)\text{BaO} \cdot \text{Al}_2\text{O}_3 \cdot 2\text{SiO}_2$, $\leq x \leq 1$),

Table 2 Mechanical properties of EBCs coating deposited by APS

Material	Vickers hardness, Hv (GPa)	Elastic modulus, E (GPa)	Fracture toughness, K_{IC} (MPa $\sqrt{\text{m}}$)	References
Mullite	10.8	126.0	1.8–2.8	[136]
Yb_2SiO_5	5.12	97.30	2–2.8	[136]
Yb_2SiO_5	6.4	119	1.97	[138]
$\text{Yb}_2\text{SiO}_2\text{O}_7$	4.28	168	2–2.8	[139]
$\text{Yb}_2\text{SiO}_2\text{O}_7$	6.2	155	2.12	[139]

and rare earth silicates such as monosilicates (RE_2SiO_5) and disilicates ($\text{RE}_2\text{Si}_2\text{O}_7$) [143].

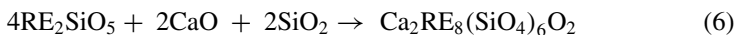
Mullite-based coatings are one of the most reported EBCs proposed in the literature due to its similar CTE to that of SiC. However, these types of coatings often develop cracks during thermal exposure, allowing corrosive species to penetrate and attack the SiC substrates. The formation of cracks is associated with the crystallization of the amorphous mullite, accompanying a volumetric contraction. For this reason, second-generation APS mullite coatings have been proposed, which present better durability at high temperatures (up to 1300 °C) under hot corrosion [144]. However, the second generation also had problems related to the loss of silica by volatilization [38]. Currently, a new generation of EBCs employs an outer layer based on a rare-earth silicates that includes Y or Yb [142].

The Yb_2SiO_5 coating has been reported as a good candidate for TC in EBCs since it can provide water vapor corrosion resistance [145]. Some studies have been carried out by Li et al. [146] who evaluated a plasma sprayed Yb_2SiO_5 coating under high-temperature water vapor and thermal cycling. The authors reported the decomposition of the Yb_2SiO_5 to form a second phase (Yb_2O_3) due to the volatilization of silica during the fabrication of the coatings by APS [139]. When the Yb_2O_3 comes in contact with water vapor $\text{Yb}(\text{OH})_3$ is produced. SEM images of the Yb_2SiO_5 coatings corroborated the presence of pores which was attributed to the volatilization of $\text{Yb}(\text{OH})_3$ and $\text{Si}(\text{OH})_4$. The authors suggest the presence of Yb_2SiO_5 because of the reaction of water vapor with the $\text{Yb}_2\text{Si}_2\text{O}_7$ coating, as shown in Eq. (5) [147].



On the other hand, EBCs are also exposed to CMAS that are molten above 1200 °C and may favor the formation of products which can be less thermomechanical compatible with the substrate or exhibit a high volatilization tendency [142]. Grant et al. [38] reported that CMAS can cause significant recession of yttrium monosilicate (Y_2SiO_5 , YMS), despite the precipitation of $\text{Ca}_2\text{Y}_8(\text{SiO}_4)_6\text{O}_2$, an oxyapatite layer, which is a nearly dense layer obtained at the YMS surface. The reaction is carried out continuously due to the presence of a thin amorphous layer at the grain boundaries within the oxyapatite layer, which provides a fast path for diffusion of the YMS-apatite reaction front.

On the other hand, Yb silicates ($\text{Yb}_2\text{SiO}_2\text{O}_7$ and Yb_2SiO_5 , mainly) also produce the formation of $\text{Ca}_2\text{Yb}_8(\text{SiO}_4)_6\text{O}_2$ -like apatite phase due to the dissolution of the CMAS according to the following reaction (Eq. 6) (see Fig. 3) [142, 148].



The presence of Yb_2O_3 phase in the Yb_2SiO_5 TC does not represent any influence on the reaction process. However, in $\text{Yb}_2\text{SiO}_2\text{O}_7$ coating, the Yb_2SiO_5 phase is distributed throughout the volume of the $\text{Yb}_2\text{SiO}_2\text{O}_7$ layer, providing a preferential path for the permeation of molten salts.

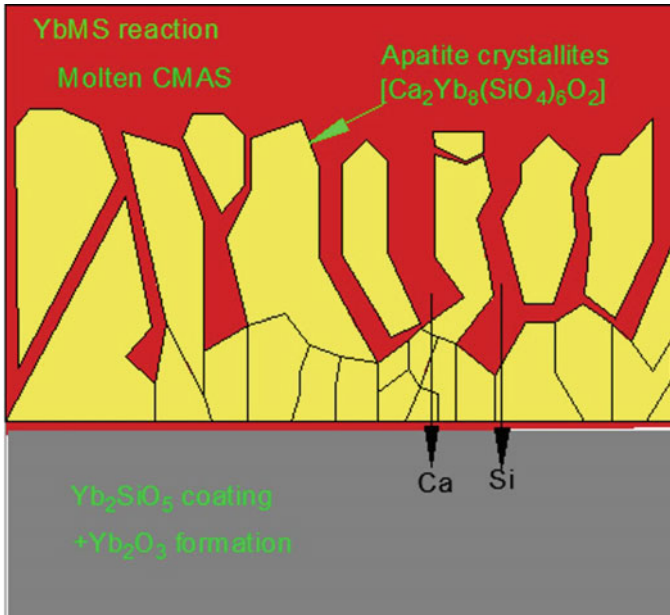


Fig. 3 Schematic representation of reaction mechanism between CMAS and Yb₂SiO₅ (YbMS)

To provide water vapor resistance, EBCs should have low silicon activity at the TC to avoid volatilization. Oxide coatings are a promising approach for providing environmental protection in advanced engine components because these materials are more resistant than silicon-based ceramics [149]. In this sense, two alternatives can be explored, firstly, modifying the optical-basicity (Λ) of crystalline oxide ceramics in order to decrease their reactivity. For example, some studies have evaluated the reactivity of EBCs with the addition of Y such as YAlO₃ ($\Lambda = 0.70$) and Y₂Si₂O₇ ($\Lambda = 0.70$) that have different behavior than CMAS ($\Lambda = 0.64$), and to the EBC without Y content Y₂Si₂O₇ ($\Lambda = 0.68$) and Sc₂Si₂O₇ ($\Lambda = 0.66$). This result suggests the promotion of stable phases, avoiding the grain-boundary penetration by the CMAS glass [44]. A second option is designing multilayer coating architectures, employing TC with the ability to resist CMAS attack. Thus, new architectures named Thermal/Environmental Barrier Coatings (TEBCs) have been developed in recent years. These coatings consist of multilayers, where the TC is based on HfO₂ or ZrO₂ modified compositions (as both show high CTEs) and intermediate layers of Yb₂SiO₅ and Yb₂SiO₇, with the Yb₂SiO₇ located just on top of the substrate (SiC) in order to have a better matching of CTEs [52].

The silicon-based bond coat normally employed on EBCs provides protection against oxidation at high temperatures. When the coating is exposed at temperatures higher than 1200 °C a β -cristobalite layer is formed at the silicon-Yb₂SiO₇ interface and provides protection against oxygen entrance to the CMC substrate. However, when the entire EBC is cooled down below ~240 °C a β - α cristobalite

transformation occurs with a 4.9% intrinsic volumetric change, increasing the probability of delamination in the system. Deijkers and Wadley [150] proposed the use of an alternative Si-based bond coat with HfO_2 additions to diminish such volume change. The authors showed that during high temperature exposure HfO_2 reacts with SiO_2 to form HfSiO_4 , a stable and thermomechanically stable phase compatible with silicon and $\text{Yb}_2\text{Si}_2\text{O}_7$.

6 Conclusions

Scientific advances related to modern applications of TBCs/EBCs rely on the increase of service temperature. Despite the efforts for the development of new multilayered coating architectures and new ceramic materials, there is a need for further detailed investigations to get a better comprehension about the need of several coating layers and their synergistic role in TBCs and EBCs. Further efforts for the development of physical and mathematical models about thermomechanical evolution of TBCs/EBCs before and after applying different mechanical constraints can be an important insight to understand and truly envision their potential as thermochemical protective systems.

Since high temperatures above 1200 °C are involved in modern gas turbines, CMAS is still a major issue. Many reports up to date suggest that CMAS infiltration is a real problem for the industry [151]. Advances in ceramic materials certainly offer some potential candidates for mitigating CMAS attack [152, 153]. Nevertheless, conventional YSZ still cannot be completely replaced since new ceramic candidates often present low fracture toughness and/or relatively high thermal conductivity under TBCs service conditions. In addition, there is an increment in the number of research and published papers in recent years about the development of new potential ceramic materials that can work as TBCs in modern gas turbines [154]. These works are mainly focused on the characterization of thermophysical properties. However, it is going to be crucial for the coming years that these new ceramic candidates can be evaluated under real harsh environments to compare the results obtained against those reported for conventional TBCs.

The industry is also moving onto new alternatives, for instance, there is a need for lower emissions due to new policies focused on green technologies. As a result, the manufacturers are trying the development of efficient combustion turbine systems and less complex cooling systems than current ones. This situation establishes a challenge on insulation capacity and performance of the TBCs. In this manner, working on porosity, porous size, and porosity distribution are real options to get progress on the technology. For instance, this strategy has been recently reported for YSZ-based TBCs where controlled porosity resulted in a better stability at substantially higher temperatures than that found in conventional YSZ coatings [155]. The combination of this strategy with new ceramic candidates for TBCs can also represent new steps further to the technology in the near future. On the other hand, efforts of the industry are also focused on sustainable and clean processes along the fabrication of aircraft

components. In this sense, there is a new tendency on exploring TBC fabrication processes that can be an alternative to APS and PS-PVD. For instance, the Low-Pressure Cold Spray (LPCS) and High-Pressure Cold Spray (HPCS) techniques are being explored as an alternative fabrication process for composite TBC systems. However, the studies are still in early stages and there is still a great deal of work to do in the incoming years. For instance, some goals for future development of TBCs by cold spray rely on understanding ceramic deposition, identification of post-processing steps, and evaluation of the performance of the TBCs obtained with respect to conventional counterparts [156].

Acknowledgements The authors acknowledge the National Council of Humanities, Science and Technology of Mexico (CONAHCYT) and the National Laboratory of Thermal Spray of Mexico (CENAPROT), and the Surface Engineering Laboratory at the Center for Engineering and Industrial Development (CIDESI) for their support during the writing of this book chapter. The authors also acknowledge the support of the program “Investigadores por Mexico” project 848.

References

1. Huda, Z., Zaharinie, T., Al-Ansary, H.A.: Enhancing power output and profitability through energy-efficiency techniques and advanced materials in today’s industrial gas turbines. *Int. J. Mech. Mater. Eng.* **9**(1), 1–12 (2014). <https://doi.org/10.1186/S40712-014-0002-Y/TABLES/4>
2. Miller, R.A.: Thermal barrier coatings for aircraft engines: history and directions. *J. Therm. Spray Technol.* **6**(1), 35–42 (1997). <https://doi.org/10.1007/BF02646310>
3. Mouritz, A. P. (2012). Introduction to aerospace materials. In: *Introduction to Aerospace Materials*, pp. 1–621. <https://doi.org/10.2514/4.869198>
4. Yin, F., Gangoli Rao, A.: Performance analysis of an aero engine with inter-stage turbine burner. *Aeronaut. J.* **121**(1245), 1605–1626 (2017). <https://doi.org/10.1017/aer.2017.93>
5. Whittle, A.C.F.: The first James Clayton lecture: the early history of the whittle jet propulsion gas turbine. *Proc. Inst. Mech. Eng.* **152**(1), 419–435 (1945). https://doi.org/10.1243/PIME_PROC_1945_152_071_02
6. Bogard, D.G., Thole, K.A.: Gas turbine film cooling. *J. Propul. Power* **22**(2), 249–270 (2006). <https://doi.org/10.2514/1.18034>
7. Sim, C.M., Oh, H.S., Kim, T.J., Lee, Y.S., Kim, Y.K., Kwak, S.S., Hwang, Y.H.: Detecting internal hot corrosion of in-service turbine blades using neutron tomography with Gd tagging. *J. Nondestr. Eval.* **33**(4), 493–503 (2014). <https://doi.org/10.1007/s10921-014-0244-x>
8. Konter, M., Thumann, M.: Materials and manufacturing of advanced industrial gas turbine components. *J. Mater. Process. Technol.* **117**(3), 386–390 (2001). [https://doi.org/10.1016/S0924-0136\(01\)00785-3](https://doi.org/10.1016/S0924-0136(01)00785-3)
9. Clarke, D.R., Oechsner, M., Padture, N.P.: Thermal-barrier coatings for more efficient gas-turbine engines. *MRS Bull.* **37**(10), 891–898 (2012). <https://doi.org/10.1557/mrs.2012.232>
10. Fouliard, Q., Hernandez, J., Northam, M., Ghosh, R., Raghavan, S.: Doped 8% yttria-stabilized zirconia for temperature measurements in thermal barrier coatings using phosphor thermometry. In: *AIAA Scitech 2020 Forum*, 1 PartF, 1–8 (2020). <https://doi.org/10.2514/6.2020-0631>
11. Reed, R.C. (2006). *The Superalloys Fundamentals and Applications*.
12. Zielińska, M., Yavorska, M., Poreba, M., Sieniawski, J.: Thermal properties of cast nickel based superalloys. *Arch. Mater. Sci. Eng.* **44**(1), 35–38 (2010)

13. Pollock, T.M., Tin, S.: Nickel-based superalloys for advanced turbine engines: chemistry, microstructure, and properties. *J. Propul. Power* **22**(2), 361–374 (2006). <https://doi.org/10.2514/1.18239>
14. Balint, D.S., Xu, T., Hutchinson, J.W., Evans, A.G.: Influence of bond coat thickness on the cyclic rumpling of thermally grown oxides. *Acta Mater.* **54**(7), 1815–1820 (2006). <https://doi.org/10.1016/j.actamat.2005.12.008>
15. Kwon, J.Y., Lee, J.H., Jung, Y.G., Paik, U.: Effect of bond coat nature and thickness on mechanical characteristic and contact damage of zirconia-based thermal barrier coatings. *Surf. Coat. Technol.* **201**(6), 3483–3490 (2006). <https://doi.org/10.1016/J.SURFCOAT.2006.07.240>
16. Haynes, J.A., Lance, M.J., Pint, B.A., Wright, I.G.: Characterization of commercial EB-PVD TBC systems with CVD (Ni, Pt)Al bond coatings. *Surf. Coat. Technol.* **146–147**, 140–146 (2001). [https://doi.org/10.1016/S0257-8972\(01\)01483-9](https://doi.org/10.1016/S0257-8972(01)01483-9)
17. Ruiz-Luna, H., Porcayo-Calderon, J., Alvarado-Orozco, J.M., García-Herrera, J.E., Martínez-Gomez, L., Trápaga-Martínez, L.G., Muñoz-Saldaña, J.: Electrochemical corrosion of HVOF-sprayed NiCoCrAlY coatings in CO₂-saturated brine. *J. Therm. Spray Technol.* **25**(7), 1330–1343 (2016). <https://doi.org/10.1007/s11666-016-0449-x>
18. Mora-García, A.G., Ruiz-Luna, H., Mosbacher, M., Popp, R., Schulz, U., Glatzel, U., Muñoz-Saldaña, J.: Microstructural analysis of Ta-containing NiCoCrAlY bond coats deposited by HVOF on different Ni-based superalloys. *Surf. Coat. Technol.* **354**(June), 214–225 (2018). <https://doi.org/10.1016/j.surfcoat.2018.09.025>
19. Kesler, O., Matejicek, J., Sampath, S., Suresh, S., Gnaeupel-Herold, T., Brand, P.C., Prask, H.J.: *Mater. Sci. Eng. A* **257**, 215–224 (1998)
20. Chen, W.R., Archer, R., Huang, X., Marple, B.R.: TGO growth and crack propagation in a thermal barrier coating. *J. Therm. Spray Technol.* **17**(5–6), 858–864 (2008). <https://doi.org/10.1007/S11666-008-9251-8/METRICS>
21. Chen, W.R., Wu, X., Marple, B.R., Nagy, D.R., Patnaik, P.C.: TGO growth behaviour in TBCs with APS and HVOF bond coats. *Surf. Coatings Technol.* **202**, 2677–2683 (2008). <https://doi.org/10.1016/j.surfcoat.2007.09.042>
22. Peng, X.: Metallic coatings for high-temperature oxidation resistance. In: *Thermal Barrier Coatings*, pp. 53–74 (2011). <https://doi.org/10.1533/9780857090829.1.53>
23. Tolpygo, V.K., Clarke, D.R.: Wrinkling of α -alumina films grown by oxidation—II. Oxide separation and failure. *Acta Mater.* **46**(14), 5167–5174 (1998). [https://doi.org/10.1016/S1359-6454\(98\)00134-7](https://doi.org/10.1016/S1359-6454(98)00134-7)
24. Thakare, J.G., Pandey, C., Mahapatra, M.M., Mulik, R.S.: Thermal barrier coatings—a state of the art review. *Metals Mater. Int.* **27**(7), 1947–1968 (2020). <https://doi.org/10.1007/S12540-020-00705-W>
25. Vaßen, R., Jarligo, M.O., Steinke, T., Mack, D.E., Stöver, D.: Overview on advanced thermal barrier coatings. *Surf. Coat. Technol.* **205**(4), 938–942 (2010). <https://doi.org/10.1016/j.surfcoat.2010.08.151>
26. Cipitria, A., Golosnoy, I.O., Clyne, T.W.: A sintering model for plasma-sprayed zirconia TBCs. Part I: Free-standing coatings. *Acta Mater.* **57**(4), 980–992 (2009). <https://doi.org/10.1016/j.actamat.2008.10.024>
27. Leoni, M., Jones, R.L., Scardi, P.: Phase stability of scandia-yttria-stabilized zirconia TBCs. *Surf. Coatings Technol.* **108–109**(October 1998), 107–113 (1998). [https://doi.org/10.1016/S0257-8972\(98\)00617-3](https://doi.org/10.1016/S0257-8972(98)00617-3)
28. Thompson, J.A., Ji, W., Klocker, T., Clyne, T.W.: Sintering of the top coat in thermal spray tbc systems under service conditions. *Superalloys*, 685–692. https://doi.org/10.7449/2000/Superalloys_2000_685_692.pdf
29. Andrievskaya, E.R.: Phase equilibria in the refractory oxide systems of zirconia, hafnia and yttria with rare-earth oxides. *J. Eur. Ceram. Soc.* **28**(12), 2363–2388 (2008). <https://doi.org/10.1016/j.jeurceramsoc.2008.01.009>
30. Chavez, J.J.G., Naraparaju, R., Mikulla, C., Mechnich, P., Kelm, K., Ramana, C.V., Schulz, U.: Comparative study of EB-PVD gadolinium-zirconate and yttria-rich zirconia coatings

- performance against Fe-containing calcium-magnesium-aluminosilicate (CMAS) infiltration. *Corros. Sci.* **190**, 109660 (2021). <https://doi.org/10.1016/J.CORSCI.2021.109660>
31. Pan, W., Phillpot, S.R., Wan, C., Chernatynskiy, A., Qu, Z.: Low thermal conductivity oxides. *MRS Bull.* **37**(10), 917–922 (2012). <https://doi.org/10.1557/mrs.2012.234>
 32. Amer, M., Curry, N., Hayat, Q., Sharma, R., Janik, V., Zhang, X., Nottingham, J., & Bai, M.: Cracking behavior of Gd₂Zr₂O₇/YSZ multi-layered thermal barrier coatings deposited by suspension plasma spray. *Coatings* **13**(1), 107 (2023). <https://doi.org/10.3390/COATINGS13010107>
 33. Guijosa-Garcia, C.Y., Rivera-Gil, M.A., Ramana, C.V., Naraparaju, R., Schulz, U., Muñoz-Saldaña, J.: Reaction products from high temperature treatments of (La_xGd_{1-x})₂Zr₂O₇ system and volcanic ash powder mixtures. *JOM* **74**(7), 2791–2808 (2022). <https://doi.org/10.1007/S11837-022-05302-3/METRICS>
 34. Lozano-Mandujano, D., Poblano-Salas, C.A., Ruiz-Luna, H., Esparza-Esparza, B., Giraldo-Betancur, A.L., Alvarado-Orozco, J.M., Trápaga-Martínez, L.G., Muñoz-Saldaña, J.: Thermal spray deposition, phase stability and mechanical properties of La₂Zr₂O₇/LaAlO₃ coatings. *J. Therm. Spray Technol.* **26**(6), 1198–1206 (2017). <https://doi.org/10.1007/s11666-017-0569-y>
 35. Moskal, G., Swadźba, L., Hetmańczyk, M., Witala, B., Mendala, B., Mendala, J., Sosnowy, P.: Characterization of microstructure and thermal properties of Gd₂Zr₂O₇-type thermal barrier coating. *J. Eur. Ceram. Soc.* **32**(9), 2025–2034 (2012). <https://doi.org/10.1016/j.jeurceram soc.2011.11.043>
 36. Saruhan, B., Francois, P., Fritscher, K., Schulz, U.: EB-PVD processing of pyrochlore-structured La₂Zr₂O₇-based TBCs. *Surf. Coat. Technol.* **182**(2–3), 175–183 (2004). <https://doi.org/10.1016/j.surfcoat.2003.08.068>
 37. Witz, G., Shklover, V., Steurer, W.: Phase evolution in yttria-stabilized zirconia thermal barrier coatings studied by rietveld refinement of X-ray powder diffraction patterns. *J. Am. Ceram. Soc.* **7820**, 1–17 (n.d.)
 38. Grant, K.M., Krämer, S., Löfvander, J.P.A., Levi, C.G.: CMAS degradation of environmental barrier coatings. *Surf. Coat. Technol.* **202**(4–7), 653–657 (2007). <https://doi.org/10.1016/J.SURFCOAT.2007.06.045>
 39. Kabir, M.R., Sirigiri, A. K., Naraparaju, R., Schulz, U.: Flow kinetics of molten silicates through thermal barrier coating: a numerical study. *Coatings*, **9**(5) (2019). <https://doi.org/10.3390/COATINGS9050332>
 40. Kakuda, T.R., Levi, C.G., Bennett, T.D.: The thermal behavior of CMAS-infiltrated thermal barrier coatings. *Surf. Coat. Technol.* **272**, 350–356 (2015). <https://doi.org/10.1016/j.surfcoat.2015.03.043>
 41. Naraparaju, R., Schulz, U., Mechnich, P., Döbber, P., Seidel, F.: Degradation study of 7wt.% yttria stabilised zirconia (7YSZ) thermal barrier coatings on aero-engine combustion chamber parts due to infiltration by different CaO-MgO-Al₂O₃-SiO₂ variants. *Surf. Coat. Technol.* **260**, 73–81 (2014). <https://doi.org/10.1016/j.surfcoat.2014.08.079>
 42. Rai, A.K., Bhattacharya, R.S., Wolfe, D.E., Eden, T.J.: CMAS-resistant thermal barrier coatings (TBC). *Int. J. Appl. Ceram. Technol.* **7**(5), 662–674 (2010). <https://doi.org/10.1111/j.1744-7402.2009.02373.x>
 43. Rivera-Gil, M.A., Gomez-Chavez, J.J., Ramana, C.V., Naraparaju, R., Schulz, U., Muñoz-Saldaña, J.: High temperature interaction of volcanic ashes with 7YSZ TBC's produced by APS: Infiltration behavior and phase stability. *Surf. Coat. Technol.* **378**(June), 124915 (2019). <https://doi.org/10.1016/j.surfcoat.2019.124915>
 44. Turcer, L.R., Padture, N.P.: Towards multifunctional thermal environmental barrier coatings (TEBCs) based on rare-earth pyrosilicate solid-solution ceramics. *Scripta Mater.* **154**, 111–117 (2018). <https://doi.org/10.1016/J.SCRIPTAMAT.2018.05.032>
 45. Bakan, E., Mack, D.E., Mauer, G., Mücke, R., Vaßen, R.: Porosity-property relationships of plasma-sprayed Gd₂Zr₂O₇ YSZ thermal barrier coatings. *J. Am. Ceram. Soc.* **98**(8), 2647–2654 (2015). <https://doi.org/10.1111/jace.13611>
 46. Habibi, M.H., Wang, L., Guo, S.M.: Evolution of hot corrosion resistance of YSZ, Gd₂Zr₂O₇, and Gd₂Zr₂O₇+YSZ composite thermal barrier coatings in Na₂SO₄+V₂O₅ at 1050 °C. *J. Eur. Ceram. Soc.* **32**(8), 1635–1642 (2012). <https://doi.org/10.1016/j.jeurceramsoc.2012.01.006>

47. Zhou, H.M., Yi, D.Q., Yu, Z.M., Xiao, L.R.: Preparation and thermophysical properties of CeO₂ doped La₂Zr₂O₇ ceramic for thermal barrier coatings. *J. Alloy. Compd.* **438**(1–2), 217–221 (2007). <https://doi.org/10.1016/j.jallcom.2006.08.005>
48. Guo, H., Guo, Y., Xue, Z., Gong, S., Xu, H.: Overview of thermal barrier coatings for advanced gas turbine engine. In: *Thermal Barrier Coatings*, 1–20 (2023). <https://doi.org/10.1016/B978-0-12-819027-2.00013-4>
49. Tejero-Martin, D., Bennett, C., Hussain, T.: A review on environmental barrier coatings: history, current state of the art and future developments. *J. Eur. Ceram. Soc.* **41**(3), 1747–1768 (2021). <https://doi.org/10.1016/J.JEURCERAMSOC.2020.10.057>
50. Zhu, D.: *Environmental Barrier Coating Development for SiC/SiC Ceramic Matrix Composites: Recent Advances and Future Directions* (n.d.)
51. Bakan, E., Marcano, D., Zhou, D., Sohn, J., Mauer, G., Vaßen, R.: Yb₂Si₂O₇ Environmental Barrier Coatings Deposited by Various Thermal Spray Techniques: A Preliminary Comparative Study (n.d.)
52. Garcia, E., Sotelo-Mazon, O., Poblano-Salas, C.A., Trapaga, G., Sampath, S.: Characterization of Yb₂Si₂O₇–Yb₂SiO₅ composite environmental barrier coatings resultant from in situ plasma spray processing. *Ceram. Int.* **46**(13), 21328–21335 (2020). <https://doi.org/10.1016/J.CERAMINT.2020.05.228>
53. Richards, B.T., Wadley, H.N.G.: Plasma spray deposition of tri-layer environmental barrier coatings. *J. Eur. Ceram. Soc.* **34**(12), 3069–3083 (2014). <https://doi.org/10.1016/J.JEURCERAMSOC.2014.04.027>
54. Levi, C.G., Hutchinson, J.W., Vidal-Sétif, M.H., Johnson, C.A.: Environmental degradation of thermal-barrier coatings by molten deposits. *MRS Bull.* **37**(10), 932–941 (2012). <https://doi.org/10.1557/mrs.2012.230>
55. Fauchais, P., Vardelle, M., Goutier, S.: Latest researches advances of plasma spraying: from splat to coating formation. *J. Therm. Spray Technol.* **25**(8), 1534–1553 (2016). <https://doi.org/10.1007/s11666-016-0435-3>
56. Fauchais, P.: Understanding plasma spraying. *J. Phys. D Appl. Phys.* **37**(9) (2004). <https://doi.org/10.1088/0022-3727/37/9/R02>
57. Craig, M., Ndamka, N.L., Wellman, R.G., Nicholls, J.R.: CMAS degradation of EB-PVD TBCs: the effect of basicity. *Surf. Coat. Technol.* **270**, 145–153 (2015). <https://doi.org/10.1016/j.surfcoat.2015.03.009>
58. Darolia, R.: Thermal barrier coatings technology: critical review, progress update, remaining challenges and prospects. *Int. Mater. Rev.* **58**(6), 315–348 (2013). <https://doi.org/10.1179/1743280413Y.0000000019>
59. Fauchais, P.L., Heberlein, J.V.R., Boulos, M.I.: *Thermal Spray Fundamentals* (2014). <https://doi.org/10.1007/978-0-387-68991-3>
60. Hospach, A., Mauer, G., Vaßen, R., Stöver, D.: Characteristics of ceramic coatings made by thin film low pressure plasma spraying (LPPS-TF). *J. Therm. Spray Technol.* **21**(3–4), 435–440 (2012). <https://doi.org/10.1007/S11666-012-9748-Z/METRICS>
61. Mauer, G., Jarligo, M.O., Rezanka, S., Hospach, A., Vaßen, R.: Novel opportunities for thermal spray by PS-PVD. *Surf. Coat. Technol.* **268**, 52–57 (2015). <https://doi.org/10.1016/j.surfcoat.2014.06.002>
62. Montavon, G., Sampath, S., Berndt, C.C., Herman, H., Coddet, C.: Effects of vacuum plasma spray processing parameters on splat morphology. *J. Therm. Spray Technol.* **4**(1), 67–74 (1995). <https://doi.org/10.1007/BF02648530/METRICS>
63. Smith, M.F., Hall, A.C., Fleetwood, J.D., Meyer, P.: Very low pressure plasma spray—a review of an emerging technology in the thermal spray community. *Coatings* **1**(2), 117–132 (2011). <https://doi.org/10.3390/COATINGS1020117>
64. VanEvery, K., Krane, M.J., Trice, R.W., Wang, H., Porter, W., Besser, M., Sordelet, D., Ilavsky, J., Almer, J.: Column formation in suspension plasma-sprayed coatings and resultant thermal properties. *J. Therm. Spray Technol.* **20**, 817–828 (2011). <https://doi.org/10.1007/s11666-011-9632-2>

65. Kassner, H., Siegert, R., Hathiramani, D., Vassen, R., Stoeber, D.: Application of suspension plasma spraying (SPS) for manufacture of ceramic coatings. *J. Therm. Spray Technol.* **17**, 115–123 (2008)
66. McCartney, D.G.: High velocity oxyfuel thermal sprayed coatings: processing, characterisation, and performance. *Surf. Eng.* **14**(2), 104–106 (2013). <https://doi.org/10.1179/SUR.1998.14.2.104>
67. Zhang, D., Harris, S.J., McCartney, D.G.: Microstructure formation and corrosion behaviour in HVOF-sprayed Inconel 625 coatings. *Mater. Sci. Eng. A* **344**(1–2), 45–56 (2003). [https://doi.org/10.1016/S0921-5093\(02\)00420-3](https://doi.org/10.1016/S0921-5093(02)00420-3)
68. Nowak, W., Naumenko, D., Mor, G., Mor, F., Mack, D.E., Vassen, R., Singheiser, L., Quadackers, W.J.: Effect of processing parameters on MCrAlY bondcoat roughness and lifetime of APS–TBC systems. *Surf. Coat. Technol.* **260**, 82–89 (2014). <https://doi.org/10.1016/J.SURFCOAT.2014.06.075>
69. Curry, N., Tang, Z., Markocsan, N., Nylén, P.: Surface & Coatings Technology influence of bond coat surface roughness on the structure of axial suspension plasma spray thermal barrier coatings—Thermal and lifetime performance. *Surf. Coat. Technol.* (2014). <https://doi.org/10.1016/j.surfcoat.2014.08.067>
70. Tawancy, H.M., Sridhar, N., Abbas, N.M., Rickerby, D.S.: Comparative performance of selected bond coats in advanced thermal barrier coating systems. *J. Mater. Sci.* **35**(14), 3615–3629 (2000). <https://doi.org/10.1023/A:1004825932601>
71. Kim, B.H., Suhr, D.S.: The influence of fuel/oxygen ratio in HVOF spraying on the deposition of Cr₃C₂ coatings. *Mater. Trans. JIM* **41**(12), 1657–1662 (2000). <https://doi.org/10.2320/MATERTRANS1989.41.1657>
72. Murugan, K., Ragupathy, A., Balasubramanian, V., Sridhar, K.: Optimizing HVOF spray process parameters to attain minimum porosity and maximum hardness in WC–10Co–4Cr coatings. *Surf. Coat. Technol.* **247**, 90–102 (2014). <https://doi.org/10.1016/J.SURFCOAT.2014.03.022>
73. Rajasekaran, B., Mauer, G., Vaßen, R.: Enhanced characteristics of HVOF-sprayed MCrAlY bond coats for TBC applications. *J. Therm. Spray Technol.* **20**(6), 1209–1216 (2011). <https://doi.org/10.1007/S11666-011-9668-3/METRICS>
74. Saaedi, J., Coyle, T.W., Arabi, H., Mirdamadi, S., Mostaghimi, J.: Effects of HVOF process parameters on the properties of Ni–Cr coatings. *J. Therm. Spray Technol.* **19**(3), 521–530 (2010). <https://doi.org/10.1007/S11666-009-9464-5/METRICS>
75. Saucedo, S., Lascano, S., Núñez, J., Parra, C., Arévalo, C., Béjar, L.: Effect of HVOF processing parameters on Cr₃C₂-NiCr hard coatings deposited on AISI 4140 steel. *Eng. Sci. Technol. Int. J.* **39**, 101342 (2023). <https://doi.org/10.1016/J.JESTCH.2023.101342>
76. Bounazef, M., Guessasma, S., Montavon, G., Coddet, C.: Effect of APS process parameters on wear behaviour of alumina–titania coatings. *Mater. Lett.* **58**(20), 2451–2455 (2004). <https://doi.org/10.1016/J.MATLET.2004.02.026>
77. Lamuta, C., Di Girolamo, G., Pagnotta, L.: Microstructural, mechanical and tribological properties of nanostructured YSZ coatings produced with different APS process parameters. *Ceram. Int.* **41**(7), 8904–8914 (2015). <https://doi.org/10.1016/J.CERAMINT.2015.03.148>
78. Chen, X., Sun, Y., Hu, J., Li, J., Deng, C., Wu, D., Zeng, D., Li, W., Liu, Y., Zou, B., Cao, X.: Thermal cycling failure of the multilayer thermal barrier coatings based on LaMgAl₁₁O₁₉/YSZ. *J. Eur. Ceram. Soc.* **40**(4), 1424–1432 (2020). <https://doi.org/10.1016/J.JEURCERAMSOC.2019.12.039>
79. Feist, J.P., Sollazzo, P.Y., Pilgrim, C., Nicholls, J.R.: Operation of a burner rig for thermal gradient cycling of thermal barrier coatings. In: *Proceedings of the ASME Turbo Expo 2014*, pp. 1–10 (2014). <https://doi.org/10.1115/GT2014-26325>
80. Kang, Y.X., Bai, Y., Yuan, T., Wang, Y., Fan, W., Gao, Y., Bao, C.G., Chen, H.Y., Li, B.Q.: Thermal cycling lives of plasma sprayed YSZ based thermal barrier coatings in a burner rig corrosion test. *Surf. Coat. Technol.* **324**, 307–317 (2017). <https://doi.org/10.1016/j.surfcoat.2017.05.066>

81. McBride, B.J., Gordon, S.: Computer Program for Calculation of Complex Chemical Equilibrium (vol. 1). NASA Lewis Research Center (1996). [https://books.google.com.mx/books?hl=en&lr=&id=1DA8AQAIAAJ&oi=fnd&pg=PA3&dq=B.+J.+McBride+and+S.+Gordon,+%22Computer+program+for+calculation+of+complex+chemical+equilibrium+compositions+and+applications,+II.+Users+manual+and+program+description,%22+NASA+reference+publication,+1311+84-85+\(1996\)&ots=hr9nON_XU&sig=ImWLNf0YygsPOGmocyU0JE9PM&redir_esc=y#v=onepage&q&f=false](https://books.google.com.mx/books?hl=en&lr=&id=1DA8AQAIAAJ&oi=fnd&pg=PA3&dq=B.+J.+McBride+and+S.+Gordon,+%22Computer+program+for+calculation+of+complex+chemical+equilibrium+compositions+and+applications,+II.+Users+manual+and+program+description,%22+NASA+reference+publication,+1311+84-85+(1996)&ots=hr9nON_XU&sig=ImWLNf0YygsPOGmocyU0JE9PM&redir_esc=y#v=onepage&q&f=false)
82. Evans, A.G., Mumm, D.R., Hutchinson, J.W., Meier, G.H., Pettit, F.S.: Mechanisms controlling the performance and durability of thermal barrier coatings. *Prog. Mater. Sci.* **46**, 505–553 (2001). <https://doi.org/10.4028/www.scientific.net/KEM.197.199>
83. Krämer, S., Yang, J., Levi, C.G., Johnson, C.A.: Thermochemical interaction of thermal barrier coatings with molten CaO–MgO–Al₂O₃–SiO₂ (CMAS) deposits. *J. Am. Ceram. Soc.* **89**(10), 3167–3175 (2006). <https://doi.org/10.1111/J.1551-2916.2006.01209.X>
84. Krämer, S., Yang, J., Levi, C.G.: Infiltration-inhibiting reaction of gadolinium zirconate thermal barrier coatings with CMAS melts. *J. Am. Ceram. Soc.* **91**(2), 576–583 (2008). <https://doi.org/10.1111/J.1551-2916.2007.02175.X>
85. Chen, X., He, M.Y., Spitsberg, I., Fleck, N.A., Hutchinson, J.W., Evans, A.G.: Mechanisms governing the high temperature erosion of thermal barrier coatings. *Wear* **256**, 735–746 (2004). [https://doi.org/10.1016/S0043-1648\(03\)00446-0](https://doi.org/10.1016/S0043-1648(03)00446-0)
86. Chen, X., Wang, R., Yao, N., Evans, A.G., Hutchinson, J.W., Bruce, R.W.: Foreign object damage in a thermal barrier system: mechanisms and simulations (n.d.). [https://doi.org/10.1016/S0921-5093\(02\)00905-X](https://doi.org/10.1016/S0921-5093(02)00905-X)
87. Dicarolo, J.A., Yun, H.-M., Morscher, G.N., Bhatt, R.T.: SiC/SiC Composites for 1200 °C and Above (2004). <http://www.sti.nasa.gov>
88. Rühle, M., Evans, A.G.: High toughness ceramics and ceramic composites. *Prog. Mater. Sci.* **33**(2), 85–167 (1989). [https://doi.org/10.1016/0079-6425\(89\)90005-4](https://doi.org/10.1016/0079-6425(89)90005-4)
89. Zhu, S., Mizuno, M., Nagano, Y., Cao, J., Kagawa, Y., Kaya, H.: Creep and fatigue behavior in an enhanced SiC/SiC composite at high temperature. *J. Am. Ceram. Soc.* **81**(9), 2269–2277 (1998). <https://doi.org/10.1111/J.1151-2916.1998.TB02621.X>
90. Lee, K.N., Miller, R., Jacobson, N.S.: New generation of plasma-sprayed mullite coatings on silicon carbide. *J. Am. Ceram. Soc.* **78**(3) (1995b). <https://ntrs.nasa.gov/api/citations/19960010009/downloads/19960010009.pdf>
91. Lee, K.N., Fox, D.S., Eldridge, J.I., Zhu, D., Robinson, R.C., Bansal, N.P., Miller, R.A.: Upper Temperature Limit of Environmental Barrier Coatings Based on Mullite and BSAS (2002). www.sti.nasa.gov
92. Lee, K.N., Fox, D.S., Bansal, N.P.: Rare earth silicate environmental barrier coatings for SiC/SiC composites and Si₃N₄ ceramics. *J. Eur. Ceram. Soc.* **25**(10), 1705–1715 (2005). <https://doi.org/10.1016/J.JEURCERAMSOC.2004.12.013>
93. Lee, K.N., Miller, R.A., Jacobson, N.S.: Plasma Sprayed Mullite Coatings on Silicon-Based Ceramics (Patent No. 5391404). United States Patent (1995a)
94. Guo, Q., He, W., He, J., Wen, J., Chen, W., Sun, J., Guo, H.: Characterization of Yb₂SiO₅-based environmental barrier coating prepared by plasma spray–physical vapor deposition. *Ceram. Int.* **48**(14), 19990–19999 (2022). <https://doi.org/10.1016/J.CERAMINT.2022.03.274>
95. Lee, K.N.: Key Durability Issues With Mullite-Based Environmental Barrier Coatings for Si-Based Ceramics (2000). <https://gasturbinespower.asmedigitalcollection.asme.org>
96. Lee, K.N., Miller, R.A.: Development and environmental durability of mullite and mullite/YSZ dual layer coatings for SiC and Si₃N₄ ceramics. *Surf. Coatings Technol.* **86–87**(PART 1), 142–148 (1996). [https://doi.org/10.1016/S0257-8972\(96\)03074-5](https://doi.org/10.1016/S0257-8972(96)03074-5)
97. He, M.Y., Hutchinson, J.W., Evans, A.G.: Simulation of Stresses and Delamination in a Plasma-Sprayed Thermal Barrier System Upon Thermal Cycling (n.d.). Retrieved 10 Mar 2023, from www.elsevier.com/locate/msea
98. Lee, K.N.: Protective coatings for gas turbines. In: *Coatings for Superalloy Components*, pp. 1–19 (2006). <https://www.netl.doe.gov/sites/default/files/gas-turbine-handbook/4-4-2.pdf>

99. Opila, E.J.: Oxidation and volatilization of silica-formers in water vapor. In: NASA (n.d.). Retrieved 10 Mar 2023, from <https://ntrs.nasa.gov/api/citations/20020070889/downloads/20020070889.pdf>
100. Richards, B.T., Sehr, S., De Franqueville, F., Begley, M.R., Wadley, H.N.G.: Fracture mechanisms of ytterbium monosilicate environmental barrier coatings during cyclic thermal exposure. *Acta Mater.* **103**, 448–460 (2016). <https://doi.org/10.1016/j.actamat.2015.10.019>
101. Zhu, D., Fox, D.S., Ghosn, L.J., Harder, B.: Creep Behavior of Hafnia and Ytterbium Silicate Environmental Barrier Coating Systems on SiC/SiC Ceramic Matrix Composites (n.d.)
102. Zhu, D., Lee, K., Miller, R.A.: Cyclic Failure Mechanisms of Thermal and Environmental Barrier Coating Systems Under Thermal Gradient Test Conditions (n.d.). Retrieved 10 Mar 2023, from <http://www.sti.nasa.gov>
103. Subanovic, M., Song, P., Wessel, E., Vassen, R., Naumenko, D., Singheiser, L., Quadackers, W.J.: Effect of exposure conditions on the oxidation of MCrAlY-bondcoats and lifetime of thermal barrier coatings—A review. *Mater. Technol.* **204**(6–7), 820–823 (2009). <https://doi.org/10.1016/j.surfcoat.2009.09.056>
104. Haubold, T., Wigren, J., Gualco, C.: Comparison of thermal cycling experiments on thick thermal barrier coatings. In: ITSC 1998, pp. 1617–1622. ASM International (1998). <https://doi.org/10.31399/asm.cp.itsc1998p1617>
105. Mehta, A., Vasudev, H., Singh, S.: Recent developments in the designing of deposition of thermal barrier coatings—A review. *Mater. Today Proc.* **26**, 1336–1342 (2020). <https://doi.org/10.1016/j.matpr.2020.02.271>
106. Torkashvand, K., Poursaeidi, E., Mohammadi, M.: Effect of TGO thickness on the thermal barrier coatings life under thermal shock and thermal cycle loading. *Ceram. Int.* **44**(8), 9283–9293 (2018). <https://doi.org/10.1016/j.ceramint.2018.02.140>
107. Keyvani, A., Saremi, M., Heydarzadeh Sohi, M., Valefi, Z.: A comparison on thermomechanical properties of plasma-sprayed conventional and nanostructured YSZ TBC coatings in thermal cycling. *J. Alloy. Compd.* **541**, 488–494 (2012). <https://doi.org/10.1016/j.jallcom.2012.06.062>
108. Zhang, Y., Jiang, H., Tian, S., Xu, W., Wang, T., Zhang, S., Zeng, S., Luo, W., Zhang, Y.: High temperature oxidation resistance of TNM alloy coated with/without 8YSZ/NiCoCrAlY thermal barrier coatings. *Appl. Surf. Sci.* **611**, 155704 (2023). <https://doi.org/10.1016/j.apsusc.2022.155704>
109. Karooglanli, A.C., Turk, A., Ozdemir, I., Ustel, F.: Comparison of oxidation and thermal shock performance of thermal barrier coatings. *Mater. Manuf. Process.* **30**(6), 717–723 (2015). <https://doi.org/10.1080/10426914.2014.952025>
110. Wang, L., Wang, Y., Sun, X.G., He, J.Q., Pan, Z.Y., Wang, C.H.: Thermal shock behavior of 8YSZ and double-ceramic-layer La₂Zr₂O₇/8YSZ thermal barrier coatings fabricated by atmospheric plasma spraying. *Ceram. Int.* **38**(5), 3595–3606 (2012). <https://doi.org/10.1016/j.ceramint.2011.12.076>
111. Pourbafrani, M., Shoja, R.R., Bakhshi, S.R., Loghman-Estarki, M.R., Jamali, H.: Effect of microstructure and phase of nanostructured YSZ thermal barrier coatings on its thermal shock behaviour. *Surf. Eng.* **31**(1), 64–73 (2015). <https://doi.org/10.1179/1743294414Y000000397>
112. Shi, M., Xue, Z., Zhang, Z., Ji, X., Byon, E., Zhang, S.: Effect of spraying powder characteristics on mechanical and thermal shock properties of plasma-sprayed YSZ thermal barrier coating. *Surf. Coatings Technol.* **395**(15) (2020). <https://doi.org/10.1016/j.surfcoat.2020.125913>
113. Bolcavage, A., Feuerstein, A., Foster, J., Moore, P.: Thermal shock testing of thermal barrier coating/bondcoat systems. *J. Mater. Eng. Perform.* **13**(4), 389–397 (2004). <https://doi.org/10.1361/10599490419883>
114. Sadri, E., Ashrafzadeh, F., Eslami, A., Jazi, H.S., Ehsaei, H.: Thermal shock performance and microstructure of advanced multilayer thermal barrier coatings with Gd₂Zr₂O₇ topcoat. *Surf. Coat. Technol.* **448**, 128892 (2022). <https://doi.org/10.1016/j.surfcoat.2022.128892>

115. Ma, X., Rivellini, K., Ruggiero, P., Wildridge, G.: Novel thermal barrier coatings with phase composite structures for extreme environment applications: concept, process, evaluation and performance. *Coatings* **13**(1), 210 (2023). <https://doi.org/10.3390/COATINGS13010210>
116. Yang, Z., Yang, K., Wang, W., Yang, T., Fang, H., Qiang, L., Zhang, X., Zhang, C.: Investigation of Thermal shock behavior of multilayer thermal barrier coatings with superior erosion resistance prepared by atmospheric plasma spraying. *Coatings* **12**(6), 804 (2022). <https://doi.org/10.3390/COATINGS12060804>
117. Guo, L., Li, B., Cheng, Y., Wang, L.: Composition optimization, high-temperature stability, and thermal cycling performance of Sc-doped Gd₂Zr₂O₇ thermal barrier coatings: theoretical and experimental studies. *J. Adv. Ceram.* **11**(3), 454–469 (2022). <https://doi.org/10.1007/S40145-021-0549-Z/METRICS>
118. Han, Y., Zong, P.-A., Huang, M., Yang, Z., Feng, Y., Pan, W., Zhang, P., & Wan, C.: In-situ synthesis of gadolinium niobate quasi-binary composites with balanced mechanical and thermal properties for thermal barrier coatings. *J. Adv. Ceram.* **2022**(9), 1445–1456 (n.d.). <https://doi.org/10.1007/s40145-022-0622-2>
119. Li, Y., Li, C.J., Zhang, Q., Xing, L.K., Yang, G.J.: Effect of chemical compositions and surface morphologies of MCrAlY coating on its isothermal oxidation behavior. *J. Therm. Spray Technol.* **20**(1–2), 121–131 (2011). <https://doi.org/10.1007/S11666-010-9590-0/METRICS>
120. Seo, D., Ogawa, K., Suzuki, Y., Ichimura, K., Shoji, T., Murata, S.: Comparative study on oxidation behavior of selected MCrAlY coatings by elemental concentration profile analysis. *Appl. Surf. Sci.* **255**(5), 2581–2590 (2008). <https://doi.org/10.1016/J.APSUSC.2008.07.141>
121. Toscano, J.: Influence of Composition and Processing on the Oxidation Behaviour of MCrAlY Coatings for TBC Applications (2008)
122. Viswanathan, V., Dwivedi, G., Sampath, S.: Engineered multilayer thermal barrier coatings for enhanced durability and functional performance. *J. Am. Ceram. Soc.* **97**(9), 2770–2778 (2014). <https://doi.org/10.1111/JACE.13033>
123. Yu, Z.X., Huang, J.B., Wang, W.Z., Yu, J.Y., Wu, L.M.: Deposition and properties of a multilayered thermal barrier coating. *Surf. Coat. Technol.* **288**, 126–134 (2016). <https://doi.org/10.1016/j.surfcoat.2016.01.001>
124. Zhong, J., Yang, D., Guo, S., Zhang, X., Liang, X., Wu, X.: Rear earth oxide multilayer deposited by plasma spray-physical vapor deposition for envisaged application as thermal/environmental barrier coating. *Coatings* **11**, 889 (2021). <https://doi.org/10.3390/COATINGS11080889>
125. Pan, Y., Liang, B., Niu, Y., Han, D., Liu, D., Zheng, X.: Research on thermal stability and properties of Ca₃ZrSi₂O₉ as potential T/EBC materials. *Coatings* **11**(5), 583 (2021). <https://doi.org/10.3390/COATINGS11050583>
126. Vassen, R., Cao, X., Tietz, F., Basu, D., Stöver, D.: Zirconates as new materials for thermal barrier coatings. *J. Am. Ceram. Soc.* **83**(8), 2023–2028 (2000). <https://doi.org/10.1111/J.1151-2916.2000.TB01506.X>
127. Kumar, R., Jordan, E., Gell, M., Roth, J., Jiang, C., Wang, J., Rommel, S.: CMAS behavior of yttrium aluminum garnet (YAG) and yttria-stabilized zirconia (YSZ) thermal barrier coatings. *Surf. Coat. Technol.* **327**, 126–138 (2017). <https://doi.org/10.1016/J.SURFCOAT.2017.08.023>
128. Carpio, P., Borrell, A., Salvador, M.D., Gómez, A., Martínez, E., Sánchez, E.: Microstructure and mechanical properties of plasma spraying coatings from YSZ feedstocks comprising nano- and submicron-sized particles. *Ceram. Int.* **41**(3), 4108–4117 (2015). <https://doi.org/10.1016/J.CERAMINT.2014.11.106>
129. Borom, M.P., Johnson, C.A., Peluso, L.A.: Role of environment deposits and operating surface temperature in spallation of air plasma sprayed thermal barrier coatings. *Surf. Coatings Technol.* **86–87**(PART 1), 116–126 (1996). [https://doi.org/10.1016/S0257-8972\(96\)02994-5](https://doi.org/10.1016/S0257-8972(96)02994-5)
130. Pujol, G., Ansart, F., Bonino, J.P., Malié, A., Hamadi, S.: Step-by-step investigation of degradation mechanisms induced by CMAS attack on YSZ materials for TBC applications. *Surf. Coat. Technol.* **237**, 71–78 (2013). <https://doi.org/10.1016/J.SURFCOAT.2013.08.055>

131. Smialek, J.L.: The Chemistry of Saudi Arabian Sand: A Deposition Problem on Helicopter Turbine Airfoils (1991)
132. Stott, F.H., De Wet, D.J., Taylor, R.: Degradation of thermal-barrier coatings at very high temperatures. *MRS Bull.* **19**(10), 46–49 (1994). <https://doi.org/10.1557/S0883769400048223>
133. Mohan, P., Yuan, B., Patterson, T., Desai, V.H., Sohn, Y.H.: Degradation of yttria-stabilized zirconia thermal barrier coatings by vanadium pentoxide, phosphorous pentoxide, and sodium sulfate. *J. Am. Ceram. Soc.* **90**(11), 3601–3607 (2007). <https://doi.org/10.1111/J.1551-2916.2007.01941.X>
134. Drexler, J.M., Shinoda, K., Ortiz, A.L., Li, D., Vasiliev, A.L., Gledhill, A.D., Sampath, S., Padture, N.P.: Air-plasma-sprayed thermal barrier coatings that are resistant to high-temperature attack by glassy deposits. *Acta Mater.* **58**(20), 6835–6844 (2010). <https://doi.org/10.1016/J.ACTAMAT.2010.09.013>
135. Chen, W.R., Zhao, L.R.: Review—volcanic ash and its influence on aircraft engine components. *Procedia Eng.* **99**, 795–803 (2015). <https://doi.org/10.1016/J.PROENG.2014.12.604>
136. Kadir, N., Garcia, E., Kirk, C., Gao, J., Guo, Z., Zhai, X., Sun, T., Fezzaa, K., Sampath, S., Chen, W.W.: Impact damage of narrow silicon carbide (SiC) ceramics with and without environmental barrier coatings (EBCs) by various foreign object debris (FOD) simulants. *Surf. Coat. Technol.* **407**, 126779 (2021). <https://doi.org/10.1016/J.SURFCOAT.2020.126779>
137. Sun, Z., Zhou, Y., Wang, J., Li, M.: γ -Y₂Si₂O₇, a machinable silicate ceramic: mechanical properties and machinability. *J. Am. Ceram. Soc.* **90**(8), 2535–2541 (2007). <https://doi.org/10.1111/J.1551-2916.2007.01803.X>
138. Kassem, R., Al Nasiri, N.: A comprehensive study on the mechanical properties of Yb₂SiO₅ as a potential environmental barrier coating. *Surf. Coat. Technol.* **426**, 127783 (2021). <https://doi.org/10.1016/J.SURFCOAT.2021.127783>
139. Zhong, X., Niu, Y., Li, H., Zeng, Y., Zheng, X., Ding, C., Sun, J.: Microstructure evolution and thermomechanical properties of plasma-sprayed Yb₂SiO₅ coating during thermal aging. *J. Am. Ceram. Soc.* **100**(5), 1896–1906 (2017). <https://doi.org/10.1111/JACE.14690>
140. Chen, L., Hu, M., Feng, J.: Mechanical properties, thermal expansion performance and intrinsic lattice thermal conductivity of AlMO₄ (M=Ta, Nb) ceramics for high-temperature applications. *Ceram. Int.* **45**(6), 6616–6623 (2019). <https://doi.org/10.1016/J.CERAMINT.2018.12.135>
141. Hu, Q., Zhou, X., Tu, Y., Lu, X., Huang, J., Jiang, J., Deng, L., Dong, S., Cao, X.: High-temperature mechanical properties and oxidation resistance of SiCf/SiC ceramic matrix composites with multi-layer environmental barrier coatings for turbine applications. *Ceram. Int.* **47**(21), 30012–30019 (2021). <https://doi.org/10.1016/J.CERAMINT.2021.07.176>
142. Zhao, H., Richards, B.T., Levi, C.G., Wadley, H.N.G.: Molten silicate reactions with plasma sprayed ytterbium silicate coatings. *Surf. Coat. Technol.* **288**, 151–162 (2016). <https://doi.org/10.1016/J.SURFCOAT.2015.12.053>
143. Li, H., Yu, Y., Fang, B., Xiao, P., Wang, S.: Study on properties of Hf₆Ta₂O₁₇/Ta₂O₅ system: a potential candidate for environmental barrier coating (EBC). *J. Eur. Ceram. Soc.* **42**(11), 4651–4662 (2022). <https://doi.org/10.1016/J.JEURCERAMSOC.2022.04.034>
144. Lee, K.N., Jacobson, N.S., Miller, R.A.: Refractory Oxide Coatings on SiC Ceramics. *MRS Bull.* **19**(10), 35–38 (1994). <https://doi.org/10.1557/S088376940004820X>
145. Al Nasiri, N., Patra, N., Jayaseelan, D.D., Lee, W.E.: Water vapour corrosion of rare earth monosilicates for environmental barrier coating application. *Ceram. Int.* **43**(10), 7393–7400 (2017). <https://doi.org/10.1016/J.CERAMINT.2017.02.123>
146. Li, G., Qin, L., Cao, X., Lu, X., Tu, Y., Zhang, H., Jiang, J., Deng, L., Dong, S., Liu, L., An, W.: Water vapor corrosion resistance and failure mechanism of SiCf/SiC composites completely coated with plasma sprayed tri-layer EBCs. *Ceram. Int.* **48**(5), 7082–7092 (2022). <https://doi.org/10.1016/J.CERAMINT.2021.11.267>
147. Richards, B.T., Young, K.A., De Francqueville, F., Sehr, S., Begley, M.R., Wadley, H.N.G.: Response of ytterbium disilicate–silicon environmental barrier coatings to thermal cycling in water vapor. *Acta Mater.* **106**, 1–14 (2016). <https://doi.org/10.1016/J.ACTAMAT.2015.12.053>

148. Chen, Z., Tian, Z., Zheng, L., Ming, K., Li, B.: Thermo-mechanical properties and CMAS resistance of (Ho_{0.4}Yb_{0.3}Lu_{0.3})₂SiO₅ solid solution for environmental barrier coating applications. *Ceram. Int.* **49**(4), 6429–6439 (2023). <https://doi.org/10.1016/J.CERAMINT.2022.10.266>
149. Lackey, W.J., Stinton, D.P., Cerny, G.A., Schaffhauser, A.C., Fehrenbacher, L.L.: Ceramic coatings for advanced heat engines—a review and projection. *Adv. Ceram. Mater. (USA)* **2**(1), 24–30 (1987). <https://doi.org/10.1111/J.1551-2916.1987.TB00048.X>
150. Deijkers, J.A., Wadley, H.N.G.: A duplex bond coat approach to environmental barrier coating systems. *Acta Mater.* **217**, 117167 (2021). <https://doi.org/10.1016/J.ACTAMAT.2021.117167>
151. Stein, Z., Kinzel, M.P., Tetard, L., Raghavan, S.: CMAS Infiltration and Mitigation Strategies for Minimizing Premature Degradation Failure of High Temperature Ceramic Coatings in Turbine Engines (2023). <https://doi.org/10.2514/6.2023-0179>
152. He, L., Pan, L., Zhou, W., Niu, Z., Chen, X., Chen, M., Zhang, Q., Pan, W., Xiao, P., Li, Y.: Thermal corrosion behavior of Yb₄Hf₃O₁₂ ceramics exposed to calcium-ferrum-alumina-silicate (CFAS) at 1400 °C. *J. Eur. Ceram. Soc.* (2023). <https://doi.org/10.1016/J.JEURCERAMSOC.2023.02.041>
153. Liu, S., Liu, Q., Hu, X., Guo, J., Zhu, W., Zhang, F., Xia, J.: CMAS corrosion resistance behavior and mechanism of Hf₆Ta₂O₁₇ ceramic as potential material for thermal barrier coatings. *Coatings* **13**(2), 404 (2023). <https://doi.org/10.3390/COATINGS13020404>
154. Pakseresht, A., Sharifianjazi, F., Esmailkhanian, A., Bazli, L., Reisi Nafchi, M., Bazli, M., Kirubakaran, K.: Failure mechanisms and structure tailoring of YSZ and new candidates for thermal barrier coatings: a systematic review. *Mater. Des.* **222**, 111044 (2022). <https://doi.org/10.1016/J.MATDES.2022.111044>
155. Rudrapatna, N., Lutz, B., Kington, H.: Next generation air plasma spray porous thermal barrier coatings for gas turbine combustors. *J. Eng. Gas Turbines Power* **145**(4), 041004 (2023). <https://doi.org/10.1115/1.4055919/1147459>
156. Maev, R.G., Tjong, J., Leshchinsky, E., Pantea, M., Leshchynsky, V.: Cold-sprayed multilayer thermal barrier–catalytic coatings for engine pistons: coatings design and properties. *Coatings* **12**(9), 1332 (2022). <https://doi.org/10.3390/COATINGS12091332>

Environmental Barrier Coatings

Environmental Barrier Coatings (EBCs) for Ceramic Matrix Composites



Feifei Zhou and Donghui Guo

Abstract With the rapid improvement of thrust-to-weight ratio of aeroengine, the internal temperature of aeroengine also gradually increases. Ceramic matrix composites (CMCs) react with water vapor and various molten salt impurities in the gas combustion environments, causing the rapid consumption of CMCs. To solve this problem, it is necessary to prepare the environmental barrier coatings (EBCs) on the surface of CMCs. To date, EBCs have experienced three generations of development. The first generation is a double-layer structure with mullite as the bonding layer and YSZ (7 wt.%) as the ceramic layer. The YSZ surface layer has an unavoidable penetrating crack due to the large difference in thermal expansion coefficient between the CMCs and YSZ. The second generation is a multi-layer structure coating with silicon and mullite as the bonding layer and $\text{Ba}_x\text{Sr}_{1-x}\text{Al}_2\text{Si}_2\text{O}_8$ (BSAS) as the ceramic layer. However, they can only be used below 1300 °C due to the poor chemical stability. As the third generation of EBCs materials, rare earth silicate ceramics have attracted the attention owing to their high melting point, excellent high-temperature phase stability, and corrosion resistance. Therefore, the selection and development of high-performance EBCs materials has become the top priority in the field of EBCs.

Keywords Environmental barrier coatings · Ceramic matrix composites · Rare earth silicate · Water oxygen corrosion · High-temperature oxidation

F. Zhou (✉)

School of Materials Science and Engineering, Harbin Institute of Technology, Harbin 150001, People's Republic of China
e-mail: snowy_hit@163.com

Zhengzhou Research Institute, Harbin Institute of Technology, Zhengzhou 450000, People's Republic of China

D. Guo

Institute of Advanced Structure Technology, Beijing Institute of Technology, Beijing, People's Republic of China

© The Author(s), under exclusive license to Springer Nature Switzerland AG 2024

215

A. Pakseresht and K. K. Amirtharaj Mosas (eds.), *Ceramic Coatings for High-Temperature Environments*, Engineering Materials, https://doi.org/10.1007/978-3-031-40809-0_7

1 Application Background of EBCs

The power equipment of aeroengines and gas turbines is an important symbol of a country's scientific, technological, industrial, economic, and national defense strength. The thrust-to-weight ratio is an important index to measure the working capacity of an aeroengine. Increasing the temperature in front of the turbine is the main way to achieve high thrust-to-weight ratio of an aeroengine [1–3]. There are three main ways to improve the thrust-to-weight ratio of the engine: to increase the pressure ratio of the press, to increase the inlet temperature in front of the turbine, and to reduce the structural weight of the engine and the aircraft as a whole. Because the cost of increasing the turbocharging ratio and the design cycle is longer, the performance is mainly improved by increasing the inlet temperature in front of the turbine and reducing the structure quality, which will put a serious test on the materials. At present, the inlet temperature of the turbine engine with a thrust-to-weight ratio of 10 has reached nearly 1750 °C, and the temperature of the tail nozzle is about 1200 °C. The thrust-to-weight ratio of the next-generation high-performance engine can reach 15–20, so the inlet temperature before the turbine will also reach 2100 °C.

Silicon carbide ceramic matrix composites (SiC-CMC) have many excellent characteristics, such as low density (2–2.5 g/cm³), high specific strength (tensile strength, ≥ 200 MPa), high specific modulus (≥ 50 GPa), insensitivity to cracks, high temperature resistance, and chemical corrosion resistance [4, 5]. It is one of the most potential structural materials to replace superalloys in the future. So far, SiC-CMC mainly focuses on carbon fiber-reinforced silicon carbide (C_f/SiC) and silicon carbide fiber-reinforced silicon carbide (SiC_f/SiC). Because the latter has more excellent oxidation resistance, SiC_f/SiC materials are more ideal application materials for high-performance aeroengine hot end components. Although SiC_f/SiC materials have excellent high-temperature mechanical properties and oxidation resistance, aircraft engines use kerosene as fuel, and the combustion products contain a lot of water vapor and excessive oxygen. Under the erosion of the gas, SiC_f/SiC materials also face serious corrosion problems [6–8]. The protective oxidation product SiO₂ generated by SiC under high temperature will react with surrounding water vapor to generate volatile substances such as Si(OH)₄, which will lead to the rapid consumption of matrix materials, which is one of the main reasons limiting the application of SiC_f/SiC materials at present [9]. In order to solve this problem, it is necessary to prepare a water oxygen corrosion resistant coating on the surface of SiC_f/SiC materials, namely environmental barrier coatings (EBCs).

EBCs have been developed for three generations, as shown in Fig. 1. At present, the main systems are Si bonding layer and rare earth silicate surface layer. With the continuous improvement of service temperature of high-performance engines in the future, its temperature exceeds 1400 °C and is close to or above the melting point of Si. The environmental barrier coating system with Si as the bonding layer cannot meet the requirements of long-term service at high temperature. At the same time, the single-component rare earth silicate has poor comprehensive performance under high-temperature environment.

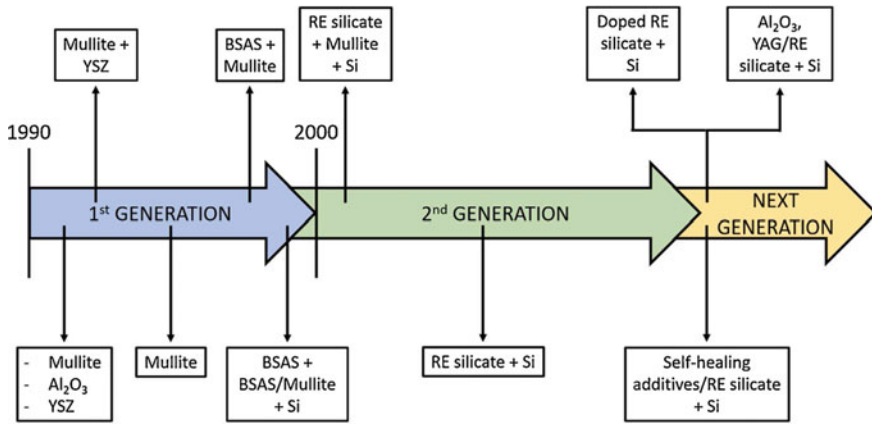


Fig. 1 Evolution timeline of EBC design [9]

Therefore, the future development trend of environmental barrier coatings mainly includes: (1) From the perspective of environmental barrier coating materials, it mainly includes the modification of Si bonding layer and rare earth silicate surface layer. The modification of Si bonding layer mainly includes HfO₂, Yb-Gd, and other modifiers to improve its melting point and bonding strength; the modification of rare earth silicate surface layer mainly includes the nanocrystallization of surface material and the use of high-entropy rare earth silicate system to improve its water oxygen corrosion resistance, thermophysical properties, and chemical stability; (2) From the perspective of environmental barrier coating structure, it mainly includes multi-layer structure and thermal/environmental barrier coating system. Among them, multi-layer structure refers to the composition gradual/continuous transition (so-called gradient structure) between the Si layer and the rare earth silicate surface layer; thermal/environmental barrier coating system refers to the application of thermal barrier coating on the basis of rare earth silicate surface layer to improve its thermal insulation and CMAS corrosion resistance. The thermal barrier coating mainly includes rare earth zirconate, rare earth hafnate, ytterbium aluminum garnet, etc.; (3) From the perspective of the preparation process of environmental barrier coatings, the plasma spraying physical vapor deposition (PS-PVD) based on the development of low-pressure plasma spraying technology combines the advantages of atmospheric plasma spraying (APS) and electron beam physical vapor deposition (EB-PVD). Through process adjustment, the gas, liquid, and solid multiphase deposition of spraying powder can be realized, and the structural and functional coatings with different requirements can be prepared. This technology has high deposition efficiency and can realize non-line of sight deposition. It has great advantages in preparing environmental barrier coatings for complex-shaped components with uniform thickness and structure. Therefore, PS-PVD has become one of the most promising methods for preparing high-performance environmental barrier coatings in the future.

2 Material Systems of EBCs

2.1 Mullite and YSZ

The natural mullite was first discovered in Malle Island, Scotland, in 1924. Mullite, as an aluminosilicate mineral, is composed of $3\text{Al}_2\text{O}_3 \cdot 2\text{SiO}_2$. It is an important ceramic material, which is the main component for preparing ceramics, porcelain, refractory materials, and clay hollow products. Mullite has the advantages of low density, similar coefficient of thermal expansion (CTE, $5 \times 10^{-6} \cdot \text{K}^{-1}$) to silicon-based matrix, and good chemical compatibility with the matrix [10]. It was first used as an environmental barrier coating. The research shows that mullite can combine well with the matrix and has a certain blocking effect on the high-temperature gas environment. After the mullite coating is prepared by atmospheric plasma spraying, the silicon-based substrate with mullite coating is heated to the crystallization temperature of amorphous mullite (1000 °C), so as to successfully obtain a stable crystalline mullite coating. And the number of cracks in the coating is greatly reduced. Figure 2a shows the section morphology of mullite coating after two cycles (24 h/cycle) from room temperature to 1000 °C. It can be seen from Fig. 2b that after two cycles of examination from room temperature to 1000 °C, the amorphous mullite coating is full of cracks, while the crystalline mullite coating only has a few cracks. This shows that crystallization plays an important role in improving the effective service time of mullite coating.

However, the activity of SiO_2 in mullite is high, and it will react with H_2O to generate volatile $\text{Si}(\text{OH})_4$ in high-temperature gas environment, resulting in porous Al_2O_3 on the surface of mullite coating, providing a channel for high-temperature water vapor to attack the silicon-based matrix. YSZ has better stability than mullite in high-temperature water and oxygen environment, but CTE is quite different from CTE of silicon matrix. Large differences in CTE will reduce the bonding strength between the coating and the substrate, so it is necessary to add mullite coating with moderate CTE between the substrate and the YSZ coating to alleviate the impact of CTE mismatch between the YSZ surface layer and the substrate on the bonding

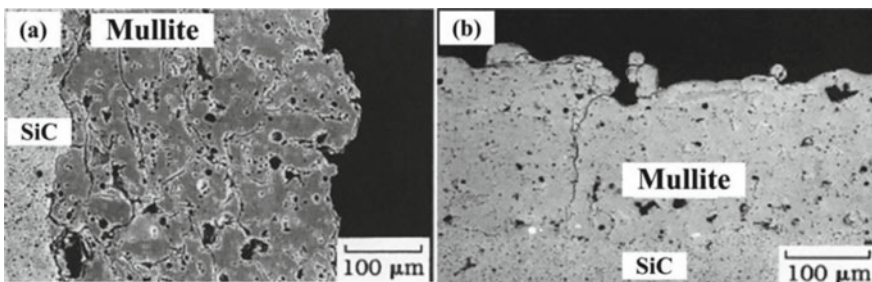


Fig. 2 Section morphology of mullite coating after 2 cycles (24 h/cycle) from room temperature to 1000 °C. **a** Conventional coating; **b** fully crystalline coating [11]

strength of the coating. The assessment found that due to the stronger resistance to water and oxygen corrosion of YSZ, the resistance to water and oxygen corrosion of mullite/YSZ system was greatly improved compared with that of single-layer mullite coating. However, due to the high CTE of YSZ (about twice higher than that of mullite and SiC), the coating cracked during multiple thermal cycles, which made the development of EBC coating encounter a bottleneck.

2.2 $Ba_xSr_{1-x}Al_2Si_2O_8$ (BSAS)

BSAS has lower SiO_2 activity, lower thermal expansion coefficient ($4\text{--}5 \times 10^{-6} \cdot K^{-1}$) and elastic modulus (≤ 50 GPa), and better physical and chemical compatibility with SiC matrix, which meets all requirements of engine gas environment for environmental barrier coating materials, and has become the research focus of environmental barrier coating at present [12, 13].

The preparation methods of BSAS spray powder can be divided into powder granulation process, granulation and sintering process, and melting and crushing process. Powder granulation is to use $BaCO_3$, $SrCO_3$, Al_2O_3 , and silica sol as raw materials. Firstly, the mixed powders are calcined for 3 h at $1300^\circ C$ by solid state reaction. Then, slurry is prepared with binder and water in a certain proportion. Finally, spray granulation is conducted to obtain BSAS powders. Granulation and sintering is first to prepare slurry in a certain proportion. Subsequently, original material microspheres are obtained by spray granulation. Finally, the BSAS powders are calcined at $1300^\circ C$ for 3 h.

The monoclinic BSAS spray powder can be successfully prepared by both the powder granulation process and the granulation and sintering process. From SEM, it can be seen that the BSAS powder prepared by melting and crushing methods has an irregular shape and incomplete grain development as shown in Fig. 3. The thermal expansion test curves of different BSAS spraying powders are shown in Fig. 4. Within the range from room temperature to $1200^\circ C$, and the thermal expansion coefficient after powder granulation and granulation sintering is $5.02 \times 10^{-6}/^\circ C^{-1}$, thermal expansion coefficient after melting and crushing is $5.39 \times 10^{-6}/^\circ C^{-1}$, which matches the thermal expansion coefficient of SiC ceramics and SiC ceramic composites, which also verifies the feasibility of monoclinic BSAS powder as the EBC coating material.

In short, BSAS has the advantages of low modulus of elasticity, coefficient of thermal expansion, and good compatibility with mullite, which makes the coating produce small thermal stress during thermal cycling, and greatly inhibits the generation of cracks.

BSAS, which is closer to mullite CTE, is used to replace the YSZ surface coating. Due to the short length of Si–O bond in BSAS, the material itself has high resistance to water and oxygen corrosion. In addition, the glass with good fluidity produced by the reaction of BSAS and SiO_2 has a good sealing effect on the cracks in the coating. Through diffusion couple experiments, it is found that mullite and SiC are mechanically bound, and there is no close chemical binding. Therefore, in order to improve

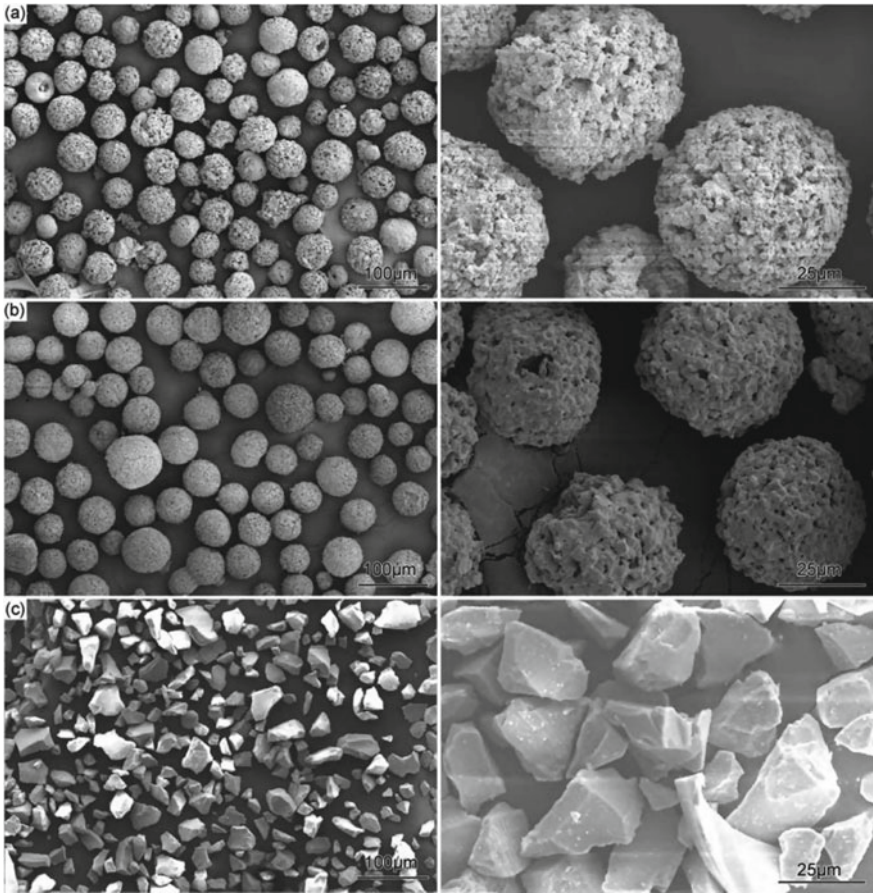


Fig. 3 SEM of different BSAS spraying powders. **a** Powder granulation; **b** granulation sintering, and **c** melting crushing [14]

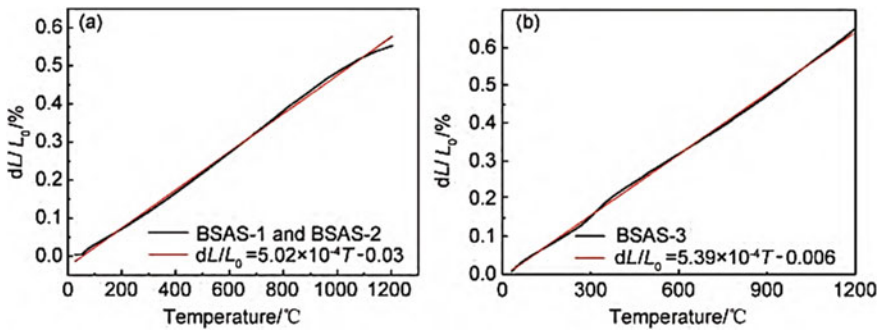


Fig. 4 Curve of thermal expansion coefficient of different powders. **a** Powder granulation and granulation sintering, **b** melt crushing [14]

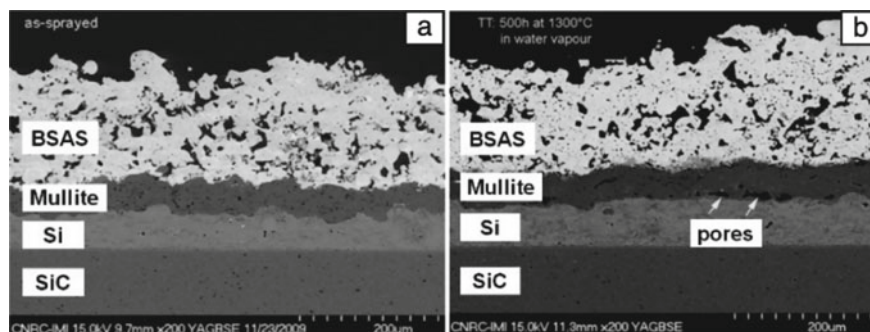


Fig. 5 Section morphology of Si/mullite/BSAS coating. **a** as sprayed, **b** water oxygen corrosion at 1300 °C for 500 h [15]

the binding force between EBCs and SiC matrix, Si with better chemical compatibility with SiC is introduced into the EBCs system as the bonding layer. Si/mullite/BSAS coating was prepared on the surface of SiC substrate by APS technology, as shown in Fig. 5. The introduction of Si bonding layer significantly improves the bonding between EBCs and matrix. Compared with the YSZ surface layer, the structural compactness of the BSAS surface layer has not been significantly improved, but the pores are mostly closed, which further strengthens the water oxygen barrier ability of EBCs. After 500 h of corrosion in water and oxygen environment at 1300 °C, the coating still maintains good structural stability, without obvious longitudinal cracks and peeling, and only a small amount of pores appear at the interface between mullite layer and Si bonding layer, as shown in Fig. 5b.

As a surface layer material for EBCs, the factors limiting its application mainly include the following two points: Firstly, BSAS will undergo degradation due to volatilization under high-temperature conditions (exceed 1300 °C). Lee et al. [12] estimated the degradation size of BSAS coatings after 1000 h of service under conditions of a total environmental pressure of 0.6 MPa, a partial water vapor pressure of 0.06 MPa, and a gas flow rate of 24 m/s through simulation as shown in Table 1. When the ambient temperature is 1500 °C, the BSAS coating deteriorates to 268 μm . This thickness far exceeds the thickness of the coating itself, and its degradation will be even more severe in high-pressure environments. Secondly, the BSAS coating will react with SiO_2 in the mullite coating at high temperatures to form a glass phase, reducing its melting temperature. Therefore, the long-term service temperature of the Si/mullite/BSAS coating system is relatively low, and the maximum service temperature is limited to 1300 °C.

Table 1 Predicted degradation of BSAS coating exposing in simulated combustion environment

Temperature/°C	1300	1400	1500
Weight loss/[$\times 10^{-4}$ mg/(cm^2 h)]	2.4	5.7	23
Predicted degradation size/ μm	28	67	268

2.3 Rare Earth Silicate

Among the rare earth silicates composed of rare earth oxide RE_2O_3 (RE is rare earth) and binary oxide SiO_2 , the most common ones are rare earth silicates with the ratio of 1:1, 1:2 and 7:9. According to the different ionic radii of rare earth elements, rare earth silicates can form a variety of polymorphic phases. The compound with the ratio of RE_2O_3 : SiO_2 (1:1) has two kinds of polymorphic phases. The one with larger radius of rare earth ions forms X1 phase, and the one with smaller radius of rare earth ions forms X2 phase as shown in Fig. 6. Seven polymorphous phases have been found in the compound with the ratio of 1:2. Finally, most of the compounds with the ratio of RE_2O_3 : SiO_2 (7:9) can generate $\text{RE}_{9.33}(\text{SiO}_4)_6\text{O}_2$ phase.

Rare earth silicate, with its good phase stability and corrosion resistance, has become a hot material for silicon-based ceramic environmental barrier coating. Among them, rare earth bisilicate $\text{RE}_2\text{Si}_2\text{O}_7$ has three obvious characteristics. First, because the structure symmetry of $\text{RE}_2\text{Si}_2\text{O}_7$ is low and the crystal structure is complex, the thermal conductivity is low. Second, $\text{Yb}_2\text{Si}_2\text{O}_7$ and $\text{Lu}_2\text{Si}_2\text{O}_7$ have no phase transition and have excellent phase stability. They are the only two types of materials with unique stable structure in $\text{RE}_2\text{Si}_2\text{O}_7$. Third, there are more rare earth elements in the middle of the ionic radius of lanthanide rare earth elements. Among them, the most typical rare earth silicate is ytterbium silicate.

Yb_2SiO_5 is composed of Si–O tetrahedron and Yb–O polyhedron and has two monoclinic crystal forms. The crystal structure of X2- Yb_2SiO_5 is shown in Fig. 7. In the crystal structure of Yb_2SiO_5 , there are 64 atoms in a unit cell, consisting of 2 Yb atomic positions, 1 Si atomic position, and 5 O atomic positions. In the case of $\text{Yb}_2\text{Si}_2\text{O}_7$, β phase in a wide temperature range (space group C2/m) is stable. Figure 8a shows the crystal structure of β - $\text{Yb}_2\text{Si}_2\text{O}_7$, which is the conformal SiO_4 tetrahedron (or Si_2O_7) connected by YbO_6 unit. Figure 8b–d are the projection of β - $\text{Yb}_2\text{Si}_2\text{O}_7$ atoms on (001), (010), and (100) planes, respectively.

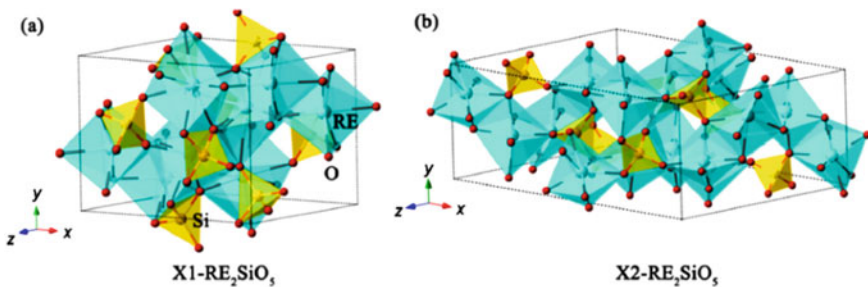


Fig. 6 Crystal structure of a X1- RE_2SiO_5 and b X2- RE_2SiO_5 [16]

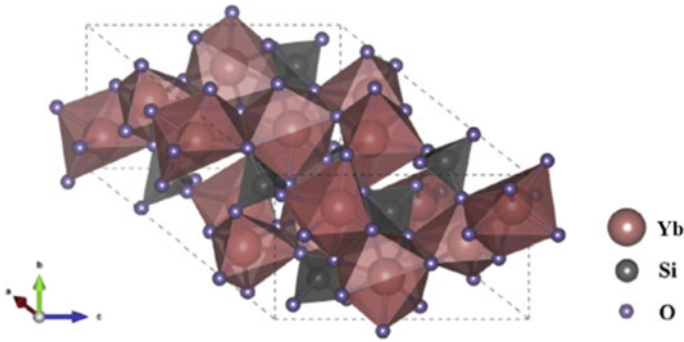


Fig. 7 Monoclinic crystal structure of X₂-Yb₂SiO₅ [17]

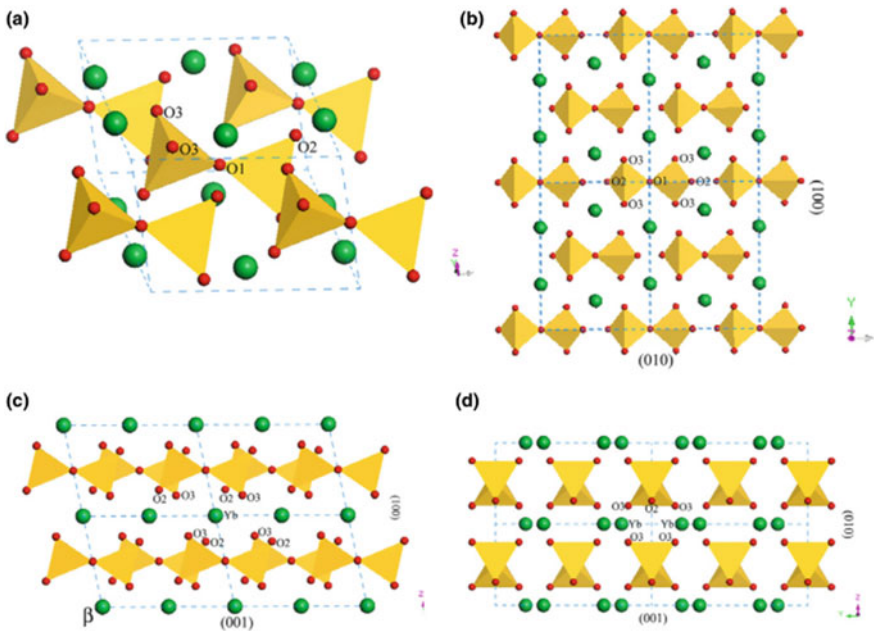


Fig. 8 a Crystal structure; b–d The projection of β -Yb₂Si₂O₇ atoms on (001), (010), and (100) planes, respectively [18]

2.4 High-Entropy Rare Earth Silicate and Modification of Si Layer

The new concepts of high-entropy ceramics and high-entropy design provide new ideas and new opportunities for people to design multi-component/high-entropy rare

earth silicate materials in the whole system of rare earth and to carry out the composition design and performance control of high-entropy rare earth silicate coating materials. Previous studies have shown that the key properties of rare earth silicate materials, such as CTE and high-temperature phase stability, are directly related to the types of rare earth elements [19]. The light or heavy rare earth elements in the first half cycle and the second half cycle can play a decisive role in the macroscopic properties of materials and have their own advantages, which provide the possibility and guiding principle for the design of multi-component rare earth/high-entropy compounds.

In recent years, researchers have tried to optimize the properties of rare earth silicate materials by using the high-entropy strategy. The high-entropy rare earth bisilicate $(\text{Yb}_{0.2}\text{Y}_{0.2}\text{Lu}_{0.2}\text{Sc}_{0.2}\text{Gd}_{0.2})_2\text{Si}_2\text{O}_7$ coating has excellent phase stability in the range of room temperature to 1300 °C and has a good match with the thermal expansion of silicon carbide matrix composites [20]. It also shows better resistance to water vapor corrosion at 1250 °C, 50% H_2O –50% O_2 water vapor environment. High-entropy rare earth silicate $(\text{Yb}_{0.25}\text{Y}_{0.25}\text{Lu}_{0.25}\text{Er}_{0.25})_2\text{SiO}_5$ has good phase stability and strong thermal expansion anisotropy in the range of room temperature to 1200 °C [21]. It is possible to match the thermal expansion of silicon carbide matrix composites by controlling the preferred orientation of the coating. In general, the performance optimization of rare earth silicate is expected to be realized through reasonable high-entropy design, and the space for performance control is relatively broad.

It can be seen from Fig. 9 that the single-phase high-entropy rare earth monosilicate $(\text{Y}_{1/4}\text{Ho}_{1/4}\text{Er}_{1/4}\text{Yb}_{1/4})_2\text{SiO}_5$ ($(4\text{RE}_{1/4})_2\text{SiO}_5$) material is $\text{X}2\text{-RE}_2\text{SiO}_5$, and the four rare earth element ions are uniformly distributed randomly at the atomic scale, which proves that the material is single phase rare earth monosilicate and high-entropy [10]. The CTE of $(4\text{RE}_{1/4})_2\text{SiO}_5$ in the range of room temperature to 1200 °C is significantly lower than that of four mono-component rare earth silicates RE_2SiO_5 ($\text{RE} = \text{Y}, \text{Ho}, \text{Er}$ and Yb), with a reduction of about 11–19%. The room-temperature thermal conductivity of $(4\text{RE}_{1/4})_2\text{SiO}_5$ is 5.40–66.8% lower than that of four kinds of single-component rare earth silicate RE_2SiO_5 . The synergetic reduction of CTE and thermal conductivity can make the CTE of high-entropy $(4\text{RE}_{1/4})_2\text{SiO}_5$ match well with SiC_f/SiC matrix, which can provide better thermal barrier while effectively reducing the stress of EBC.

To improve the life of EBC, a reasonable method is to reduce the growth rate of thermally grown oxide (TGO). As for thermal barrier coating (TBC), the life of TBC is significantly increased by reducing the TGO growth rate of the bonding layer. Therefore, there is a way to reduce the permeability of oxidant through the coating. The failure due to TGO growth can be inhibited by reducing the oxidant reaching the surface of TGO or reducing the thermal mechanical stress generated in the coating during cooling.

Recently, a study on the oxidation of silicon particles dispersed in HfO_2 matrix proposed a method to reduce the thermo-mechanical driving force [23]. Oxidation of silicon particles above 1250 °C initially result in the formation of silicon particles β -cristobalite SiO_2 and then react with monoclinic HfO_2 to form HfSiO_4 . Thermal

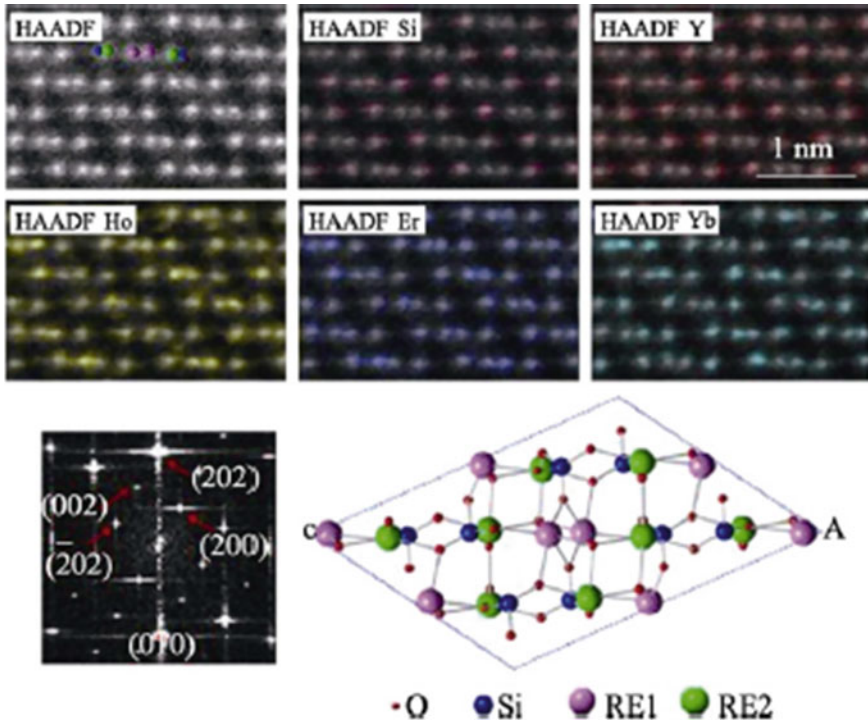


Fig. 9 HAADF-STEM photos of high-entropy rare earth monosilicate $(Y_{1/4}Ho_{1/4}Er_{1/4}Yb_{1/4})_2SiO_5$ and its atomic-scale element distribution [22]

expansion coefficient CTE of $HfSiO_4$ ($3.6 \times 10^{-6} \text{ }^\circ\text{C}^{-1}$) is similar to silicon ($4.1 \times 10^{-6} \text{ }^\circ\text{C}^{-1}$) and SiC ($4.7 \times 10^{-6} \text{ }^\circ\text{C}^{-1}$) [24], and the conversion of SiO_2 to $HfSiO_4$ may reduce the TGO-induced storage strain energy and delay the coating delamination. In addition, some researchers first prepare composite powder and then prepare corresponding coating. Figure 10 shows the morphologies of the HfO_2 - SiO_2 pre-mixed powders.

2.5 Aluminate

In RE_2O_3 - Al_2O_3 system, there are mainly $REAlO_3$ with perovskite structure, $RE_3Al_5O_{12}$ with garnet structure and $RE_4Al_2O_9$ with monoclinic structure. When $RE_2O_3:Al_2O_3 = 2:1$, rare earth aluminates with the molecular formula of $RE_4Al_2O_9$ can be produced ($RE = La, Nd, Eu, Gd, Tb, Dy, Ho, Er, Yb, Lu$ and Y). $RE_4Al_2O_9$ series of compounds have similar crystal structure and belong to monoclinic system. The space group is $P2_1/c$. The lattice constant decreases with the increase of atomic number, as shown in Table 2.

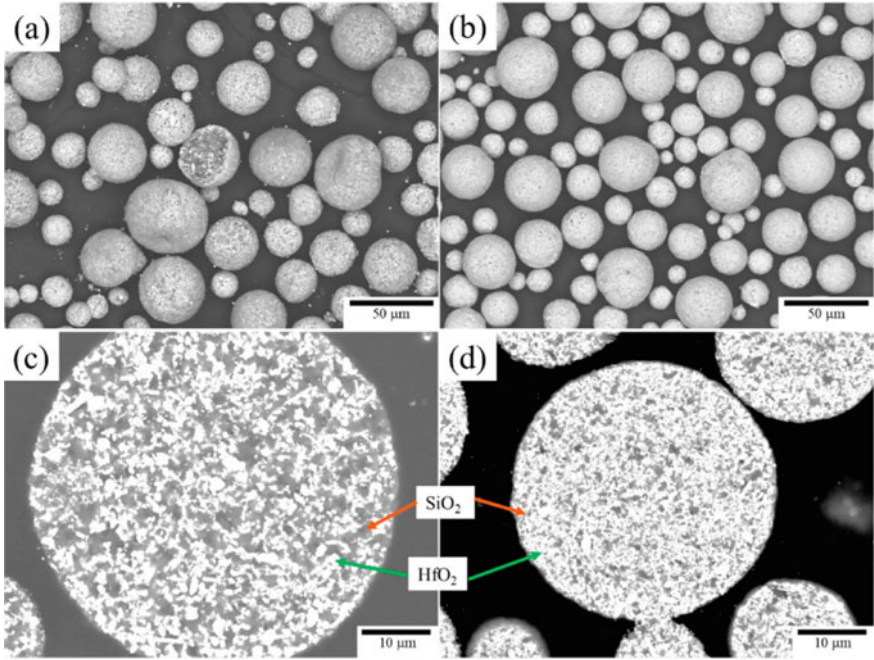


Fig. 10 Morphologies of $\text{HfO}_2\text{-SiO}_2$ pre-mixed powders. **a, c** $5\text{HfO}_2\text{-}5\text{SiO}_2$ powders, **b, d** $7\text{HfO}_2\text{-}3\text{SiO}_2$ powders [25]

Table 2 Crystal structure of $\text{RE}_4\text{Al}_2\text{O}_9$ [26]

Compound	Space group	Crystal structure	Lattice parameter				
			a (Å)	b (Å)	c (Å)	β (deg)	V (Å ³)
$\text{La}_4\text{Al}_2\text{O}_9$	$P2_1/c$	Monoclinic	7.970	11.090	11.410	108.800	954.7
$\text{Nd}_4\text{Al}_2\text{O}_9$	$P2_1/c$	Monoclinic	7.720	10.840	11.300	109.500	891.4
$\text{Sm}_4\text{Al}_2\text{O}_9$	$P2_1/c$	Monoclinic	7.635	10.730	11.234	109.237	869.0
$\text{Eu}_4\text{Al}_2\text{O}_9$	$P2_1/c$	Monoclinic	7.586	10.684	11.202	109.127	857.9
$\text{Gd}_4\text{Al}_2\text{O}_9$	$P2_1/c$	Monoclinic	7.533	10.635	11.206	108.976	849.1
$\text{Tb}_4\text{Al}_2\text{O}_9$	$P2_1/c$	Monoclinic	7.483	10.563	11.161	108.888	834.8
$\text{Dy}_4\text{Al}_2\text{O}_9$	$P2_1/c$	Monoclinic	7.435	10.520	11.127	108.746	824.2
$\text{Ho}_4\text{Al}_2\text{O}_9$	$P2_1/c$	Monoclinic	7.384	10.469	11.115	108.618	814.3
$\text{Er}_4\text{Al}_2\text{O}_9$	$P2_1/c$	Monoclinic	7.338	10.421	11.093	108.489	804.5
$\text{Yb}_4\text{Al}_2\text{O}_9$	$P2_1/c$	Monoclinic	7.263	10.337	11.026	108.293	786.0
$\text{Lu}_4\text{Al}_2\text{O}_9$	$P2_1/c$	Monoclinic	–	–	–	–	–
$\text{Y}_4\text{Al}_2\text{O}_9$	$P2_1/c$	Monoclinic	7.375	10.462	11.110	108.575	812.6

The rare earth aluminate $RE_4Al_2O_9$ has the advantages of high melting point, good high-temperature stability, low Young's modulus, low thermal conductivity, similar thermal expansion coefficient and weak anisotropy to mullite and is considered to be an environmental barrier coating outer material with important application prospects. From the phase diagram of RE_2O_3 - Al_2O_3 system, it can be seen that $RE_4Al_2O_9$ is stable in other systems except La_2O_3 - Al_2O_3 system. In addition to $Y_4Al_2O_9$, other $RE_4Al_2O_9$ ($RE = Sm, Eu, Gd, Tb$) after heat treatment at 1000 °C for 200 h appear $REAlO_3$ phase. According to the different content of $REAlO_3$ phase, the thermal stability order of $RE_4Al_2O_9$ ($RE = Y, Sm, Eu, Gd, Tb$) can be described as follows: $Y_4Al_2O_9 > Eu_4Al_2O_9 > Gd_4Al_2O_9 > Tb_4Al_2O_9 > Sm_4Al_2O_9$. In addition, the study found that the phase transition temperature of $Y_4Al_2O_9$ is 1377 °C, which indicates that the phase transition temperature is not only related to the radius of the cation, but also related to the electronic structure of the cation.

At present, the environmental barrier coating matched with silicon-based ceramics and its composites is usually composed of three layers: outer layer, mullite inner layer, and silicon adhesive layer. Among them, the outer layer materials that are widely studied are rare earth silicate, mainly Yb_2SiO_5 and $Yb_2Si_2O_7$. However, due to the strong anisotropy of its elastic modulus and thermal expansion coefficient, its application is limited. The Young's modulus anisotropy of $Y_4Al_2O_9$ and $Yb_4Al_2O_9$ is smaller than that of Yb_2SiO_5 . Therefore, $Y_4Al_2O_9$ and $Yb_4Al_2O_9$ can be used as the next generation of thermal/environmental barrier coating materials instead of rare earth silicate.

3 Preparation Technology of EBCs

3.1 Atmospheric Plasma Spraying (APS)

Atmospheric plasma spraying (APS) is to heat ceramic powder to the melting state through plasma arc, spray it at high speed with the flame flow, and deposit it on the pretreated substrate surface, thus forming a coating with special properties. Plasma spraying technology has been widely used in the EBC preparation of engine combustion chamber and other hot end components. At present, the process has been developed and put into commercial application. NASA took the lead in adopting plasma spraying technology to spray various types of EBC on SiC-based ceramic and its composite hot end components.

APS has the advantages of fast deposition rate and low cost and is the most common method to prepare ceramic environmental barrier coatings. Because plasma spraying involves rapid heating and rapid cooling, the heat-affected zone of the substrate is small, and some amorphous and nanocrystalline particles may be produced in the sprayed coating. The specific process of atmospheric plasma spraying is shown in Fig. 11.

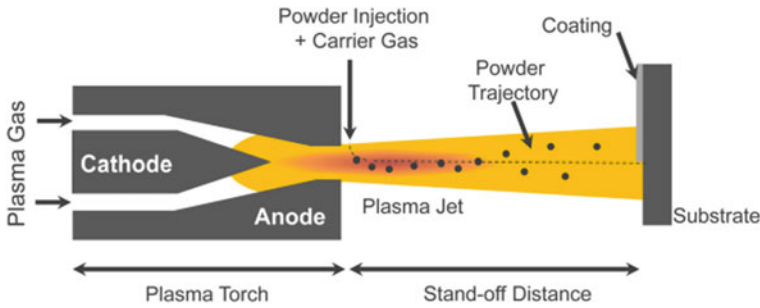


Fig. 11 Schematic diagram of atmospheric plasma spraying [27]

APS is widely used, such as environmental/thermal barrier coating, anti-corrosion coating, material surface decoration, repair of mechanical parts, and precise molding of precision ceramics. This technology has the characteristics of fast, relatively low cost, and wide application, especially suitable for coating preparation.

3.2 Electron Beam Physical Vapor Deposition (EB-PVD)

EB-PVD heats the material with the help of a focused high-energy electron beam, makes it melt and evaporate rapidly, and then deposits the vapor on a certain substrate. It can evaporate both metal and ceramic. Its high deposition rate makes it have a wide application market, such as thermal barrier coating, environmental barrier coating, and other components. In the late 1960s, a German company first prepared the first set of EB-PVD equipment with thermal barrier coating for gas turbine blades.

The basic working principle is as follows: Firstly, the workroom is pumped to a certain vacuum state through a vacuum pump, and then, the electron beam is emitted by the electron gun onto the target source material. The emission energy of the electron beam enables it to rapidly heat and diffuse to vaporize the material, and the material vapor moves from the target source to the vicinity of the substrate and finally deposits on the surface of the substrate in the form of atoms or molecules and solidifies to form a coating as shown in Fig. 12. The structure of environmental barrier coating prepared by EB-PVD is columnar crystal. Compared with the coating prepared by APS, the coating prepared by EB-PVD has high strain tolerance, high compactness, and significantly enhanced bonding strength. However, its thermal conductivity is relatively high, its deposition rate is slow, and its cost is high.

For ceramic coating, loose structure has better thermal insulation property and impact resistance than dense structure. Some studies have shown that the thermal cycle life of coatings with a porosity of about 15% is the longest [29, 30]. There are many factors affecting the coating quality, including the structure design of the plasma spray gun, the distance between the spray gun and the substrate, the size of the spray power, the gas flow rate, the speed of powder delivery, the properties of the

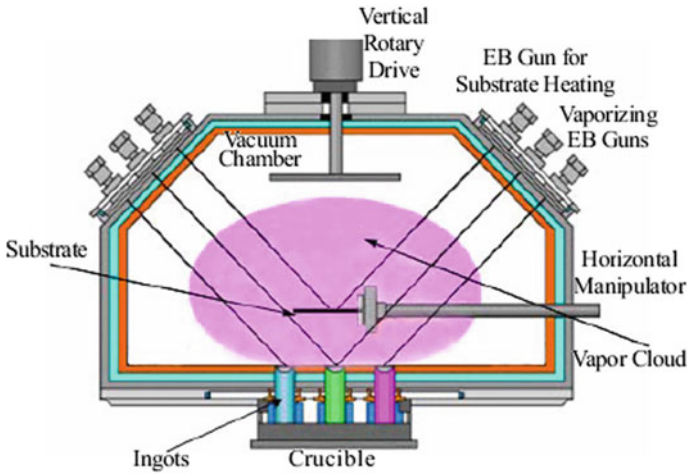


Fig. 12 Schematic diagram of EB-PVD [28]

powder itself, and the surface roughness of the substrate. APS equipment is relatively simple, the coating preparation speed is fast, the deposition efficiency is high, and the cost is low. It has a wide range of applications, especially in the preparation of large area and thick coating, such as the combustion chamber and tail nozzle of gas turbine, which has a strong competitive advantage, which EB-PVD cannot complete. The most important application of EB-PVD is the preparation of gas turbine blades. The columnar crystal structure formed by EB-PVD can reduce the internal stress of the coating to nearly zero, so the prepared coating has particularly excellent thermal shock resistance [9, 31]. The thermal cycle life of the coating prepared by EB-PVD is much longer than that of APS coating. However, EB-PVD equipment is very complex, expensive, and inefficient and is not suitable for coating preparation of large structural components. Table 3 shows the comparison of coating properties prepared by EB-PVD and PS methods.

Table 3 Performance comparison of EB-PVD and APS coatings [32]

Performance	EB-PVD	APS
Thermal conductivity/[W/(m·K)]	1.5–1.9	0.8–1.1
Surface roughness $R_a/\mu\text{m}$	1.0	10.0
Bonding strength/MPa	40	20–40
Young’s modulus/GPa	90	200
Relative corrosion rate	1	7
Coating formation rate/ $(\mu\text{m}/\text{min})$	3–5	50–200
Cost	Very high	Low

3.3 Plasma Spraying Physical Vapor Deposition (PS-PVD)

PS-PVD is a newly developed new method for coating preparation. In the low-pressure spraying room, the PS-PVD uses a high-power plasma spray gun (the maximum power can reach 200 kW) to generate plasma flame. The length and diameter of the flame can reach 2 m and 0.2–0.4 m, respectively (Fig. 13). At different parts of the plasma flame direction, the evaporation state of the coating material is different, and the coating structure formed is also different. The material powder rapidly melts in the plasma flame, and part of it vaporizes. The formed vapor deposits on the substrate surface above the plasma flame to form a coating. The coating has a columnar crystal structure similar to EB-PVD [33]. However, the molten droplets without evaporation are sprayed on the substrate surface to form a coating, which has the layered structure characteristics of plasma spraying. Therefore, PS-PVD combines the advantages of PS and EB-PVD to obtain a coating with the dual characteristics of columnar crystal and layered structure.

The gas, liquid, and solid multiphase deposition of spray powder can be realized by adjusting the process parameters, and the structural and functional coatings with different requirements can be prepared. The deposition efficiency is high, which can realize non-line of sight deposition. It has great advantages for the coating of complex parts with uniform coating thickness and structure, especially for the environmental barrier coating of silicon carbide reinforced silicon carbide matrix composite turbine blades. In the advanced PS-PVD deposition system, all operations are carried out in a vacuum environment. The width of the plasma flame can be controlled by changing the vacuum degree. In addition, the addition of inert gas can also control the plasma flame flow and regulate the ion beam and energy. The addition of hydrogen can greatly increase the width and temperature of the plasma flame flow, and can make the powder deposit in the form of gas phase. Specifically, hydrogen will make the plasma flame flow wider, and inert gas can make the plasma flame flow stable. Finally, by changing the gas ratio of the plasma, adjusting the process parameters such as current, spraying distance, and powder feeding rate to deposit different powders, the layered and columnar composite coatings are obtained.

PS-PVD can realize solid, liquid, and gas multiphase deposition and non-line of sight deposition. By adjusting the spraying parameters, the environmental barrier

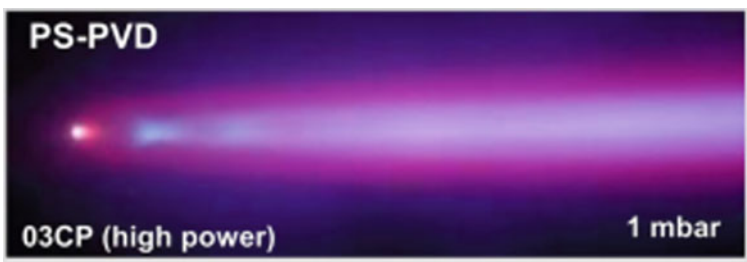


Fig. 13 Plasma flame flow of PS-PVD [34]

coatings with layered, columnar, and layered mixed structures can be obtained. Therefore, PS-PVD, as an advanced preparation technology of environmental barrier coatings, has great application prospects in the preparation of high-performance high-temperature/ultra-high-temperature environmental barrier coatings in the future [35]. However, PS-PVD is a newly developed coating preparation process in recent years, and its application is still slightly inadequate. For example, the action mechanism of different kinds of material particles and plasma jet is different, and the deposition mechanism is also different; at present, the PS-PVD technology mostly uses nano-ceramic powder, which is easy to sinter in the process of transportation, and needs to change the transportation mode to send the powder into the plasma flame. These problems need to be studied. In addition, the PS-PVD equipment is expensive, which makes the coating preparation cost too high, and is not suitable for widespread use in ordinary engines. To date, the preparation of EBC coating by APS and EB-PVD methods is relatively extensive in practical production, and the PS-PVD method is still in the research stage.

3.4 Other Preparation Technology

Other common preparation processes mainly include slurry impregnation, sol-gel, chemical vapor deposition, and supersonic flame spraying.

The preparation process of the slurry method is relatively simple, and the basic steps include: (1) first, mix the required dispersant, binder, solvent, and powder material used for preparing the coating to prepare the slurry. (2) Immerse the matrix into the prepared slurry and then pull it out slowly. When pulling it out, it must maintain a constant speed to prevent the thickness difference of the slurry adhered by the matrix from too large; or paint the slurry onto the substrate. (3) Put the coating + substrate into the oven for drying and heat preservation to remove the solvent in the coating. (4) EBCs coating is prepared by high-temperature sintering [36].

The slurry impregnation method has low cost and simple process, but its disadvantages are also obvious. In the process of impregnation and brushing, the consistency of coating thickness cannot be guaranteed, especially when the impregnation method is used, the influence of gravity on the thickness is more obvious, and the uneven thickness will make the coating easy to crack when used in high-temperature environment, resulting in premature failure of the coating. In addition, the drying process before sintering can prolong the process cycle of slurry method by nearly half, which is not the best process for preparing EBC in terms of time cost.

Sol-gel method is a traditional method for preparing thin films and coatings, and its operation process is relatively simple [37]. The raw material of sol-gel method is inorganic compound solution. Firstly, there are dispersed submicron sized particulate sols in the solution generated through hydrolysis and condensation reactions. Then, it is combined with the particles to form a solidified gel. Finally, oxides or other compound solids are successfully prepared after heat treatment. Sol-gel method for

preparing oxide coatings has considerable advantages: simple process and equipment, without vacuum conditions and equipment. The process temperature is low. The coating can be prepared on various substrates with different shapes and materials in a large area. Moreover, it can effectively control the composition and microstructure of the coating, so it is often used. However, it is difficult to prepare a dense uniform continuous coating with a certain thickness.

Chemical vapor deposition (CVD) is a method of producing solid films by means of atomic and intermolecular chemical reactions using gaseous precursor reactants [38]. The chemical vapor deposition process is usually carried out at relatively high temperature (usually ≥ 700 °C) and pressure environment, because higher temperature and pressure help to improve the deposition rate of the film.

Supersonic flame spraying refers to taking the flame generated by the combustion of fuel such as kerosene and propane in oxygen as the heat source, generating supersonic flame flow through Laval nozzle, sending powder feed into the flame for heating and melting, and then rapidly depositing on the substrate surface to form a coating, as shown in Fig. 14. Because its flame speed exceeds the sound speed, the coating has low oxidation degree, high compactness, and good bonding strength. Compared with the temperature of plasma flame, the temperature of supersonic flame is lower, and it is generally used to deposit the adhesive layer in the coating. Compared with low-pressure plasma spraying, supersonic flame spraying coating has lower preparation cost and simple operation.

In conclusion, there are many methods to prepare EBCs. However, from its maturity, cost, coating quality, operational process feasibility, and other aspects, the APS method is the most efficient and most suitable process for preparing the environmental barrier coating of large engine turbine blades. In addition to the above methods, there are also polymer conversion ceramic method, oxidation binding reaction, sputtering impregnation method, and other coating preparation methods. These methods are

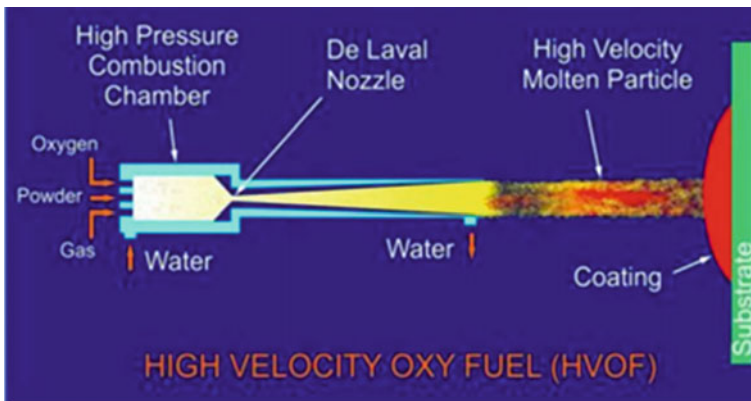


Fig. 14 Schematic diagram of supersonic flame spraying

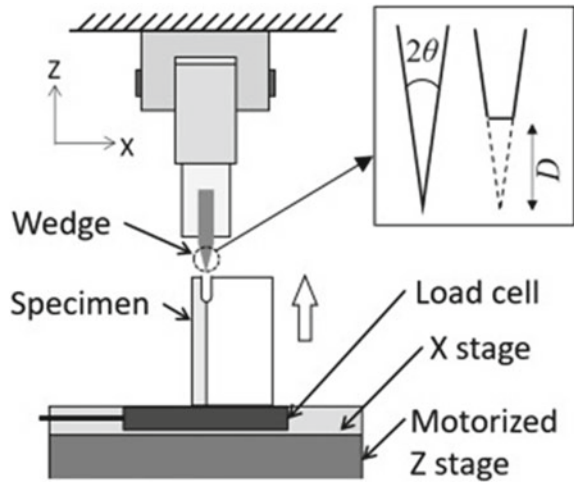
widely used in various preparation conditions, providing a variety of options for coating preparation in different regions and fields.

4 Mechanical Properties of EBCs

4.1 Fracture Toughness

Based on Irwin theory, the fracture toughness K_{IC} represents the limit value of the applied stress field strength that the mode I crack system can bear. When the strength K of the applied stress field reaches or exceeds the fracture toughness K_{IC} of the material, the crack will expand. Irwin considers the crack system in isotropic uniform continuous material. For the crack system with certain geometric shape, the fracture toughness K_{IC} defined by Irwin should be a material constant. In order to obtain the specific fracture toughness value from the experiment, the American Society for Testing and Materials has developed a test standard ASTM E-24, which has made an authoritative definition of fracture toughness from the experiment. To other words, fracture toughness is the resistance of crack growth under the plane strain condition. To date, there have been some techniques to test the fracture toughness of ceramic materials. On the one hand, the test methods of different geometric components, such as single-sided notched beam method (SENB), double-torsion method (DT), double-cantilever beam method (DCB), mountain-shaped notch method (CHV), and indentation method (ID). On the other hand, the method of wedge pressing and pre-sintering crack preparation can explore the preparation methods of ideal tip crack.

Kakisawa et al. [39] proposed a simple test method for interfacial fracture of ceramic matrix composites (CMCs) and ceramic environmental barrier coatings (EBCs), as shown in Fig. 15. A method of changing the asymmetric double-cantilever beam (ADCB) test is adopted, so that the interface toughness can be measured in a small sample with simple shape without applying interlayer load. This test is applicable to single-layer SiC substrate composed of mullite layer and silicon bonded coating. Pre-cracks are introduced through pop-up cracks, and then notches with overlapping pre-cracks are processed. Insert the wedge into the gap and open the pre-crack. The crack propagation is started from the critical notch opening displacement, and the interfacial toughness is calculated. The measured interfacial toughness is 4.1 J/m^2 . Finally, the applicable scope of the test is discussed, and suggestions for introducing notch and pre-crack are put forward.

Fig. 15 Toughness test [39]

4.2 Bonding Strength

The bonding strength of the coating includes the cohesion strength between the coating particles, the bonding strength of the coating itself, and the bonding strength between the coating and the substrate material. Generally, only the bonding strength between the coating and the substrate is measured, which is called bonding strength.

The measurement method of coating bonding strength is mainly tensile test. Tensile strength is the most important index for evaluating the bonding strength of coatings. During the test, use the test tool or equipment to make the sample bear the tensile force perpendicular to the coating surface until the sample is pulled away, that is, the coating is peeled off, record the load at the time of failure, divide the load value by the cross-sectional area of the sample, and then calculate the tensile strength of the coating.

$$R_H = \frac{F_m}{S}$$

where R_H is the tensile bonding strength (N/mm^2), F_m is the maximum load (N), and S is the cross-sectional area of the fracture surface (mm^2).

The coating prepared by low-pressure plasma spraying (LPPS) is more dense than that of air plasma spraying (APS), and its bonding strength is relatively high. However, densification will also increase the residual stress in the coating, which is an adverse factor to the bonding strength. The spraying process includes spraying methods and conditions. The impact on the bond strength can be more objectively evaluated by comprehensive consideration.

Chen et al. [40] prepared $Yb_2Si_2O_7/Si$ environmental barrier coatings (EBCs) using APS and LPPS processes. The phase composition, microstructure, and bonding

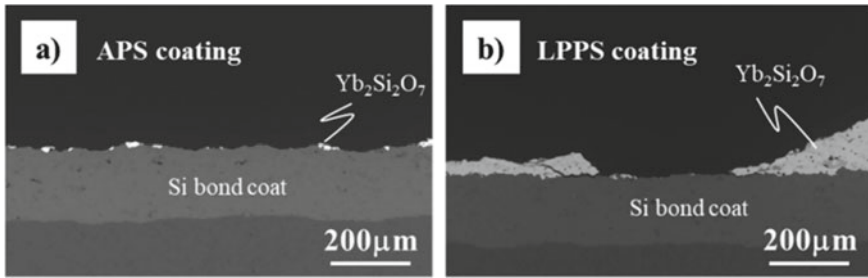


Fig. 16 a Cross section microstructure of APS and b LPPS EBC after bonding strength test [40]

strength of APS and LPPS composites were studied. The bonding strength of APS $\text{Yb}_2\text{Si}_2\text{O}_7/\text{Si}$ coating is 17.6 ± 1.6 MPa, and that of LPPS $\text{Yb}_2\text{Si}_2\text{O}_7/\text{Si}$ coating is 29.1 ± 0.75 MPa. The bonding strength of LPPS is about 65% higher than that of APS. The section microstructure after the bond strength test is shown in Fig. 16. The failure of APS and LPPS $\text{Yb}_2\text{Si}_2\text{O}_7/\text{Si}$ coating mainly occurs at the interface between the coating and the adhesive layer. The LPPS coating has a certain degree of adhesive failure, and the failure of APS coating is more similar to the classic adhesive layer. In both cases, SEM observation shows that the Si bonded coating has strong adhesion. It is reported that at higher deposition temperature, the contact between sputter-substrate and sputtering is significantly improved, thus reducing porosity and improving adhesion strength. The deposition temperature of LPPS process (900°C) is significantly higher than that of APS process (100°C). Therefore, it can be expected that the sputtered bonding and sputtered silicon bonding of EBCs (LPPS) will be improved compared with EBCs (APS). In addition, in the LPPS electron beam, the higher kinetic energy generated by the higher particle velocity will further enhance the adhesion between the sputtering plate and the silicon bonding layer. Therefore, higher bonding strength can be observed in LPPS EBCs.

5 High-Temperature Failure Behavior of EBCs

5.1 Water Oxygen Corrosion

EBCs are often impacted by water vapor, molten salt, and other foreign matters when serving in the engine environment. Therefore, the selected coating material must have excellent corrosion resistance. Among them, the coatings are most sensitive to water vapor corrosion.

The water vapor corrosion resistance of materials can be predicted from the perspectives of SiO_2 activity, hydrophobicity, and optical basicity (OB). Low activity of SiO_2 , good hydrophobicity at normal temperature, and large OB value mean good stability of water vapor [41, 42]. EBCs should have good high-temperature phase

stability. In other words, no phase change occurs during high-temperature exposure, or the CTE and volume change of new crystal after phase change is very small. Most of the rare earth monosilicates have a single crystal form and basically have no phase change from room temperature to high temperature, while most of the rare earth bisilicates show a complex polycrystalline state [43]. They undergo polycrystalline phase change when heating up and generate phase change stress during service. In addition, EBCs materials should have good chemical compatibility [44]. At present, no single material has been found to meet all the requirements of EBCs.

Compared with mullite, YSZ, and BSAS, rare earth silicate materials have excellent high-temperature phase stability, low thermal conductivity, and good thermal compatibility with SiC matrix and become the most potential EBCs surface materials. It is found that rare earth silicate has excellent resistance to water and oxygen corrosion. Under the extreme water and oxygen corrosion conditions of 1450 °C and water vapor flow rate of 100 m/s, the weight loss rate of rare earth silicate represented by $\text{Yb}_2\text{Si}_2\text{O}_7$ is about $0.002 \text{ mg} (\text{cm}^2 \cdot \text{h})^{-1}$. The weight loss rate of mullite is $0.039 \text{ mg} (\text{cm}^2 \cdot \text{h})^{-1}$ [45].

In summary, the reaction of rare earth silicate with water vapor is a complex process. The water oxygen corrosion resistance of single/double silicates containing different rare earth elements is different, and it is difficult to uniformly summarize as RE_2SiO_5 is better or worse than $\text{RE}_2\text{Si}_2\text{O}_7$. However, according to a large number of tests, it can be determined that the resistance of rare earth silicate to water oxygen corrosion is absolutely superior to the first and second-generation EBCs and also superior to most ceramic materials. At present, the law of the water oxygen corrosion resistance of the substances in the rare earth silicate system needs further study.

5.2 High-Temperature Oxidation

No matter at the crack tip or at the side edge exposed to the environment, the long-term high temperature will oxidize the Si bonding layer and form the thermal growth oxide $\beta\text{-SiO}_2$ (TGO) [46, 47]. Figure 17 shows the TGO growth diagram of the environmental barrier coating system under high-temperature cycling. During the thermal cycle, when the temperature increases to 1316 °C, the TGO composition is $\beta\text{-SiO}_2$. When the temperature decreases to 220 °C, the $\beta\text{-SiO}_2$ will be transformed into α phase. The structure of TGO layer has been seriously damaged by the repetition of reversible phase transition, resulting in the loss of its antioxidant capacity. The average thickness of TGO increases with the increase of exposure time under high-temperature conditions, and its thickness can reach several microns after 2000 thermal cycles. The TGO layer contains many vertical cracks that completely penetrate the oxide layer. This phenomenon is particularly obvious in the region where the thickness of TGO changes. With the increase of the number of cycles, the silicate coating will crack prematurely.

It is reported that PS-PVD technology is used in SiC_f/SiC matrix. Subsequently, the prepared coating was isothermal oxidized for 1000 h in air at 1300 °C. No obvious

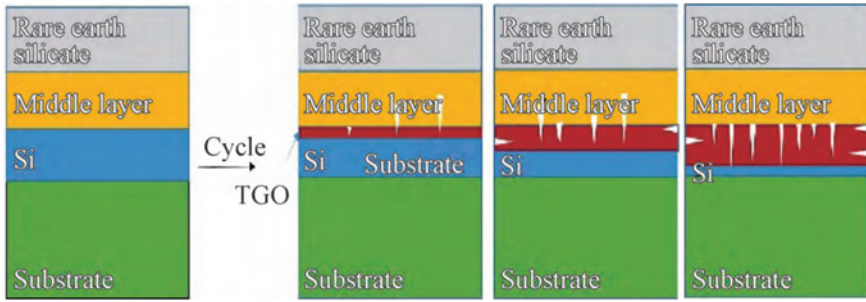


Fig. 17 Schematic diagram of TGO growth and crack growth

cracks were formed at the interface of Yb_2SiO_5 /mullite coating. However, many cracks appear at the interface of mullite/Si coating, as shown in Fig. 18c. On the one hand, due to the different thermal expansion coefficient between mullite and silicon coating, tensile stress appears in mullite coating. On the other hand, the Si coating will form a TGO layer (calcite phase), resulting in volume expansion, and the CTE of the SiO_2 layer is much higher than CTE of mullite. When the cracks propagate laterally, they are interconnected to form horizontal cracks, leading to premature delamination of EBCs. In addition, there are two cristobalite crystal forms at about 200 °C, and there is a reversible phase transition between the two crystal forms. Therefore, brittle fracture is easy to occur at the interface of mullite/Si coating during thermal cycling. Cracks also appear in the internal mullite coating, as shown in Fig. 18a, which is caused by the volume expansion of the mullite/Si coating interface. At the same time, the internal Si coating also produced some cracks, which may be due to the oxidation of SiO_2 in the coating.

5.3 Calcium-Magnesium-Alumino-Silicate Melts (CMAS) Corrosion

In the engine environment, EBCs also have molten salt erosion. The key to prevent molten salt corrosion of EBCs is to reduce their reactivity with molten salt [49–51]. The corrosion mechanism of CMAS and RE_2SiO_5 is also complex due to the complex structure of RE_2SiO_5 . Figure 19 shows the corrosion mechanism of RE_2SiO_5 and CMAS. At a corrosion temperature of 1200 °C (lower than the initial melting temperature of CMAS), CMAS was deposited on the surface of RE_2SiO_5 sample and reacted with RE_2SiO_5 . Some RE_2SiO_5 grains interact with SiO_2 in CMAS to form $\text{RE}_2\text{Si}_2\text{O}_7$. In addition, RE_2O_3 can react with SiO_2 to produce rare earth silicate. RE_2SiO_5 and $\text{RE}_2\text{Si}_2\text{O}_7$ further react with CMAS to form oxyapatite phase and garnet phase. However, the main phases in CMAS are anorthite and cyano-wollastonite, with low SiO_2 content. Therefore, only a small amount of $\text{RE}_2\text{Si}_2\text{O}_7$ is formed by the reaction of RE_2SiO_5 and SiO_2 . In addition, the composition of CMAS glass phase changes

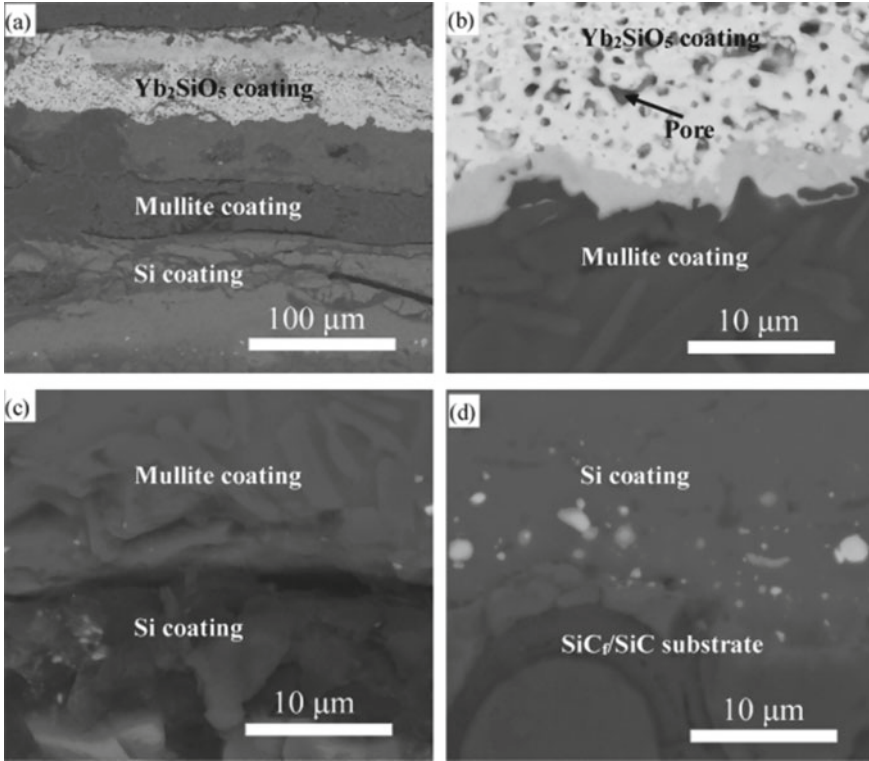


Fig. 18 Microstructure of Si/mullite/Yb₂SiO₅ coating under isothermal oxidation at 1300 °C and 1000 h **a** Overall coating, **b** Yb₂SiO₅/mullite coating interface, **c** mullite/Si coating interface, **d** Si/matrix interface [48]

from wollastonite (CaSiO₃) to anorthite doped with rare earth elements (CaAl₂Si₂O₈) due to the rapid accumulation of Al and the diffusion of rare earth elements.

The CMAS corrosion resistance of RE₂SiO₅ has been found in multitudinous experimental results, which is related to the ionic radius of rare earth elements.

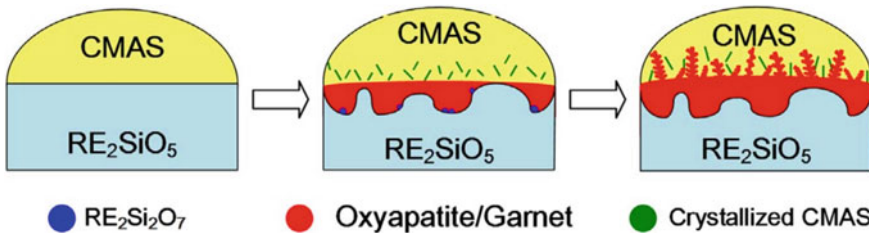


Fig. 19 Schematic illustration of the proposed corrosion mechanism of RE₂SiO₅-CMAS system [52]

RE_2SiO_5 with smaller RE^{3+} radius showed better CMAS resistance than RE_2SiO_5 with larger RE^{3+} radius. RE_2SiO_5 with larger RE^{3+} radius is easier to form apatite phase after CMAS-induced corrosion, and RE_2SiO_5 with smaller RE^{3+} radius is easier to form garnet phase.

6 Summary and Future Direction

The material systems, preparation technologies, mechanical properties, and high-temperature failure behaviors of EBCs are systematically analyzed. The Si bonding layer/rare earth silicate surface layer system is currently the most promising EBCs. However, there are many factors that limit the development of this material system. The resistance to water oxygen corrosion of rare earth silicate materials and the quality of the surface layer determine the protective ability of EBCs for aircraft engines. The low melting point of the silicon bonding layer limits the service temperature of the EBCs. Easy oxidation is an important cause of coating failure. The improvement measures for the EBCs have been summarized by analyzing existing researches.

To date, most studies on rare earth silicate EBCs have only improved the protective performance of coatings from a single perspective. Therefore, multifunctional coupled EBCs will be an important direction for the development of future EBCs. The multifunctional coupling EBCs is as follows:

- (1) High-entropy rare earth silicates and self-healing material coupling surface layer. Coupling high-entropy rare earth silicates with excellent resistance to water oxygen corrosion with self-healing materials (SiC , MoSi_2), to prepare a mixed surface layer of EBCs. The mixed surface layer is expected to exhibit stronger resistance to water oxygen corrosion.
- (2) High melting point oxide and silicon coupling bonding layer. Mixing high melting point oxides with silicon can effectively overcome the shortcomings of silicon materials, such as low usage temperature and easy generation of TGO.
- (3) Combination of coupling surface layer and coupling bonding layer. It is expected to obtain the EBCs with excellent water oxygen corrosion resistance, strong high-temperature oxidation resistance, and high service temperature.

References

1. Lee, K.N., Zhu, D.M., Lima, R.S.: Perspectives on environmental barrier coatings (EBCs) manufactured via air plasma spray (APS) on ceramic matrix composites (CMCs): a tutorial paper. *J Therm Spray Tech.* **30**, 40–58 (2021)
2. Ali, A.A.: Durability modeling review of thermal- and environmental-barrier-coated fiber-reinforced ceramic matrix composites part I. *Materials* **11**, 1251 (2018)

3. Fang, G.W., Gao, X.G., Song, Y.D.: A review on ceramic matrix composites and environmental barrier coatings for aero-engine: material development and failure analysis. *Coatings* **13**, 357 (2023)
4. Yin, X.W., Cheng, L.F., Zhang, L.T.: Fibre-reinforced multifunctional SiC matrix composite materials. *Int. Mater. Rev.* **62**, 117–172 (2017)
5. Kane, K.A., Pint, B.A., Mitchell, D.: Oxidation of ultrahigh temperature ceramics: kinetics, mechanisms, and applications. *J. Eur. Ceram. Soc.* **41**, 6130–6150 (2021)
6. Dayi, E.N., Nasiri, N.A.: Diffusion study of rare-earth oxides into silica layer for environmental barrier coating applications. *J. Eur. Ceram. Soc.* **39**, 4216–4222 (2019)
7. Rohbeck, N., Morrell, P., Xiao, P.: Degradation of ytterbium disilicate environmental barrier coatings in high temperature steam atmosphere. *J. Eur. Ceram. Soc.* **39**, 3153–3163 (2019)
8. Lv, B.W., Jin, X.C., Cao, J.: Advances in numerical modeling of environmental barrier coating systems for gas turbines. *J. Eur. Ceram. Soc.* **40**, 3363–3379 (2020)
9. Daniel, T.M., Chris, B., Tanvir, H.: A review on environmental barrier coatings: History, current state of the art and future developments. *J. Eur. Ceram. Soc.* **41**, 1747–1768 (2021)
10. Jecha, D., Čelko, L., Remešová, M.: Influence of isothermal oxidation on microstructure of YSZ and Mullite-YSZ thermal barrier coatings. *Procedia Struct. Integr.* **23**, 378–383 (2019)
11. Lee, K.N.: Key Durability issues with mullite-based environmental barrier coatings for Si-based ceramics. *J. Eng. Gas Turbines Power* **122**, 632–636 (2000)
12. Lee, K.N., Fox, D.S., Eldridge, J.I.: Upper temperature limit of environmental barrier coatings based on mullite and BSAS. *J. Am. Ceram. Soc.* **86**, 1299–1306 (2003)
13. Luan, S.L., Zhang, S., Ren, K.: Hot corrosion behavior of multialkaline-earth aluminosilicate for environmental barrier coatings. *J. Eur. Ceram. Soc.* **43**, 2175–2184 (2023)
14. Cojocar, C.V., Kruger, S.E., Moreau, C.: Elastic Modulus evolution and behavior of Si/Mullite/BSAS-based environmental barrier coatings exposed to high temperature in water vapor environment. *J. Therm. Spray Technol.* **20**, 92–99 (2010)
15. Cojocar, C.V., Lévesque, D., Moreau, C.: Performance of thermally sprayed Si/mullite/BSAS environmental barrier coatings exposed to thermal cycling in water vapor environment. *Surf. Coat. Technol.* **216**, 215–223 (2013)
16. Lia, Y.R., Wang, J.M., Wang, J.Y.: Theoretical investigation of phonon contributions to thermal expansion coefficients for rare earth monosilicates RE₂SiO₅ (RE = Dy, Ho, Er, Tm, Yb and Lu). *J. Eur. Ceram. Soc.* **40**, 2658–2666 (2020)
17. Ogawa, T., Otani, N., Yokoi, T.: Density functional study of phase stabilities and Raman spectra of Yb₂O₃, Yb₂SiO₅ and Yb₂Si₂O₇ under pressure. *Phys. Chem. Chem. Phys.* 1–10 (2018)
18. Zhou, Y.C., Zhao, C., Wang, F.: Theoretical prediction and experimental investigation on the thermal and mechanical properties of bulk β-Yb₂Si₂O₇. *J. Am. Ceram. Soc.* **96**(12), 3891–3900 (2013)
19. Guo, X.T., Zhang, Y.L., Li, T.: High-entropy rare-earth disilicate (Lu_{0.2}Yb_{0.2}Er_{0.2}Tm_{0.2}Sc_{0.2})₂Si₂O₇: a potential environmental barrier coating material. *J. Eur. Ceram. Soc.* **42**, 3570–3578 (2022)
20. Dong, Y., Ren, K., Lu, Y.: High-entropy environmental barrier coating for the ceramic matrix composites. *J. Eur. Ceram. Soc.* **39**(7), 2574–2579 (2019)
21. Chen, H., Xiang, H., Dai, F.Z.: High entropy (Yb_{0.25}Y_{0.25}Lu_{0.25}Er_{0.25})₂SiO₅ with strong anisotropy in thermal expansion. *J. Mater. Sci. Technol.* **36**, 134–139 (2020)
22. Ren, X., Tian, Z., Zhang, J.: Equiatomic quaternary (Y_{1/4}Ho_{1/4}Er_{1/4}Yb_{1/4})₂SiO₅ silicate: a perspective multifunctional thermal and environmental barrier coating material. *Scripta Mater.* **168**, 47–50 (2019)
23. Deijkers, J.A., Wadley, H.N.G.: Hafnium silicate formation during oxidation of a permeable silicon + HfO₂ powder composite system. *Acta Mater. Mater.* **201**, 448–461 (2020)
24. Nakano, K., Fukatsu, N., Kanno, Y.: Thermodynamics of Zr/Hf-mixed silicates as a potential for environmental barrier coatings for tyranno-hex materials. *Surf. Coat. Technol.* **203**, 1997–2002 (2009)
25. Zhang, Z.Y., Park, Y.J., Xue, Z.L.: Effect of the HfO₂/SiO₂ pre-mixing ratio and heating temperature on the formation of HfSiO₄ as a bond coat of environmental barrier coatings. *Ceram. Int.* **48**, 15657–15667 (2022)

26. Hisanoli, Y., Kazuhiro, O., Mamoru, O.: Phase transition of rare-earth aluminates (RE₄Al₂O₉) and rare-earth gallates (RE₄Ga₂O₉). *J. Am. Ceram. Soc.* **78**(9), 2385–2390 (1995)
27. Bakan, E., Vassen, R.: Ceramic top coats of plasma-sprayed thermal barrier coatings: materials, processes, and properties. *J. Therm. Spray Technol.* **26**(6), 992–1010 (2017)
28. Guo, H.B., Peng, L.Q., Gong, S.K.: Progress in EB-PVD thermal barrier coatings. *Therm. Spray Technol.* **2**, 8 (2009)
29. Zhang, Z.Y., Park, Y.J., Xue, Z.L.: Cyclic oxidation performances of new environmental barrier coatings of HfO₂-SiO₂/Yb₂Si₂O₇ coated SiC at 1375 °C and 1475 °C in the air environment. *J. Eur. Ceram. Soc.* **42**, 4663–4675 (2022)
30. Zhang, Z.Y., Park, Y.J., Kim, D.H.: High-temperature oxidation performance of novel environmental barrier coating 50HfO₂-50SiO₂/Y_xYb_(2-x)Si₂O₇ at 1475 °C. *J. Eur. Ceram. Soc.* **43**, 1127–1140 (2023)
31. Ding, Q.J., Tan, X., Jiang, L.W.: High-temperature performances of Si-HfO₂-based environmental barrier coatings via atmospheric plasma spraying. *Ceram. Int.* **48**, 23127–23136 (2022)
32. Reinhold, E., Deus, C., Wenzel, B.D.: EB-preheating of turbine blades—The completion of EB-technology for thermal barrier coating. *Surf. Coat. Technol.* **111**(1), 10–15 (1999)
33. Lv, B.W., Zhuo, X.S., Wang, C.: Mechanisms of crack healing in dense Yb-Si-O environmental barrier coatings by plasma spray-physical vapor deposition. *Ceram. Int.* **48**, 15975–15983 (2022)
34. Vardelle, A., Moreau, C., Akedo, J.: The 2016 Thermal spray roadmap. *J. Therm. Spray Technol.* **25**(8), 1376–1440 (2016)
35. Wu, J., Yang, W.C., Zhang, X.F.: Corrosion behavior of PS-PVD spray Yb₂Si₂O₇ environmental barrier coatings during continuous water vapor exposure. *Corros. Sci.* **210**, 110831 (2023)
36. Tian, Y.S., Chen, C.Z., Wang, D.Y.: Recent developments in zirconia thermal barrier coatings. *Surf. Rev. Lett.* **12**(3), 369–378 (2005)
37. Ueno, S., Jayaseelan, D.D., Kondo, N.: Development of EBC for Silicon Nitride. *Key Eng. Mater.* **287**, 449–456 (2005)
38. Zhang, S., Xu, Q., Tu, R.: Growth mechanism and defects of < 111 > -oriented β-SiC films deposited by laser chemical vapor deposition. *J. Am. Ceram. Soc.* **98**(1), 236–241 (2015)
39. Kakisawa, H., Nishimura, T.: A method for testing the toughness of ceramic environmental barrier coatings (EBCs) on ceramic matrix composites (CMCs). *J. Eur. Ceram. Soc.* **38**(2), 655–663 (2018)
40. Chen, D., Pegler, A., Dwivedi, G.: Thermal cycling behavior of air plasma-sprayed and low-pressure plasma-sprayed environmental barrier coatings. *Coatings* **11**, 7 (2021)
41. Chen, Z.Y., Lin, C.C., Zheng, W.: A high-entropy (Yb_{0.2}Y_{0.2}Lu_{0.2}Ho_{0.2}Er_{0.2})₂Si₂O₇ environmental barrier coating prepared by atmospheric plasma-spray. *Ceram. Int.* **49**, 11323–11333 (2023)
42. Lee, K.N., Garg, A., Jennings, W.D.: Effects of the chemistry of coating and substrate on the steam oxidation kinetics of environmental barrier coatings for ceramic matrix composites. *J. Eur. Ceram. Soc.* **41**, 5675–5685 (2021)
43. Zhong, X., Zhu, T., Niu, Y.R.: Effect of microstructure evolution and crystal structure on thermal properties for plasma-sprayed RE₂SiO₅; (RE=Gd, Y, Er) environmental barrier coatings. *J. Mater. Sci. Technol.* **85**, 141–151 (2021)
44. Zhang, Q., Zhang, X.Q., Ma, Z.: Water vapor and CMAS corrosion tests of Y₂SiO₅/Si thermal and environmental barrier coating. *Heliyon* **8**, e10262 (2022)
45. Klemm, H.: Silicon nitride for high-temperature applications. *J. Am. Ceram. Soc.* **93**, 1501–1522 (2010)
46. Lee, K.N.: Yb₂Si₂O₇ Environmental barrier coatings with reduced bond coat oxidation rates via chemical modifications for long life. *J. Am. Ceram. Soc.* **102**, 1507–1521 (2019)
47. Stack, P., Kane, K., Sweet, M.: Dry air cyclic oxidation of mixed Y/Yb disilicate environmental barrier coatings and bare silica formers. *J. Eur. Ceram. Soc.* **42**, 3345–3350 (2022)

48. Zhang, X.F., Song, J.B., Deng, Z.Q.: Interface evolution of Si/Mullite/Yb₂SiO₅ PS-PVD environmental barrier coatings under high temperature. *J. Eur. Ceram. Soc.* **40**, 1478–1487 (2020)
49. Kim, S.H., Nagashima, N., Matsushita, Y.: Interaction of Gd₂Si₂O₇ with CMAS melts for environmental barrier coatings. *J. Eur. Ceram. Soc.* **43**, 593–599 (2023)
50. Kim, S.H., Fisher, C.A.J., Nagashima, N.: Reaction between environmental barrier coatings material Er₂Si₂O₇ and a calcia-magnesia-alumina-silica melt. *Ceram. Int.* **48**, 17369–17375 (2022)
51. Wiesner, V.L., Scales, D., Johnson, N.S.: Calcium–magnesium aluminosilicate (CMAS) interactions with ytterbium silicate environmental barrier coating material at elevated temperatures. *Ceram. Int.* **46**, 16733–16742 (2020)
52. Jiang, F., Cheng, L., Wang, Y.: Hot corrosion of RE₂SiO₅ with different cation substitution under calcium-magnesium-aluminosilicate attack. *Ceram. Int.* **43**, 9019–9023 (2017)

Environmental Barrier Coatings (EBCs) for Silicon-Based Ceramics and Composites



Jia-Hu Ouyang, Gui Cao, and Shu-Qi Wang

Abstract Silicon-based ceramics and composites are promising materials for hot-section structural components of high-temperature turbines due to their excellent mechanical properties at elevated temperatures. However, corrosive gas and foreign particles in the service environment, such as water vapor/oxygen and some silicate dusts may attack silicon-based ceramics, which finally result in lifetime recession and sometimes severe failure. Therefore, Environmental Barrier Coatings (EBCs) have been proposed to isolate these corrosive media. EBCs system has developed over several decades to the most common structure consisting of bond coat/interlayer/topcoat. Main performance requirements for EBCs include low-thermal conductivity, thermal expansion coefficients matched with silicon-based Ceramic Matrix Composites (CMCs), and chemical compatibility with CMCs. Meanwhile, higher fracture toughness and bonding strength with CMCs can prolong the service life of EBCs. Therefore, EBCs are usually composed of three layers: the bonding layer, interlayer, and topcoat. Nowadays, EBCs have promoted to the third generation. The topcoat of EBCs in direct contact with the environment is crucial. Rare-earth silicates are considered as the most promising materials of the EBCs topcoats, owing to their appropriate thermophysical properties and excellent chemical compatibility. Additionally, mullites or rare-earth disilicates are usually selected as the interlayer material, meanwhile the bonding layer is generally silicon. During high-temperature service, corrosive media sometimes destroy the integrity of EBCs. In order to improve the service life of EBCs, different strategies have been adopted, such as solid-solutionizing treatment and high-entropy engineering. The thermal protective system of EBCs for silicon-based ceramics and composites has been developed rapidly to the promising rare-earth silicates as topcoats for the requirements of long-term service. Based on explorations of high-temperature corrosion mechanisms under attacks of water vapor

J.-H. Ouyang (✉) · G. Cao · S.-Q. Wang
School of Materials Science and Engineering, Harbin Institute of Technology, Harbin 150001, China
e-mail: ouyangjh@hit.edu.cn

S.-Q. Wang
e-mail: wang-shuqi@hit.edu.cn

and CMAS, scientists are still struggling to perfect EBCs by different strategies in order to meet the needs of practical applications.

Keywords EBCs · Silicon-based ceramics · Coating materials properties · High-temperature corrosion behavior · Failure mechanism

Abbreviations

APS	Atmospheric plasma spraying
BSAS	Barium-strontium aluminosilicate
CMAS	Calcium-magnesia-aluminosilicate
CMCs	Ceramic matrix composites
CTEs	Coefficients of thermal expansion
EBCs	Environmental barrier coatings
EB-PVD	Electron beam physical vapor deposition
PS-PVD	Plasma spray-physical vapor deposition
T/EBCs	Thermal/environmental barrier coatings
TBC	Thermal barrier coating
TGOs	Thermal growth oxides
YSZ	Yttria-stabilized zirconia

1 Introduction

Gas turbine engines for aerospace and energy generation represent the cornerstone of a rapidly growing sector, with an estimation of two trillion USD for the cumulative sales of gas turbine engines in the 2017–2031 period [1]. With such considerable economic presence, people are very interested in the development of high-performance components. Nickel-based superalloys have been the standard for hot section components of gas turbine engines, in the past decades. Improvements in thermal barrier coatings and cooling mechanisms have enabled the industry to increase the gas inlet temperature up to 1500 °C [2], thereby improving thermal efficiency, thrust-to-weight ratio, and reducing emissions of noxious by-products. However, this strategy is approaching the inherent limit of the operation temperature of Ni-based superalloys. A new approach is required for the breakthrough in the next generation of engines, and silicon-based CMCs are the most promising material to fulfil the role.

1.1 Mechanical Properties of Silicon-Based Ceramics and Composites

The development of thermal engines with high flow ratio, high thrust-to-weight ratio, high inlet temperature has been a hot spot for decades, of which high inlet temperature is the key for heat engines to achieve high thrust-weight ratio and high thermal efficiency [3, 4]. When the thrust-to-weight ratio reaches 8, the outlet temperature of the combustion chamber reaches 1650 °C, and when the thrust-to-weight ratio increases to 10–12 or higher, the outlet temperature can reach above 1850 °C [3]. Currently, nickel-based alloys used in turbines usually withstand temperatures of only 1075 °C (Fig. 1) [2], which is difficult to meet the service requirements for advanced aero-engines [4]. New materials, such as SiC, Si₃N₄, CMCs, have gradually replaced metals as a mutual material for aero-engines due to their lightweight, high operating temperatures, and superb mechanical properties. As well as, these Si-based ceramics can withstand high temperatures of 1000–1500 °C, whose density is only one-third that of superalloy [5]. However, as a high-temperature structural material, the low toughness of ceramic material is its fatal weakness in the application of engine high-temperature structural parts. Silicon carbide matrix composites (C_f/SiC, SiC_f/SiC, etc.) toughened by continuous fibers have become one of the preferred materials for aero-engines and aerospace high-temperature structural components, which is attributed to the fact that silicon carbide matrix composites retain the advantages of high temperature resistance, oxidation resistance and thermal shock resistance of SiC ceramics, simultaneously, the strengthening and toughening effect of C or SiC fibers overcomes the congenital drawbacks of low fracture toughness and poor impact load resistance of SiC ceramics. Physical and chemical properties of silicon carbide matrix composites are shown in Table 1. Thus, it can be seen that silicon-based composites with low density, high specific strength, high specific modulus, high toughness and thermal shock resistance are the most promising material to meet the service requirements of the combustion chamber with high outlet temperature (1500 °C or above) for the next generation of aero-engine.

1.2 Failure of Silicon-Based Ceramics and Composites in Service

SiC and CMCs can provide excellent high-temperature mechanical properties for engines, but the combustion environment (including oxygen, water vapor, volcanic ash, high temperature, etc.) leads to serious degradation and rapid attenuation of high-temperature mechanical properties. Silica-based ceramics are typically oxidized to form a dense SiO₂ film, that can react with water vapor to form gaseous Si(OH)₄ (Fig. 2). This causes the recession and failure of silicon-based ceramics, where the recession rate of CMCs approach 1–10 μm/h at 1300–1500 °C in the combustion [6], the reaction formulas are as follows:

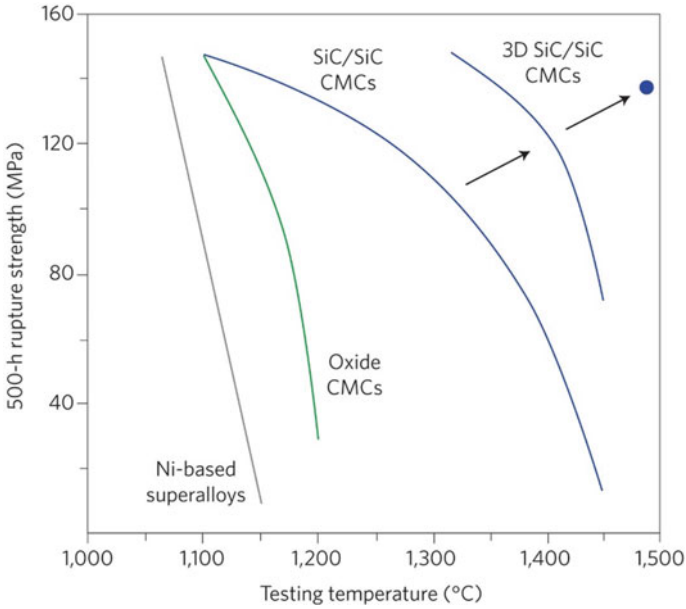
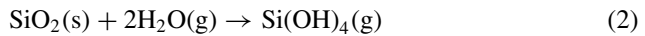
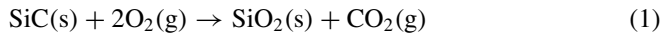


Fig. 1 Rupture strength after 500 h of continuous exposure versus testing temperature of Ni-based superalloys, oxide CMCs and various SiC_f/SiC CMCs. The blue point is the 300 h rupture strength [2]

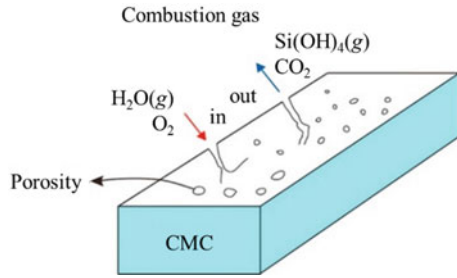
Table 1 Physical and chemical properties of silicon carbide matrix composites

	SiC	C _f /SiC	SiC _f /SiC
Density/g cm ⁻³	3.2	2.25	3.07–3.15
Expansion coefficient/10 ⁻⁶ K ⁻¹	4.3	3.8	4.0–5.1
Thermal conductivity/W (m ⁻¹ K ⁻¹)	270	120–160	80–150
Hardness/kg mm ⁻²	2500	1700	2200
Young modulus/GPa	448	291	380–430
Poisson ratio	0.168	–	–



In addition, aero-engines and gas turbines can absorb silicates existing in-service environments that originate from airborne dust, runway pieces, volcanic ash, and ambient dust or fly ash in the turbine, which is collectively referred to as CMAS (Calcium-Magnesia-Alumino-Silicate). CMAS crash the inner surface of the steam

Fig. 2 CMCs reacting with oxygen and water vapor at elevated temperatures [3]



turbine and deposit on it, which will lead to serious corrosion or molten state [7–9]. The failures of engine components due to corrosion and subsequent blockage of cooling holes cause disastrous consequences, as shown in Fig. 3 [8]. Hence, Environmental Barrier Coatings (EBCs) are prepared on the silicon-based nonoxide ceramic surface to prevent it from corrosion attacks in a harsh chemical environment [10, 11]. That is, EBCs are used to protect silicon-based nonoxide ceramic to improve their oxidation resistance, water vapor corrosion resistance and CMCs corrosion resistance, as well as reduce damage at high temperatures.



Fig. 3 Military aircraft flying during a sand storm in an arid region. Image insert-mineral dust particles passing through the gas turbine and corroding the ceramic coatings and metallic surfaces of the hot section components [8]

1.3 Performance Requirements of EBCs for Hot-Section Components

Based on the above analysis, EBCs are necessary to improve the service life of silicon-based ceramics in harsh environment of oxygen, water vapor and volcanic ash. Hence, as the EBC materials on the silicon-based ceramic surface to resist environmental corrosion, the following properties are required [12]:

- (a) Excellent phase stability at high temperatures that can avoid the failure of coating integrity. That is, during the multiple thermal cycles service, good phase stability can prevent thermal stress caused by phase transformation, as well as avoid cracking and premature failure of the coating.
- (b) Coefficients of Thermal Expansions (CTEs) close to substrate materials of Si-based ceramics or CMCs, which avert coating delamination or cracking of coating caused by mismatch of CTEs. Namely, in the process of preparation and subsequent application of coatings, the volume change of coatings caused by the variations of temperature can produce the stress between different layers in EBCs, which induces the formation of cracks or even exfoliation of coating.
- (c) Excellent hot-corrosion resistances. Specifically, on the one hand, water-oxygen and CMAS corrosion can easily lead to phase transformation of EBC materials; on the other hand, water-oxygen and CMAS corrosion media can also spread to the substrate through the defects in the coatings. These two different corrosion forms cause the reduction of effective coating thickness, and overall cracking even complete spallation of coatings.
- (d) Good chemical compatibility is necessary to avoid harmful reactions with substrates.
- (e) Low thermal conductivity, which can decrease the substrate temperature and the corrosion rate.

2 Development for EBCs Materials

The development of EBCs is generally classified as different generations according to the main composition used. In this section, the EBCs materials of different generations are reviewed in detail.

2.1 The First-Generation EBCs

(a) Mullite/YSZ Coating

Mullite ($3\text{Al}_2\text{O}_3 \cdot 2\text{SiO}_2$) coating originates from the research on the corrosion of silicon-based ceramics by $\text{CaO-MgO-Al}_2\text{O}_3\text{-SiO}_2$ molten salts. Mullite coatings with low density, low-thermal conductivity, thermal expansion coefficient close to

non-oxide ceramics, high-temperature oxidation resistance and molten-salt corrosion resistance can prolong the service life of silicon-based ceramics. Price et al. [13] prepared a durable mullite coating by air plasma spraying (APS) to prevent corrosion of SiC heat exchange tube; however, more penetrating cracks were produced on the coating, which resulted in the destruction of the matrix during the service process. The cracks formation mechanism of mullite coating was investigated by NASA's Glenn research center [14], which resulted from many amorphous phases in mullite coating prepared by APS. Specifically, at high temperature, the metastable amorphous phase mullite was transformed into a crystal phase with lower free energy, accompanied by volume shrinkage. On the other hand, the decomposition of mullite during spraying led to the formation of Al₂O₃ phase in the coating, while the difference in coefficients of thermal expansion between mullite and Al₂O₃ caused residual stress, finally resulting in cracks [15]. Additionally, mullite has a high SiO₂ activity (~0.4) and a low activation energy of reaction with water vapor (about 78 ± 10 kJ/mol). This means that SiO₂ in the coating reacts easily with water vapor to form volatile Si(OH)₄ and loose Al₂O₃ layer [16]. Thus, it can be seen that mullite has a poor resistance to water-oxygen corrosion, which can be compensated by adding more stable compounds in the water-oxygen environment as the top coating. Based on the advantages of yttria stabilized zirconia (YSZ) in thermal barrier coating (TBC) system, meanwhile considering its cost and practicability, YSZ and mullite were used to form a double-layer coating [17]. Lee et al. [18] tested the oxidation weight change of the mullite/YSZ coating after thermal exposure in 50 vol% H₂O–50 vol% O₂ environment at 1573 K for 100 h and found that mullite/YSZ coating can reduce the volatilization of SiO₂ in high-temperature water-oxygen environment, which exhibited a good water-oxygen corrosion resistance. Unfortunately, it is easy to produce penetrating cracks under long-term service conditions. Mesquita et al. [17] prepared two types of mullite/YSZ coatings on the SiC substrate by APS. The thermal cycling experiments were carried out in 90 vol% H₂O–10 vol% O₂ environment with the flow rate of 3.5 cm/s and the pressure of 1 atm, at 1300 °C for 2 h, and then cooled to room temperature for 0.5 h. As a result, obvious microstructural damage occurred in the coating. As shown in Fig. 4 [17], microcracks and openings were first produced in the top YSZ layer. Obvious cracks appeared in the coating after 100 cycles, which propagated to the Si bonding layer and resulted in a certain stress relaxation in the YSZ layer and lots of pores simultaneously. The reason is that the mismatch of thermal expansion coefficient of mullite and YSZ caused residual stress during the thermal cycling process, inducing crack initiation and propagation, which provided rapid diffusion channels for the corrosive medium (water-oxygen and CMAS) to further speed up the corrosion process.

(b) **Si/mullite/BSAS coating**

Although mullite/YSZ coating can provide protection for hundreds of hours in a water vapor environment of about 1300 °C, the crack initiation caused by the mismatch of the thermal expansion coefficient between YSZ and Mullite/SiC leads to the premature failure of EBCs. Hence, the top layer of YSZ is replaced by barium-strontium aluminosilicate (BSAS). BSAS has a relatively low coefficient of thermal

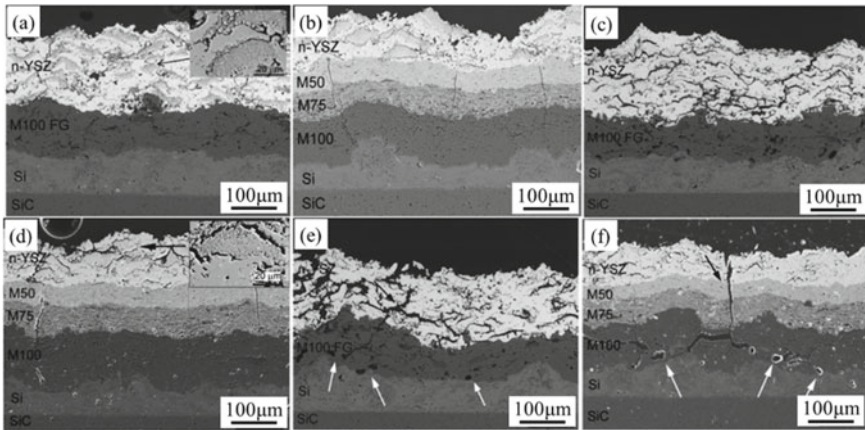


Fig. 4 Microstructural morphologies of two types of mullite/YSZ coatings (a, b); SEM micrographs of the cross sections of two types of coatings architectures thermally aged 50 (c, d) and 100 cycles (e, f), respectively [17]

expansion, low elastic modulus, high fracture resistance and good water-oxygen corrosion resistance, so it is not easy to produce thermal stress between BSAS and mullite layer. Meanwhile, a Si layer is added as a bonding layer between mullite and the substrate material (SiC, Si_3N_4 or CMCs) to improve the adhesion of the whole system [19, 20]. Lee et al. [19] investigated the corrosion behavior of the BSAS/mullite/Si coating during the 300 thermal cycles (1 h for 1 cycle) at 1400 °C in the 90 vol% H_2O –10 vol% O_2 environment. As shown in Fig. 5a, the Si bonding layer was oxidized to produce SiO_2 into the BSAS layer after 300 thermal cycles. Since BSAS and SiO_2 exist a co-melting point, the melting point of BSAS– SiO_2 decreases with the composition towards the co-melting point, producing a glass phase resulting in spalling of the coating. Therefore, it is found that the service life of the Si/mullite/BSAS coating is longer than that of the first generation mullite/YSZ coating, but when the working temperature reaches 1400 °C and the working time is more than 300 h, the resulting glass phase can cause the spalling failure of the coating. Cojocaru et al. [21] also investigated the porosity of Si/mullite/BSAS coating caused by water–oxygen corrosion and the thermal growth oxides (TGOs) formed on the interface of Si/mullite, as well as their failure behavior.

2.2 The Second-Generation EBCs

Although the service life of Si/mullite/BSAS coating is longer than that of mullite/YSZ coating, its service temperature is still difficult to meet the requirements of higher thrust-to-weight ratio of advanced aero-engines. The application requirement of coatings proposed by NASA in 1999 was that the coating surface can withstand

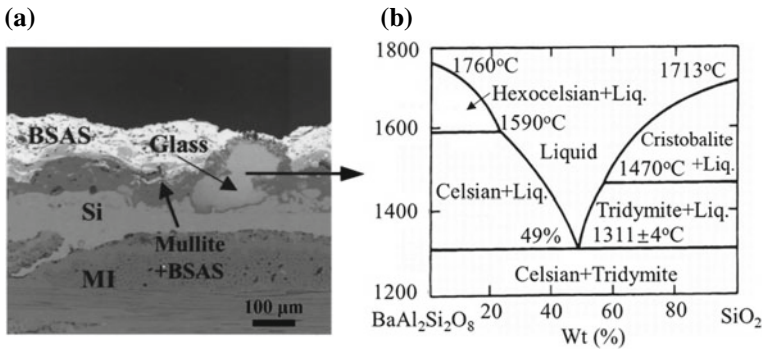


Fig. 5 Cross-sectional morphology (a) of the Si/(mullite + BSAS)/BSAS coating after 300 cycles (1 h for 1 cycle) at 1400 °C in the 90 vol% H_2O –10 vol% O_2 environment the phase diagram of BAS– SiO_2 (b) [19]

high temperature water-oxygen corrosion at 1482 °C and ensure that the interface temperature of the coating/substrate was lower than 1316 °C. To overcome the limitations of the above two generations of EBCs, researchers try to find a top coating with good chemical compatibility with mullite interlayer at higher temperature and low-thermal stress during thermal cycling. Rare-earth silicates have many advantages, such as high melting point, low thermal conductivity, good chemical stability at high temperature and thermal expansion coefficient similar to that of silicon-based ceramics. Therefore, rare-earth silicates show better resistance to high-temperature water-oxygen corrosion than BSAS, and have become the most potential candidate material for the top layer of EBCs [22, 23].

Lee et al. [24] prepared EBCs on the surfaces of SiC and Si₃N₄ with different rare earth silicates as top layers by APS, and the high-temperature water-oxygen corrosion resistance and chemical compatibility with mullite layers at 1300–1500 °C were characterized. The rare-earth silicate materials were verified to have a better resistance to high temperature water-oxygen corrosion than BSAS (as shown in Fig. 6 [24]), which indicated that rare-earth silicate as the top-layer material can make EBCs serve at higher temperatures. But the service lifetime is still difficult to meet the requirements of NASA, so searching for the best rare-earth silicate materials and designing reasonable multi-layer EBCs have become the key breakthrough.

2.3 The Third-Generation EBCs

On the basis of the structure and material systems of the second-generation EBCs, to further improve the service lifetime of the EBCs, it is necessary to modify the topcoat rare earth silicate materials, so as to derive the third-generation EBCs, that is, the optimized rare earth monosilicate system. In recent years, researchers have explored a variety of effective modification methods including solid solution doping [25] and

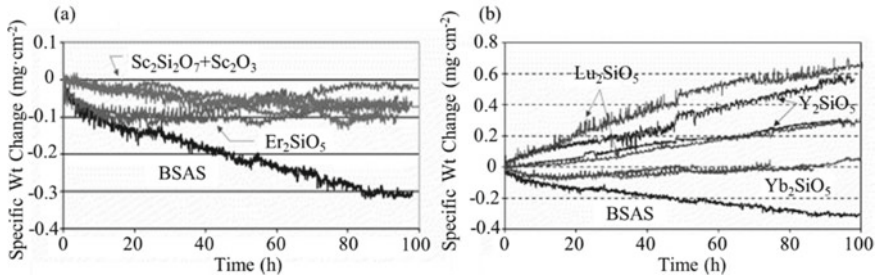


Fig. 6 Volatilization weight loss of hot-pressed rare-earth silicates exposed to 50 vol% H₂O–50 vol% O₂ with a velocity of 4.4 cm s⁻¹ at 1500 °C under a total pressure of 1 atm: **a** Sc₂Si₂O₇ + Sc₂O₃ and Er₂SiO₅; **b** Lu₂SiO₅, Y₂SiO₅ and Yb₂SiO₅ [24]

composite modification [26, 27], to tailor the thermal expansion coefficient, thermal conductivity, mechanical properties and high temperature corrosion resistance of top-layer materials. Of all the rare-earth silicate coatings studied recently, the yttrium silicate composition appears to have present advantages in its industrial applications [28]. Further research is still needed, especially with regard to the appropriate deposition techniques needed to meet successful EBC. Although this preference is based on its inherent properties and high-temperature behavior, there is still plenty of room for improvement, and future studies of more complex constituents based on ytterbium silicate might represent the future of the field. Besides, adding self-healing particles (such as SiC, MoSi₂) to the top-layer materials is also a new idea, which is attributed to the fact that the local compressive stress produced by high-temperature oxidation can close the cracks in the EBCs during the thermal cycling to improve the service life of coatings [29].

3 Fabrication and Characterization of EBCs

3.1 Fabrication Methods

The fabrication methods of EBCs include APS, slurry impregnation, EB-PVD, chemical vapor deposition, sol–gel, and hydrothermal electrophoretic deposition, etc.

APS is the most commonly used EBCs preparation technique reported at present [30], mainly using plasma flame to heat and melt the spraying powder. The spraying materials are impacted to the workpiece surface at high speed under the action of high-speed plasma flame flow, forming a flat layer with a laminar structure that consists of numerous deformed particles interlocked and hooked in a wave-like stacking. Some pores or voids are inevitably produced between layers (the porosity is generally between 4 and 20%) due to the temperature gradient of the plasma arc. There also

exist some oxide inclusions in the coatings due to the extremely high temperature of the plasma arc. These defects are conducive to reducing the thermal conductivity of coatings, relieving the internal stress in the coating and preventing the propagation of cracks. However, these defects in the coating may also provide channels for oxygen, water vapor and other corrosive gases in the engine environment.

The slurry impregnation mainly consists of the following steps: (1) the substrate material is immersed in a slurry; (2) the substrate material is lifted out of the slurry uniformly and slowly to form a wetted thin layer on the surface; (3) the coating is dried, cured and shaped. The advantages of the slurry method are associated with a simple preparation process, low cost, and suitable for complex components. However, the coating thickness prepared at one time is thin due to the cracking tendency in an excessive-thickness coating. Hence, the slurry-prepared coating requires multiple preparations and multiple sintering, which may cause damage to the fibers in the CMC–SiC composites, especially the SiC fibers, decreasing the mechanical properties.

EB-PVD [31] is also a common technique for preparing thermal barrier coatings. EB-PVD coatings generally have a columnar structure with a large number of inter-columnar pores perpendicular to the coating surface and small intra-columnar crystalline pores. The coating with such a structure has a good adhesive strength with the matrix and the thermal stress is relieved. However, the heat flow transfer cannot effectively impede due to the inter-column pores being strips perpendicular to the coating surface. Thus, the thermal conductivity of coating prepared by EB-PVD is generally higher than that by plasma spraying. In addition, the corrosive media are easy to permeate the inside of the coating along the inter-column pores in the high-temperature water vapor or CMAS environment, accelerating the corrosion of the coating. Recently, a new method by combining their advantages may be available to prepare high-performance EBCs by plasma spray-physical vapor deposition (PS-PVD) [32], as well as the new in situ generating coating method with dense structure need to be further explored [33].

3.2 Structure and Performance Characterization

3.2.1 Structural Characterization

Common basic characterizations include scanning electron microscope attaching energy spectrometer, Transmission electron microscopy, XRD, Fourier transform infrared spectroscopy, Raman spectroscopy, X-ray photoelectron spectroscopy, Image-J software, etc. In addition, there are other means of structural characterization, such as 3D-CT, scanning precession electron diffraction, synchrotron radiation, Electron Backscattered Diffraction, Brunauer–Emmett–Teller Focused Ion beam, Special Aberration Corrected Transmission Electron Microscope, etc.

3.2.2 Performance Characterization

(1) Adhesive Strength

According to the ASTM-C633 standard, the adhesive strength of the coating was measured by dual tensile method. The experimental conditions were as follows: the loading rate was 2 mm/min, until the tensile fracture of the coating sample. The load of tensile fracture was recorded, and the adhesive strength σ (MPa) of the coating was calculated according to Eq. (3):

$$\sigma = \frac{F}{S} \quad (3)$$

where F (kN) is the tensile load of the coating fracture, S (m²) is the coating surface area.

(2) Vickers Hardness and Crack Propagation Resistance

The hardness (HV) of ceramic coating was tested by Vickers hardness tester. The coating hardness was calculated by Eq. (4), and the average value represents the actual hardness of the coating.

$$HV = 1.8544 \frac{F}{\left(\frac{D_1 + D_2}{2}\right)^2} \quad (4)$$

where F (kgf) represents load, D_1 and D_2 (mm) are the diagonal lengths of the indentation.

Besides, the crack propagation resistance was analyzed using the crack propagation length (L) at the indentation tip. Under the same load, the larger the crack length at the indentation tip, the lower the crack propagation resistance of the coating. By analyzing crack propagation resistance of different coatings, the indentation fracture toughness of different coatings can be qualitatively compared.

(3) Thermal Shock

Thermal shock resistance of coatings was evaluated by the method of heating followed by water-quenching. Thermal cycle process was repeated until the peeled-off part of the coating surface reached nearly 20%, and the number of thermal cycles after thermal shock failure is defined as its thermal cycle life.

(4) Phase Stability Test

The ceramic material was sintered at high temperature for 500 h to test whether the phase transition occurred and whether the weight loss was less than 0.1%.

(5) Coefficient of Thermal Expansion

CTEs of ceramic materials was measured by high-temperature thermal dilatometer. The test temperature was 30–1500 °C.

(6) Thermal Conductivity

The thermal conductivity of ceramics and coatings was measured by instantaneous dotting method, that is, the thermal diffusivity (mm^2/s) of samples was tested by laser stroboscopic equipment, and then the thermal conductivity λ ($\text{W m}^{-1} \text{K}^{-1}$) can be calculated from Eq. (5).

$$\lambda = \alpha \cdot \rho \cdot C_p \quad (5)$$

where ρ (g cm^{-3}) and C_p ($\text{J g}^{-1} \text{K}^{-1}$) are the material density and the specific heat capacity, respectively.

The density of ceramic materials was measured by the Archimedes buoyancy method and calculated by Eq. (6).

$$\rho = \frac{m_1}{m_1 - m_2} \quad (6)$$

where m_1 (g) and m_2 (g) are mass of sample in air and mass of sample under buoyancy force in water, respectively.

The coating density ρ_2 can be calculated by the Eq. (7).

$$\rho_0 = \frac{\rho_1 x_1 + \rho_2 x_2}{x_1 + x_2} \quad (7)$$

where ρ_0 (g cm^{-3}) is the total density of matrix + coating, ρ_1 (g cm^{-3}) is the density of matrix, x_1 (mm) is the thickness of matrix, x_2 (mm) is coating thickness.

The specific heat capacity (C_p) of ceramic materials was characterized by differential scanning calorimeter. The specific heat capacity of the coating material used the test results of the above ceramic material. For the coating sample, the thermal conductivity can be obtained by inputting the density ρ_1 , thickness x_1 , specific heat capacity, thermal conductivity of matrix and the density ρ_2 , thickness x_2 and specific heat capacity of the coating into the testing equipment.

The thermal conductivity of ceramic materials was modified by Eq. (8) to obtain the real thermal conductivity [34].

$$\frac{\lambda}{\lambda_0} = 1 - \frac{3}{4}\phi \quad (8)$$

where λ is test thermal conductivity, λ_0 is actual thermal conductivity, ϕ is ceramic porosity.

(7) Construction of High Temperature Water–Oxygen Corrosion Platform and Corrosion Test Design

The schematic diagram of the high-temperature water–oxygen corrosion platform is shown in Fig. 7, which mainly includes a precision liquid gas generator that provides water-oxygen atmosphere, a tube furnace that provides a high-temperature

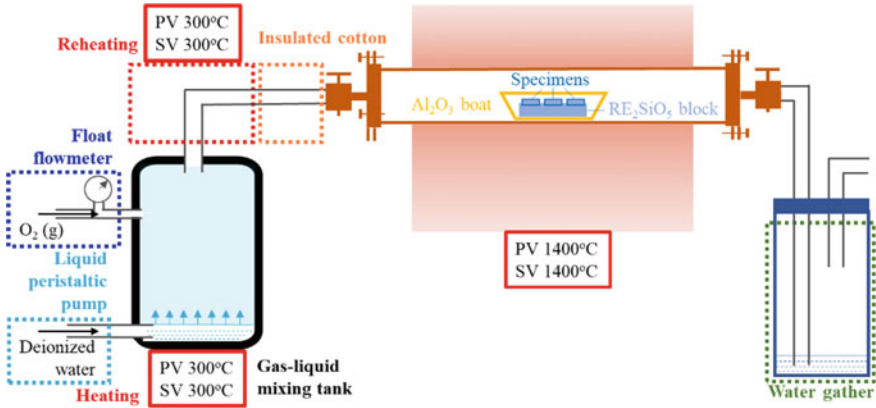


Fig. 7 Schematic diagram of water–vapor–oxygen corrosion device [35]

environment, and a tail collector located in the outlet section of the tube furnace to verify the water-oxygen ratio in the corrosion environment [35].

Corrosion test design: In the part of the precision liquid gas phase generator, the temperature of the gas–liquid mixing tank and the reheating zone was set to 573 K to ensure that the deionized water quickly evaporate into water vapor and mix with oxygen and enter the tube furnace to provide a water-oxygen corrosion atmosphere, and water vapor condensation will not occur before entering the tube furnace. In order to provide the water-oxygen mixture gas with water-oxygen ratio of 50 vol%–50 vol% and $1.7 \times 10^{-3} \text{ m s}^{-1}$ air flow speed to the tube furnace with inner diameter $\Phi 50 \text{ mm}$, the peristaltic pump rate was set to 0.08 mL min^{-1} and the inlet end float Flowmeter was set to 100 mL min^{-1} . In the part of the tube furnace, the water oxygen corrosion temperature and time set were 1300, 1400, 1500 °C and 4, 16, 36, 64, 100 h, respectively, and the heating rate was 10 K min^{-1} . The function of the tail collector was to collect the mixed gas of water and oxygen from the outlet in the process of high-temperature water-oxygen corrosion, and a certain amount of liquid was added at the beginning of the test to ensure that the mixed gas of water and oxygen can be condensed into liquid phase water here. Whether the ratio of water to oxygen in the test process was correct or not was verified by calculating the volume difference of the liquid phase before and after corrosion. Finally, the sample was placed in the central temperature zone of the tubular furnace to ensure the corrosion temperature during the high temperature water oxygen corrosion process.

(8) High-Temperature Contact Angle Test

The main body of the high-temperature CMAS contact angle testing platform is composed of a tube furnace and a high-speed CCD camera. The metal material flange of the air outlet is replaced by a perspective flange in order to record the melting and wetting spreading behavior of CMAS at high temperature. The schematic diagram of the high-temperature contact angle testing device is shown in Fig. 8. The end temperature of the high-temperature wetting angle test was set to 1400 °C and kept

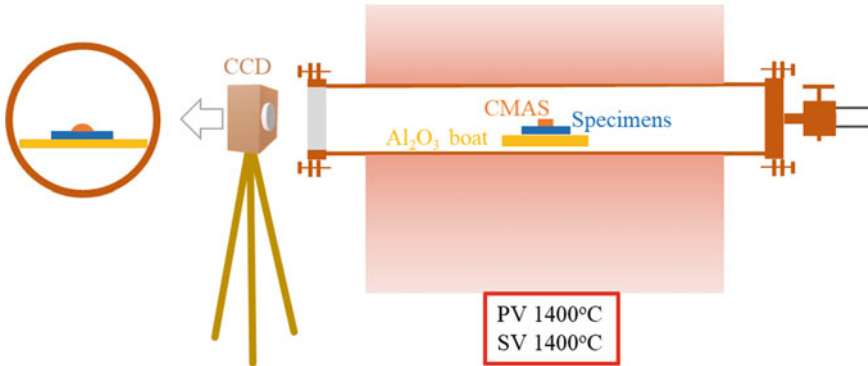


Fig. 8 Schematic diagram of contact angle measurement device at high temperatures

at that temperature for 30 min; the heating rate from room temperature to 1100 °C was 10 °C min⁻¹; the heating rate was 3 °C min⁻¹ at 1400 °C; the ambient atmosphere was air atmosphere.

(9) CMAS Corrosion Test Design

The sample surface was polished to 1 μm and cleaned with acetone. Before and after placing the CMAS powder on the surface, samples were weighed to ensure the weight of the added CMAS powder to provide a CMAS surface concentration of ~30 mg/cm². Subsequently, the samples coated with CMAS powder were heated in constant temperature air at 1300 °C, 1400°C for hot corrosion reaction, respectively.

3.3 Properties

3.3.1 Thermal Expansion Coefficients and Damage Tolerance

For EBCs, it should be stable to undergo temperature variations, and possess strong adhesion with Si-based ceramics. Therefore, high-temperature mechanical properties and thermophysical properties of layers in EBCs should be evaluated carefully. Also, EBCs should be effectively resistant to corrosive media during long service to play the environmental barrier role well.

Appropriate design of EBC system can fundamentally reduce thermal stresses between layers in EBCs system. On the one hand, coatings sprayed by APS, as the most usual coating preparation method, usually produce thermal stresses during the cooling down process. On the other hand, all the layers in EBCs suffer from expansion and shrinkage due to temperature shocks during service life. With similar CTEs, CTEs mismatches among layers and between bond layer and silicon-based ceramic can be reduced, which restrain void cracks and spallation of coatings effectively, prolonging service life. As simplified module, during the cooling down process of

EBCs spraying, with temperature decrease of ΔT , the coating modulus, passion's ratio and CTE of E_{EBC} , ν_{EBC} and α_{EBC} , thermal mismatch stress σ_t can be estimated by Eq. (9) [36]. Therefore, screening materials with appropriate modulus, passion's ratio and CTE are necessary for EBCs system design. Although bond strength is a concern, multilayer EBCs are promising to provide small CTE gradients between layers and hence reduce thermal stresses.

$$\sigma_t = \Delta T \times E_{\text{EBC}} \times \frac{\alpha_{\text{EBC}} - \alpha_{\text{Substrate}}}{1 - \nu_{\text{EBC}}} \quad (9)$$

Table 2 lists thermal expansion coefficients, elasticity modulus and passion's ratios of some rare-earth silicates. Rare-earth disilicates with beta or gamma crystal structure generally possess CTEs close to silicon-based ceramics. Therefore, they are usually applied as the layer connecting directly to substrate or bond layer. However, as introduced in a later section, rare-earth disilicates usually suffer from more severe corrosion from both water vapor and CMAS. As a result, only rare-earth disilicates as topcoats of EBCs cannot meet the corrosion resistance requirement. Therefore, rare-earth monosilicates have been usually chosen as the topcoats materials to provide lower volatilization rates when attacked by water vapor and oxygen, as well as higher crystallinity ability in CMAS to form a barrier layer to resistant further CMAS corrosion.

Besides monitoring the length deviation between ends of the strip specimens, CTE can also be evaluated by the analysis of minor changes in XRD patterns of specimens placed at different temperatures. By this way, the intrinsic lattice expansion can be evaluated. As results, there exist significant CTE differences among axes of rare-earth monosilicate crystal structures. CTE in *b*-axis is similar to the linear measured CTE, in *a*-axis is higher, while in *c*-axis is as low as $\sim 2 \times 10^6 \text{ K}^{-1}$ which is not sensitive to types of rare-earth elements [43, 44]. Therefore, when considering the application of rare-earth monosilicates as layers in EBCs, the higher anisotropic CTEs have to be carefully designed to meet lower thermal stresses. For rare-earth oxyapatites, they are rarely applied in EBCs due to the excessive CTEs, although some literatures pointed out their potential resistance to CMAS corrosion at elevated temperatures [45, 46]. However, the relatively low modulus may be complementary for their excessive CTEs to reduce thermal stresses, which still needs further research.

3.3.2 Thermal Conductivity

Low thermal conductivity of coatings could, to some degree, keep the substrate materials at lower temperatures and maintain higher mechanical properties. Nowadays, a concept of thermal/environmental barrier coatings (T/EBCs) raises, which means the barrier role of coatings for both thermal attack and environmental corrosive media [43, 47–49]. Therefore, lower thermal conductivity also becomes as a criterion if materials can be applied in EBCs. For rare-earth silicates, all the

Table 2 Mechanical properties and CTEs of some rare-earth silicates

Compound	Density (g cm ⁻³)	Elastic modulus <i>E</i> at RT (GPa)	Poisson's ratios ν	CTE ($\times 10^{-6}$ K ⁻¹)	Refs.	
Tb ₂ SiO ₅	6.35	144	0.229	8.86 (RT–1473 K)	[37]	
Dy ₂ SiO ₅	6.49	151	0.225	7.62 (RT–1473 K)		
Ho ₂ SiO ₅	6.56	148	0.214	7.61 (RT–1473 K)		
Er ₂ SiO ₅	6.73	157	0.219	7.63 (RT–1473 K)		
Tm ₂ SiO ₅	6.9	163	0.225	7.65 (RT–1473 K)		
Yb ₂ SiO ₅	7.1	158	0.221	7.33 (RT–1473 K)		
Lu ₂ SiO ₅	7.24	172	0.226	6.95 (RT–1473 K)		
Y ₂ SiO ₅	4.22	155	0.200	7.45 (RT–1473 K)		
β -Y ₂ Si ₂ O ₇	3.93	170	–	4.1 (293–1673 K)		[38–41]
β -Lu ₂ Si ₂ O ₇	6.25	178	0.306	4.2 (303–1873 K)		
β -Yb ₂ Si ₂ O ₇	6.13	168	0.30	4.0 (303–1873 K)		
γ -Y ₂ Si ₂ O ₇	4.04	155	0.270	3.9 (300–1573 K)		
La _{0.33} Si ₆ O ₂₆	5.31	141	–	9.6 (300–1073 K)	[42]	

rare-earth disilicates, monosilicates, and oxyapatites possess low thermal conductivities, especially at high temperatures, which is due to the complex monoclinic crystal structure and heavy rare-earth atoms. As a simulated result by Slack module, intrinsic thermal conductivity of rare-earth monosilicates can reach very low, close to 1 W (m⁻¹ K⁻¹)[41]. Experimental measurements of thermal conductivities are shown in Table 3. Although affected by thermal radiation at high temperatures, the measured thermal conductivities of X₂-Ho₂SiO₅ of a quite low value of 1.11 W m⁻¹ K⁻¹ at 1000 °C. Also, some of β -RE₂Si₂O₇ has low thermal conductivities of 1.6–1.9 W m⁻¹ K⁻¹ at 1000 °C. Simultaneously, all of rare-earth oxyapatites possess low thermal conductivities ranging from 1.10 to 1.14 W m⁻¹ K⁻¹ at 1000 °C [50]. Furthermore, thermal conductivity is easy to mediate by introducing dopants, which destroys the lattice periodicity.

Table 3 Experimental thermal conductivities (λ) of rare-earth silicates at 1000 °C ($\text{W m}^{-1} \text{K}^{-1}$) [37–40]

	RE ₂ SiO ₅							RE ₂ Si ₂ O ₇			
RE	Dy	Ho	Er	Tm	Yb	Lu	Y	Y, β	Lu, β	Yb, β	Y, γ
λ	1.53	1.10	1.41	1.53	1.25	2.06	1.52	1.64	1.74	1.83	3.25

3.3.3 CMAS Corrosion

CMAS is mainly composed of CaO, MgO, Al₂O₃ and SiO₂, with some trace oxides like Na₂O and Fe₂O₃. The viscosity of CMAS glass reduces with increasing temperature [51]. Another helpful finding is that the calculated value by Fluegel and FactSage models approach experimental viscosity of CMAS glass. Verified by both calculations and experiments, viscosity of CMAS glass reduces as the concentration ratio of SiO₂ to CaO decreases [52], which is attributed to the variations on the glass network structure. This reveals CMAS with a high concentration ratio of SiO₂ to CaO usually infiltrates along grain boundaries or other microstructural defects more quickly. In consideration of the initial contact between CMAS and EBCs, CMAS clusters generally crash to the top surface of EBCs in a form of melting droplets. The splash morphology tends to form on smooth surfaces with radial jetting and break-up, while circular- and disc-like splats tend to form on rough surfaces because the asperities on rough surfaces limits the flow [53]. By sessile drop method, the diffusing and wetting behaviors of CMAS are acquired. CMAS clusters become dense driven by surface tension, until forming large droplets, with internal bubbles and crystals unfolding on the surface. When the crystals in the droplet dissolve into the melt, the wetting state changes from heterogeneous to homogeneous [54]. Besides experiments, simulations show some interesting and meaningful intrinsic wetting mechanisms of CMAS on coating surfaces. For example, molecular dynamics simulations are used to investigate the wetting process of CMAS on surface of YSZ, revealing that the distribution of oxygen anion is the main factor determining the wetting behavior and even the corrosion behavior [55].

More than that, possibly the thermal hazard is underestimated while sticking temperature is overestimated, which results from the inaccurate substitution of sand or dust proxy for volcanic ash. Hence, some experimental data of volcanic ash at home and abroad were collected and then the behavior of volcanic ash adhesion was parameterized. On this basis, a model is established to evaluate the probability of volcanic ash deposition in the engine. As shown in Fig. 9, during thermal heating, various volcanic ashes undergo approximately four stages, corresponding to four characteristic temperatures composed of a shrinkage temperature (ST), a deformation temperature (DT), a hemispherical temperature (HT) and a flow temperature (FT). These characteristic temperatures express the initial contacting behavior of volcanic ashes on the surface. Apparently noted, there exist strong differences in characteristic temperatures for different volcanic ashes. This finding is meaningful for evaluating initial sticking behaviors, which can forward guide analysis of the

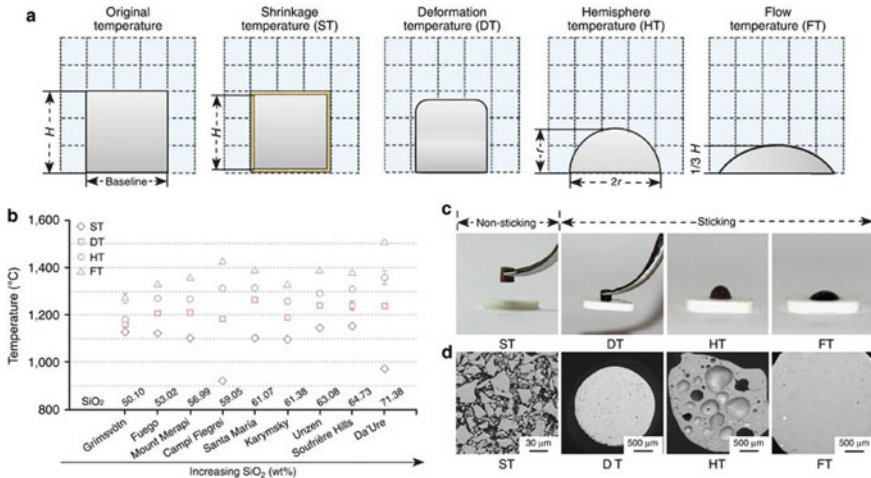


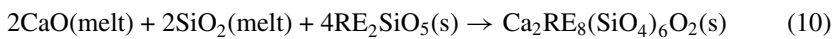
Fig. 9 Geometric characteristics of volcanic ash after compaction at the different characteristic temperatures: **a** Geometrical definition of four characteristic temperatures (ST, DT, HT and FT) during the volcanic ash melting process, **b** distribution of the four characteristic temperatures for the nine volcanic ash, **c** typical behavior observed in the experiment, **d** SEM images of corresponding microstructures of the volcanic ash at the four characteristic temperatures [56]

CMAS hot corrosion behavior. Therefore, properties of CMAS glass depend on their components and compositions, which affect the CMAS corrosion behavior significantly. The viscosity of glass contributes to the infiltration of CMAS glass into the topcoat of EBCs, and leading to the CTE mismatch between CMAS, apatite and rare-earth silicate [56].

When it comes to interactions between CMAS and EBCs, the CMAS hot corrosion behavior of rare-earth silicates can be commonly considered as a dissolution-precipitation process [57–62]. It means during the CMAS corrosion process, topcoats also dissolve into high-temperature melts besides react with them, even sometimes the generated products also dissolve again. The reprecipitation is originated from the local constituent supersaturation after dissolution of some cations from topcoats or corrosion products. Due to the complex composition variations during the CMAS corrosion process, reprecipitated products are different, containing oxyapatite, garnet, or even cyclosilicate, reprecipitated rare-earth monosilicates and disilicates. The corrosion products are determined by thermodynamics combined with composition. Larger rare-earth cations tend to form stable oxyapatite phase with rod-like feature, even without participant of large Ca^{2+} , like La^{3+} and Gd^{3+} . As cationic radius decreasing, rare-earth cations require more amount of Ca^{2+} to form thermostable oxyapatite, which means a lower growth rate of the apatite corrosion layer. However, rare-earth cations with smaller radii tend to combine with Ca, Mg, Al and Si to form garnet phase with sphere-like feature. It is usually formed around the oxyapatite layer near the melt side, due to the local concentration enhancement by expelling Ca, Mg, Al cations during the oxyapatite formation. Some scientist

considered that the formation of garnet phase is more efficient to consume the melt than oxyapatite phase, owing to its consumption of all species of main compositions in CMAS. It's worth noting here that both the formed oxyapatite and garnet are normally non-stoichiometric, whose stoichiometry depends on the melt composition and varies with the temperature and time durations [63–65].

However, new corrosion products seem to form more easily in rare-earth monosilicates other than disilicates [44]. This is probably resulting from the role difference of silica playing in the corrosion reaction. Taking the oxyapatite reaction for example, the formulas of reactions are Eqs. (10) and (11) for rare-earth monosilicates and disilicates, respectively. For rare-earth monosilicates, the reaction consumes silica in melt and resulting in the concentration enhancement of calcia, however the reaction generates silica for rare-earth disilicates. Some previous study indicated that the reprecipitation of oxyapatite generally leaves off once the ratio of $c(\text{CaO})/c(\text{SiO}_2)$ decreasing to the critical value [66]. Therefore, the rare-earth monosilicates are more effective crystallizing agent for CMAS compared with rare-earth disilicates. Furthermore, rare-earth disilicates also exhibit less reaction activity with CMAS, which usually leads to a catastrophic failure when combined with the low CTE of $\sim 4.0 \times 10^{-6} \text{ K}^{-1}$ (for $\beta\text{-RE}_2\text{Si}_2\text{O}_7$). For example, CMAS rarely reacts with $\beta\text{-Yb}_2\text{Si}_2\text{O}_7$ but infiltrates into the interior along microstructural defects or grain boundaries. CMAS existing among grain boundaries possess CTE quite higher than $\beta\text{-Yb}_2\text{Si}_2\text{O}_7$, which leads to huge thermal stress when temperature decreasing or thermal shocking, and further inducing the so-called “blister” cracks through most of the topcoat, as shown in Fig. 10 [67]. Therefore, screening appropriate materials to crystallize CMAS according to the actual service environment (temperature, composition of CMAS, etc.) is more important to improve reliability of EBCs under the CMAS attack. It is equally important that the grain boundary stability of rare-earth silicates requires to improve for inhibiting the infiltration of high-temperature CMAS melt, which will be introduced in the Sect. 3.3.4.



In terms of the current research, characterization of CMAS corrosion resistances can be divided into approximately three aspects. First are the properties of CMAS glass, like the critical temperature of sticking, and viscosity which determines infiltration rate and sticking temperatures. Second is the thermodynamic equilibrium phase diagram of the system composed of multiple oxides including rare-earth oxides. Based on the phase diagram, probable crystallized products for different coatings combined with CMAS of different components can be forward predicted. Third are the observations on the interaction effects between EBCs composed of specific layers or the corresponding ceramic substitutes and CMAS of specific components. However, CMAS corrosion resistances of EBCs are hard to evaluate and compare

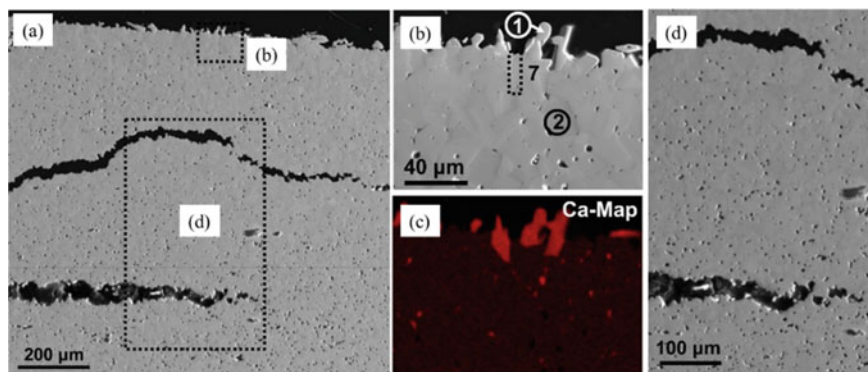


Fig. 10 SEM images of cross section of β - $\text{Yb}_2\text{Si}_2\text{O}_7$ pellet interacted with CMAS at 1500 °C for 24 h: **a** low (whole pellet) and **b**, **d** high magnification. **c** Ca elemental mapping corresponding to **d**. The dashed boxes in **a** illustrate regions where high magnification SEM images in **b** and **d** were collected from [67]

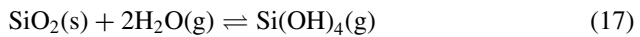
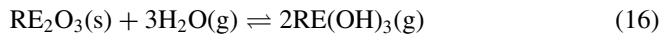
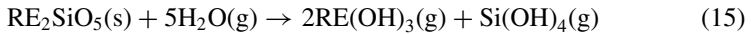
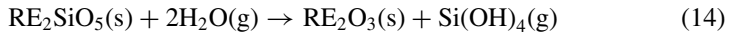
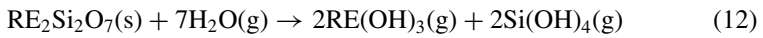
for different types of coatings, due to the variation on temperature, CMAS composition and failure forms. For rare-earth monosilicates, the recession rate is mostly equal to the growth rate of interfacial apatite layer. Thinner thickness of apatite layer normally means better CMAS corrosion resistance. However, for rare-earth disilicates, coating failure should be evaluated by both the recession rate of topcoats and cracks or fracture induced by interior thermal stress.

3.3.4 Water Vapor/Oxygen Corrosion

In water vapor/oxygen corrosion environment, EBCs are corroded to failure due to two aspects, namely interactions between water/oxygen and topcoats, as well as between corrosive media (water/oxygen) diffused into EBCs and bond layer. For the first interaction, topcoats tend to react with water vapor to generate volatile hydroxides, leading to reduction of the effective thickness of topcoat in EBCs system. Meanwhile, some interactions result in some solid-phase products undergoing phase transitions, which sometimes induce thermal stress and further spallation [68–70]. For the interaction at the bond layer, the main concern is the formation of thermal growth oxide (silica) by reaction between silicon and oxygen. Silica usually undergoes phase transition, which can give rise to the spallation of entire EBCs when combined with thermal shocks during service [71–73].

Rare-earth silicates usually react with water vapor to form volatile rare-earth or silicon hydroxides. For rare-earth disilicates, they may generate volatile rare-earth or silicon hydroxides directly, as Eq. (12), or generate rare-earth monosilicates and silicon hydroxides firstly, as Eq. (13). Monosilicates also subsequently generate rare-earth oxides/hydroxides and silicon hydroxides, as Eqs. (14) and (15) [74]. As shown in Table 4, the specific reaction products depend on the type of rare-earth element and

the partial pressure of water vapor, gas flow velocity, temperature, time and so on [35, 75–80]. Wherein, both partial pressure of water vapor and temperature determines the partial volatilization pressure of rare-earth oxide and silica. Meanwhile, gas flow velocity influences the vapor pressures of oxides in the atmosphere, which determine the balance of reversible reaction, as shown by Eqs. (16) and (17). Sometimes even metastable apatite phase rises after water vapor corrosion if there exist even a few impurities, like Na, Ca, etc. Of course, some rare-earth silicates with large rare-earth radii, X1-Gd₂SiO₅ for example, tend to generate stable apatite phase even without impurities. Besides, it deserves to be mentioned that appearance of the garnet phase during some corrosion process is formed due to the participant of the aluminum hydroxide impurities volatilized from alundum tube.



Nowadays, there exist two main predictions for the water vapor corrosion rate of rare-earth silicates. The first proposed that the surrounding electron state determines the water vapor corrosion resistances. On one aspect, the stronger the chemical bonds, the lower the corrosion rate is. It means that combined Mulliken population and bond length may predict the corrosion resistance to water vapor [81, 82]. On the other aspect, the outermost electrons of rare-earth endows them with hydrophobic property, even at high temperatures [83], which means the water contact angel at room is, to some degree, negatively correlated with high-temperature volatilization rate. However, this explanation seems to ignore the steam partial pressure, which actually affects the corrosion reaction types, namely products. Thus, the other explanation and prediction method seems more promising to estimate both corrosion products and volatilization rates. Once thermal activities of rare-earth oxides and silica are known, the partial pressures of hydroxides, namely volatilization rate are achievable [84–86]. Also, thermodynamic calculations were verified to support the results of BSAS under water vapor attack at different temperatures, where the reaction mechanism is volatilization of all oxide constituents as gaseous hydroxide species, mainly consisting of Ba(OH)₂, Sr(OH)₂, Al(OH)₃, and Si(OH)₄. So, different types of calculation combined with experimental results confirm the effectivity of thermodynamic

Table 4 Corrosion products of yttrium/ytterbium silicates fabricated by different methods after being corrosion-tested in different water vapor environment [35, 75–80]

Material	Fabrication method	Parameters used for corrosion tests	Corrosion products	Reference
$Y_2Si_2O_7$	Pressureless sintering	30% H_2O –70%Air, 13 cm/s 1500 °C, 20/50/120/310 h	Garnet, apatite	[75]
$Y_2Si_2O_7$	SPS	$P(H_2O) = 1$ atm, 200 m/s 1400 °C, 60 h	Y_2SiO_5 , Y_2O_3	[76]
$Yb_2Si_2O_7$	Pressureless sintering	30% H_2O –70%Air, 13 cm/s 1500 °C, 20/50/120/310 h	Garnet	[75]
$Yb_2Si_2O_7$	SPS	$P(H_2O) = 1$ atm, ~200 m/s 1400 °C, 250 h	Yb_2SiO_5 , Yb_2O_3	[77]
Y_2SiO_5	Pressureless sintering	90% H_2O –10%Air 1350 °C, 50/100 h	Apatite, $Y_2Si_2O_7$, SiO_2	[78]
Y_2SiO_5	SPS	$P(H_2O) = 1$ atm, 200 m/s 1400 °C, 60 h	Y_2O_3	[76]
$Y_2SiO_5 + Y_2O_3$	APS	30% H_2O –70%Air, 0.025 cm/s 1400 °C, 100/200/300 h	Y_2SiO_5	[80]
$Y_2SiO_5 + Y_2Si_2O_7$ (few)	SPS	$v = 4$ mL/min 1350 °C, 12 h	Apatite	[79]
Yb_2SiO_5	Pressureless sintering	90% H_2O –10%Air 1350 °C 50/100 h	$Yb_2Si_2O_7$, SiO_2	[78]
$Yb_2SiO_5 + Yb_2O_3$	APS	30% H_2O –70%Air, 0.025 cm/s 1400 °C, 100/200/300 h	Yb_2SiO_5	[80]
Y_2SiO_5	Hot-pressing sintering	50% H_2O –50% O_2 , 0.17 cm/s 1300/1400/1500 °C, 100 h	Apatite, garnet	[35]
Yb_2SiO_5	Hot-pressing sintering	50% H_2O –50% O_2 , 0.17 cm/s 1300/1400/1500 °C, 100 h	Garnet	[35]

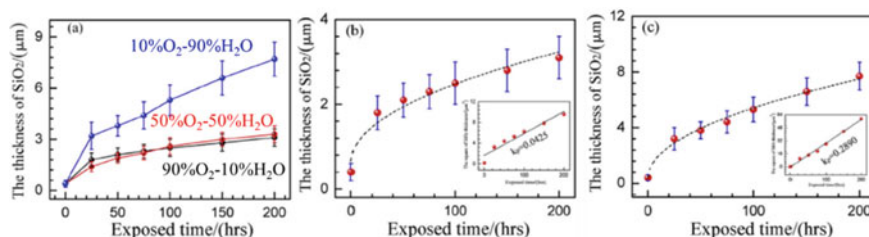


Fig. 11 The thickness growth of SiO_2 versus exposed durations (a) of under different ratios of oxygen to water vapor, b fitted in $90\% \text{O}_2\text{-}10\% \text{H}_2\text{O}$ environment and c fitted in $10\% \text{O}_2\text{-}90\% \text{H}_2\text{O}$ [73]

prediction [87]. However, although some RE–Si–O systems have been evaluated and can mostly match the experiment results, many more systems remain to be explored. This veritably benefits evaluation and screening rare-earth silicates for applying as a topcoat in EBCs.

Except interaction with topcoats, some of oxygen combined water vapor diffused into bond layer through microstructural defects or lattice, reacting with silicon and producing thermal growth oxides. Both of rare-earth silicate types and water vapor partial pressure affects oxidation kinetics. Some previous studies illustrated that the growth index of TGO is approximately 2, meaning that the formation of TGO is controlled by diffusion other than interfacial reaction [73]. As investigated, $\text{Y}_2\text{Si}_2\text{O}_7$ exhibits lower TGO growth rate compared with some other disilicates, which is consistent with the essential diffusion research by time of flight secondary ion mass spectrometry (TOF–SIMS) [88]. In addition, water vapor partial pressure also contributes to the oxidation kinetics, as shown in Fig. 11. When combined with a high water vapor partial pressure of 90%, the growth rate of TGO increases, by nearly 6 times compared to that with water vapor partial pressure of 10–50%. This reveals the concern on the bond layer quality when EBCs service in environment of high water vapor pressure [73].

Therefore, the resistance of EBCs to water vapor and oxygen corrosion at high temperatures should be evaluated by several aspects. Firstly, the mass loss speed of EBCs due to volatilization is regarded as one criterion to simply evaluate the stability of topcoats. However, limited by the furnace tube made by aluminum oxides, the mass weighed contains the aluminum deposition on the coating surface, sometimes even exhibiting negative values owing to the large aluminum contamination and low volatilization rate. Secondly, the observations on thickness of reaction layer basically reflect the corrosion depth along vertical axis. However, the main corrosion reaction is volatilization, meaning the reaction layer is hard to observe and evaluate. Both for this reason and excluding aluminum contamination, some scholars proposed an improved method, namely improving local gas velocity at the local outlet of a long and narrow admission pipeline. As the gas velocity increased to approximately 200 m s^{-1} , aluminum contamination is avoided and apparent corrosion layers with loose structure are observed. Subsequently, corrosion resistance to water vapor and

oxygen can be evaluated by reaction rate constants calculated by fitting curves of the reaction layer growth. Thirdly, the TGO growth rate constant is an effective criterion to evaluate O transmittance of coatings. For basic study, then TOF-SIMS is a useful characterization method to describe the intrinsic properties of materials for better understanding of O transmittance.

3.4 Improvement Strategies for Properties of EBCs

3.4.1 Solid-Solutionizing Treatment and Entropy-Stabilized Engineering

As a usual strategy to mediate material properties, solid-solutionizing is verified as an available treatment to reduce thermal conductivity, alleviate CTE mismatches, and tuning corrosion resistances to water vapor and CMAS at high temperatures. In recent years, configurational entropy has been introduced to explore materials with specific properties. Because of the core effect of multicomponent elements with similar equal molar ratios, some high entropy alloys exhibit exciting properties such as high stability, excellent mechanical and thermophysical properties. Not uniquely, high-entropy ceramics also exhibit low thermal conductivities due to lattice distortions of high-entropy effect and high corrosion resistances due to sluggish diffusion [43, 49, 89–95].

Although rare-earth monosilicates exhibit beneficial corrosion resistances, their CTEs quite higher than silicon-based ceramics limit their application in direct connection to substrates or bond layers. As Si–O bonds have been verified as an insignificant role in thermal expansion, RE–O bonds are thought to contribute most on thermal expansion. As evidence, rare-earth monosilicates show quite high CTEs along *c* axis without [SiO₄] tetrahedron inhibiting expansion of RE–O in that direction, while significant low CTEs along *a* axis with [SiO₄] tetrahedron. Therefore, solid-solutionizing by rare-earth atoms is widely introduced into rare-earth monosilicates to achieve CTEs close to silicon-based ceramics and meanwhile reduce thermal conductivities. The thermal conductivity reduction is basically due to the decreased phonon mean free path involving point defects, which is dependent on lattice mass differences and lattice distortions raised by doping point defects. Table 5 lists mechanical and thermophysical properties of some rare-earth monosilicates with solid-solutionizing and entropy-stabilized engineering [43, 49, 89–91]. CTEs of rare-earth monosilicates have been effectively reduced to approach expected values, and simultaneously thermal conductivities also reduce to lower values.

Generally explaining, various polyhedra units containing [REO_{*m*}] and [SiO₄] in crystal structure determine resistances to thermal deformation, which involves stretch, bend and rotation. A proposed module of CTE reduction is that the distortions of polyhedra are improved by heterogeneous rare-earth atoms into the lattice, but with no actual verification until now. For rare-earth disilicates, based on the first principle calculation, thermal expansion behaviors of β -, γ -, and δ -RE₂Si₂O₇

Table 5 Mechanical and thermophysical properties of some rare-earth monosilicates with solid-solutionizing and entropy-stabilized engineering [43, 49, 89–91]

Compounds	Elastic modulus (GPa)	CTE ($\times 10^{-6} \text{ K}^{-1}$)	Thermal conductivity ($\text{W m}^{-1} \text{ K}^{-1}$)
$(\text{Yb}_{0.2}\text{Y}_{0.2}\text{Lu}_{0.2}\text{Sc}_{0.2}\text{Gd}_{0.2})_2\text{Si}_2\text{O}_7$	–	3.7–5.7 (RT–1400 °C)	–
$(\text{Y}_{1/3}\text{Ho}_{2/3})_2\text{SiO}_5$	–	6.86 (RT–1200 °C)	2.27
$(\text{Y}_{2/3}\text{Ho}_{1/3})_2\text{SiO}_5$	–	5.89 (RT–1200 °C)	2.11
$(\text{Yb}_{0.25}\text{Ho}_{0.25}\text{Er}_{0.25}\text{Y}_{0.25})_2\text{SiO}_5$	172	6.42 (RT–1200 °C)	2.2
$(\text{Yb}_{0.25}\text{Y}_{0.25}\text{Lu}_{0.25}\text{Er}_{0.25})_2\text{SiO}_5$	–	7.63 (RT–1200 °C)	–
$(\text{Lu}_{0.2}\text{Yb}_{0.2}\text{Er}_{0.2}\text{Y}_{0.2}\text{Ho}_{0.2})_2\text{SiO}_5$	160	7.09 (RT–1200 °C)	1.61
$(\text{Yb}_{0.2}\text{Er}_{0.2}\text{Y}_{0.2}\text{Ho}_{0.2}\text{Dy}_{0.2})_2\text{SiO}_5$	168	7.14 (RT–1200 °C)	1.68
$(\text{Lu}_{0.2}\text{Yb}_{0.2}\text{Er}_{0.2}\text{Y}_{0.2}\text{Gd}_{0.2})_2\text{SiO}_5$	170	7.5 (RT–1200 °C)	2.11
$(\text{Yb}_{0.2}\text{Er}_{0.2}\text{Y}_{0.2}\text{Dy}_{0.2}\text{Gd}_{0.2})_2\text{SiO}_5$	165	7.44 (RT–1200 °C)	1.86

are revealed. The low CTEs of these rare-earth disilicates result from the linear or bending structure of $[\text{O}_3\text{Si}]-\text{O}_\text{B}-[\text{SiO}_3]$ units and strength of the interaction between bridge oxygen (O_B) and neighboring rare-earth atoms. Therefore, with the introduced local lattice distortion around $[\text{O}_3\text{Si}]-\text{O}_\text{B}-[\text{SiO}_3]$ units, γ - $(\text{Dy}_{0.15}\text{Y}_{0.85})_2\text{Si}_2\text{O}_7$ shows the 5–19% improvement in CTE compared with γ - $\text{Y}_2\text{Si}_2\text{O}_7$ at temperatures ranging from 300 to 1200 °C, closer to silicon-based ceramics.

In addition to thermophysical properties, the corrosion resistance of rare-earth silicates is also tunable by solid-solutionizing. Rare-earth monosilicates with introducing one or more rare-earth elements almost possess higher resistances to both water vapor and CMAS, in respects of the lower weight loss rates at same temperatures and thinner thicknesses of the reaction layer at same temperatures for same durations [49, 58, 89]. This shows the superiority of multi-component rare-earth monosilicates than single-component rare-earth monosilicates in corrosion resistances other than the thermophysical property improvements. Although the inner mechanisms are not very clear, the entropy stabilization effect may be a possible explanation. For rare-earth disilicates, blister cracks originated from the infiltration of high-temperature CMAS into layers like β - $\text{Yb}_2\text{Si}_2\text{O}_7$ are generally inhibited by introducing Y, which provides higher reactivity with CMAS to form barrier layer (apatite phase here) at the interface [96]. Also, some multi-component rare-earth monosilicates were also confirmed to possess higher stability of grain boundaries to resist the infiltration of CMAS along grain boundaries. As shown in Fig. 12,

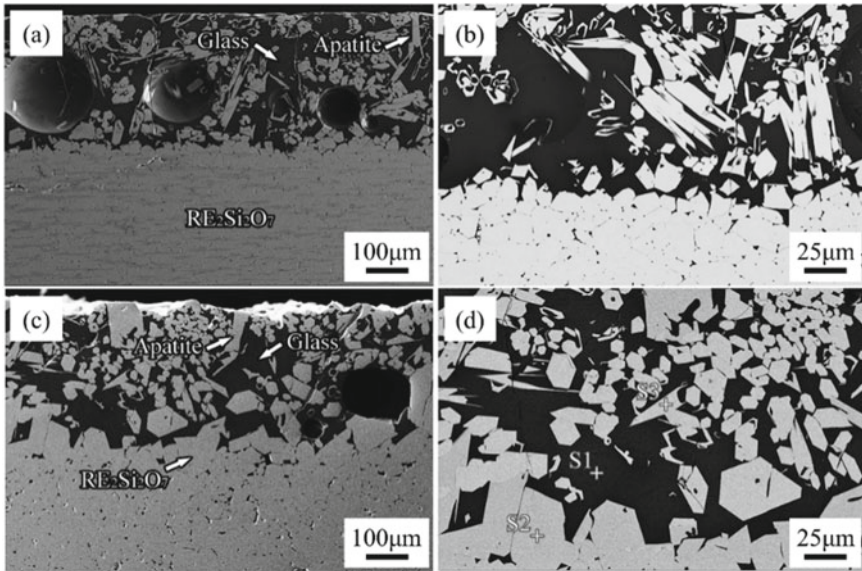


Fig. 12 Cross-sectional morphologies of the reaction front of $(\text{Er}_{0.25}\text{Tm}_{0.25}\text{Yb}_{0.25}\text{Lu}_{0.25})_2\text{Si}_2\text{O}_7$ after CMAS corrosion at 1500 °C for **a, b** 4 h and **c, d** 50 h [58]

$(\text{Er}_{0.25}\text{Tm}_{0.25}\text{Yb}_{0.25}\text{Lu}_{0.25})_2\text{Si}_2\text{O}_7$ ceramics exhibit excellent resistances to CMAS at high temperatures, with no observation on cracks or spallation even at 1500 °C for 50 h [58]. Also, the high-entropy disilicate $(\text{Yb}_{0.2}\text{Y}_{0.2}\text{Sc}_{0.2}\text{Lu}_{0.2}\text{Gd}_{0.2})_2\text{Si}_2\text{O}_7$ with single β phase shows a high strength retention of 86% and approximately no weight variations even after corroded in 50% H_2O –50% O_2 at 1250 °C for 300 h [89].

3.4.2 Compositing Treatment

Compositing treatment is usually applied to improve comprehensive mechanical properties of both alloys and ceramics. It also contributes on performance improvement in both mechanical properties and corrosion resistances of EBCs. Additives play different roles in prolonging the service life of EBCs.

Usually, some additives added improves corrosion resistances of rare-earth silicates to CMAS corrosion. A thin aluminum film deposited on the top surface of Si/Mullite/ Yb_2SiO_5 triple-layer EBCs sprayed by PS-PVD benefits to form an effective barrier composed of interfacial reaction products. Furthermore, aluminum additives reduce the formation of nonstoichiometric products with higher concentration of anions, cation vacancies and defects, as well as inhibiting elemental diffusion from CMAS to the Yb_2SiO_5 topcoat. Additionally, with addition of YSZ, CMAS corrosion products of Yb_2SiO_5 transfer to mainly $\text{Ca}_2\text{Al}_2\text{SiO}_5$, $\text{Ca}_3\text{ZrSi}_2\text{O}_9$ and $\text{Y}_3\text{Al}_5\text{O}_{12}$, other than apatite phase, inhibiting the further infiltration of CMAS [97]. A promising system of mixed ytterbium silicates provide a lower thickness of reaction layer than

both Yb_2SiO_5 and $\beta\text{-Yb}_2\text{Si}_2\text{O}_7$, when attacked by CMAS. A convincing explanation is that thermal activity of $\text{RE}_x\text{Si}_y\text{O}_{1.5x+2y}$ with x/y ratio ranging from 1 to 2 is lower, which changes the interaction between CMAS and mixed silicates. Another benefit is the CTE tuned to approach that of silicon-based ceramics, which probably reduces thermal stresses [98]. Si bond layer with the HfO_2 additive is a concept for the improvement in high-temperature capability and creep properties of the bond layer. In this system, silicon acts as an oxygen gatherer. While after SiO_2 is formed, HfO_2 reacts with it at high temperatures to form HfSiO_4 (hafnon) phase. Hafnon is stable at high temperatures, with a CTE matching well to that of silicon, and it is expected to form quickly enough at the temperatures required for EBC applications. By consumption of silica in the hafnon formation reaction, coating spallation induced by generated silica can be avoided [99].

Not only that, self-healing materials generally investigated and applied in thermal barrier coatings exhibit efficient crack-healing ability. Thermal shock and phase transition due to corrosion reaction are prone to induce cracks, which are probably healed by fluid glass. Nano $\beta\text{-SiC}$ is applied as self-healing particles in $\text{Yb}_2\text{Si}_2\text{O}_7\text{-Yb}_2\text{SiO}_5$ composites. As researched, filling cracks by silica oxidized by $\beta\text{-SiC}$ and volume expansion originated from a new formation of $\text{Yb}_2\text{Si}_2\text{O}_7$ are two main mechanisms promoting crack healing of composite materials [100]. Moreover, $\gamma\text{-Y}_2\text{Si}_2\text{O}_7$ composited with TiSi_2 shows lower weight loss in water vapor environment. Although cracks are wider than un-composited due to mismatch, they are totally occlusive by fillers. Even fillers are denser with extending corrosion duration, which is believed to inhibit transfer of water vapor into SiC beneath effectively and thus raise the endurance of EBCs [101].

4 Main Failure Mechanisms of EBCs

EBCs undergo failure usually due to thermal stress and consumption of effective coatings when attacked by corrosive media in the service environment. By simulating test, failure mechanisms referring to coating recession, thermal stress distribution and spallation are comprehended, which favorable for predicting coatings life and further improvement on the EBCs system.

4.1 *Intrinsic Failure in EBCs Without Interaction to Corrosive Media*

In the service of EBCs, thermal stresses are the most prominent problems, due to their release majorly induces cracks and even spallation. With ignoring water vapor and CMAS attacks, thermal attacks also lead to some thermal stresses during heating

and cooling processes, which is due to thermal expansion or some possible reactions between layers in EBCs. For instance, mullite is usually applied as a transition layer between the silicon bond layer and the rare-earth monosilicate topcoat to balance their thermal expansion mismatch. However, this type of tri-layer EBC sprayed by APS also generates cracks even during isothermal oxidation, although the heating treatment makes it denser. During the oxidation process, pores arise near the Yb_2SiO_5 /mullite interface due to the formation of rod-like garnet phase from Yb_2O_3 in monosilicates and Al_2O_3 in mullite. When combined with the thermal expansion mismatch, cracks are formed and lead to buckling in the mullite layer [102].

Amorphous phase and the stoichiometric shift are verified as undesirable and inevitable, which probably promote the formation of byproducts during service process. Fortunately, appropriate thermal treatment, adjusting plasma power and chemistry allow tuning chemistry of coatings based on comprehends on the gradient thermal and chemical effects. Evolution dynamics show the great effect of metastability and phase transition on the mechanical and thermophysical properties of coatings. For example, with metastable $P21/c$ Yb_2SiO_5 transferring to $C2/c$ Yb_2SiO_5 , the expansion in lattice volume contributes to coating expansion, and thus promoting healing of microcracks formed in the spraying process. Besides phase transition, the grain growth is another issue requiring concern. Generally, layers with lower activation energy of grain growth exhibit more observable microstructural evolution. Due to amounts of grain boundary decreasing, properties like hardness, elastic modulus, thermal conductivities and fracture strength are all affected, which forward changes the thermal stress distribution among layers [102–109].

Thermal shock resistance defines as the resistance of EBC coatings to rapid temperature variations during both the heating and cooling processes. In this aspect, thermal expansion mismatch between layers is thought to be prominent. For example, $\text{Yb}_2\text{Si}_2\text{O}_7/\text{Si}$ system shows apparent improvement compared with Yb_2SiO_5 system, due to the quite small thermal expansion differences between $\text{Yb}_2\text{Si}_2\text{O}_7$ and Si [110]. However, due to high-thermal conductivity and poor resistances to water vapor and CMAS, only rare-earth disilicates are hard to play the role of topcoats in EBCs. A type of tri-layer EBCs composed of Yb_2SiO_5 , $\text{Yb}_2\text{Si}_2\text{O}_7$ and Si is investigated. Although microcracks arise in the Yb_2SiO_5 layer after thermal shock experiments at 1350 °C, but they are almost eliminated at the $\text{Yb}_2\text{SiO}_5/\text{Yb}_2\text{Si}_2\text{O}_7$ interface. As verified by TEM, twinings and dislocations contribute to plastic deformation of $\text{Yb}_2\text{Si}_2\text{O}_7$ coatings, which is probably the factor inhibiting crack propagation [111].

4.2 Failure Mechanisms of EBCs Under Attacks of Corrosive Media

In this section, interactions between topcoats and corrosive media are introduced, where the corrosion degradation is more complex. In an easy aspect, corrosive media interact with topcoat materials to generate corrosion products by interfacial reaction

or dissolution-precipitation. Topcoat materials both volatilize and undergo phase transition in water vapor environment, which means consumption of the EBC effective thickness. While by the CMAS attack at elevated temperatures, topcoat dissolves in CMAS, and furthermore some solid phases precipitate from supersaturated melt. Besides direct interaction at the interface, both water vapor combined with oxygen and CMAS can diffuse into the inner coatings and probably lead to more severe failures.

For water vapor corrosion, phase transition sometimes leads to volume change. For example, Y_2SiO_5 sometimes reacts with water vapor to generate apatite phase with part of Y volatilizing, which leads to the volume reduction and thus tensile stresses. Surface cracks thus produce and propagate [35]. With ultra-high velocity of water vapor, the surface of topcoat produces many pores due to the combined action of volatilization and volume change of phase transitions. Although the thickness degradation is not much high, but the pores distributed in depth become channels for corrosive media, which cannot inhibit the further corrosion [76, 77]. Oxygen combined with water vapor attacks some non-oxide layers like the silicon bond layer, to generate some TGOs. Phase transition accompanied with volume change usually leads to large thermal stress and damage the interfacial bonding strength, which sometimes leads to spallation of the whole EBCs from substrates [71–73].

For CMAS corrosion, its stress analysis is more complicated. It is a combination process of dissolution, precipitation, and infiltration. Taking $Y_2Si_2O_7$ as an example, its reactivity with CMAS is high enough to generate a large amount of apatite product, as shown in Fig. 13. It has to be noted that CTE of CMAS increases as the amount of CaO increasing. With prolonging corrosion duration, CaO is consumed, and thus, CTE of CMAS is lower. However, CTE of the generated oxyapatite phase is much higher than silicon-based ceramics, which leads to stress when cooling down. While the residual compressive stress contributes to the termination of cracks within EBCs. The balance between residual compressive stress and residual tensile stress determines the transformation from cracking to spallation. Penetrating cracks are preferable with a positive CTE mismatch between EBC and substrate. If taking $Yb_2Si_2O_7$ as an example, corrosion mechanism changes [112]. As talked before, some rare-earth disilicates rarely react with CMAS. Without corrosion products at the interface, CMAS infiltrates along grain boundaries or microstructural defects. The CTE mismatch between intergranular CMAS and disilicates results in stresses and generate ‘blister’ cracks [35]. The interaction between CMAS and $Yb_2Si_2O_7$ -based multilayer EBCs has been investigated by high-energy synchrotron X-ray techniques, concentration on stresses analysis on the EBC topcoat. There exists a transformation between Ca in CMAS and Yb in $Yb_2Si_2O_7$, leading to the lattice parameters decrease. Thus, compressive stress arises in EBC topcoat when cooling down combined with the solidification of CMAS, and causes cracks originated from the CMAS surface [113]. It is worth noting the necessity of avoiding sharp horizontal microstructures for tuning the coating structure.

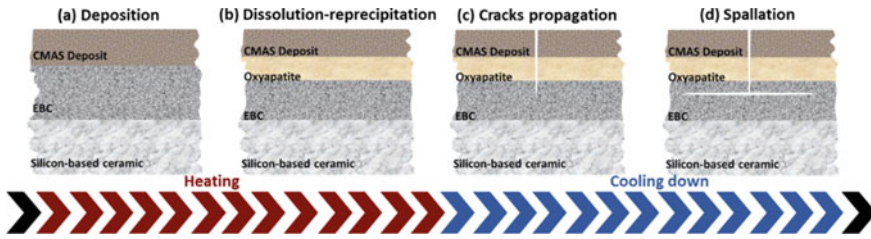


Fig. 13 EBC on the silicon-based ceramic undergoing CMAS corrosion: **a** initial CMAS deposition and accumulation, **b** dissolution-precipitation in CMAS-EBC system, **c** crack initiation and propagation, **d** spallation

5 Conclusions and Outlook

EBCs sprayed on the surface of silicon-based ceramics and composites are mainly requirements for preventing them from attacks of corrosive media in service environments when applied as thermos-structural components of advanced turbines. When screening materials for application on EBCs, appropriate mechanical properties, low thermal conductivities and CTEs close to silicon-based ceramics are required, as well as corrosion resistances to water vapor, oxygen and CMAS. Through large amounts of previous studies, EBCs have developed to the third generation, which is composed of topcoat, bond layer, and sometimes transition layer to relieve thermal stresses. The topcoat is mainly composed of rare-earth silicates with effective modification strategies, bond layer is silicon, while for transition layer, both mullites and rare-earth disilicates have applications.

For optimizing thermal stresses in sprayed coatings, both tuning materials properties and appropriate thermal treatments are effective, by optimization on crystal structures and microstructural evolution. This is most important for prolonging the service lifetime of the third-generation EBCs. Although vague knowledge on the tunable properties of rare-earth monosilicates by solid-solutionizing is helpful to develop new materials for EBCs applications, more intrinsic and accurate relationships between properties and types and amounts of rare-earth silicates are required for screening the most appropriate materials.

The forward concern is corrosion resistances of EBCs to corrosive media. Lots of studies allow us to unveil the underlying corrosion mechanisms. For water vapor corrosion combined with oxygen, the surface phase transition, volatilization of the original topcoat and the formation of TGOs are three main factors inducing stresses and failure of EBCs. For CMAS corrosion, dissolution-precipitation and infiltration of the high-temperature melt along grain boundaries are two main factors, which lead to consumption of topcoat and thermal stresses during the cooling stage. However, it still is urgently needed to develop the comprehensive corrosion experiment platforms, for simulating realistic service environments, like high water vapor velocity and molten CMAS clusters with velocities. Investigations on the corrosion behavior subjected to water vapor, oxygen and CMAS are also in development. There are still

a lot to explore for in-depth comprehension on corrosion behaviors, evaluation and prediction on service lifetime of EBCs.

Overall, researches so far allow us acquire most mechanical and thermo-physical properties applied as coatings in the EBCs system. A certain understanding on corrosion behaviors under attacks from water vapor, oxygen and CMAS proposed improvement directions for enhancing properties and prolonging service lifetime of EBCs. However, deeper comprehension on failure mechanisms related to stress distribution still requires more exploration. When combined with directional mediation in mechanical and thermophysical properties, new EBCs system will exhibit longer service life in operation environment of advanced turbine engines.

Acknowledgements The financial support from the National Science and Technology Major Project (2017-VI-0020-0093) and the Heilongjiang Postdoctoral Science Foundation are gratefully acknowledged.

References

1. Padture, N.P.: Environmental degradation of high-temperature protective coatings for ceramic-matrix composites in gas-turbine engines. *NPJ Mat Degrad.* (2019)
2. Padture, N.P.: Advanced structural ceramics in aerospace propulsion. *Nat. Mater.* **15**(8), 804–809 (2016). <https://doi.org/10.1038/nmat4687>
3. Xu, Y., Hu, X.X., Xu, F.F., Li, K.W.: Rare earth silicate environmental barrier coatings: present status and prospective. *Ceram. Int.* **43**(8), 5847–5855 (2017). <https://doi.org/10.1016/j.ceramint.2017.01.153>
4. Padture, N.P., Gell, M., Jordan, E.H.: Thermal barrier coatings for gas-turbine engine applications. *Science* **296**(5566), 280–284 (2002). <https://doi.org/10.1126/science.1068609>
5. Ohnabe, H., Masaki, S., Onozuka, M., Miyahara, K., Sasa, T.: Potential application of ceramic matrix composites to aero-engine components. *Compos. Part A-Appl. Sci.* **30**(4), 489–496 (1999). [https://doi.org/10.1016/S1359-835x\(98\)00139-0](https://doi.org/10.1016/S1359-835x(98)00139-0)
6. Parthasarathy, T.A., Cox, B., Sudre, O., Przybyla, C., Cinibulk, M.K.: Modeling environmentally induced property degradation of SiC/BN/SiC ceramic matrix composites. *J. Am. Ceram. Soc.* **101**(3), 973–997 (2018). <https://doi.org/10.1111/jace.15325>
7. Poerschke, D.L., Jackson, R.W., Levi, C.G.: Silicate deposit degradation of engineered coatings in gas turbines: progress toward models and materials solutions. *Annu. Rev. Mater. Res.* **47**, 297–330 (2017). <https://doi.org/10.1146/annurev-matsci-010917-105000>
8. Costa, G., Harder, B.J., Wiesner, V.L., Zhu, D.M., Bansal, N., Lee, K.N., Jacobson, N.S., Kapush, D., Ushakov, S.V., Navrotsky, A.: Thermodynamics of reaction between gas-turbine ceramic coatings and ingested CMAS corrodents. *J. Am. Ceram. Soc.* **102**(5), 2948–2964 (2019). <https://doi.org/10.1111/jace.16113>
9. Levi, C.G., Hutchinson, J.W., Vidal-Setif, M.H., Johnson, C.A.: Environmental degradation of thermal-barrier coatings by molten deposits. *Mrs Bull.* **37**(10), 932–941 (2012). <https://doi.org/10.1557/mrs.2012.230>
10. Gunthner, M., Schutz, A., Glatzel, U., Wang, K.S., Bordia, R.K., Greissl, O., Krenkel, W., Motz, G.: High performance environmental barrier coatings, Part I: passive filler loaded SiCN system for steel. *J. Eur. Ceram. Soc.* **31**(15), 3003–3010 (2011). <https://doi.org/10.1016/j.jeurceramsoc.2011.05.027>
11. Liu, J., Zhang, L.T., Liu, Q.M., Cheng, L.F., Wang, Y.G.: Polymer-derived SiOC-barium-strontium aluminosilicate coatings as an environmental barrier for C/SiC composites. *J. Am. Ceram. Soc.* **93**(12), 4148–4152 (2010). <https://doi.org/10.1111/j.1551-2916.2010.04000.x>

12. Lee, K.N.: Current status of environmental barrier coatings for Si-based ceramics. *Surf Coat Tech.* **133**, 1–7 (2000). [https://doi.org/10.1016/S0257-8972\(00\)00889-6](https://doi.org/10.1016/S0257-8972(00)00889-6)
13. Price, J., Van-Roode, M., Stala, C.: Ceramic oxide-coated silicon carbide for high temperature corrosive environments. *Key Eng. Mater.* **72–74**, 71–84 (1992). <https://doi.org/10.4028/www.scientific.net/KEM.72-74.71>
14. Lee, K.N., Miller, R.A.: Oxidation behavior of mullite-coated SiC and SiC/SiC composites under thermal cycling between room temperature and 1200–1400 °C. *J. Am. Ceram. Soc.* **79**(3), 620–626 (1996). <https://doi.org/10.1111/j.1151-2916.1996.tb07920.x>
15. Lee, K.N.: Key durability issues with mullite-based environmental barrier coatings for Si-based ceramics. *J. Eng. Gas Turb. Power* **122**(4), 632–636 (2000). <https://doi.org/10.1115/1.1287584>
16. Fritsch, M., Klemm, H., Herrmann, M., Schenk, B.: Corrosion of selected ceramic materials in hot gas environment. *J. Eur. Ceram. Soc.* **26**(16), 3557–3565 (2006). <https://doi.org/10.1016/j.jeurceramsoc.2006.01.015>
17. Mesquita-Guimaraes, J., Garcia, E., Miranzo, P., Osendi, M.I., Cojocar, C.V., Lima, R.S.: Mullite-YSZ multilayered environmental barrier coatings tested in cycling conditions under water vapor atmosphere. *Surf. Coat. Tech.* **209**, 103–109 (2012). <https://doi.org/10.1016/j.surfcoat.2012.08.044>
18. Lee, K.N., Miller, R.A.: Development and environmental durability of mullite and mullite/YSZ dual layer coatings for SiC and Si₃N₄ ceramics. *Surf. Coat. Tech.* **86**(1–3), 142–148 (1996). [https://doi.org/10.1016/S0257-8972\(96\)03074-5](https://doi.org/10.1016/S0257-8972(96)03074-5)
19. Lee, K.N., Fox, D.S., Eldridge, J.I., Zhu, D.M., Robinson, R.C., Bansal, N.P., Miller, R.A.: Upper temperature limit of environmental barrier coatings based on mullite and BSAS. *J. Am. Ceram. Soc.* **86**(8), 1299–1306 (2003). <https://doi.org/10.1111/j.1151-2916.2003.tb03466.x>
20. Liu, D., Kyaw, S.T., Flewitt, P.E.J., Seraffon, M., Simms, N.J., Pavier, M., Jones, I.A.: Residual stresses in environmental and thermal barrier coatings on curved superalloy substrates: experimental measurements and modelling. *Mat. Sci. Eng. A-Struct.* **606**, 117–126 (2014). <https://doi.org/10.1016/j.msea.2014.03.014>
21. Cojocar, C.V., Levesque, D., Moreau, C., Lima, R.S.: Performance of thermally sprayed Si/mullite/BSAS environmental barrier coatings exposed to thermal cycling in water vapor environment. *Surf. Coat. Tech.* **216**, 215–223 (2013). <https://doi.org/10.1016/j.surfcoat.2012.11.043>
22. Richards, B.T., Zhao, H.B., Wadley, H.N.G.: Structure, composition, and defect control during plasma spray deposition of ytterbium silicate coatings. *J. Mater. Sci.* **50**(24), 7939–7957 (2015). <https://doi.org/10.1007/s10853-015-9358-5>
23. Zhou, Y.C., Zhao, C., Wang, F., Sun, Y.J., Zheng, L.Y., Wang, X.H.: Theoretical prediction and experimental investigation on the thermal and mechanical properties of Bulk beta-Yb₂Si₂O₇. *J. Am. Ceram. Soc.* **96**(12), 3891–3900 (2013). <https://doi.org/10.1111/jace.12618>
24. Lee, K.N., Fox, D.S., Bansal, N.P.: Rare earth silicate environmental barrier coatings for SiC/SiC composites and Si₃N₄ ceramics. *J. Eur. Ceram. Soc.* **25**(10), 1705–1715 (2005). <https://doi.org/10.1016/j.jeurceramsoc.2004.12.013>
25. Tian, Z.L., Lin, C.F., Zheng, L.Y., Sun, L.C., Li, J.L., Wang, J.Y.: Defect-mediated multiple-enhancement of phonon scattering and decrement of thermal conductivity in (Y_xYb_{1-x})₂SiO₅ solid solution. *Acta Mater.* **144**, 292–304 (2018). <https://doi.org/10.1016/j.actamat.2017.10.064>
26. Boakye, E.E., Mogilevsky, P., Parthasarathy, T.A., Keller, K.A., Hay, R.S., Cinibulk, M.K.: Processing and testing of RE₂Si₂O₇ fiber-matrix interphases for SiC-SiC composites. *J. Am. Ceram. Soc.* **99**(2), 415–423 (2016). <https://doi.org/10.1111/jace.13935>
27. Wolf, M., Mack, D.E., Guillon, O., Vassen, R.: Resistance of pure and mixed rare earth silicates against calcium-magnesium-aluminosilicate (CMAS): a comparative study. *J. Am. Ceram. Soc.* **103**(12), 7056–7071 (2020). <https://doi.org/10.1111/jace.17328>
28. Tejero-Martin, D., Bennett, C., Hussain, T.: A review on environmental barrier coatings: history, current state of the art and future developments. *J. Eur. Ceram. Soc.* **41**(3), 1747–1768 (2021). <https://doi.org/10.1016/j.jeurceramsoc.2020.10.057>

29. Nguyen, S.T., Nakayama, T., Suematsu, H., Suzuki, T., He, L.F., Cho, H.B., Niihara, K.: Strength improvement and purification of $\text{Yb}_2\text{Si}_2\text{O}_7$ -SiC nanocomposites by surface oxidation treatment. *J. Am. Ceram. Soc.* **100**(7), 3122–3131 (2017). <https://doi.org/10.1111/jace.14831>
30. Chen, W.R., Wu, X., Marple, B.R., Lima, R.S., Patnaik, P.C.: Pre-oxidation and TGO growth behaviour of an air-plasma-sprayed thermal barrier coating. *Surf Coat Tech.* **202**(16), 3787–3796 (2008). <https://doi.org/10.1016/j.surfcoat.2008.01.021>
31. Peters, M., Leyens, C., Schulz, U., Kaysser, W.A.: EB-PVD thermal barrier coatings for aeroengines and gas turbines. *Adv. Eng. Mater.* **3**(4), 193–204 (2001). [https://doi.org/10.1002/1527-2648\(200104\)3:4%3c193::AID-ADEM193%3e3.0.CO;2-U](https://doi.org/10.1002/1527-2648(200104)3:4%3c193::AID-ADEM193%3e3.0.CO;2-U)
32. Wu, J., Yang, W.C., Zhang, X.F., Wang, C., Zhuo, X.S., Zhan, Y.Z., Liu, M., Zhou, K.S.: Corrosion behavior of PS-PVD spray $\text{Yb}_2\text{Si}_2\text{O}_7$ environmental barrier coatings during continuous water vapor exposure. *Corros Sci.* **210**, 110831 (2023). <https://doi.org/10.1016/j.corsci.2022.110831>
33. Lenz-Leite, M., Degenhardt, U., Krenkel, W., Schafföner, S., Motz, G.: In situ generated $\text{Yb}_2\text{Si}_2\text{O}_7$ environmental barrier coatings for protection of ceramic components in the next generation of gas turbines. *Adv. Mater. Interfaces* **9**(11) (2022). <https://doi.org/10.1002/admi.202102255>
34. Chen, X.G., Li, H.D., Zhang, H.S., Zhang, H.M., Tang, A., Su, S.: Influence of Yb substitution for La on thermophysical property of $\text{La}_2\text{AlTaO}_7$ ceramics. *Ceram. Int.* **43**(10), 7537–7542 (2017). <https://doi.org/10.1016/j.ceramint.2017.03.044>
35. Cao, G., Wang, S.Q., Ding, Z.Y., Wang, Y.H., Liu, Z.G., Ouyang, J.H., Wang, Y.M., Wang, Y.J.: High temperature corrosion behavior and the inhibition of apatite formation evolving from corrosion of $(\text{Y}_{1-x}\text{Yb}_x)_2\text{SiO}_5$ in water vapor environment. *Appl. Surf. Sci.* **601**, 154284 (2022). <https://doi.org/10.1016/j.apsusc.2022.154284>
36. Richards, B.T., Wadley, H.N.G.: Plasma spray deposition of tri-layer environmental barrier coatings. *J. Eur. Ceram. Soc.* **34**(12), 3069–3083 (2014). <https://doi.org/10.1016/j.jeurceram.2014.04.027>
37. Chen, H., Xiang, H., Dai, F.Z., Liu, J., Zhou, Y.: High entropy $(\text{Yb}_{0.25}\text{Y}_{0.25}\text{Lu}_{0.25}\text{Er}_{0.25})_2\text{SiO}_5$ with strong anisotropy in thermal expansion. *J. Mater. Sci. Technol.* **36**, 134–139 (2020). <https://doi.org/10.1016/j.jmst.2019.07.022>
38. Ridley, M., Gaskins, J., Hopkins, P., Opila, E.: Tailoring thermal properties of multi-component rare earth monosilicates. *Acta Mater.* **195**, 698–707 (2020). <https://doi.org/10.1016/j.actamat.2020.06.012>
39. Zhang, H., Lu, J., Shan, X., Wu, D., Zhao, X., Guo, F., Xiao, P.: A promising molten silicate resistant material: rare-earth oxy-apatite $\text{RE}_{9,33}(\text{SiO}_4)_6\text{O}_2$ (RE = Gd, Nd or La). *J. Eur. Ceram. Soc.* **40**(12), 4101–4110 (2020). <https://doi.org/10.1016/j.jeurceramsoc.2020.04.021>
40. Sleeper, J., Garg, A., Wiesner, V.L., Bansal, N.P.: Thermochemical interactions between CMAS and $\text{Ca}_2\text{Y}_8(\text{SiO}_4)_6\text{O}_2$ apatite environmental barrier coating material. *J. Eur. Ceram. Soc.* **39**(16), 5380–5390 (2019). <https://doi.org/10.1016/j.jeurceramsoc.2019.08.040>
41. Tian, Z., Zheng, L., Wang, J., Wan, P., Li, J., Wang, J.: Theoretical and experimental determination of the major thermo-mechanical properties of RE_2SiO_5 (RE = Tb, Dy, Ho, Er, Tm, Yb, Lu, and Y) for environmental and thermal barrier coating applications. *J. Eur. Ceram. Soc.* **36**(1), 189–202 (2016). <https://doi.org/10.1016/j.jeurceramsoc.2015.09.013>
42. Turcer, L.R., Padture, N.P.: Towards multifunctional thermal environmental barrier coatings (TEBCs) based on rare-earth pyrosilicate solid-solution ceramics. *Scripta Mater.* **154**, 111–117 (2018). <https://doi.org/10.1016/j.scriptamat.2018.05.032>
43. Tian, Z., Zheng, L., Li, Z., Li, J., Wang, J.: Exploration of the low thermal conductivities of γ - $\text{Y}_2\text{Si}_2\text{O}_7$, β - $\text{Y}_2\text{Si}_2\text{O}_7$, β - $\text{Yb}_2\text{Si}_2\text{O}_7$, and β - $\text{Lu}_2\text{Si}_2\text{O}_7$ as novel environmental barrier coating candidates. *J. Eur. Ceram. Soc.* **36**(11), 2813–2823 (2016). <https://doi.org/10.1016/j.jeurceramsoc.2016.04.022>
44. Luo, Y., Wang, J., Li, J., Hu, Z., Wang, J.: Theoretical study on crystal structures, elastic stiffness, and intrinsic thermal conductivities of β -, γ -, and δ - $\text{Y}_2\text{Si}_2\text{O}_7$. *J. Mater. Res.* **30**(4), 493–502 (2015). <https://doi.org/10.1557/jmr.2015.1>

45. Fernandez-Carrion, A.J., Allix, M., Becerro, A.I.: Thermal expansion of rare-earth pyrosilicates. *J. Am. Ceram. Soc.* **96**(7), 2298–2305 (2013). <https://doi.org/10.1111/jace.12388>
46. Tian, C., Liu, J., Cai, J., Zeng, Y.: Direct synthesis of $\text{La}_{0.33}\text{Si}_6\text{O}_{26}$ ultrafine powder via sol-gel self-combustion method. *J. Alloys Compd.* **458**(1–2), 378–382 (2008). <https://doi.org/10.1016/j.jallcom.2007.03.128>
47. Zhao, Z., Chen, H., Xiang, H., Dai, F.Z., Wang, X., Xu, W., Sun, K., Peng, Z., Zhou, Y.: $(\text{Y}_{0.25}\text{Yb}_{0.25}\text{Er}_{0.25}\text{Lu}_{0.25})_2(\text{Zr}_{0.5}\text{Hf}_{0.5})_2\text{O}_7$: a defective fluorite structured high entropy ceramic with low thermal conductivity and close thermal expansion coefficient to Al_2O_3 . *J. Mater. Sci. Technol.* **39**, 167–172 (2020). <https://doi.org/10.1016/j.jmst.2019.08.018>
48. Sun, L., Luo, Y., Ren, X., Gao, Z., Du, T., Wu, Z., Wang, J.: A multicomponent γ -type $(\text{Gd}_{1/6}\text{Tb}_{1/6}\text{Dy}_{1/6}\text{Tm}_{1/6}\text{Yb}_{1/6}\text{Lu}_{1/6})_2\text{Si}_2\text{O}_7$ disilicate with outstanding thermal stability. *Mater Res Lett.* **8**(11), 424–430 (2020). <https://doi.org/10.1080/21663831.2020.1783007>
49. Ren, X.M., Tian, Z.L., Zhang, J., Wang, J.Y.: Equiatomic Quaternary $(\text{Y}_{1/4}\text{Ho}_{1/4}\text{Er}_{1/4}\text{Yb}_{1/4})_2\text{SiO}_5$ silicate: a perspective multifunctional thermal and environmental barrier coating material. *Scripta Mater.* **168**, 47–50 (2019). <https://doi.org/10.1016/j.scriptamat.2019.04.018>
50. Wu, R., Pan, W., Ren, X., Wan, C., Qu, Z., Du, A.: An extremely low thermal conduction ceramic: $\text{RE}_{9.33}(\text{SiO}_4)_6\text{O}_2$ silicate oxyapatite. *Acta Mater.* **60**(15), 5536–5544 (2012). <https://doi.org/10.1016/j.actamat.2012.06.051>
51. Wiesner, V.L., Vempati, U.K., Bansal, N.P.: High temperature viscosity of calcium-magnesium-aluminosilicate glass from synthetic sand. *Scripta Mater.* **124**, 189–192 (2016). <https://doi.org/10.1016/j.scriptamat.2016.07.020>
52. Jia, R.D., Deng, L.B., Yun, F., Li, H., Zhang, X.F., Jia, X.L.: Effects of SiO_2/CaO ratio on viscosity, structure, and mechanical properties of blast furnace slag glass ceramics. *Mater. Chem. Phys.* **233**, 155–162 (2019). <https://doi.org/10.1016/j.matchemphys.2019.05.065>
53. Song, W.J., Yang, S.J., Fukumoto, M., Lavalley, Y., Lokachari, S., Guo, H.B., You, Y.C., Dingwell, D.B.: Impact interaction of in-flight high-energy molten volcanic ash droplets with jet engines. *Acta Mater.* **171**, 119–131 (2019). <https://doi.org/10.1016/j.actamat.2019.04.011>
54. Song, W., Lavalley, Y., Wadsworth, F.B., Hess, K.U., Dingwell, D.B.: Wetting and spreading of molten volcanic ash in jet engines. *J. Phys. Chem. Lett.* **8**(8), 1878–1884 (2017). <https://doi.org/10.1021/acs.jpcclett.7b00417>
55. Li, B.T., Chen, Z., Zheng, H.Z., Li, G.F., Li, H.J., Peng, P.: Wetting mechanism of CMAS melt on YSZ surface at high temperature: first-principles calculation. *Appl. Surf. Sci.* **483**, 811–818 (2019). <https://doi.org/10.1016/j.apsusc.2019.04.009>
56. Song, W., Lavalley, Y., Hess, K.U., Kueppers, U., Cimarelli, C., Dingwell, D.B.: Volcanic ash melting under conditions relevant to ash turbine interactions. *Nat. Commun.* **7**, 10795 (2016). <https://doi.org/10.1038/ncomms10795>
57. Wiesner, V.L., Scales, D., Johnson, N.S., Harder, B.J., Garg, A., Bansal, N.P.: Calcium–magnesium aluminosilicate (CMAS) interactions with ytterbium silicate environmental barrier coating material at elevated temperatures. *Ceram. Int.* **46**(10), 16733–16742 (2020). <https://doi.org/10.1016/j.ceramint.2020.03.249>
58. Sun, L., Luo, Y., Tian, Z., Du, T., Ren, X., Li, J., Hu, W., Zhang, J., Wang, J.: High temperature corrosion of $(\text{Er}_{0.25}\text{Tm}_{0.25}\text{Yb}_{0.25}\text{Lu}_{0.25})_2\text{Si}_2\text{O}_7$ environmental barrier coating material subjected to water vapor and molten calcium–magnesium–aluminosilicate (CMAS). *Corros Sci.* **175**, 108881 (2020). <https://doi.org/10.1016/j.corsci.2020.108881>
59. Wiesner, V.L., Harder, B.J., Bansal, N.P.: High-temperature interactions of desert sand CMAS glass with yttrium disilicate environmental barrier coating material. *Ceram. Int.* **44**(18), 22738–22743 (2018). <https://doi.org/10.1016/j.ceramint.2018.09.058>
60. Turcer, L.R., Krause, A.R., Garces, H.F., Zhang, L., Padture, N.P.: Environmental-barrier coating ceramics for resistance against attack by molten calcia-magnesia-aluminosilicate (CMAS) glass: Part I, YAlO_3 and $\gamma\text{-Y}_2\text{Si}_2\text{O}_7$. *J. Eur. Ceram. Soc.* **38**(11), 3905–3913 (2018). <https://doi.org/10.1016/j.jeurceramsoc.2018.03.021>
61. Poerschke, D.L., Hass, D.D., Eustis, S., Seward, G.G.E.V., Sluytman, J.S., Levi, C.G., Sampath, S.: Stability and CMAS resistance of Ytterbium-Silicate/Hafnate EBCs/TBC for

- SiC composites. *J. Am. Ceram. Soc.* **98**(1), 278–286 (2015). <https://doi.org/10.1111/jace.13262>
62. Grant, K.M., Krämer, S., Löfvander, J.P.A., Levi, C.G.: CMAS degradation of environmental barrier coatings. *Surf. Coat. Technol.* **202**(4–7), 653–657 (2007). <https://doi.org/10.1016/j.surfcoat.2007.06.045>
 63. Costa, G., Harder, B.J., Bansal, N.P., Kowalski, B.A., Stokes, J.L.: Thermochemistry of calcium rare-earth silicate oxyapatites. *J. Am. Ceram. Soc.* **103**(2), 1446–1453 (2019). <https://doi.org/10.1111/jace.16816>
 64. Mao, H., Selleby, M., Fabrichnaya, O.: Thermodynamic reassessment of the Y_2O_3 - Al_2O_3 - SiO_2 system and its subsystems. *Calphad* **32**(2), 399–412 (2008). <https://doi.org/10.1016/j.calphad.2008.03.003>
 65. Godbole, E., Handt, A., Poerschke, D.: Apatite and garnet stability in the Al-Ca-Mg-Si-(Gd/Y/Yb)-O systems and implications for T/EBC: CMAS reactions. *J. Am. Ceram. Soc.* **105**(2), 1596–1609 (2022). <https://doi.org/10.1111/jace.18179>
 66. Poerschke, D.L., Shaw, J.H., Verma, N., Zok, F.W., Levi, C.G.: Interaction of yttrium disilicate environmental barrier coatings with calcium-magnesium-iron aluminosilicate melts. *Acta Mater.* **145**, 451–461 (2018). <https://doi.org/10.1016/j.actamat.2017.12.004>
 67. Turcer, L.R., Krause, A.R., Garces, H.F., Zhang, L., Padture, N.P.: Environmental-barrier coating ceramics for resistance against attack by molten calcium-magnesia-aluminosilicate (CMAS) glass: Part II, β - $Yb_2Si_2O_7$ and β - $Sc_2Si_2O_7$. *J. Eur. Ceram. Soc.* **38**(11), 3914–3924 (2018). <https://doi.org/10.1016/j.jeurceramsoc.2018.03.010>
 68. Ueno, S., Ohji, T., Lin, H.T.: Recession behavior of $Yb_2Si_2O_7$ phase under high speed steam jet at high temperatures. *Corros. Sci.* **50**(1), 178–182 (2008). <https://doi.org/10.1016/j.corsci.2007.06.014>
 69. Richards, B.T., Begley, M.R., Wadley, H.N.G., Smialek, J.L.: Mechanisms of ytterbium monosilicate/mullite/silicon coating failure during thermal cycling in water vapor. *J. Am. Ceram. Soc.* **98**(12), 4066–4075 (2015). <https://doi.org/10.1111/jace.13792>
 70. Richards, B.T., Young, K.A., Francqueville, D.F., Sehr, S., Begley, M.R., Wadley, H.N.G.: Response of ytterbium disilicate–silicon environmental barrier coatings to thermal cycling in water vapor. *Acta Mater.* **106**, 1–14 (2016). <https://doi.org/10.1016/j.actamat.2015.12.053>
 71. Lu, Y., Luo, L., Liu, J., Zhu, C., Wang, Y., Jacobson, N.: Failure mechanism associated with the thermally grown silica scale in environmental barrier coated C/SiC composites. *J. Am. Ceram. Soc.* **99**(8), 2713–2719 (2016). <https://doi.org/10.1111/jace.14273>
 72. Lu, Y.H., Wang, Y.G.: Effects of oxygen and water vapor on the formation and growth of silica layer beneath barium strontium aluminosilicate coatings. *Ceram. Int.* **44**(7), 8570–8575 (2018). <https://doi.org/10.1016/j.ceramint.2018.02.062>
 73. Lu, Y., Cao, Y., Zhao, X.: Optimal rare-earth disilicates as top coat in multilayer environmental barrier coatings. *J. Alloys Compd.* **769**, 1026–1033 (2018). <https://doi.org/10.1016/j.jallcom.2018.08.084>
 74. Courcot, E., Rebillat, F., Teyssandier, F., Louchet-Pouillier, C.: Stability of rare earth oxides in a moist environment at elevated temperatures-experimental and thermodynamic studies. *J. Eur. Ceram. Soc.* **30**(9), 1911–1917 (2010). <https://doi.org/10.1016/j.jeurceramsoc.2010.02.012>
 75. Maier, N., Nickel, K.G., Rixecker, G.: High temperature water vapour corrosion of rare earth disilicates (Y, Yb, Lu) $_2Si_2O_7$ in the presence of $Al(OH)_3$ impurities. *J. Eur. Ceram. Soc.* **27**(7), 2705–2713 (2007). <https://doi.org/10.1016/j.jeurceramsoc.2006.09.013>
 76. Parker, C.G., Opila, E.J.: Stability of the Y_2O_3 - SiO_2 system in high-temperature, high-velocity water vapor. *J. Am. Ceram. Soc.* **103**(4), 2715–2726 (2019). <https://doi.org/10.1111/jace.16915>
 77. Ridley, M., Opila, E.: Thermochemical stability and microstructural evolution of $Yb_2Si_2O_7$ in high-velocity high-temperature water vapor. *J. Eur. Ceram. Soc.* **41**(5), 3141–3149 (2021). <https://doi.org/10.1016/j.jeurceramsoc.2020.05.071>
 78. Al-Nasiri, N., Patra, N., Jayaseelan, D.D., Lee, W.E.: Water vapour corrosion of rare earth monosilicates for environmental barrier coating application. *Ceram. Int.* **43**(10), 7393–7400 (2017). <https://doi.org/10.1016/j.ceramint.2017.02.123>

79. García, E., Miranzo, P., Osendi, M.I.: The prospect of Y_2SiO_5 -based materials as protective layer in environmental barrier coatings. *J. Therm. Spray Technol.* **22**(5), 680–689 (2013). <https://doi.org/10.1007/s11666-013-9917-8>
80. Wang, Y.W., Niu, Y.R., Zhong, X., Shi, M.H., Mao, F.Q., Zhang, L., Li, Q.L., Zheng, X.B.: Water vapor corrosion behaviors of plasma sprayed ytterbium silicate coatings. *Ceram. Int.* **46**(18), 28237–28243 (2020). <https://doi.org/10.1016/j.ceramint.2020.07.324>
81. Wang, Y., Liu, J.: Corrosion of barium aluminosilicates by water-vapour: an investigation from first principles. *Corros. Sci.* **51**(9), 2126–2129 (2009). <https://doi.org/10.1016/j.corsci.2009.05.040>
82. Wang, Y.W., Niu, Y.R., Zhong, X., Shi, M.H., Mao, F.Q., Zhang, L., Li, Q.L., Zheng, X.B.: Water vapor corrosion behaviors of plasma sprayed RE_2SiO_5 ($RE = Gd, Y, Er$) coatings. *Corros. Sci.* **167**, 108529 (2020). <https://doi.org/10.1016/j.corsci.2020.108529>
83. Tian, Z.L., Zhang, J., Sun, L.C., Zheng, L.Y., Wang, J.Y.: Robust hydrophobicity and evaporation inertness of rare-earth monosilicates in hot steam at very high temperature. *J. Am. Ceram. Soc.* **102**(6), 3076–3080 (2019). <https://doi.org/10.1111/jace.16315>
84. Jacobson, N.S., Butt, D.: Silica activity measurements in the Y_2O_3 - SiO_2 system and applications to modeling of coating volatility. *J. Am. Ceram. Soc.* **97**(6), 1959–1965 (2014). <https://doi.org/10.1111/jace.12974>
85. Costa, G.C.C., Jacobson, N.S.: Mass spectrometric measurements of the silica activity in the Yb_2O_3 - SiO_2 system and implications to assess the degradation of silicate-based coatings in combustion environments. *J. Eur. Ceram. Soc.* **35**(15), 4259–4267 (2015). <https://doi.org/10.1016/j.jeurceramsoc.2015.07.019>
86. Kowalski, B.A., Jacobson, N.S., Bodenschatz, C., Costa, G.: Thermodynamics of the Lu_2O_3 - SiO_2 system and comparison to other rare earth silicates. *J. Chem. Thermodyn.* **161**, 106483 (2021). <https://doi.org/10.1016/j.jct.2021.106483>
87. Ridley, M.J., Opila, E.J.: High-temperature water-vapor reaction mechanism of barium strontium aluminosilicate (BSAS). *J. Eur. Ceram. Soc.* **42**(7), 3305–3312 (2022). <https://doi.org/10.1016/j.jeurceramsoc.2022.02.004>
88. Zhao, G., Xu, B., Ren, K., Shao, G., Wang, Y.: Oxygen diffusion through environmental barrier coating materials. *Ceram. Int.* **46**(11), 19545–19549 (2020). <https://doi.org/10.1016/j.ceramint.2020.05.007>
89. Dong, Y., Ren, K., Lu, Y., Wang, Q., Liu, J., Wang, Y.: High-entropy environmental barrier coating for the ceramic matrix composites. *J. Eur. Ceram. Soc.* **39**(7), 2574–2579 (2019). <https://doi.org/10.1016/j.jeurceramsoc.2019.02.022>
90. Tian, Z.L., Zheng, L.Y., Hu, W.P., Sun, L.C., Zhang, J., Wang, J.Y.: Tunable properties of $(Ho_xY_{1-x})_2SiO_5$ as damage self-monitoring environmental/thermal barrier coating candidates. *Sci. Rep.-UK* **9**, 415 (2019). <https://doi.org/10.1038/s41598-018-36883-2>
91. Cao, G., Ouyang, J.H., Li, Y., Liu, Z.G., Ding, Z.Y., Wang, Y.H., Jin, Y.J., Wang, Y.M., Wang, Y.J.: Improved thermophysical properties of rare-earth monosilicates applied as environmental barrier coatings by adjusting structural distortion with RE-doping. *J. Eur. Ceram. Soc.* **41**(14), 7222–7232 (2021). <https://doi.org/10.1016/j.jeurceramsoc.2021.07.029>
92. Guo, X., Zhang, Y., Li, T., Zhang, P., Shuai, K., Li, J., Shi, X.: High-entropy rare-earth disilicate $(Lu_{0.2}Yb_{0.2}Er_{0.2}Tm_{0.2}Sc_{0.2})_2Si_2O_7$: a potential environmental barrier coating material. *J. Eur. Ceram. Soc.* **42**(8):3570–3578 (2022). <https://doi.org/10.1016/j.jeurceramsoc.2022.03.006>
93. Chen, Z., Tian, Z., Zheng, L., Ming, K., Ren, X., Wang, J., Li, B.: $(Ho_{0.25}Lu_{0.25}Yb_{0.25}Eu_{0.25})_2SiO_5$ high-entropy ceramic with low thermal conductivity, tunable thermal expansion coefficient, and excellent resistance to CMAS corrosion. *J. Adv. Ceram.* **11**(8), 1279–1293 (2022). <https://doi.org/10.1007/s40145-022-0609-z>
94. Wang, X., He, Y., Wang, C., Bai, Y., Zhang, F., Wu, Y., Song, G., Wang, Z.J.: Thermal performance regulation of high-entropy rare-earth disilicate for thermal environmental barrier coating materials. *J. Am. Ceram. Soc.* **105**(7), 4588–4594 (2022). <https://doi.org/10.1111/jace.18456>
95. Luo, Y., Sun, L., Wang, J., Du, T., Zhou, C., Zhang, J., Wang, J.: Phase formation capability and compositional design of beta-phase multiple rare-earth principal component disilicates. *Nat. Commun.* **14**(1), 1275 (2023). <https://doi.org/10.1038/s41467-023-36947-6>

96. Turcer, L.R., Padture, N.P.: Rare-earth pyrosilicate solid-solution environmental-barrier coating ceramics for resistance against attack by molten calcia–magnesia–aluminosilicate (CMAS) glass. *J. Mater. Res.* **35**(17), 2373–2384 (2020). <https://doi.org/10.1557/jmr.2020.132>
97. Zhang, X., Zhou, K., Liu, M., Deng, C., Deng, C., Niu, S., Xu, S., Su, Y.: CMAS corrosion and thermal cycle of Al-modified PS-PVD environmental barrier coating. *Ceram. Int.* **44**(13), 15959–15964 (2018). <https://doi.org/10.1016/j.ceramint.2018.06.019>
98. Wolf, M., Mack, D.E., Guillon, O., Vaßen, R.: Resistance of pure and mixed rare earth silicates against calcium-magnesium-aluminosilicate (CMAS): a comparative study. *J. Am. Ceram. Soc.* **103**(12), 7056–7071 (2020). <https://doi.org/10.1111/jace.17328>
99. Harder, B.J.: Oxidation performance of Si-HfO₂ environmental barrier coating bond coats deposited via plasma spray-physical vapor deposition. *Surf. Coat. Technol.* **384** (2020). <https://doi.org/10.1016/j.surfcoat.2019.125311>
100. Nguyen, S.T., Nakayama, T., Suematsu, H., Iwasawa, H., Suzuki, T., Otsuka, Y., He, L., Takahashi, T., Niihara, K.: Self-healing behavior and strength recovery of ytterbium disilicate ceramic reinforced with silicon carbide nanofillers. *J. Eur. Ceram. Soc.* **39**(10), 3139–3152 (2019). <https://doi.org/10.1016/j.jeurceramsoc.2019.03.040>
101. Chen, Y., Lu, Y., Ye, Q., Wang, Y.: A self-healing environmental barrier coating: TiSi₂-doped Y₂Si₂O₇/barium strontium aluminosilicate coating. *Surf. Coat. Technol.* **307**, 436–440 (2016). <https://doi.org/10.1016/j.surfcoat.2016.09.020>
102. Zhang, X., Song, J., Deng, Z., Wang, C., Niu, S., Liu, G., Deng, C., Deng, C., Liu, M., Zhou, K., Lu, J.: Interface evolution of Si/Mullite/Yb₂SiO₅ PS-PVD environmental barrier coatings under high temperature. *J. Eur. Ceram. Soc.* **40**(4), 1478–1487 (2020). <https://doi.org/10.1016/j.jeurceramsoc.2019.10.062>
103. Jang, B.K., Nagashima, N., Kim, S., Oh, Y.S., Lee, S.M., Kim, H.T.: Mechanical properties and microstructure of Yb₂SiO₅ environmental barrier coatings under isothermal heat treatment. *J. Eur. Ceram. Soc.* **40**(7), 2667–2673 (2020). <https://doi.org/10.1016/j.jeurceramsoc.2019.12.057>
104. Summers, W.D., Begley, M.R., Zok, F.W.: Transition from penetration cracking to spallation in environmental barrier coatings on ceramic composites. *Surf. Coat. Technol.* **378**(25), 125083 (2019). <https://doi.org/10.1016/j.surfcoat.2019.125083>
105. Zhai, Z., Wang, W., Mei, X., Li, M., Cui, J., Wang, F., Pan, A.: Effect of the surface microstructure ablated by femtosecond laser on the bonding strength of EBCs for SiC/SiC composites. *Opt. Commun.* **424**, 137–144 (2018). <https://doi.org/10.1016/j.optcom.2018.04.055>
106. Zhong, X., Niu, Y., Li, H., Zeng, Y., Zheng, X., Ding, C., Sun, J.: Microstructure evolution and thermomechanical properties of plasma-sprayed Yb₂SiO₅ coating during thermal aging. *J. Am. Ceram. Soc.* **100**(5), 1896–1906 (2017). <https://doi.org/10.1111/jace.14690>
107. Appleby, M.P., Zhu, D., Morscher, G.N.: Mechanical properties and real-time damage evaluations of environmental barrier coated SiC/SiC CMCs subjected to tensile loading under thermal gradients. *Surf. Coat. Technol.* **284**, 318–326 (2015). <https://doi.org/10.1016/j.surfcoat.2015.07.042>
108. Hong, Z., Cheng, L., Zhang, L., Wang, Y.: Internal friction behavior of C/SiC composites with environmental barrier coatings in corrosive environment. *Int. J. Appl. Ceram. Technol.* **8**(2), 342–350 (2011). <https://doi.org/10.1111/j.1744-7402.2010.02589.x>
109. Xu, Y., Yan, Z.: Investigation on the preparation of Si/Mullite/Yb₂Si₂O₇ environmental barrier coatings onto silicon carbide. *J. Rare Earths* **28**(3), 399–402 (2010). [https://doi.org/10.1016/S1002-0721\(09\)60120-4](https://doi.org/10.1016/S1002-0721(09)60120-4)
110. Zhong, X., Niu, Y., Li, H., Zhu, T., Song, X., Zeng, Y., Zheng, X., Ding, C., Sun, J.: Comparative study on high-temperature performance and thermal shock behavior of plasma-sprayed Yb₂SiO₅ and Yb₂Si₂O₇ coatings. *Surf. Coat. Technol.* **349**, 636–646 (2018). <https://doi.org/10.1016/j.surfcoat.2018.06.056>
111. Zhong, X., Niu, Y., Li, H., Zhou, H., Dong, S., Zheng, X., Ding, C., Sun, J.: Thermal shock resistance of tri-layer Yb₂SiO₅/Yb₂Si₂O₇/Si coating for SiC and SiC-matrix composites. *J. Am. Ceram. Soc.* **101**(10), 4743–4752 (2018). <https://doi.org/10.1111/jace.15713>

112. Summers, W.D., Poerschke, D.L., Begley, M.R., Levi, C.G., Zok, F.W.: A computational modeling framework for reaction and failure of environmental barrier coatings under silicate deposits. *J. Am. Ceram. Soc.* **103**, 5196–5213 (2020). <https://doi.org/10.1111/jace.17187>
113. Stolzenburg, F., Kenesei, P., Almer, J., Lee, K.N., Johnson, M.T., Faber, K.T.: The influence of calcium–magnesium–aluminosilicate deposits on internal stresses in $\text{Yb}_2\text{Si}_2\text{O}_7$ multilayer environmental barrier coatings. *Acta Mater.* **105**, 189–198 (2016). <https://doi.org/10.1016/j.actamat.2015.12.016>

Development of Silicates and Spraying Techniques for Environmental Barrier Coatings



Ayahisa Okawa, Son Thanh Nguyen, Tadachika Nakayama,
Hisayuki Suematsu, Takashi Goto, and Koichi Niihara

Abstract Currently, silicon carbide fibre-reinforced silicon carbide matrix ceramic matrix composites are widely used as high-temperature components for next-generation gas-turbine engines. However, hot steam and volcanic ash degrade the mechanical properties of silicon carbide. Environmental barrier coatings (EBCs) play an important role in mitigating corrosion under the harsh operating conditions required for next-generation turbines. In addition to corrosion resistance, the coefficient of thermal expansion and phase stability are important for EBC material selection to stabilise the layer structure during thermal cycling. Various silicates have been considered as candidates for EBCs, where rare-earth silicates have shown promising results. Moreover, various spraying techniques that can achieve a layered EBC structure have been considered in addition to appropriate material selection as key strategies for improving the reliability and lifetime of EBCs. Crystallisation, porosity, and crack formation caused by the formation of secondary phases due to Si evaporation are controlled by thermal spraying techniques. This chapter comprehensively evaluates the selection of silicates and spraying techniques for EBCs and discusses their prospects.

Keywords Turbine engine · Coatings · Thermal spraying · Ceramic composite · Rare-earth silicate

A. Okawa (✉)

Institute of Multidisciplinary Research for Advanced Materials, Tohoku University,
Sendai 980-8577, Japan
e-mail: ayahisa.okawa@tohoku.ac.jp

S. T. Nguyen

Department of Creative Engineering, National Institute of Technology, Kushiro College,
Kushiro 084-0916, Japan

T. Nakayama · H. Suematsu · T. Goto · K. Niihara

Extreme Energy-Density Research Institute, Nagaoka University of Technology,
Nagaoka 940-2188, Japan
e-mail: nky15@vos.nagaokaut.ac.jp

Abbreviation

CTE	Coefficient of thermal expansion
CMC	Ceramics matrix composite
EBC	Environmental barrier coating
TBC	Thermal barrier coating
SiC	Silicon carbide
SiC _f /SiC _m	Silicon carbide fibre-reinforced silicon carbide matrix
CMAS	Calcium magnesium aluminosilicate
Mullite	Al ₆ Si ₂ O ₁₃
BSAS	Ba _{1-x} Sr _x Al ₂ Si ₂ O ₈
RE	Rare-earth
CIP	Cold isostatic press
HP	Hot press
SPS	Spark plasma sintering
APS	Atmospheric plasma spraying
XRD	X-ray diffraction
SEM	Scanning electron microscope
TEM	Transmission electron microscope
SPS	Suspension plasma spraying
LPPS	Low-pressure plasma spraying
HVOF	High-velocity oxygen fuel
TGO	Thermally grown oxide

1 Background

The rapid development of gas-turbine engines over the past few decades owing to the fabrication of advanced materials has significantly contributed to the development of various fields such as the power generation and aerospace industry. Nickel-based superalloys and thermal barrier coatings (TBCs) are key inventions that have enabled the increase in the inlet temperature of gas-turbine engines and significantly improved fuel efficiency [1]. Rare-earth-based A₂B₂O₇ materials are preferred as TBCs because of their low thermal conductivities and coefficients of thermal expansion (CTE), which are close to those of nickel-based superalloys [2, 3]. However, turbine gas temperatures are expected to exceed 1500 °C in the near future, and nickel-based superalloys cannot withstand such high temperatures, even with the help of TBCs and cooling technology [4].

To further improve fuel consumption, it is necessary to decrease the weight of turbine components and improve their resistance to high temperatures. A silicon carbide (SiC) fibre-reinforced silicon carbide matrix (SiC_f/SiC_m) is the most promising material for next-generation aircraft engine turbine blades [1]. Figure 9.1 shows the transition and future projections of the operating temperature of an aircraft

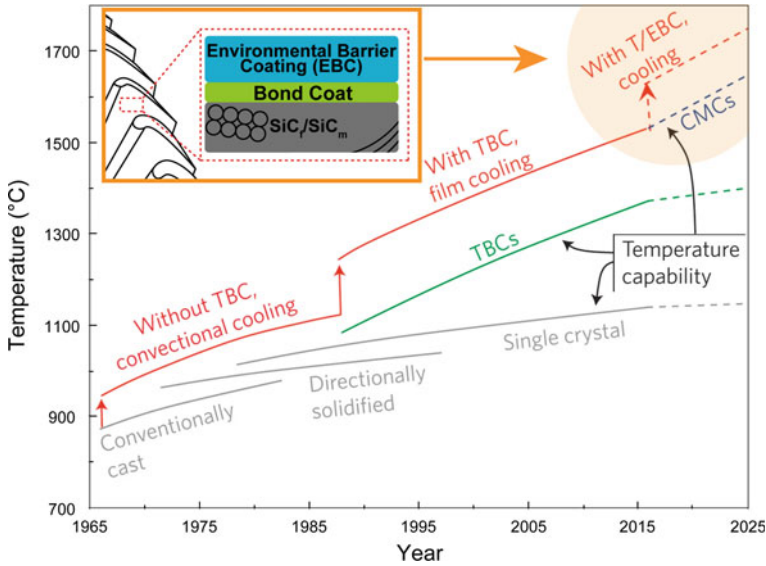
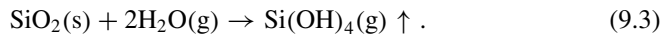
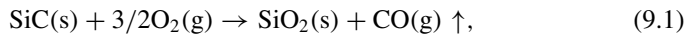


Fig. 9.1 Trends and projections of the temperature capabilities of materials for gas-turbine engines; and a schematic of the CMC, bond coat, and EBC system (Reproduced and redrawn with permission. Copyright 2016, Springer [1])

gas turbine and a schematic of the widely used ceramic matrix composite (CMC), bond coat, and environmental barrier coating (EBC) systems.

SiC has high damage tolerance, good fatigue resistance, and thermal stability at high temperatures. As previously mentioned, SiC_f/SiC_m has been studied as a component of gas-turbine engines; however, several technical issues remain. Particularly, SiC undergoes rapid recession in combustion atmospheres containing water vapour.

This recession can be described by the following reactions [5, 6]:



Therefore, next-generation aircraft engine turbine blades consist of an EBC, which is a water vapour shielding layer, and a bond coat that provides good adhesion between the EBC and SiC_f/SiC_m. The EBC is an essential system for improving the reliability of the CMC; however, it is susceptible to destruction by various hazards in severe operating environments. As shown in Fig. 9.2a, the minimum requirement for the material selection of EBCs is excellent water vapour corrosion resistance, in addition to properties such as follows: (a) the CTE should be compatible with

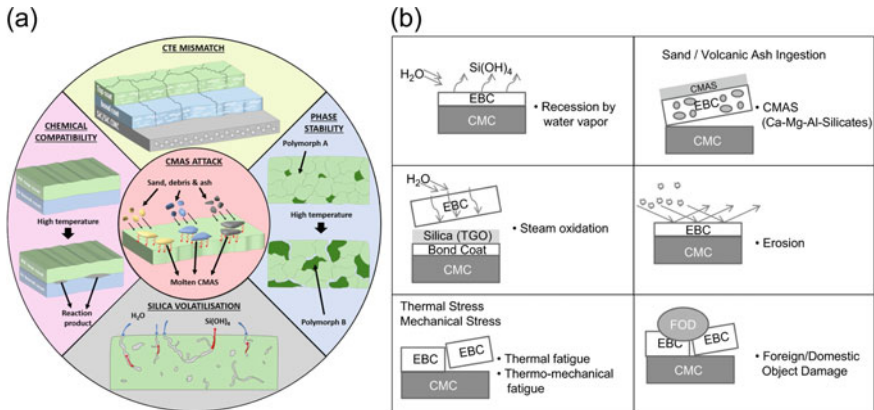


Fig. 9.2 a Five main EBC requirements [7], and b key EBC failure modes [8] (Reproduced with permission, copyright 2021, Elsevier [7], copyright 2019, Wiley–VCH [8])

that of SiC. A large CTE difference between the EBC and SiC causes the delamination of the EBC owing to thermal stress. (b) The material should be nonpolymorphic, and the crystalline phase should be stable because different crystalline phases have different CTEs, which may increase the thermal stress. (c) Reactions involving volcanic ash and calcium magnesium aluminosilicate (CMAS) as the main phases should be minimal. Particularly, the formation of apatite with a large CTE difference results in vertical mud cracks, which act as a path for the supply of water vapour to the SiC matrix. (d) The chemical stability between the layers should be maintained at high temperatures. For example, TBC materials often react with Si; thus, it is necessary to experimentally demonstrate that coating systems exhibit excellent resistance to these hazards. A schematic of the destruction mechanism is presented in Fig. 9.2b.

2 EBC Material Candidates

2.1 $Al_6Si_2O_{13}$ (Mullite) and $Ba_{1-x}Sr_xAl_2Si_2O_8$ (BSAS)

Early EBC studies focused on mullite as a candidate material; however, water vapour volatilises the silica, causing the mullite to recede. Yttria-stabilised zirconia was added as a water vapour corrosion-resistant coating on top of the mullite coating; however, rapid fracture occurred at the interface owing to the stress caused by the CTE difference. This indicates the importance of the CTE and water vapour in EBC development.

To improve the thermal stability of second-generation mullite EBCs, NASA used Si in the bonding layer, and BSAS was introduced to reduce the thermal and physical mismatch of the coating. Si is generally accepted as a bond coat because it possesses

high adhesion, has a CTE value close to that of SiC, and is able to prevent the oxidation of the substrate $\text{SiC}_f/\text{SiC}_m$ by forming a suitable thermally grown oxide (TGO) SiO_2 . This system has a high thermal stability and good CTE compatibility. However, when the Si bond coat was oxidised and reacted with BSAS, glass was formed, and the structure was degraded. In addition, BSAS volatilised and largely receded at temperatures above 1400 °C in a water vapour-rich atmosphere [9].

2.2 Rare-Earth Silicates

Being a third-generation EBC, rare-earth silicates ($\text{RE}_2\text{Si}_2\text{O}_7$ or RE_2SiO_5) are now widely accepted as the most promising materials apart from the aforementioned BSAS. As shown in Fig. 9.3, rare-earth (RE) silicates exhibit better water vapour corrosion resistance than the BSAS silicates.

Because EBCs have a layered structure, the CTE mismatch is a critical property because it induces stress during thermal cycling. Figure 9.4 shows the water vapour corrosion resistance and CTE of the EBC candidates. RE_2SiO_5 has a relatively high CTE and excellent resistance to corrosion by water vapour volatilization. In contrast, $\text{RE}_2\text{Si}_2\text{O}_7$ has good CTE compatibility with SiC but poor resistance to corrosion by water vapour volatilisation.

Currently, the most widely used EBC is Yb silicate, which is promising because it meets the required functions relatively well; however, it is not yet sufficient for practical applications as an EBC. Recently, multicomponent $\text{RE}_2\text{Si}_2\text{O}_7$ [12–14] and RE_2SiO_5 [15, 16] have exhibited excellent thermal properties and resistance to corrosion by water vapour and volcanic ash. Wang et al. proposed the concept of high-entropy components in EBCs [12]. In the same year, high-entropy EBC materials were also reported for the first time in different RE_2SiO_5 systems [15]. The entropy of mixing ΔS_{mix} is described by the following equation:

$$\Delta S_{\text{mix}} = -R \sum_{i=1}^n x_i \ln x_i, \quad (9.4)$$

Fig. 9.3 Volatility of rare-earth silicates and BSAS when exposed to 50% H_2O -50% O_2 with a flow velocity of 4.4 cm/s at a total pressure of 1 atm and temperature of 1500 °C (Reproduced with permission. Copyright 2004, Elsevier [10])

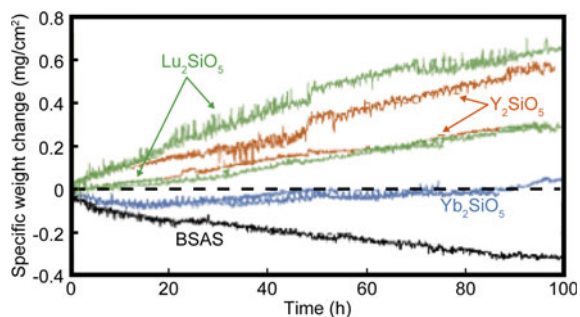
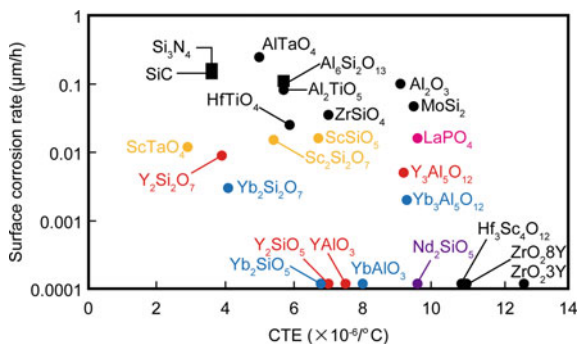


Fig. 9.4 Surface water vapour corrosion rate at 1450 °C and CTE of the EBC candidate materials (Reproduced and redrawn with permission. Copyright 2010, Wiley-VCH [11])



where R is the gas constant, x_i is the mole fraction of component i , and n is the number of components. Multicomponent oxides are considered to have high entropy when $\Delta S_{\text{mix}} \geq 1.5R$, and medium entropy when $1.0R \leq \Delta S_{\text{mix}} \leq 1.5R$. High-entropy RE silicates require precursor treatment and high temperatures for synthesis to obtain a uniform distribution. The synthesis of the multicomponent RE silicates and their fabrication methods are listed in Table 9.1. The different sintering methods include cold isostatic pressing (CIP), hot pressing (HP), and spark plasma sintering (SPS). In the sol-gel method, hydrous RE nitrate and tetraethyl orthosilicate are commonly used as raw materials. However, when ball milling, RE₂O₃ and SiO₂ are generally selected as raw powders, and there exists a route that utilises pre-reacted RE silicate powders. Feedstock powder synthesis can be a bottleneck in thermal spraying, a widely accepted deposition method for EBCs. Fine feedstock powders reduce the porosity of coatings. However, high temperatures are required for the synthesis of uniformly distributed multicomponent silicates; thus, agglomeration of the powder is inevitable. The development of low-cost methods to obtain powders at a relatively low temperatures and in short periods of time will be an issue for the future studies.

3 Properties and Corrosion Behaviour of Rare-Earth Silicates for EBC

Section 1 describes the requirements for EBCs. This section describes in detail the adaptability of RE silicates (RE₂Si₂O₇ or RE₂SiO₅) to the main requirements such as the CTE, water vapour corrosion, and volcanic ash corrosion.

3.1 Phase Stability and Thermal Properties

Compared with TBCs, EBCs must have a low porosity to prevent water vapour from entering the CMC. This requirement results in a high Young's modulus for

Table 9.1 Components of equiatomic multicomponent RE silicates and fabrication methods for bulk samples

Component	Mixture and calcination	Sintering	Ref
$(Y_{1/5}Y_{1/5}Lu_{1/5}Sc_{1/5}Gd_{1/5})_2Si_2O_7$	Sol-gel method, calcinated at 1500 °C for 2 h in air	CIP under 200 MPa, and then sintered at 1600 °C for 3 h in Ar	[12, 17]
$(Y_{1/4}Ho_{1/4}Er_{1/4}Yb_{1/4})_2SiO_5$	Planetary ball milling, calcinated at 1550 °C for 1 h	HP, 1600 °C for 1 h under 30 MPa in Ar	[15, 18]
$(Sc_{1/5}Y_{1/5}Dy_{1/5}Er_{1/5}Yb_{1/5})_2SiO_5$	Dry ball milling	SPS, 1550–1700 °C for 10–20 min under 65–70 MPa in Ar	[16]
$(Er_{1/4}Tm_{1/4}Yb_{1/4}Lu_{1/4})_2Si_2O_7$	Planetary ball milling, calcinated at 1550 °C for 1 h	HP, 1800 °C for 2 h under 30 MPa	[13]
$(Gd_{1/6}Tb_{1/6}Dy_{1/6}Tm_{1/6}Yb_{1/6}Lu_{1/6})_2Si_2O_7$	Planetary ball milling, calcinated at 1550 °C for 6 h	HP, 1800 °C for 2 h under 30 MPa	[14, 19]
$(Y_{1/5}Yb_{1/5}Sc_{1/5}Gd_{1/5}Lu_{1/5})_2Si_2O_7$	Wet (ethanol) ball milling, calcinated at 1600 °C for 4 h	SPS, 1500 °C for 5 min under 75 MPa	[20]

(continued)

Table 9.1 (continued)

Component	Mixture and calcination	Sintering	Ref
$(Y_{1/4}B_{1/4}Er_{1/4}Sc_{1/4})_2Si_2O_7$	Sol-gel method, calcinated at 1500 °C for 2 h	Pressed under 4 MPa, and then 1600 °C for 5, 10, 15 h in air	[21]
$(Yb_{1/5}Y_{1/5}Lu_{1/5}Ho_{1/5}Er_{1/5})_2Si_2O_7$ $(Yb_{1/4}Lu_{1/4}Ho_{1/4}Er_{1/4})_2Si_2O_7$	Wet (ethanol) ball milling	CIP, 1600 °C for 10 h	[22, 23]
$(Lu_{1/5}Yb_{1/5}Er_{1/5}Tm_{1/5}Sc_{1/5})_2Si_2O_7$	Planetary ball milling, calcinated at 1500 °C for 10 h	HP, 1550 °C for 3 h under 30 MPa in Ar	[24]
$(Y_{1/2}Yb_{1/2})_2Si_2O_7$ $(Y_{1/3}Yb_{1/3}Er_{1/3})_2Si_2O_7$ $(Y_{1/4}Yb_{1/4}Er_{1/4}Sc_{1/4})_2Si_2O_7$ $(Y_{1/5}Yb_{1/5}Er_{1/5}Sc_{1/5}Gd_{1/5})_2Si_2O_7$ $(Y_{1/6}Yb_{1/6}Er_{1/6}Sc_{1/6}Gd_{1/6}Eu_{1/6})_2Si_2O_7$	Sol-gel method, calcinated at 1500 °C for 2 h	Pressed under 2 MPa, and then 1600 °C for 10 h in air	[25]
$(Ho_{1/4}Lu_{1/4}Yb_{1/4}Eu_{1/4})_2SiO_5$	Wet (ethanol) ball milling, calcinated at 1650 °C for 8 h	CIP under 200 MPa, and then sintered at 1550 °C for 12 h	[26]
$(Sc_{1/5}Nd_{1/5}Er_{1/5}Yb_{1/5}Lu_{1/5})_2Si_2O_7$	Dry ball milling, calcinated at 900 °C for 30 min	SPS, 1525 °C for 1 h under 65 MPa	[27]
$(Yb_{1/4}Er_{1/4}Y_{1/4}Dy_{1/4})_2Si_2O_7$	Sol-gel method, calcinated at 1400 °C for 18 h in air	N.A	[28]

(continued)

Table 9.1 (continued)

Component	Mixture and calcination	Sintering	Ref
$(Y_{1/5}Dy_{1/5}Er_{1/5}Yb_{1/5}Ho_{1/5})_2Si_2O_7$	Planetary ball milling, calcinated at 1500 °C for 1 h in air	CIP under 200 MPa, and then sintered at 1600 °C for 3 h	[29]
$(Dy_{1/5}Ho_{1/5}Er_{1/5}Tm_{1/5}Yb_{1/5})_2SiO_5$ $(Dy_{1/5}Ho_{1/5}Er_{1/5}Y_{1/5}Lu_{1/5})_2SiO_5$ $(Dy_{1/5}Ho_{1/5}Er_{1/5}Y_{1/5}Tm_{1/5})_2SiO_5$ $(Dy_{1/5}Ho_{1/5}Er_{1/5}Y_{1/5}Yb_{1/5})_2SiO_5$	Ball milling, calcinated at 1600 °C for 4 h	SPS, 1800°C for 5 min under 75 MPa	[30]
$(Yb_{1/4}Y_{1/4}Lu_{1/4}Er_{1/4})_2SiO_5$	Wet (ethanol) ball milling	Pressed under 30 MPa, and then 1600 °C for 13h in air	[31]
$(Y_{1/4}Dy_{1/4}Ho_{1/4}Er_{1/4})_2SiO_5$ $(Yb_{1/4}Dy_{1/4}Ho_{1/4}Er_{1/4})_2SiO_5$ $(Y_{1/3}Dy_{1/3}Er_{1/3})_2SiO_5$ $(Y_{1/3}Dy_{1/3}Lu_{1/3})_2SiO_5$	Wet (ethanol) ball milling, calcinated at 1600 °C for 2 h in air	HP, 1700 °C for 1 h under 30 MPa	[32]
$(Sm_{1/5}Eu_{1/5}Tb_{1/5}Dy_{1/5}Lu_{1/5})_2Si_2O_7$ -Porous	Sol-gel method, calcinated at 1200 °C for 2 h	CIP under 200 MPa, and then sintered at 1300 °C for 2 h	[33]

the EBCs. However, a high Young's modulus can increase the stored elastic energy, thereby increasing the risk of coating failure if the energy release rate (G) exceeds a critical value (G_c). Under planar stress conditions and a homogeneous coating stress (σ), the energy release rate for an infinite crack can be calculated as follows:

$$G = \frac{\sigma^2 h}{2E_{\text{EBC}}}, \quad (9.5)$$

where h is the thickness of the coating and E_{EBC} is the Young's modulus of the EBC. The residual stress in a thin coating at room temperature is then determined as the difference in the CTE assuming that the stress in the coating relaxes at elevated temperatures.

$$\sigma = E_{\text{EBC}}(\alpha_{\text{EBC}} - \alpha_{\text{CMC}})\Delta T, \quad (9.6)$$

where α_{EBC} is the CTE of the EBC, α_{CMC} is the CTE of the CMC, and ΔT is the temperature difference. Given that the energy release rate in (9.5) is proportional to the square of the CTE mismatch, it is advisable to avoid substantial disparities. Additionally, the energy release rate is linearly influenced by both the coating thickness and Young's modulus [34].

As mentioned previously, the CTE of $\text{RE}_2\text{Si}_2\text{O}_7$ is relatively close to that of SiC . However, $\text{RE}_2\text{Si}_2\text{O}_7$ with RE sites other than Lu and Yb show polymorphism (α , β , γ , δ , A, G and F), resulting in different CTEs [35]. Consequently, phase transformations can lead to significant stress during thermal cycling. Therefore, EBC candidates should not exhibit polymorphisms. Figure 9.5 shows the correlation between the temperature and crystalline phase. $\text{Yb}_2\text{Si}_2\text{O}_7$ and $\text{Lu}_2\text{Si}_2\text{O}_7$ exhibit only the β -phase, and high-entropy $\text{RE}_2\text{Si}_2\text{O}_7$ exhibits a stable γ -phase up to the melting point. Therefore, these elements are considered as ideal candidates for EBC.

RE_2SiO_5 displays commendable corrosion resistance to water vapour but exhibits a substantially higher CTE than $\text{RE}_2\text{Si}_2\text{O}_7$. Additionally, thermal properties such as the thermal conductivity and CTE were reduced by introducing multicomponent RE_2SiO_5 , as shown in Fig. 9.6. Figure 9.7a, b shows the CTE of the multicomponent RE silicates. The adjustment of the CTE due to the multicomponents is also similar for $\text{RE}_2\text{Si}_2\text{O}_7$ and RE_2SiO_5 .

Compared to the single-component system, the multicomponent system has a higher Young's modulus, suggesting that it is more resistant to internal thermal pressure at high temperatures [15]. When an ion with a relatively small radius is substituted, the interatomic distance gradually decreases, increasing the lattice energy and decreasing the CTE. In high-entropy compounds, even if the interatomic distance slightly increases, the lattice distortion is so large that the lattice vibrations become non-coordinated and the amplitude vibrations of the atoms are inhibited, thus suppressing the decrease in the lattice energy [25]. Another factor may be the phonon behaviour that is unique to RE silicates. X2- RE_2SiO_5 (I2/a) has two types of phonons with Grüneisen constants of different signs, each of which contributes to the

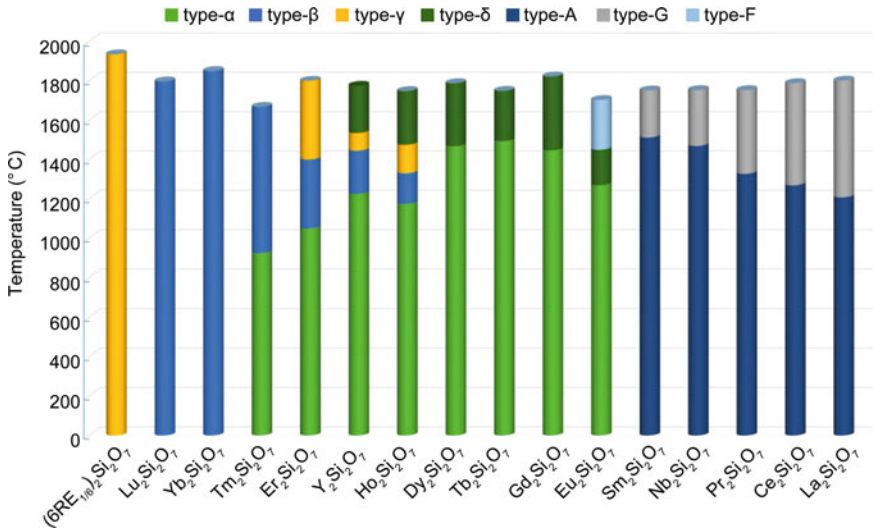


Fig. 9.5 Schematics of the polymorphic transformation temperatures of RE₂Si₂O₇. The RE in the multicomponent silicate is Gd, Tb, Dy, Tm, Yb and Lu (Reproduced and redrawn with permission. Copyright 2020, Taylor & Francis [14])

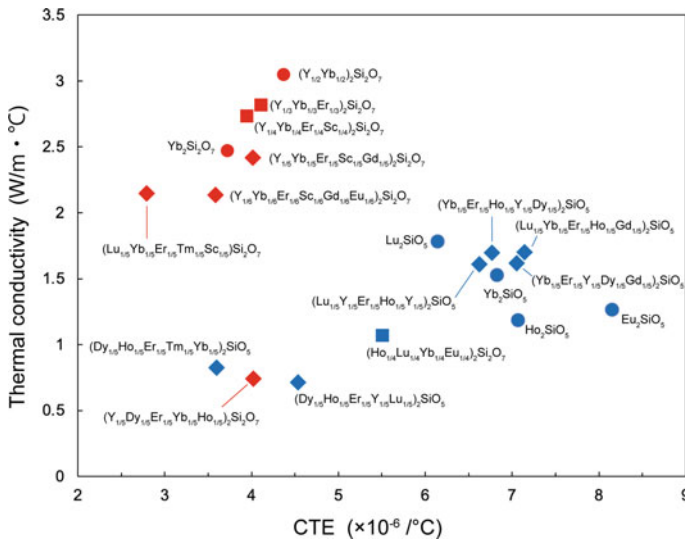


Fig. 9.6 CTE and thermal conductivity of the RE silicate at 600 °C. ◆ and ■ denote high and medium entropy, respectively [24–26, 29, 30, 36, 37]

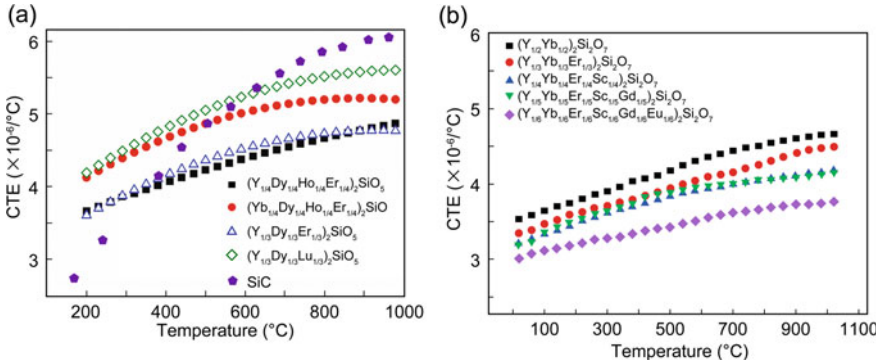
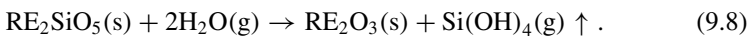


Fig. 9.7 CTE of the multicomponents: **a** RE_2SiO_5 [32] and **b** $\text{RE}_2\text{Si}_2\text{O}_7$ [25] (Reproduced and redrawn with permission. Copyright 2021, Springer, and 2022, Wiley–VCH [25, 32])

positive and negative thermal expansions [38]. Thus, multicomponent substitution can effectively control both the phase stability and thermal properties.

3.2 Resistance to Corrosion by Water Vapour

RE silicates were proposed as EBC candidates to protect the SiC from water vapour corrosion. However, these RE silicates also receded because of water vapour corrosion via the following reactions [39–42]:



Cracking during thermal cycling was also inevitable because the formed products have different CTEs, as shown in Fig. 9.8A, a–c. Additionally, as shown in Fig. 9.8B, a, b, the recession and pore formation facilitated the supply of oxygen to the Si bond coat. Consequently, this contributed to the rapid growth of the TGO, which caused delamination.

For the water vapour volatilization model, the volatility of SiO_2 is obtained as shown below [5, 9]:

$$\text{volatility} \propto v^{1/2} (P_{\text{H}_2\text{O}})^2 P^{-1/2} \quad (9.9)$$

where v is the gas velocity, $P_{\text{H}_2\text{O}}$ is the partial pressure of the water vapour, and P is the total pressure. The susceptibility of RE silicates to water vapour corrosion is based on mechanisms similar to those of the SiC evaporation model, which is dependent on the temperature, flow rate, and water vapour partial pressure. Therefore, water vapour

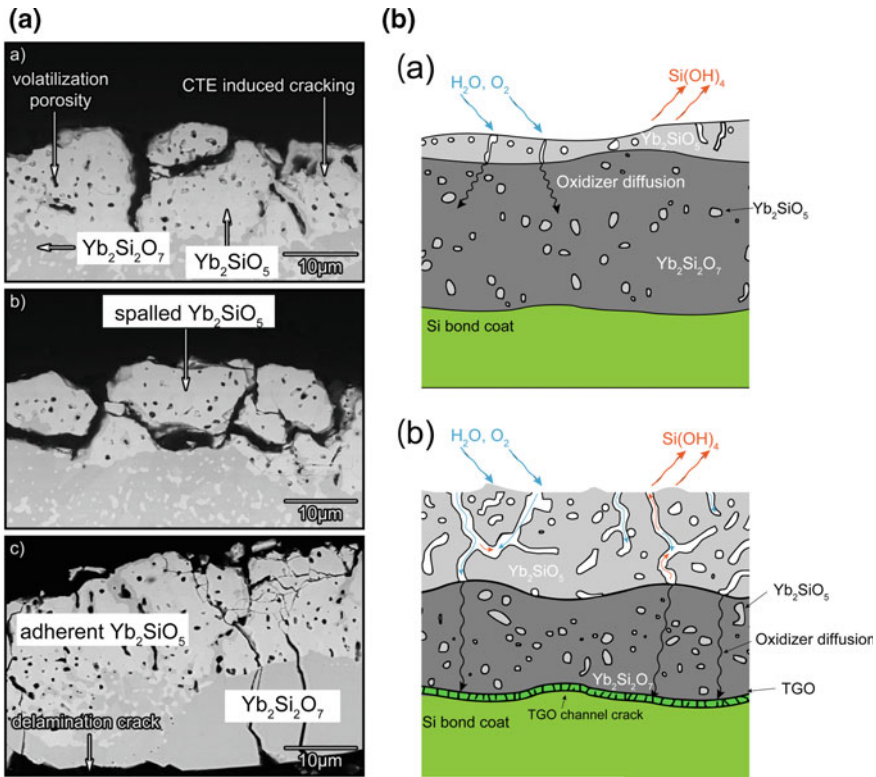


Fig. 9.8 A, a–c Cross-sectional images of $\text{Yb}_2\text{Si}_2\text{O}_7$ after exposure to high temperatures in a water vapour-rich atmosphere. Schematic illustrations of the recession mechanism caused by water vapour corrosion: **B-a** initial stage, and **B-b** late stage of water vapour corrosion (Reproduced and redrawn with permission. Copyright 2016, Elsevier [39])

corrosion tests are typically performed at high velocity and water vapour partial pressures, and at temperatures above 1200 °C [43]. The water vapour corrosion is generally evaluated through gravimetric measurements, X-ray diffraction (XRD), scanning electron microscopy (SEM), and transmission electron microscopy (TEM). XRD can identify corrosion products such as RE_2SiO_5 and RE_2O_3 , enabling a simple evaluation of the surface corrosion. In addition, SEM can be used to observe pores and easily distinguish $\text{RE}_2\text{Si}_2\text{O}_7$ from RE_2SiO_5 and RE_2O_3 based on contrast differences and EDS analyses, whereas TEM provides detailed observations of reactions at grain boundaries, which can be useful in understanding corrosion mechanisms. In severe steam tests such as steam jets, cross-sectional observations are made because corrosion occurs both on the surface and internally. Therefore, after testing, the sample was encapsulated in resin and cut, and its cross-section was observed after polishing.

The cost of equipment and time required for the water vapour corrosion tests were high. The correlation between the surface hydrophobicity and water vapour reaction is significant, with silicate exhibiting the highest hydrophobicity, as quantified by its

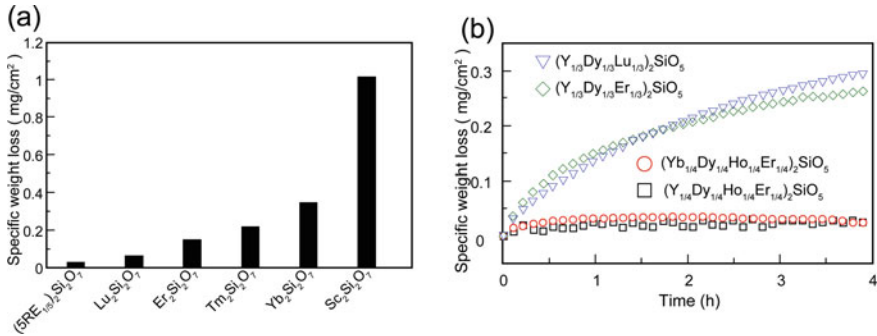


Fig. 9.9 Weight loss after the water vapour corrosion test of **a** RE₂Si₂O₇ [24], and **b** RE₂SiO₅ [32]. The RE in (SRE_{1/5})Si₂O₇ is Lu, Yb, Er, Tm and Sc (Reproduced and redrawn with permission. Copyright 2021 and 2022, Elsevier [24, 32])

water contact angle, and the least weight loss due to the water vapour reaction [13, 23, 44]. This water contact angle measurement can serve as a simple screening test for the selection of materials with high water vapour corrosion resistance.

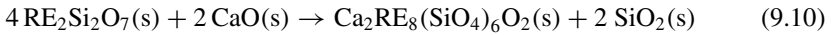
The strategy of using multicomponent compounds has been proposed as a means of increasing the corrosion resistance to water vapour, as shown in Fig. 9.9, which illustrates the relationship between the weight loss and time after the water vapour corrosion testing of RE silicates. Here, the corrosion resistance increased with RE doping. It should also be noted that multicomponent compounds do not guarantee improved water vapour corrosion resistance, as other studies have shown [15, 23]. For example, Lu₂Si₂O₇ has been shown to have higher water vapour corrosion resistance than high-entropy materials. The corrosion of high-entropy RE₂Si₂O₇ under static (extremely slow velocity) water vapour-rich conditions is initiated at the inner surface of the RE₂Si₂O₇ grains, and is accompanied by the formation and growth of the corrosion product, RE₂SiO₅ [23]. Conversely, many reports have indicated that corrosion occurs at the grain boundaries [32, 45]. Currently, as given in Table 9.2, the parameters for water vapour corrosion testing are limited and not standardised; therefore, a more comprehensive study is required.

3.3 Resistance to Corrosion by Volcanic Ash

Volcanic ash is a serious threat to the reliability of EBCs because it immediately melts and reacts with them at operating temperatures of approximately 1200 °C or higher, thereby destroying their structures. The main component of volcanic ash is CMAS, which has been investigated in numerous corrosion studies. Figure 9.10 shows a cross-sectional image after CMAS corrosion. The RE₂Si₂O₇ with relatively large ionic radii such as Y and Er, react with CMAS and melt to form a Ca₂RE₈(SiO₄)₆O₂ (apatite) phase, which prevents CMAS penetration via the following reaction [46, 47]:

Table 9.2 Water vapour corrosion testing of multicomponent RE silicates at 1 atm

Materials	Test condition	Refs
$(Y_{1/4}Ho_{1/4}Er_{1/4}Yb_{1/4})_2SiO_5$	1400 °C for 5 h in 4.9% H ₂ O-95.1% air under a gas flow rate of 40 ml/min	[18]
$(Y_{1/4}Ho_{1/4}Er_{1/4}Yb_{1/4})_2SiO_5$	1400 °C for 5 h in 9.2% H ₂ O + 90.8% air under a gas flow rate of 40 ml/min	[15]
$(Er_{1/4}Tm_{1/4}Yb_{1/4}Lu_{1/4})_2Si_2O_7$	1400 °C for 5 h in 90% H ₂ O + 10% air under a gas flow rate of 40 ml/min	[13]
$(Yb_{1/5}Y_{1/5}Lu_{1/5}Ho_{1/5}Er_{1/5})_2Si_2O_7$ $(Yb_{1/4}Lu_{1/4}Ho_{1/4}Er_{1/4})_2Si_2O_7$	1350 °C for 50 or 100 h in 30% H ₂ O-70% air under a gas velocity of 2.5×10^{-4} m/s	[23]
$(Dy_{1/5}Ho_{1/5}Er_{1/5}Tm_{1/5}Yb_{1/5})_2SiO_5$ $(Dy_{1/5}Ho_{1/5}Er_{1/5}Y_{1/5}Lu_{1/5})_2SiO_5$ $(Y_{1/4}Dy_{1/4}Ho_{1/4}Er_{1/4})_2SiO_5$ $(Yb_{1/4}Dy_{1/4}Ho_{1/4}Er_{1/4})_2SiO_5$ $(Y_{1/3}Dy_{1/3}Er_{1/3})_2SiO_5$ $(Y_{1/3}Dy_{1/3}Lu_{1/3})_2SiO_5$	1400 °C for 4 h in 90% H ₂ O-10% Ar under a flow rate of 10 ml/min	[30, 32]
$(Lu_{1/5}Yb_{1/5}Er_{1/5}Tm_{1/5}Sc_{1/5})_2Si_2O_7$	1500 °C for 200 h in 50% H ₂ O-50% O ₂ under a gas flow rate of 100 ml/min	[24]
$(Sc_{1/5}Nd_{1/5}Er_{1/5}Yb_{1/5}Lu_{1/5})_2Si_2O_7$	1400 °C for 125 h in 100% H ₂ O under a gas velocity of 240 m/s	[27]
$(Yb_{1/5}Y_{1/5}Lu_{1/5}Sc_{1/5}Gd_{1/5})_2Si_2O_7$	1500 °C for 200 h in 50% H ₂ O-50% O ₂ under a gas velocity of 0.1 cm/s	[12]



However, the formation of apatite was induced by vertical mud cracks due to the thermal mismatch caused by the high CTE. Conversely, the $\text{RE}_2\text{Si}_2\text{O}_7$ with relatively small ionic radii such as Sc and Yb did not react with the CMAS melt, but instead penetrated the interior [48]. The penetration of CMAS causes volume expansion and excessive stress, eventually leading to crack initiation. The reactions of the RE silicates with CMAS can be divided into three stages [22]. First, the RE silicate was dissolved in the CMAS melt. Second, when RE_2O_3 was saturated in the CMAS melt, apatite began to precipitate. Finally, the CaO in CMAS was depleted owing to crystallisation and stopped driving apatite formation, and the remaining CMAS reached equilibrium with $\text{RE}_2\text{Si}_2\text{O}_7$. However, apatite formation due to the consumption of the RE silicate causes the degradation of the EBC.

Multicomponent rare-earth silicates exhibit better corrosion resistance in volcanic ash than single-component rare-earth silicates. Two main factors contribute to the increase in the CMAS corrosion resistance of multicomponent RE silicates. One is the slow dissolution rate of high-entropy $\text{RE}_2\text{Si}_2\text{O}_7$ in molten CMAS [13, 17]. The lattice

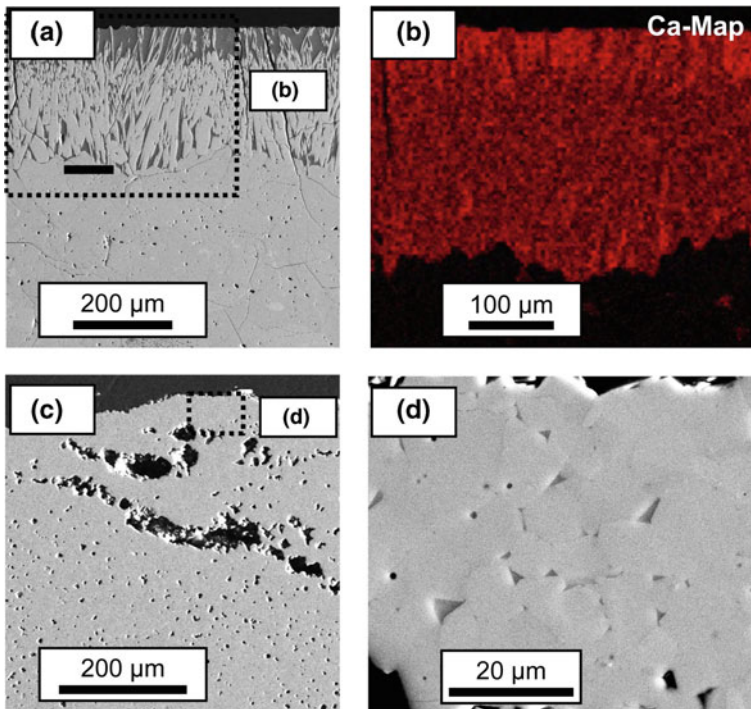


Fig. 9.10 Cross-section images after exposure at 1500 °C for 24 h using CMAS, (A-B) $\gamma\text{-Y}_2\text{Si}_2\text{O}_7$ [46], and (C-D) $\beta\text{-Yb}_2\text{Si}_2\text{O}_7$ [48] (Reproduced and redrawn with permission. Copyright 2018, Elsevier [46, 48])

distortion results of the random occupation of lattice sites by multiple RE elements with different ion sizes show that a large lattice distortion leads to fluctuations in the lattice potential energy of the migration paths from one site to another during diffusion. Consequently, high-entropy $\text{RE}_2\text{Si}_2\text{O}_7$ has a slower diffusion rate and higher activation energy for atomic diffusion than the single-component $\text{RE}_2\text{Si}_2\text{O}_7$. Therefore, the formation of new phases owing to the interaction between high-entropy $\text{RE}_2\text{Si}_2\text{O}_7$ and CMAS was delayed. Another factor is the effect of the ionic radius. The formation and penetration of apatite depend on the ionic radius, as described earlier [19, 26]. Additionally, $\text{Lu}_2\text{Si}_2\text{O}_7$ did not react with volcanic ash. In contrast, a dense layer of apatite, $\text{Ca}_2\text{RE}_8(\text{SiO}_4)_6\text{O}_2$ (RE = Yb, Lu, Ho, or Er), is formed in $(\text{Yb}_{1/4}\text{Lu}_{1/4}\text{Ho}_{1/4}\text{Er}_{1/4})_2\text{Si}_2\text{O}_7$ [22]. The formation of apatite crystals is favoured when the ionic radius of the incorporated RE^{3+} approaches that of Ca^{2+} [27, 49–51]. This suggests that the controlled dissolution of $\text{RE}_2\text{Si}_2\text{O}_7$ into the CMAS melt or apatite formation improves the corrosion resistance to volcanic ash.

4 Thermal Spraying Techniques for EBCs

Thermal spraying is widely accepted as an important strategy for improving the reliability and lifetime of EBCs. The thermal spraying process has several advantages over alternative methods such as unlimited dimensions, from which the required EBC coating thickness of 100 μm can be achieved, and its relatively high speed compared to CVD and other coating techniques. With the accumulation of knowledge on candidate EBC materials, the number of studies on thermal spraying has increased. Four thermal spraying processes, namely atmospheric plasma spraying (APS), suspension plasma spraying (SPS), low-pressure plasma spraying (LPPS), and high-velocity oxygen fuel (HVOF), have been studied considering RE silicates [34, 52]. The primary requirements for each process are the temperature and velocity of the feedstock powder to ensure the dense deposition of the EBC.

The four thermal spray processes, are shown in Fig. 9.11a considering the plasma/flame temperature and feedstock velocity. A major challenge in EBC deposition is the prevention of vertical mud cracks after thermal spraying. The failure mechanism of the TGO growth is shown in Fig. 9.11b, c, where small vertical cracks functioned as stress relaxants. However, the presence of vertical mud cracks provides a pathway for oxidised species through cracks in the Si bond coat, resulting in TGO growth beyond the critical delamination point and causing the EBC to delaminate.

The formation of vertical mud cracks in the coating is attributed to two main sources of stress: (1) shrinkage stress during the crystallisation of amorphous particles caused by the rapid cooling of particles due to the cold substrate, and (2) thermal stress due to the formation of secondary phases with a divergent CTE such as Yb_2O_3 or Yb_2SiO_5 , which is attributed to SiO evaporation [54]. In traditional APS systems, SiO evaporation was an unavoidable consequence of using high plasma power to achieve dense microstructures with robust interfacial bonding. Recently, the limitations of the traditional thermal spray processes have been addressed through the development of

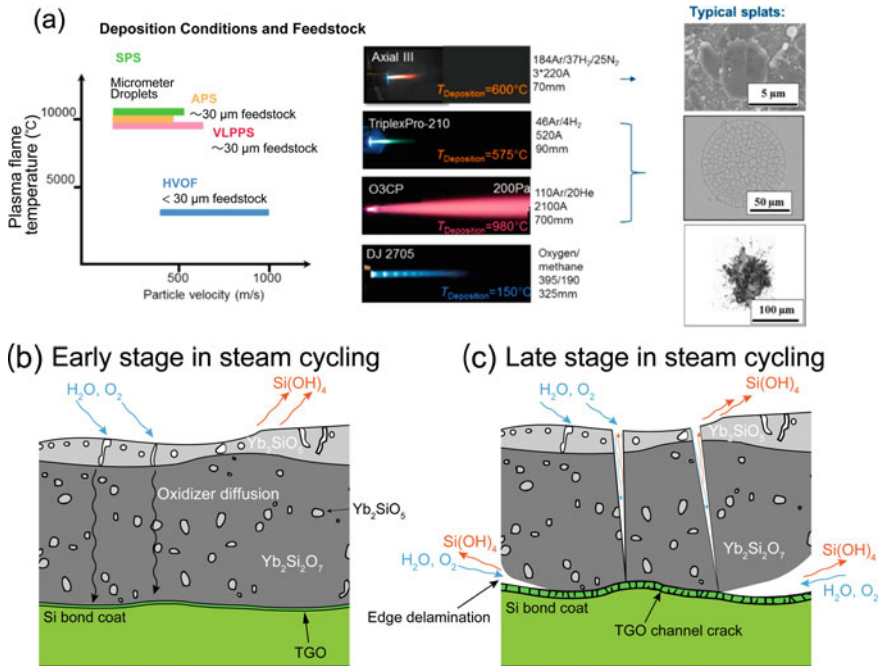


Fig. 9.11 a Characteristics of the four kinds of thermal spray processes [34]. Schematics of EBC delamination owing to accelerated TGO formation by vertical mud cracks and edge failure during steam cycling: **b** early stage, and **c** later stage [39, 53] (Reproduced and redrawn with permission. Copyright 2016, Elsevier [39])

advanced techniques. Additionally, some of these techniques have reached the cycle testing stage. Thus, this paper provides a comprehensive review of each of these advanced thermal spraying methods.

4.1 Atmospheric Plasma Spraying (APS)

Atmospheric plasma spraying (APS) is a method of spraying using a high-temperature thermal plasma jet at 10,000 °C or higher, which is produced by applying a voltage between a tungsten electrode and water-cooled nozzle and allowing a plasma gas such as argon to flow and generate a plasma discharge. The APS is the most widely used processing technology for fabricating EBCs. One of the main reasons for this is that TBCs are applied to gas-turbine blades using APS. Additionally, a high-density and vertical mud crack formation due to amorphous or SiO evaporation are trade-offs. At higher plasma temperatures, Yb₂Si₂O₇, Yb₂SiO₅ and Yb₂O₃ are formed owing to the evaporation of SiO [54]. The percentage of the Yb₂SiO₅ phase increased from 11.7% at an input current of 225 A to 44.1% at 520 A. In addition, the

residual thermal stress of the coating almost doubled, and the coating with a higher percentage of the $\text{Yb}_2\text{Si}_2\text{O}_7$ phase had a lower tensile stress [55]. Clear interface cracks were also observed in the APS deposits [52]. These cracks were caused by tensile stresses in the highly amorphous and dense films during cooling from high deposition temperatures to room temperature, resulting in an incommensurate CTE.

However, lowering the plasma temperature increased the porosity. During cooling, inhomogeneous nucleation occurred at the splat boundaries; however, the centre of the splat remained amorphous. Inadequate heating leads to a decrease in the volume and increase in the density of the crystallised region, resulting in the development of elastic tensile stress in the amorphous region. Pores can form in a splat under sufficient stress [41]. Such pores not only reduce the bonding between the splats and degrade the mechanical properties of the $\text{Yb}_2\text{Si}_2\text{O}_7$ coating, but also act as a permeation pathway for oxygen to the substrate, resulting in the destruction of the EBC due to the growth of the TGO.

In APS, plasma-heated particles have a very high temperature, but the substrate is cold and thus amorphous. The substrate temperature initially reaches 800–900 °C before rapidly dropping to 400–600 °C until the start of thermal spraying, and remaining in this temperature range during deposition [52]. In contrast, coatings with smaller sample sizes exhibit a high crystallinity of 76 wt% at approximately 800–900 °C, as shown in Fig. 9.12a, b [34].

Therefore, substrate-assisted heating during deposition is a promising approach [54]. Figure 9.12c shows a schematic of heat-assisted APS. The substrate was kept in a furnace at a high temperature of approximately 1200 °C, which is generally higher than the stable phase crystallisation temperature of the sprayed RE silicate [56]. Therefore, the cooling rate of the sprayed particles reaching the substrate can be reduced, and crystallisation can be promoted. Another method involves maintaining the substrate at a high temperature by shortening the standoff distance (SD) [57]. A combination of a short SD, high plasma current, and small specimens can be used to maintain the substrate at a high temperature and achieve a highly crystalline coating. In addition, a short SD of 50 mm suppressed the evaporation of SiO during spraying because of the reduced dwell time, and the optimum proportion (less than 20 wt%) of the second phase was uniformly distributed in the final deposit. Consequently, desirable microstructures such as dense structures with a uniform distribution of small pores were observed.

Additionally, the coating must be sufficiently crystallised to obtain a robust EBC. Therefore, post-heating treatments are commonly used. When the sprayed $\text{Yb}_2\text{Si}_2\text{O}_7$ was heat treated, three metastable phases, $\alpha\text{-Yb}_2\text{Si}_2\text{O}_7$ (P-1), $\text{X1-Yb}_2\text{SiO}_5$ (P2₁/c) and $\text{Yb}_{4.67}\text{Si}_3\text{O}_{13}$ (P6₃/m), were formed at approximately 1000 °C; and finally, two stable phases, $\beta\text{-Yb}_2\text{Si}_2\text{O}_7$ (C2/m) and $\text{X2-Yb}_2\text{SiO}_5$ (I2/a), were formed at 1200 °C [56]. Phase transition behaviour is important in heat treatment strategies. For example, microcracks can be healed not only by the sintering effect [43], but also through volume expansion during the metastable to stable phase transition of Yb_2SiO_5 [58]. In addition, the sprayed high-entropy RE silicates showed five stable phases such as γ , β , $\delta\text{-RE}_2\text{Si}_2\text{O}_7$, $\text{RE}_{4.67}\text{Si}_3\text{O}_{13}$ and $\text{X2-Yb}_2\text{SiO}_5$ after heat treatment

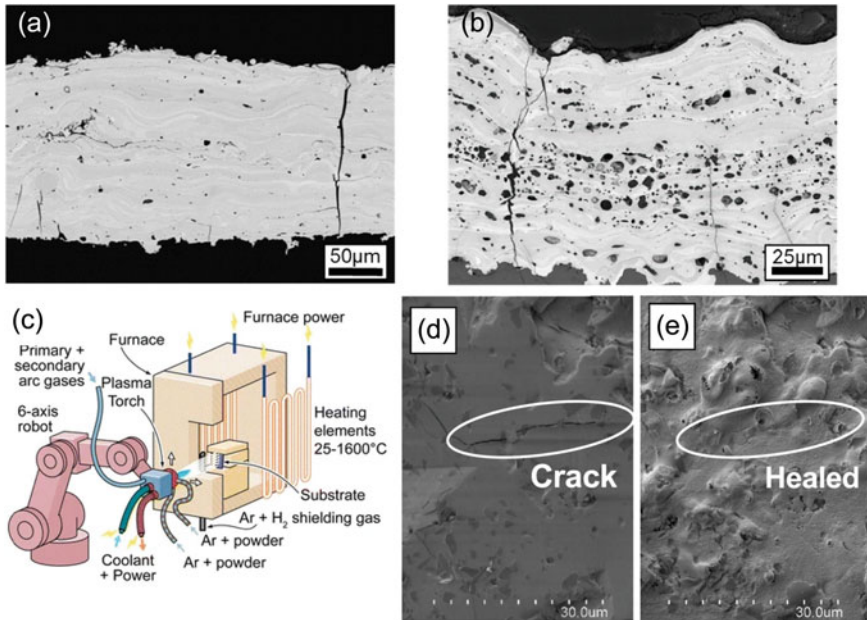


Fig. 9.12 Cross-sectional images of coating deposited via thermal spraying. The deposition temperature is **a** 550 °C and **b** 900 °C [34]. **c** Structure of plasma spray deposition with heat assist [54]. Surface images of the **d** as-indentated **e** after exposure at 1300 °C for 5 h in air [60] (Reproduced and redrawn with permission. Copyright 2015, Springer [54], Copyright 2022, Springer [60])

[59]. The details of crystallisation from the amorphous phase and phase transition are still unclear, and further research is needed to optimise the heat treatment.

A novel approach for the addition of SiC has also been demonstrated [60]. Figure 9.12d, e show the Vickers indentations before and after annealing. SiC oxidation via heat treatment not only healed cracks caused by volume expansion during oxidation, but also induced the reaction between SiO_2 and Yb_2SiO_5 to form $\text{Yb}_2\text{Si}_2\text{O}_7$ [61].

4.2 Suspension Plasma Spraying (SPS)

Suspension plasma spraying (SPS) is a spray coating process in which a suspension of fine feedstock powder, which directly influences the microstructure of the coating, is dispersed in water or ethanol and injected into a plasma jet as a thermal spray material. For example, the size and shape of feedstock powders have a direct impact on the pore size. In SPS, fine powders of 1 μm or less are usually dispersed in a liquid and injected. When particles with a diameter of a few microns are used, a denser coating can be obtained than with APS. Similar to other thermal spraying

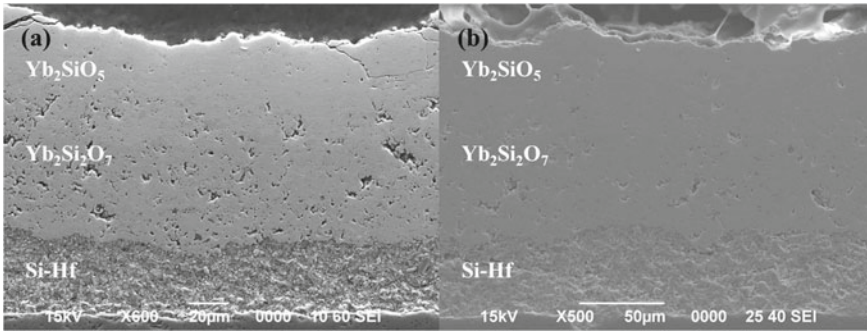


Fig. 9.13 Cross-sectional images **a** before and **b** after secondary densification (Reproduced with permission. Copyright 2021, Springer [64])

methods, the challenge for SPS is preventing the occurrence of the amorphous phase via rapid cooling and the prevention of Yb_2SiO_5 formation by the volatilisation of SiO [52]. The SD affects the substrate temperature, and reducing the distance not only achieves higher crystallisation but also stronger splat bonds [34]. Additionally, reducing the particle size of the feedstock powder improves heat conduction and enhances crystallisation [62].

However, for the volatilisation of SiO , the heat transfer of the particles in the liquid can be controlled using the plasma gas mixing ratio or by adding water to the existing ethanol solvent. The unmelted particles resulted in a high porosity and the formation of a coating layer, and highly crystalline $\text{Yb}_2\text{Si}_2\text{O}_7$ was obtained [63]. In addition, the volatilisation can be reduced by increasing the particle velocity during flight and decreasing the exposure time to the plasma flame [62]. The advantage of a smaller particle size for crystallization is mentioned above; however, larger fine particle surface area promotes SiO volatilization, resulting in the formation of more Yb_2SiO_5 [62].

Recently, a secondary densification technique was proposed [64]. Figure 9.13 (a-b) shows cross-sectional images before and after the secondary densification process. Ytterbium (III) nitrate pentahydrate ($\text{Yb}(\text{NO}_3)_3 \cdot 5\text{H}_2\text{O}$) and tetraethyl orthosilicate ($(\text{C}_2\text{H}_5\text{O})_4\text{Si}$) were applied to the surface of the coating, which comprises amorphous Yb_2SiO_5 via SPS and heat treatment at 1200°C . The conversion of amorphous Yb_2SiO_5 to crystalline $\text{Yb}_2\text{Si}_2\text{O}_7$ was confirmed through X-ray diffraction after the secondary heat treatment. This resulted in reduced cracks and pores and improved durability at high temperatures.

4.3 Low-Pressure Plasma Spraying (LPPS)

Low-pressure plasma spraying (LPPS) is a method of plasma spraying in inert and reduced-pressure atmospheres. The particle velocity of the LPPS process was higher

than those of the APS and SPS processes [34]. The high particle velocity at the time of substrate impact improves the adhesion between the molten splats, which is advantageous for the formation of the dense coatings required for EBC development. In addition, plasma heating temperatures lower than those of the APS and SPS can suppress SiO volatilisation. Another significant advantage is that the substrate temperature can be maintained until the start of deposition owing to the low heat transfer in a vacuum. The high deposition temperatures and post-deposition plasma heating in a low-pressure chamber enabled the deposition of $\text{Yb}_2\text{Si}_2\text{O}_7$ coatings with near-perfect crystallinity (~98%), high density (~4% porosity) and low SiO volatilisation [52]. The cross-sectional views of $\text{Yb}_2\text{Si}_2\text{O}_7$ coatings deposited via LPPS are shown in Fig. 9.14: (a) treated using post-deposition plasma heating, and (b) without post-deposition plasma heating. No vertical mud cracks were formed owing to the high crystallinity and few secondary phases. A vertical mud crack-free coating was achieved by gradually decreasing the plasma power used for heating within a given time and allowing the samples to cool to room temperature. In the sample without post-deposition plasma heating, vertical mud cracks were observed, including in the coating [52]. Additionally, increasing the cooling rate also increased the amorphous content of the thermally-sprayed coating, resulting in higher stresses. Therefore, it is important to control the cooling rate to achieve crack-free coatings.

In the steam cycling test at 1316 °C in 90% H_2O + 10% air atmosphere, the LPPS EBC did not fail during the 1000 cycles. This test was also performed for pure Si samples; however, the TGO growth rate of the LPPS EBCs was significantly lower than that of pure Si sample [65, 66]. Although the LPPS plasma temperature was relatively low, SiO volatilisation still occurred and approximately 15.5 vol% Yb_2SiO_5 was formed. Efforts to realise $\text{Yb}_2\text{Si}_2\text{O}_7$ coatings for plasma spraying are

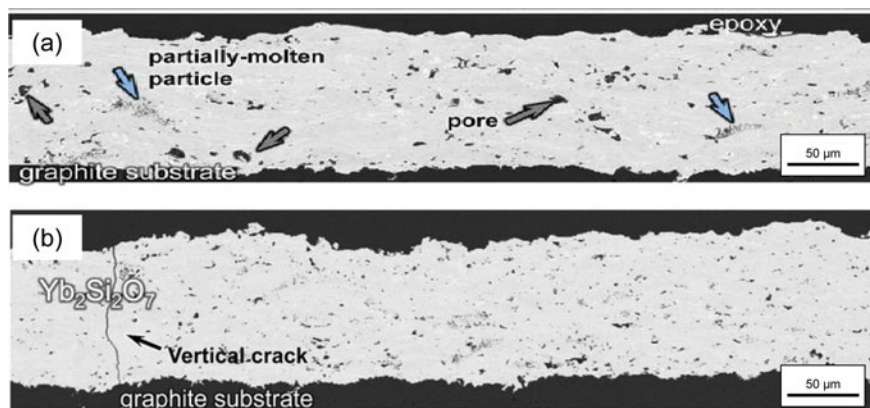


Fig. 9.14 Cross-sectional views of the LPPS coating deposited via **a** post-deposition plasma heating, and **b** without post-deposition plasma heating (Reproduced with permission. Copyright 2017, Springer [52])

ongoing [34]. However, the fact that 15.5vol% Yb_2SiO_5 could withstand thermal cycling supports the idea that $\text{Yb}_2\text{Si}_2\text{O}_7$ is a promising EBC.

4.4 High-Velocity Oxygen Fuel (HVOF)

High-velocity oxygen fuel (HVOF) is a thermal spraying process that uses a gas flame as the heat source. By increasing the pressure in the combustion chamber, a high-speed flame, comparable to a continuous flame, can be generated. $\text{Yb}_2\text{Si}_2\text{O}_7$ coatings with more than 90% crystallinity, less than 10% porosity, and a small number of cracks were obtained via HVOF spraying at a short SD [67]. Compared to other plasma spraying methods, HVOF has the advantages of a low deposition temperature and high speed. The low temperature (150–170 °C), in addition to preventing SiO evaporation, minimises thermal stresses in the thermal spraying process [68]. Furthermore, the kinetic energy of the particles at high speeds allows them to be coated with unmelted or partially melted particles; that is, the particles remain mostly crystallised. Compressive stresses can also increase owing to the peening effect of the particles on the substrate and the previously deposited layers. The porosity and cohesion of the coating depend mainly on the kinetic energy of the particles, which in turn, depends on the ductility and strain resistance of the substrate [67]. If the kinetic energy of the particles and ductility of the substrate are sufficiently high to allow compression, a coating with low porosity and high crystallinity is formed from the particles with a low melting point. Thus, the resulting coating is vertically mud-crack-free. However, the disadvantages include delamination and increased porosity owing to unmelted particles. Partial delamination occurred when loose, unmelted particles were in contact with the bond coat. Delamination is correlated with the gas velocity and is largely determined by the velocity and kinetic energy of the colliding particles. There was an incomplete transformation of the released kinetic energy into ductile deformation, which introduced stress in the deposited layers that continued to accumulate with successive depositions. In addition, the presence of loosely bound particles reduces the interfacial bond strength. Eventually, this effect was mitigated by the formation of cracks at the interface. Macroscopic delamination was observed under a high particle velocity, an absence of an amorphous phase and a low coating porosity. In addition, as noted above, a high-velocity injection decreases the porosity, and the porosity tends to increase with an increasing number of unmelted particles.

To obtain highly dense, highly crystalline and delamination-free $\text{Yb}_2\text{Si}_2\text{O}_7$ coatings, surface modification of the substrate is required to improve the adhesion of the initial coating layer. Alternatively, by increasing the heat transfer to avoid SiO evaporation, it is possible to improve the adhesion and prevent delamination by partially melting more impacted particles. The incomplete melting of brittle oxide particles can result in destruction owing to the high-speed impact on the Si bond coat substrate. However, if the core remains unmelted, the outer surface of the particles melts, and adhesion to the substrate or existing coating layer is possible, wherein shorter distances accelerate heat irradiation. The substrate temperatures observed at

short SDs (up to 767 °C) are clearly higher than those at longer SDs (up to 227 °C), and the ductility of the material increases with increasing temperature. The initial ductile coating layer was compressed via peening with hard particles at relatively high speeds, thereby promoting the formation of a dense coating with low porosity, and the crystallinity of all coatings was 90% or more at 100 mm SD [67]. Additionally, reducing the feedstock powder size further improved the wettability and densification by eliminating unmelted particles. However, the amorphous content and number of Yb_2SiO_5 phases increased.

In the suspension HVOF (SHVOF) process, nano- or submicron-particles are dispersed in a solvent such as water or ethanol to form a suspension that is then injected into an HVOF torch [69]. The suspension experiences solvent evaporation and melting of the particles, which in turn induces the formation of a coating. The high velocity of the particles upon impact results in better intersplat adhesion, which results in a denser coating. As shown in Fig. 9.15, a smaller distance can cause the formation of a dense coating. Thermal spray coatings are typically highly amorphous; however, heat treatment at 1300 °C for 10 h transformed the amorphous phase into the crystalline $\text{Yb}_2\text{Si}_2\text{O}_7$ and Yb_2SiO_5 . The appearance of the Yb_2SiO_5 secondary phase in the SHVOF coating is attributed to the loss of SiO during the thermal spraying process, and the TGO growth rate of the SHVOF EBCs was found to be less than one-third that of the air-plasma-sprayed EBCs under the same test conditions. In addition to using much finer particles ($<3\ \mu\text{m}$) than those used in conventional powder spray processes, the SHVOF process can form coatings with more sophisticated features owing to the better adhesion.

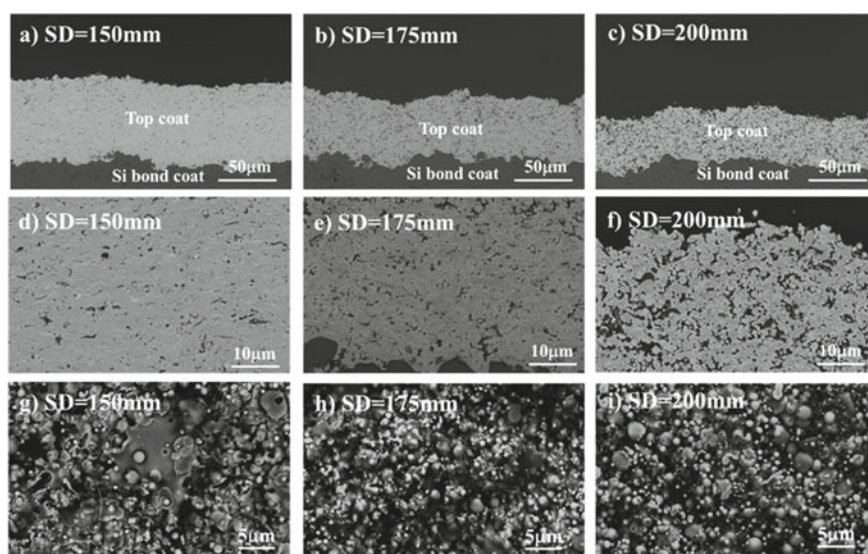


Fig. 9.15 a–f Cross-sectional and g–i surface images of as-sprayed SHVOF coatings at various SD (Reproduced with permission. Copyright 2023, Springer [69])

5 Summary and Perspectives

Currently, $\text{SiC}_f/\text{SiC}_m$ is being investigated as an alternative to current Ni-based superalloys for turbine blades; however, water vapour corrosion in high-temperature combustion environments is still a problem. Numerous attempts have been made over the years to overcome water vapour corrosion in environmental barrier coating structures, where researchers have focused on silicates.

The main requirements for EBCs are thermal properties such as the CTE, thermal conductivity and resistance to corrosion by water vapour and volcanic ash. Currently, RE silicates are considered to be the most promising materials.

In particular, multicomponent RE silicates have the potential to overcome the aforementioned issues, which cannot be achieved using a single-component silicate. However, several challenges remain unaddressed. Clear guidelines for element selection to optimise different properties and a method for particle synthesis are lacking. Not only is the synthesis of high-entropy RE silicates costly, but particle agglomeration is also inevitable when they are calcined at high temperatures. Because the feedstock powder system that was used for thermal spraying has a significant impact on the density of the coating, it is necessary to develop a method for synthesising the nanoparticles.

For thermal spraying methods, attempts have been made to deposit coatings using APS, SPS, LPPS and HVOF. Table 9.3 provides a comparison of thermal spraying techniques.

The APS method has been widely used in EBCs because of its success in TBCs. However, the formation of an amorphous phase due to the rapid cooling caused by a low-temperature substrate, and the formation of secondary phases such as Yb_2SiO_5 and Yb_2O_3 due to SiO evaporation are drawbacks. Recent advances have suggested that these problems can be overcome by controlling the substrate temperature using the heating support method and a short SD. In addition, the use of fine particles in suspension techniques to obtain low-porosity coatings is effective, and the benefits of these techniques are similar to those of HVOF. Although LPPS can produce the best quality coatings, other methods that have a lower cost should be investigated.

The phase transitions and crystallisation of the amorphous coatings produced by thermal spraying exhibit different behaviours depending on the RE ions. Thus, the

Table 9.3 Comparison of the thermal spraying techniques

	SiO evaporation	Crystallinity	Density	Crack	Adhesion	Cost
APS	2	3	3	2	4	5
SPS	2	4	4	2	4	3
LPPS	4	5	5	4	5	1
HVOF	4	4	3	4	2	3

1: bad, 3: average, 5: good

heat treatment needs to be optimised based on a detailed analysis of other sprayed EBC candidates.

Finally, this chapter focuses on the EBC; thermal and environmental barrier coatings are being proposed as next-generation gas-turbine coating systems. Recently, structures with a thermal barrier function that mitigates the thermal stress due to CTE differences such as three-layered structures ($(\text{Gd}_{0.9}\text{Yb}_{0.1})_2\text{Zr}_2\text{O}_7/\text{Yb}_2\text{SiO}_5/\text{Si}$) [70] and four-layered structures ($\text{LaMgAl}_{11}\text{O}_{19}/\text{Yb}_2\text{SiO}_5/\text{Yb}_2\text{Si}_2\text{O}_7/\text{Si}$ [71] and $\text{LaMgAl}_{11}\text{O}_{19}/\text{LiAlSiO}_4\text{-LaMgAl}_{11}\text{O}_{19}/\text{Yb}_2\text{Si}_2\text{O}_7/\text{Si}$ [72]) have been developed. In the future, the adhesion and thermal cycling resistance of these structures should be evaluated.

Research on EBCs is divided into diverse themes to meet different requirements, which require not only a fast research pace but also a broad perspective. Ultimately, this research is meant to contribute to existing industry knowledge; hence, there is a need for collaboration across research fields. In the past few decades, reports on novel approaches to overcome these challenges have made this field an interesting one with considerable potential.

Acknowledgements The authors would like to thank Editage (www.editage.jp) for English language review.

References

1. Padture, N.P.: Advanced structural ceramics in aerospace propulsion. *Nat. Mater.* **15**, 804–809 (2016). <https://doi.org/10.1038/nmat4687>
2. Zhang, J., Guo, X., Jung, Y.G., Li, L., Knapp, J.: Lanthanum zirconate based thermal barrier coatings: a review. *Surf. Coat. Technol.* **323**, 18–29 (2017). <https://doi.org/10.1016/j.surfcoat.2016.10.019>
3. Nguyen, S.T., Nakayama, T., Suematsu, H., Suzuki, T., Takeda, M., Niihara, K.: Low thermal conductivity $\text{Y}_2\text{Ti}_2\text{O}_7$ as a candidate material for thermal/environmental barrier coatings. *Ceram. Int.* **42**, 11314–11323 (2016). <https://doi.org/10.1016/j.ceramint.2016.04.052>
4. Richards, B.T., Wadley, H.N.G.: Plasma spray deposition of tri-layer environmental barrier coatings. *J. Eur. Ceram. Soc.* **34**, 3069–3083 (2014). <https://doi.org/10.1016/j.jeurceramsoc.2014.04.027>
5. Opila, E.J., Hann, R.E.: Paralineer oxidation of CVD SiC in water vapour. *J. Am. Ceram. Soc.* **80**, 197–205 (1997). <https://doi.org/10.1111/j.1151-2916.1997.tb02810.x>
6. Opila, E.J.: Oxidation and volatilization of silica formers in water vapor. *J. Am. Ceram. Soc.* **86**, 1238–1248 (2003). <https://doi.org/10.1111/j.1151-2916.2003.tb03459.x>
7. Tejero-Martin, D., Bennett, C., Hussain, T.: A review on environmental barrier coatings: History, current state of the art and future developments. *J. Eur. Ceram. Soc.* **41**, 1747–1768 (2021). <https://doi.org/10.1016/j.jeurceramsoc.2020.10.057>
8. Lee, K.N.: $\text{Yb}_2\text{Si}_2\text{O}_7$ Environmental barrier coatings with reduced bond coat oxidation rates via chemical modifications for long life. *J. Am. Ceram. Soc.* **102**, 1507–1521 (2019). <https://doi.org/10.1111/jace.15978>
9. Lee, K.N., Fox, D.S., Eldridge, J.I., Zhu, D., Robinson, R.C., Bansal, N.P., Miller, R.A.: Upper temperature limit of environmental barrier coatings based on mullite and BSAS. *J. Am. Ceram. Soc.* **86**, 1299–1306 (2003). <https://doi.org/10.1111/j.1151-2916.2003.tb03466.x>

10. Lee, K.N., Fox, D.S., Bansal, N.P.: Rare earth silicate environmental barrier coatings for SiC/SiC composites and Si₃N₄ ceramics. *J. Eur. Ceram. Soc.* **25**, 1705–1715 (2005). <https://doi.org/10.1016/j.jeurceramsoc.2004.12.013>
11. Klemm, H.: Silicon nitride for high-temperature applications. *J. Am. Ceram. Soc.* **93**, 1501–1522 (2010). <https://doi.org/10.1111/j.1551-2916.2010.03839.x>
12. Dong, Y., Ren, K., Lu, Y., Wang, Q., Liu, J., Wang, Y.: High-entropy environmental barrier coating for the ceramic matrix composites. *J. Eur. Ceram. Soc.* **39**, 2574–2579 (2019). <https://doi.org/10.1016/j.jeurceramsoc.2019.02.022>
13. Sun, L., Luo, Y., Tian, Z., Du, T., Ren, X., Li, J., Hu, W., Zhang, J., Wang, J.: High temperature corrosion of (Er_{0.25}Tm_{0.25}Yb_{0.25}Lu_{0.25})₂Si₂O₇ environmental barrier coating material subjected to water vapour and molten calcium–magnesium–aluminosilicate (CMAS). *Corros Sci.* **175**, 108881 (2020). <https://doi.org/10.1016/j.corsci.2020.108881>
14. Sun, L., Luo, Y., Ren, X., Gao, Z., Du, T., Wu, Z., Wang, J.: A multicomponent γ -type (Gd_{1/6}Tb_{1/6}Dy_{1/6}Tm_{1/6}Yb_{1/6}Lu_{1/6})₂Si₂O₇ disilicate with outstanding thermal stability. *Mater Res Lett.* **8**, 424–430 (2020). <https://doi.org/10.1080/21663831.2020.1783007>
15. Ren, X., Tian, Z., Zhang, J., Wang, J.: Equiatomic quaternary (Y_{1/4}Ho_{1/4}Er_{1/4}Yb_{1/4})₂SiO₅ silicate: a perspective multifunctional thermal and environmental barrier coating material. *Scr. Mater.* **168**, 47–50 (2019). <https://doi.org/10.1016/j.scriptamat.2019.04.018>
16. Ridley, M., Gaskins, J., Hopkins, P., Opila, E.: Tailoring thermal properties of multi-component rare earth monosilicates. *Acta Mater.* **195**, 698–707 (2020). <https://doi.org/10.1016/j.actamat.2020.06.012>
17. Dong, Y., Ren, K., Wang, Q., Shao, G., Wang, Y.: Interaction of multicomponent disilicate (Yb_{0.2}Y_{0.2}Lu_{0.2}Sc_{0.2}Gd_{0.2})₂Si₂O₇ with molten calcia–magnesia–aluminosilicate. *J. Adv. Ceram.* **11**, 66–74 (2022). <https://doi.org/10.1007/s40145-021-0517-7>
18. Ren, X., Zhang, J., Wang, J.: Composition effects on elastic, thermal and corrosion properties of multiple-RE silicate (Ho_{1/4}Er_{1/4}Yb_{1/4}Lu_{1/4})₂SiO₅ as a promising thermal and environmental barrier coating material. *J. Eur. Ceram. Soc.* **42**, 7258–7266 (2022). <https://doi.org/10.1016/j.jeurceramsoc.2022.08.034>
19. Sun, L., Ren, X., Luo, Y., Lv, X., Wang, J., Oh, Y., Wang, J.: Exploration of the mechanism of enhanced CMAS corrosion resistance at 1500 °C for multicomponent (Er_{0.25}Tm_{0.25}Yb_{0.25}Lu_{0.25})₂Si₂O₇ disilicate. *Corros Sci.* **203**, 110343 (2022). <https://doi.org/10.1016/j.corsci.2022.110343>
20. Turcer, L.R., Sengupta, A., Pature, N.P.: Low thermal conductivity in high-entropy rare-earth pyrosilicate solid-solutions for thermal environmental barrier coatings. *Scr. Mater.* **191**, 40–45 (2021). <https://doi.org/10.1016/j.scriptamat.2020.09.008>
21. Wang, X., Cheng, M., Xiao, G., Wang, C., Qiao, R., Zhang, F., Bai, Y., Li, Y., Wu, Y., Wang, Z.: Preparation and corrosion resistance of high-entropy disilicate (Y_{0.25}Yb_{0.25}Er_{0.25}Sc_{0.25})₂Si₂O₇ ceramics. *Corros Sci.* **192**, 109786 (2021). <https://doi.org/10.1016/j.corsci.2021.109786>
22. Chen, Z., Lin, C., Zheng, W., Zeng, Y., Niu, Y.: Investigation on improving corrosion resistance of rare earth pyrosilicates by high-entropy design with RE-doping. *Corros. Sci.* **199**, 110217 (2022). <https://doi.org/10.1016/j.corsci.2022.110217>
23. Chen, Z., Lin, C., Zheng, W., Jiang, C., Zeng, Y., Song, X.: Water vapour corrosion behaviors of high-entropy pyrosilicates. *J. Materiomics.* **8**, 992–1000 (2022). <https://doi.org/10.1016/j.jmat.2022.03.002>
24. Guo, X., Zhang, Y., Li, T., Zhang, P., Shuai, K., Li, J., Shi, X.: High-entropy rare-earth disilicate (Lu_{0.2}Yb_{0.2}Er_{0.2}Tm_{0.2}Sc_{0.2})₂Si₂O₇: A potential environmental barrier coating material. *J. Eur. Ceram. Soc.* **42**, 3570–3578 (2022). <https://doi.org/10.1016/j.jeurceramsoc.2022.03.006>
25. Wang, X., He, Y., Wang, C., Bai, Y., Zhang, F., Wu, Y., Song, G., Wang, Z.J.: Thermal performance regulation of high-entropy rare-earth disilicate for thermal environmental barrier coating materials. *J. Am. Ceram. Soc.* **105**, 4588–4594 (2022). <https://doi.org/10.1111/jace.18456>
26. Chen, Z., Tian, Z., Zheng, L., Ming, K., Ren, X., Wang, J., Li, B.: (Ho_{0.25}Lu_{0.25}Yb_{0.25}Eu_{0.25})₂SiO₅ high-entropy ceramic with low thermal conductivity, tunable thermal expansion coefficient, and excellent resistance to CMAS corrosion. *J. Adv. Ceram.* **11**, 1279–1293 (2022). <https://doi.org/10.1007/s40145-022-0609-z>

27. Ridley, M.J., Tomko, K.Q., Tomko, J.A., Hoglund, E.R., Howe, J.M., Hopkins, P.E., Opila, E.J.: Tailoring thermal and chemical properties of a multi-component environmental barrier coating candidate ($\text{Sc}_{0.2}\text{Nd}_{0.2}\text{Er}_{0.2}\text{Yb}_{0.2}\text{Lu}_{0.2}\text{Si}_2\text{O}_7$). *Materialia (Oxf)*. **26**, (2022). <https://doi.org/10.1016/j.mta.2022.101557>
28. Salanova, A., Brummel, I.A., Yakovenko, A.A., Opila, E.J., Ihlefeld, J.F.: Phase stability and tensorial thermal expansion properties of single to high-entropy rare-earth disilicates. *J. Am. Ceram. Soc.* (2023). <https://doi.org/10.1111/jace.18986>
29. Abrar, S., Ma, Z., Liu, L., Nazeer, F., Malik, A.: Ultra-low thermal conductivity and excellent high temperature resistance against calcium-magnesium-alumina-silicate of a novel β -type pyrosilicates. *J Alloys Compd.* **169001** (2023). <https://doi.org/10.1016/j.jallcom.2023.169001>
30. Tan, Y., Liao, W., Zeng, S., Jia, P., Teng, Z., Zhou, X., Zhang, H.: Microstructures, thermophysical properties and corrosion behaviours of equiatomic five-component rare-earth monosilicates. *J Alloys Compd.* **907**, (2022). <https://doi.org/10.1016/j.jallcom.2022.164334>
31. Chen, H., Xiang, H., Dai, F.Z., Liu, J., Zhou, Y.: High entropy ($\text{Yb}_{0.25}\text{Y}_{0.25}\text{Lu}_{0.25}\text{Er}_{0.25}$) SiO_5 with strong anisotropy in thermal expansion. *J Mater Sci Technol.* **36**, 134–139 (2020). <https://doi.org/10.1016/j.jmst.2019.07.022>
32. Liao, W., Tan, Y., Zhu, C., Teng, Z., Jia, P., Zhang, H.: Synthesis, microstructures, and corrosion behaviors of multi-components rare-earth silicates. *Ceram. Int.* **47**, 32641–32647 (2021). <https://doi.org/10.1016/j.ceramint.2021.08.160>
33. Liu, D., Jia, X., Shi, B., Wang, Y., Xu, B.: ($\text{Sm}_{0.2}\text{Eu}_{0.2}\text{Tb}_{0.2}\text{Dy}_{0.2}\text{Lu}_{0.2}$) Si_2O_7 : A novel high-entropy rare earth disilicate porous ceramics with high porosity and low thermal conductivity. *Mater Chem Phys.* **286**, (2022). <https://doi.org/10.1016/j.matchemphys.2022.126181>
34. Vaßen, R., Bakan, E., Gatzten, C., Kim, S., Mack, D.E., Guillon, O.: Environmental barrier coatings made by different thermal spray technologies. *Coatings.* **9**, (2019). <https://doi.org/10.3390/coatings9120784>
35. Fernández-Carrión, A.J., Allix, M., Becerro, A.I.: Thermal expansion of rare-earth pyrosilicates. *J. Am. Ceram. Soc.* **96**, 2298–2305 (2013). <https://doi.org/10.1111/jace.12388>
36. Cao, G., Ouyang, J.-H., Li, Y., Liu, Z.-G., Ding, Z.-Y., Wang, Y.-H., Jin, Y.-J., Wang, Y.-M., Wang, Y.-J.: Improved thermophysical properties of rare-earth monosilicates applied as environmental barrier coatings by adjusting structural distortion with RE-doping. *J. Eur. Ceram. Soc.* **41**, 7222–7232 (2021). <https://doi.org/10.1016/j.jeurceramsoc.2021.07.029>
37. Zhou, Y.C., Zhao, C., Wang, F., Sun, Y.J., Zheng, L.Y., Wang, X.H.: Theoretical prediction and experimental investigation on the thermal and mechanical properties of bulk β - $\text{Yb}_2\text{Si}_2\text{O}_7$. *J. Am. Ceram. Soc.* **96**, 3891–3900 (2013). <https://doi.org/10.1111/jace.12618>
38. Li, Y., Luo, Y., Tian, Z., Wang, J., Wang, J.: Theoretical exploration of the abnormal trend in lattice thermal conductivity for monosilicates RE_2SiO_5 (RE = Dy, Ho, Er, Tm, Yb and Lu). *J. Eur. Ceram. Soc.* **38**, 3539–3546 (2018). <https://doi.org/10.1016/j.jeurceramsoc.2018.04.014>
39. Richards, B.T., Young, K.A., de Francqueville, F., Sehr, S., Begley, M.R., Wadley, H.N.G.: Response of ytterbium disilicate-silicon environmental barrier coatings to thermal cycling in water vapour. *Acta Mater.* **106**, 1–14 (2016). <https://doi.org/10.1016/j.actamat.2015.12.053>
40. Bakan, E., Mack, D.E., Lobe, S., Koch, D., Vaßen, R.: An investigation on burner rig testing of environmental barrier coatings for aerospace applications. *J. Eur. Ceram. Soc.* **40**, 6236–6240 (2020). <https://doi.org/10.1016/j.jeurceramsoc.2020.06.016>
41. Bakan, E., Sohn, Y.J., Kunz, W., Klemm, H., Vaßen, R.: Effect of processing on high-velocity water vapour recession behaviour of Yb-silicate environmental barrier coatings. *J. Eur. Ceram. Soc.* **39**, 1507–1513 (2019). <https://doi.org/10.1016/j.jeurceramsoc.2018.11.048>
42. Ueno, S., Ohji, T., Lin, H.-T.: Recession behaviour of $\text{Yb}_2\text{Si}_2\text{O}_7$ phase under high speed steam jet at high temperatures. *Corros. Sci.* **50**, 178–182 (2008). <https://doi.org/10.1016/j.corsci.2007.06.014>
43. Okawa, A., Nguyen, S.T., Wiff, J.P., Son, H.W., Nakayama, T., Hashimoto, H., Sekino, T., Do, T.M.D., Suematsu, H., Suzuki, T., Goto, T., Niihara, K.: Self-healing ability, strength enhancement, and high-temperature oxidation behaviour of silicon carbide-dispersed ytterbium disilicate composite for environmental barrier coatings under isothermal heat treatment. *J. Eur. Ceram. Soc.* (2022). <https://doi.org/10.1016/j.jeurceramsoc.2022.05.057>

44. Tian, Z., Zhang, J., Sun, L., Zheng, L., Wang, J.: Robust hydrophobicity and evaporation inertness of rare-earth monosilicates in hot steam at very high temperature. *J. Am. Ceram. Soc.* **102**, 3076–3080 (2019). <https://doi.org/10.1111/jace.16315>
45. Lv, X., Cui, J., Zhang, J., Wang, J.: Phase composition and property evolution of $(Yb_{1-x}Ho_x)_2Si_2O_7$ solid solution as environmental/thermal barrier coating candidates. *J. Eur. Ceram. Soc.* **36**, 2813–2823 (2022). <https://doi.org/10.1016/j.jeurceramsoc.2022.04.020>
46. Turcer, L.R., Krause, A.R., Garces, H.F., Zhang, L., Pature, N.P.: Environmental-barrier coating ceramics for resistance against attack by molten calcia-magnesia-aluminosilicate (CMAS) glass: Part I, $YAlO_3$ and γ - $Y_2Si_2O_7$. *J. Eur. Ceram. Soc.* **38**, 3905–3913 (2018). <https://doi.org/10.1016/j.jeurceramsoc.2018.03.021>
47. Kim, S.H., Fisher, C.A.J., Nagashima, N., Matsushita, Y., Jang, B.K.: Reaction between environmental barrier coatings material $Er_2Si_2O_7$ and a calcia-magnesia-alumina-silica melt. *Ceram. Int.* **48**, 17369–17375 (2022). <https://doi.org/10.1016/j.ceramint.2022.03.001>
48. Turcer, L.R., Krause, A.R., Garces, H.F., Zhang, L., Pature, N.P.: Environmental-barrier coating ceramics for resistance against attack by molten calcia-magnesia-aluminosilicate (CMAS) glass: Part II, β - $Yb_2Si_2O_7$ and β - $Sc_2Si_2O_7$. *J. Eur. Ceram. Soc.* **38**, 3914–3924 (2018). <https://doi.org/10.1016/j.jeurceramsoc.2018.03.010>
49. Quintas, A., Caurant, D., Majérous, O., Dussossoy, J.L., Charpentier, T.: Effect of changing the rare earth cation type on the structure and crystallisation behaviour of an aluminoborosilicate glass. *Phys. Chem. Glass.: Phys Chem Glasses-B.* **49**, 192–197 (2008)
50. Tian, Z., Zhang, J., Zheng, L., Hu, W., Ren, X., Lei, Y., Wang, J.: General trend on the phase stability and corrosion resistance of rare earth monosilicates to molten calcium–magnesium–aluminosilicate at 1300 °C. *Corros. Sci.* **148**, 281–292 (2019). <https://doi.org/10.1016/j.corsci.2018.12.032>
51. Costa, G., Harder, B.J., Bansal, N.P., Kowalski, B.A., Stokes, J.L.: Thermochemistry of calcium rare-earth silicate oxyapatites. *J. Am. Ceram. Soc.* **103**, 1446–1453 (2020). <https://doi.org/10.1111/jace.16816>
52. Bakan, E., Marcano, D., Zhou, D., Sohn, Y.J., Mauer, G., Vaßen, R.: $Yb_2Si_2O_7$ environmental barrier coatings deposited by various thermal spray techniques: a preliminary comparative study. *J. Therm. Spray Technol.* **26**, 1011–1024 (2017). <https://doi.org/10.1007/s11666-017-0574-1>
53. Richards, B.T., Sehr, S., de Franqueville, F., Begley, M.R., Wadley, H.N.G.: Fracture mechanisms of ytterbium monosilicate environmental barrier coatings during cyclic thermal exposure. *Acta Mater.* **103**, 448–460 (2016). <https://doi.org/10.1016/j.actamat.2015.10.019>
54. Richards, B.T., Zhao, H., Wadley, H.N.G.: Structure, composition, and defect control during plasma spray deposition of ytterbium silicate coatings. *J. Mater. Sci.* **50**, 7939–7957 (2015). <https://doi.org/10.1007/s10853-015-9358-5>
55. Wang, H., Zhang, J., Sun, L., Wang, J.: Microstructure and phase composition evolution of dual-phase ytterbium silicate coatings plasma sprayed from stoichiometric $Yb_2Si_2O_7$ feedstock powder. *Surf Coat Technol.* **437**, (2022). <https://doi.org/10.1016/j.surfcoat.2022.128373>
56. Bakan, E., Sohn, Y.J., Vaßen, R.: Metastable to stable phase transformation in atmospheric plasma sprayed Yb-silicate coating during post-heat treatment. *Scr Mater.* **225**, (2023). <https://doi.org/10.1016/j.scriptamat.2022.115169>
57. Arhami, F., ben Ettouil, F., Moreau, C.: As-Sprayed Highly Crystalline $Yb_2Si_2O_7$ Environmental Barrier Coatings (EBCs) by Atmospheric Plasma Spray (APS). *J Therm Spray Technol.* (2023). <https://doi.org/10.1007/s11666-022-01526-6>
58. Garcia, E., Lee, H., Sampath, S.: Phase and microstructure evolution in plasma sprayed $Yb_2Si_2O_7$ coatings. *J. Eur. Ceram. Soc.* **39**, 1477–1486 (2019). <https://doi.org/10.1016/j.jeurceramsoc.2018.11.018>
59. Peng, Y., Luo, Z., Wang, H., Du, T., Zhang, J., Sun, L., Wang, J.: Crystallization and phase evolution in novel $(Gd_{1/6}Tb_{1/6}Dy_{1/6}Tm_{1/6}Yb_{1/6}Lu_{1/6})_2Si_2O_7$ environmental barrier coating. *Int J Appl Ceram Technol.* (2022). <https://doi.org/10.1111/ijac.14210>
60. Kitahara, T., Mitani, K., Saito, H., Ichikawa, Y., Ogawa, K., Masuda, T.: Improvement in the self-healing property of plasma-sprayed environmental barrier coatings by SiC addition. *J Therm Spray Technol.* (2022). <https://doi.org/10.1007/s11666-022-01441-w>

61. Nguyen, S.T., Takahashi, T., Okawa, A., Suematsu, H., Niihara, K., Nakayama, T.: Improving self-healing ability and flexural strength of ytterbium silicate-based nanocomposites with silicon carbide nanoparticles and whiskers. *J Ceram Soc JAPAN*. **129**, 209–216 (2021). <https://doi.org/10.2109/jcersj2.20179>
62. Yanaoka, R., Ichikawa, Y., Ogawa, K., Masuda, T., Sato, K.: Fundamental study of suspension plasma sprayed silicate coatings. *Mater. Trans.* **61**, 1390–1395 (2020). <https://doi.org/10.2320/matertrans.T-M2020826>
63. Ryu, H.L., Lee, S.M., Han, Y.S., Choi, K., An, G.S., Nahm, S., Oh, Y.S.: Preparation of crystalline ytterbium disilicate environmental barrier coatings using suspension plasma spray. *Ceram. Int.* **45**, 5801–5807 (2019). <https://doi.org/10.1016/j.ceramint.2018.12.048>
64. Park, S.M., Nahm, S., Oh, Y.S.: Thermal durability of ytterbium silicate environmental barrier coating prepared by suspension plasma spray. *J. Korean Ceram. Soc.* **58**, 192–200 (2021). <https://doi.org/10.1007/s43207-020-00086-1>
65. Chen, D., Pegler, A., Dwivedi, G., de Wet, D., Dorfman, M.: Thermal cycling behaviour of air plasma-sprayed and low-pressure plasma-sprayed environmental barrier coatings. *Coatings*. **11**, (2021). <https://doi.org/10.3390/coatings11070868>
66. Chen, D., Pegler, A., Dorfman, M.: Environmental barrier coatings using low pressure plasma spray process. *J. Am. Ceram. Soc.* **103**, 4840–4845 (2020). <https://doi.org/10.1111/jace.17199>
67. Wolf, M., Mack, D.E., Mauer, G., Guillon, O., Vaßen, R.: Crystalline ytterbium disilicate environmental barrier coatings made by high velocity oxygen fuel spraying. *Int. J. Appl. Ceram. Technol.* **19**, 210–220 (2022). <https://doi.org/10.1111/ijac.13829>
68. Bakan, E., Mauer, G., Sohn, Y.J., Koch, D., Vaßen, R.: Application of high-velocity oxygen-fuel (HVOF) spraying to the fabrication of Yb-silicate environmental barrier coatings. *Coatings*. **7**, (2017). <https://doi.org/10.3390/coatings7040055>
69. Chen, D.: Suspension HVOF sprayed ytterbium disilicate environmental barrier coatings. *J. Therm. Spray Technol.* **31**, 429–435 (2022). <https://doi.org/10.1007/s11666-022-01343-x>
70. Chen, W., He, W., He, J., Guo, Q., Li, S., Guo, H.: Failure mechanisms of $(\text{Gd}_{0.9}\text{Yb}_{0.1})_2\text{Zr}_2\text{O}_7/\text{Yb}_2\text{SiO}_5/\text{Si}$ thermal/environmental barrier coatings during thermal exposure at 1300°C/1400°C. *J Eur Ceram Soc.* **42**, 3297–3304 (2022). <https://doi.org/10.1016/j.jeurceramsoc.2022.02.023>
71. Lü, K., Dong, S., Huang, Y., Mao, C., Jiang, J., Deng, L., Cao, X.: Thermal shock behaviour of $\text{LaMgAl}_{11}\text{O}_{19}/\text{Yb}_2\text{Si}_2\text{O}_7/\text{Si}$ thermal/environmental barrier coatings with $\text{LaMgAl}_{11}\text{O}_{19}$ - LiAlSiO_4 transition layer. *Surf Coat Technol.* **443**, (2022). <https://doi.org/10.1016/j.surfcoat.2022.128594>
72. Fan, W., Zou, B., Fan, C., Wang, Y., Cai, X., Tao, S., Xu, J., Wang, C., Cao, X., Zhu, L.: Fabrication and oxidation resistant behaviour of plasma sprayed $\text{Si}/\text{Yb}_2\text{Si}_2\text{O}_7/\text{LaMgAl}_{11}\text{O}_{19}$ coating for Cf/SiC composites at 1673K. *Ceram. Int.* **43**, 392–398 (2017). <https://doi.org/10.1016/j.ceramint.2016.09.171>

1D Micro/Nanomaterial Toughened Ceramic Coatings for Carbon/Carbon Composites



Xuemin Yin, Huimin Liu, Xin Zhang, and Hejun Li

Abstract Carbon/carbon (C/C) composites, due to their unique structural characteristics and excellent properties, are one of the most promising materials for high-temperature application in aerospace propulsion systems. However, this composite material is susceptible to high-temperature oxidation in oxygen-containing environment. Coating with Si-based ceramics or ultra-high temperature ceramic (UHTC) materials is proven to be an efficient method for improving the resistances of the C/C composites against oxidation and ablation. Unfortunately, there still remain some challenges in the coating technology, such as the mismatch of C/C substrates and ceramic coatings, as well as the intrinsic brittleness of coating ceramics. To solve these problems, numerous studies were conducted on reinforcing the ceramic coatings with 1D micro/nanomaterials, which exhibit varied structural advantages, such as small size in nanometer scale, large aspect ratio and high structural stability. The research status of 1D micro/nanomaterials reinforced ceramic coatings for C/C composites are discussed in this review.

Keywords Carbon/carbon composite · Ceramic coatings · 1D micro/nanomaterials · Oxidation · Ablation

1 Introduction

With the recent rapid development in aerospace and aviation industries, high-performance thermal structural materials become increasingly important [1]. During the lifetime in practical applications, thermal structural materials often encounter severe and complex conditions, such as ultra-high temperatures, high speeds and complex loadings [2]. Therefore, under the strong requirements for future aircrafts, an

X. Yin (✉) · H. Liu · X. Zhang · H. Li

State Key Laboratory of Solidification Processing, Shaanxi Key Laboratory of Fiber Reinforced Light Composite Materials, Northwestern Polytechnical University, Xi'an, PR China
e-mail: yinxuemin@nwpu.edu.cn

URL: <https://www.scopus.com/authid/detail.uri?authorId=56643646900>

enormous amount of research efforts are put into development of high-performance thermal structural materials [3, 4].

The C/C composite is a carbon matrix reinforced by carbon fibers. It has excellent structural properties, including low bulk density ($<2.0 \text{ g/cm}^3$) and coefficient of thermal expansion (CTE), good reliability, superior specific strength and modulus, as well as excellent high-temperature retention of mechanical performance [5]. However, the C/C composites oxidation in air at temperature above $450 \text{ }^\circ\text{C}$ may cause failures and even catastrophic accidents in serious cases, which greatly restrict the C/C composites from broad and long-term applications in oxygen-containing conditions [6–9].

To enhance the resistances of the C/C composites against oxidation and ablation, a large number of studies were conducted and various methods were proposed, including preform structure design, pyrolytic carbon texture control, matrix modification and coating technologies [10]. Particularly, the coating methods are considered as the most efficient strategy for improving the long-term anti-oxidation/ablation performances of C/C composite. Ceramics, especially UHTCs, have been widely applied as potential candidate materials in anti-oxidation/ablation coatings [2, 11, 12].

In spite of the improved anti-oxidation/ablation capabilities of the C/C composites with ceramic coatings, it is still challenging to meet the practical requirements for high durability and long lifetime in ultra-high temperature environments. The intrinsic brittleness of conventional ceramic coating materials and the inconsistent CTEs of the coating layer and the substrate can result in cracking and debonding of the coating layer. This failure could significantly lower the coating protection function for C/C composites [13]. To address these problems, different one-dimensional (1D) micro/nano-scaled filler materials have been used to reinforce the ceramic coatings, including CNTs, SiC whiskers/nanowires, HfC/ZrC nanowires and core-shell structured nanowires, which were selected due to their unique structural and mechanical characteristics, e.g., large aspect ratio, super-high strength, good ductility smaller microstructure and superior high-temperature stability. Besides, in order to achieve long-term application in extremely harsh conditions, additional optimizations of the one-dimensional nanostructures are required, such as reducing the C/C defects, increasing fiber/matrix interface binding, improving the stress distribution and further enhancing the mechanical properties. The researches on 1D micro/nanomaterials reinforced ceramic coatings on the C/C composites are summarized and discussed in the following sections.

2 Preparation Methods of Ceramic Coatings

(1) Pack Cementation (PC)

As a simple method, PC is commonly adopted to prepare ceramic coating layers on the C/C composites (Fig. 1a) [14]. Typically, the C/C composite is first immersed into the reactive powder mixture, and the reaction system is then heated to high

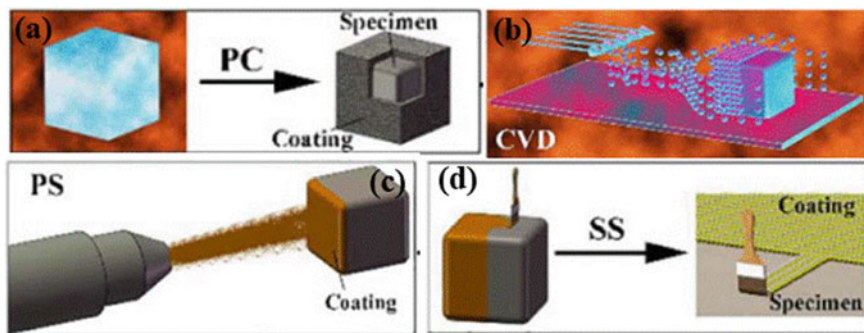


Fig. 1 Schematic diagram of the typical fabrication methods of ceramic coatings for C/C composites: **a** pack cementation (PC); **b** chemical vapor deposition (CVD); **c** plasma spray (PS); **d** slurry-sintering (SS) [11]. Copyright © 2021, The Author(s)

temperatures. In this thermal treatment process, the molten reactants react with the carbon matrix or migrate onto the C/C composite to form the ceramic coating [15–17]. The composition of the ceramic coating could be easily controlled by changing the mass ratio of raw materials [18, 19]. The simple PC process can usually provide high bonding force between the substrate and the coating layer; however, the high-temperature treatment and reaction may lower the C/C composites performances. Besides, the coating thickness in this method is difficult to be controlled.

Actually, PC is a method for preparing coatings by pressure-less sintering. However, it is difficult to sinter ceramics, especially UHTCs with covalent bonds and intrinsic brittleness. The densification level of the coating prepared by PC is low, which cannot meet the application requirements. Hot press sintering is an effective way to solve this problem. It could induce dense coatings with strong interface bonding. However, the hot pressing process has special requirements for the equipments, and it is unsuitable to fabricate ceramic coatings on C/C substrates with complex shapes.

(2) Chemical Vapor Deposition (CVD)

As one of the common coating techniques, the CVD method is also widely applied for synthesizing high-quality and high-purity coatings (Fig. 1b) [20, 21]. The CVD process for ceramic coatings is similar to that for 1D micro/nanomaterials [9, 22]. One of its advantages is that the microstructure, morphology, crystallinity, composition, purity as well as thickness of ceramic coatings can be easily controlled via changing the CVD parameters, e.g., temperature, pressure, reaction time and gas flow rate [21, 23]. In addition, the reaction temperature for CVD is usually low, which could avoid the high-temperature-induced damage or defects in C/C composite substrates [24]. With respect to the disadvantages of the CVD method, they are known as slow process, high cost, corrosive byproducts, as well as requirements for vacuum or inert atmosphere and special preparation equipments.

(3) Plasma Spray (PS)

A simple thermal spraying technique is involved in the PS coating preparation method, in which the spray materials are melted and sprayed onto the C/C composite surface (Fig. 1c). During the preparation process, a plasma flame with ultra-high temperature is used to melt the injected raw material powders [8, 25]. The molten or semi-molten powders are then sprayed with high velocity to C/C substrates and cooled down rapidly afterward to form a coating with uniform thickness and well-controlled composition [26, 27]. However, the ceramic coatings prepared by PS possess and have also some disadvantages, e.g., high porosity, large surface roughness as well as weak binding force between the substrate and the coating layer.

(4) Slurry Sintering (SS)

For preparing coatings on various substrates for different applications, SS is the most widely used technique (Fig. 1d) [28, 29]. In a typical SS process, ceramic powders or precursors are dispersed first in a solvent to form a slurry, which is then brushed onto the C/C substrates. After the solvent is removed by drying, the system is finally heat treated under the protection of an inert gas [30, 31]. The as-prepared ceramic coatings have usually porous structures [18]. To improve the coating densification level, the brushing-drying-heating process cycle can be repeated for several times. On the other hand, the coating-substrate bonding from this process is usually weak and the carbon components generated from pyrolysis remain in the coatings. To solve these problems, the SS method is normally used combining other methods, e.g., gas and liquid silicon infiltration.

3 Fabrication of 1D Micro/nanomaterial-Reinforced Ceramic Coatings for C/C Composites

In general, physical method and chemical growth method are the two common ways for introducing 1D micro/nanomaterials onto C/C composites. In this paper, the physical method mainly represents the electrophoretic deposition (EPD), while the chemical growth method mainly includes the chemical vapor deposition and the pyrolysis of polymer precursors. In addition, some hybrid and heterostructure 1D micro/nanomaterials were also applied as nanoreinforcements for ceramic coatings in recent years. They were normally synthesized via a composed process comprising multiple steps or different methods.

EPD is an electrochemical process in colloidal solution. Driven by an externally applied electric field, the electrically charged colloidal particles are transferred onto an oppositely charged conductive substrate and deposited there to form a coating film. EPD is an easy approach to fabricate 1D micro/nanomaterials on C/C composites [32]. However, the bonding strength at interface of 1D micro/nanomaterials and C/C substrates is usually low, which may easily lead to the shedding of 1D reinforcement layers.

One-dimensional carbon- and ceramic-based micro/nanomaterials are usually in-situ fabricated on the substrates by CVD method [33, 34]. Generally, reactants in

gas phase are directed into the systems and reacted afterward at high temperature to growth 1D micro/nanomaterials in a specific direction. In addition, catalysts are often adopted to promote the growth process of the 1D micro/nanomaterials. By adjusting the process parameters, including catalyst type, temperature, gas flow velocity, reaction pressure and time, the morphology and distribution of 1D micro/nanomaterials could be easily controlled. However, CVD requires complex equipments and the remaining metallic catalysts in the system could cause damages in the C/C substrates and ceramic coatings.

In addition, liquid polymeric precursors are a common raw material for fabricating different ceramics via high-temperature thermal treatment. During the pyrolysis process, gaseous species are produced and reacted with each other over the metallic catalysts to form ceramic nanomaterials, e.g., SiCNWs [35], Si₃N₄NWs [36], HfCNWs [37] and ZrCNWs [38]. Although this method is simple and efficient, it is difficult to control the morphology of nanomaterials. Besides, ceramic residues remain also on the C/C substrates.

4 CNT-Reinforced Ceramic Coatings on C/C Composites

Due to the unique structural characteristics of excellent mechanical capability, low CTE and density, high aspect ratio (length to radius ratio) and thermal conductivity, carbon nanotubes (CNTs) are an idea reinforcement material for different composites to improve their structural and functional performances [39, 40]. Therefore, CNTs are selected to be introduced into C/C composites as well as their ceramic coatings [41]. For coatings, the introduction of CNTs could not only increase the toughness of protective layers, but also lower the CTE mismatch at interface of the C/C substrate and the ceramic coating.

Zheng et al. fabricated CNTs and PyC on C/C composite surface using CVD with carbon sources of C₂H₂ and CH₄, respectively. Afterwards, SiC coatings were deposited on CNTs or CNTs-PyC [24] (Fig. 2a–c). The reinforced SiC coatings are composed of outer layer of pure SiC as well as inner layer of CNTs-SiC or CNTs-PyC-SiC (Fig. 2b, c). In comparison with pure SiC coating with 55% of mass loss, CNTs-PyC reinforced SiC coatings show less cracks and higher oxidation resistance (mass loss of 15%) in oxidation at 1200 °C for 2 h. The CNTs-PyC-SiC layer could serve as a buffer layer, comprising a large number of phase interfaces, which can alleviate the thermal stress at interface of the substrate and the SiC coating layer, suppressing the SiC coating from crack propagation.

Feng and co-workers fabricated double-layer coating structure of SiC/CNTs-SiC by depositing CNTs first on C/C substrates with EPD and then depositing SiC with CVD [44]. By varying the EPD time, it is possible to control the loading of the CNTs on the substrates. After the EPD process, a porous layer of randomly oriented CNTs on C/C substrates was observed. After the deposition of SiC, a dense inner layer of CNTs-SiC and an outer layer of SiC were formed. In comparison with the CNT-free pure SiC coating, the double-layer coating of SiC/CNTs-SiC exhibits less

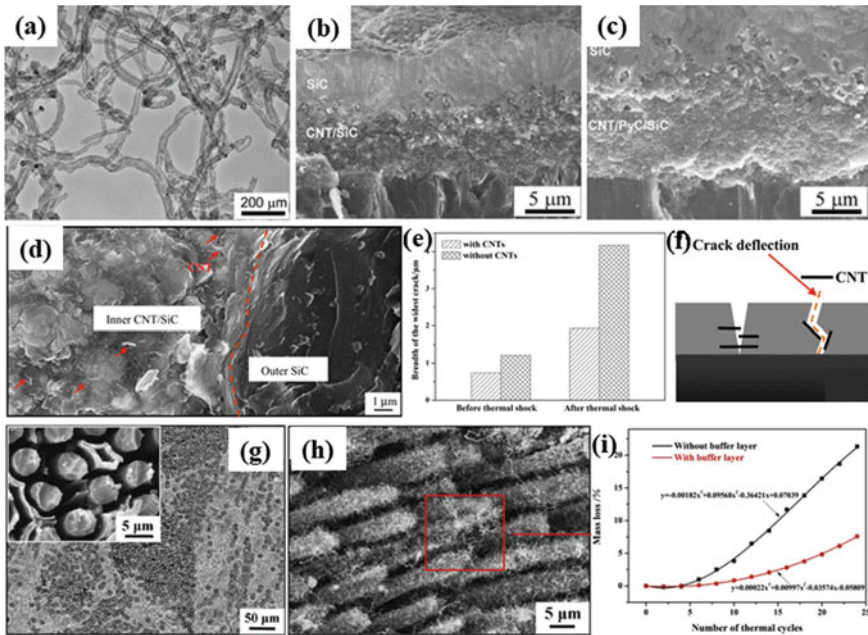


Fig. 2 a TEM image of CNTs; SEM images of b CNT-SiC coating cross-section and c CNT-PyC-SiC coating cross-section [24]. Copyright © 2011 Elsevier Ltd. All rights reserved. d SEM image of CNTs-SiC coating cross-section before polishing; e Width of the largest microcrack on coated composites before and after thermal cycling; f Illustration diagram of CNTs coating [42]. Copyright © 2015 Elsevier B.V. All rights reserved. g Images of C/C-ZrC-SiC composites surface after pre-oxidation; h SEM images of CNTs on C/C-ZrC-SiC composite after pre-oxidation; i Thermal shock curves of the coated composites [43]. Copyright © 2015 The Chinese Ceramic Society. Production and hosting by Elsevier B.V

and smaller cracks, as well as higher resistance to thermal shocks. After 15 times of thermal cycling in temperature range of 298–1473 K, the C/C composites coated by SiC/CNTs-SiC via 85 s of EPD-CNTs show the best resistance to thermal shock with a decrease in the mass loss from 15.82% to 11.84%. The enhanced resistance against thermal shock is mainly due to the inner layer of CNTs-SiC.

In addition to pure C/C substrates, Fu et al. also fabricated CNTs on surface of ZrC-SiC-coated C/C composite with injection chemical vapor deposition (ICVD) to reinforce CVD-SiC coatings [42] (Fig. 2d). The introduction of CNTs reduces the crack size and leads to crack deflection in ceramic coatings, originating from the bridging and pulling out of CNTs (Fig. 2e, f). Because of the enhanced binding force at interface of the SiC coating and the C/C-ZrC-SiC substrate, the CNT-coated composite system shows a mass loss decrease from 5.98% to 1.98% after 15 times of thermal shock cycling at temperature range of 298–1773 K.

Furthermore, aiming at further improving the performances of SiC coating layer on the C/C-ZrC-SiC composite, including the interface adhesion strength as well

as the resistance against thermal shock, the C/C-ZrC-SiC substrate was firstly pre-oxidized before the growth of CNTs [43]. After the pre-treatment, a porous structured surface was obtained and some carbon fibers were exposed (Fig. 2g), where CNTs as well as the SiC coating could be deposited easily, facilitating further construction of a CNT-reinforced SiC interlocking buffer layer (Fig. 2h). Because of the formation of the buffer layer, an increase in adhesion strength from 2.3 to 6.8 N was observed at interface of SiC coating and C/C-ZrC-SiC substrate. Additionally, after 25 times of the thermal shock cycling in temperature range of 298–1773 K, the samples with and without CNTs-reinforced buffer layer show mass loss of 7.58% and 21.33%, respectively, indicating a significant improvement of the thermal shock resistance for the CNT-reinforced interlocking structure (Fig. 2i). The enhanced interface bonding strength as well as the elevated resistance against thermal shock could be attributed to the co-existence of the reinforcement capability of nanosized CNTs and the “pinning effect” of inlaid microscaled CVD-SiC coating.

5 SiC Whisker/nanowire-Reinforced Ceramic Coatings for C/C Composites

5.1 SiC Whisker-Reinforced Ceramic Coatings on C/C Composites

SiO₂ coating layers fabricated by oxidation of SiC whisker show multiple excellent structural characteristics, e.g., low CTE, high chemical and thermal stability, superior fracture toughness and resistance against thermal shock, as well as outstanding self-healing ability. Therefore, SiC whisker is considered as an excellent reinforcement material [45–47].

To date, different methods including CVD, PC, sol–gel process and slurry dipping have been adopted to prepare SiC whisker with different structures [48–50]. Li et al. [47] first employed SiC whisker-reinforced SiC ceramic coating to protect C/C composites from the oxidations via a two-step procedure containing slurry and pack cementations. The as-obtained SiC coating with a SiC whisker content of 10 wt.% shows a mass loss of 1.7% in high temperature (1773 K) oxidation with a duration of 48 h. Later, Wen et al. [51] utilized sol–gel method to deposit SiC whisker-reinforced mullite coating layer onto SiC-coated C/C substrates. With the SiC whisker content increase up to 10 wt.%, the crack propagation resistance of the coating was remarkably enhanced owing to the increased coating toughness and suppression of microcracks formation. Only a little of microcracks were detected in the thermal cycled sample (Fig. 3a, b). The crack deflection and energy dissipation mechanism originating from the whisker bridging lead to improved thermal cycling resistance. The sample with 10 wt.% of SiC whisker shows a mass loss per unit area of only 3.0628 mg/cm² (Fig. 3c). The SiC whiskers could also be also introduced in the C/C composites with CVD to obtain SiC whisker-reinforced C/C-Cu composites

with superior anti-ablation ability at ultra-high temperatures (Fig. 3d) [52]. An elastic modulus around 138.32 GPa was detected, which could be ascribed to the inhibition effects of SiC whiskers for crack growth and fiber pulling-out (Fig. 3e). SiC whiskers have high dispersion homogeneity, large specific surface area and a continuous dense oxide (SiO_2) layer covering the matrix surface, promoting the anti-ablation ability of the composites (Fig. 3f). Wang et al. [19] used finite element analysis to study the effect of SiC whiskers on toughening HfB_2 -SiC-Si/SiC coating. As the sample was treated with a heat flux under 1500 °C in static air for 200 s, the maximum thermal stress corresponding to the SiC whisker-HfB₂-SiC-Si/SiC structured coating is 239 MPa. It is significantly lower than the corresponding value of SiC whisker-free HfB₂-SiC-Si/SiC coating (267 MPa). In addition, analysis results indicate that the SiC whiskers can effectively eliminate the CTE mismatch and significantly suppress crack formation/growth in virtue of their reinforcement capability including whisker extraction and bridge strengthening, which can efficiently alleviate the thermal stress from temperature changes. With the rapid developments of fabrication technologies, many other types of multilayer or multiphase coatings toughened by SiC whisker have also been extensively studied [19, 53–56]. After introducing SiC whisker, longer lifetime in extreme conditions was achieved for the reinforced coatings.

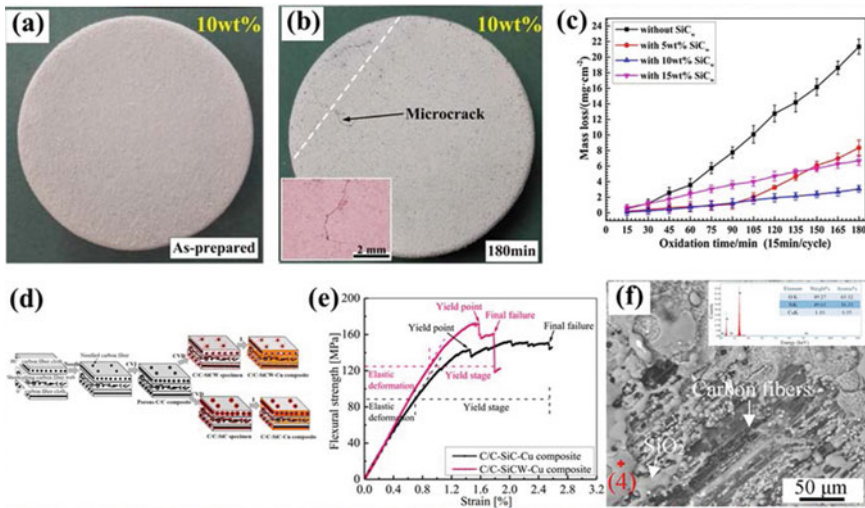


Fig. 3 Surface photographs of 10 wt.% SiC whisker-reinforced mullite coatings **a** before and **b** after the thermal cycling (the inset shows the coating surface with higher magnifications), **c** Different mass loss per unit surface area with the oxidation time/thermal cycle (15 min/cycle) of the coated samples with different content of SiC whiskers [51]. Copyright © 2016 Elsevier Ltd. All rights reserved. C/C-SiCW-Cu composite: **d** schematic diagram of the fabrications, **e** flexural stress/strain curves, **f** SEM images of the surfaces after 30 s of ablation testing (the inset shows the corresponding EDS image of point (4)) [52]. © 2021 Elsevier Ltd and Techna Group S.r.l. All rights reserved

5.2 SiC Nanowire-Reinforced Ceramic Coatings on C/C Composites

SiC nanowire has aroused increasingly research interests because of their extremely excellent mechanical properties, including superior wear resistance and thermal stability, as well as high compatibility with Si-based coatings [57]. Both experimental and theoretical studies have revealed that SiC nanowire is a promising 1D nanomaterial as an effective reinforcement agent for ceramic composites and ultra-high temperature anti-oxidation coating. Moreover, as reinforcement material, SiC nanowire shows better mechanical properties than SiC whisker.

A large number of research works on the fabrication methods and techniques for SiC nanowire have been reported, such as sol-gel process, carbothermal reduction, CVD, polymeric precursor pyrolysis, EPD, slurry painting (SP) and template methods [35, 58–61]. Li et al. [62] used SP and catalyst-free high-temperature treatment processes to in-situ grow high-purity SiC nanowire porous layer through vapor-solid (VS) mechanism (Fig. 4a). An increase in the elastic modulus by 35% was observed after reinforcement of the SiC coating with SiC nanowire. Moreover, the SP process mentioned above is very efficient and relatively simple. Huang et al. [63] prepared SiC nanowire-reinforced mullite coating layer on C/C composite pre-coated with SiC via a two-step procedure comprising a hydrothermal EPD and a subsequent pulse arc discharge deposition (Fig. 4b, c). The reinforcement effect from mullite devitrification, bridging, pulling-out and the crack deflection improved resistance of the coating against thermal shocks. Figure 4d–g illustrate four conventional toughening mechanisms, which could absorb a large amount of energy from the fracturing process and decline the crack thickness, enhancing the toughness of the coatings [64, 65]. In another research, by combining the CVD and PC methods, SiC nanowire was introduced as the reinforcement material into a coating layer of CrSi_2 -SiC-Si on SiC-coated C/C composite to improve their oxidation protective ability [66]. The size of microcracks in the coating could be reduced by SiC nanowire, further improving the resistance of the coating against oxidation in temperature range of 25–1500 °C. Moreover, with combined CVD and PC approaches, various coatings like SiC nanowire-reinforced MoSi_2 -SiC, SiC- MoSi_2 - CrSi_2 , CrSi_2 -SiC-Si et al. were also developed by Fu and Chu for C/C composites to enhance their resistance against oxidation [67, 68].

Up to date, various SiC nanowires with different micro- and nano-structures have been developed to improve the performances of ceramic coatings, such as straight line shaped nanowires [67], bamboo-shaped nanowires [69], nanoribbons [70] and ultra-long SiC nanowires [71] (Fig. 5a–d). Particularly, bamboo-shaped SiC nanowires could increase the contact area at interface of nanowires and the coating, further improving the load transfer efficiency [69, 72]. Chu et al. [71] prepared continuous mesh structure of super-long SiC nanowires (Fig. 5d) to enhance the SiC-Si coating. Test results show that the super-long SiC nanowires can effectively inhibit the coating from cracking and protect C/C composite against oxidation in the air at 1773 K.

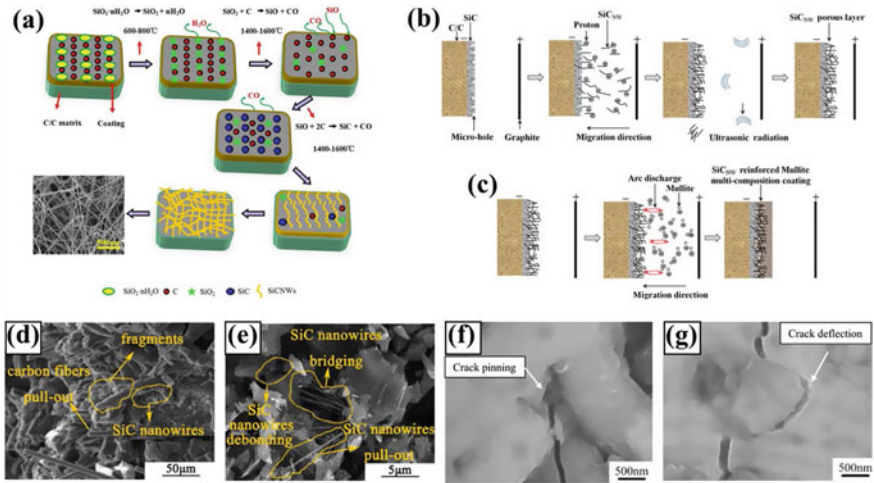


Fig. 4 Schematic diagrams: **a** Growth model of SiCNWs in SP and catalyst-free high-temperature treatment processes [62]; © 2021 Elsevier Ltd and Techna Group S.r.l. All rights reserved. **b** synthesis of SiC nanowire porous layer, **c** preparation of SiC nanowire-reinforced mullite coating [63]. Copyright © 2016 Elsevier Ltd. All rights reserved. Typical toughening mechanisms: **d** pull-out, **e** bridging, **f** crack pinning, **g** crack deflection [64, 65]. © 2022 Published by Elsevier Ltd on behalf of The editorial office of journal of Materials Science and Technology. © 2016 Elsevier B.V. All rights reserved

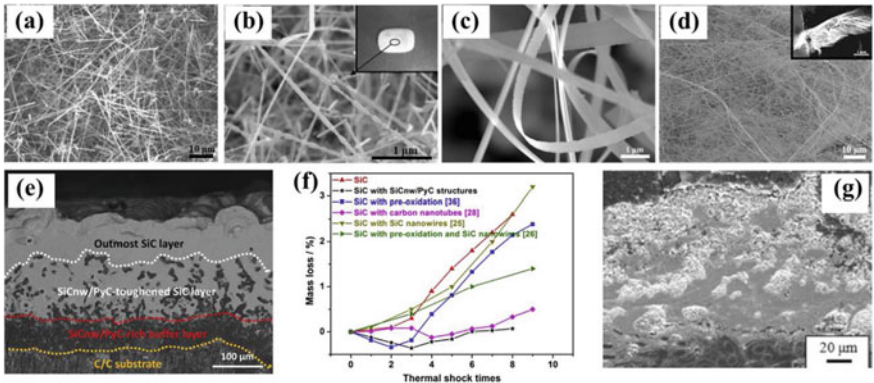


Fig. 5 SiC morphologies: **a** straight line shaped SiC nanowires [67] Copyright © 2010 Elsevier Ltd. All rights reserved. **b** bamboo-shaped nanowires [69], Copyright © 2013 Elsevier Ltd. All rights reserved. **c** nanoribbons [70], Copyright © 2014 Elsevier Ltd. All rights reserved. **d** ultra-long SiC nanowires [71]. Copyright © 2014 Elsevier Ltd. All rights reserved. CVD-SiC coating reinforced with SiC nanowire/PyC core-shell structured material: **e** morphology of the SiC coating cross-section, **f** thermal shock curves in air and temperature range of 198–1773 K for coated composite systems [73]. © 2018 Elsevier Ltd. All rights reserved. **g** cross-section morphology of SiC nanowire-toughened HfC coating after ablation [74]. Copyright © 2014 Published by Elsevier Ltd

In addition to the enhancement of anti-oxidation ability, improvement in resistances of coatings against thermal shock and ablation could also be achieved by SiCNWs reinforcement. Fu et al. [75] prepared SiC nanowire-reinforced inlaid transition coating layer of SiC-MoSi₂-ZrB₂ on the C/C composite. The as-obtained composite system with a pre-oxidation and CVD-SiC nanowire shows a line slope of 0.2495 and a mass loss per unit area of only 0.0037 g/cm², indicating a good thermal shock resistance of the coating. Besides, Zhuang et al. [73] developed CVD-SiC coating reinforced with SiC nanowire/PyC core-shell structured material. The multi-interface core-shell structure shown in Fig. 5e provides excellent toughening effect. The mass loss was measured to be only 0.07% after eight thermal cycles (Fig. 5f). However, Si-based ceramics are not suitable for ablative coating systems because of their low melting points. Introduction of UHTCs like ZrC and HfC is also an efficient way to promote the resistance of C/C composites against ablation [76, 77]. For example, Li et al. [74] introduced SiC nanowires into the HfC coating with high melting point to further improve its ablation resistance. The thick HfO₂ layer on the SiC nanowire-reinforced HfC coating shows good adhesion to the inner coating (Fig. 5g). In addition, the results also suggest monolithic layer HfO₂ for application due to its stronger ablative protection effect.

6 UHTC Nanowire-Reinforced Ceramic Coatings on C/C Composites

6.1 HfC Nanowire-Reinforced Ceramic Coatings on C/C Composites

In comparison with SiCNWs, superior thermal stability at high temperatures and better mechanical performance are observed for HfCNWs, which are considered as an ideal reinforcing and toughening material for ceramic coatings on C/C substrates in ablation environments with ultra-high temperatures and strong erosion forces [78–80].

In previous works, a lot of attentions have been attracted to the fabrication of HfCNWs with techniques of CVD [81], precursor pyrolysis [82], carbon nanotube template [83], etc. Among the techniques, CVD is a widely used method to incorporate HfCNWs into ceramic coatings.

Ren and co-workers [84] fabricated HfCNWs modified HfC coating on the C/C substrate via CVD (Fig. 6a, b), and revealed that HfCNWs can alleviate the coating/substrate CTE mismatch by decreasing the CTE of HfC coating. Besides, after addition of HfCNWs, an increase in the bonding strength from 4 to 5.7 N at interface of the coating layer and the substrate was observed, which could be attributed to the pull-out and debonding effects of HfCNWs. It should also be mentioned that the HfCNWs toughened ceramic coating with low CTE and higher toughness could

effectively suppress coating cracking and therefore significantly improve the anti-ablation property of the HfC coating. In an ablation test with oxyacetylene flame and exposure time of 60 s, the HfC-coated C/C Composite with HfCNWs reinforcement shows a decrease of the mass ablation rate from original 0.44 mg/s to 0.26 mg/s.

HfCNWs are able to greatly reduce the size and number of microcracks, inhibit the microcrack propagation in multiphase or multilayer coatings, and prevent the delamination and debonding of outer coatings through toughening mechanisms such as HfCNWs pull-out, debonding, bridging and crack deflection [84, 85] (Fig. 6c-f). Therefore, the HfCNWs toughened coatings seem to have superior long-term resistance against isothermal oxidation and thermal shock. HfCNW-reinforced Si-Mo-Cr/SiC multilayer coating was fabricated with CVD and subsequent PC for C/C composite [85]. After introducing HfCNWs, the sample showed a mass loss decrease of 33.71% in thermal shock with 30 cycles at temperatures of 298–1773 K, and a

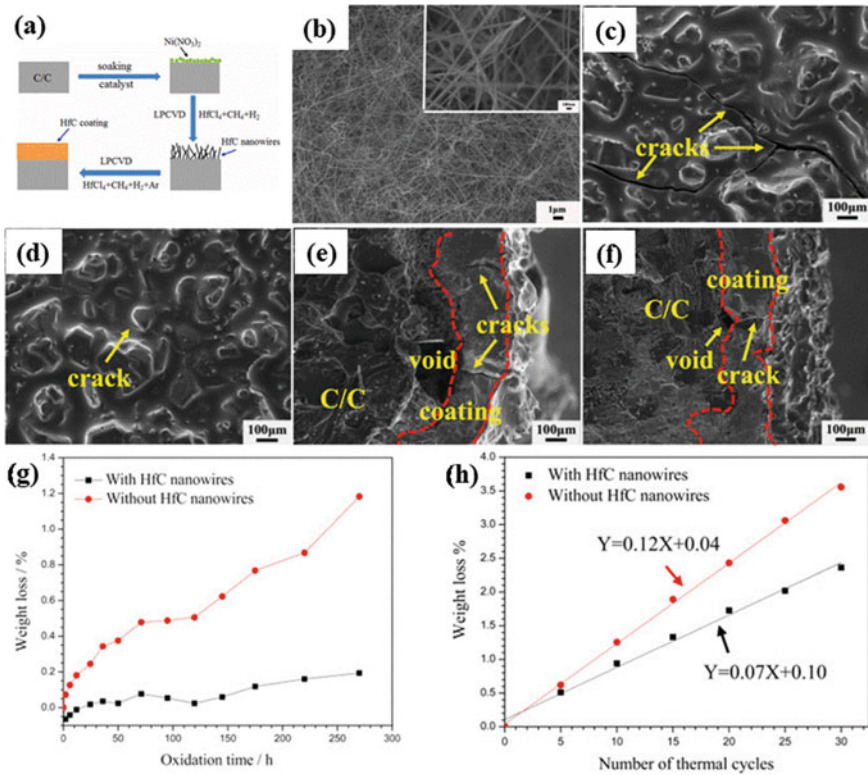


Fig. 6 a Schematic of the fabrication procedures of HfCNW-reinforced HfC coating for C/C composite; b SEM image of HfCNWs [84]. © 2018 Elsevier Ltd and Techna Group S.r.l. All rights reserved. SEM images of coating surface and cross-section after oxidation under 1773 K for 270 h: c, e in the absence of HfC nanowires; d, f in the presence of HfC nanowires; mass loss curves of coated C/C systems g in thermal shock under temperature of 298–1773 K, and h in isothermal oxidation in air at 1773 K [85]. © 2016 Elsevier Ltd and Techna Group S.r.l. All rights reserved

83.90% of mass loss rate decrease after 270 h of isothermal oxidation under 1773 K in air (Fig. 6g, h). Additionally, HfCNWs toughened multiphase and multilayer coatings prepared by combination of different techniques exhibited excellent ablation resistance under harsh conditions. HfCNWs toughened HfC/SiC [86] and ZrB₂-SiC/SiC coatings [87] were prepared on C/C samples through CVD, PC as well as supersonic atmosphere plasma spray (SAPS). After oxyacetylene flame ablation cycle of 60 s for 3 times, the mass ablation rate of HfC/SiC-coated C/C samples with HfCNWs addition decreased by 66.89% and 130.33%, respectively. While the corresponding value for ZrB₂-SiC/SiC-coated C/C samples with HfCNWs decreased by 160% after 90 s of oxyacetylene ablation.

6.2 ZrC Nanowire-Reinforced Ceramic Coatings for C/C Composites

In addition to HfCNWs, the ZrCNWs materials also have high melting points, superior mechanical properties and excellent thermal/chemical stability at elevated temperatures. Therefore, ZrCNWs are also promising reinforcement agents for applications in extremely harsh environments. Typically, ZrCNWs are synthesized by CVD, precursor pyrolysis [38, 88], carbothermal reduction [89], microwave hydrothermal processing [90], etc.

Regarding the application of ZrCNWs as reinforcement agents in ceramic coatings, Li and co-workers [91] synthesized ZrCNW-modified ZrC coatings on the C/C composite with a two-step CVD approach (Fig. 7a-d). The ZrC-coated C/C composites with the addition of ZrCNWs showed high interface bonding strength (Fig. 7e) and excellent ablation resistance with 81.96% and 1.08% of reduction in mass and linear ablation rates, respectively (Fig. 7f). Moreover, the coating with ZrCNWs incorporation shows an obviously greater enhancement in ablation resistance than the coating with SiCNWs addition, suggesting higher stability and compatibility of ZrCNW-reinforced ZrC coatings. After ZrCNWs introduction, ZrO₂ rod-like structures were formed, which could alleviate thermal stress concentrations at interface of the substrate and coating layer, suppress the propagation of cracks in coatings, and therefore improve the coating stability against ultra-high temperatures as well as the strong flame scouring during ablation (Fig. 7g-i).

7 Core-shell Structured Nanowire-Reinforced Ceramic Coatings for C/C Composites

Cheng and co-workers [92] reported that SiCNWs have a poor thermal stability at ultra-high temperatures, which restricts the applications of SiCNWs in ceramic coatings for oxidation and ablation resistances. The morphology stability of SiCNWs

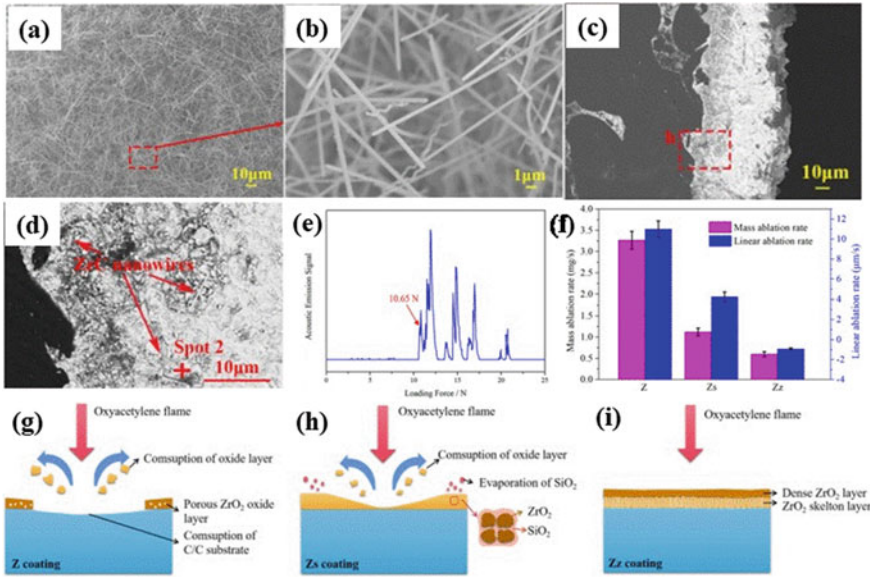


Fig. 7 a, b SEM image of ZrCNWs; c, d BSE images of ZrCNW-reinforced ZrC coating cross-section; e Bonding strength of ZrCNW-reinforced ZrC coating; f Mass and linear ablation rates of different samples. g–i Illustration diagram of ablation mechanism for different samples [91]. © 2022 Elsevier B.V. All rights reserved

could be improved by surface deposition of PyC. In this process, the PyC layer could consume the SiO₂ layer formed at SiCNWs surface and modify the SiCNWs bare surface by nucleation and growth of PyC on the surface. Therefore, the atomic glides of stacking faults (SFs) could be prevented with the high bonding strength in the thermal treatment process.

With inspiration from the above work, novel core–shell structured SiCNW@PyC nanowires were introduced into various ceramic coating layers, which could greatly enhance the ultra-high temperatures stability of SiCNWs, improve the binding force and diminish the thermal stress of ceramic coatings [93, 94]. The network of SiCNWs could be well maintained after PyC deposition and the obtained nanowires show a typical core–shell structure (Fig. 8a–c) [94]. The core–shell structured SiCNW@PyC nanowires can effectively lower the substrate/coating CTE mismatch, improving the interface bonding. Additionally, the increased interfaces in the ceramic coatings may cause multiple deflections of cracks and consume more energy, which are favorable for improving the mechanical property of the coatings. For example, Fu et al. applied core–shell SiCNW@PyC nanowires to reinforce the ZrB₂-SiC coating [93], ZrB₂-ZrC coating [73] and SiC coating [94], which were prepared by PC, SAPC and CVD methods, respectively. The resistances of ceramic coatings against oxidation, ablation and thermal shock could be enhanced simultaneously after the introduction of SiCNW@PyC nanowires.

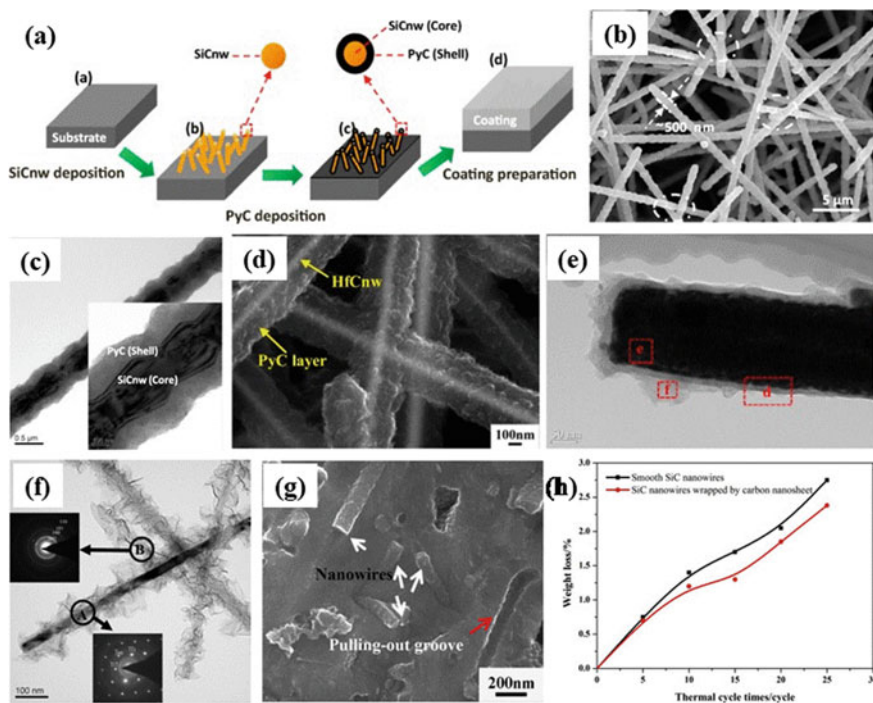


Fig. 8 a Schematic of ZrB₂-ZrC coating with SiCNWs/PyC on C/C-ZrB₂-ZrC-SiC substrate; **b** SEM and **c** TEM images of SiCNWs/PyC [94]. © 2018 Elsevier Ltd. All rights reserved. **d** SEM and **e** TEM images of HfCNWs/PyC [95]. © 2021 Elsevier Ltd. All rights reserved. **f** TEM image of CNSs-SiCNWs (inset: SAED pattern of A and B areas); **g** Fracture surface of SiC coating with SiC nanowires wrapped by CNSs; **h** Thermal cycling curves in temperature range of 298–1773 K [96]. © 2016 Elsevier B.V. All rights reserved

Based on the above strategy, PyC was also deposited onto HfCNWs surface to construct HfCNWs/PyC core-shell structured nanowires. Ren et al. used core-shell structured HfC/PyC nanowires to reinforce Hf_{1-x}Zr_xC coating for C/C composites through three-step CVD method (Fig. 8d, e) [95]. After the incorporation of HfCNWs/PyC, the crystal structure of Hf_{1-x}Zr_xC coating was changed from columnar to isometric phase. The PyC layer could reduce the coating hardness and the elastic modulus, and improve the fracture toughness and binding force of the coating. In comparison with HfCNWs, HfCNWs/PyC reinforced Hf_{1-x}Zr_xC coating exhibited improved anti-ablation capabilities with mass and linear ablation rates of 0.13 mg s⁻¹ and -0.46 μm s⁻¹, respectively, which can be attributed to the skeleton structure of HfO₂ nanowires formed during the ablation tests.

Porous carbon nanosheets (CNSs)-wrapped SiCNWs (CNSs-SiCNWs) could also be used to reinforce SiC coatings (Fig. 8f, g). The SiC coating toughness and resistance to thermal shock could be efficiently elevated via introduction of CNSs-SiCNWs, which exhibit crack pinning and deflection effects on the coating system. In

thermal shock tests with 23 cycles in temperature range of 298–1773 K, the mass loss of CNSs-SiCNWs reinforced sample was found to be 2.38%, while the corresponding value of smooth SiCNWs reinforced sample is much higher (13.45%) (Fig. 8h) [96].

With a layered structure, hexagonal boron nitride (BN) could also be used to adjust the binding force between SiCNWs and ceramic coatings. When compared with carbon-based shells, BN exhibits more pronounced thermal stability and resistance to oxidation at high temperatures. In recent work, Tong et al. prepared core-shell SiCNWs@BN nanowires modified HfC coating with a multi-step CVD method (Fig. 9a–c). In comparison with SiCNWs@PyC/HfC coating, the SiCNWs@BN/HfC coating showed a significantly improved ablation resistance and decreased mass and linear ablation rate. After the ablation tests, the whole SiCNWs@PyC/HfC structure was transformed into a loose layer of HfO₂ with a poor oxygen-blocking ability, whereas a compact film of HfO₂ was generated on the SiCNWs@BN/HfC coating, which could further protect the C/C composite from oxidation. Besides, with the introduction of BN, a Hf-Si-B-O type glass was formed, which exhibited a self-healing effect on defects (Fig. 9d, e) [97].

In addition to the single-layer shell, double-layer shell interface was also constructed on SiCNWs to optimize the properties of ceramic coatings. Double-layered PyC-SiC phase was prepared on the surface of SiCNWs by Tong et al. (Fig. 9f–h) [98]. It was interesting to find that the cracks in double-layer reinforced coating (SiCNWs@PyC-SiC/HfC) after impacting tests were obviously smaller than those of single-layer reinforced coating (SiCNWs@PyC/HfC). Furthermore, in ablation tests with oxyacetylene flame, the SiCNWs@PyC-SiC/HfC coating showed more superior anti-ablation properties than the SiCNWss@PyC/HfC coating. Due to the introduction of double-layer PyC-SiC interface, an increase of the interface number in the HfC coating is expected and two-grade pull-out of nanowires could occur during crack propagation, which would consume more energy, decrease the crack dimension and further enhance the anti-ablation ability of the coatings (Fig. 9i, j).

8 Multiple Nano/micro-materials Co-reinforced Ceramic Coatings for C/C Composites

Combining a variety of nano/micro-materials or to fabricate hierarchical structured nanomaterials as reinforcement agents for ceramic coating structures on the C/C substrates is theoretically a highly efficient strategy to intensively and extensively improve the coating properties, which can make the best use of the structural and mechanical advantages of the varied reinforcement materials.

Huo and co-workers [99] deposited nanostructured SiCNWs and CNTs hybrid material on the C/C composites surface by EPD (Fig. 10a), which were used to co-toughen SiC coatings by PC method. As shown in Fig. 10b and c, the co-deposited SiCNWs and CNTs formed an uniform 3D porous network on C/C composite surface,

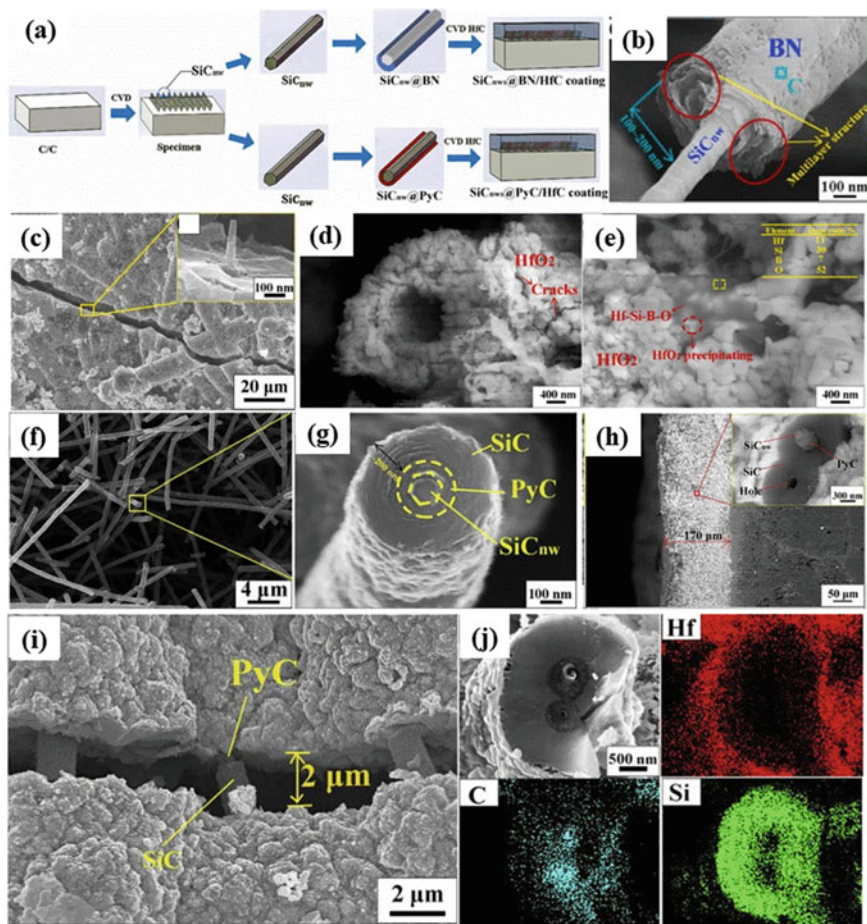


Fig. 9 a Illustration diagram of preparation procedure for SiCNWs@PyC/HfC coating and SiCNWs@BN/HfC coating; b SEM image of SiCNWs@BN structure; c SEM images of impacted SiCNWs@BN/HfC coating; SEM images of impacted-ablated d SiCNWs@PyC/HfC coating and e SiCNWs@BN/HfC coating on transitional ablation region [97]. © 2022 Elsevier Ltd. All rights reserved. f, g SEM images of SiCNWs@PyC-SiC; h Cross-section of SiCNWs@PyC-SiC reinforced coating; i SEM image and j EDS results of cracking area at coating surface after impact [98] © 2021 Elsevier Ltd. All rights reserved

which could effectively refine the SiC grains and simultaneously suppress crack deflection in coating layers. Due to the reinforcement effects of the hybrid nanomaterial, including crack deflection, bridging and pull-out, the reinforced SiC-coated C/C composites showed a weight loss of 1.08% after 100 h of oxidation test at 1773 K (Fig. 10d-f). This value is much lower than that of the sample without the hybrid material reinforcement. The improved resistance of SiC coatings against oxidation

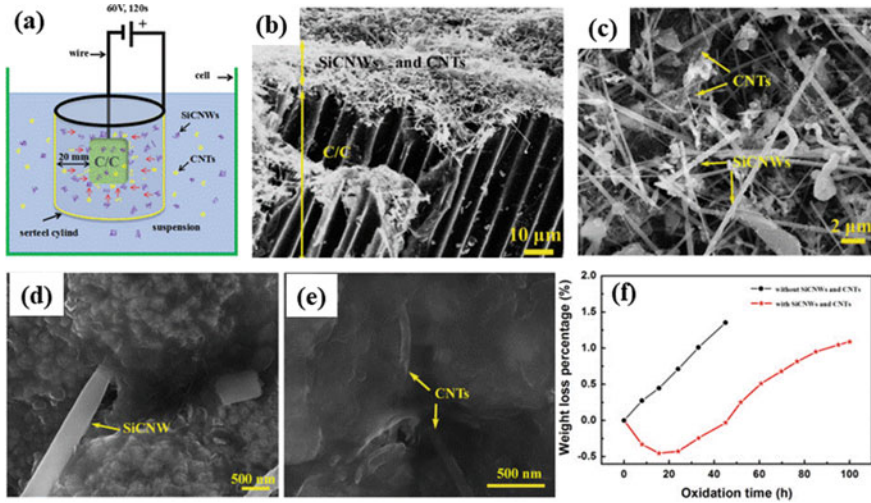


Fig. 10 a Illustration diagram for co-deposition of SiCNWs and CNTs on C/C composite in EPD cell; b, c SEM images of samples after co-deposition of SiCNWs and CNTs by EPD for 120 s; d, e Magnified SEM images of SiC coating with SiCNWs and CNTs; f Weight loss curves of SiC-coated C/C composite during exposure to the atmosphere [99]. © 2016 Elsevier Ltd and Techna Group S.r.l. All rights reserved

could be interpreted by the enhanced coating-substrate adhesion bonding and the formed continuous SiO₂ glass layer.

9 Summary

As mentioned in this review, 1D micro/nanomaterials have the advantages of high strength, nanometer scale, good structural stability and large aspect ratio, which could improve the bonding strength at interface of ceramic coating layers and C/C composite substrates, and enhance the ceramic coating toughness by crack deflection, bridging as well as pulling out effects. Therefore, introduction of 1D micro/nanomaterials is an efficient route to improve the anti-oxidation and anti-ablation property of ceramic coatings.

There still remain some challenges in reinforcement of ceramic coatings on C/C composite, which are summarized as follows. (1) The substrate/coating CET mismatch could lead to coating cracking and even coating failure. Although the cracking could be suppressed to some extent by introduction of 1D micro/nanomaterials, it is still unavoidable, especially in severe conditions, e.g., under thermal shock. (2) Ceramic coatings with capability for broad temperature range applications are required for C/C composites to achieve high performances. In laboratory conditions, the oxidation and ablation resistances of the coatings are

mostly tested at specific temperatures, which is difficult to meet the requirements for more severe and complex temperature environments. The application temperature range of ceramic coatings is generally very narrow, and the effect of 1D micro/nanomaterials on this aspect is limited. (3) In the published work and laboratory studies, C/C composites with small size and uniform shape are usually used. However, C/C composites in practical applications are mostly with large sizes and mixed shapes. The introduction of 1D micro/nanomaterials onto small and uniform C/C composites can be well controlled, but it is difficult to keep the homogeneity of 1D micro/nanomaterials on surface of large and special-shaped C/C composites, where aggregation of the micro/nanomaterials may also happen.

Some scope and future study directions are suggested as follows: (1) To meet the requirements of rapid developments in aerospace and aviation industries (e.g., rocket propulsion systems), further improvement in the binding force at interface of the ceramic coating layers and the C/C composite substrates is desired to prevent the coating layers from removal by strong gas or particle scouring at high temperatures. Combining computational techniques with experimental results can provide a deeper understanding on the reinforcement mechanism and effectively address the aforementioned issues. (2) Developing novel coatings, such as gradient coatings and alternative coatings, to broaden the application temperature range of ceramic coatings is a task for future studies. (3) Novel and suitable methods also need to be developed to realize the highly efficient and well controllable fabrication of 1D micro/nanomaterials and ceramic coatings on surfaces of C/C composites with large sizes and complex shapes.

Acknowledgements The authors are thankful for funding from the National Natural Science Foundation of China (52202047, 52293371), Natural Science Basic Research Plan in Shaanxi Province (2022JQ-324), China Postdoctoral Science Foundation (2021M702659) and Young Talent Fund of Association for Science and Technology in Shaanxi, China (20220435).

References

1. Prameela, S.E., Pollock, T.M., Raabe, D., Meyers, M.A., Aitkaliyeva, A., Chintersingh, K.L., Cordero, Z.C., Graham-Brady, L.: Materials for extreme environments. *Nat. Rev. Mater.* **8**, 81–88 (2023). <https://doi.org/10.1038/s41578-022-00496-z>
2. Padture, N.P.: Advanced structural ceramics in aerospace propulsion. *Nat. Mater.* **15**, 804–809 (2016). <https://doi.org/10.1038/nmat4687>
3. Zeng, Y., Wang, D.N., Xiong, X., Zhang, X., Withers, P.J., Sun, W., Smith, M., Bai, M., Xiao, P.: Ablation-resistant carbide $Zr_{0.8}Ti_{0.2}C_{0.74}B_{0.26}$ for oxidizing environments up to 3,000 °C, *Nat. Commun.* **8**, 15836 (2017). <https://doi.org/10.1038/ncomms15836>.
4. Centeno, A., Santamaría, R., Granda, M., Menéndez, R., Blanco, C.: Improvement of thermal conductivity in 2D carbon-carbon composites by doping with TiC nanoparticles. *Mater. Chem. Phys.* **122**, 102–107 (2010). <https://doi.org/10.1016/j.matchemphys.2010.02.072>
5. Yin, X.M., Han, L.Y., Liu, H.M., Li, N., Song, Q., Fu, Q.G., Zhang, Y.L., Li, H.J.: Recent progress in 1D nanostructures reinforced Carbon/Carbon composites. *Adv. Funct. Mater.* **32**, 2204965 (2022). <https://doi.org/10.1002/adfm.202204965>

6. He, Q.C., Li, H.J., Yin, X.M., Lu, J.H.: Effects of PyC shell thickness on the microstructure, ablation resistance of SiCnws/PyC-C/C-ZrC-SiC composites. *J. Mater. Sci. Technol.* **71**, 55–66 (2021). <https://doi.org/10.1016/j.jmst.2020.08.047>
7. He, Q.C., Li, H.J., Tan, Q., Lu, J.H., Yin, X.M.: Effects of ZrC particle size on ablation behavior of C/C-SiC-ZrC composites prepared by chemical liquid vapor deposition, *Corros. Sci.* **205** (2022). <https://doi.org/10.1016/j.corsci.2022.110469>
8. Kim, H.S., Kang, B.R., Choi, S.M.: Fabrication and characteristics of a HfC/TiC multilayer coating by a vacuum plasma spray process to protect C/C composites against oxidation. *Corros. Sci.* **178**, 109068 (2021). <https://doi.org/10.1016/j.corsci.2020.109068>
9. Kim, J.L., Kim, W.J., Choi, D.J., Park, J.Y., Ryu, W.S.: Design of a C/SiC functionally graded coating for the oxidation protection of C/C composites. *Carbon* **43**, 1749–1757 (2005). <https://doi.org/10.1016/j.carbon.2005.02.025>
10. Jin, X.C., Fan, X.L., Lu, C.S., Wang, T.J.: Advances in oxidation and ablation resistance of high and ultra-high temperature ceramics modified or coated carbon/carbon composites. *J. Eur. Ceram. Soc.* **38**, 1–28 (2018). <https://doi.org/10.1016/j.jeurceramsoc.2017.08.013>
11. Ni, D.W., Cheng, Y., Zhang, J.P., Liu, J.X., Zou, J., Chen, B.W., Wu, H.Y., Li, H.J., Dong, S.M., Han, J.C., Zhang, X.H., Fu, Q.G., Zhang, G.J.: Advances in ultra-high temperature ceramics, composites, and coatings. *J. Adv. Ceram.* **11**, 1–56 (2022). <https://doi.org/10.1007/s40145-021-0550-6>
12. Walker, L.S., Corral, E.L., Parthasar, T.: Self-generating high-temperature oxidation-resistant glass-ceramic coatings for C-C composites using UHTCs. *J. Am. Ceram. Soc.* **97**, 3004–3011 (2014). <https://doi.org/10.1111/jace.13017>
13. Fu, Q.G., Zhang, P., Zhuang, L., Zhou, L., Zhang, J.P., Wang, J., Hou, X.H., Riedel, R., Li, H.J.: Micro/nano multiscale reinforcing strategies toward extreme high-temperature applications: take carbon/carbon composites and their coatings as the examples. *J. Mater. Sci. Technol.* **96**, 31–68 (2022). <https://doi.org/10.1016/j.jmst.2021.03.076>
14. Ren, X.R., Li, H.J., Fu, Q.G., Chu, Y.H., Li, K.Z.: TaB₂-SiC-Si multiphase oxidation protective coating for SiC-coated carbon/carbon composites. *J. Eur. Ceram. Soc.* **33**, 2953–2959 (2013). <https://doi.org/10.1016/j.jeurceramsoc.2013.06.028>
15. Bezzi, F., Burgio, F., Fabbri, P., Grilli, S., Magnani, G., Salernitano, E., Scafè, M.: SiC/MoSi₂ based coatings for C_f/C composites by two step pack cementation. *J. Eur. Ceram. Soc.* **39**, 79–84 (2019). <https://doi.org/10.1016/j.jeurceramsoc.2018.01.024>
16. Zhuang, L., Fu, Q.G.: Bonding strength, thermal shock and oxidation resistance of interlocking (Zr, Hf)C-SiC/SiC double-layer coating for C/C composites. *Surf. Coat. Technol.* **315**, 436–442 (2017). <https://doi.org/10.1016/j.surfcoat.2017.02.072>
17. Zhang, Y.L., Fei, T., Zeng, W.Y., Yang, B.X., Li, H.J., Li, K.Z.: Microstructure and oxidation behavior of C/C-ZrB₂-SiC composites coated with SiC coating at high temperature. *Corros. Sci.* **100**, 421–427 (2015). <https://doi.org/10.1016/j.corsci.2015.08.015>
18. Li, H.J., Fu, Q.G., Shi, X.H., Li, K.Z., Hu, Z.B.: SiC whisker-toughened SiC oxidation protective coating for carbon/carbon composites. *Carbon* **44**, 602–605 (2006). <https://doi.org/10.1016/j.carbon.2005.09.026>
19. Wang, T.Y., Luo, R.Y.: Oxidation protection and mechanism of the HfB₂-SiC-Si/SiC coatings modified by in-situ strengthening of SiC whiskers for C/C composites. *Ceram. Int.* **44**, 12370–12380 (2018). <https://doi.org/10.1016/j.ceramint.2018.04.025>
20. Ren, J.C., Feng, E.R., Zhang, Y.L., Zhang, J., Li, L.: Microstructure and anti-ablation performance of HfC-TaC and HfC-ZrC coatings synthesized by CVD on C/C composites. *Ceram. Int.* **46**, 10147–10158 (2020). <https://doi.org/10.1016/j.ceramint.2020.01.006>
21. Zhang, J., Zhang, Y.L., Fu, Y.Q., Zhu, X.F., Chen, R.C.: Long-time ablation behavior of the multilayer alternating CVD-(SiC/HfC)₃ coating for carbon/carbon composites. *Corros. Sci.* **189**, 109586 (2021). <https://doi.org/10.1016/j.corsci.2021.109586>
22. Wei, L., Yang, X., Bi feng, Z., Song, W., Jun, L., Qing guo, L., Jun, Y.: Degradation of CVD-SiC coated C/SiC composites exposed to the monopropellant combustion products based on Hydroxylammonium nitrate (HAN), *Corros. Sci.* **74**, 149–153 (2013). <https://doi.org/10.1016/j.corsci.2013.04.036>

23. Ren, J.C., Duan, Y.T., Lv, C.F., Luo, J.Y., Zhang, Y.L., Fu, Y.Q.: Effects of HfC/PyC core-shell structure nanowires on the microstructure and mechanical properties of $\text{Hf}_{1-x}\text{Zr}_x\text{C}$ coating. *Ceram. Int.* **47**, 7853–7863 (2021). <https://doi.org/10.1016/j.ceramint.2020.11.132>
24. Zheng, G.B., Sano, H., Uchiyama, Y.: A carbon nanotube-enhanced SiC coating for the oxidation protection of C/C composite materials. *Compos. B Eng.* **42**, 2158–2162 (2011). <https://doi.org/10.1016/j.compositesb.2011.05.012>
25. Ma, C., Li, H., Wu, H., Fu, Q., Sun, C., Shi, X., Zhang, Y., Zhang, Z., Tao, J., Han, Z.: Mullite oxidation resistant coating for SiC-coated carbon/carbon composites by supersonic plasma spraying. *J. Mater. Sci. Technol.* **29**, 29–33 (2013). <https://doi.org/10.1016/j.jmst.2012.11.001>
26. Yao, D.J., Li, H.J., Wu, H., Fu, Q.G., Qiang, X.F.: Ablation resistance of ZrC/SiC gradient coating for SiC-coated carbon/carbon composites prepared by supersonic plasma spraying. *J. Eur. Ceram. Soc.* **36**, 3739–3746 (2016). <https://doi.org/10.1016/j.jeurceramsoc.2016.02.047>
27. Yoo, H.I., Kim, H.S., Hong, B.G., Sihn, I.C., Lim, K.H., Lim, B.J., Moon, S.Y.: Hafnium carbide protective layer coatings on carbon/carbon composites deposited with a vacuum plasma spray coating method. *J. Eur. Ceram. Soc.* **36**, 1581–1587 (2016). <https://doi.org/10.1016/j.jeurceramsoc.2016.01.032>
28. Feng, G.H., Li, H.J., Yao, X.Y., Zhou, H., Yu, Y.L., Lu, J.H.: Ablation resistance of HfC-TaC/HfC-SiC alternate coating for SiC-coated carbon/carbon composites under cyclic ablation. *J. Eur. Ceram. Soc.* **41**, 3207–3218 (2021). <https://doi.org/10.1016/j.jeurceramsoc.2021.01.050>
29. Feng, G.H., Li, H.J., Yao, X.Y., Yu, Y.L.: Investigation on the relationship between multi-layer architecture and ablation behavior using an oxyacetylene torch. *Corros. Sci.* **198**, 110104 (2022). <https://doi.org/10.1016/j.corsci.2022.110104>
30. Li, H., Zhang, Y.L., Fu, Q.G., Li, K.Z., Wei, J., Hou, D.S.: Oxidation behavior of SiC nanoparticle-SiC oxidation protective coating for carbon/carbon composites at 1773K. *Carbon* **45**, 2704–2707 (2007). <https://doi.org/10.1016/j.carbon.2007.08.013>
31. Zhang, Y.L., Li, H.J., Fu, Q.G., Li, K.Z.: High performance SiC oxidation protective coating with ZrO_2 particle dispersion for carbon/carbon composites. *Adv. Energy Mater.* **10**, 986–989 (2008). <https://doi.org/10.1002/adem.200800016>
32. Shen, Q.L., Li, H.J., Zhao, F.L., Song, Q., Fu, Q.G.: Electrophoretic deposition of carbon nanotubes for improved ablation resistance of carbon/carbon composites. *Corros. Sci.* **132**, 204–213 (2018). <https://doi.org/10.1016/j.corsci.2018.01.001>
33. Han, L.Y., Xiao, C.X., Song, Q., Yin, X.M., Li, W., Li, K.Z., Li, Y.Y.: Nano-interface effect of graphene on carbon nanotube reinforced carbon/carbon composites. *Carbon* **190**, 422–429 (2022). <https://doi.org/10.1016/j.carbon.2022.01.010>
34. Liu, H.M., Li, K.Z., Chen, H., Liu, B., Yin, X.M.: Facile growth of oriented SiC nanowires arrays on carbon fiber cloth via CVD. *Ceram. Int.* **48**, 34543–34549 (2022). <https://doi.org/10.1016/j.ceramint.2022.08.038>
35. Fu, Q.G., Tan, B.Y., Zhuang, L., Jing, J.Y.: Significant improvement of mechanical properties of carbon/carbon composites by in situ growth of SiC nanowires. *Mater. Sci. Eng. A* **672**, 121–128 (2016). <https://doi.org/10.1016/j.msea.2016.07.001>
36. Yin, X.M., Li, H.J., Han, L.Y., Meng, J.C., Lu, J.H., Song, Q.: All Si_3N_4 nanowires membrane based high-performance flexible solid-state asymmetric supercapacitor. *Small* **17**, 2008056 (2021). <https://doi.org/10.1002/sml.202008056>
37. Fu, Y.Q., Zhang, Y.L., Ren, J.C., Li, T., Wang, H.H.: Large-scale synthesis of hafnium carbide nanowires via a Ni-assisted polymer infiltration and pyrolysis. *J. Am. Ceram. Soc.* **102**, 2924–2931 (2019). <https://doi.org/10.1111/jace.16107>
38. Yan, N.N., Shi, X.H., Li, K., Fu, Q.G., Xie, W., Zhang, H.R., Song, Q.: In-situ homogeneous growth of ZrC nanowires on carbon cloth and their effects on flexural properties of carbon/carbon composites. *Compos. B Eng.* **154**, 200–208 (2018). <https://doi.org/10.1016/j.compositesb.2018.08.021>
39. Han, L.Y., Li, K.Z., Xiao, C.X., Yin, X.M., Gui, X.C., Song, Q., Ye, F.: Carbon nanotube-vertical edge rich graphene hybrid sponge as multifunctional reinforcements for high performance epoxy composites. *Carbon* **201**, 871–880 (2023). <https://doi.org/10.1016/j.carbon.2022.09.074>

40. Song, Q., Li, K.Z., Li, H.J., Fu, Q.G.: Increasing the tensile property of unidirectional carbon/carbon composites by grafting carbon nanotubes onto carbon fibers by electrophoretic deposition. *J. Mater. Sci. Technol.* **29**, 711–714 (2013). <https://doi.org/10.1016/j.jmst.2013.05.015>
41. Zheng, G.B., Mizuki, H., Sano, H., Uchiyama, Y.: CNT-PyC-SiC/SiC double-layer oxidation-protection coating on C/C composite. *Carbon* **46**, 1808–1811 (2008). <https://doi.org/10.1016/j.carbon.2008.07.014>
42. Fu, Q.G., Zhuang, L., Li, H.J., Feng, L., Jing, J.Y., Tan, B.Y.: Effect of carbon nanotubes on the toughness, bonding strength and thermal shock resistance of SiC coating for C/C-ZrC-SiC composites. *J. Alloys Compd.* **645**, 206–212 (2015). <https://doi.org/10.1016/j.jallcom.2015.04.223>
43. Fu, Q.G., Zhuang, L., Ren, Q.W., Feng, L., Li, H.J., Guo, Y.A.: Carbon nanotube-toughened interlocking buffer layer to improve the adhesion strength and thermal shock resistance of SiC coating for C/C-ZrC-SiC composites. *J. Materiomics.* **1**, 245–252 (2015). <https://doi.org/10.1016/j.jmat.2015.07.006>
44. Feng, L., Li, K.Z., Si, Z.S., Li, H.J., Song, Q., Shan, Y.C., Wen, S.: Microstructure and thermal shock resistance of SiC/CNT-SiC double-layer coating for carbon/carbon composites. *Ceram. Int.* **40**, 13683–13689 (2014). <https://doi.org/10.1016/j.ceramint.2014.04.127>
45. Li, S., Zhang, Y.M., Han, J.C., Zhou, Y.F.: Fabrication and characterization of SiC whisker reinforced reaction bonded SiC composite. *Ceram. Int.* **39**, 449–455 (2013). <https://doi.org/10.1016/j.ceramint.2012.06.047>
46. Garnier, V., Fantozzi, G., Nguyen, D., Dubois, J., Thollet, G.: Influence of SiC whisker morphology and nature of SiC/Al₂O₃ interface on thermomechanical properties of SiC reinforced Al₂O₃ composites. *J. Eur. Ceram. Soc.* **25**, 3485–3493 (2005). <https://doi.org/10.1016/j.jeurceramsoc.2004.09.026>
47. Campbell, G.H., Ruhle, M., Dalgleish, B.J., Evans, A.G.: Whisker toughening: a comparison between aluminum oxide and silicon nitride toughened with silicon carbide. *J. Am. Ceram. Soc.* **73**, 521–530 (1990). <https://doi.org/10.1111/j.1151-2916.1990.tb06548.x>
48. Xu, Z.J., Chi, W.D., Liu, H., Yu, J.M., Yang, X.K.: Oxidation protective coating on carbon/carbon composite prepared by two-step processes of pack cementation and sol-gel. *Hot Working Technol.* **41**, 107–110 (2012)
49. Du, B., Hong, C.Q., Zhou, S.B., Liu, C., Zhang, X.H.: Multi-composition coating for oxidation protection of modified carbon-bonded carbon fiber composites. *J. Eur. Ceram. Soc.* **36**, 3303–3310 (2016). <https://doi.org/10.1016/j.jeurceramsoc.2016.05.028>
50. Fu, Q.G., Li, H.J., Li, K.Z., Shi, X.H., Huang, M., Sun, G.D.: Effect of SiC whiskers on the microstructure and oxidation protective ability of SiC-CrSi₂ coating for carbon/carbon composites. *Mater. Sci. Eng. A* **445**, 386–391 (2007). <https://doi.org/10.1016/j.msea.2006.09.067>
51. Wen, Z.L., Xiao, P., Li, Z., Yu, X.Y., Li, Y.: Thermal cycling behavior and oxidation resistance of SiC whisker-toughened-mullite/SiC coated carbon/carbon composites in burner rig tests. *Corros. Sci.* **106**, 179–187 (2016). <https://doi.org/10.1016/j.corsci.2016.02.003>
52. Wang, P., Wei, F.C., Zhang, H.B., Yin, J., Hao, Z.H., Zhou, J.W.: Effect of SiC whiskers on the mechanical and ablation performances of Cu modified C/C composite. *Ceram. Int.* **48**, 5369–5376 (2022). <https://doi.org/10.1016/j.ceramint.2021.11.080>
53. Fu, Q.G., Li, H.J., Shi, X.H., Li, K.Z., Zhang, W., Huang, M.: A SiC whisker-toughened SiC-CrSi₂ oxidation protective coating for carbon/carbon composites. *Appl. Surf. Sci.* **253**, 3757–3760 (2007). <https://doi.org/10.1016/j.apsusc.2006.07.092>
54. Fu, Q.G., Li, H.J., Li, K.Z., Shi, X.H., Hu, Z.B., Huang, M.: SiC whisker-toughened MoSi₂-SiC-Si coating to protect carbon/carbon composites against oxidation. *Carbon* **44**, 1866–1869 (2006). <https://doi.org/10.1016/j.carbon.2006.03.002>
55. Pu, D.M., Chen, P.J., Xiao, P., Li, Z., Deng, P.Y., Pang, L., Li, J.W., Li, Y.: Oxidation and thermal cycling behavior of c-AlPO₄ and SiC whisker co-modified mullite deposited on SiC-C/SiC composites. *Surf. Coat. Technol.* **400** (2020). <https://doi.org/10.1016/j.surfcoat.2020.126201>

56. Xie, C., Song, S.L., He, G.Z., Mao, Z.H., Ma, C.C., Zhang, T., Hu, P.F., Zhen, Q.: The toughening design of multi-layer antioxidation coating on C/C matrix via SiC-SiCw transition layer grown in-situ. *J. Eur. Ceram. Soc.* **42**, 43–51 (2022). <https://doi.org/10.1016/j.jeurceramsoc.2021.09.043>
57. Kowbel, W., Bruce, C., Withers, J.C., Ransone, P.O.: Effect of carbon fabric whiskerization on mechanical properties of C-C composites, *Composites, Part A*. **28**, 993–1000 (1997). [https://doi.org/10.1016/S1359-835X\(97\)00007-9](https://doi.org/10.1016/S1359-835X(97)00007-9)
58. Chu, Y.H., Fu, Q.G., Li, H.J., Shi, X.H., Li, K.Z., Wen, X., Shang, G.N.: Effect of SiC nanowires on the mechanical and oxidation protective ability of SiC coating for C/C composites. *J. Am. Ceram. Soc.* **95**, 739–745 (2012). <https://doi.org/10.1111/j.1551-2916.2011.04979.x>
59. Ye, H.H., Titchenal, N., Gogotsi, Y., Ko, F.: SiC nanowires synthesized from electrospun nanofiber templates. *Adv. Mater.* **17**, 1531–1535 (2005). <https://doi.org/10.1002/adma.200500094>
60. Chu, Y.H., Li, H.J., Fu, Q.G., Qi, L.H., Zou, X.: Toughening by SiC nanowires in a dense SiC-Si ceramic coating for oxidation protection of C/C composites. *J. Am. Ceram. Soc.* **95**, 3691–3697 (2012). <https://doi.org/10.1111/j.1551-2916.2012.05412.x>
61. Fu, Q.G., Nan, X.Y., Chen, X., Wang, W.L., Li, H.J., Li, Y.Y., Jia, L.T.: Electrophoretic deposition of SiC nanowires onto carbon/carbon composites to improve the interface bonding of Ti-Ni-Si joint. *Mater. Des.* **80**, 137–143 (2015). <https://doi.org/10.1016/j.matdes.2015.04.042>
62. Li, T., Zhang, Y.L., Sun, J., Ren, J.C., Zhang, P.F., Fu, Y.Q., Wang, H.H., Zhang, L.L.: In situ synthesis of SiC nanowire porous layer on carbon/carbon composites. *J. Am. Ceram. Soc.* **101**, 1371–1380 (2018). <https://doi.org/10.1111/jace.15296>
63. Huang, J.F., Zhou, L., Cao, L.Y., Ouyang, H.B., Hao, W., Li, C.Y., Fei, J.: Effect of the incorporation of SiC nanowire on mullite/SiC protective coating for carbon/carbon composites. *Corros. Sci.* **107**, 85–95 (2016). <https://doi.org/10.1016/j.corsci.2016.02.022>
64. Tian, X.F., Li, H.J., Shi, X.H., Lin, H.J., Yan, N.N., Feng, T.: Morphologies evolution and mechanical behaviors of SiC nanowires reinforced C/(PyC-SiC)_n multilayered matrix composites. *J. Mater. Sci. Technol.* **96**, 190–198 (2022). <https://doi.org/10.1016/j.jmst.2021.05.004>
65. Qiang, X.F., Li, H.J., Zhang, Y.L., Wang, Z.Z., Ba, Z.X., Zhang, X.B.: Mechanical and oxidation protective properties of SiC nanowires-toughened SiC coating prepared in-situ by a CVD process on C/C composites. *Surf. Coat. Technol.* **307**, 91–98 (2016). <https://doi.org/10.1016/j.surfcoat.2016.08.072>
66. Chu, Y.H., Li, H.J., Fu, Q.G., Qi, L.H., Wei, B.B.: Oxidation protection of SiC-coated C/C composites by SiC nanowire-toughened CrSi₂-SiC-Si coating. *Corros. Sci.* **55**, 394–400 (2012). <https://doi.org/10.1016/j.corsci.2011.11.001>
67. Fu, Q.G., Li, H.J., Zhang, Z.Z., Zeng, X.R., Li, K.Z.: SiC nanowire-toughened MoSi₂-SiC coating to protect carbon/carbon composites against oxidation. *Corros. Sci.* **52**, 1879–1882 (2010). <https://doi.org/10.1016/j.corsci.2010.01.031>
68. Hui, C.Y., Gang, F.Q., Wei, C.C., Jun, L.H., Zhi, L.K., Qin, L.: SiC nanowire-toughened SiC-MoSi₂-CrSi₂ oxidation protective coating for carbon/carbon composites. *Surf. Coat. Technol.* **205**, 413–418 (2010). <https://doi.org/10.1016/j.surfcoat.2010.07.001>
69. Li, H.J., Yang, X., Chu, Y.H., Li, L., Fu, Q.G., Qi, L.H.: Oxidation protection of C/C composites with in situ bamboo-shaped SiC nanowire-toughened Si-Cr coating. *Corros. Sci.* **74**, 419–423 (2013). <https://doi.org/10.1016/j.corsci.2013.05.006>
70. Chu, Y.H., Li, H.J., Luo, H.J., Li, L., Qi, L.H.: Oxidation protection of carbon/carbon composites by a novel SiC nanoribbon-reinforced SiC-Si ceramic coating. *Corros. Sci.* **92**, 272–279 (2015). <https://doi.org/10.1016/j.corsci.2014.12.013>
71. Chu, Y.H., Li, H.J., Li, L., Qi, L.H.: Oxidation protection of C/C composites by ultra long SiC nanowire-reinforced SiC-Si coating. *Corros. Sci.* **84**, 204–208 (2014). <https://doi.org/10.1016/j.corsci.2014.03.029>
72. Chu, Y.H., Li, H.J., Fu, Q.G., Qi, L.H., Li, L.: Bamboo-shaped SiC nanowire-toughened SiC coating for oxidation protection of C/C composites. *Corros. Sci.* **70**, 11–16 (2013). <https://doi.org/10.1016/j.corsci.2012.12.009>

73. Zhuang, L., Fu, Q.G., Li, H.J.: SiCnw/PyC core-shell networks to improve the bonding strength and oxyacetylene ablation resistance of ZrB₂-ZrC coating for C/C-ZrB₂-ZrC-SiC composites. *Carbon* **124**, 675–684 (2017). <https://doi.org/10.1016/j.carbon.2017.09.019>
74. Li, H.J., Wang, Y.J., Fu, Q.G., Chu, Y.H.: SiC nanowires toughened HfC ablative coating for C/C composites. *J. Mater. Sci. Technol.* **31**, 70–76 (2015). <https://doi.org/10.1016/j.jmst.2014.03.024>
75. Fu, Q.G., Jing, J.Y., Tan, B.Y., Yuan, R.M., Zhuang, L., Li, L.: Nanowire-toughened transition layer to improve the oxidation resistance of SiC-MoSi₂-ZrB₂ coating for C/C composites. *Corros. Sci.* **111**, 259–266 (2016). <https://doi.org/10.1016/j.corsci.2016.05.013>
76. Zhuang, L., Fu, Q.G., Tan, B.Y., Guo, Y.A., Ren, Q.W., Li, H.J., Li, B., Zhang, J.P.: Ablation behaviour of C/C and C/C-ZrC-SiC composites with cone-shaped holes under an oxyacetylene flame. *Corros. Sci.* **102**, 84–92 (2016). <https://doi.org/10.1016/j.corsci.2015.09.022>
77. Tian, X.F., Shi, X.H., Yang, L., Li, H.J., Lin, H.J.: Preparation and ablation properties of SiC nanowire-reinforced ZrC-SiC coating-matrix integrated C/C composites. *Ceram. Int.* **47**, 31251–31258 (2021). <https://doi.org/10.1016/j.ceramint.2021.07.301>
78. Fu, Y.Q., Zhang, Y.L., Yin, X.M., Han, L.Y., Fu, Q.G., Li, H.J.: Two birds with one stone: Simultaneous fabrication of HfC nanowires and CNTs through efficient utilization of polymer-derived ceramics. *J. Mater. Sci. Technol.* **129**, 163–172 (2022). <https://doi.org/10.1016/j.jmst.2022.04.037>
79. Fu, Y.Q., Zhang, Y.L., Chen, H., Yin, X.M., Zhang, J., Sun, J., Fu, Q.G.: Ultra-high temperature resistance of one-dimensional hafnium carbide wrapped with pyrolytic carbon up to 2450 °C. *Corros. Sci.* **195**, 110015 (2022). <https://doi.org/10.1016/j.corsci.2021.110015>
80. Fu, Y.Q., Zhang, Y.L., Chen, H., Han, L.Y., Yin, X.M., Fu, Q.G., Sun, J.: Ultra-high temperature performance of carbon fiber composite reinforced by HfC nanowires: a promising lightweight composites for aerospace engineering. *Compos. B Eng.* **250**, 110453 (2023). <https://doi.org/10.1016/j.compositesb.2022.110453>
81. Yin, X.M., Li, H.J., Fu, Y.Q., Yuan, R.M., Lu, J.H.: Hierarchical core-shell structure of NiCo₂O₄ nanosheets@HfC nanowires networks for high performance flexible solid-state hybrid supercapacitor. *Chem. Eng. J.* **392**, 124820 (2020). <https://doi.org/10.1016/j.cej.2020.124820>
82. Fu, Y.Q., Zhang, Y.L., Yin, X.M., Li, T., Zhang, J.: Awl-like HfC nanowires grown on carbon cloth via Fe-catalyzed in a polymer pyrolysis route. *J. Am. Ceram. Soc.* **103**, 3458–3465 (2020). <https://doi.org/10.1111/jace.17073>
83. Mu, J.R., Shi, X.H., Zhang, H.R., Yang, L., Han, X.: Microstructures and enhanced flexural properties of single-crystalline HfC nanowires in-situ modified carbon/carbon composites by electrophoresis-thermal evaporation using CNTs as the template. *Ceram. Int.* **47**, 3063–3069 (2021). <https://doi.org/10.1016/j.ceramint.2020.09.142>
84. Ren, J.C., Zhang, Y.L., Fu, Y.Q., Zhang, J.: Influence of HfC nanowires on the growth behavior, microstructure and ablation resistance of CVD-HfC coating. *Ceram. Int.* **45**, 5321–5331 (2019). <https://doi.org/10.1016/j.ceramint.2018.11.230>
85. Ren, J.C., Zhang, Y.L., Hu, H., Zhang, P.F., Fei, T., Zhang, L.L.: HfC nanowires to improve the toughness and oxidation resistance of Si-Mo-Cr/SiC coating for C/C composites. *Ceram. Int.* **42**, 14518–14525 (2016). <https://doi.org/10.1016/j.ceramint.2016.06.064>
86. Ren, J.C., Zhang, Y.L., Zhang, P.F., Li, T., Li, J.H., Yang, Y.: Ablation resistance of HfC coating reinforced by HfC nanowires in cyclic ablation environment. *J. Eur. Ceram. Soc.* **37**, 2759–2768 (2017). <https://doi.org/10.1016/j.jeurceramsoc.2017.02.057>
87. Ren, J.C., Zhang, Y.L., Zhang, P.F., Li, T., Hu, H.: UHTC coating reinforced by HfC nanowires against ablation for C/C composites. *Surf. Coat. Technol.* **311**, 191–198 (2017). <https://doi.org/10.1016/j.surfcoat.2017.01.014>
88. Kim, J.G., Park, S.J., Park, J.Y., Choi, D.J.: The effect of temperature on the growth and properties of chemical vapor deposited ZrC films on SiC-coated graphite substrates. *Ceram. Int.* **41**, 211–216 (2015). <https://doi.org/10.1016/j.ceramint.2014.08.060>
89. Xu, L., Huang, C.Z., Liu, H.L., Zou, B., Zhu, H.T., Zhao, G.L., Wang, J.: Study on the synthesis and growth mechanisms of the refractory ZrC whiskers. *Int. J. Refract. Met. Hard Mater.* **42**, 116–119 (2014). <https://doi.org/10.1016/j.ijrmhm.2013.08.011>

90. Li, K.Z., Zhou, X., Zhao, Z.G., Chen, C.Y., Wang, C.C., Ren, B.Y., Zhang, L.L.: Synthesis of zirconium carbide whiskers by a combination of microwave hydrothermal and carbothermal reduction. *J. Solid State Chem.* **258**, 383–390 (2018). <https://doi.org/10.1016/j.jssc.2017.11.002>
91. Li, B., Li, H.J., Yao, X.Y., Zhu, X.F., Liu, N.K.: Preparation and ablation resistance of ZrC nanowires-reinforced CVD-ZrC coating on sharp leading edge C/C composites. *Appl. Surf. Sci.* **584**, 152617 (2022). <https://doi.org/10.1016/j.apsusc.2022.152617>
92. Cheng, C.Y., Li, H.J., Fu, Q.G., Li, L., Guo, L.P., Yin, X.M., Tian, X.F.: Effects of pyrocarbon on morphology stability of SiC nanowires at high temperatures. *J. Am. Ceram. Soc.* **101**, 3694–3702 (2018). <https://doi.org/10.1111/jace.15524>
93. Cheng, C.Y., Li, H.J., Fu, Q.G., Guo, L.P.: A SiCnw/PyC-toughened ZrB₂-SiC coating for protecting Si-SiC coated C/C composites against oxidation. *Appl. Surf. Sci.* **457**, 360–366 (2018). <https://doi.org/10.1016/j.apsusc.2018.06.246>
94. Zhuang, L., Fu, Q.G., Yu, X.: Improved thermal shock resistance of SiCnw/PyC core-shell structure toughened CVD-SiC coating. *J. Eur. Ceram. Soc.* **38**, 2808–2814 (2018). <https://doi.org/10.1016/j.jeurceramsoc.2018.02.017>
95. Ren, J.C., Lv, C.F., Duan, Y.T., Zhang, Y.L., Zhang, J.: Microstructure and ablation performance of HfC/PyC core-shell structure nanowire-reinforced Hf_{1-x}Zr_xC coating. *J. Eur. Ceram. Soc.* **41**, 7450–7463 (2021). <https://doi.org/10.1016/j.jeurceramsoc.2021.08.036>
96. Qiang, X.F., Li, H.J., Zhang, Y.L., Wang, Z.Z., Ba, Z.X.: Synthesis and toughening effect of SiC nanowires wrapped by carbon nanosheet on C/C composites. *J. Alloys Compd.* **676**, 245–250 (2016). <https://doi.org/10.1016/j.jallcom.2016.03.197>
97. Tong, M.D., Ding, J.H., Li, N., Feng, T., Fu, Q.G.: Effect of SiCnws@BN core shell upon impact-ablation performance of HfC coating on C/C composites. *Corros. Sci.* **209**, 110707 (2022). <https://doi.org/10.1016/j.corsci.2022.110707>
98. Tong, M.D., Fu, Q.G., Liang, M.Y., Feng, T., Hou, W.B., Sun, J., Shi, X.H.: Effect of PyC-SiC double-layer interface on ablation behaviour of impacted CVD-SiCnws/HfC coating. *Corros. Sci.* **191**, 109741 (2021). <https://doi.org/10.1016/j.corsci.2021.109741>
99. Huo, C.X., Guo, L.J., Li, Y.Y., Wang, C.C., Feng, L., Liu, N.K., Zhang, Y.L., Dong, K.Y., Song, Q.: Effect of co-deposited SiC nanowires and carbon nanotubes on oxidation resistance for SiC-coated C/C composites. *Ceram. Int.* **43**, 1722–1730 (2017). <https://doi.org/10.1016/j.ceramint.2016.08.196>

Oxidation and Thermal Cycle Behavior of $\text{Yb}_2\text{Si}_2\text{O}_7$ -*c*- AlPO_4 - SiC_w -Mullite Multilayer Coatings



Pengju Chen, Peng Xiao, and Yang Li

Abstract The mullite ceramic coating has excellent oxidation resistance in static environments, but it is easy to generate micro-cracks during the thermal cycling process due to the low toughness. Therefore, a novel cristobalite aluminum phosphate particle (*c*- AlPO_4) and SiC whisker toughened mullite middle coating (*c*- AlPO_4 - SiC_w -mullite, ASM) were prepared on the SiC coated carbon fiber reinforced SiC composites (C/SiC) by a novel sol–gel combined with air spraying method. Meanwhile, the ytterbium disilicate ($\text{Yb}_2\text{Si}_2\text{O}_7$) top coating was prepared on the surface of the ASM middle coating to avoid excessive oxidation of SiC whiskers (Fig. 1). Results show that the bi-layer ASM/SiC coating with 20 wt.% of *c*- AlPO_4 showed the most excellent oxidation resistance, the weight loss rate after the oxidation in ambient air for 210 h at 1773 K was merely $3.00 \times 10^{-5} \text{ g cm}^{-2} \text{ h}^{-1}$. After 16 thermal cycles (240 min) between 1773 K and room temperature in burner rig tests, the weight loss of mullite/SiC coating coated samples was up to $38.49 \times 10^{-3} \text{ g cm}^{-2}$, while the weight losses of SM/SiC and ASM/SiC coatings coated samples were reduced to $14.09 \times 10^{-3} \text{ g cm}^{-2}$ and $5.59 \times 10^{-3} \text{ g cm}^{-2}$, respectively. However, although *c*- AlPO_4 particles further improved the service life of SM coating in high-temperature environment, the overflow of PO_x gas aggravated the formation and expansion of cracks in the $\text{Yb}_2\text{Si}_2\text{O}_7$ outer coating and caused the service life of overall $\text{Yb}_2\text{Si}_2\text{O}_7$ /ASM/SiC coating to be slightly lower than that of $\text{Yb}_2\text{Si}_2\text{O}_7$ /SM/SiC coating. This study guides the design of modified bi-layer and tri-layer EBCs with long service life in high-temperature and complex environments.

Keywords $\text{Yb}_2\text{Si}_2\text{O}_7$ · SiC whisker · *c*- AlPO_4 particle · EBC coatings · Oxidation behavior

P. Chen

School of Nuclear Science and Technology, University of South China, Hengyang 421001, China

P. Xiao · Y. Li (✉)

National Key Laboratory of Science and Technology on High-strength Structural Materials, Central South University, Changsha 410083, China

e-mail: liyong16@csu.edu.cn

© The Author(s), under exclusive license to Springer Nature Switzerland AG 2024

339

A. Pakseresht and K. K. Amirtharaj Mosas (eds.), *Ceramic Coatings*

for *High-Temperature Environments*, Engineering Materials,

https://doi.org/10.1007/978-3-031-40809-0_11

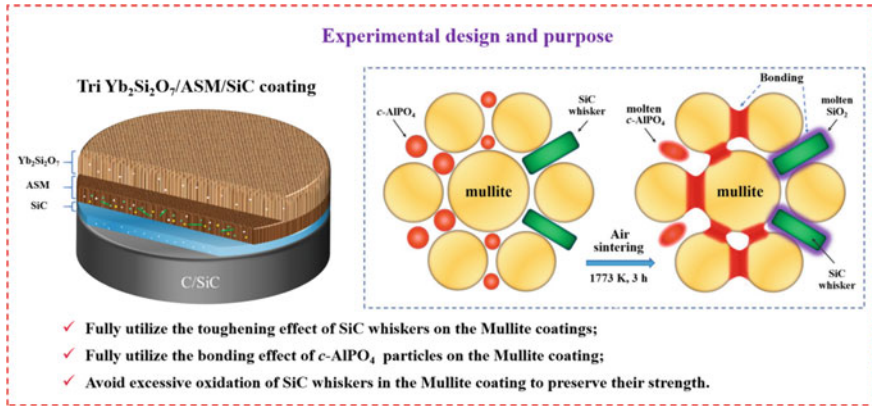


Fig. 1 The design and purpose of preparing the tri-layer $\text{Yb}_2\text{Si}_2\text{O}_7/\text{ASM}/\text{SiC}$ coating on the C/SiC composites in this experiment

1 Introduction

Silicon carbide ceramics (SiC) and their composite materials (SiC_f/SiC , C_f/SiC , etc.) have received high attention due to their good ablation thermal shock resistance, high-temperature strength and modulus, low density, and excellent mechanical properties [1–5]. Among them, carbon fiber reinforced silicon carbide ceramic matrix composite (C_f/SiC) has the highest specific strength and higher working temperature and is considered as candidates materials for high-temperature applications (gas turbine, rocket nozzles, nuclear industry, heat-exchanger parts, etc.) [6–9]. However, the gradual oxidation of carbon fibers or matrix may reduce the mechanical properties of C/SiC composites (≥ 723 K), this limits its application in high-temperature oxygen-containing environments [10–12]. Therefore, it is necessary to modify the composite matrix or prepare environmental barrier coatings (EBCs) on the surface of the composites matrix to improve its performance and service life in high-temperature extreme environments [13–18].

In the past decades, a number of bi-layer and tri-layer EBCs systems, especially the silicide and silicon oxide coatings system have been explored to improve the isothermal oxidation and thermal shock resistance for SiC-ceramic matrix composites. In general, the EBCs systems have experienced several generations of development, and the service performance of tri-layer EBCs is better than bi-layer EBCs in high-temperature extreme environment because each layer of the tri-layer EBCs can exert its unique performance [19]. The first generation of EBCs is the YSZ (Ytria-stabilized zirconia)/Mullite system, which improves the corrosion resistance of single-layer mullite coating in steam corrosion environment. However, the coefficient of thermal expansion (CTE) of YSZ is almost twice that of mullite and SiC ceramics, resulting in cracks, delamination and even spalling during the thermal cycling process [19–23]. To improve crack resistance, the YSZ top coating is replaced

by BSAS ($\text{BaO}_{1-x}\text{-SrO}_x\text{-Al}_2\text{O}_3\text{-2SiO}_2$, $0 \leq x \leq 1$). Meanwhile, in the second generation of EBCs, a Si bonding layer is prepared between the mullite coating and the SiC matrix to improve the bonding strength between the EBCs and the SiC matrix [19]. However, while improving crack resistance, the durability of the second generation EBCs still exists and limits the service temperature and life of the EBCs [24, 25]. The evaporation rate of the BSAS top coating is relatively high under the condition of high-speed gas washing, and the reaction between BSAS and silica forms a glass phase with a low melting point (~ 1573 K), resulting in a long-term service temperature should not exceed 1573 K.

Rare-earth silicate ceramics (Re = Yb, Er, Lu, etc.) have attracted extensive attention due to their low volatility in high-temperature steam corrosion environments, which is considered an excellent top coating for the third generation of EBCs [26–29]. Rare-earth silicate ceramics are divided into disilicate ($\text{RE}_2\text{Si}_2\text{O}_7$) and monosilicate (RE_2SiO_5). Therein, RE_2SiO_5 has better phase stability than $\text{RE}_2\text{Si}_2\text{O}_7$ in high-temperature steam corrosion environment, but the higher CTE of RE_2SiO_5 ($6.0\text{--}10.0 \times 10^{-6}/\text{K}$) limits its long-life applications [30–32]. However, $\text{RE}_2\text{Si}_2\text{O}_7$ ceramic has a similar CTE to SiC-ceramic matrix composites (CMCs), so researchers have gradually shifted their focus to $\text{RE}_2\text{Si}_2\text{O}_7$ ceramic. At the same time, both the experimental results and theoretical calculations show that the $\text{Yb}_2\text{Si}_2\text{O}_7$ ceramic has the best stability in the steam corrosion environment [33, 34]. Among them, the $\text{Yb}_2\text{Si}_2\text{O}_7$ ceramic is selected as the top coating for EBCs due to it exists only a single β phase at high temperatures and the CTE ($4.1 \times 10^{-6}/\text{K}$) is similar to SiC ($4.3\text{--}5.4 \times 10^{-6}/\text{K}$) and mullite ($5.0\text{--}6.0 \times 10^{-6}/\text{K}$) ceramics [35–38].

Up to now, atmospheric plasma spraying (APS) and electron beam physical vapor deposition (EB-PVD) are two commonly used methods for preparing EBCs on the surface of composites [39, 40]. Moreover, many other methods have been developed to prepare EBCs, for example, chemical vapor deposition (CVD), sol–gel methods, electrophoretic deposition, etc. [41–44]. However, due to the uneven thickness and easy cracking of the coating prepared by sol–gel method, the complex preparation process of CVD method and electrophoretic deposition method are mainly used for the preparation of small samples in the laboratory, so that the above methods are limited in the preparation and application of EBCs. Our previous research shows that the combination of sol–gel method and air spraying process has high efficiency in preparation and a simple preparation process, which can meet the consistency requirements for EBCs preparing uniform and large and complex parts [36–38].

Currently, EBCs is mainly tested in static air and water vapor environment. However, the static environment corrosion behavior can only reflect the phase stability between individual EBCs. It is difficult to reflect the long-life reliability and stability of the EBCs in practical work. Therefore, it is necessary to conduct an appropriate evaluation of the long-term stability and reliability of the EBCs. The thermal cycle life is one of the key factors in evaluating the long-term stability and reliability of EBC coatings. Extending the thermal cycle life of the EBC coating can improve the thermal cycle life of CMC parts in aero-engine and reduce the tedious maintenance activities. The thermal cycle life of EBCs is usually measured by testing burner equipment, special design electric furnace, spalling furnace, etc.

[45–50]. Among them, the testing in burner rig equipment can simulate the actual operating conditions to a large extent and is the best method to provide the reliable results as actual working conditions.

In our present work, the tri-layer $\text{Yb}_2\text{Si}_2\text{O}_7/\text{Mullite}/\text{SiC}$ EBCs were prepared via the CVD and sol–gel method combined with air spraying process. At the same time, a burner test facility was designed and manufactured to test the thermal cycle performance of the EBCs. Although mullite coating exhibits excellent oxidation resistance in static environments [37], due to its low toughness, micro-cracks are easily generated during the thermal cycling process [38]. Therefore, the SiC whisker toughening phase and $c\text{-AlPO}_4$ bonding phase were added to the mullite coating to improve its thermal cycle performance. To understand the effect of the SiC whisker toughening phase and $c\text{-AlPO}_4$ bonding phase on the isothermal oxidation and thermal cycling performance of the bi-layer Mullite/SiC and tri-layer $\text{Yb}_2\text{Si}_2\text{O}_7/\text{Mullite}/\text{SiC}$ coatings, the phase compositions, microstructures, isothermal oxidation and thermal cycling performance of the bi-layer Mullite/SiC, $\text{SiC}_w\text{-Mullite}/\text{SiC}$, $c\text{-AlPO}_4\text{-SiC}_w\text{-Mullite}/\text{SiC}$ and tri-layer $\text{Yb}_2\text{Si}_2\text{O}_7/\text{Mullite}/\text{SiC}$, $\text{Yb}_2\text{Si}_2\text{O}_7/(\text{SiC}_w\text{-Mullite, SM})/\text{SiC}$, $\text{Yb}_2\text{Si}_2\text{O}_7/(c\text{-AlPO}_4\text{-SiC}_w\text{-Mullite, ASM})/\text{SiC}$ coated C/SiC composites were intensively studied. Wherein, the SiC inner layer was prepared via CVD method, the mullite, SM, ASM middle coatings, and $\text{Yb}_2\text{Si}_2\text{O}_7$ outer coating were prepared via the combination of sol–gel method and air spraying process.

2 Experimental

2.1 Coating Preparation

The preparation of the tri-layer $\text{Yb}_2\text{Si}_2\text{O}_7/\text{ASM}/\text{SiC}$ coating is illustrated in Fig. 2. Using the CVD method to deposit the SiC inner coating on the surface of C/SiC samples [51]. Mullite precursor sol, mullite powder (mass ratio of the mullite precursor sol to the mullite powder was 1:4), AlPO_4 and $c\text{-AlPO}_4$ powder (mass fractions of 10, 20, 30, and 40 wt.% of the total mixture; AlPO_4 corresponds to 30 wt.% of the total AlPO_4 and $c\text{-AlPO}_4$ powder to further improve the bonding strength of the coating), and alcohol were mixed in a high-energy planetary ball-mill at 200 rpm for 1.5 h. Polyvinylpyrrolidone (PVP, about 1 wt.% of the total mixture) was used as a crack-sealing agent, while oxalic acid (approximately 2 wt.%) was used as a drying control chemical additive (DCCA) during the ball milling process. Acetone was added to adjust the solution viscosity at 200 rpm for 0.5 h. Finally, high-purity $\beta\text{-SiC}$ whiskers (Hongwu, China) with average length of 20 μm and diameters of 2 μm (obtained from the manufacturers) were added to obtain the ASM coating precursor solution. The SiC whiskers (mass fractions of 10 wt. % of the total mixture) were pre-dispersed by ultrasonication with carboxy methylcellulose (CMC, molecular weight 20,000, GONSO, China) as the dispersant before the addition. The ball milling speed and time were controlled at 100 rpm and 0.5 h to protect the

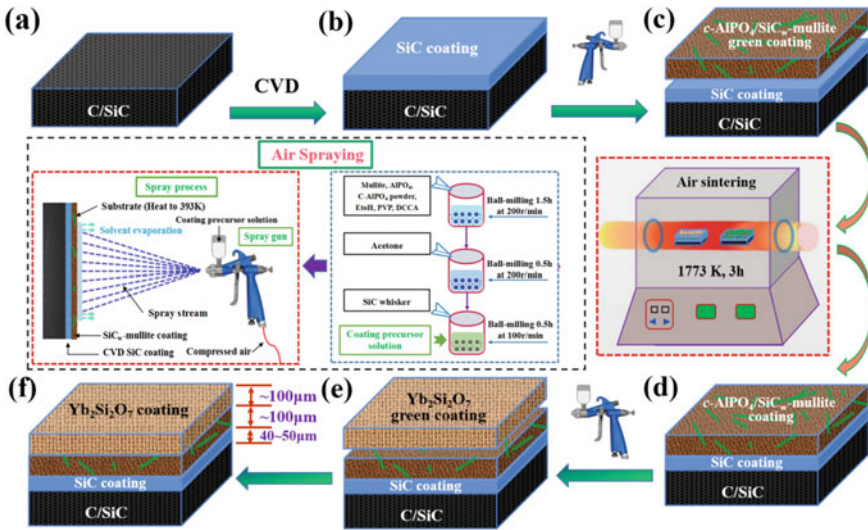


Fig. 2 Schematic diagram showing the preparation process of the tri-layer $Yb_2Si_2O_7/ASM/SiC$ coating on the C/SiC samples

SiC whiskers from damage, respectively. The mass ratio of the alcohol and acetone solvents should be controlled at 1:4. The optimal solid concentration of the mullite precursor sol, mullite powder, $AlPO_4$, and $c-AlPO_4$ powder in the ASM coating precursor solution was in the range of 20 to 30 wt.%. The target thicknesses for the SiC inner coating and ASM top coating were (40–50) μm and 100 μm , respectively.

The ASM coating precursor suspension was sprayed onto the surface of the SiC-C/SiC substrate using an improved air spray gun (R2-F, FRVNK). In the spraying process, the SiC-C/SiC substrate was heated to 393 K in a drying furnace, and then removed for spraying. The distance between the spray gun and substrate was about (15–20) cm. Each spraying process takes approximately 1 s, which was regarded as one cycle. After every five cycles, the SiC-C/SiC matrix must be reheated to 393 K in the drying furnace to ensure uniformity of the coating in the spraying process. After the spraying, the coated SiC-C/SiC matrix was air-sintered for 3 h in an electric furnace at 1773 K to form the ASM coatings.

In addition, the $Yb_2Si_2O_7$ top coating was deposited on the surface of mullite intermediate layer by the combination of sol-gel method and air spraying process too. All surfaces of the samples were coated with the coating. The $Yb_2Si_2O_7$ precursor sol, $Yb_2Si_2O_7$ powder was used as a drying control chemical additive (DCCA) in the ball milling process. Acetone was then added to adjust the solution viscosity at 200 rpm for 0.5 h. The optimal solid concentration of $Yb_2Si_2O_7$ precursor sol and $Yb_2Si_2O_7$ powder in the $Yb_2Si_2O_7$ coating precursor solution was in the range of 40–60 wt.%. The $Yb_2Si_2O_7$ coating precursor suspension was then sprayed on the surface of the samples using a modified air spray gun (R2-F, FRVNK). Each spraying process lasted about 1 s and counted as one cycle. After every five cycles,

the samples need to be reheated to 393 K to ensure uniformity of the coating in the spraying process. After the spraying, the samples were sintered in air at 1673 K for 3 h in an electric furnace to form the $\text{Yb}_2\text{Si}_2\text{O}_7$ top coating. The target thickness of the SiC coating is (40–50) μm . The target thickness of $\text{Yb}_2\text{Si}_2\text{O}_7$ top coating is 100 μm .

2.2 Isothermal Oxidation Tests

The samples were subjected to isothermal oxidation tests at 1773 K or 1673 K in electric furnace. The five samples were simultaneously held at 1773 K or 1673 K for a fixed time in static air. They were then removed directly from the furnace and cooled to room temperature. The samples were then put back into the furnace for another oxidation process. The weight change data were recorded after every 5 h. An electronic balance (SHIMADZUAUY220) with a sensitivity of ± 0.1 mg was used to record the weight loss data of the isothermal oxidation experiments. The weight loss and weight loss rates of the samples were calculated by formula (1) and (2).

$$\text{WL} = (m_0 - m_1)/s \quad (1)$$

$$\text{WLR} = (m_0 - m_1)/s \cdot t \quad (2)$$

where WL is the weight loss of the coated samples, g cm^{-2} . WLR is the weight loss rate of the coated samples, $\text{g cm}^{-2} \text{h}^{-1}$. m_0 is the starting weight of the coated samples, g. m_1 is the weight of the coated samples after oxidation for a period time, g. s is the surface area of coated specimen, cm^2 , t is the actual oxidation time, h.

2.3 Burner Rig Tests

Figure 3 indicates a high-speed gas scour experiment on a circular sample in our laboratory on a burner bench facility. Standard aviation-grade kerosene (No. 3 jet fuel) was used as the fuel for the burner bench facility test. The complete combustion of aviation-grade kerosene was realized to form the main products CO_2 and H_2O by controlling the ratio of high-purity oxygen and aviation-grade kerosene in the facility. The speed of high-temperature and high-speed flame was about (30–50 m)/s. Firstly, after the circular sample is fixed on a ceramic support to form a stable high-speed high-temperature gas, the sample is rapidly heated in a high-speed high-temperature gas environment. The temperature at the center of the surface was measured with an infrared temperature measuring instrument (MR1SBSF, Raytek, USA). Subsequently, the sample surface temperature was then stabilized at $1773 \pm$

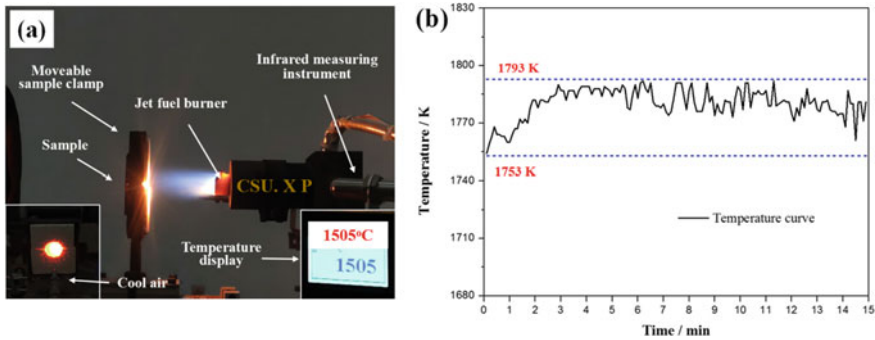


Fig. 3 Photograph of a circular specimen under the burner rig test in burner bench facility (a), Temperature curves of the sample surface during burner rig test (b)

20 K or 1673 ± 20 K by rapidly adjusting the ratio of high-purity oxygen to aviation-grade kerosene and was then kept at this temperature for 15 min. The samples were taken directly from the high-speed gas flame and cooled to room temperature with compressed air within 1 min, and then weighed by an electronic balance when cooled to room temperature. Finally, the samples were again put into the high-speed and high-temperature gas flame for the next burner rig tests. The weight loss of unit surface area was collected after every two cycles, and the weight loss of unit surface area was calculated by the formula (1). The surface temperature curve of the sample during a thermal cycle of burner rig tests was shown in Fig. 3b.

2.4 Coating Characterization

Before and after the oxidation, X-ray diffraction (XRD, Rigaku D/max 2550, Japan) at 40 kV and 200 mA using Cu K radiation was used to analyze phase compositions of the coatings. Scanning electron microscopy (SEM, Nova NanoSEM230, Japan) equipped with energy-dispersive spectroscopy (EDS) at 20.0 kV was used to analyze the morphologies and elemental distributions of the coatings. Electron probe micro-analysis instrument (EPMA JEOL CO, Jxa-8230, Japan) with a wavelength dispersive spectrometer (WDS) was used to analyze the elemental compositions and the microstructures of the coatings. Water-immersion technique using the Archimedes method was used to analyze the open porosity volumes of the coatings with the average value of three samples. Super-high magnification lens zoom 3D microscopy (VHX-5000, Japan) was used to analyze the three-dimensional (3D) erosive surface of different tri-layer coating after the burner rig tests.

3 Results and Discussion

3.1 Microstructure and Phase Composition of the Coatings

Figure 4 shows the surface and cross-section micrographs of the bi-layer Mullite/SiC, SM/SiC, and ASM/SiC coatings with different *c*-AlPO₄ contents. The average thicknesses of the SM and ASM top coatings with 10, 20, 30, 40 wt.% of *c*-AlPO₄ on the surfaces of the SiC-C/SiC sample are 110, 98, 101, 97, and 90 μm, respectively (error range; ±10 μm). Therein, the average thickness of the mullite top coating was 120 μm, which has the largest thickness as the resistance of the mullite coating precursor slurry (without large SiC whiskers) is minimum during the spraying process. The minimum resistance means that more slurry was sprayed per unit time. Notably, no obvious cracks are observed on the surfaces of the mullite, SM, and ASM coatings after the sintering for 3 h at 1773 K due to a well-matched in coefficient of thermal expansion between SiC and mullite. The open porosity of the SM coating (1.62%) is greater than that of the mullite coating (1.34%) due to the aggregation of SiC whiskers in the coating. The open porosities of the ASM coatings with 10, 20, 30, and 40 wt.% of *c*-AlPO₄ are 1.72, 1.84, 2.19 and 2.56%, respectively, which is due to the certain volume shrinkage of AlPO₄ on *c*-AlPO₄ during sintering at 1773 K for 3 h.

Figure 5 shows the SEM images and EDS line scans analysis of the concentration distributions of C, O, Al, Si, and P elements in a cross-section of the ASM/SiC coating with 20 wt.% of *c*-AlPO₄. Figure 5a shows that the interface of each coating is tightly bonded. The average thickness of the SiC inner coating prepared by CVD method is about 45.8 μm. Meanwhile, the ASM coating prepared by the sol-gel method combined with air spraying is about 95.1 μm. During sintering at 1773 K, some holes were observed in the coating because of the aggregation of SiC whiskers and certain volume contraction of AlPO₄ to *c*-AlPO₄. Figure 5b indicates that the bi-layer coating can be divided into three parts, denoted as A, B, and C. According to the EDS line scan analysis, Part A is a C/SiC composite matrix. Part B is a SiC bonding layer prepared by CVD. Part C is the ASM top coating with 20 wt.% of *c*-AlPO₄ prepared by the sol-gel method combined with air spraying.

To fully understand the distributions of different ceramic phases in the ASM coating with 20 wt.% of *c*-AlPO₄, the EMPA was performed to study the element distributions (Fig. 6). As shown in Fig. 6b, c, in addition to the distribution of carbon in the SiC whiskers, a large and even distribution of carbon element was observed in the ASM coating because some SiC whiskers were damaged during the ball milling process. In addition, a small portion of SiC particles accompanied the SiC whiskers supplied by the manufacturer. Figure 6c–e indicates the uniform distribution of Al, Si, and O elements in the mullite phase of the ASM coating, respectively. Figure 6f indicates the distribution of P elements in the *c*-AlPO₄ phase of the coating, which is uniform in the coating and considerably large in the local *c*-AlPO₄ particles.

Figure 7 shows the surface XRD patterns of the mullite, SM, and ASM coatings with different *c*-AlPO₄ contents. The peaks only belong to mullite, *c*-AlPO₄, and

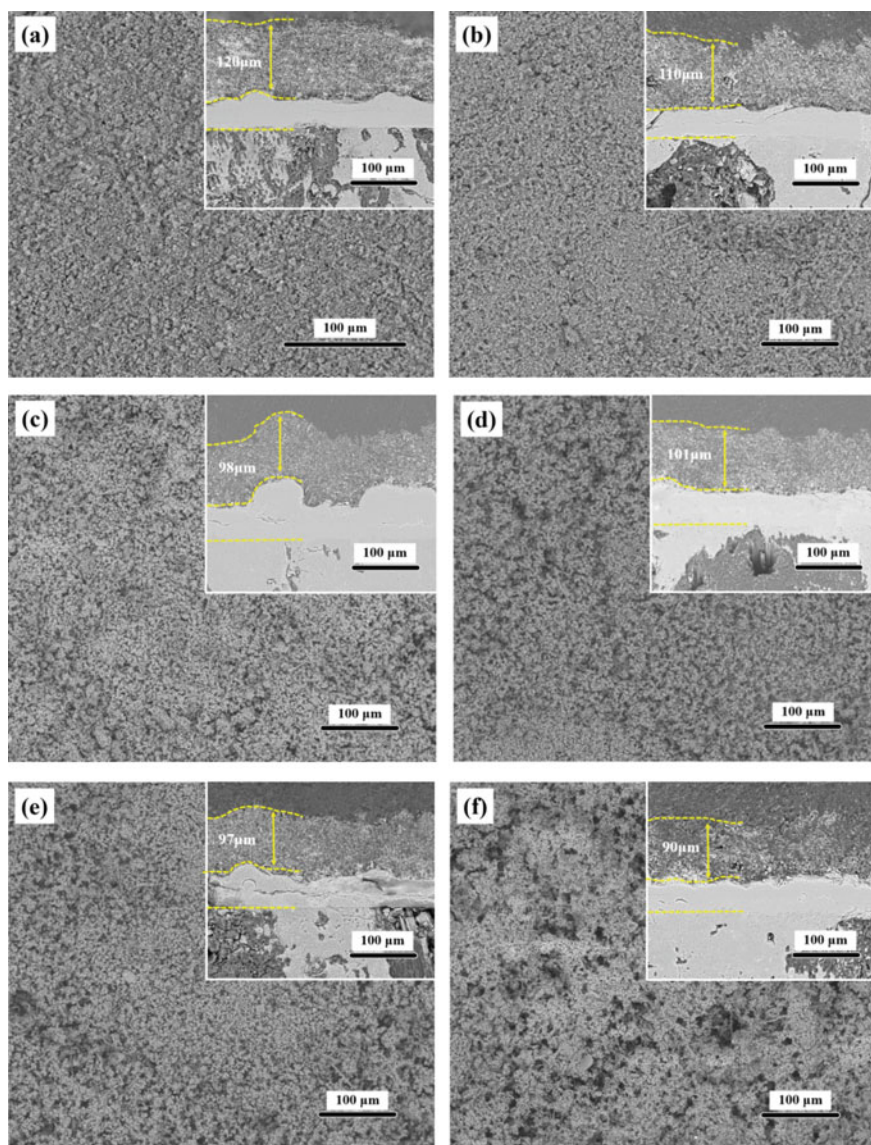


Fig. 4 Surface and cross-section SEM images of the bi-layer Mullite/SiC (a), SM/SiC (b), ASM/SiC coatings with different c -AlPO₄ contents coated C/SiC samples: c 10 wt.%, d 20 wt.%, e 30 wt.%, f 40 wt.%

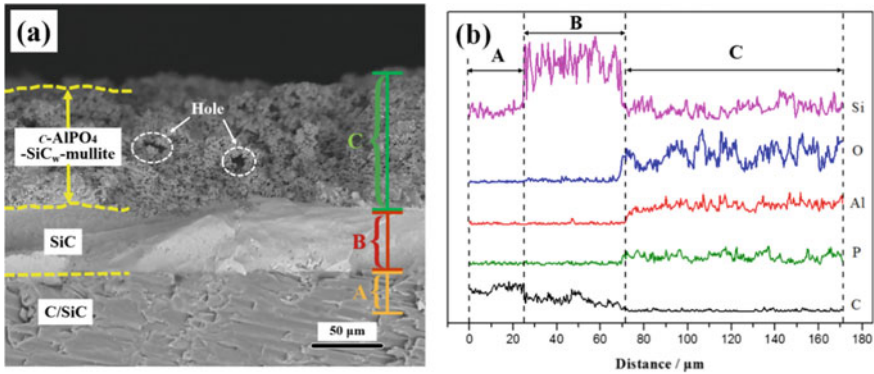


Fig. 5 Cross-section SEM image (a) and EDS element line scan analysis (b) of the bi-layer ASM/SiC coating with 20 wt.% of *c*-AlPO₄ coated C/SiC sample

SiC_w of the ASM coating, which is in agreement with the original phase of the mullite, *c*-AlPO₄, and SiC whiskers. The AlPO₄ was completely converted to *c*-AlPO₄ when the temperature was above 1573 K in the sintering process. In addition, the peak intensity of *c*-AlPO₄ increased with the increase of *c*-AlPO₄ content.

Figure 8 shows the microstructure of the surface and XRD patterns of the Yb₂Si₂O₇ outer coating in the tri-layer Yb₂Si₂O₇/Mullite/SiC coating. No visible cracks on the surface of Yb₂Si₂O₇ outer coating. However, during the air spraying and sintering, there are some micro-holes distributed in Yb₂Si₂O₇ outer coating due to the volatilization of solvents. There is only the Yb₂Si₂O₇ diffraction peak is observed on the surface of tri-layer Yb₂Si₂O₇/Mullite/SiC coating coated C/SiC sample, showing the Yb₂Si₂O₇ outer coating is uniformly distributed along the thickness direction. Figure 9 shows the cross-section microstructure of tri-layer Yb₂Si₂O₇/(Mullite, SM, ASM)/SiC coatings coated C/SiC composites substrate. As shown in Fig. 9a, the thickness of each layer of Yb₂Si₂O₇/Mullite/SiC coating is evenly distributed, and the coatings are closely bonded. Moreover, no visible holes and obvious penetrating cracks appear in the tri-layer Yb₂Si₂O₇/Mullite/SiC EBCs, indicating that the bonding between the coating and the C/SiC matrix is very close. Figure 9b, c show that there are certain holes in the SM and ASM intermediate coatings because of the agglomeration of SiC whiskers. The cross-section microstructure of sample needs to be embedded in the resin, impurities such as resin enter the holes during the grinding process, making the pores in the cross-section microstructure less clear than the surface microstructure. The overall thickness of tri-layer Yb₂Si₂O₇/(Mullite, SM, ASM)/SiC coatings are basically the same, the average thickness is between 260 and 270 μm. Therein, the average thickness of the SiC inner layer deposited via the CVD process is about 57.3 μm, the average thickness of mullite, SM, and ASM intermediate coatings and Yb₂Si₂O₇ outer coating prepared by the sol-gel method combined with air spraying method are about 110 and 100 μm, respectively. The thickness of SiC inner layer, mullite, SM and ASM intermediate coating, and Yb₂Si₂O₇ outer coating is very close to the value of the experimental

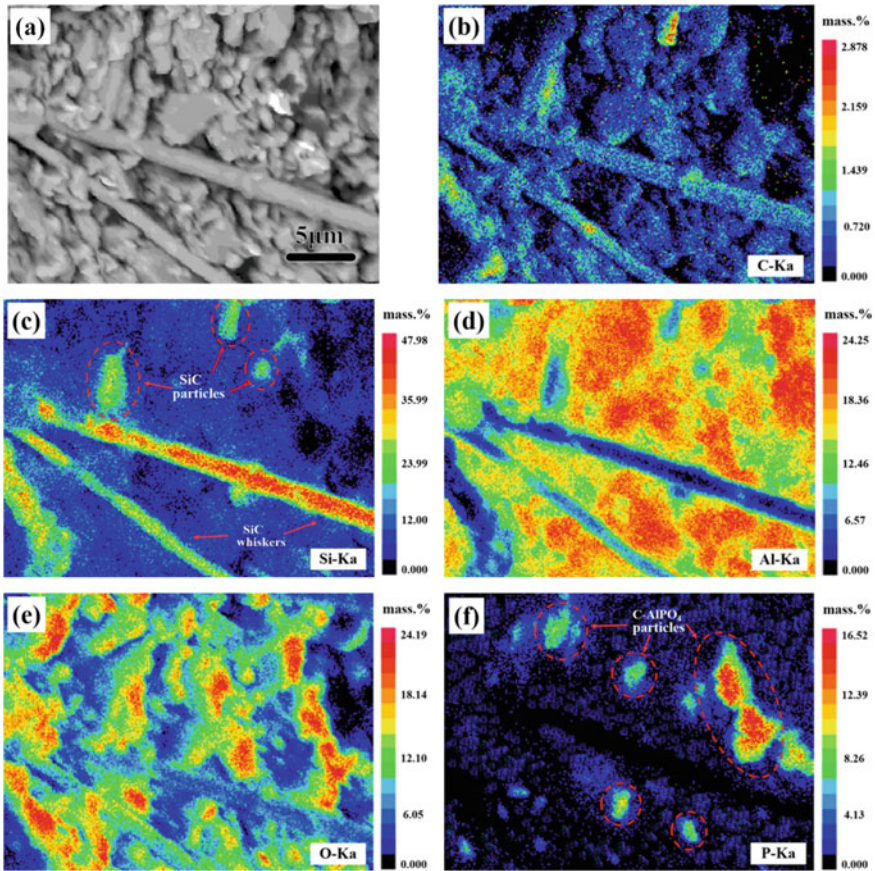


Fig. 6 Morphology and element distribution of the bi-layer ASM/SiC coating with 20 wt.% of *c*-AlPO₄: **a** Morphology, **b** C distribution, **c** Si distribution, **d** Al distribution, **e** O distribution, **f** P distribution

design (inner coating: 50 μm, middle coating: 100 μm, and outer coating: 100 μm). In addition, the tri-layer Yb₂Si₂O₇/SM/SiC coating with uniform thickness can be prepared at the high curvature position of the coating sample (Fig. 9d).

3.2 Isothermal Oxidation Properties of Coatings

Figure 10 shows the isothermal oxidation curve of the bi-layer Mullite/SiC coating coated C/SiC sample in the air at 1773 K. After 100 h of oxidation, the weight loss of the coated C/SiC sample is only $7.26 \times 10^{-3} \text{ g cm}^{-2}$ with the corresponding weight loss rate of $7.26 \times 10^{-5} \text{ g cm}^{-2} \text{ h}^{-1}$, indicating that the Mullite/SiC coating can

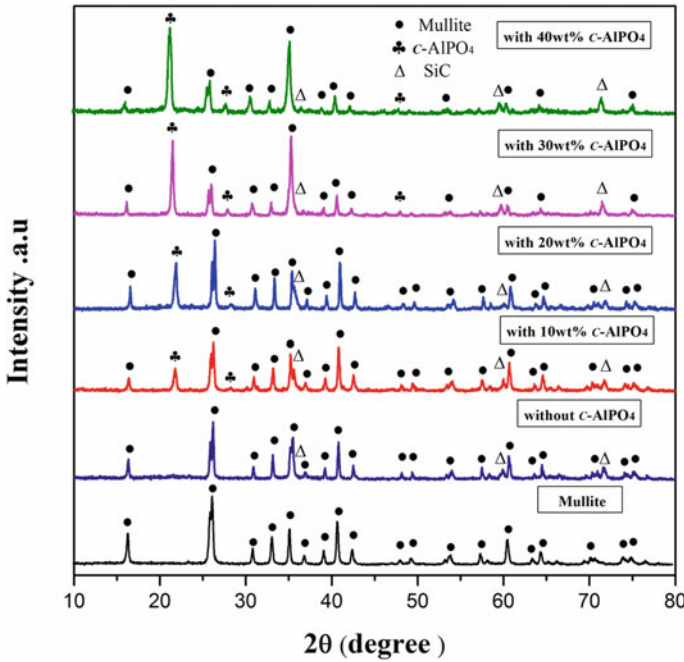


Fig. 7 Surface XRD patterns of the mullite, SM, and ASM coatings with different *c*-AlPO₄ contents after sintering at 1773 K for 3 h

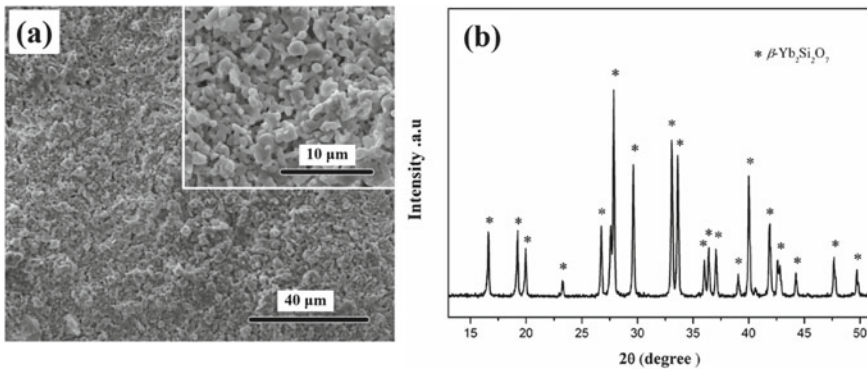


Fig. 8 Surface SEM image (a) and XRD patterns (b) of the Yb₂Si₂O₇ outer coating in tri-layer Yb₂Si₂O₇/Mullite/SiC coating coated C/SiC sample

effectively protect the oxidation of C/SiC sample. For comparison, the isothermal oxidation curves of the bi-layer SM/SiC, ASM/SiC coatings with different *c*-AlPO₄ contents on the C/SiC sample are shown in Fig. 11. The weight loss of the SM/SiC coated C/SiC sample is up to $18.07 \times 10^{-3} \text{ g cm}^{-2}$ after the oxidation for 100 h,

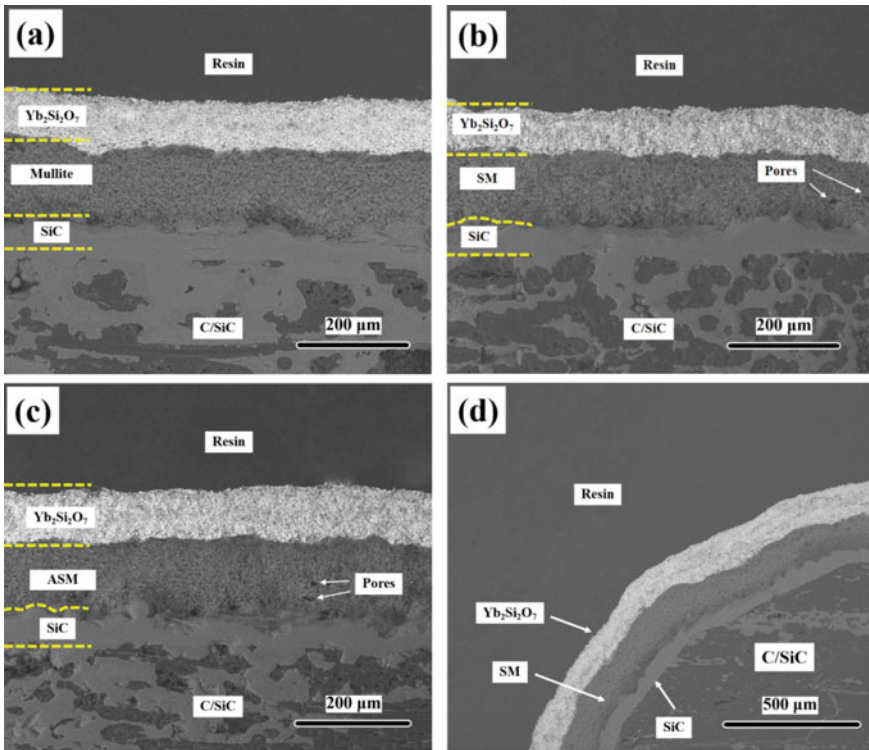


Fig. 9 Cross-section microstructure images of the Yb₂Si₂O₇/[Mullite (a), SM (b), ASM (c)]/SiC coated C/SiC sample, and the Yb₂Si₂O₇/SM/SiC coating at high curvature (d)

which is almost three times that of the mullite coated sample. The weight loss of the ASM/SiC coated C/SiC sample tended to decrease with the increase of *c*-AlPO₄ content is 10 to 20 wt.%. The weight loss of the ASM/SiC coating with 10 wt.% of *c*-AlPO₄ after the oxidation for 100 h was $12.43 \times 10^{-3} \text{ g cm}^{-2}$. When the content of *c*-AlPO₄ increases to 20 wt.%, the weight loss of the ASM/SiC coating is only $3.66 \times 10^{-3} \text{ g cm}^{-2}$. However, the weight loss of the ASM/SiC coated the sample rapidly increased with the increase of *c*-AlPO₄ (30 to 40 wt. %). The weight losses of the ASM/SiC coatings with 30 and 40 wt.% of *c*-AlPO₄ after the oxidation for 80 h are $20.21 \times 10^{-3} \text{ g cm}^{-2}$ and $29.99 \times 10^{-3} \text{ g cm}^{-2}$, respectively, even higher than that of the SM coating after the oxidation for 100 h. The larger formation of gaseous PO_x leads to the emergence of penetrating pores in the ASM coatings with 30 and 40 wt.% of *c*-AlPO₄, this provided a channels for oxygen diffusion to the surface of the C/SiC matrix.

Figure 12 shows the isothermal oxidation curve of the bi-layer ASM/SiC coating with 20 wt. % of *c*-AlPO₄ on the C/SiC sample in the air at 1773 K. When the oxidation time is 210 h, the weight loss of the coated sample is only $6.29 \times 10^{-3} \text{ g cm}^{-2}$, with the corresponding weight loss rate of $3.00 \times 10^{-5} \text{ g cm}^{-2} \text{ h}^{-1}$. This indicates

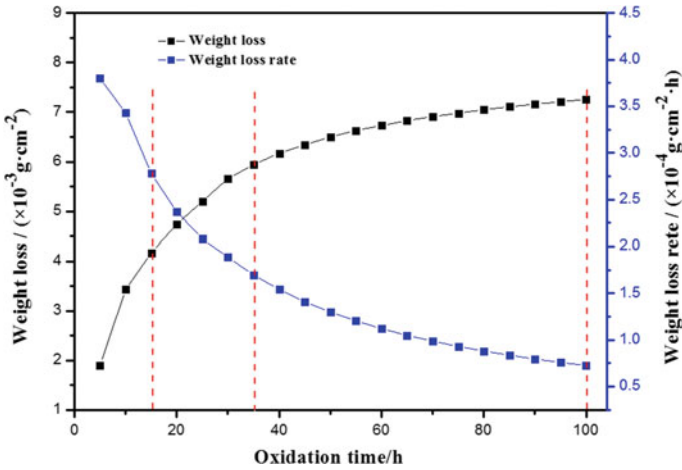


Fig. 10 Isothermal oxidation curves of the bi-layer Mullite/SiC coated C/SiC composites in the air at 1773 K

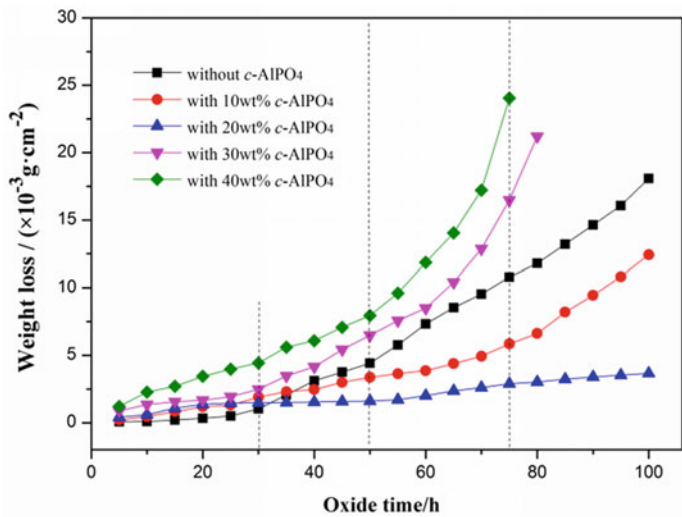


Fig. 11 Isothermal oxidation curves of the bi-layer SM/SiC, ASM/SiC coatings with different *c*-AlPO₄ contents coated C/SiC composites in the air at 1773 K

that the ASM coating with 20 wt. % of *c*-AlPO₄ has excellent oxidation resistance. Based on curve fitting of the weight loss using the Origin software in Fig. 12, the oxidation behavior of the ASM with 20 wt.% of *c*-AlPO₄ can be divided into four processes denoted as A, B, C, and D. The corresponding oxidation kinetic equations are presented as Eqs. (3)–(6), respectively, where $\Delta W (\times 10^{-3} \text{ g cm}^{-2})$ is the weight loss of the sample and t (h) is the oxidation time.

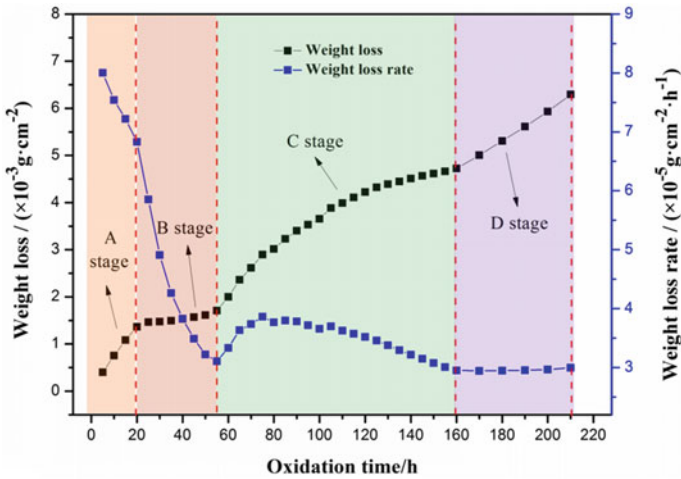


Fig. 12 Isothermal oxidation curves of the bi-layer ASM/SiC coating with 20 wt.% of *c*-AlPO₄ coated C/SiC composites in the air at 1773 K

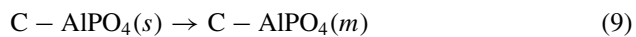
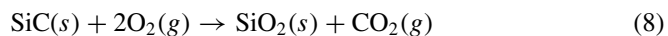
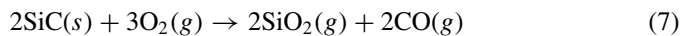
$$\Delta W_A = 0.0051 + 0.08234 t - 0.000712 t^2 \quad (0 < t \leq 20) \quad (3)$$

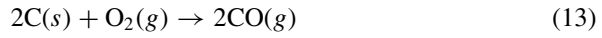
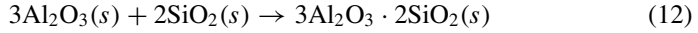
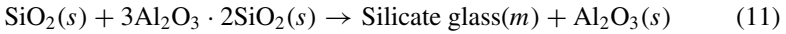
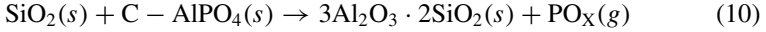
$$\Delta W_B = 1.62946 - 0.01304 t + 0.0002602 t^2 \quad (20 < t \leq 55) \quad (4)$$

$$\Delta W_C = -1.73139 + 0.07848 t - 0.0002406 t^2 \quad (55 < t \leq 160) \quad (5)$$

$$\Delta W_D = 3.04679 - 0.00502 t + 0.00009742 t^2 \quad (160 < t \leq 210) \quad (6)$$

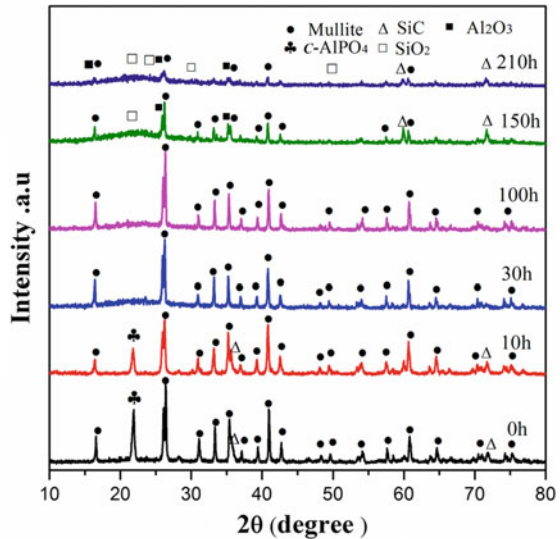
After oxidation of 1773 K in the air for a period, the surface XRD patterns of the ASM coating with 20 wt. % of *c*-AlPO₄ on the C/SiC composite are shown in Fig. 13. According to the XRD analysis results, the chemical reactions of the ASM coating with 20 wt. % of *c*-AlPO₄ can be summarized as Eqs. (7)–(14). To better understand the changes in micro-morphology and phase composition of the coating during the oxidation at 1773 K in the air, corresponding surface and cross-section SEM images of the bi-layer ASM coating with 20 wt.% of *c*-AlPO₄ on C/SiC composite after the oxidation at 1773 K in the air for periods of time are shown in Fig. 14.





As shown in Fig. 12, the weight loss rate of the sample remains at a higher level in the initial oxidation stage A (0–20 h). According to the SEM observation, a small amount of SiC whiskers were not completely oxidized, and the surface of the coating was still rough and porous after the oxidation for 10 h (Fig. 14a). Oxygen diffuses through the micro-holes to the surface of the SiC inner coating and C/SiC composite led to the oxidation of the SiC inner coating and C/SiC matrix. Moreover, a part of the SiC whiskers, particles, and SiC layer were gradually oxidized to form molten SiO₂ (Eqs. 7 and 8), and *c*-AlPO₄ particles were transformed into the molten phase (Eq. 9). Subsequently, the molten SiO₂ reacted with the molten *c*-AlPO₄ to generate fine mullite and PO_x (Eq. 10). The oxidation of the C/SiC matrix and the losses of CO, CO₂, and PO_x were the main factors contributing to the high weight loss rate of the sample at the initial oxidation stage A (0–20 h).

Fig. 13 Surface XRD patterns of ASM coating with 20 wt.% of *c*-AlPO₄ after oxidation at 1773 K in the air for different hours



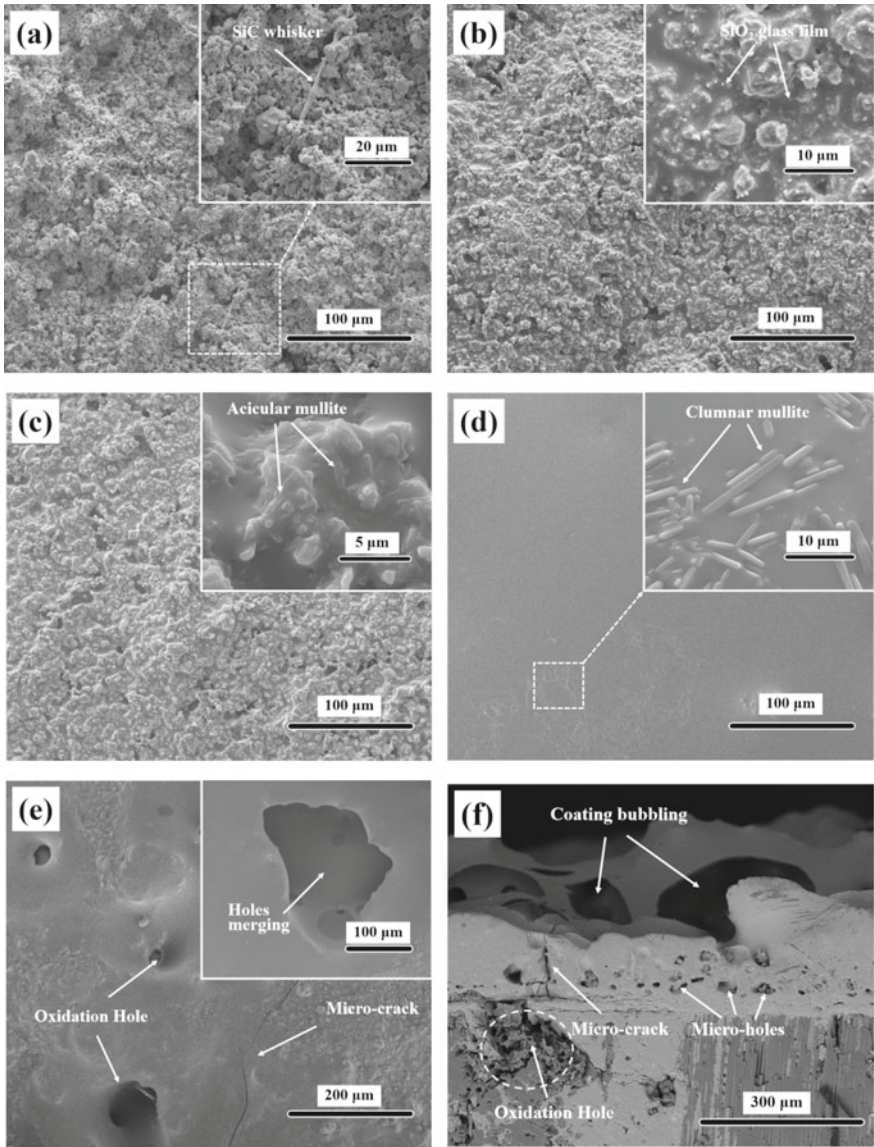


Fig. 14 Surface (a–e) and cross-section (f) SEM images of the bi-layer ASM/SiC coating with 20 wt.% of *c*-AlPO₄ coated C/SiC sample after oxidation at 1773 K in the air for different hours. **a** 10 h; **b** 30 h; **c** 100 h; **d** 150 h; **e** 210 h; **f** 210 h

After the oxidation for 30 h, due to the excess SiC whiskers and powders, the *c*-AlPO₄ phase was not observed in the coating (Fig. 13) in Eqs. (7)–(10). The oxidation of the excessive SiC whiskers and particles formed a SiO₂ glass layer on the surface of and inside the coating (Fig. 14b) due to the uniform distributions of C and Si elements in the coating, which gradually sealed the micro-cracks and micro-holes of the SiC inner layer and top coating so that the weight loss of the sample was considerably reduced. The average weight loss rate of the sample decreased from $6.83 \times 10^{-5} \text{ g cm}^{-2} \text{ h}^{-1}$ to $3.33 \times 10^{-5} \text{ g cm}^{-2} \text{ h}^{-1}$ at the oxidation stage B (20–60 h).

With the increase in oxidation time, new micro-cracks appeared in the top coating because of the CTE difference between the C/SiC composite and top coating. However, as shown in Fig. 14c, d, the mullite skeleton in the coating gradually reacts with the SiO₂ glass layer, forming a uniform and dense silicate glass layer with a good self-healing ability (Eq. 11) [52, 53]. The weight loss rate of the sample initially increases and then decreases with the oxidation time at the oxidation stage C (60–160 h) could be explained mainly by the above phenomena. The oxidation rate is mainly controlled by the diffusion rate of oxygen along the silicate glass layer at the late oxidation stage C. As the contents of SiO₂ and silicate glass film are lower than the sensitivity in the XRD analysis, no significant SiO₂ and silicate glass film peaks are detected after the oxidation at 1773 K in the air for 30 and 100 h, respectively. Moreover, the free Al₂O₃ and SiO₂ on the surfaces of mullite particles or in the silicate glass film reform acicular or columnar secondary mullite at the high temperature of 1773 K (Eq. 12 and Fig. 14c, d).

After the oxidation time reaches 160 h (stage D), due to the volatilization of the silicate glass layer and oxidation of the C/SiC composite, with the passage of oxidation time, the weight loss of the coated samples rapidly increases. The peak of the SiC inner coating is detected along with the decrease in coating thickness. Simultaneously, micro-cracks will appear due to the frequent thermal shocks in the range of 1773 K to room temperature (Fig. 14e). This is the channel for oxygen diffusion to the surface of the C/SiC matrix. The oxygen reacts with the C/SiC matrix (Eqs. 13 and 14) leads to the formation of penetrating micro-holes in the silicate glass layer (Fig. 14e, f) due to the escape of CO and CO₂. The weight loss of the sample further accelerates, and small micro-pores gather together to form larger micro-holes (Fig. 14f).

To understand the oxidation mechanism of the coating and demonstrate that the glass film on the surface of the mullite particles is molten SiO₂ (Fig. 14b), the morphology and element distribution of the ASM coating with 20 wt.% of *c*-AlPO₄ after the oxidation for 30 h are shown in Fig. 15. Figure 15a indicates an obvious molten glass film with a good self-healing ability distributed on and around the mullite particle skeleton. The mullite particle skeleton has a lower color depth in the Si element distribution map (Fig. 15b) and higher color depth in the Al element distribution map (Fig. 15c). Oppositely, the glass film has a higher color depth in the Si element distribution map (Fig. 15b) and lower color depth in the Al element distribution map (Fig. 15c). The above results confirm that the glass film on and around the mullite particle skeleton is a SiO₂ film formed by the oxidation of redundant SiC whiskers and SiC particles in the coating.

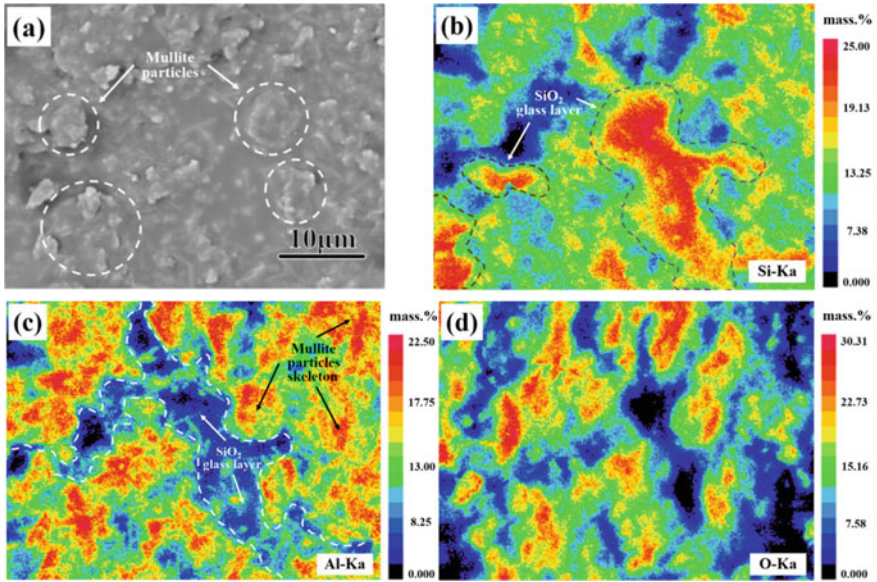


Fig. 15 Morphology and element distribution of the ASM coating with 20 wt.% of *c*-AlPO₄ after oxidation at 1773 K in air for 30 h: **a** Morphology, **b** Si distribution, **c** Al distribution, **d** O distribution

Figure 16 shows the oxidation resistance curves of the tri-layer Yb₂Si₂O₇/Mullite/SiC coated C/SiC composites in the air at 1673 K. After 200 h of oxidation, the weight loss of the tri-layer Yb₂Si₂O₇/Mullite/SiC coating sample is only $2.840 \times 10^{-3} \text{ g cm}^{-2}$ with the corresponding weight loss rate of $1.420 \times 10^{-5} \text{ g cm}^{-2} \text{ h}^{-1}$, showing that the tri-layer Yb₂Si₂O₇/Mullite/SiC coating has good oxidation resistance for C/SiC matrix. The oxidation behavior of tri-layer Yb₂Si₂O₇/Mullite/SiC coated matrix includes three stages marked as A, B, and C. According to oxidation curve characteristics, the corresponding oxidation equation fitted by origin 9.0 is represented in Eqs. (15) to (17).

$$\Delta W_A = 0.11 + 0.131t - 0.0026t^2 \quad (0 < t \leq 20) \quad (15)$$

$$\Delta W_B = 1.24 + 0.02516t - 1.36 \times 10^{-4}t^2 \quad (20 < t \leq 60) \quad (16)$$

$$\Delta W_C = 1.90 + 0.0074t - 1.36 \times 10^{-5}t^2 \quad (60 < t \leq 200) \quad (17)$$

After adding SiC whiskers to the mullite intermediate coating in the tri-layer Yb₂Si₂O₇/Mullite/SiC coating, the anti-oxidation characteristics of the tri-layer Yb₂Si₂O₇/SM/SiC coated C/SiC matrix in the air at 1673 K is shown in Fig. 17. After 200 h of oxidation, the weight loss of the tri-layer Yb₂Si₂O₇/SM/SiC coated

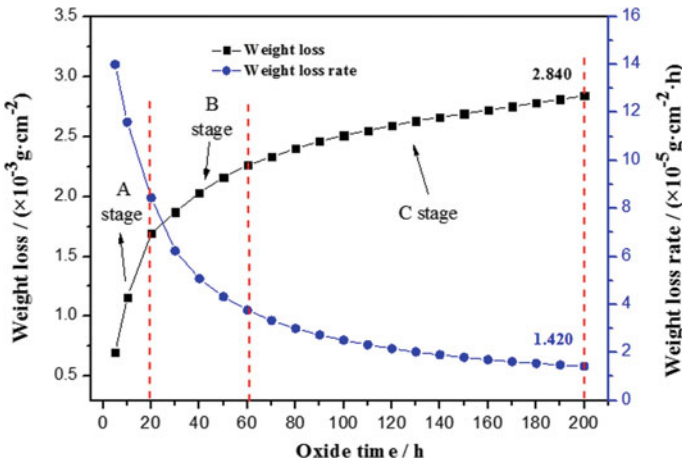


Fig. 16 Isothermal oxidation curves of the tri-layer $\text{Yb}_2\text{Si}_2\text{O}_7/\text{Mullite}/\text{SiC}$ coated C/SiC composites in the air at 1673 K

sample is only $0.150 \times 10^{-3} \text{ g cm}^{-2}$ with the homologous weight loss rate of $0.075 \times 10^{-5} \text{ g cm}^{-2} \text{ h}^{-1}$, which indicates the tri-layer $\text{Yb}_2\text{Si}_2\text{O}_7/\text{Mullite}/\text{SiC}$ coating has better oxidation resistance for C/SiC composites. The oxidation behavior of tri-layer $\text{Yb}_2\text{Si}_2\text{O}_7/\text{SM}/\text{SiC}$ coated matrix includes three stages marked as A, B, and C according to oxidation curve characteristics, the corresponding oxidation equation fitted by origin 9.0 is represented in Eqs. (18) to (20).

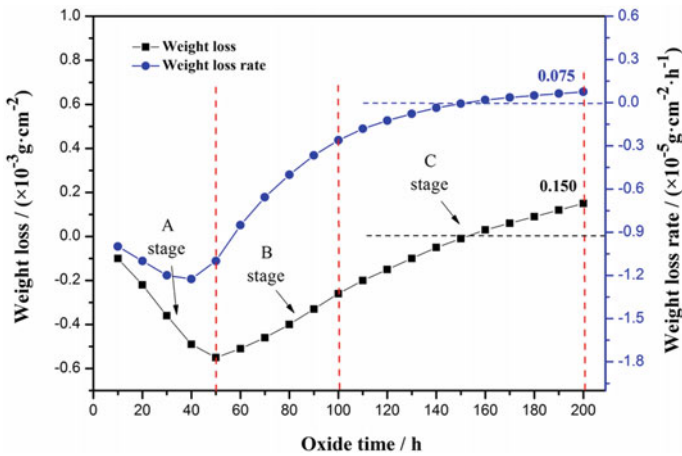


Fig. 17 Isothermal oxidation curves of the tri-layer $\text{Yb}_2\text{Si}_2\text{O}_7/\text{SM}/\text{SiC}$ coated C/SiC composites in the air at 1673 K

$$\Delta W_A = 0.072 - 0.01727 t + 9.29 \times 10^{-5} t^2 \quad (0 < t \leq 50) \quad (18)$$

$$\Delta W_B = -0.675 + 5.857 \times 10^{-4} t + 3.571 \times 10^{-5} t^2 \quad (50 < t \leq 100) \quad (19)$$

$$\Delta W_C = -1.008 + 0.00926 t - 1.742 \times 10^{-5} t^2 \quad (100 < t \leq 200) \quad (20)$$

In the starting oxidation stage of A (0–50 h), the tri-layer $\text{Yb}_2\text{Si}_2\text{O}_7/\text{SM}/\text{SiC}$ coated matrix indicates a state of continuous weight gain, the weight gain of the sample is $0.55 \times 10^{-3} \text{ g cm}^{-2}$ with the homologous weight gain rate of $1.11 \times 10^{-5} \text{ g cm}^{-2} \text{ h}^{-1}$ after oxidation for 50 h. After the oxygen diffusion to the surface of SM intermediate coating through the micro-pores in $\text{Yb}_2\text{Si}_2\text{O}_7$ outer coating, the SiC whiskers in SM intermediate coating are oxidized (Eqs. 7 and 8). As a result, the weight of the sample is increased. Subsequently, in the middle oxidation stage of B (50–100 h), the oxidation reaction of SiC whiskers is about to end or complete, making the weight of the sample no longer increase. A very small amount of oxygen diffuses to the surface of the SiC inner coating through the micro-pores in $\text{Yb}_2\text{Si}_2\text{O}_7$ outer and SM intermediate coatings, and then diffuses to the surface of the C/SiC matrix through the micro-cracks in the SiC inner coating, causing slight oxidation of carbon fibers and matrix in the C/SiC sample (Eqs. 13 and 14). As a result, the tri-layer $\text{Yb}_2\text{Si}_2\text{O}_7/\text{SM}/\text{SiC}$ coated sample subsequently indicates constant weight loss. However, at this time, the total weight of the coated matrix still maintains in an increased state of weight. The weight increase of coated sample is $0.26 \times 10^{-3} \text{ g cm}^{-2}$ with the homologous weight gain rate of $0.26 \times 10^{-5} \text{ g cm}^{-2} \text{ h}^{-1}$ after oxidation for 100 h. Finally, during the oxidation stage of C (100–200 h), with the progress of the sintering and densification of the $\text{Yb}_2\text{Si}_2\text{O}_7$ outer coating, the number of micro-pores in the coating continues to decrease, and the ability of the coating to prevent oxygen diffusion is increased. On the other hand, the SiO_2 glass phase retains to heal the micro-pores between mullite particles in the SM intermediate coating or reacts with mullite powders to form a silicoaluminate glass phase (Eq. 11). Finally, the ability of SM intermediate coating to prevent oxygen diffusion is increased owing to the decrease of the number of micro-pores. The weight loss rate of the coating sample indicates a decreasing trend.

Figure 18 shows the macro morphology, microstructure, and section microstructure of tri-layer $\text{Yb}_2\text{Si}_2\text{O}_7/\text{SM}/\text{SiC}$ coating coated C/SiC samples after oxidation at 1673 K for 200 h. As shown in Fig. 18a, the tri-layer $\text{Yb}_2\text{Si}_2\text{O}_7/\text{SM}/\text{SiC}$ coating sample remains unchanged after oxidation in air environment for 200 h, and no visible cracks and peeling are found on the surface and edge of the coating. The surface of the $\text{Yb}_2\text{Si}_2\text{O}_7$ outer coating is very dense and no obvious micro-cracks are found (Fig. 18b), indicating excellent resistance to oxygen diffusion. Figure 18c shows that the tri-layer $\text{Yb}_2\text{Si}_2\text{O}_7/\text{SM}/\text{SiC}$ coating maintains strong adhesion between the coatings without the penetrating crack generated. In SM intermediate coating, the SiO_2 glass phase is formed by the oxidation of SiC whiskers, and aluminosilicate glass phase is formed by a portion of SiO_2 and mullite have a good healing effect, which can continuously heal the micro-pores and cracks in the SM middle coating.

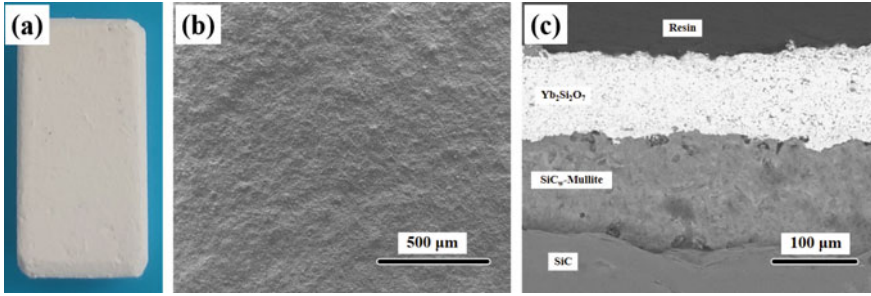


Fig. 18 Surface macro morphology (a), microstructure (b), and section microstructure (c), of tri-layer $\text{Yb}_2\text{Si}_2\text{O}_7/\text{SM}/\text{SiC}$ coating coated C/SiC samples after oxidation at 1673 K for 200 h

Finally, a dense middle coating with very few micro-pores is formed. At this time, the tri-layer $\text{Yb}_2\text{Si}_2\text{O}_7/\text{SM}/\text{SiC}$ coating has an excellent ability to prevent the diffusion of oxygen in the C/SiC matrix and indicates a very good resistance for C/SiC composite to oxidation in the air environment. The above results are the reason for the tri-layer $\text{Yb}_2\text{Si}_2\text{O}_7/\text{SM}/\text{SiC}$ coating which has better oxidation resistance than tri-layer $\text{Yb}_2\text{Si}_2\text{O}_7/\text{Mullite}/\text{SiC}$ coating for C/SiC sample in the air environment.

After further adding $c\text{-AlPO}_4$ powders to SM intermediate coating, the isothermal oxidation curves of tri-layer $\text{Yb}_2\text{Si}_2\text{O}_7/\text{ASM}/\text{SiC}$ coating coated C/SiC samples in the air at 1673 K are shown in Fig. 19. After 200 h of oxidation, the tri-layer $\text{Yb}_2\text{Si}_2\text{O}_7/\text{ASM}/\text{SiC}$ coating samples with a weight loss up to $2.530 \times 10^{-3} \text{ g cm}^{-2}$, which is much higher than that of tri-layer $\text{Yb}_2\text{Si}_2\text{O}_7/\text{SM}/\text{SiC}$ coating samples ($0.150 \times 10^{-3} \text{ g cm}^{-2}$) and slightly lower than that of tri-layer $\text{Yb}_2\text{Si}_2\text{O}_7/\text{Mullite}/\text{SiC}$ ($2.840 \times 10^{-3} \text{ g cm}^{-2}$). The oxidation behavior of tri-layer $\text{Yb}_2\text{Si}_2\text{O}_7/\text{ASM}/\text{SiC}$ coated matrix includes four stages marked as A, B, C, and D. According to oxidation curve characteristics, the corresponding oxidation equation fitted by origin 9.0 is represented in Eqs. (21) to (24).

$$\Delta W_A = 0.040 - 0.0095t + 0.00025t^2 \quad (0 < t \leq 30) \quad (21)$$

$$\Delta W_B = -0.02829 - 0.00224t + 9.286 \times 10^{-5}t^2 \quad (30 < t \leq 80) \quad (22)$$

$$\Delta W_C = -0.57643 + 0.01468t - 3.214 \times 10^{-5}t^2 \quad (80 < t \leq 160) \quad (23)$$

$$\Delta W_D = \text{Coating peeling} \quad (160 < t \leq 200) \quad (24)$$

In the initial oxidation stage of A (0–30 h), the tri-layer $\text{Yb}_2\text{Si}_2\text{O}_7/\text{ASM}/\text{SiC}$ coating samples show an increase in weight, the weight gain of sample after 30 h of oxidation is $0.020 \times 10^{-3} \text{ g cm}^{-2}$ with the homologous weight gain rate of $0.067 \times 10^{-5} \text{ g cm}^{-2} \text{ h}^{-1}$. Comparison of the initial oxidation stage of tri-layer $\text{Yb}_2\text{Si}_2\text{O}_7/\text{SM}/\text{SiC}$ coating samples, despite the oxidation of SiC whiskers leading to an increase

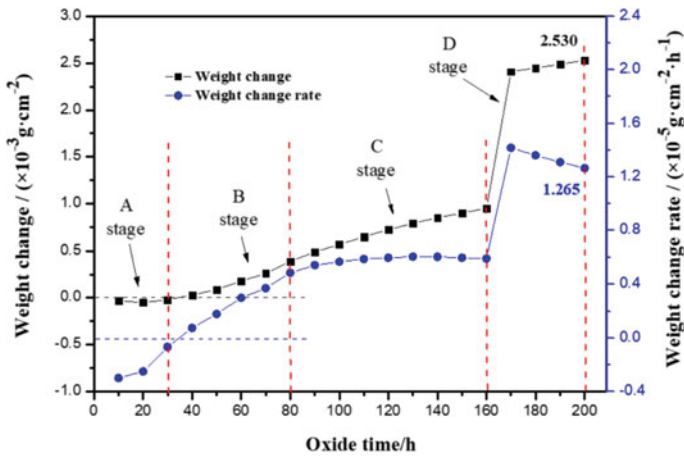


Fig. 19 Isothermal oxidation curves of the tri-layer $\text{Yb}_2\text{Si}_2\text{O}_7/\text{ASM}/\text{SiC}$ coating coated C/SiC sample in the air at 1673 K

in sample weight, the PO_x gas leakage caused by the reaction of SiO_2 and $c\text{-AlPO}_4$ resulted in a loss of samples weight. As a result, the sample weight slightly increased. Subsequently, in the oxidation stage of B (30–80 h), the oxidation reaction of SiC whiskers is coming to an end or completed. However, the process of forming mullite phase in ASM intermediate coating by the reaction of SiO_2 and $c\text{-AlPO}_4$ continues. Therefore, the PO_x gas leakage caused a rapid increase in the weight loss rate of the coating sample, and the coating sample showed an overall weight loss state. After 80 h of oxidation, the weight gain of sample is $0.390 \times 10^{-3} \text{ g cm}^{-2}$ with the homologous weight gain rate of $0.49 \times 10^{-5} \text{ g cm}^{-2} \text{ h}^{-1}$. When entering the C oxidation stage (80–160 h), the $c\text{-AlPO}_4$ phase in the ASM intermediate coating is consumed so that the PO_x gas leakage is also terminated. The excess SiO_2 glass phase continues to react with mullite particles to form a silicoaluminate glass layer/phase with self-healing ability or heal the micro-pores between mullite particles. As a result, the ability of ASM intermediate coating to hinder oxygen diffusion is increased because of the decrease of the number of micro-pores. Therefore, the weight loss rate of the coating sample may decrease. However, in the oxidation stage of D (160–200 h), the weight loss of the sample is suddenly increased, the peeling of $\text{Yb}_2\text{Si}_2\text{O}_7$ outer coating at the edge of coating samples is the main reason for the sudden increase in weight loss of coating samples.

Figure 20 shows the surface macro morphology, microstructure, and section microstructure of tri-layer $\text{Yb}_2\text{Si}_2\text{O}_7/\text{ASM}/\text{SiC}$ coating coated C/SiC samples after oxidation at 1673 K for 200 h. Compared with the tri-layer $\text{Yb}_2\text{Si}_2\text{O}_7/\text{SM}/\text{SiC}$ coating samples (Fig. 18a), the surface of $\text{Yb}_2\text{Si}_2\text{O}_7$ outer coating has many macroscopic cracks, and the coating falls off at the edge of the sample (Fig. 20a). Although the $c\text{-AlPO}_4$ particles improve the oxidation resistance of the SM intermediate coating in the air environment, the PO_x gas formed in the ASM middle coating leads to the

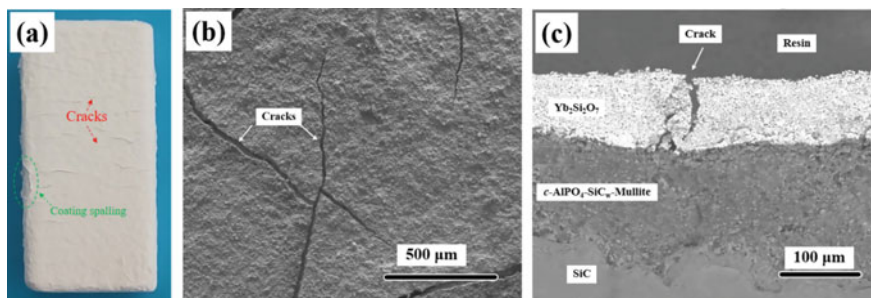


Fig. 20 Surface macro morphology (a), microstructure (b), and section microstructure (c), of tri-layer $\text{Yb}_2\text{Si}_2\text{O}_7/\text{ASM}/\text{SiC}$ coating coated C/SiC samples after oxidation at 1673 K for 200 h

increase of internal stress in $\text{Yb}_2\text{Si}_2\text{O}_7$ outer coating and finally forms penetrating cracks to provide a channel for the overflow of PO_x gas. As shown in Fig. 20b, there are obvious cracks on the surface of $\text{Yb}_2\text{Si}_2\text{O}_7$ outer coating, and the ASM intermediate coating can be clearly seen through a wider crack width. The cross-sectional microstructure shows that there is an obvious penetrating cracks in $\text{Yb}_2\text{Si}_2\text{O}_7$ outer coating but no penetrating cracks are found in ASM intermediate coating (Fig. 20c). Meanwhile, when the $c\text{-AlPO}_4$ particles in ASM intermediate coating are completely consumed by the SiO_2 oxidation product of SiC whiskers. The excess SiO_2 or silicoaluminate glass phase caused by the reaction between SiO_2 and mullite gradually heals the micro-pores in the ASM intermediate coating. However, due to the lower SiO_2 content in ASM coating compared to SM coating, the healing degree of SiO_2 and silicoaluminate glass phase on the micro-pores in the ASM middle coating is lower than that of the SM middle coating.

3.3 Thermal Cycle Properties of Coatings

Figure 21 shows the change in surface macrophotograph of bi-layer Mullite/SiC, SM/SiC, ASM/SiC coatings coated C/SiC sample in the burner rig test at 1773 K. After 8 times thermal cycles, macroscopic cracks visible to the naked eye appear on the surface of the Mullite/SiC coating. The cracks penetrate all mullite coating, and the surface of mullite coating will not peel off. At the same time, no macroscopic cracks were detected on the surface of the SM/SiC, ASM/SiC coatings. After 16 times thermal cycles, the mullite coating at the edge of Mullite/SiC coating exhibits obvious peeling phenomenon. There are many irregular “cracks” on the surface of mullite coating. The edge of the SM/SiC coating remains intact without shedding, but there are still a few macroscopic cracks on the surface of it. However, the surface of ASM/SiC coating remains intact without cracking and peeling. The above results indicate that the SiC whiskers can improve the thermal cycle resistance of Mullite/

SiC coating, and *c*-AlPO₄ particles can also improve the thermal cycle resistance of SM/SiC coating.

Figure 22 indicates the weight loss curves of bi-layer Mullite/SiC, SM/SiC, ASM/SiC coatings coated C/SiC sample with the thermal cycle process. After 240 min thermal cycles (16 times), the weight loss of the Mullite/SiC coating coated sample reaches $38.49 \times 10^{-3} \text{ g cm}^{-2}$, the formation of penetrating cracks and partial coating peeling are the main reasons for the high weight loss. By comparison, the weight loss of the SM/SiC and ASM/SiC coated samples is $14.09 \times 10^{-3} \text{ g cm}^{-2}$ and $5.59 \times 10^{-3} \text{ g cm}^{-2}$ after 16 thermal cycles, showing that adding SiC_w can effectively prevent the formation of cracks. Moreover, the addition of *c*-AlPO₄ can also prevent the formation of cracks and reduce the weight loss of the coating sample.

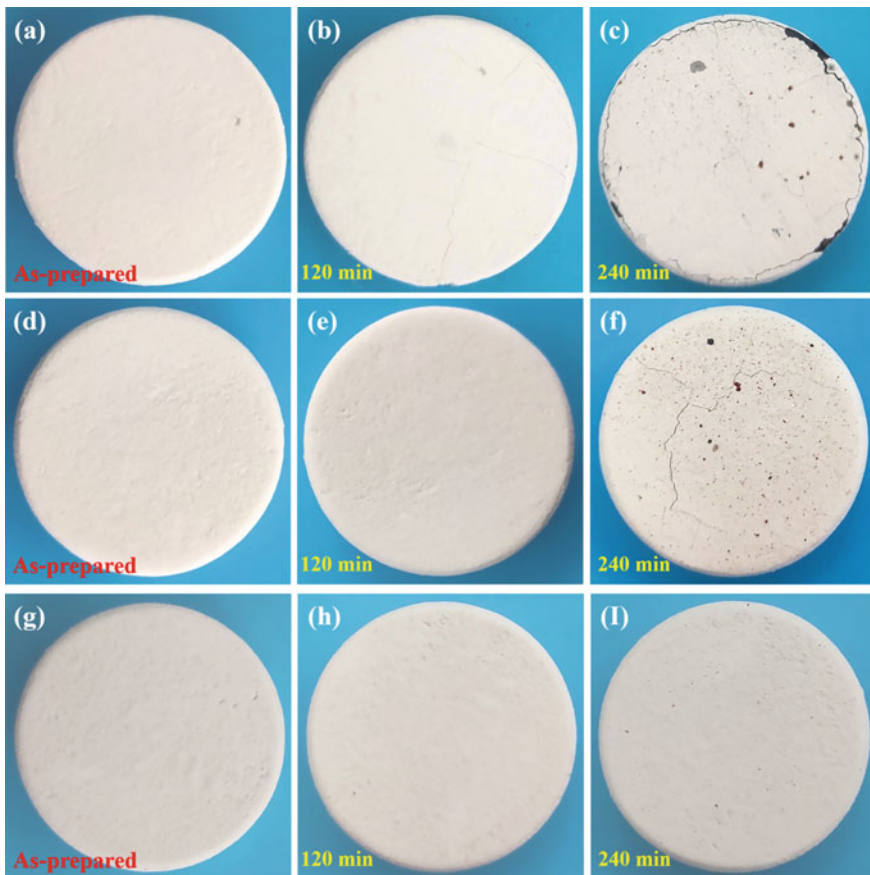


Fig. 21 The change of surface morphology of bi-layer Mullite/SiC (a–c), SM/SiC (d–f), ASM/SiC (g–i) coating coated C/SiC samples under 1773 K at high-speed gas scouring environment with oxidation time

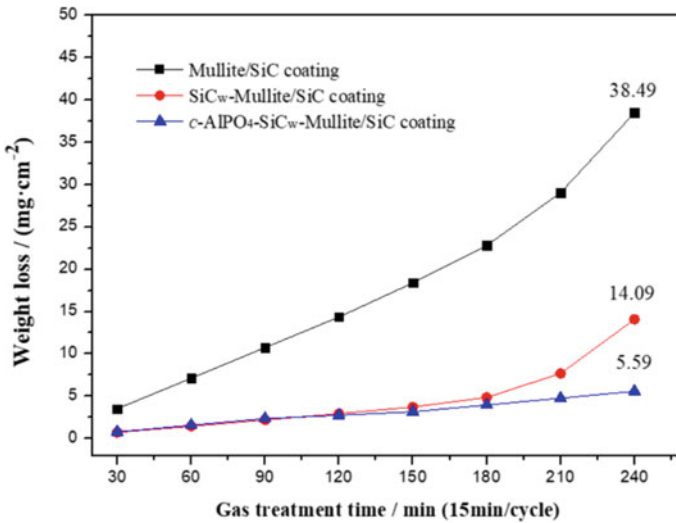


Fig. 22 The weight loss curves of the bi-layer Mullite/SiC, SM/SiC, ASM/SiC coating coated C/SiC composites at high-speed gas scouring environment with oxidation time

Figure 23 indicates the microstructure of the bi-layer Mullite/SiC coating coated C/SiC sample after 16 thermal cycles at 1773 K in the burner rig test. There are many irregular cracks on the surface of mullite coating due to the CTE differences between the mullite coating and SiC inner coating or the existence of stress caused by the direct scouring of high-speed gas (Fig. 23a, b). At the same time, it is accompanied by the occurrence of part of mullite coating peeling off. A large number of chapping cracks provide a direct channel for the diffusion of oxygen in mullite coating, resulting in rapid weight loss of coating samples (Fig. 23c, d). Compared with the bi-layer Mullite/SiC coating, there is no irregular crack on the surface of SM coating after 16 thermal cycles owing to the excellent mechanical properties of SiC_w in SM coating, but many micro-cracks were distributed around the visible cracks (Fig. 24a, b). Compared with the bi-layer SM/SiC coating, after 16 thermal cycles, there are only a few micro-cracks on the surface and edge surface of ASM coating. Therefore, c-AlPO₄ particles enhanced the interface adhesion between ASM coating and SiC inner coating so that the thermal shock resistance of ASM coating was improved (Fig. 25a, b).

Figure 26 shows the SEM images and schematics diagram of various toughening mechanisms of SiC whiskers or pores. Figure 26a indicates a typical image of the bridging feature of the SiC whiskers between the cracks. The “whiskers bridging” is the most important reinforcement mechanism of SiC whiskers [38, 44, 54]. The SiC whiskers introduce compressive stress to prevent expansion cracks in the coating. Due to the high strength and modulus of the SiC whiskers, more energy is needed for the destruction of whiskers bridging (Fig. 26b) [44]. In addition, if the bonding force of the SiC_w/coating matrix interface is lower than the whiskers strength (Fig. 26c),

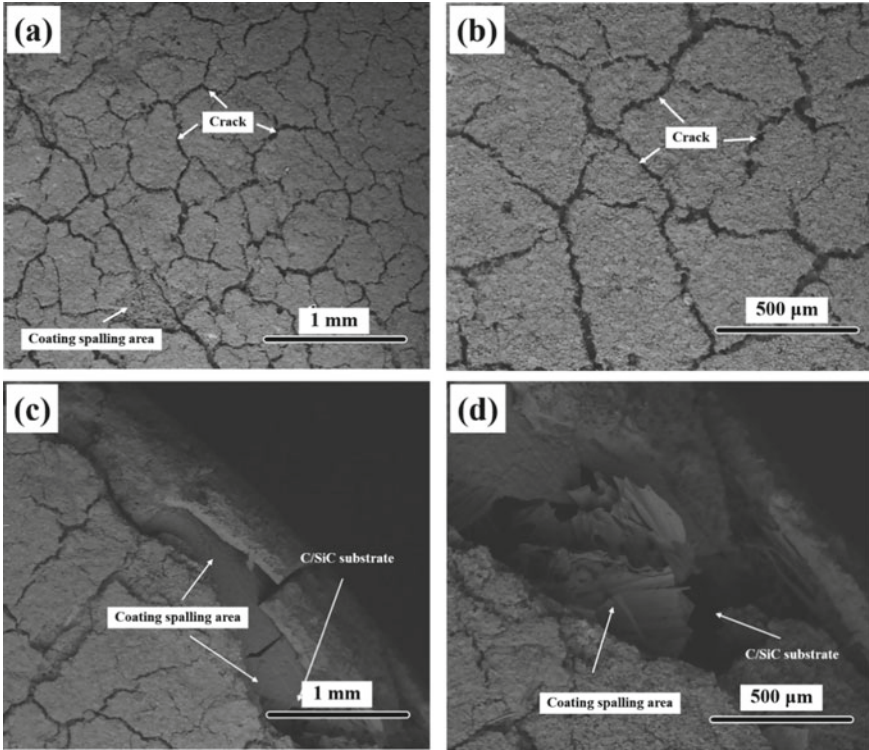


Fig. 23 Microstructure of the bi-layer Mullite/SiC coating coated C/SiC composite after 16 thermal cycles in high-speed gas environment

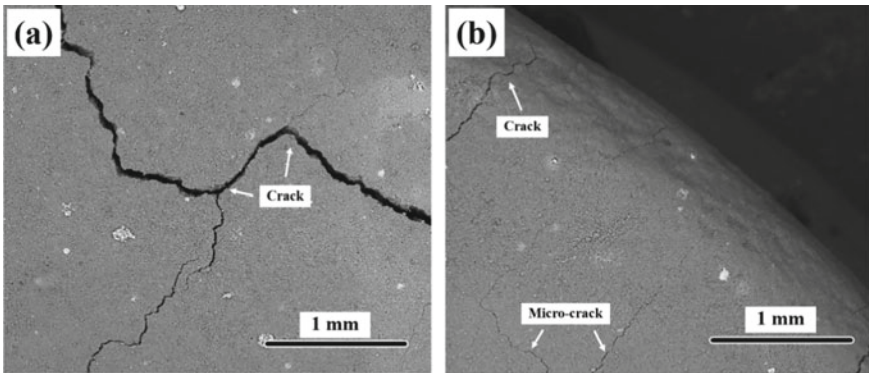


Fig. 24 Microstructure of the bi-layer SM/SiC coating coated C/SiC composite after 16 thermal cycles in high-speed gas environment

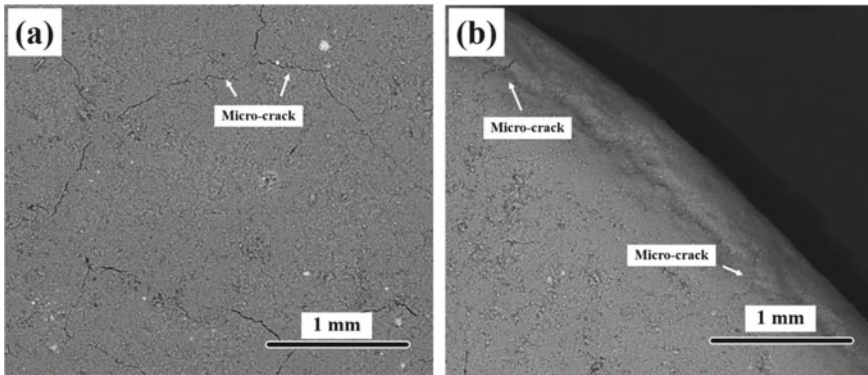


Fig. 25 Microstructure of the bi-layer ASM/SiC coating coated C/SiC composite after 16 thermal cycles in high-speed gas environment

SiC whiskers will be pulled out of the substrate during the crack expansion process. Some energy is expended during the “whiskers pull-out” from the coating because of the friction between the whiskers and coatings [55, 56]. When the crack extends at a certain angle to the SiC_w, due to the high strength and modulus of SiC_w [57–59], it is not easy to pass through SiC_w and continue to propagate in the original direction. Figure 26e indicates that the crack extends to the SiC_w and then deflects to other directions around the SiC_w. The “crack deflection” leads to the formation of new cracks and thus a large fracture energy should be absorbed to improve the toughness of the coating [60, 61]. In addition, the pores formed by the agglomeration of SiC_w and the volume shrinkage process of AlPO₄ to *c*-AlPO₄ can change the direction and path of crack expansion (see Fig. 26g, h), which will improve the toughness of the coating by consuming and absorbing energy during the formation of new cracks. All the above results indicate that the ASM coating has the best thermal shock resistance between room temperature and 1773 K.

Figure 27 indicates the schematic of *c*-AlPO₄ particles and SiC whiskers improving the bond strength of the ASM coating after sintering in the air at 1773 K for 3 h. The molten SiO₂ on the surface of SiC whiskers has a certain bonding ability to powder particles and SiC inner coating, resulting the bonding strength of the SM coating is higher than that of the mullite coating. Moreover, the melting point of *c*-AlPO₄ particles we used was between 1723 and 1773 K; all AlPO₄ particles were converted into *c*-AlPO₄ particles during the sintering process in the air at 1773 K; and the molten *c*-AlPO₄ phase with excellent bonding ability was gradually formed between mullite particles. Finally, the ASM coating has the highest bonding strength with SiC inner coating.

Figure 28 indicates the change in surface macrophotograph of tri-layer Yb₂Si₂O₇/ (Mullite, SM, ASM)/SiC coatings coated C/SiC sample in the burner rig test at 1673 K with scouring time. Different properties of middle coatings have an obvious effect on the thermal cycling performance of the tri-layer coating system [62]. After 180 min thermal cycles (12 times), a lot of irregular cracks appear around the center

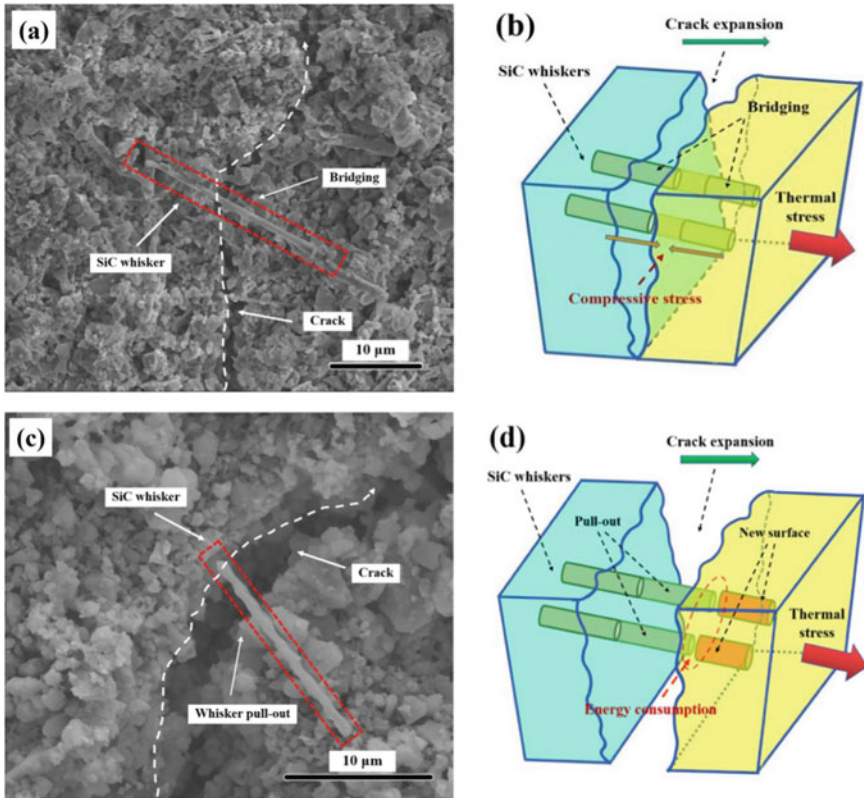


Fig. 26 Representative SEM images and schematic diagrams of the ASM/SiC coating after 24 thermal cycles: **a, b** micro-crack bridging by the SiC_w; **c, d** SiC_w pull-out from the coating substrate; **e, f** micro-crack deflection near the SiC_w; **g, h** micro-crack deflection near the micro-pores

of Yb₂Si₂O₇ outer coating in the Yb₂Si₂O₇/Mullite/SiC coated sample, and a part of Yb₂Si₂O₇ outer coating on the edge of the ring sample are peeling off. Moreover, as the number of thermal cycle times increases, the number of irregular cracks in the Yb₂Si₂O₇ outer coating is increased. In addition, the coating peeling phenomenon becomes more obvious. For comparison, after 12 thermal cycle times (Fig. 28f), no visible cracks were found on the surface Yb₂Si₂O₇ outer coating in the Yb₂Si₂O₇/SM/SiC coated sample. Even after a 360 min thermal cycles (24 times), there are still no visible cracks and the coating peeling phenomenon on the surface of Yb₂Si₂O₇ outer coating (Fig. 28h), indicating that the Yb₂Si₂O₇/SM/SiC coating has excellent thermal cycle performance under high-temperature and high-speed gas corrosion environment. However, in the Yb₂Si₂O₇/ASM/SiC coated sample (Fig. 28j), there are some visible and irregular cracks around the center of Yb₂Si₂O₇ outer coating. Moreover, the size of irregular cracks is larger than tri-layer Yb₂Si₂O₇/Mullite/SiC coated sample. As the scouring time increased to 360 min (24 times), the irregular cracks in the Yb₂Si₂O₇ outer coating slightly increased (Fig. 28j-l).

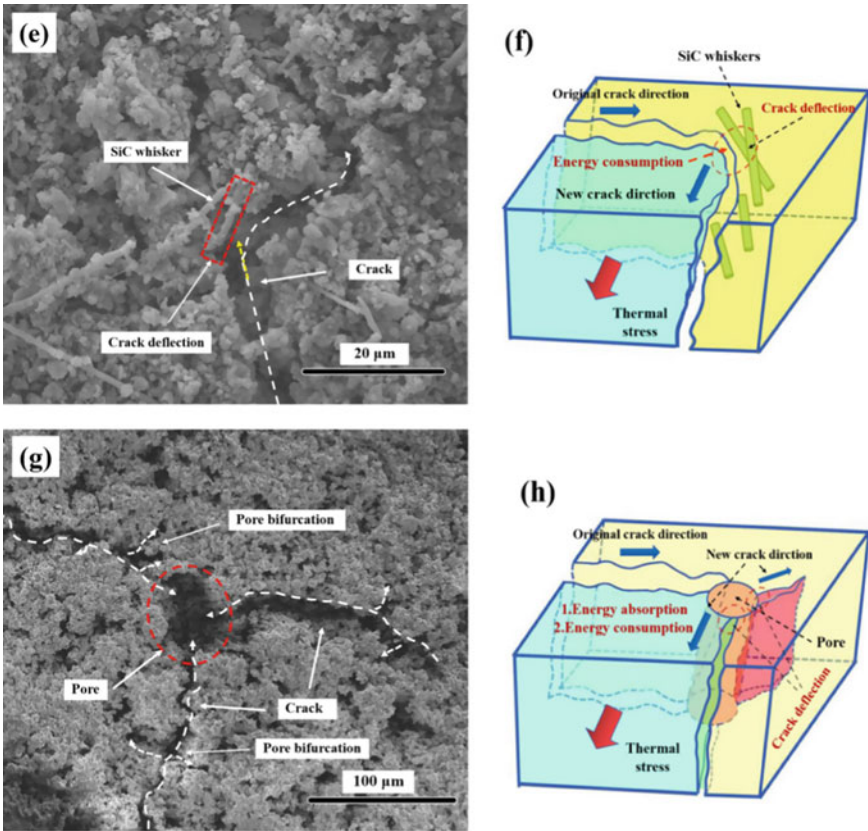


Fig. 26 (continued)

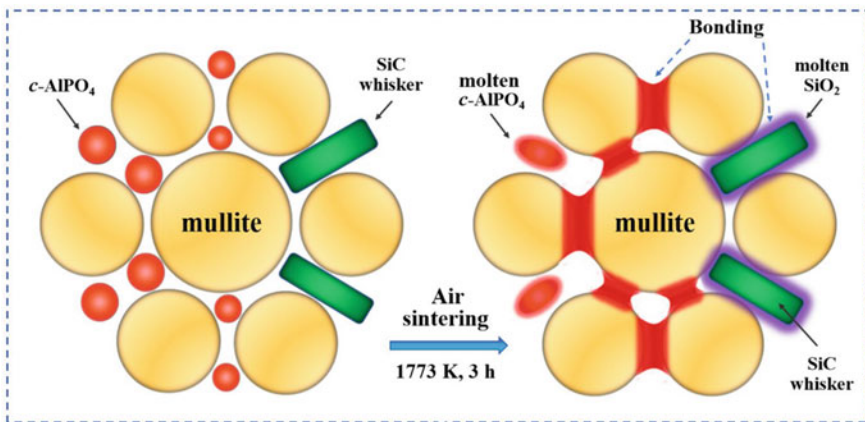


Fig. 27 Schematic diagram of *c*-AlPO₄ and SiC whisker improving the bond strength of the *c*-AlPO₄-SiC_w-mullite coating after sintering at 1773 K for 3 h in the air

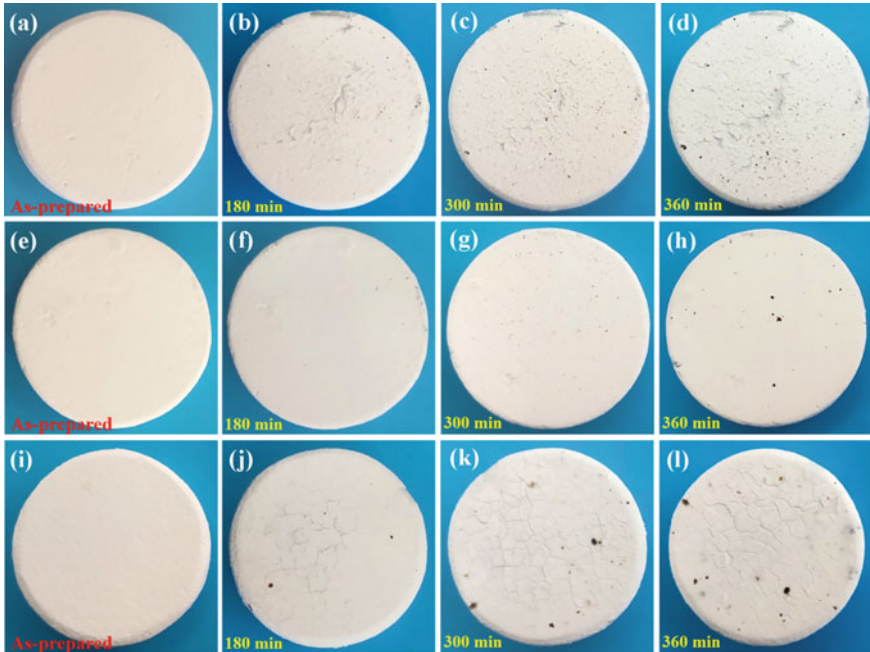


Fig. 28 The change in morphology of tri-layer $\text{Yb}_2\text{Si}_2\text{O}_7/\text{Mullite}/\text{SiC}$ (a–d), $\text{Yb}_2\text{Si}_2\text{O}_7/\text{SM}/\text{SiC}$ (e–h), $\text{Yb}_2\text{Si}_2\text{O}_7/\text{ASM}/\text{SiC}$ (i–l) coatings coated C/SiC samples in the burner rig test at 1673 K with scouring time

Figure 29 shows the surface microstructure of tri-layer $\text{Yb}_2\text{Si}_2\text{O}_7/(\text{Mullite}, \text{SM}, \text{ASM})/\text{SiC}$ coatings coated C/SiC samples in the burner rig test at 1673 K after 360 min thermal cycles (24 times). Figure 29a indicates that there are a lot of cracks on the surface of $\text{Yb}_2\text{Si}_2\text{O}_7$ outer coating in $\text{Yb}_2\text{Si}_2\text{O}_7/\text{Mullite}/\text{SiC}$ coated sample, and the exposed mullite intermediate coating can be clearly seen through the cracks in $\text{Yb}_2\text{Si}_2\text{O}_7$ outer coating. Meanwhile, Fig. 29b shows that the number and size of irregular cracks in $\text{Yb}_2\text{Si}_2\text{O}_7$ outer coating are decreased along the center of the sample to the edge (arrow direction in Fig. 29b), indicating that the formation of irregular cracks in $\text{Yb}_2\text{Si}_2\text{O}_7$ outer coating is not only related to the CTE difference between mullite intermediate and $\text{Yb}_2\text{Si}_2\text{O}_7$ outer coatings, but also directly related to the high-speed gas scouring on the straight surface of $\text{Yb}_2\text{Si}_2\text{O}_7$ coating. Therefore, the increase of internal stress in $\text{Yb}_2\text{Si}_2\text{O}_7$ coating will exacerbate the formation of irregular cracks. In contrast, only slight micro-cracks are detected at the center and edge of $\text{Yb}_2\text{Si}_2\text{O}_7$ outer coating in $\text{Yb}_2\text{Si}_2\text{O}_7/\text{SM}/\text{SiC}$ coated sample (Fig. 29c, d). However, in the $\text{Yb}_2\text{Si}_2\text{O}_7/\text{ASM}/\text{SiC}$ coated sample, the width of irregular cracks on the surface of $\text{Yb}_2\text{Si}_2\text{O}_7$ outer coating is greater than that of $\text{Yb}_2\text{Si}_2\text{O}_7/\text{SM}/\text{SiC}$ coated sample (Fig. 29e), and the width of irregular cracks in $\text{Yb}_2\text{Si}_2\text{O}_7$ outer coating is decreased along the center of the sample to the edge too (arrow direction in Fig. 29f). Meanwhile, when the wide cracks appear (Fig. 29e), a small part of

the $\text{Yb}_2\text{Si}_2\text{O}_7$ coating will peel off under the erosion of high-speed combustion gas. The above results indicate that the SiC whiskers toughening phase in the mullite intermediate coating can significantly improve the thermal cycle performance of the tri-layer $\text{Yb}_2\text{Si}_2\text{O}_7$ /Mullite/SiC coated sample. However, after further adding *c*- AlPO_4 powders to the SM intermediate coating, the thermal cycle performance of the $\text{Yb}_2\text{Si}_2\text{O}_7$ /ASM/SiC coated sample did not improve. Table 1 shows the quantitative analysis of cracks on the surface of $\text{Yb}_2\text{Si}_2\text{O}_7$ outer coating in tri-layer $\text{Yb}_2\text{Si}_2\text{O}_7$ /(Mullite, SM, ASM)/SiC coatings coated C/SiC samples after 360 min corrosion. The crack densities on the surfaces of the $\text{Yb}_2\text{Si}_2\text{O}_7$ outer coating in tri-layer $\text{Yb}_2\text{Si}_2\text{O}_7$ /(Mullite, SM, ASM)/SiC coatings are 5.5, 1.4, 1.9 mm^2 , respectively. The average crack widths on the surfaces of the $\text{Yb}_2\text{Si}_2\text{O}_7$ outer coating in tri-layer $\text{Yb}_2\text{Si}_2\text{O}_7$ /(Mullite, SM, ASM)/SiC coatings are 101.5, 3.3, 125.7 μm , respectively. Meanwhile, the maximum crack widths on the surfaces of the $\text{Yb}_2\text{Si}_2\text{O}_7$ outer coating in the $\text{Yb}_2\text{Si}_2\text{O}_7$ /SM/SiC coating is only 5.5 μm , which is much lower than that of the $\text{Yb}_2\text{Si}_2\text{O}_7$ /Mullite/SiC (161.2 μm) and $\text{Yb}_2\text{Si}_2\text{O}_7$ /ASM/SiC (228.9 μm) coatings.

Figure 30 shows the cross-section microstructure of tri-layer $\text{Yb}_2\text{Si}_2\text{O}_7$ /(Mullite, SM, ASM)/SiC coatings coated C/SiC sample after 360 min thermal cycles (24 times) in the burner rig test at 1673 K. Figure 30a indicates that there is an obvious penetrating crack in the $\text{Yb}_2\text{Si}_2\text{O}_7$ /Mullite/SiC coated C/SiC matrix due to the CTE difference between the coatings or matrix. The penetrating crack is a channel for oxygen diffusion to the C/SiC substrate, and the width of penetrating cracks increases with the increase of the thermal cycling times. As a result, due to the oxidation of carbon fibers or substrate near the coating side, many oxidation pores are formed on the C/SiC substrate. In contrast, Fig. 30b shows that there are few penetrating micro-cracks in the $\text{Yb}_2\text{Si}_2\text{O}_7$ /SM/SiC coated C/SiC matrix. Figure 30c, d display the cracks deflection or disappearance of tri-layer $\text{Yb}_2\text{Si}_2\text{O}_7$ /SM/SiC coating during the thermal cycling process. Because of the excellent mechanical properties of SiC whiskers, after the crack extends to the surface of the SM intermediate coating, it does not directly penetrate the SM coating, but extends along the interface between SM middle and $\text{Yb}_2\text{Si}_2\text{O}_7$ outer coatings on both sides. Finally, new penetrating cracks are formed on the SM coating far away from the crack in the $\text{Yb}_2\text{Si}_2\text{O}_7$ outer coating (Fig. 30c) or directly disappeared in SM intermediate coating (Fig. 30d). However, after 360 min thermal cycling time, Fig. 30e, f show the cracks width in $\text{Yb}_2\text{Si}_2\text{O}_7$ outer coating of the $\text{Yb}_2\text{Si}_2\text{O}_7$ /ASM/SiC coating is greater than that of the $\text{Yb}_2\text{Si}_2\text{O}_7$ /SM/SiC coating, and even higher than that of the $\text{Yb}_2\text{Si}_2\text{O}_7$ /Mullite/SiC coating. The structural damage of the $\text{Yb}_2\text{Si}_2\text{O}_7$ /ASM/SiC coating mainly occurs at the interface between the ASM intermediate and $\text{Yb}_2\text{Si}_2\text{O}_7$ outer coatings. The structure of ASM intermediate coating will not be damaged due to the *c*- AlPO_4 bonding phase further enhancing the thermal cycle performance of SM intermediate coating. However, when the oxygen diffuses to the ASM intermediate coating along the penetrating cracks and micro-pores in $\text{Yb}_2\text{Si}_2\text{O}_7$ outer coating, the SiC whisker is oxidized to molten SiO_2 and reacts with molten *c*- AlPO_4 . Finally, a secondary mullite is formed accompanied via the overflow of PO_x gas, which aggravates the formation and expansion of cracks in the $\text{Yb}_2\text{Si}_2\text{O}_7$ outer coating. When the width of cracks increases to a certain value, the interface between the $\text{Yb}_2\text{Si}_2\text{O}_7$ outer coating and

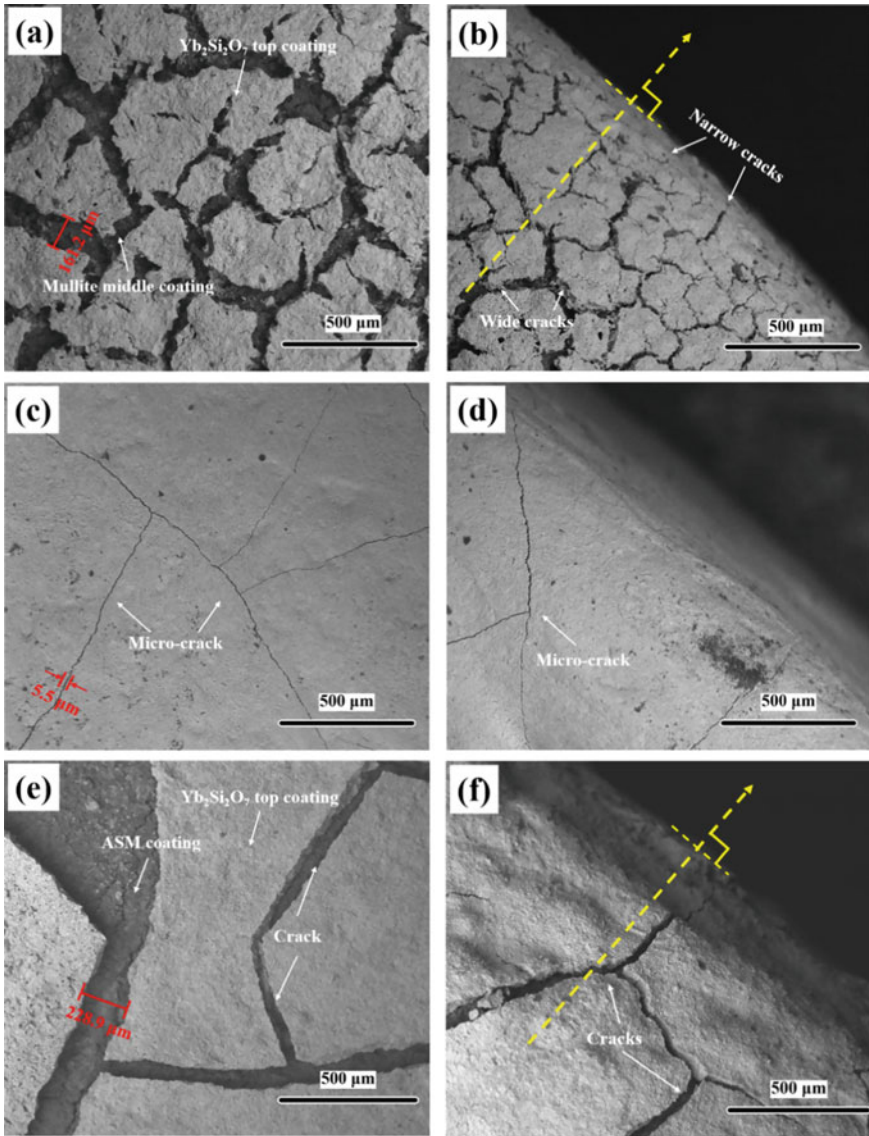


Fig. 29 Surface microstructure of tri-layer $\text{Yb}_2\text{Si}_2\text{O}_7/\text{Mullite}/\text{SiC}$ (a, b), $\text{Yb}_2\text{Si}_2\text{O}_7/\text{SM}/\text{SiC}$ (c, d), $\text{Yb}_2\text{Si}_2\text{O}_7/\text{ASM}/\text{SiC}$ (e, f) coatings coated C/SiC samples after 360 min corrosion in the burner rig test at 1673 K

Table 1 The quantitative analysis of cracks in tri-layer $\text{Yb}_2\text{Si}_2\text{O}_7$ /(Mullite, SM, ASM)/SiC coatings coated C/SiC samples after 360 min corrosion in the burner rig test at 1673 K

Coating	Crack density/mm ²	Average crack width/ μm	Maximum crack width/ μm
$\text{Yb}_2\text{Si}_2\text{O}_7$ /Mullite/SiC	5.5	101.5	161.2
$\text{Yb}_2\text{Si}_2\text{O}_7$ /SM/SiC	1.4	3.3	5.5
$\text{Yb}_2\text{Si}_2\text{O}_7$ /ASM/SiC	1.9	125.7	228.9

the ASM intermediate coating is peeled off because of the gas eroding force after the high-speed combustion gas reaches the surface of ASM intermediate coating. Moreover, the rebound gas generated by the ASM coating causes a certain degree of warping outwards. The surface and cross-sectional analysis results from Figs. 28, 29 and 30 show that the tri-layer $\text{Yb}_2\text{Si}_2\text{O}_7$ /SM/SiC coating coated sample has the best thermal cycle performance among tri-layer $\text{Yb}_2\text{Si}_2\text{O}_7$ /(Mullite, SM, ASM)/SiC coatings coated sample under a high-speed combustion gas environment.

Figure 31 shows the change in macrophotograph of tri-layer $\text{Yb}_2\text{Si}_2\text{O}_7$ /SM/SiC coated sample during 480 min thermal cycles (32 times) to 540 min thermal cycles (36 times) after the burner rig tests at 1673 K. As shown in Fig. 31a, after 480 min thermal cycling, some visible and irregular cracks began to appear on the surface of the $\text{Yb}_2\text{Si}_2\text{O}_7$ /SM/SiC coated sample. Meanwhile, a small portion of $\text{Yb}_2\text{Si}_2\text{O}_7$ outer coating began to peel off. Figure 31b shows that the number and size of visible and irregular cracks on the surface of the $\text{Yb}_2\text{Si}_2\text{O}_7$ /SM/SiC coated sample further increase with the increase of the thermal cycling times. Figure 32 shows the typical cross-section microstructure of tri-layer $\text{Yb}_2\text{Si}_2\text{O}_7$ /SM/SiC coated C/SiC matrix after 540 min corrosion. Under the long-term eroding of high-speed combustion gas, the $\text{Yb}_2\text{Si}_2\text{O}_7$ outer coating gradually peels off, and the SM intermediate coating is slowly eroded. Finally, the $\text{Yb}_2\text{Si}_2\text{O}_7$ outer and SM middle coatings from obvious arc “corrosion pit.” After the oxygen reaches the surface of C/SiC substrate along the micro-cracks in the SiC inner coating, the C/SiC composites substrate is slight oxidation.

Figure 33 shows the weight loss curves of tri-layer $\text{Yb}_2\text{Si}_2\text{O}_7$ /(Mullite, SM, ASM)/SiC coating coated C/SiC composites with the thermal cycle process. After 24 thermal cycles (360 min), the tri-layer $\text{Yb}_2\text{Si}_2\text{O}_7$ /Mullite/SiC coating coated sample with a weight loss up to $29.53 \times 10^{-3} \text{ g cm}^{-2}$. During the thermal cycles process, the formation of a large number of penetrating cracks is the main reason for the rapid weight loss of the sample. However, the weight loss of tri-layer $\text{Yb}_2\text{Si}_2\text{O}_7$ /SM/SiC coating coated sample is only $6.19 \times 10^{-3} \text{ g cm}^{-2}$, which is only one-fifth of tri-layer $\text{Yb}_2\text{Si}_2\text{O}_7$ /Mullite/SiC coating coated sample and a half that of tri-layer $\text{Yb}_2\text{Si}_2\text{O}_7$ /ASM/SiC coating coated sample ($13.24 \times 10^{-3} \text{ g cm}^{-2}$). When the number of thermal cycles exceeds 24 times, the weight loss of tri-layer $\text{Yb}_2\text{Si}_2\text{O}_7$ /SM/SiC coating coated sample rapidly increases with the increase of thermal cycling. After 36 thermal cycles (540 min), the weight loss of tri-layer $\text{Yb}_2\text{Si}_2\text{O}_7$ /SM/SiC coating coated sample

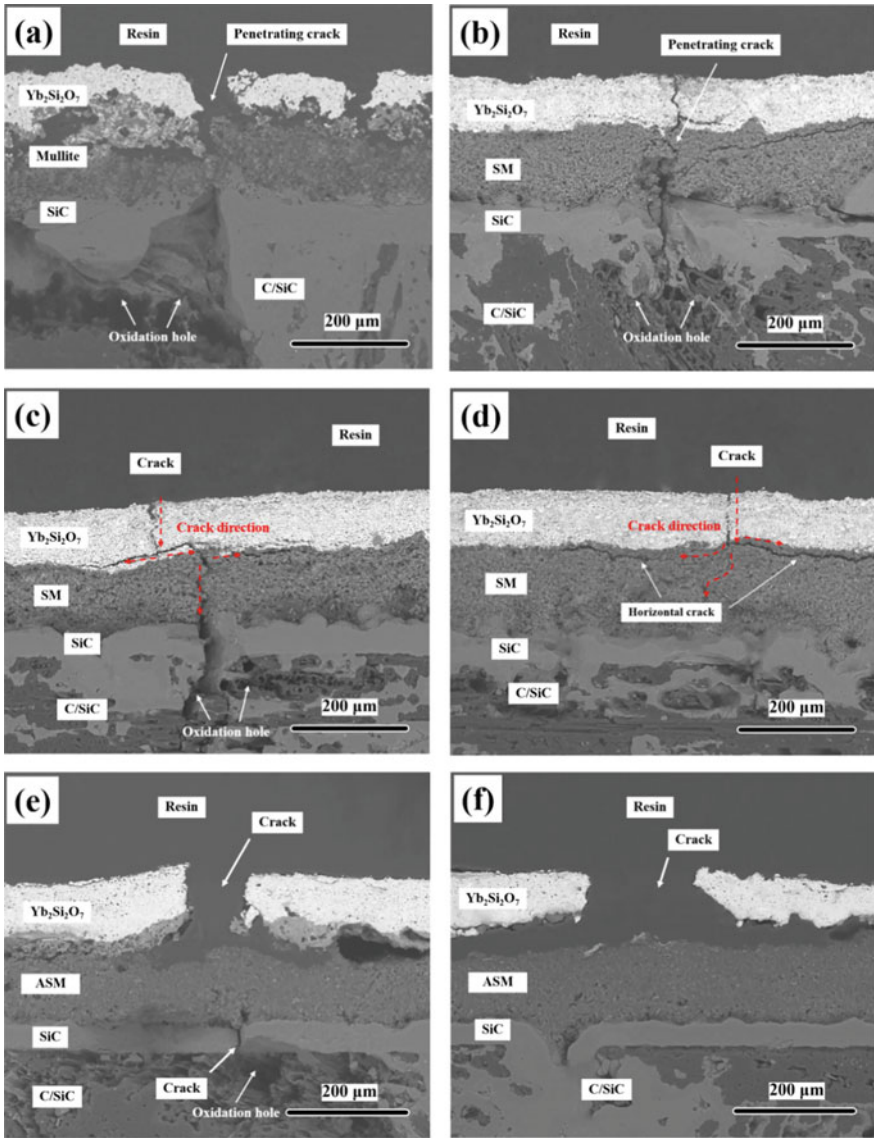


Fig. 30 Cross-section microstructure of tri-layer $\text{Yb}_2\text{Si}_2\text{O}_7/\text{Mullite}/\text{SiC}$ (a), $\text{Yb}_2\text{Si}_2\text{O}_7/\text{SM}/\text{SiC}$ (b–d), $\text{Yb}_2\text{Si}_2\text{O}_7/\text{ASM}/\text{SiC}$ (e, f) coatings coated C/SiC samples after 360 min corrosion in the burner rig test at 1673 K

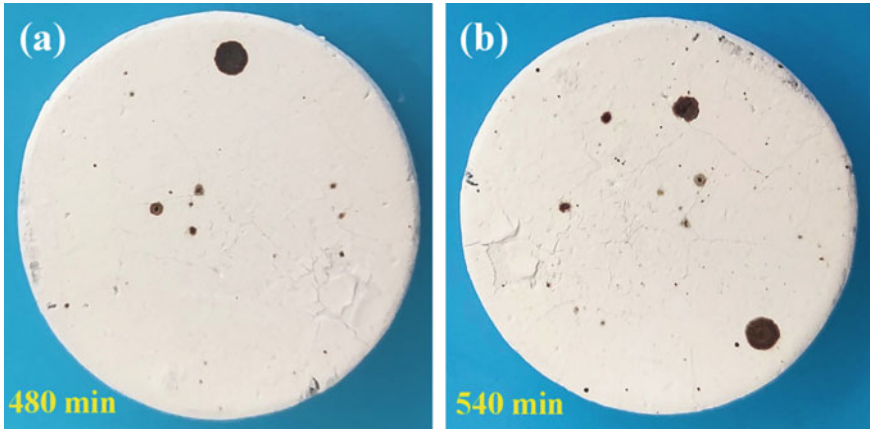


Fig. 31 The change in morphology of tri-layer $\text{Yb}_2\text{Si}_2\text{O}_7/\text{SM}/\text{SiC}$ coating coated C/SiC samples in the burner rig test at 1673 K with scouring time **a** 480 min, **b** 540 min

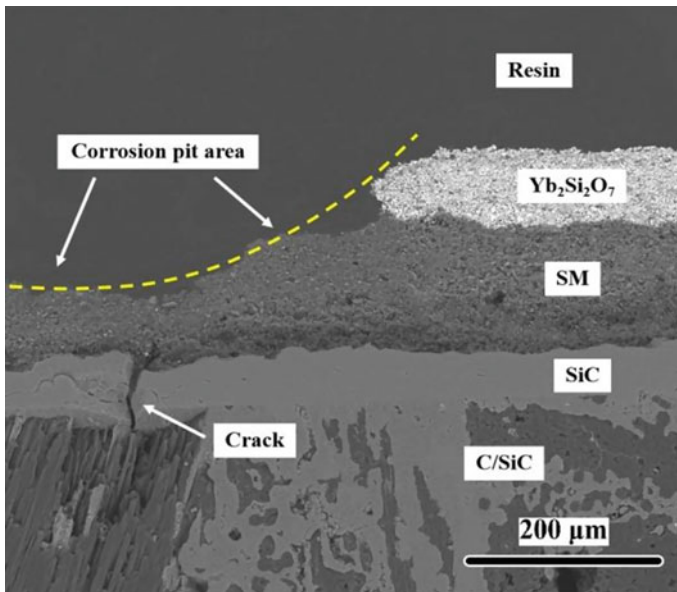


Fig. 32 Cross-section microstructure of tri-layer $\text{Yb}_2\text{Si}_2\text{O}_7/\text{SM}/\text{SiC}$ coating coated C/SiC samples after 540 min corrosion in the burner rig test at 1673 K

reached as high as $32.67 \times 10^{-3} \text{ g cm}^{-2}$, due to the formation of cracks in the coating and the peeling off of a small part of the coating.

To better observe the different surface morphology of tri-layer coatings after high-temperature and high-speed gas corrosion, the 3D morphology of different tri-layer

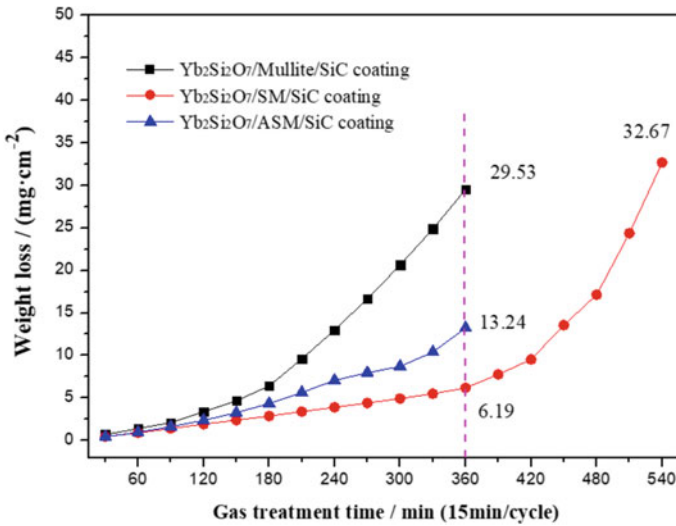


Fig. 33 The weight loss curves of tri-layer $\text{Yb}_2\text{Si}_2\text{O}_7/\text{Mullite}/\text{SiC}$, $\text{Yb}_2\text{Si}_2\text{O}_7/\text{SM}/\text{SiC}$, $\text{Yb}_2\text{Si}_2\text{O}_7/\text{ASM}/\text{SiC}$ coating coated C/SiC composites during high-speed gas experiment

samples is observed. Figure 34 shows the surface 3D patterns of the $\text{Yb}_2\text{Si}_2\text{O}_7/\text{Mullite}/\text{SiC}$ and $\text{Yb}_2\text{Si}_2\text{O}_7/\text{ASM}/\text{SiC}$ coatings coated sample after 360 min thermal cycles (24 times), and the $\text{Yb}_2\text{Si}_2\text{O}_7/\text{SM}/\text{SiC}$ coated sample after 540 min thermal cycles (36 times). Figure 34a shows that the $\text{Yb}_2\text{Si}_2\text{O}_7$ outer coating has rich colors, while the mullite intermediate coating is gray. According to the analysis of the depth distribution curve of the line segment, the damage of the $\text{Yb}_2\text{Si}_2\text{O}_7$ outer coating structure mainly includes the following three categories: The first category, the initial micro-crack caused by the CTE difference between the mullite intermediate and $\text{Yb}_2\text{Si}_2\text{O}_7$ outer coatings during the thermal cycling process; the second category, after the initial micro-crack is formed, the $\text{Yb}_2\text{Si}_2\text{O}_7$ outer coating is broken and peeled off under the eroding force of high-temperature and high-speed combustion gas; the third category, the $\text{Yb}_2\text{Si}_2\text{O}_7$ outer coating continuously erodes under the action of combustion gas, ultimately forming arc-shaped corrosion pits. Figure 34b shows that the structural damage of the tri-layer $\text{Yb}_2\text{Si}_2\text{O}_7/\text{ASM}/\text{SiC}$ coating mainly occurs in $\text{Yb}_2\text{Si}_2\text{O}_7$ outer coating. There is clear demolding coating at the intersection of cracks, which consistent with the warping of $\text{Yb}_2\text{Si}_2\text{O}_7$ outer coating observed in Fig. 30e, f. According to the depth distribution curve of tri-layer $\text{Yb}_2\text{Si}_2\text{O}_7/\text{ASM}/\text{SiC}$ coating in the coating the line section, the coating fracture zone not only has a complete fracture zone but also has an arc-shaped corrosion pits. As shown in Fig. 34c, an obvious annular corrosion pit is formed on the surface of the $\text{Yb}_2\text{Si}_2\text{O}_7/\text{SM}/\text{SiC}$ coating, and some cracks are detected around the annular corrosion pit. According to the analysis of the depth distribution curve, the depth of the annular corrosion pit is about 200 μm (almost reaches the sum of the thickness of $\text{Yb}_2\text{Si}_2\text{O}_7$

outer and SM middle coatings). In the scouring force in burner rig test, the structural damage of $\text{Yb}_2\text{Si}_2\text{O}_7/\text{SM}/\text{SiC}$ coating includes the following two categories: The first category, the initial micro-cracks in $\text{Yb}_2\text{Si}_2\text{O}_7$ outer coating are caused by the CTE difference between the SM intermediate and the $\text{Yb}_2\text{Si}_2\text{O}_7$ outer coatings during thermal cycling. It is much lower than that of the $\text{Yb}_2\text{Si}_2\text{O}_7/\text{Mullite}/\text{SiC}$ and $\text{Yb}_2\text{Si}_2\text{O}_7/\text{ASM}/\text{SiC}$ coatings. The second type, after the initial formation of micro-cracks, the $\text{Yb}_2\text{Si}_2\text{O}_7$ outer coating is continuously scoured and corroded by high-speed gas at the cracks locating, and ultimately extends to the SM intermediate coating, forming an obvious circular corrosion pits in the SM intermediate and $\text{Yb}_2\text{Si}_2\text{O}_7$ outer coatings. Compared with the $\text{Yb}_2\text{Si}_2\text{O}_7/\text{ASM}/\text{SiC}$ coated sample, due to the small crack width in the $\text{Yb}_2\text{Si}_2\text{O}_7$ outer coating, there is no $\text{Yb}_2\text{Si}_2\text{O}_7$ outer coating warping phenomenon, and no PO_x gas overflow to induce the destruction of the interface between SM intermediate coating and $\text{Yb}_2\text{Si}_2\text{O}_7$ outer coating.

Summarizing the analysis results in Figs. 28, 29, 30, 31, 32, 33 and 34, the protection and failure mechanism diagram of the tri-layer $\text{Yb}_2\text{Si}_2\text{O}_7/(\text{Mullite}, \text{SM}, \text{ASM})/\text{SiC}$ coated C/SiC sample in burner rig test is presented in Fig. 35. When the tri-layer coating sample is exposed to the leaching conditions on the burner rig test equipment, the coating surface is directly eroded by high-temperature and high-speed combustion gas, and the high-speed gas will exert a certain amount of physical stress on the $\text{Yb}_2\text{Si}_2\text{O}_7$ outer coating. Meanwhile, during thermal cycling, the sample undergoes multiple rapid cooling and heating processes at 1673 K-room temperature or room temperature-1673 K. A lot of thermal stress is generated in the three layer coating due to the CTE difference between the C/SiC matrix and the tri-layer coating or the each layer in the tri-layer coating. Under the interaction of thermal stress and physical eroding stress, many irregular micro-cracks appear in $\text{Yb}_2\text{Si}_2\text{O}_7$ outer coating and mullite intermediate coating due to their poor thermal cycling performance (Fig. 35a, b). The width of irregular micro-cracks is increased with the increase of thermal times. If the cracks increase to a certain extent, the coating will peel off. Moreover, the width and size of irregular cracks decrease continuously from the center to the edge position (Fig. 35b). A large amount of oxygen diffuses along the irregular cracks in $\text{Yb}_2\text{Si}_2\text{O}_7$ outer and mullite intermediate coatings to the SiC inner layer and continues to diffuse to C/SiC matrix along the micro-cracks in the SiC inner layer, and this can lead to serious oxidation in C/SiC composite samples.

However, the SiC whiskers ($4.5\text{--}5.5 \times 10^{-6}/\text{K}$) toughening phase reduces the difference in CTE between the mullite ($5\text{--}6 \times 10^{-6}/\text{K}$) and the $\text{Yb}_2\text{Si}_2\text{O}_7$ ($3.6\text{--}4.5 \times 10^{-6}/\text{K}$) coatings in the $\text{Yb}_2\text{Si}_2\text{O}_7/\text{SM}/\text{SiC}$ coating [29, 36, 37] and further reduces the possibility of crack formation caused by thermal stress (Eq. 25) [45]. Due to the addition of SiC whiskers with excellent mechanical properties, the thermal cycle performance of mullite middle coating is greatly improved, resulting in the increase and propagation of the micro-crack width in $\text{Yb}_2\text{Si}_2\text{O}_7$ top coating being restrained. Compared to the $\text{Yb}_2\text{Si}_2\text{O}_7/\text{Mullite}/\text{SiC}$ EBCs coated sample, after testing the sample through the same number of heating cycles, only small micro-cracks were detected in the SM intermediate and the $\text{Yb}_2\text{Si}_2\text{O}_7$ outer coatings, and there is no $\text{Yb}_2\text{Si}_2\text{O}_7$ outer coating fell off in coating coated sample (Fig. 35d). Only a small amount of

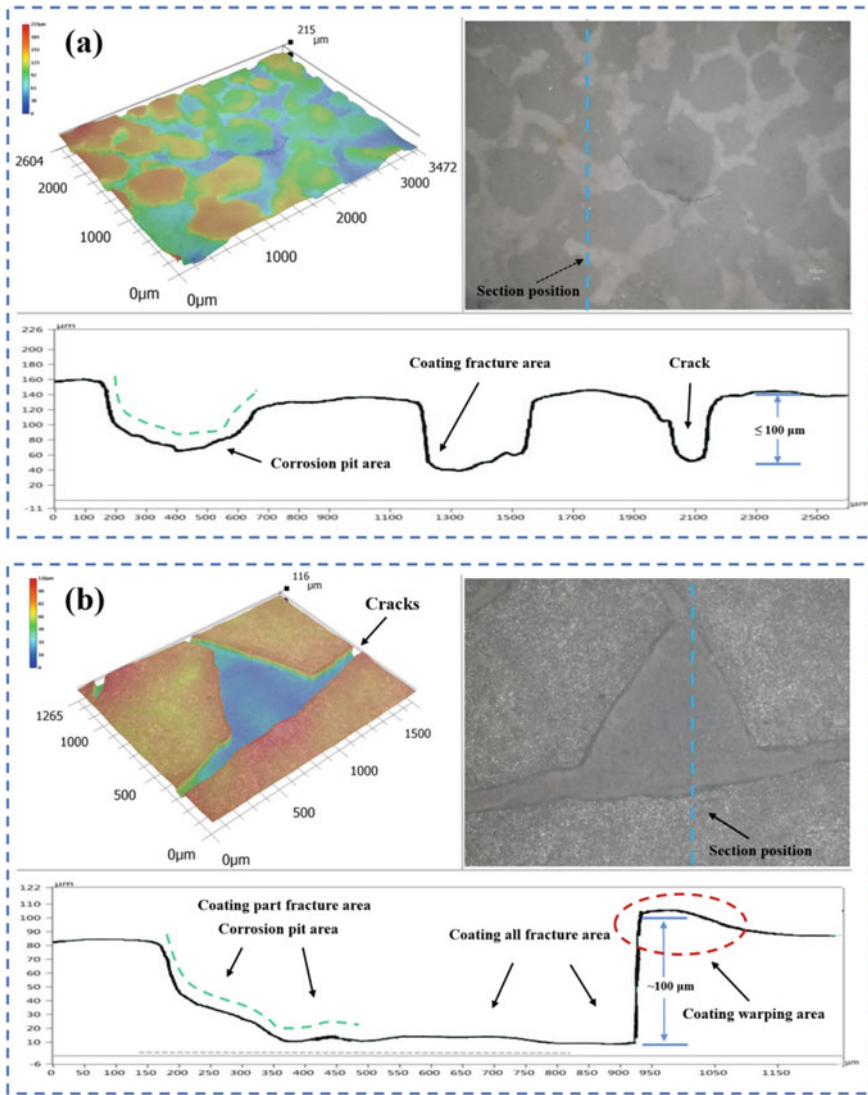


Fig. 34 Surface 3D morphology of tri-layer $Yb_2Si_2O_7/[Mullite (a), ASM (b)]/SiC$ coatings coated C/SiC sample after 24 thermal cycles, and $Yb_2Si_2O_7/SM/SiC$ (c) coated C/SiC sample after 36 thermal cycles at 1673 K

oxygen diffused to the composites substrate based on micro-cracks in the $Yb_2Si_2O_7/SM/SiC$ coating, resulting in a slight oxidation of the composites substrate.

After further adding the $c-AlPO_4$ bonding phase to the SM middle coating, only a few micro-cracks were detected in ASM middle coating due to $c-AlPO_4$ powder further improving the thermal cycle performance of SM middle coating. However,

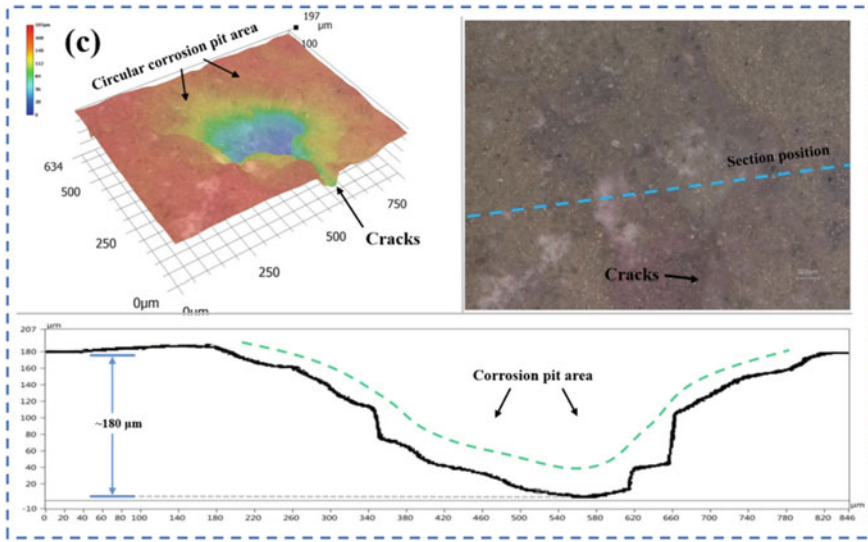


Fig. 34 (continued)

when oxygen diffuses along the small pores in the $Yb_2Si_2O_7$ outer coating to the ASM intermediate coating, SiC whiskers are oxidized to form molten SiO_2 and react with molten $c-AlPO_4$. Finally, when PO_x gas overflows, it becomes a secondary mullite. PO_x gas leaks when the crack width increases to a certain value, and it can increase the formation and expansion of cracks in the $Yb_2Si_2O_7$ outer coating. Due to the physical erosion of the high-temperature and high-speed combustion gases (Fig. 35f), the $Yb_2Si_2O_7$ outer coating in the contact between the ASM intermediate and $Yb_2Si_2O_7$ outer coating will fall off and bend outward.

$$\sigma_c = \frac{\Delta\alpha \cdot \Delta T \cdot E_c}{(1 - \nu_c^2)} \tag{25}$$

where, ν_c and E_c are the poisson ratio and elastic modulus of the outer coating; ΔT is the temperature difference; $\Delta\alpha$ is the CTE difference between the outer coating and the inner coating or substrate.

4 Conclusions and Outlook

1. The bi-layer Mullite/SiC, SM/SiC, ASM/SiC coatings and tri-layer $Yb_2Si_2O_7$ /Mullite/SiC, $Yb_2Si_2O_7$ /SM/SiC, $Yb_2Si_2O_7$ /ASM/SiC coatings were prepared by the CVD and a novel sol-gel method combined with air spraying process. The sol-gel method combined with air spraying process has been proved to

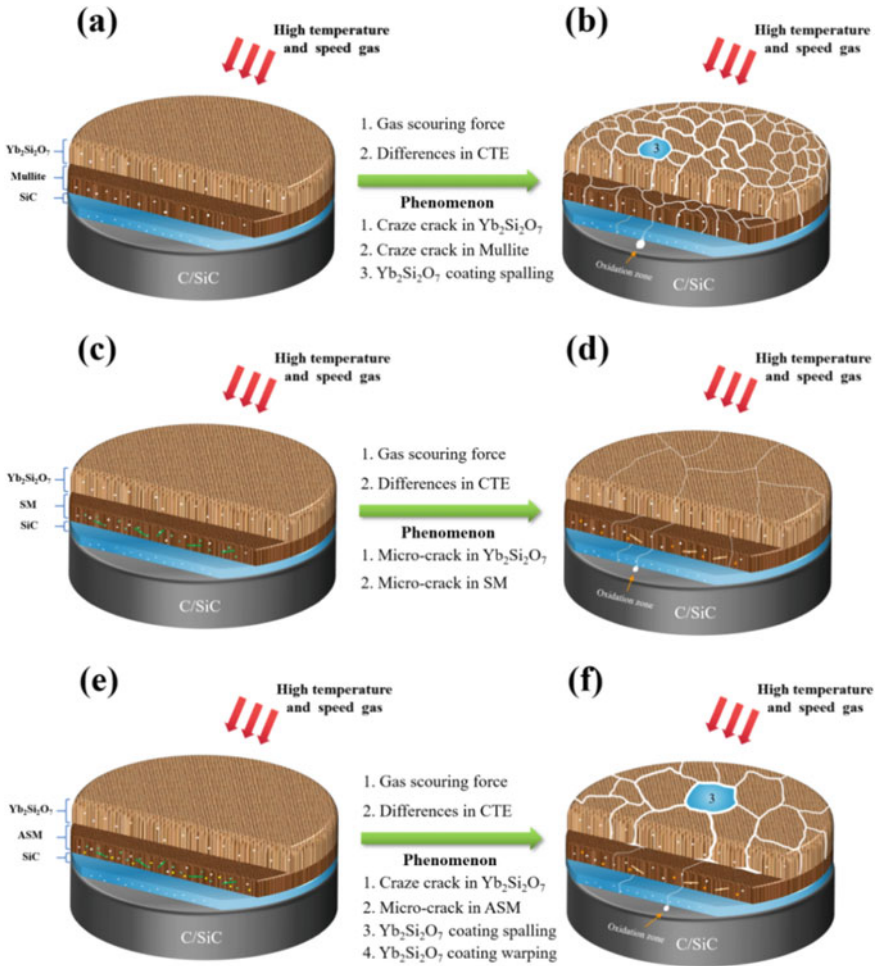


Fig. 35 The oxidation resistance and failure mechanism of the tri-layer Yb₂Si₂O₇/(Mullite, SM, ASM)/SiC coating coated C/SiC sample at 1673 K in the burner rig test

have the characteristics of high preparation efficiency and simple preparation process, which can meet the requirements of preparing uniform EBCs on large and complex components.

- In the isothermal oxidation test of the coating, the weight loss of bi-layer Mullite/SiC, SM/SiC, and ASM/SiC coating with 10, 20, 30, 40 wt.% *c*-AlPO₄ content coated C/SiC composites after the oxidation in the air for 100 h at 1773 K is $7.26 \times 10^{-3} \text{ g cm}^{-2}$, $18.07 \times 10^{-3} \text{ g cm}^{-2}$, $12.43 \times 10^{-3} \text{ g cm}^{-2}$, $3.66 \times 10^{-3} \text{ g cm}^{-2}$, $20.21 \times 10^{-3} \text{ g cm}^{-2}$, $29.99 \times 10^{-3} \text{ g cm}^{-2}$, respectively. After adding SiC_w into the mullite coating, the static oxidation resistance of mullite coating decreased, but the static oxidation resistance of SM coating first increased and then decreased

after further addition of *c*-AlPO₄ particles. The ASM/SiC coating sample with 10 wt.% SiC whisker and 20 wt.% *c*-AlPO₄ powder particles has the best oxidation resistance; the weight loss is only $6.29 \times 10^{-3} \text{ g cm}^{-2}$ after the oxidation in the air for 210 h at 1773 K. The weight loss of tri-layer Yb₂Si₂O₇/Mullite/SiC, Yb₂Si₂O₇/SM/SiC, Yb₂Si₂O₇/ASM/SiC coatings coated C/SiC composites after the oxidation in the air for 200 h at 1673 K is $2.84 \times 10^{-3} \text{ g cm}^{-2}$, $0.15 \times 10^{-3} \text{ g cm}^{-2}$, $2.53 \times 10^{-3} \text{ g cm}^{-2}$, respectively. The Yb₂Si₂O₇/SM/SiC coating sample has the best oxidation resistance owing to the healing effect of SiO₂ formed by oxidation of SiC_w and no gas phase waste generation.

3. In the burner rig test of the coating, the weight loss of bi-layer Mullite/SiC, SM/SiC, and ASM/SiC coating with 20 wt.% *c*-AlPO₄ content coated C/SiC composites after 240 min thermal cycles (16 times) at 1773 K is $38.49 \times 10^{-3} \text{ g cm}^{-2}$, $14.09 \times 10^{-3} \text{ g cm}^{-2}$, $5.59 \times 10^{-3} \text{ g cm}^{-2}$, respectively. The ASM/SiC coating has the best thermal cycle resistance to gas erosion environment due to the excellent mechanical properties of SiC whiskers and the bonding properties of *c*-AlPO₄ particles. The weight loss of tri-layer Yb₂Si₂O₇/Mullite/SiC, Yb₂Si₂O₇/SM/SiC, Yb₂Si₂O₇/ASM/SiC coatings coated C/SiC composites after 360 min thermal cycles (24 times) at 1673 K is $29.53 \times 10^{-3} \text{ g cm}^{-2}$, $6.19 \times 10^{-3} \text{ g cm}^{-2}$, $13.24 \times 10^{-3} \text{ g cm}^{-2}$, respectively. For tri-layer coating, although *c*-AlPO₄ particles improve the thermal cycle resistance of the SM middle layer, the generated PO_x waste gas is easy to cause cracks in the Yb₂Si₂O₇ outer coating.

The results in this paper show that the addition of SiC whiskers and *c*-AlPO₄ particles has different action mechanism on the static air environment oxidation resistance and thermal cycling performance of bi-layer and tri-layer environmental barrier coatings. In summary, in addition to having specific properties, the coating modification component shall not have any harmful chemical reaction with the coating itself and SiC matrix. Moreover, it is necessary to develop online testing and characterization means to more easily grasp the changes of the morphology, weight, structure, and phase compositions of the coating samples with the examination time, so as to more accurately understand and explain the performance evolution and failure mechanism of EBCs under the different examination environment.

Acknowledgements The authors gratefully acknowledge the financial support from the National Natural Science Foundation of China (Grant No. 52102122 and 12305304).

References

1. Ai, S.G., Song, W.L., Chen, Y.F.: Stress field and damage evolution in C/SiC woven composites: Image-based finite element analysis and in situ X-ray computed tomography tests. *J. Eur. Ceram. Soc.* **341**(4), 2323–2334 (2021). <https://doi.org/10.1016/j.jeurceramsoc.2020.12.026>
2. Song, C.K., Liu, Y.S., Ye, F., et al.: Enhanced mechanical property and tunable dielectric property of SiC_f/SiC-SiBCN composites by CVI combined with PIP. *J. Adv. Ceram.* **10**(4), 758–767 (2021). <https://doi.org/10.1007/s40145-021-0470-5>

3. Ma, D.H., Hou, Z.H., Li, J.P., et al.: Interface Type on the Static Mechanical Properties and Internal Friction of 3D-SiC/SiC Composites. *J. Inorg. Mater.* **36**(1), 55–60 (2021). <http://www.jim.org.cn/EN/10.15541/jim20200272>
4. Kumar, P., Srivastava, V.K.: Tribological behaviour of C/C–SiC composites—A review. *J. Adv. Ceram.* **5**(1), 1–12 (2016). <https://link.springer.com/article/10.1007/s40145-015-0171-z>
5. Zhang, J.M., Chen, X.W., Liao, C.J., et al.: Optimizing microstructure and properties of SiC_f/SiC composites prepared by reactive melt infiltration. *J. Inorg. Mater.* **36**(10) (2021) 1103–1110. <http://www.jim.org.cn/EN/10.15541/jim20210091>
6. Qian, Y.B., Zhang, X.G., Ge, M., et al.: Frictional response of a novel C/C–ZrB₂–ZrC–SiC composite under simulated braking. *J. Adv. Ceram.* **2**(2), 157–161 (2013). <https://link.springer.com/article/10.1007/s40145-013-0055-z>
7. Wang, Z., Wang, J.T., Song, H.W., et al.: Laser ablation behavior of C/SiC composites subjected to transverse hypersonic airflow. *Corros. Sci.* **183**, 109345 (2021). <https://doi.org/10.1016/j.corros.2021.109345>
8. Li, Y., Xiao, P., Luo, H., et al.: Fatigue behavior and residual strength evolution of 2.5D C/C–SiC composites. *J. Eur. Ceram. Soc.* **36**(16), 3977–3985 (2016). <https://doi.org/10.1016/j.jeurceramsoc.2016.07.009>
9. Wang, J., Cao, L.Y., Zhang, Y.H., et al.: Effect of mass transfer channels on flexural strength of C/SiC composites fabricated by femtosecond laser assisted CVI method with optimized laser power. *J. Adv. Ceram.* **10**(2), 227–236 (2021). <https://link.springer.com/article/10.1007/s40145-020-0433-2>
10. Ma, X.K., Yin, X.W., Fan, X.M., et al.: Evolution of mechanical and electromagnetic interference shielding properties of C/SiC during oxidation at 700 °C. *Carbon* **157**(2), 1–11 (2019). <https://doi.org/10.1016/j.carbon.2019.09.088>
11. Luo, L., Wang, Y.G., Liu, L., et al.: Ablation behavior of C/SiC composites in plasma wind tunnel. *Carbon* **103**, 73–83 (2016). <https://doi.org/10.1016/j.carbon.2016.02.085>
12. Cheng, L.F., Xu, Y.D., Zhang, L.T., et al.: Oxidation behavior of three dimensional C/SiC composites in air and combustion gas environments. *Carbon* **38**(15), 2103–2108 (2000). [https://doi.org/10.1016/S0008-6223\(00\)00068-3](https://doi.org/10.1016/S0008-6223(00)00068-3)
13. Yan, Z.Q., Xiang, X., Xiao, P., et al.: A multilayer coating of dense SiC alternated with porous Si–Mo for the oxidation protection of carbon/carbon silicon carbide composites. *Carbon* **46**(1), 149–153 (2008). <https://doi.org/10.1016/j.carbon.2007.10.035>
14. Chen, X.G., Zhang, H.M., Zhang, H.S., et al.: Ce_{1-x}Sm_xO_{2-x/2} -A novel type of ceramic material for thermal barrier coatings. *J. Adv. Ceram.* **5**(3), 244–252 (2016). <https://link.springer.com/article/10.1007/s40145-016-0196-y>
15. Niu, Z.B., Li, Z., Xiao, P., et al.: Influence of h-BN as additive on microstructure and oxidation mechanism of C/C–SiC composite. *J. Eur. Ceram. Soc.* **39**(15), 4634–4644 (2019). <https://doi.org/10.1016/j.jeurceramsoc.2019.06.032>
16. Kakisawa, H., Nishimura, T.: A method for testing the interface toughness of ceramic environmental barrier coatings (EBCs) on ceramic matrix composites (CMCs). *J. Eur. Ceram. Soc.* **38**(2), 655–663 (2018). <https://doi.org/10.1016/j.jeurceramsoc.2017.09.032>
17. Guo, L., Li, G., Gan, Z.L.: Effects of surface roughness on CMAS corrosion behavior for thermal barrier coating applications. *J. Adv. Ceram.* **10**(3), 472–481 (2021). <https://link.springer.com/article/10.1007/s40145-020-0449-7>
18. Sun, Y.N., Xiang, H.M., Dai, F.Z., et al.: Preparation and properties of CMAS resistant bixbyite structured high-entropy oxides RE₂O₃ (RE=Sm, Eu, Er, Lu, Y, and Yb): Promising environmental barrier coating materials for Al₂O₃f/Al₂O₃ composites. *J. Adv. Ceram.* **10**(3), 596–613 (2021). <https://link.springer.com/article/10.1007/s40145-021-0461-6>
19. Daniel, T.M., Chris, B., Tanvir, H.: A review on environmental barrier coatings: history, current state of the art and future developments. *J. Eur. Ceram. Soc.* **41**(3), 1747–1768 (2021). <https://doi.org/10.1016/j.jeurceramsoc.2020.10.057>
20. Xue, Y., Zhao, Y.L., An, Y.L., et al.: High-entropy (La_{0.2}Nd_{0.2}Sm_{0.2}Eu_{0.2}Gd_{0.2})₂Ce₂O₇: A potential thermal barrier material with improved thermo-physical properties. *J. Adv. Ceram.* **11**(4), 615–628 (2022). <https://link.springer.com/article/10.1007/s40145-021-0563-1>

21. Kang, N.L., Fox, D.S., Bansal, N.P.: Rare earth silicate environmental barrier coatings for SiC/SiC composites and Si₃N₄ ceramics. *J. Eur. Ceram. Soc.* **25**(10), 1705–1715 (2005). <https://doi.org/10.1016/j.jeurceramsoc.2004.12.013>
22. Fan, W.Q., Song, X.M., Huang, Y.L., et al.: Structure change and phase transition distribution of YSZ coating caused by CMAS corrosion. *J. Inorg. Mater.* **36**(10), 1059–1066 (2021). <http://www.jim.org.cn/EN/10.15541/jim20210013>
23. Kang, N.L., Miller, R.A.: Development and environmental durability of mullite and mullite/YSZ dual layer coatings for SiC and Si₃N₄ ceramics. *Surf. Coat. Tech* **86–87**, 142–148 (1996). [https://doi.org/10.1016/S0257-8972\(96\)03074-5](https://doi.org/10.1016/S0257-8972(96)03074-5)
24. Cojocaru, C.V., Kruger, S.E., Moreau, C., et al.: Elastic modulus evolution and behavior of Si/Mullite/BSAS-based environmental barrier coatings exposed to high temperature in water vapor environment. *J. Therm. Spray. Technol.* **20**(1–2), 92–99 (2011). <https://link.springer.com/article/10.1007/s11666-010-9599-4>
25. Cojocaru, C.V., Lévesque, D., Moreau, C., et al.: Performance of thermally sprayed Si/mullite/BSAS environmental barrier coatings exposed to thermal cycling in water vapor environment. *Surf. Coat. Tech.* **216**, 215–223 (2013). <https://doi.org/10.1016/j.surfcoat.2012.11.043>
26. Rohbeck, N., Morrell, P., Xiao, P.: Degradation of ytterbium disilicate environmental barrier coatings in high temperature steam atmosphere. *J. Eur. Ceram. Soc.* **39**(10), 3153–3163 (2019). <https://doi.org/10.1016/j.jeurceramsoc.2019.04.034>
27. Bakan, E., Sohn, Y.J., Kunz, W., et al.: Effect of processing on high-velocity water vapor recession behavior of Yb-silicate environmental barrier coatings. *J. Eur. Ceram. Soc.* **39**(4), 1507–1513 (2019). <https://doi.org/10.1016/j.jeurceramsoc.2018.11.048>
28. Tian, Z.L., Ren, X.M., Lei, Y.M., et al.: Corrosion of RE₂Si₂O₇ (RE=Y, Yb, and Lu) environmental barrier coating materials by molten calcium-magnesium-alumino-silicate glass at high temperatures. *J. Eur. Ceram. Soc.* **39**(14), 4245–4254 (2019). <https://doi.org/10.1016/j.jeurceramsoc.2019.05.036>
29. Chen, P.J., Xiao, P., Li, Z., et al.: Water vapor corrosion behavior and failure mechanism of air sprayed bi-layer Yb₂Si₂O₇/SiC and tri-layer Yb₂Si₂O₇/ (SiC_w-Mullite)/SiC environmental barrier coating. *Adv. Pow. Mater* **2**(1), 100064 (2022). <https://doi.org/10.1016/j.apmate.2022.100064>
30. Richards, B.T., Wadley, H.N.G.: Plasma spray deposition of tri-layer environmental barrier coatings. *J. Eur. Ceram. Soc.* **34**(12), 3069–3083 (2014). <https://doi.org/10.1016/j.jeurceram soc.2014.04.027>
31. Zhang, Z.F., Zhou, K.S., Liu, M., et al.: Preparation of Si/Mullite/Yb₂Si₂O₅ environment barrier coating (EBC) by plasma spray-physical vapor deposition (PS-PVD). *J. Inorg. Mater.* **33**(3), 325–330 (2018). <http://www.jim.org.cn/EN/10.15541/jim20170194>
32. Nasiri, N. A., Patra, N., Horlait, D., et al. Thermal properties of rare-earth monosilicates for EBC on Si-based ceramic composites. *J. Am. Ceram. Soc.* **99**, 589–596 (2015). <https://ceramics.onlinelibrary.wiley.com/doi/10.1111/jace.13982>
33. Wang, Y.Q., Liu, J.L.: First-principles investigation on the corrosion resistance of rare earth disilicates in water vapor. *J. Eur. Ceram. Soc.* **29**(11), 2163–2167 (2009). <https://doi.org/10.1016/j.jeurceramsoc.2009.02.005>
34. Maier, N., Nickel, K.G., Rixecke, G.: High temperature water vapour corrosion of rare earth disilicates (Y, Yb, Lu)₂Si₂O₇ in the presence of Al(OH)₃ impurities. *J. Eur. Ceram. Soc.* **27**(7), 2705–2713 (2007). <https://doi.org/10.1016/j.jeurceramsoc.2006.09.013>
35. Turcer, L.R., Padture, N.P.: Towards multifunctional thermal environmental barrier coatings (TEBCs) based on rare-earth pyrosilicate solid-solution ceramics. *Scripta Mater.* **154**, 111–117 (2018). <https://doi.org/10.1016/j.scriptamat.2018.05.032>
36. Chen, P.J., Pan, L., Xiao, P., et al.: Microstructure and anti-oxidation properties of Yb₂Si₂O₇/SiC bilayer coating for C/SiC composites. *Ceram. Int.* **45**(1), 854–860 (2019). <https://doi.org/10.1016/j.ceramint.2019.08.132>
37. Chen, P.J., Xiao, P., Li, Z., et al.: Microstructure and oxidation behavior of a novel bilayer (c-AlPO₄-SiC_w-mullite)/SiC coating for carbon fiber reinforced CMCs. *J. Eur. Ceram. Soc.* **39**(14), 3988–3999 (2019). <https://doi.org/10.1016/j.jeurceramsoc.2019.06.026>

38. Chen, P.J., Xiao, P., Li, Z., et al.: Bonding strength and thermal shock resistance of a novel bilayer (c-AlPO₄-SiC_w-mullite)/SiC coated carbon fiber reinforced CMCs. *J. Am. Ceram. Soc.* **103**(1), 82–93 (2020). <https://ceramics.onlinelibrary.wiley.com/doi/10.1111/jace.16697>
39. Song, X.M., Meng, F.L., Kong, M.G., et al.: Relationship between cracks and microstructures in APS YSZ coatings at elevated temperatures. *Mater Charact.* **131**, 277–284 (2017). <https://doi.org/10.1016/j.matchar.2017.07.008>
40. Su, L.C., Yi, C.H.: Effects of CMAS penetration on the delamination cracks in EB-PVD thermal barrier coatings with curved interface. *Ceram. Int.* **43**(12), 8893–8897 (2013). <https://doi.org/10.1016/j.ceramint.2017.04.025>
41. Pu, D.M., Chen, P.J., Xiao, P., et al.: Oxidation and thermal cycling behavior of c-AlPO₄ and SiC whisker co-modified mullite deposited on SiC-C/SiC composites. *Surf. Coat. Tech.* **400**, 126201 (2020). <https://doi.org/10.1016/j.surfcoat.2020.126201>
42. Qi, Z., Lv, X.X., Zhao, W.Q., et al.: BN/SiC coating on SiC tows prepared by chemical vapor infiltration. *Mater. Sci. Eng.* **678**, 012062 (2019)
43. Pu, D.M., Chen, P.J., Xiao, P., et al.: Microstructure evolution and isothermal oxidation properties of c-AlPO₄ and SiC whisker co-modified mullite coated SiC-C/SiC composites. *Ceram. Int.* **45**(16), 20704–20713 (2019). <https://doi.org/10.1016/j.ceramint.2019.07.054>
44. Wen, Z.L., Xiao, P., Li, Z., et al.: Thermal cycling behavior and oxidation resistance of SiC whisker-toughened-mullite/SiC coated carbon/carbon composites in burner rig tests. *Corros. Sci.* **106**, 179–187 (2016). <https://doi.org/10.1016/j.corsci.2016.02.003>
45. Jana, P., Jayan, P.S., Mandal, S., et al.: Thermal cycling life and failure analysis of rare earth magnesium hexaaluminate based advanced thermal barrier coatings at 1400 °C. *Surf. Coat. Tech.* **328**, 398–409 (2017). <https://doi.org/10.1016/j.surfcoat.2017.09.019>
46. Chen, S.A., Chen, P.J., Duan, J.J., et al.: Thermal cycling behavior of bi-layer Yb₂Si₂O₇/SiC EBC-coated C₇/SiC composites in burner rig tests. *Adv. Compos. Hybrid. Mater.* **5**, 2184–2192 (2022). <https://link.springer.com/article/10.1007/s42114-021-00270-9>
47. Smialek, J.L., Cuy, M.D., Harder, B.J., et al.: Durability of YSZ coated Ti₂AlC in 1300°C high velocity burner rig tests. *J. Am. Ceram. Soc.* **103**(12), 7014–7030 (2020). <https://ceramics.onlinelibrary.wiley.com/doi/10.1111/jace.17154>
48. Chen, P.J., Xiao, P., Li, Z., et al.: Thermal cycling behavior of La₂Zr₂O₇/Yb₂Si₂O₇/SiC coated PIP C₇/SiC composites under burner rig tests. *J. Eur. Ceram. Soc.* **41**(7), 4058–4066 (2021). <https://doi.org/10.1016/j.jeurceramsoc.2021.02.005>
49. Morelli, S., Testa, V., Bolelli, G., et al.: CMAS corrosion of YSZ thermal barrier coatings obtained by different thermal spray processes. *J. Eur. Ceram. Soc.* **40**(12), 4084–4100 (2020). <https://doi.org/10.1016/j.jeurceramsoc.2020.04.058>
50. Wang, T.X., Shao, F., Ni, J.X., et al.: Corrosion behavior of air plasma spraying zirconia-based thermal barrier coatings subject to Calcium-Magnesium-Aluminum-Silicate (CMAS) via burner rig test. *Ceram. Int.* **46**(11), 18698–18706 (2020). <https://doi.org/10.1016/j.ceramint.2020.04.184>
51. Zhou, W., Long, Y.: Mechanical properties of CVD-SiC coatings with Si impurity. *Ceram. Int.* **44**(2), 21730–21733 (2018). <https://doi.org/10.1016/j.ceramint.2018.08.266>
52. Wang, K.T., Wang, L.Y., Huang, J.F., et al.: Microstructure and oxidation resistance of C-AlPO₄-mullite coating prepared by hydrothermal electrophoretic deposition for SiC-C/C composites. *Ceram. Int.* **39**(2), 1037–1044 (2013). <https://doi.org/10.1016/j.ceramint.2012.07.024>
53. Jiang, Y., Chang, L.F., Ru, H.Q.: Microstructure and oxidation behaviors of dense mullite-silicon carbidesilicon coating for graphite fabricated by dipping-pyrolysis and reactive infiltration. *Surf. Coat. Tech.* **350**, 410–418 (2018). <https://doi.org/10.1016/j.surfcoat.2018.07.041>
54. Lei, Z., Huang, J.F., Haibo, O.Y., et al.: In-situ mullite whisker to improve the thermal shock resistance of silicate glass coating for SiC coated carbon/carbon composites. *J. Alloy. Compd.* **712**, 288–295 (2017). <https://doi.org/10.1016/j.jallcom.2017.03.205>
55. Zhou, W., Xiao, P., Luo, W., et al.: Microstructural evolution of SiC coating on C/C composites exposed to 1500 °C in ambient air. *Ceram. Int.* **45**(1), 854–860 (2019). <https://doi.org/10.1016/j.ceramint.2018.09.255>

56. Fang, Y.C., Cui, X.F., Jin, G., et al.: Influence of SiC fiber on thermal cycling lifetime of SiC fibers /YSZ thermal barrier coatings by atmospheric plasma spraying. *Ceram. Int.* **44**(15), 18285–18293 (2013). <https://doi.org/10.1016/j.ceramint.2018.07.040>
57. Ma, F.J., Huang, C.Z., Niu, J.H., et al.: Toughening mechanisms of Al₂O₃-matrix composites with SiC whiskers. *Ceram. Int.* **48**(15), 17556–17563 (2022). <https://doi.org/10.1016/j.ceramint.2022.03.021>
58. Luo, Y., Zheng, S.L., Ma, S.H., et al.: Mullite-bonded SiC-whisker-reinforced SiC matrix composites: preparation, characterization, and toughening mechanisms. *J. Eur. Ceram. Soc.* **38**(16), 5282–5293 (2018). <https://doi.org/10.1016/j.jeurceramsoc.2018.08.022>
59. Fu, Q.G., Li, H.J., Hong, S.X., et al.: A SiC whisker-toughened SiC-CrSi₂ oxidation protective coating for carbon/carbon composites. *Appl. Surf. Sci.* **3253**(8), 3757–3760 (2007). <https://doi.org/10.1016/j.apsusc.2006.07.092>
60. Fan, X.Y., Sun, R.J., Dong, J., et al.: Fabrication and thermal shock behavior of Si₃N₄ whiskers toughened γ -Y₂Si₂O₇ coating on porous Si₃N₄ ceramics. *Ceram. Int.* **46**(13), 21681–21688 (2020). <https://doi.org/10.1016/j.ceramint.2020.05.275>
61. Li, S., Wei, C.C., Wang, P., et al.: Fabrication of ZrO₂ whisker modified ZrO₂ ceramics by oscillatory pressure sintering. *Ceram. Int.* **46**(11), 17684–17690 (2020). <https://doi.org/10.1016/j.ceramint.2020.04.071>
62. Chen, P.J., Xiao, P., Tang, X., et al.: Corrosion behavior and failure mechanism of SiC whisker and *c*-AlPO₄ particle-modified novel tri-layer Yb₂Si₂O₇/mullite/SiC coating in burner rig tests. *J. Adv. Ceram.* **11**(12), 1901–1917 (2022). <https://link.springer.com/article/10.1007/s40145-022-0655-6>

Space Environment Effects on Advanced Ceramic Coating for Aerospace Thermal-Proof Re-entry Systems



Roberto Pastore, Andrea Delfini, Marta Albano, Fabio Santoni, Fabrizio Piergentili, and Mario Marchetti

Abstract Advanced carbon-based composites, such as carbon/carbon (C/C) or carbon/silicon carbide (C/SiC), are ceramics matrix composites (CMC) employed in aerospace industry for thermal protection systems (TPS) to face the dramatic thermo-mechanical stress suffered by spacecraft structures during re-entry into Earth atmosphere. A branch of current aerospace research is focused in finding ever more effective coating solutions to preserve CMCs from oxidation due to prolonged exposure of the spacecraft surfaces to low Earth orbit (LEO) environment: in long-time missions, in fact, this may lead to so high TPS damaging that its main thermo-mechanical functionality (i.e., withstanding re-entry conditions) would be compromised. This chapter gives an overview of the experimental activity developed during recent years at the Aerospace Systems Laboratory (LSA) of Sapienza University of Rome about the study of C/C materials for protecting aerospace structures from thermal shock in re-entry missions. In particular, advanced coating treatments using ceramic-based (SiC-Al₂O₃-ZrO₂) refractory varnishes, even reinforced by ceramic filling nanoparticles (SiO₂ powder), are analyzed by space environment simulation ground-testing: in particular, the activity currently performed by means of LSA dedicate facilities concerns the reproduction of LEO aggressive aging in terms of atomic oxygen/UV irradiation, thermal cycling, and high-temperature ultra-high vacuum conditions.

Keywords Ceramic coating · Carbon/Carbon materials · Space environment simulation · Thermo-mechanical stress · Atomic oxygen · Outgassing

R. Pastore (✉) · A. Delfini · F. Santoni · M. Marchetti
Department of Astronautics, Electric and Energy Engineering, Sapienza University of Rome, Via Salaria 851, 00138 Rome, Italy
e-mail: roberto.pastore@uniroma1.it

M. Albano
Italian Space Agency, Via del Politecnico Snc, 00133 Rome, Italy

F. Piergentili
Department of Mechanical and Aerospace Engineering, Sapienza University of Rome, Via Eudossiana 18, 00184 Rome, Italy

1 Introduction

From the commencement of the Space Age, the re-entry phase has been a crucial element for both manned and unmanned aerospace missions. This is due to the harsh thermo-mechanical stress experienced by spacecraft upon entering the atmosphere, which can result in loss of mass (ablation) or even complete disintegration of structures. The development of space missions that include re-entry into the atmosphere necessitates low-cost routines for accessibility to space. Reusable integrated systems give the possibility to extend the range of services by increasing the annual mission rate, which can be short or long term (even several months).

Prolonged living in space raises the issue of spacecraft structures aging, particularly for space structures operating in long-term missions within low Earth orbit (LEO) regions. These regions are characterized by ultra-high vacuum and large thermal oscillations, which cause outgassing from the exposed surfaces, the presence of atomic oxygen (AtOx), high-energy ultraviolet (UV) radiation, and other phenomena that can cause critical degradation of material performance. Therefore, the development of re-entry missions requires the outgrowth of reusable integrated systems that can deal with harsh space environmental conditions during both the re-entry and on-orbit phase [1–6].

Advanced carbon-based composites such as carbon/carbon (C/C) or carbon/silicon carbide (C/SiC) are ceramics matrix composites (CMC) that are used in the aerospace industry to address the critical thermo-mechanical stress experienced by spacecraft structures during re-entry into Earth's atmosphere. These materials prove to be highly stable at extreme temperatures due to a very low thermal expansion, making them ideal candidates for reusable space integrated components such as thermal protection systems (TPS), nozzle throats, and ablation thermal-proof structures [7–12].

However, the continuous and extended exposure of spacecraft surfaces to a damaging oxidative environment must be carefully considered for long-term missions. LEO working conditions, in particular, induce ceramic material aging due to combined effects of severe vacuum thermal cycles and harsh UV/AtOx irradiation. Such inconveniences may impede the use of C/C as a re-entry protection material since significant surface oxidation may lead to TPS degradation that compromises the thermo-mechanical functionality to be exploited during re-entry phase partially or even fully [13–18]. Oxidation in CMCs may result in different damaging. Typically, the fiber/matrix interface is attacked, resulting in delamination cracking between plies. However, at high temperatures, a more tough oxidation attack occurs within the fiber bundles, causing cross-bundle cracking. The fracture behavior and, therefore, the crack propagation due to increasing temperature and harsh environment are drawbacks that need to be taken into account and deeply analyzed. Thus, it is mandatory to preserve the CMC exposed surface from both oxidation and erosion.

Currently, the application of thin coating films on composite materials is a technique of strategic relevance for several industrial fields. Thin films are employed for a variety of technological solutions, such as insulation layers for cabling and

fiberglass, processing of space components and so on. Alongside, a number of methodologies have been developed for coatings composition and surface application, such as ceramic layering applied by pack cementation, reaction sintering, matrix impregnation and pyrolysis, or surface deposition treatments [19–24].

Particularly in the aerospace sector, coating design and thickness optimization, as well as the knowledge of the impact on its effectiveness due to the environmental aging (in particular to thermo-mechanical loads, outgassing, UV and atomic oxygen exposure) represent basic requirements. The coating's effectiveness depends on its continuity, porosity, degree of adhesion to the substrate, and resistance to the operating conditions. Beyond the technical reasons, factors such as cost or convenience of treatment in relation to aspects related to maintenance and reparability are fundamental in the selection of a specific coating for any given aerospace application.

In the present chapter, the scientific activity developed during last years at the Aerospace Systems Laboratory (LSA) of Sapienza University of Rome is summarized, highlighting the research aimed at developing surface coatings on materials and structures for space applications (i.e., on vehicles for atmospheric re-entry and orbital stationing) [6, 11, 12, 20, 21, 25–27]. In particular, advanced coating treatments using ceramic-based ($\text{SiC}-\text{Al}_2\text{O}_3-\text{ZrO}_2$) refractory varnishes, even reinforced by ceramic filling nanoparticles (SiO_2 powder), were proposed to preserve C/C ceramic substrates, such material being widely studied as bulk TPS core constituent. The experimental characterization was performed by means of the several LSA ground-testing facilities available, which are able to simulate the space aging effects on materials by reproducing LEO aggressive conditions in terms of AtOx/UV irradiation, thermal cycling, and high-temperature/ultra-high vacuum environment. Tackling this task should be of aid for improving the design of spacecraft protective systems, with particular regard to CMC-based advanced TPS for re-entry vehicles and, more generally, for applications in large space structures—as, for example, the ISS—operating in long-term missions within LEO regions. Hierarchical carbon-based ceramic structures are expected to be successfully used for aerospace applications, providing the multi-functional behavior (i.e., bulk thermo-mechanical strength and surface shielding from aging agents) mandatory for being compliant with the severe long-term/re-entry mission requirements.

2 Materials

2.1 Ceramic Substrates

C/C composites are a type of engineered ceramics that utilize a dense graphitic matrix interspersed with carbon fiber plies. Further components may also be incorporated in particulate or fibrous form. These composites can be customized by adjusting the fiber arrangement and/or the matrix densification process, resulting in a wide range

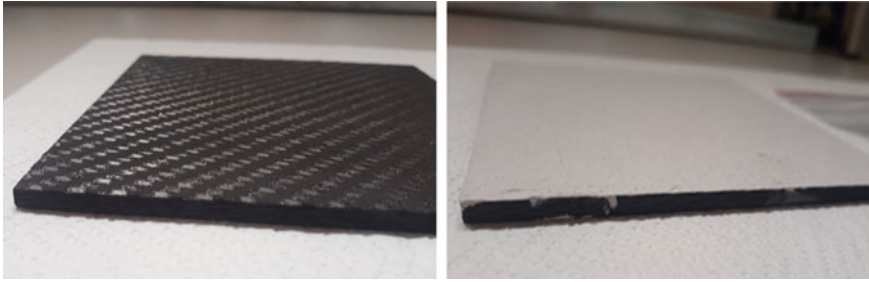


Fig. 1 C/C-based specimens: naked square slab (left), sample coated by Pyro-paint 634 ALP thin film (right). [26]

of products. C/C materials and components are designed simultaneously to optimize the composite properties and enhance the performance of the components. The optimal thermal resistance and stability of carbon/carbon ceramics, as well as their ability to provide mechanical properties competitive or better than heavier materials at high temperatures, establish such materials as very promising for aerospace applications. This is due to the coupling of a relatively lightweight (density 1.4–1.8 g/cm³) with significant strength, stiffness, fracture toughness, frictional properties, thermal conductivity, and resistance to oxidation.

The physical and chemical evolution that occurs during the processing phase affect the ultimate properties of a C/C composite: that is particularly inherent to the fiber–matrix bonding and the differential dimensional changes related to heat treatment and consequent thermal stresses. Weak fiber–matrix interfaces are advantageous because they allow matrix cracking without propagating through the fibers, which can continue to carry high loads. Strong interfaces produce brittle composites with low strengths in the fiber directions.

Commercial C/C slabs [Mitsubishi Chemical Carbon Fiber and Composites] with density of 1.437 g/cm³ were considered as main substrate material of hybrid structures to be characterized by space environment simulation testing. The pristine items were cut by water-jet technique to obtain a wide range of specimens suite for any specific test, such as thin square plates for thermal properties analysis (Fig. 1) or small pieces for exposure to harsh agents ground-test (Figs. 2 and 3); all the samples were pre-conditioned in high vacuum atmosphere ($\sim 10^{-5}$ mbar) for 8–12 h before every treatment and application, with the aim of removing pollutants and prevent unwanted effects of moisture.

2.2 Ceramic Coating

Commercial varnishes were analyzed for coating treatments, and a ceramic nanopowder was considered as supplementary filler. The family of materials adopted for the coating treatment is a series of “Pyro-paint” liquid-based solvents [Aremco

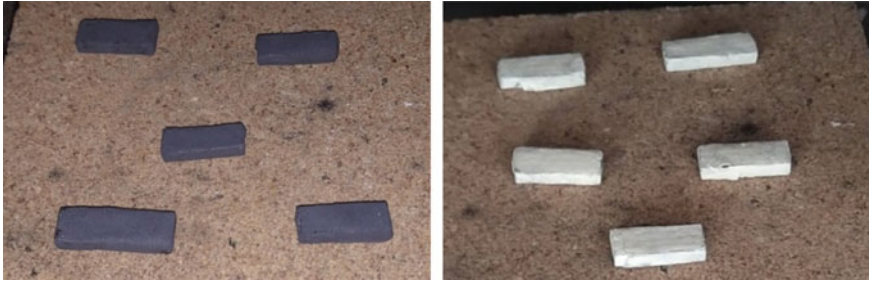
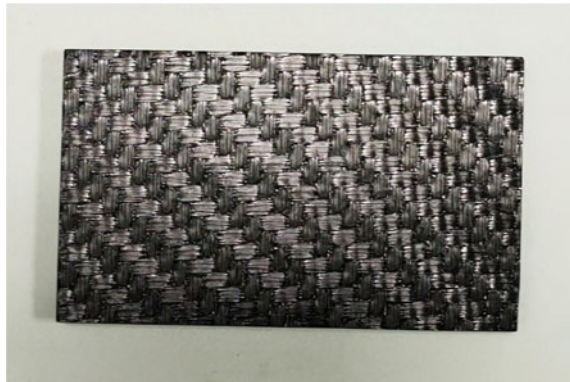


Fig. 2 Coated C/C small specimens (left—SiC-based Pyro-paint varnish; right—ALP-based Pyro-paint varnish) prepared for CTE and outgassing measurements. [25]

Fig. 3 Naked C/C small specimens dimensioned for AtOx/UV exposure test



Products Inc.], which can be employed in conditions characterized by operative temperatures up to 1800 °C. Using these items was suggested by a state-of-the-art analysis conducted on materials providing advanced thermal behavior: such components are frequently adopted where the requirement of safeguarding C/C surfaces up to 1600 °C has to be addressed. The characteristics of three selected products are given hereafter, as from technical data sheets: (i) Pyro-paint 634 ALP: white odorless varnish composed by Al₂O₃ at 70 wt% and AlPO₄ at 25 wt%, with a remaining 5 wt% of water, high abrasion and corrosion resistance for working temperatures up to 1760 °C; (ii) Pyro-paint 634 SiC: grey odorless varnish composed by SiC at 60 wt%, AlPO₄ at 20 wt% and Al₂O₃ at 10 wt% with a remaining 10wt% of water, oxidation resistance improved by silicon carbide single part at 1400 °C; (iii) Pyro-paint 634 ZO: white odorless varnish composed by ZrO₂ at 50 wt%, aluminum silicate (20 wt%), silicate solution (20 wt%) and water (10 wt%), oxidation resistant coating on carbon provided by zirconium oxide single part up to 1800 °C.

The varnishes were modified by adding up to 1 wt% of nanospheres made of silicon oxide [Sigma-Aldrich Co.]. The average diameter of the spheres is 12 nm, and their surface area ranges from 175 to 225 m²/g. The nanoparticles were mechanically mixed with the varnishes, as silica nanomaterials are commonly used to reduce

thermal conductivity and improve insulation. Although many studies have been conducted on this issue, new types of ceramic-based coatings still require laboratory validation. The use of nanoparticles is expected to be useful in improving the mechanical characteristics of the coating and increasing the life of the underlying structure. To ensure the homogeneity of the specimens, the as-prepared solutions were brushed onto C/C substrates in a fixed amount, leveling the treated surfaces to obtain a uniform layered 0.5-mm-thick coating for all the specimens. It is worth noting that the final coating thickness is not affected by the inclusion of nanoparticles, until the limit of particles blending inside the varnish is not exceeded. A maximum of 1% was considered to achieve good mixing, proper brushing, and optimal coating infiltration in the substrate bulk. The curing phase included two hours in air at room temperature, two hours in oven at 98 °C, and one hour in oven at 427 °C (except for the ZO-based treatment).

3 Experimental Setup

3.1 Thermal Characterization

The first analysis of the thermal behavior of the materials under test was carried out by measuring the linear coefficient of thermal expansion (CTE), which was carried out by means of a dedicate facility according to ASTM E228D standard. The adopted horizontal dilatometer L75HX1600 is equipped by an outer tube which constitutes the thermal conditioning chamber, including the sample housing and a pushrod (Fig. 4). The temperature range of the facility is RT-1600 °C; the measuring head, connected to the pushrod, records the sample linear expansion which is used for data processing and CTE evaluation. The adopted facility is worthwhile for an effective evaluation of materials envisaged to be used for aerospace applications: compared to usual optical sensor-based devices, in fact, such experimental setup is expected to simulate the thermo-mechanical loads experienced by a component integrated within the whole spacecraft structure, thus providing reliable results about the actual response of structures during thermal cycles or after sharp temperature raising. A thermal cycle is defined as any recursive thermal test in which the temperature is regularly altered, touching high–low temperature peaks, usually at increasing rates of variation. It is an environmental stress test used in evaluating product reliability as well as in manufacturing to catch early-term and latent defects by inducing failure through thermal fatigue. A single thermal cycle is considered complete when the temperature returns to the starting values, but in most tests, the procedure must be repeated a minimum number of times to obtain the desired results. Main purpose of the test is to perform a thermal balance for space qualification as described in the reference ECSS standard. The adopted equipment consists basically in a small vacuum chamber able to accommodate thin slabs, which are kept in contact to the thermal control components (Fig. 5). The pumping system (rotary pump Edwards



Fig. 4 CTE measurement setup: dilatometer L75HX1600 in closed configuration, device display showing sample and furnace temperatures, pushrod/sample (left—SiC; right—ALP) arrangement before the test. [26]

XDS 10, turbo-molecular pump Edwards TC-600) allows to reach a vacuum level down to 10^{-5} mbar, while thermal oscillations up to ± 150 °C are obtained by means of resistive heaters and liquid nitrogen cooling system. The tests on coated CMCs were carried out considering the thermal range -60 °C/ $+90$ °C with ten minutes of static stage (dwell time) at the target temperatures and a gradient of 2.5 °C/min (single cycle length: two hours and twenty minutes). Five cycles were conducted in the vacuum chamber (pressure around 1.5×10^{-5} mbar). The working parameters—i.e., temperatures, gradient, and dwell time—were selected to reproduce the real orbital conditions for a standard cube-sat mission.

3.2 Outgassing Test

LSA's outgassing test facility (OTF) provides the capability to perform testing of space materials in accordance with outgassing ASTM and ECSS standards. The test method is a screening technique that determines the volatile content of materials exposed to vacuum environments at high temperatures. The equipment includes a vacuum chamber (Fig. 6) that can achieve pressures as low as 10^{-5} mbar using a rotary/turbo-molecular pumping system. The chamber includes two metallic grids facing each other. The first is a copper plate that acts as samples housing and is connected to the warming system used to increase the temperature of the chamber to 125 °C. The second is an aluminum–chromium-coated plate that acts as a collector

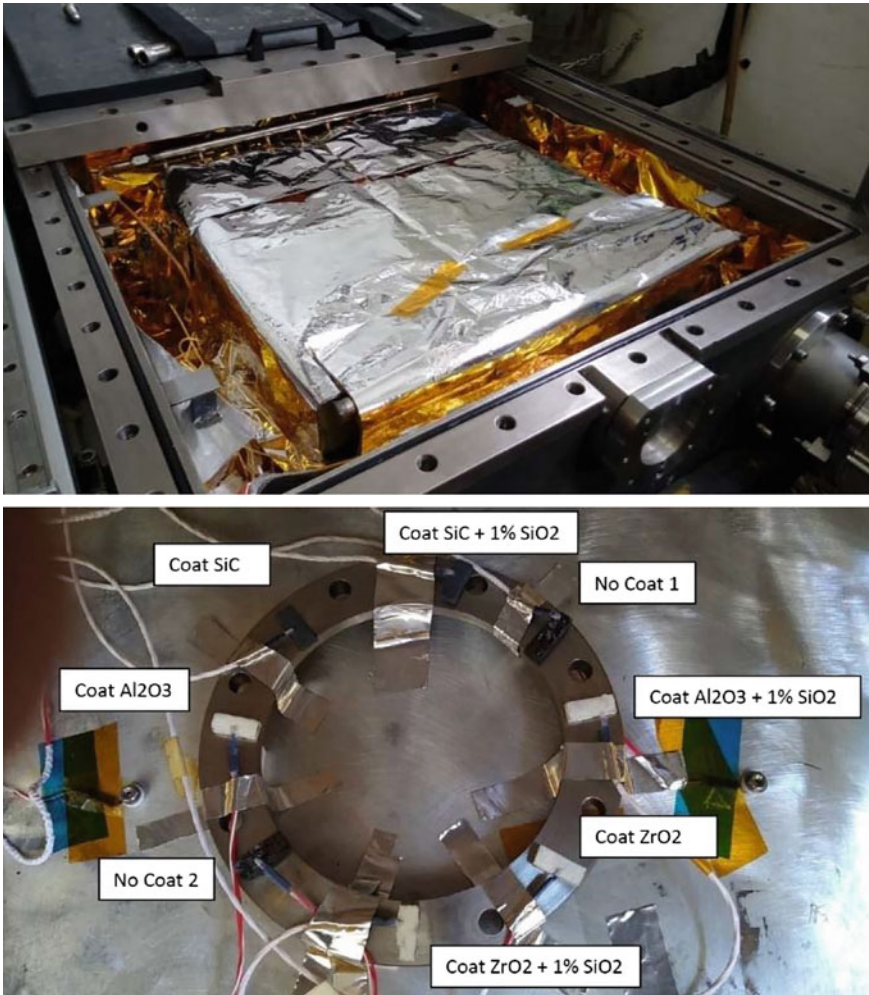


Fig. 5 Thermal cycling test setup and coated C/C specimen arrangement within the chamber. [27]

box and can be maintained at 25 °C by an oil cooling chiller system. The outgassing properties of a sample is established by measuring the mass loss by vaporization from the specimen's surface and the amount of matter re-condensed on the corresponding collector. Weights are evaluated using a Mettler-Toledo XP26DR facility, which allows to appreciate mass variation in the micrograms range. The whole outgassing equipment is set within an ISO-7 certified clean room where all test operations are conducted.

Prior to be placed into the OTF, every specimen is maintained under controlled atmosphere for 24 h (23 °C, RH 50%, standard room pressure) to eliminate possible

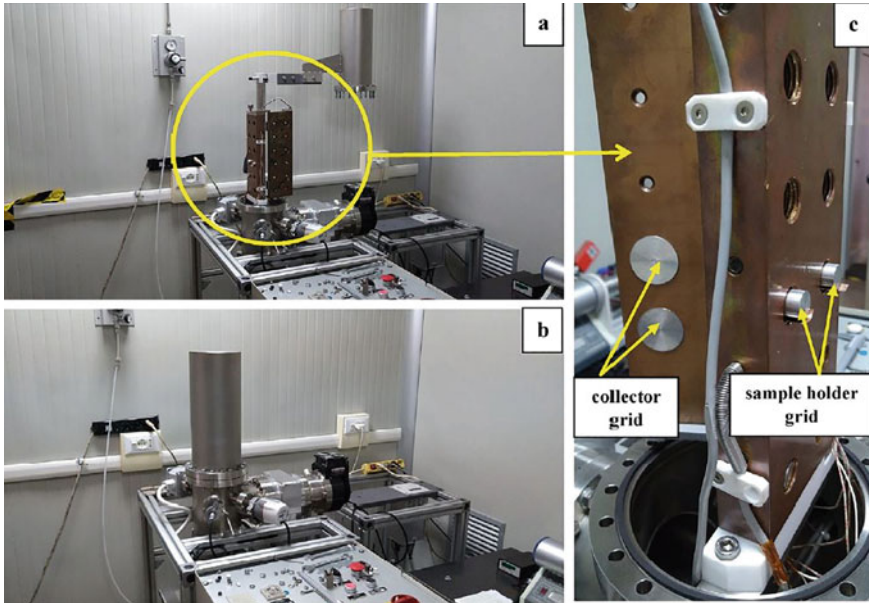


Fig. 6 Outgassing facility inside ISO-7 certified clean room @ LSA: **a** open configuration (specimens fixing and removing), **b** closed configuration (running test), **c** particular of the inner hot and cold plates. [6]

unwanted effects of previous handling and storage stages on the weight measurements. Metallic sample holders and collectors undergo a bake-out cycle in ultra-high vacuum at 125 °C for 16 h, followed by further conditioning in a dry vessel (RH 0%) at room temperature for 24 h to minimize mass loss during the test. The pre-test weight of all objects is then recorded. The holders, each containing a sample weighing between 100 and 300 mg, are fixed to the hot grid hollows, while the collectors are locked to corresponding slots on the cold plate.

The OTF chamber can accommodate twelve specimens for simultaneous testing, each specimen/collector pair being isolated from the others by a compartmented separator to prevent cross-contamination. Typically, two materials are analyzed in a single test by inserting five samples for each type within the OTF chamber. The remaining two spots on the plates are filled with empty holders and cleaned collectors as blank references. The vacuum chamber is then sealed and evacuated to a pressure of around 10^{-5} mbar. At the same time, the temperature of the specimen compartment is raised to 125 °C (a temperature chosen to be about ten degrees above any typical space operating temperature to provide accelerated aging effects), while the collector box is maintained at 25 °C. This condition is expected to cause vapor from the heated samples to stream from the holes of their compartment toward the cooled collectors, where a portion of the released gaseous species may condense. The standard length of an outgassing test is 24 h. At the end of the test, the chamber is cooled, re-pressurized with dry nitrogen gas, and opened to gather sample holders and collectors. The

latter are extracted from the OTF using sterilized tweezers and promptly weighed. Comparing the weights measured before the test, the “total mass loss” (TML) and “collected volatile condensable materials” (CVCM) are calculated and expressed as percentages of the initial specimen mass. Two additional parameters may be evaluated after a further conditioning step, storing the samples for 24 h at 23 °C and RH 50% to allow water vapor rehydration and finally weighing the samples again: the “regained mass loss” (RML) represents the percentage of effective mass loss by outgassing considering the partial mass increasing after humidity absorption, whereas the “water vapor regained” ($WVR = TML - RML$) is the relative amount of vapor re-absorbed by the sample. Standard validation rules are typically defined by the end user, depending on the specific performances required to components and systems under test. Usually, TML of 1.00% and CVCM of 0.10% are indicated as screening levels for rejection of spacecraft materials; nevertheless, the restriction may be less or even more stringent depending on the structure’s assembly/functionality, as well as on the mission itself peculiarity.

3.3 *AtOx/UV Exposure*

The AtOx ground-test facility is based on an OS-PREY Plasma Source manufactured by Oxford Scientific Instruments (Fig. 7): the system works through the dissociation of molecular oxygen flowing in a vacuum chamber (allowable pressure $\sim 10^{-3}$ Pa) controlled by high precision flowmeters, by means of energy from a radio frequency source (13.56 MHz). Such a procedure gives rise to an oxygen-based beam constituted by 99% of neutral species (about 60% of monoatomic O and 40% of molecular O₂) with energy in a range 5–10 eV. A mercury-xenon lamp (Hamamatsu—model LC8 Lightning Cure) is adopted to simulate UV irradiation: such device is assembled to the AtOx chamber, providing high-intensity UV spectral lines with an elliptical reflector (UV cold mirror) having reflectivity higher than 90% in the UV range and a quartz light guide with UV transmittance. The spectral emittance field is in the range 200–600 nm, with a maximum emission value at 365 nm, and the radiation intensity of the lamp system is 410 mW/cm² (around 10 Suns) at a working distance of 60 mm. During the tests, the mean environmental temperature is recorded by means of a sensor placed under the sample holder, measuring the chamber’s heating as a consequence of the generation of AtOx plasma and UV rays. Images of the experimental facility and of a C/C naked sample during AtOx/UV combined exposure test are given in Fig. 6. The sample holder can be rotated to obtain different angle of inclination respect to the two impinging fluxes, which are oriented as schematically depicted in Fig. 8.

The tests are performed considering a fixed time of exposure, with AtOx base flux measured a posteriori by analyzing the damage due to normal irradiation of Kapton HN reference samples, as for ASTM E-2089 standard. The analysis of the surface damaging is carried out by mass loss measurements (following the same procedure adopted for the outgassing test) and the consequent evaluation of the AtOx-driven

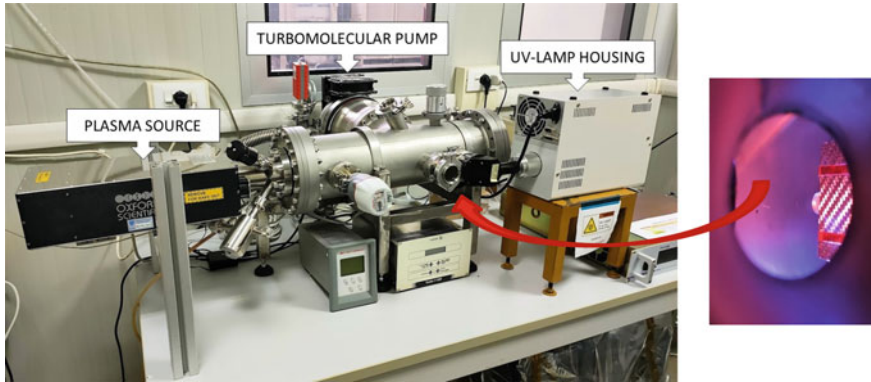
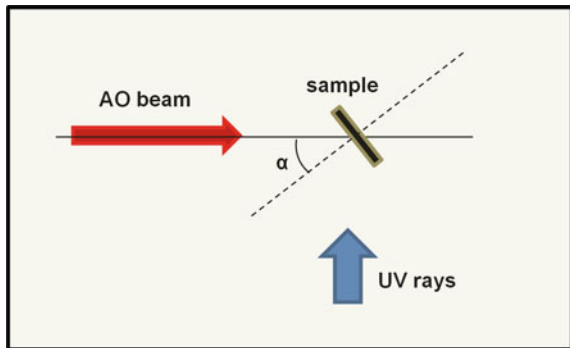


Fig. 7 AtOx/UV experimental setup available inside ISO-7 certified clean room @ LSA; at right, picture of a C/C sample during AtOx/UV irradiation test taken from the indicated view-port. [20]

Fig. 8 Sketch of the AtOx/UV exposure geometrical setup



erosion yield. The basic background lies within the operative expression of the as-called erosion rate E_Y , which is given in $[cm^3/n.at.]$ —i.e., as eroded volume for impinging oxygen atom—by the relationship

$$E_Y = \frac{\Delta M}{\rho \cdot F \cdot A}, \quad F = f \cdot \Delta t \tag{1}$$

where ΔM is the mass loss [g], ρ is the material density $[g/cm^3]$, A is the exposed surface $[cm^2]$, and F is the fluence, which is given as total number of impacts for surface unit $[n.at./cm^2]$; the latter quantity takes account of the whole time of exposure Δt [s] and is typically related to a supposed constant AtOx flux f , which is expressed in $[n.at./(s \cdot cm^2)]$, as indicated by the second relationship in Eq. (1).

4 Experimental Results

4.1 Thermal Stress Behavior

The measurements of the thermal dilatation coefficient of C/C substrates coated with AIP products, both uncoated and enriched with 1wt% of SiO₂ nanospheres, are presented in Fig. 9. The results of two samples for each type, labeled as “sn1” and “sn2,” are provided. A high degree of thermal stability was observed for all tested samples over a broad thermal range. At temperatures approaching 1400 °C, a weak decrease in averaged CTE was revealed, indicating a strong adhesion at higher temperatures and suggesting the formation of an additional bulk material due to the coating embedding. Any delamination of the coating was identified by noticeable spikes and discontinuities in the plots, which were not present in the samples that exhibited good adhesion. The absence of damage or cracks on the samples further confirmed their good adhesion. The addition of silicon dioxide nanospheres led to a slight increase in average CTE compared to the un-reinforced coating, likely due to the dispersion of nanoparticles within the aluminum oxide matrix and the nanosilica’s thermal insulation. However, the filling percentage was very low in weight compared to the alumina varnish, making the effect of the nanosilica’s low CTE on the overall thermal expansion negligible. Higher percentages of powder inclusion, as reported in the literature, would lead to a decrease in CTE. The filled samples exhibited an improved overall behavior at higher temperatures, with increased stability in the range of analysis. These results are consistent with the properties of C/C materials. However, it should be noted that an increase in CTE is inevitable when transitioning from virgin to coated material (CTE values for naked C/C are approximately $1.9 \times 10^{-6}/^{\circ}\text{C}$ at 1000 °C and $2.2 \times 10^{-6}/^{\circ}\text{C}$ at 1400 °C, as reported in [28–30]). The most characteristic values for stand-alone CTE testing were observed around 800 °C, when the material was thermally stabilized. In the initial phase (i.e., from approximately 200 °C to 700 °C), the CTE plot contained spurious effects due to both the material’s residual pyrolysis and the instrumentation’s thermo-mechanical stress. Based on the plots of the samples treated with un-reinforced coating, an average CTE value of approximately $3.0 \times 10^{-6}/^{\circ}\text{C}$ can be considered around 800 °C. For the nanocoated material, the stabilized part of the CTE trend was slightly further ahead, around 1000 degrees, with an average value of around $4.4 \times 10^{-6}/^{\circ}\text{C}$. Such results indicated that along the curing phase in the oven at 427 °C the coating solution infiltrated the carbon/carbon surface’s pores, thus becoming an integral part of the structure without creating significant structural weakening or damage (cracks).

A compendium of all the experimental outcomes acquired through the analysis with the dilatometer set up is depicted in Fig. 10, where the averaged CTE is charted for the diverse various materials under examination. The remarkable thermal stability of C/C pure material (black line) across the extensive temperature range analyzed was readily noticeable (consistent value about $2.0 \times 10^{-6}/\text{K}$ from 300 up to 1400 °C, as anticipated), while every surface treatment causes CTE noteworthy variations based on temperature. ZrO₂ coating (red line) offered excellent performance up to

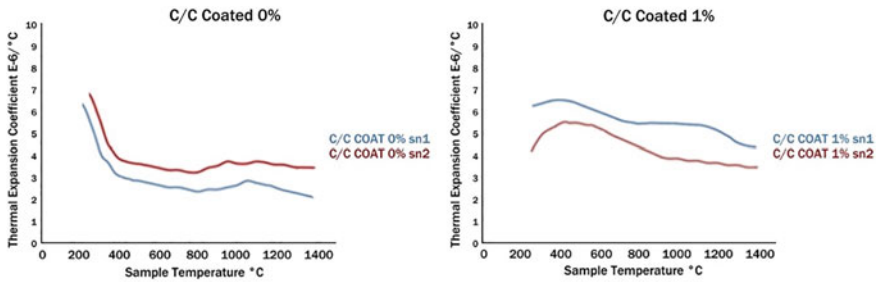


Fig. 9 CTE measurements of C/C treated by Al₂O₃ Pyro-paint (left) and of C/C coated by Al₂O₃ varnish filled by SiO₂ nanosphere at 1wt% (right). [26]

600 °C, but a steep rise at the highest temperatures was detected. Both Al₂O₃ and SiC coatings (green and gray lines, respectively) exhibited good thermal stability ($2.5\text{--}4.0 \times 10^{-6}/\text{K}$) within the intermediate hot region 800–1200 °C, but thermal stresses would be expected at lower temperatures and, furthermore, SiC behavior pointed out a phase transition around the critical temperatures above 1200 °C. All the nanoreinforced coatings (dotted lines) exhibited a fluctuating trend over the broad temperature range, with averaged CTE values rather higher than C/C substrate ($3.0\text{--}5.0 \times 10^{-6}/\text{K}$); on the other hand, noteworthy results were achieved around the key temperatures—i.e., up to 200 °C (representative of stay-on-orbit environment) and beyond 1200 °C (toward re-entry conditions)—where small values approaching C/C performances were detected. CTE decrease and stabilization at highest temperatures indicated a good degree of adhesion, thus testifying the coating embedding and the formation of further bulk material; it is believed that the thermal insulation provided by high surface area nanosized SiO₂ particles dispersion within the matrix may be effective in reducing the risk of thermo-mechanical residual stresses at very high temperatures, thanks to an established thermal and dimensional stability. The impact of nanosilica addition is particularly important considering the ZrO₂-based materials behavior: at “ordinary” temperatures the volumetric filler inclusion affected the dense packaging of the naked matrix, thus increasing its thermal expansion, while the ongoing blending at raising temperature allowed for a better mechanical stability in harsh thermal conditions.

The residual thermal stress was evaluated by means of thermal cycling between the extreme temperatures of +90 °C and –60 °C, as typical orbital thermal reference points. The coated samples showed very good insulation properties, being much more inert than not coated samples in a thermal-vacuum environment (Fig. 11). The nanofilled samples displayed the best insulation behavior as the silica nanopowder reduced the thermal conductivity of the samples. No modification in shape or color was found after the test, as well as no cracks on the coating. From a zoom of the hot dwell time of the sample, some significant aspects can be observed. First of all, the not coated samples, made of naked C/C composite, showed to be the most reactive to the heating as expected, reaching the overall highest temperatures (56.7 °C and 56.3 °C, respectively) and following a much more rapid cooling path with respect

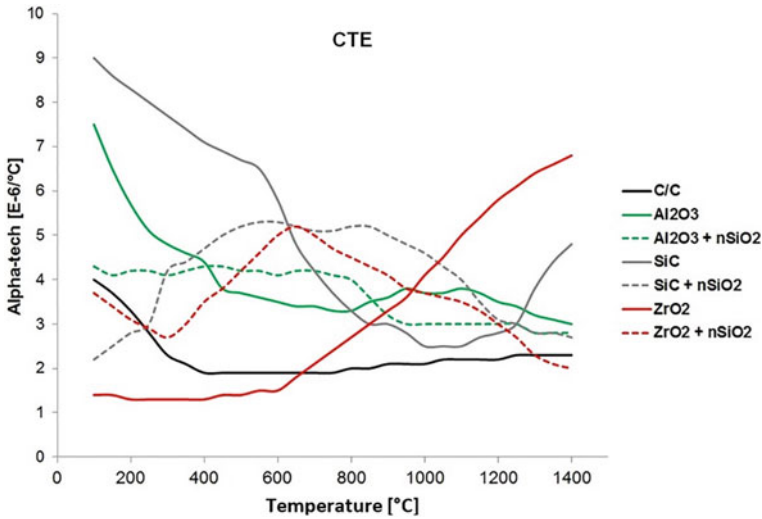


Fig. 10 Averaged CTE of pristine C/C and of the substrate coated by hybrid ceramic-based varnishes. [25]

to the other samples. For the simple-coated samples, the plots lead to some significant considerations. The Al_2O_3 -coated sample, because of the high thermal conductivity of its chemical components, showed the third highest value, stopping its rise at 55.8°C , while the SiC-coated sample is the fourth one, reaching 55.2°C . The thermal conductivity is then influenced by the use of nanosilica particles, leading to another significant aspect: the charged Al_2O_3 samples displayed the fifth highest value (55°C), followed by the analogue SiC-coated items (53.9°C). In general, the thermal conductivity was decreased due to the presence of silica nanoparticles within the coating bulk. A peculiar behavior can be noticed for the zirconia-based coating, which lead to the lowest thermal transport behavior, thus resulting in the most inert material in the batch. A similar trend is revealed by analyzing the cooling region and the relative stage step. The uncoated materials showed the highest reactivity (-21°C and -19.9°C); this latter was lowered for the substrates with Al_2O_3 and SiC basic protective layer (-18.5°C and -16.9°C , respectively) and for the corresponding nanoreinforced materials (-15.5°C and -12.5°C , respectively), whereas the ZrO_2 samples confirmed to be the most inert (-11.8°C and -9.4°C for the basic and nanocoating case, respectively).

4.2 Outgassing Properties

Naked C/C, basic coating, and 0.5–1 wt% of nanometric silica-enriched coating were examined by OTF experiments, as summarized in Fig. 12. All the substances

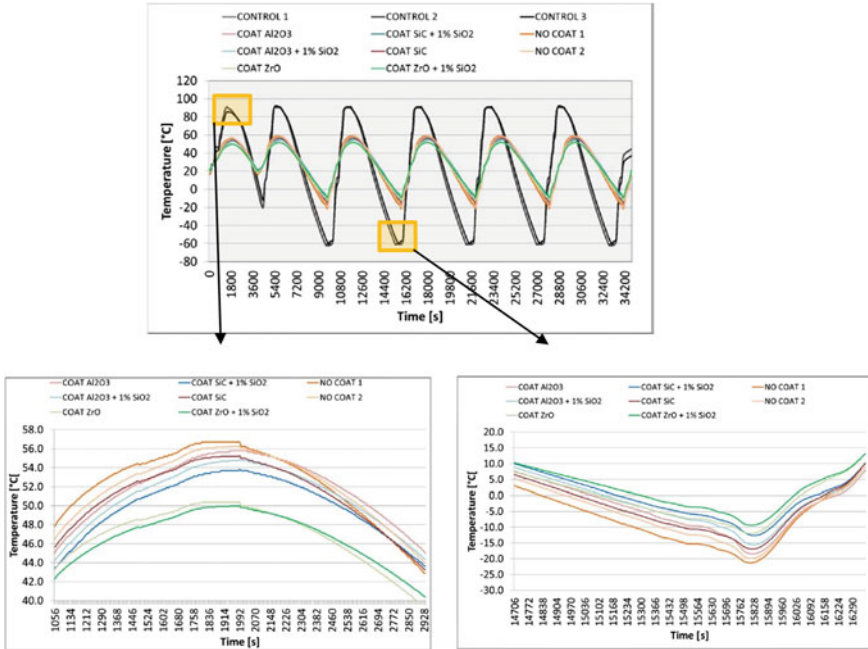


Fig. 11 Thermal cycling test results: full temperature behavior (up) and hot/cold phases insets (down). [27]

scrutinized manifested satisfactory performances, remaining well below the standard thresholds as for ECSS reference. The most interesting outcomes were obtained with the 1 wt% charged samples, thereby validating the efficiency of the Pyro-paint boost via nanoscale particles integration. Specifically, all the tested materials exhibited good opposition to vacuum-induced outgassing: the presence of the coating, without nanoscale particles, with 0.5% and 1% in mass of SiO₂, curtails the proportion of all the outgassing volumes—i.e., conserving the C/C substrate. For Al₂O₃ specimens, the CVCM value imparted consequential hints, since a decrement is readily evident as the percentage of SiO₂ inside the coating was raised. This is possibly because of the characteristics of the coating: although the TML marginally increases from 0.5 to 1%, both for plate and shell, the coating can be construed as a barricade of the internal humidity of material samples, and the escalating quantity of SiO₂ amplifies this behavior. All kinds of coatings are extremely well-suited for aerospace usage, as for ECSS Q-ST-70-02 and ASTM E595 standards. The decision regarding the material used for supplementary inquiry can be made by weighing both TML and CVCM values. For Al₂O₃ specimens, even if TML marginally increased from 0.028 for 0.5% to 0.061 for 1%, the CVCM value is noticeably reduced, from 0.027 for 0.5% to 0.014 for 1%, so the preference would fall on the slightest condensable substance. Since the diminishing of TML was remarkable for both SiC and ZrO₂ at elevating percentages of nanometric alumina, and the CVCM remains fundamentally

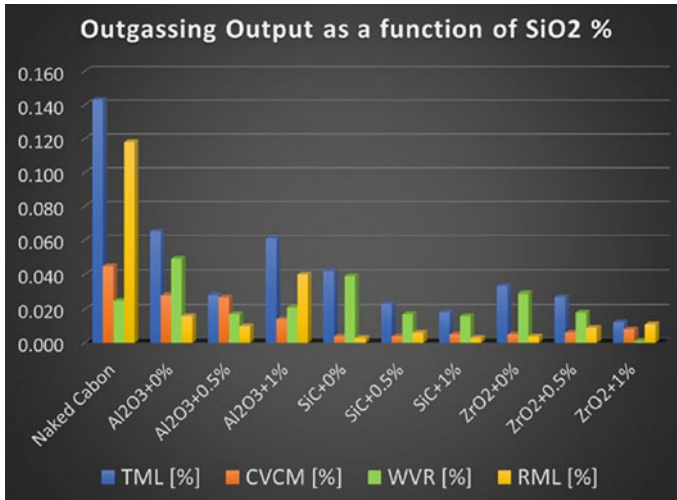


Fig. 12 Outgassing test results, comparing C/C substrate, basic and reinforced coating performances. [27]

unaltered from 0.5 to 1%, the TML value is presumed to embody the crux for the SiC and ZrO₂ coatings.

4.3 AtOx/UV Oxidative Erosion

Samples of naked and nanoreinforced coated C/C substrate were tested within the AtOx simulator chamber for erosion rate evaluation. Such quantity is expressed as eroded volume by impinging atom, as reported in Table 1, by following the framework outlined in Eq. (1) where the averaged results are given for AtOx/UV exposure testing performed in the following conditions:

- the time of exposure was 39,600 s (11 h) for an AtOx flux of about 1.9×10^{15} n.at./(s cm²), as estimated by the analyzed fluence effects on polyimide (Kapton HN) reference samples;
- the measurement of C/C samples density gives resulted around 1.35 g/cm³;

Table 1 AtOx exposure test results

Material	E_{γ} (cm ³ /at)
C/C	2.4×10^{-25}
Al ₂ O ₃ + 1 wt% nSiO ₂	3.8×10^{-26}
SiC + 1 wt% nSiO ₂	5.6×10^{-26}
ZrO ₂ + 1 wt% nSiO ₂	3.2×10^{-26}

- the area free to be irradiated turned to be different each time due to unavoidable fluctuations related to the adopted sample clamping system, varying in the range 11–17 cm².

It can be noticed that the coating protection reduced the AtOx damaging of about 75% and 85% by using nanoreinforced SiC and Al₂O₃, respectively, and of almost one order of magnitude by means of the denser zirconia-based varnish application, as expected [31, 32]. In order to get a quantitative feel about the coating efficacy, such results can be easily claimed to estimate the surface erosion after, for instance, one-year missions at typical LEO AtOx flux (10¹⁵ at./s cm²): referring to the simplified relationships given in Eq. (1), the naked C/C substrate would be penetrated by AtOx at a depth of about 75 μm, while the several coated surfaces might be effectively protected by coating layer thicknesses of 10–15 μm.

The reported experimental findings suggest that ceramic coating treatments are absolutely required to avoid (or, at least, mitigate) the C/C substrate damaging due to prolonged exposure to AtOx irradiation [33]. Nevertheless, the actual coating effectiveness would disregard the performances expected from ground-test results, if the influence of thermal shock/stress is not considered. A trial modeling can be introduced in order to give a preliminary approach to this task. As every chemical process, the mechanism of erosion by atomic oxygen impact—i.e., as effective consequence, the extraction of surface matter—generally depends on two competing factors: the energy that enhances the chemical reaction, in this case related to the AtOx impact intensity, and the resistance to the ongoing process, here accounted for by the materials surface cohesion. A chemical reaction rate is conventionally expressed as function of such variables within the Arrhenius framework defined by $\exp[-\Delta E/RT]$, ΔE being the activation threshold (a slower reaction is expected for a higher potential wall) and RT referring to the available thermal energy (a reaction takes place faster at increasing temperatures). The erosion rate may be thus qualitatively written as

$$E_Y \propto \exp\left(-\frac{H}{K}\right) \quad (2)$$

where H represents the resistance related to the work required for matter extraction, while K is the boost provided by the AtOx (relative) kinetic energy. This latter (around 8 km/s \rightarrow \sim 10 eV) is practically unaffected by temperature variations, even of hundreds of degrees (thermal energy \sim tens eV). Rather, temperature raising should have much more influence in reducing the work needed for extracting surface atoms, since the thermal dilatation—i.e., the lattice distances enlargement—lowers the interatomic/molecular bound forces, mainly on the surface (where they are already weakened respect to what happens within the bulk) as schematically depicted in Fig. 13. The AtOx erosion rate can be thus expressed as function of the absolute temperature

$$E_Y(T) = E_Y^{(0)} \cdot \exp\left(\frac{\Delta H(T)}{K}\right) \quad (3)$$

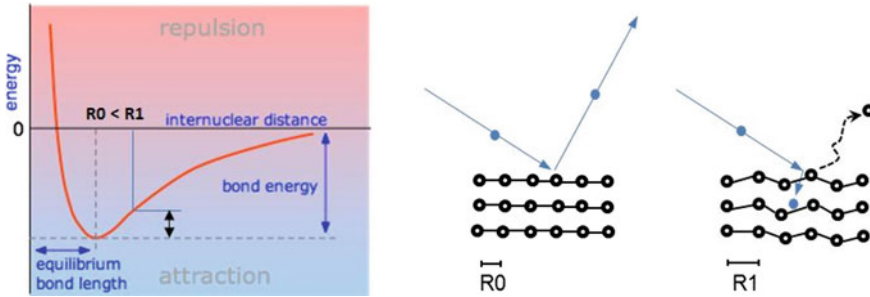


Fig. 13 Schematic representation of the thermal expansion influence on the consequences of an AtOx impact. [25]

where the basic rate $E_Y^{(0)} = E_Y(T = 0K)$ is fixed by the working conditions (flight orbit/AtOx flux and incidence angle, target cohesion, oxygen/surface chemical affinity, etc.), whereas the variation of atomization enthalpy explains the expected raising of erosion at $T > 0$ K. This framework can be used to evaluate the reaction rate modulation due to thermal oscillations with respect to what is typical measured at room temperature, thus allowing to predict the expected enhancement of AtOx erosion due to typical thermal cycle warming ($\Delta T \sim +100$ °C).

5 Conclusions and Outlooks

The evolution of reusable launch vehicles (RLV) must encompass a significant cutback in payload shipping expenses. One of the costliest components of an RLV is the thermal protection system (TPS), which safeguards the spaceship from the high heat loads during re-entry. Reusability and the on-orbit atmosphere are vital considerations in TPS design, primarily with respect to the selected materials. This chapter has summarized an extensive test program designed to examine a new TPS concept by proposing a hybrid multiscale ceramic coating—i.e., ceramic refractory varnishes enriched with silica nanoparticles—to be applied on carbon/carbon substrates. The technique is intended to conserve the thermo-mechanical properties of the ceramic substrate from harmful space environment conditions, such as low Earth orbit (LEO) thermal cycles, outgassing caused by ultra-high vacuum, as well as atomic oxygen/UV radiation. The results indicated that the proposed carbon-based ceramic structures could be successfully used in aerospace applications, providing the multi-functional performance needed to cope with harsh space environmental conditions. The optimal thermo-mechanical features of the lightweight carbon/carbon bulk, which are essential for materials exposed to the critical re-entry phase, are coupled with the qualities of the actualized thin ceramic nanocoatings, which can generally protect the base core from the detrimental aging effects due to LEO environment. In particular, the carbon/carbon-coated samples were characterized by measuring the linear coefficient of

thermal expansion using an experimental setup capable of reproducing the conditions of thermo-mechanical stress experienced by space structures and subsystems during typical thermal cycles: the results showed the effectiveness of the nanofiller addition to the ceramic varnishes versus the performance provided by un-reinforced coatings. Additionally, a thermal cycling full characterization between the extreme temperatures of +90 and -60 °C demonstrated that the coated samples exhibit excellent insulation properties in a thermal-vacuum environment, with the nanofilled samples demonstrating the best performance. Furthermore, an outgassing test on simple and nanocharged coated substrates ensured that all the materials analyzed comply with the limits imposed by the ECSS reference standard. Finally, the improved treatments were evaluated in terms of resistance to atomic oxygen exposure using dedicated equipment capable of carrying out ground-test setups to simulate the actual rate of irradiation in LEO regions: the measurements of mass loss demonstrated that the nanoreinforced ceramic coatings can successfully preserve the underlying carbon/carbon surface from the damaging atomic oxygen erosion. Basically, the results suggest that the proposed hybrid ceramic coating is a reliable technical strategy for preserving TPS C/C substrates from the oxidative conditions of the space environment, thanks to both enhanced protection effectiveness and LCC safety. While good reproducibility has been achieved based on previous works, further analyses will be conducted to correlate the current results with those related to future tests on different types of nanocoated samples. Furthermore, as an ongoing study, the material manufacturing process will be upgraded to gain production feasibility and complete coating stability. In particular, it would be necessary to monitor the coating thickness, as a magnification of surface defects may occur on the exposed material. Further investigations will be carried out to perform a full space environment characterization of carbon-based ceramic materials to be used for spacecraft components and subsystems. As a continuation and a planned application of the present activity, a prototype of Space Environment Protective Plates will be installed on a cube-sat designed and realized by the Aerospace Systems Laboratory of Sapienza University of Rome and tested in orbit as technological demonstrator. Besides, analysis extension and refinement will be addressed by ongoing experimental activities of reinforced C/C structures ground-testing. In particular, a complete physical modeling of AtOx interaction with coated C/C surfaces will be pursued by taking directly into account the material thermal properties, in order to get a reliable evaluation of the effective behavior of such structures serving long-term mission in space environment conditions. Particularly, the coupling of the specific space mission parameters (a priori defined) to the materials' constitutive properties (measured by ground-test) is expected to be established as powerful strategy for predicting the actual behavior of aerospace structures in LEO environment. The research development will be thus focused on the analysis of coated C/C structures by combining AO/UV irradiation test and thermal/outgassing characterization, in order to achieve a full knowledge of the materials' effective behavior within the LEO space environment, thus allowing a reliable estimation of the structural degradation due to all the synergic aging agents.

Tackling this task is expected to be of great aid to improve the design of spacecraft protective systems, with particular regard to C/C-based advanced TPS for re-entry vehicles and, more generally, for applications in large space structures—as, for example, the ISS—operating in long-term missions within LEO regions.

References

1. Finckenor, M. M., de Groh, K. K.: Space Environmental Effects—A researcher's Guide to: International Space Station. NASA ISS Program Science Office (2015)
2. Yang, J.C., de Groh, K.K.: Materials issues in the space environment. *MRS Bull.* **35**, 12–19 (2010)
3. James, B.F., Norton, O.W., Alexander, M.B.: The natural space environment: Effects on spacecraft. NASA STI/Recon. Technical. Rep. N **95**, 25875 (1994)
4. Dever, J.A., Banks, B.A., de Groh, K.K., Miller, S.K.: Degradation of spacecraft materials. In: Kutz, M. (ed.) *Handbook of Environmental Degradation of Materials*, pp. 465–501. William Andrew Publishing, Norwich, NY (2005)
5. Grossman, E., Gouzman, I.: Space environment effects on polymers in low earth orbit. *Nucl. Instrum. Methods Phys. Res. B: Beam Interact. Mater. Atoms* **208**, 48–57 (2003)
6. Pastore, R., Delfini, A., Albano, M., Vricella, A., Marchetti, M., Santoni, F., Piergentili, F.: Outgassing effect in polymeric composites exposed to space environment thermal-vacuum conditions. *Acta Astronaut.* **170**, 466–471 (2020)
7. Windhorst, T., Blount, G.: Carbon-carbon composites: a summary of recent developments and applications. *Mater. Des.* **18–1**, 11–15 (1997)
8. Morgan, P.: Carbon fibers and their composites. Taylor & Francis Group, USA, (2005)
9. Sheehan, J.E., Buesking, K.W., Sullivan, B.J.: Carbon-carbon composite. *Annu. Rev. Mater. Sci.* **24**, 19–44 (1994)
10. Savage, G.: Carbon–Carbon Composites, pp. 85–113, 227–382. Chapman & Hall London (1993)
11. Albano, M., Delfini, A., Pastore, R., Micheli, D., Marchetti, M.: A new technology for production of high thickness carbon/carbon composites for launchers application. *Acta Astronaut.* **128**, 277–285 (2016)
12. Albano, M., Pastore, R., Delfini, A., Micheli, D., Volpini, F., Marchetti, M.: Densification of high thickness C/C composites by chemical vapor infiltration. *Procedia Eng.* **109**, 381–389 (2015)
13. Bacos, M.P.: Carbon-carbon composites: oxidation behavior and coatings protection. *J. De Phys.* **4**, 51–59 (2010)
14. Liu, X., Cheng, L., Zhang, L., Luan, X., Mei, H.: Behavior of pure and modified carbon/carbon composites in atomic oxygen environment. *Int. J. Miner. Metall. Mater.* **21–2**, 190–195 (2014)
15. Dworak, D.P., Soucek, M.D.: Protective space coatings: a ceramer approach for nanoscale materials. *Prog. Org. Coat.* **47**, 448–457 (2003)
16. Chen, Z., Wu, W., Cheng, H., Liu, Y., Wang, S., Xue, R.: Microstructure and evolution of iridium coating on the C/C composites ablated by oxyacetylene torch. *Acta Astronaut.* **66**, 682–687 (2010)
17. Shi, X., Jin, X., Yan, N., Yang, L.: Influence of micro-oxidation on joints of C/C composites and GH3044 for large-size aerospace parts. *Acta Astronaut.* **140**, 478–484 (2017)
18. Hsu, S.-E., Wu, H.-D., Wu, T.-M., Chou, S.-T., Wang, K.-L., Chen, C.-I.: Oxidation protection for 3D carbon/carbon composites. *Acta Astronaut.* **35**, 35–41 (1995)
19. Friedrich, C., Gadow, R., Speicher, M.: Protective multilayer coatings for carbon–carbon composites. *Surf. Coat. Technol.* **151–152**, 405–411 (2002)

20. Delfini, A., Santoni, F., Bisegna, F., Piergentili, F., Pastore, R., Vricella, A., Albano, M., Familiari, G., Battaglione, E., Matassa, R., Marchetti, M.: Evaluation of atomic oxygen effects on nano-coated carbon-carbon structures for re-entry applications. *Acta Astronaut.* **161**, 276–282 (2019)
21. Delfini, A., Vricella, A., Bueno Morles, R., Pastore, R., Micheli, D., Gugliermetti, F., Marchetti, M.: CVD nano-coating of carbon composites for space materials atomic oxygen shielding. *Procedia Struct. Integrity* **3**, 208–216 (2017)
22. Shirshneva-Vaschenko, E.V., Shirshnev, P.S., Snezhnaia, Zh.G., Sokura, L.A., Bougrov, V.E., Romanov, A.E.: Zinc oxide aluminum doped slabs for heat-eliminating coatings of spacecrafts. *Acta Astronaut.* **163**, 107–111 (2019)
23. Lespade, P., Richet, N., Goursat, P.: Oxidation resistance of HfB₂-SiC composites for protection of carbon-based materials. *Acta Astronaut.* **60**, 858–864 (2007)
24. Schulte-Fischedick, J., Zern, A., Mayer, J., Ruhle, M., Frieß, M., Krenkel, W., Kochendo, R.: The morphology of silicon carbide in C/C-SiC composites. *Mater. Sci. Eng., A* **332**, 146–152 (2002)
25. Pastore, R., Delfini, A., Santoni, F., Marchetti, M., Albano, M., Piergentili, F., Matassa, R.: Space environment exposure effects on ceramic coating for thermal protection systems. *J. Spacecr. Rocket.* **58**(5), 1387–1393 (2021)
26. Delfini, A., Pastore, R., Santoni, F., Piergetili, F., Albano, M., Alifanov, O., Budnik, S., Morzhukhina, A.V., Nenarokomov, A.V., Titov, D.M., Marchetti, M.: Thermal analysis of advanced plate structures based on ceramic coating on carbon/carbon substrates for aerospace Re-entry Re-useable systems. *Acta Astronaut.* **183**, 153–161 (2021)
27. Delfini, A., Pastore, R., Santoni, F., Piergetili, M.M.: Ground simulation of the effects of the space environment on ceramic nano-coated panels for space environment protection. *Proceedings of 7th IEEE International Workshop on Metrology for AeroSpace, MetroAeroSpace 2020*, pp. 124–129, Article number 9160167 (June 2020)
28. Zhao, J., Li, K., Li, H., Wang, C., Zhai, Y.: The thermal expansion of carbon/carbon composites from room temperature to 1400 °C. *J. Mater. Sci.* **41**, 8356–8358 (2006)
29. Chen, S., Qiu, X., Zhang, B., Xu, J., Zhong, F., Zhu, B., Zhang, Y., Yang, J.O., Yang, X.: Advances in antioxidation coating materials for carbon/carbon composites. *J. Alloy. Compd.* **886**, 161143 (2021)
30. Sciti, D., Zoli, L., Reimer, T., Vinci, A., Galizia, P.: A systematic approach for horizontal and vertical scale up of sintered ultra-high temperature ceramic matrix composites for aerospace—advances and perspectives. *Compos. B Eng.* **234**, 109709 (2022)
31. Liu, G., Cheng, L., Luan, X., Zhang, J.: Damage behavior of atomic oxygen on CVD SiC coating-modified carbon/carbon composite in low earth orbit environment. *J. Mater. Sci. Technol.* **35**(12), 2957–2965 (2019)
32. Wei, Q., Guo, Z., Xu, J., Ye, W., Huang, Q.: Atomic oxygen effect of Zr-Al-C coatings on ZrNb alloys used in space environment. *Appl. Surf. Sci.* **564**, 150420 (2021)
33. Huo, C., Guo, L., Cao, A., Wang, Z., Wang, C., Kou, G., Zhang, Y.: The degradation behavior of C/C composites in high-energy atomic oxygen. *Vacuum* **146**, 120–129 (2017)

Ultra High Temperature and High Temperature Coatings

Recent Advances in Ultra-High-Temperature Ceramic Coatings for Various Applications



K. Deepthi Jayan

Abstract In the past, the research on high-temperature applications of materials has focussed mainly on SiC and Si₃N₄ only. The recent advances in propulsion and hypersonic concepts and the related applications have resulted in the search for new categories of materials capable of withstanding very high temperature. The borides, nitrides and carbides of various transition metals can be employed for synthesising ultra-high-temperature ceramic (UHTC) coatings. These materials possess excessively huge melting point along with substantial mechanical properties at extreme temperature, making them suitable for several high-temperature structural and other environmental applications such as in rockets, hypersonic vehicles and engine components. The inherent brittleness as well as extremely feeble shock resistance of ceramic materials can be overcome to a greater extent with the application of ultra-high-temperature ceramic coatings and fibre-reinforced ultra-high-temperature ceramic materials. UHTC coatings are extremely useful as thermal shock absorbers, surface seals and leak minimisers. The carbothermal reduction method is the oldest method employed for the synthesis of UHTCs. However, many other solid-state powders-based and solution-based methods have been employed recently to enhance the unique properties of them. The synthesis methods face a few challenges and require highly refined approaches to synthesis high purity UHTC powders, suitable chemical synthesis reactions and proper selection of precursors delivering excellent chemical yield and less degradation. The microstructural aspects of the synthesised UHTCs can be identified through suitable characterisation techniques including in situ characterisation. Apart from the excellent mechanical properties like excellent elasticity, flexural strength, and fracture toughness, UHTCs must be assessed for its machinability when they are employed for hypersonic and space applications. The thermodynamic properties such as the coefficient of thermal expansion, thermal conductivity and total hemispherical conductivity play a significant role in determining the high-temperature applications of UHTCs. Oxidation resistance at high-temperature environment is the most wanted property of materials especially when

K. D. Jayan (✉)

Department of Basic Sciences and Humanities, Rajagiri School of Engineering and Technology (Autonomous), Rajagiri Valley, Kakkanad, Kochi, Kerala 682039, India
e-mail: deepthij@rajagiritech.edu.in

they are employed for various space applications. Recent advances show that the use of multilayers of the high-temperature ceramic protective coating reduces oxidation of carbon–carbon (C–C) composite materials and protect them from aerothermal heating at temperatures above 3273 K. Hence, the mechanisms, kinetics and the end products of oxidation mechanisms help the researchers to identify the strengths and weaknesses of the UHTCs when employed for specific applications. This chapter focusses mainly on the recent advances in the synthesis and characterisation techniques of UHTCs giving due importance to their various properties and oxidation mechanisms. The atomistic computational modelling and simulation studies on the impacts of defects on the thermal and mechanical properties of UHTCs are found to be extremely useful to identify their drawbacks prior to their employment in various device configurations. In a similar way, the computational studies on UHTCs by employing thermal shock modelling tools provide useful information about their thermal shock resistance. This chapter also provides a brief overview of the applications of UHTCs along with a description of the properties and applications of the emerging high entropy UHTCs.

Keywords Ultra-high-temperature composites · Sintering · Simulation · High entropy materials

1 Introduction

Both the preservation of existing natural resources and their optimal and cost-effective utilisation in the design and manufacture of all high-temperature equipment are the guiding concerns behind the selection of materials today. In account of these considerations, scientists have concentrated on enhancing energy production efficiency of the equipment while concurrently reducing hazardous emissions, primarily CO_2 and NO_x , from them through a wise selection of raw materials [1]. One way to achieve this is to keep the engines and turbines at high temperature with a simultaneous reduction in the size and weight of its components, thereby creating a high-temperature environment with no cooling system in its vicinity. This will result in the development of ultra-high thrust resulting from a reduced fuel utilisation leading to a reduction in the emission of toxic gases. In the past, the research on high-temperature applications of materials has focussed mainly on super alloys such as SiC and Si_3N_4 only. However, these alloys possess some disadvantages under such operating environments and hence require the best materials including ceramic materials and composites, for such applications. In the quest for identifying suitable materials for high-temperature applications, researchers have tried several transition metals and their derivatives. The study shows that carbides, nitrides, as well as borides of transition metals can be employed as a suitable material for high-temperature applications [2, 3]. The ceramic metal composites (CMCs), thermal and environmental barrier coatings, etc., can be employed in high-temperature applications for various industries. These coatings when employed in fuel cells improve the efficiency of

power generation while keeping the emission of toxic gases to a lower level. The solid oxide fuel cells composed of ceramic metal composites can operate with the help of the fuels such as hydrogen or light hydrocarbons at high-temperature range, still maintaining a low rate of performance degradation and generating ultraclean energy.

Currently, above 3000 materials that possess high melting points, generally above 2273 K, including the popularly used high-temperature material, SiC exists [4]. The other high-temperature materials of interest include refractory metals, viz. Hf, Ir, Nb, etc., oxides of Hf, U, Th, Zr and a wide group of borides, carbides and nitrides of transition metals and their composites. Refractory diboride compounds possess excellent oxidation resistance and hence the group IV and V element-based refractory diboride materials have gained research focus. Among these materials, the diborides of Hf and Zr form the most potential candidates in ultra-high-temperature application fields [5, 6]. The high melting point and the hardness of these metals arise from the strong covalent bonding between the constituent elements of the material. They also possess a high negative free energy of formation, which accounts for the good thermal and chemical stability of the diboride compounds. The high thermal shock resistance of these diboride compounds arises from their excellent thermal conductivity and hence they can be employed for various high-temperature applications. In a similar way, non-oxide ceramic matrix composites (CMCs) formed of carbon or SiC fibres-reinforced SiC-based materials find significant importance in high-temperature applications owing to their excellent thermal conductivity, high thermal shock stability, creep, oxidation and wear resistance along with enhanced toughness compared to the monolithic material. When employed for high-temperature applications, the fibre-matrix interface in non-oxide CMCs controls the fracture toughness of material thereby hinders its transversal fracture via deflections of cracks present initially in the structure [7].

The study on UHTCs started in the late 1800s, however, technologies based on UHTCs have emerged during the 1950s only, with the increasing interest in developing new space technologies that can withstand high-temperature conditions. The research interest in UHTCs has further enhanced with the development of aerospace applications such as rocket motors, hypersonic aerospace vehicles and scramjet propulsion [8]. One of the difficulties faced during aerospace applications include the production of very high-temperature above 2000 °C at the sharp leading edges and control surfaces when the device is operated at hypersonic speeds, thus leading to heat flux and the emission of reactive gas species. Such applications employ diboride-based UHTCs due to their excellent thermal conductivity, mechanical strength and oxidation resistance, while dicarbide and dinitride-based UHTCs can be employed for the device components such as nozzle throats, divert/attitude control thrusters and nozzle liners that need to withstand heavy loads and hence require excellent mechanical strength [9, 10]. Despite the advances in the knowledge of several factors related to UHTCs such as the synthesis, processing, thermochemical properties and oxidation, a few key challenges in the understandings of UHTCs do prevail. This chapter focusses on the advances that occurred in the research of various UHTC materials and their applications in various fields.

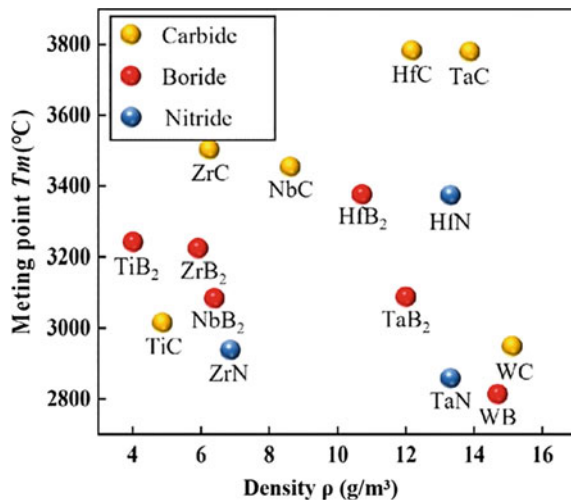
2 New UHTC Material Systems

A wide utilisation of the UHTCs for very high-temperature applications necessitates the need for the availability of a broad category of materials capable of exhibiting excellent thermodynamic properties at high temperature. The UHTC materials usually are formed by developing a strong covalent bond between the early transition elements and carbon, nitrogen or boron. The strong covalent bond is responsible for the ultra-hardness, stiffness and melting point of these compounds. These materials also possess certain degree of metallic bond character and is responsible for their high thermal and electrical conductivities in comparison with other oxide materials. Such a combination of metal like and ceramic like properties enable them to overcome extreme temperature, mechanical loads, heat flux and radiation levels. Figure 1 shows a comparison of the melting point and the density of various boride, carbide or nitride-based UHTCs that have prominent applications in various fields at high temperature [11]. The subsequent subsections discuss the properties and applications of various types of UHTCs that are carbides, nitrides or borides of early transition metals.

2.1 Boride-Based UHTCs

Recent advances in the field of aerodynamics and propulsion systems indicate the requirement of next generation aircrafts with speeds exceeding the speed of modern supersonic aircrafts, which in turn necessitates the inclusion of thin and sharp leading-edge profiles that enhances the manoeuvrability, safety and the performance of the

Fig. 1 Plot indicating the melting point of various UHTCs as a function of its density [11]. Copyright 2021. Reproduced with permission from MDPI



aircrafts while reducing the drag experienced during its operation. Transfer of fractional energy to the surface and the resulting concentration at the stagnation points of the leading edges of the aircraft occurs when the flight speed exceeds 5 Mach. At high speeds, chemical heating occurs due to the dissociation of oxygen and nitrogen in air and their subsequent recombination at the surface. These factors contribute to a very high surface temperature above 2273 K at the leading-edge region of the aircraft [6]. The melting point of conventional aircraft materials is well below this temperature and hence may result in the damage of the aircraft when operated under high operating temperature conditions. This can be avoided by the deposition of temperature resistant and highly conductive coating materials on the surface of the leading-edge region of the aircraft. Such coating materials are made up of a combination of materials that possess high thermal conductivity and high melting temperatures, so as to withstand the extremely high-temperature environments and to dissipate the heat from the thinner leading edge of the aircraft to other thicker regions without damaging the environment. In this regard, the boride-based ultra-high-temperature coating materials are extremely useful which in turn can protect the environment also [12, 13].

The refractory metal diborides of Zr and Hf are excellent thermal protection system (TPS) coating materials that possess excellent thermal conductivity and high melting points. The melting temperature of ZrB_2 and HfB_2 is 3523 K and 3653 K, respectively. ZrB_2 and HfB_2 possess a thermal conductivity of 60 W/m K and 100 W/m K, respectively. These materials also possess excellent mechanical and elastic properties along with corrosion and wear resistance and chemical stability. A group of researchers have developed a high strength zirconium diboride-based ceramic material by employing hot-pressing technique. They have developed ZrB_2 by incorporating 10, 20 and 30 vol% of SiC particulate materials in the powder form [14]. To measure the mechanical strength of the material, the four-points bend strength, fracture strength, various elastic constants, elastic modulus as well as hardness have been estimated. The mechanical strength and the hardness of the ZrB_2 material was improved with the addition of SiC. The addition of 20 to 30 vol% of SiC has improved the strength of the ZrB_2 to 1000 MPa, while the material in the absence of SiC provided a mechanical strength of 565 MPa only. It was identified that the improvement in the strength of the material is due to the increase in the grain size of the material. Another study employed a number of Hf-based carbides and W-based materials in combination with SiC and HfC to improve the oxidation [15]. Oxidation tests were performed on HfB_2 -SiC, HfB_2 -HfC, HfB_2 -WC-SiC and HfB_2 -WSi₂ ceramics with the help of oxyacetylene torch by oxidising the samples between 2373 and 2573 K. Another study focussed on estimating the thermal conductivity of HfB_2 -based UHTC material by employing laser flash diffusivity studies in the temperature range of 298 K to 873 K. A 20 vol% SiC was added to the commercially available HfB_2 to prepare the HfB_2 -SiC composites. Conventional hot pressing or spark plasma sintering was employed to consolidate the samples. The differences in processing result in changes with magnitude of thermal conductivity and its dependence on temperature. A network model of effective thermal conductivity has been developed

by including the influences of porosity, grain size, Kapitza resistance and individual thermal conductivities.

The strength and oxidation resistance of diboride UHTCs can be enhanced further by combining it with other refractory metals such as SiC or MoSi₂. The application of hot pressing at a temperature above 2273 K results in borides and boride-based particulate composites. The addition of C, B₄C and MoSi₂ to the boride materials via pressureless sintering methods results in the development of near net-shaped diboride ceramics. The flexure strengths of HfB₂ and ZrB₂ ceramics at room temperature are typically in the range of 300 MPa to 500 MPa. The flexure strengths can be improved to 800 MPa to 1000 MPa with the application of additives such as a trace concentration of SiC or MoSi₂ [14]. A major concern with boride ceramic materials is the retention of strength at high temperatures. When the temperature reaches 1273 K, the strength of fine-grained ceramics that contain particulate reinforcements tend to increase by a small amount [16]. However, when the temperature reaches 1473 K, the strength of the material decreases by 50%. A study on HfB₂ indicated a strength retention at temperature as high as 1773 K, via spark plasma sintering process [17].

2.2 Carbide-Based UHTCs

The research on carbide ceramic materials has been limited due to their high cost and the need for sophisticated equipment and technique for their preparation. Due to the abundance of Ti-based carbides in earth crust, the most studied carbide ceramic material is TiC. The high melting point, low density, excellent thermal conductivity and ultra-high hardness of TiC ceramic material make it suitable for high-temperature applications. TiC can also act as a thermal protection material for aircraft applications [18–20]. The ideal and defect crystal structure of TiC material is shown in Fig. 2. The study performed by Mao et al. demonstrated that hardness of TiC ceramic material can be enhanced by increasing the C content in the compound [11]. The Zr-based UHTC composites possess supreme mechanical and physical characteristics including high electrical and thermal conductivity, hardness, mechanical strength, etc. Though ZrC is cheap and abundant, the issues associated with sintering and the moderate value of fracture toughness of the material hinder it from wide spread applications at high temperature. However, the ZrC materials can be further toughened by reinforcing it with fibres, graphene flakes and layered structures, etc. [21].

A recent study on the optical properties of boride- and carbide-based UHTC materials indicates that adding SiC to the materials enhanced the solar energy absorption properties of them. The study focussed on estimating the optical properties of a few materials such as diborides of Hf and carbides of Hf, HfB₂–SiC and HfB₂–HfC–SiC. The above-mentioned materials were synthesised via spark plasma sintering method from ceramic powders. The synthesised materials exhibited a relative density of 95% that arises from the addition of SiC to the material, which in turn helps in improving the oxidation resistance of composites [22]. The ZrB₂ as well as HfB₂ materials are considered as potential candidates for high-temperature uses as they possess

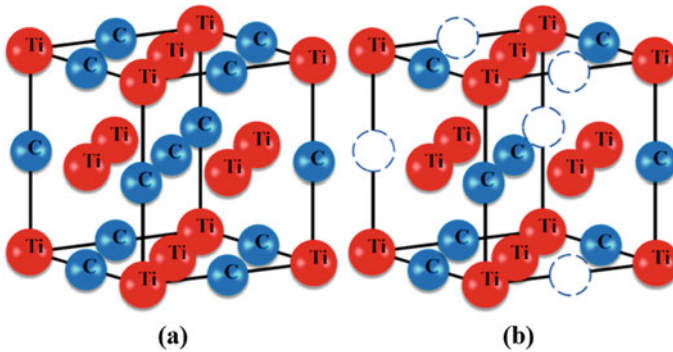


Fig. 2 **a** Ideal crystal structure and **b** defect crystal structure of TiC [11]. Copyright 2021. Reproduced with permission from MDPI

excellent oxidation resistance at an extreme temperature of 1773 K. However, rapid evaporation of boron oxides at high-temperature results in the loss of material and the monolithic ZrB_2 fails to its low thermal shock resistance and poor toughness when employed for high-temperature applications [23, 24]. A mixed boride- and carbide-based composite UHTC, $Zr_{0.8}Ti_{0.2}C_{0.74}B_{0.26}$ showed that it possesses excellent ablation resistance in the temperature range 2273 K to 3273 K when compared to the conventional ZrC-based UHTCs [25]. The composite was prepared by reactive melt infiltration and pack cementation and is identified as suitable for hypersonic vehicles, rockets and other defence systems.

Among various potential candidates for UHTCs, the ternary $Ta_xHf_{1-x}C$ ($0 < x < 1$) ceramics have attracted great attention owing to their ultra-high melting temperature above 3973 K. The simple crystal structure of these ternary ceramic compounds resembles the Fm3m space group of NaCl, which in turn helps in the generation of a continuous solid solution of $Ta_xHf_{1-x}C$ ($0 < x < 1$) with TaC and HfC in all possible compositional ranges. The ablation resistance of materials is a significant parameter that determines its suitability for high-temperature deployment as is determined by the melting point and integrity of oxide scale exposed to extreme scouting of heat fluxes. In a study, a group of researchers estimated the ablation resistance of $Ta_{0.8}Hf_{0.2}C$ and $Ta_{0.8}Hf_{0.2}C$ -10 vol% SiC ceramics via a plasma flame test in air. A 20 μm thick unstable single oxide layer of monolithic $Ta_{0.8}Hf_{0.2}C$ was detected on the completion of ablation test, while a more stable double reaction layer was identified for the $Ta_{0.8}Hf_{0.2}C$ -10 vol% SiC ceramic on the completion of ablation [26].

2.3 Nitride-Based UHTCs

Nitride-based UHTCs are generally employed for industrial applications such as hard coatings, diffusion barriers, heat mirrors and decorative coatings. The UHTC material, ZrN, can be employed as an IR reflective material. ZrN undergoes oxidation at room temperature and hence requires densification via pressureless sintering, hot pressing or hot isostatic pressing. However, these methods require a high temperature of 2273 K, along with high applied loads due to the high melting point of the material, strong covalent bonding and the presence of ZrO₂ oxide layer in the powder surface [27, 28]. Selective laser reaction sintering (SLRS) method can be employed for manufacturing nearly net-shaped UHTC materials including HfN, ZrN and TiN along with carbides and borides of transition metal elements. The group IV transition metals and their oxides are chemically transformed and incorporated into very thin layers of UHTCs via the selective laser interaction sintering in presence of 100% vol of CH₄ or NH₃ gas. The SLRS processing of transition metals and their oxides resulted in the development of near stoichiometric single phases of UHTCs [29].

In a study, a group of researchers synthesised non-stoichiometric hafnium carbonitrides (HfC_xN_y) by employing a short-term high-energy ball milling of Hf and C powders. This was followed by the combustion of Hf/C composite particles in a nitrogen environment at a pressure of 0.8 MPa. The synthesised composite material exhibited a high melting point much greater than that for HfC. The non-stoichiometric hafnium carbonitride thus developed further processed to bulk ceramic material via spark plasma sintering. The bulk composite exhibited a relative density of 98%, along with excellent fracture toughness and hardness [30]. Due to the beneficial properties and application suitability of boride- and carbide-based UHTCs, not much research studies have been done so far on the nitride-based UHTCs, and the field of nitride-based UHTCs is still developing at a great pace.

3 Synthesis Techniques of UHTCs

The boride- and carbide-based UHTCs can be employed for a number of applications including the coating for re-entry vehicles in space applications. Such applications require high-quality coating materials with sufficient hardness and mechanical strength along with high heat conductivity [31]. There are a number of preparation methods available for the development of UHTCs. Depending on the type of application for which UHTCs are employed, a specific preparation method may be employed. The following subsections discuss the various synthesis techniques employed for the preparation of UHTCs.

3.1 Powder Synthesis Method

In certain applications, the purity of UHTC composite powder employed must be high for ensuring the desired properties and microstructures for the synthesised UHTC materials. The powder synthesis method is a suitable method for applications that require the synthesis of diborides of Zr and Hf. It includes the synthesis from the reaction between elements, borothermic or carbothermic or metallothermic reduction of metal oxides, boron carbide reduction of metal oxides in carbon rich environment, molten salt electrolysis, solution-based methods and synthesis from polymer precursors.

3.1.1 Synthesis of UHTCs from Elements

The simplest method for the production of boride powder includes the chemical reaction between boron and powdered metals and thereby establishing a control over the stoichiometry of the boride powder [32]. The densification of the generated ZrB_2 or HfB_2 can be done by plasma sintering method or hot-pressing method. A method known as self-propagating high-temperature synthesis (SHS) that utilises the high exothermic energy of reactions in developing a high-temperature environment necessary for completion of chemical reactions between the boron and metal can also be employed for the synthesis of diboride-based UHTCs. Low-cost equipment requirement, low energy consumption, short process time and excellent purity are some of the benefits of employing this method. However, the retention of more than 50% of porosity along with incompleteness of chemical reactions due to fast heating is some drawbacks of this method [33].

3.1.2 Borothermic Reduction of Metal Oxide

Borothermic reduction of metal oxides at a temperature above 1273 K leads to the development of pure boride materials. A drawback of this method is the wastage of boron via the formation of boron oxide and hence is not deployed for industrial applications. This is evident from reduction in boron content of product thus prepared. By introducing mechanical milling, it is possible to lower the reaction temperature, enhance the mixing of chemicals via reduction of grain size and introduces lattice deformations leading to faster diffusion and mass transfer rates [34].

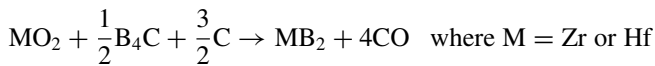
3.1.3 Carbothermic Reduction of Metal Oxide

Carbothermic reduction of metal oxide and boron oxide (B_2O_3) is an easy and simple method for the formation of boride materials at a high temperature of 2073 K [35]. A non-stoichiometric compound is formed via carbothermal reduction of the metal

oxide and leads to a loss of B_2O_3 during the reduction process and the deposition of residual carbon. The same method can be employed for the formation of boride whiskers. Nickel or cobalt can act as a catalyst during the process, however, nickel acts as a better catalyst during the process that also results in the formation of defects necessary for heat and mass transfer.

3.1.4 Boron Carbide Reduction of Metal Oxide

Here, powdered boride can be prepared at a temperature above 2073 K and keeping time for more than one hour, by the following reaction:

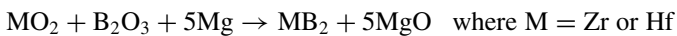


This reaction results in wastage of boron from boride powder and leads to the development of residual carbon and non-stoichiometric boride. The presence of unwanted oxygen can be removed by employing high vacuum during the reduction process.

The synthesis of boride is followed by its densification, which may be affected by the variation in size of the particle with the synthesis temperature. The synthesis stability and particle size are inversely related to the synthesis temperature [36].

3.1.5 Metallothermic Reduction

The metallothermic reduction can produce boride powder by employing the following the chemical reaction with magnesium as the reducing agent.



In metallothermic reduction, magnesium is employed as the reducing agent because of the ability of the formed MgO to leach out from the material, thus forming a pure boride phase. This reaction route also employs mechanical alloying to reduce the reaction temperature. Since it is an exothermic process, it can employ the SHS process. The sudden cooling and heating process via SHS generates a number of defects in the material and enhances the mass transfer rate. In order to overcome the incomplete reaction via SHS arising during the production of ZrB_2 from ZrO_2 , Mg and H_3BO_3 , a double SHS (DSHS) is generally performed, in which product of the first SHS reaction is mixed to Mg and H_3BO_3 and then a second SHS is performed on the mixture, thereby enhancing conversion process [37].

3.1.6 Solution-Based Techniques

Solution-based techniques can be employed for the synthesis of fine powders of borides, carbides and nitrides of transition metals due to the close contact between the reactants. At a low temperature of 1773 K, a group of researchers have prepared ZrB_2 powder employing hybrid precursor made of zirconium oxychloride ($ZrOCl_2 \cdot 0.8H_2O$), boric acid and phenolic resin which provide zirconia, boron oxide and carbon, respectively. The ZrB_2 powder thus synthesised is found to contain larger surface area and lower oxygen content in comparison with the surface area and oxygen content of commercially available ZrB_2 powder [38].

3.1.7 Molten Salt Electrolysis

Molten salt electrolysis method is employed for the preparation of diverse metal borides. One such metal boride, namely ZrB_2 can be deposited on nickel cathode from a mixture of ZrO_2 as well as B_2O_3 by dissolving with molten Na_3AlF_6 at 1293 K. The anode was prepared from graphite crucible. ZrB_2 deposit was found to be dendritic as well as fully non-adherent. A study tried to develop ZrB_2 on a Ni cathode from cryolite-alumina melts that contains Zr and B_2O_3 [39].

3.1.8 Synthesis by Polymer Precursor Route

A processible polymeric precursor for the preparation of boride materials can be developed via thoroughly dispersing a metal oxide in boron carbide polymeric precursor. This mixture with an increase of temperature will lead to formation of boron carbide as well as carbon, which is assisted subsequently by a chemical reaction to develop boride or a direct chemical reaction of a metal oxide with a polymer to form the final boride product [40].

3.2 Sol-Gel Method

Sol-gel method can be employed for the synthesis of diverse forms of UHTCs. It involves many steps including the mixing of chemicals in a solution followed by the gelation, drying and a post-treatment to get the final UHTC product. In this method, a homogeneous liquid state is employed initially that results in the development of nanopowders, fibres, thin films or porous monoliths of UHTCs with refined microstructures and mechanical properties. There are three commonly employed sol-gel methods for the synthesis of UHTCs as depicted in Fig. 3. In the templating method, infiltration or impregnation of the porous template is done with the pre-ceramic sol, followed by drying the green body and heating it up to 1873 K for the development of porous UHTCs by means of a reduction reaction. The template

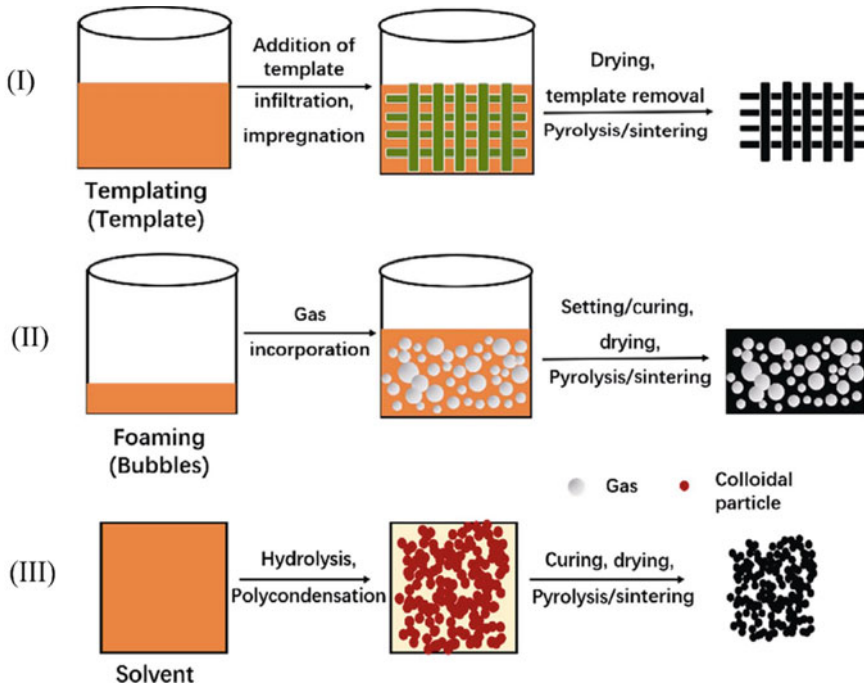


Fig. 3 Schematic representation of sol-gel process employed for the synthesis of porous UHTCs [41]. Copyright 2020. Reproduced with permission from SpringerLink

is later removed to form a stand-alone porous UHTC. The porous UHTC exhibits the same morphology as that of the original porous template, and however, undergoes shrinking during the process. In the second sol-gel method known as foaming, bubbles are developed initially with the help of air or any other volatile agents into the preceramic sol and results in green body after leaving it for setting. The third method, known as solvent evaporation, is a template free method, in which a preceramic sol-gel is transformed to a preceramic wet gel. The solvent is then evaporated to form porous UHTCs at the end [41].

4 Densification Methods for UHTCs

The poor intrinsic self-diffusion properties, strong covalent bonding and the extremely high melting points prevent the densification of UHTCs, which is required for the further employment of these materials in diverse applications. The UHTC surfaces get covered with metal oxides and it prevents the contact between boride particles, which in turn adversely affects the densification process. At high temperature, an excess growth of grains occur that leads to poor mechanical properties.

Densification process of UHTCs can be performed only at extreme pressure and temperature conditions. Some important densification processes include pressureless sintering, hot pressing, spark plasma sintering, microwave sintering and laser-assisted sintering. The following subsections briefly describe these methods employed for the densification of various types of UHTCs.

4.1 Pressureless Sintering

Ceramic materials with very dense shape can be prepared by means of pressureless sintering techniques. In the method, a cold isostatic pressing may be applied to prepare green compacts with excellent strength and then green pellets are fired in an induction furnace at a particular temperature under a controlled experimental environment. This method can be employed to produce near finished UHTCs, that do not require any additional finishing techniques such as diamond machining. One drawback of pressureless sintering is that the properties of the UHTCs developed are much inferior to that developed by means of other types of densification techniques. This arises due to the dominant nature of evaporation–condensation mechanisms during this process. Diverse additives have been added during the densification process to form boride-based UHTCs. It is also possible to add metals, carbides and silicides to improve the process of densification. Adding carbon and carbides help in the densification of borides to a high relative density of 95% at a high temperature of 2273 K. The interaction of additives with the surface oxide layer leads to the enhancement of surface energy, which in turn leads to the enhancement in densification. This method can be employed for the generation of UHTCs which do not require a high-density value. The porosity of the material results in lowering the stiffness of the material and thereby its thermal conductivity also. In a study, the pressureless sintering technique was employed by a group of researchers for the fabrication of a UHTC composite material ZrB_2 –SiC at a high temperature of 2273 K to 2473 K for 1 h in an argon environment. The composite was found to exhibit a relative density of 98.12% and a hardness of 15.02 GPa at 2473 K [42]. In a recent study, a ZrB_2 –SiC– Cr_xC_y , ZrB_2 –SiC– Mo_xC_y , ZrB_2 –CrC, ZrB_2 –MoC as well as ZrB_2 –WC composites were densified via a pressureless sintering method. As per the study, WC exhibited the highest ability to densify ZrB_2 and ZrB_2 –SiC, while Cr_3C_2 exhibited the lowest ability to densify them [43].

4.2 Reactive Sintering

UHTCs formed of the composites ZrB_2 –SiC are employed for extreme high-temperature applications, wherein the temperature exceeds 2273 K. The oxidation resistant nature of UHTCs revealed various methods for enhancing the oxidation performance that include the control of powders used at the beginning of the process,

composition of the initial materials and size distribution, type of additives, mixing of these materials and the densification methods employed. This helps in improving the viscosity of the liquid phases developed at high temperature. The addition of SiC is suitable for low temperature densification while La addition leads to the formation of ZrO_2 via liquid phase sintering. These methods result in the generation of self-generating refractory oxidation barriers, which are of superior importance in the field of high-temperature coating materials.

In this regard, the pressureless reactive sintering provides high purity products at low processing temperature and time and results in modifying grain boundary of materials. A green body having a lower porosity produces a product with high density. This process generates defects and dislocations via shock consolidation process, leading to diffusivity, which in turn enhances the density and thermal conductivity of the material. In a study, a group of researchers have employed a selective laser reaction sintering (SLRS) to prepare net-shaped UHTCs including HfC, ZrC, HfN, ZrN and TiN. The method was able to produce near stoichiometric UHTCs, however, some volumetric changes were observed due to gas–solid reactivity in the case of single component precursors. The volume changes of the metal or metal oxide precursors were compensated by the inclusion of composite metal/metal oxide precursors, which induces conversion induced stresses [44].

4.3 Hot Pressing

Dense UHTCs can be synthesised by means of hot-pressing method as the pressureless sintering of UHTCs in the absence of additives is a complicated process. Hot-pressing method employs an extremely high pressure and temperature to a powder compact. On applying pressure, diffusion of particles at the contact points occurs, which in turn is affected by the particle size. A ball milling is employed to generate UHTC powder with a size of $2\ \mu\text{m}$ approximately before the employment of hot-pressing method. The powder obtained after milling is enriched with graphite die, which is subsequently subjected to high temperature in an argon rich environment. A UHTC composite ZrB_2 –HfC–C_f was developed by employing a low temperature hot-pressing method using nanosized ZrB_2 powder. The composite material was found to exhibit non-brittleness, excellent work of fracture and a comparatively high thermal shock resistance. The material also exhibited excellent oxidation resistance, which is required for high-temperature applications [45].

4.4 Reactive Hot Pressing

This represents a technique of densification, wherein the reaction proceeds at a slow pace via the diffusion of solid-state particles. In this method, thermodynamically favourable reactions occur in a completely controlled manner that ensures the perfect

conversion of reactants to products. This reaction proceeds via simultaneous application of pressure that ensures the formation of dense bodies of UHTCs. This also eliminates the need for further powder processing of the densified UHTC. With the help of Si, Hf and B_4C as the precursors, a HfB_2 -SiC UHTC composite was synthesised by employing a reactive hot-pressing method for its densification. The reduction in size of precursors was tested by employing a vibration milling and was identified as a critical parameter that determines the microstructure of the UHTCs. The vibration milled sample exhibited a uniform oxidation, while the bare sample exhibited non-uniform oxidation. The mechanical properties of the material were tested and it was identified that the reduction in size of the precursors via vibration milling leads to an increased flexural strength also [46].

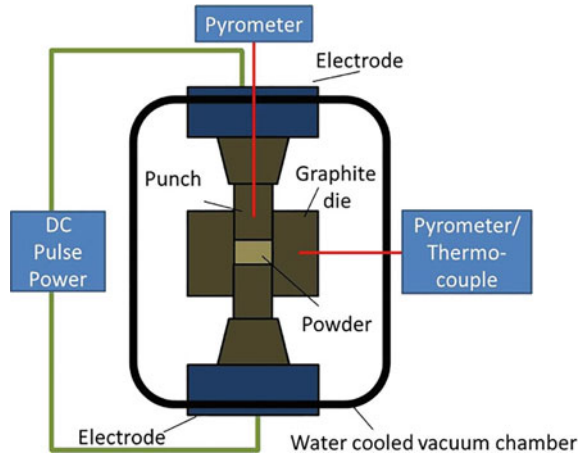
4.5 Spark Plasma Sintering

It is an advanced method for the densification of UHTCs, wherein it is possible to develop high-density UHTCs at a low reaction temperature during a very short span of time. A pulsed direct current is allowed to flow through the graphite plungers and dies along with the applications of pressure. The schematic representation of a SPS is shown in Fig. 4. This method is alternatively called as field-assisted sintering technique (FAST). It consists of a mechanical loading system, which can also act as a high-power electrical circuit kept in a controlled experimental condition. The simultaneous applications of current and pressure result in the densification of the UHTC [47]. SPS can be employed for homogeneous distribution of whiskers in UHTC composites. In a work, a group of researchers have employed SPS to densify a UHTC composite composed of B_4C and SiC_w powder mixtures. The method employed the densification of B_4C -SiC_w composite by using various wt% of SiC approximately ranging up to 12 wt% of the composite at a high temperature of 2073 K for a duration of 10 min at 50 MPa pressure. The study showed that the B_4C -SiC_w formed with a 9 wt% of SiC provided excellent Vicker's hardness, flexural strength and fracture toughness [48].

4.6 Microwave Sintering

Microwave sintering is a method employed for densifying UHTCs, in which heating of powder compact is attained via the application of microwaves to sample. Some materials do not possess the ability to absorb microwaves at room temperature; however, they can absorb microwaves if some microwave absorbing second phase is added. This technique involves a uniform and rapid heating of the sample since the microwave energy is directly given to the specimen without conducting it to the specimen. In a study, Ni was employed as a second microwave absorbing phase for

Fig. 4 Schematic representation of a SPS employed for the densification of UHTCs [47]. Copyright 2014. Reproduced with permission from Wiley online library



the densification of TiC. The study showed that density of microwave sintered specimen is 8–10% above that densified by means of conventional sintering techniques [49]. Another study employed microwave sintering method for the densification of ZrB₂-SiC composite and investigated its mechanical and other metallurgical characteristics. The study showed the highest relative density and Vickers hardness values of 97.72% and 17.03 GPa, respectively, for ZrB₂-25 vol% SiC composite [50].

4.7 Laser Sintering

This method produces dense material by sintering the powder layer by layer with the help of laser. The sample in the powder form is irradiated with a laser beam, resulting in a rise in temperature of sample leading to a size increment for the grain and eventually densification of sample. This method ensures high purity sample densification due to minimum contact between the particles. A group of researchers have developed a ZrB₂ UHTC with uniform surface morphology via laser sintering technique. The laser sintering also employs rapid cooling and leads in developing needle like nanostructures on material surface [51].

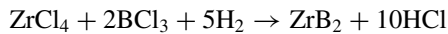
5 Coating Methods

Certain applications require UHTCs in coating form, which can be achieved by diverse methods. However, not all coating methods are applicable for UHTCs composed of borides of Zr and Hf. Vapour deposition process is the most suitable method for the development of refractory UHTCs. Some useful coating methods such as chemical vapour deposition, physical vapour deposition and plasma spray

that are employed for the coating of refractory borides are briefly described in the following subsections.

5.1 Chemical Vapour Deposition (CVD) Method

The chemical reaction of reactant vapours on a substrate results in the development of UHTC coatings via chemical vapour deposition (CVD) method. The ZrB₂ coating can be developed by employing a hydrogen reduction of ZrCl₄ and BCl₃ with argon gas as the carrier gas for the reactant vapour as per the following chemical reaction:



The precursors employed for the CVD method include Zr(BH)₄ and Hf(BH)₄, thus leading to the formation of ZrB₂ and HfB₂, respectively. By employing the CVD method, a group of researchers have developed TaC coatings on a C/C composite by maintaining a temperature beyond 2373 K. The study showed that the ablative characteristics of the UHTC coating thus prepared are highly altered by the morphology of crystal. The study also showed that an acicular crystal TaC coating exhibits excellent ablation resistance, while acute oxidation results in the conversion of the coating to its powder form [52]. The schematic representation of the CVD employed for the preparation of the UHTCs is shown in Fig. 5. With the selection of the precursors for the preparation of UHTCs, the reaction occurs within the reaction chamber at high temperature and results in the deposition of the UHTCs as depicted in Fig. 5.

5.2 Physical Vapour Deposition Method

In this method, the physical removal of a material from a sample by means of evaporation or ejection is used in preparing a thin film of UHTC coatings without incorporating chemical reactions. But it involves some procedures including high-temperature vacuum deposition, plasma sputtering, etc., to coat the UHTC material on the surface of a substrate. A sputtering method that involves the ejection of atoms from a solid material via collision with particle of high energy, was employed by researchers to form a UHTC thin film of ZrB₂ having a thickness of 800 nm on silicon substrate [54]. The schematic representation of the physical vapour deposition method for the preparation of UHTCs is shown in Fig. 6.

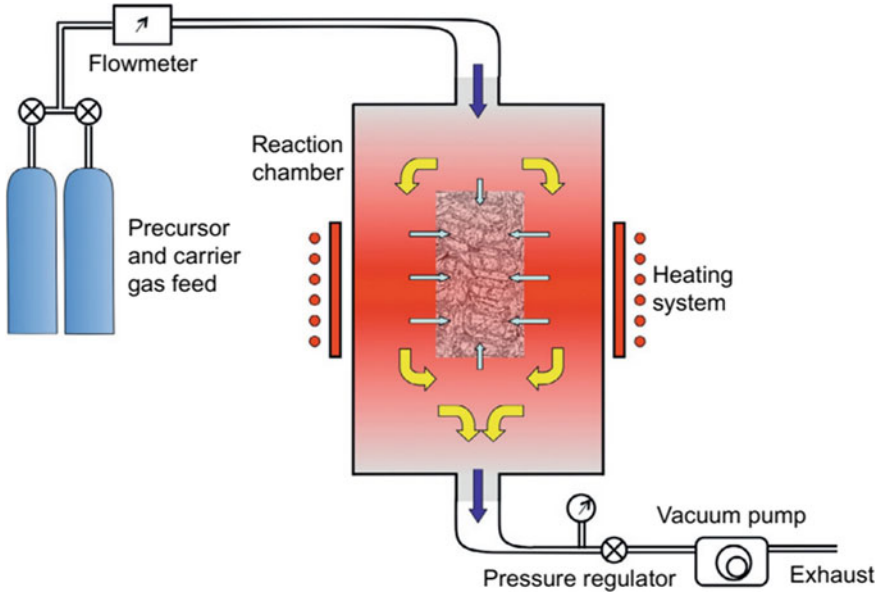


Fig. 5 Schematic representation of chemical vapour deposition/infiltration employed for the preparation of UHTCs [53]. Copyright 2015. Reproduced with permission from Elsevier

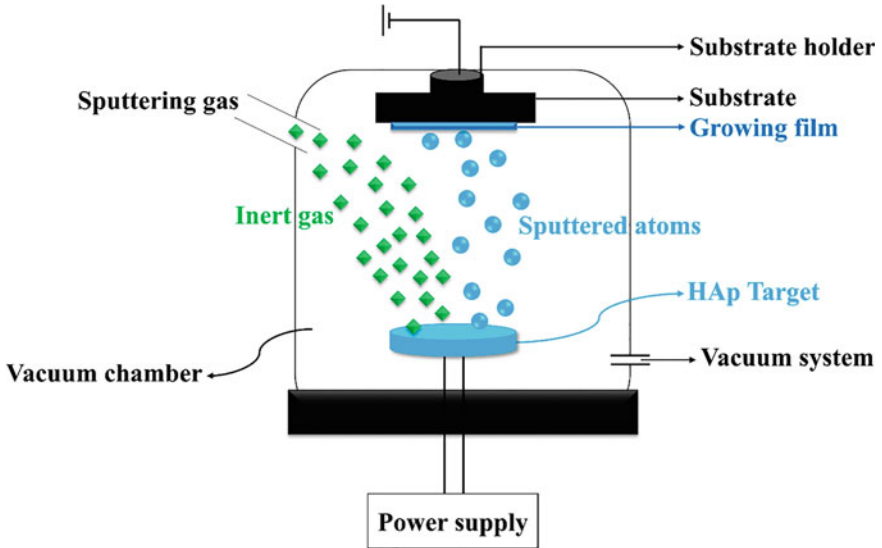


Fig. 6 Schematic of physical vapour deposition method for the preparation of UHTCs [55]. Copyright 2021. Reproduced with permission from MDPI

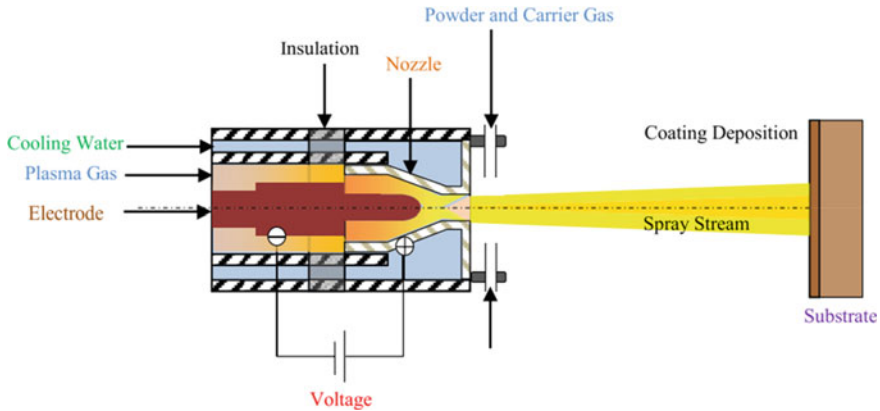


Fig. 7 Schematic of plasma gun employed for the preparation of UHTCs [57]. Copyright 2019. Reproduced with permission from Elsevier

5.3 Plasma Spray Method

This technique is employed in preparing UHTC coatings having large thickness, usually in the range of 4–5 mm. Through this method, it is also possible to develop free standing UHTC coatings by removing the substrate. The quality of developed coating depends mainly on the properties of starting powders employed for the development of UHTCs in powder form. The oxidation resistance of UHTC is improved by depositing them via vacuum plasma spray method. The schematic of plasma gun employed for the preparation of UHTCs is shown in Fig. 7. In one such study, a group of researchers have deposited a UHTC coating of HfC and TiC on a substrate via plasma spray technique. The materials exhibited excellent hardness and mechanical properties. The hardness of HfC and TiC coatings was 1650.70 HV and 753.60 HV, respectively, while for HfC and TiC layers in the multilayer sample, the values were 1563.50 HV and 1059.20 HV, respectively. The roughness values were estimated as 5.710 μm for HfC coating, 4.300 μm for TiC coating and 3.320 μm for HfC/TiC coatings [56]. The Vicker's hardness obtained for single and multilayer coatings of HfC, TiC and HfC/TiC is depicted in Fig. 8.

6 Properties of UHTCs

The popular UHTC materials such as borides, carbides and nitrides of transition metals possess diverse mechanical and thermodynamic properties, which need to be optimized for specific applications. The important mechanical and thermodynamic properties of UHTCs are described in the subsequent subsections.

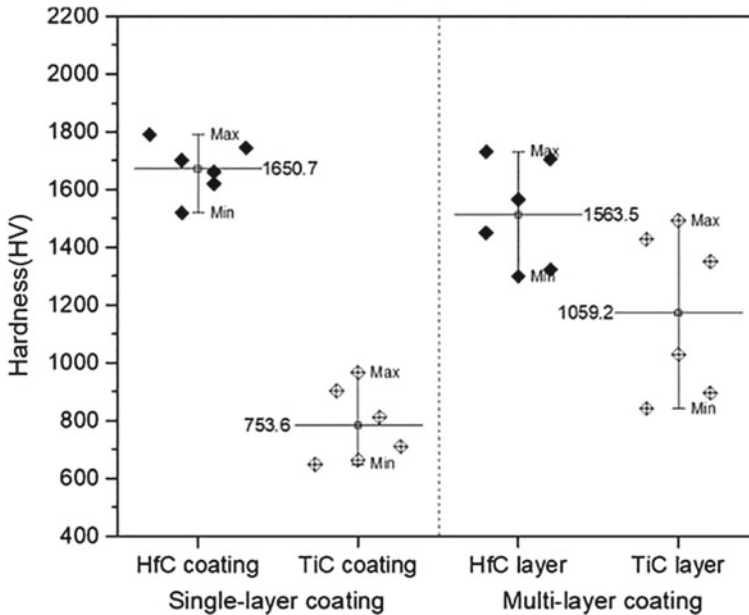


Fig. 8 Vicker's hardness of single and multilayer coatings of HfC, TiC and HfC/TiC formed by plasma spray method [56]. Copyright 2020. Reproduced with permission from MDPI

6.1 Mechanical Properties of UHTCs

Mechanical properties of UHTCs are of prime importance in various high-temperature applications. The important mechanical properties of UHTCs include elastic modulus, hardness, flexural strength, fracture toughness and grain size after sintering. The two mechanical properties of boride-based UHTCs, namely the elasticity and hardness are deeply related to the density of the material. However, the room temperature flexural strength depends on grain size of particles in UHTCs. But, grain size of particles is dependent on particle size at the initial stage, reinforcement phase content and the type of processing technique employed.

In a study, different composites composed of ZrB_2-B_4C were fabricated with 5, 15, 20 and 25 wt% of B_4C which were synthesised via a spark plasma sintering method at a temperature of 2273 K. All composite materials of ZrB_2-B_4C thus formed were found to possess a relative density value in the range of 96.14–97.78%. However, adding B_4C to ZrB_2 matrix resulted in the improvement of the hardness of the composite material. The hardness of the composite material varied to a high value of 20 GPa when the wt% of B_4C is increased from 5 to 20. The fracture toughness of the composite material also varied from 2.93 $MPa\cdot m^{0.5}$ to 4.13 $MPa\cdot m^{0.5}$ when the wt% of B_4C is increased from 5 to 25. A highest machining speed of 10.56 mm^2/min was exhibited by the ZrB_2-25 wt% B_4C composite [58]. Nanoindentation can be employed to identify the mechanical properties of UHTCs. In a recent study,

researchers have performed a nanoindentation under 6 strain rates to estimate the mechanical properties of UHTCs formed of the composite ZrB_2-SiC . The ZrB_2-SiC composite ceramic was fabricated by means of spark plasma sintering process and attained a relative density of 99.1%. The study showed that the hardness of the material increases with an increase in strain rate [59].

The joining of UHTC parts is a crucial process and it requires demanding conditions as it is difficult to manufacture large and complex components of the material. In a recent study, a Ni foil was employed as a filler to join UHTC parts and resulted in the fabrication of $ZrB_2-SiC/Ni/ZrB_2-SiC$ (ZS/Ni/ZS) joint. The joint exhibited satisfactory mechanical properties by delivering a high shear strength, while the elastic modulus at the joint was found to be lower than that exhibited by the composite material. The oxidation resistance of the joint ZS/Ni/ZS joint was found to be extremely good, thus indicating that the joint can be employed for various experimental conditions over a range of temperature varying from 1073 to 1473 K [60]. In a recent research work, a sol-gel method was used in preparing UHTCs and developed a porous UHTC with grain size varying from 1 to 500 urn and a porosity in a range of 60% to 95% at a low temperature. This implies that the mechanical properties, specifically the grain properties, can be modified to a great extent by choosing a suitable synthesis method for UHTCs [41].

6.2 Thermal Shock Resistance of UHTCs

The brittleness of UHTCs leads to thermal shock failure of them under extreme conditions of temperature and pressure and is a critical concern when employed for various applications. Thermal shock fracture parameters and thermal shock damage parameters that define the thermal properties of UHTC materials. It is possible to improve the thermal shock resistance of the UHTCs by increasing its flexural strength keeping the elastic modulus, thermal expansion coefficient and the Poisson's ratio constant.

The thermal shock resistance of UHTCs can be improved by means of optimising the microstructure designs of the UHTC materials. The symmetric distribution of strong covalent bonds in UHTCs results in low damage resistance of UHTCs due to their intrinsic brittleness. Particle toughening is a suitable mechanism for improving the mechanical properties of UHTCs. In this method, the addition of second phase dispersion particles improves the corrosion and impact resistance of UHTCs. The toughening of whiskers is another mechanism by means of which the hardness, elastic modulus, tensile strength and thermal shock resistance of the UHTCs can be improved largely. A study employed slurry injection in combination with vacuum infiltration for developing carbon filler-reinforced ZrB_2-SiC ceramics. An improvement in mechanical properties of the composite ceramics ZrB_2-SiC was achieved via a homogeneous distribution between the nanofiller and the ceramics. A critical thermal shock temperature difference of 1087 K was attained, which is found to be greater than that for the traditional ZrB_2 based ceramics [61]. In another recent

research work, the researchers have improved the thermal shock resistance of a $\text{ZrB}_2\text{-SiC-Al}_3\text{BC}_3$ UHTC synthesised via spark plasma sintering. The critical shock resistance temperature of the sample was found to be increasing with an increase in sintering temperature. In addition, the other mechanical properties of the material such as fracture toughness and flexural strength were also found to be improved to a great extent. The critical thermal shock resistance temperature of the specimen was found to be 865 K [62].

7 Simulation and Modelling Studies on UHTCs

The temperature distribution during the sintering process for the densification of UHTCs is very crucial as it decides the application suitability of many UHTCs. A prior numerical analysis will enable the researchers to identify the cons and pros of employing a particular technique for synthesis, densification or coating of UHTCs. The microstructure and the other related thermodynamic properties of the prepared sample are determined largely by the distribution temperature within the sample. Hence, in a study, researchers have performed a numerical analysis of the temperature distribution TiB_2 UHTCs during the densification process by employing a spark plasma sintering method. In this study, the current density distribution and the generated heat arising from Joule heating effect were determined during spark plasma sintering process. By employing a finite element method, it was identified that the point where the specimen is clamped to the die produces high heat and it dissipates to the sample from the centre and finally to the surroundings. A homogeneous temperature distribution was identified in the sample and the maximum temperature difference was 348 K at the sample/die interface when maintaining a sintering temperature of 2473 K [63]. A numerical study was conducted on SPS of a cylindrical sample of TiC. A finite element method was employed for solving differential equations such as heat diffusion equation and the electricity distribution equation. Stefan Boltzmann law and Newton's cooling law were employed to solve the radiation heat transfer and the convective cooling mechanisms. The study showed that the temperature of the sample is maximum at the centre. A gradient distribution of temperature was identified in the sample along the radial direction with the minimum and the maximum values of temperature as 2193 K and 2273 K, respectively, while no gradient distribution of temperature was noticed along the vertical direction [64].

The effect of flaws on the flexural strength of UHTCs can be modelled via a numerical modelling and analysis. In a numerical modelling study, the UHTC composite materials, ZrB_2 , $\text{ZrB}_2\text{-SiC}$ and $\text{ZrB}_2\text{-SiC-G}$ composed of micro flaws, with adjustable size, shape and orientation have been modelled considering the properties of the material and the geometry of the flaws. The study indicated that the flaws have an impact on the flexural strength of the UHTC can be estimated from the value of elastic modulus and the related mechanical properties [65]. A phase field numerical modelling study was employed to measure the fracture toughness of the $\text{ZrB}_2\text{-C}$ ceramics possessing various engineered microarchitectures. The modelling study

was verified by considering a fibrous monolith consisting of various volume fractions of C-rich phase. The modelled samples containing 10 and 30 vol% of C-rich phase exhibited an effective fracture toughness values 42% above than that of pure ZrB_2 sample. If the C-rich phase is increased further to 50 vol%, the fracture toughness value was found to drop to a great extent as per the numerical study and was validated from the experimental results also [66].

A recent modelling study based on the finite element method with the governing equations such as balanced heat equation and transport equation was employed to analyse the suitability of UHTCs in hypersonic flight conditions. The mathematical modelling study was performed on the assumptions that the induced porosity follows the linear and parabolic solutions of Laplace equations. The critical heat flux for the modelling study was varied between 7 and 44 MW/m². Simulation study was performed for four diverse UHTC composites and the results indicated a temperature rise crossing 4973 K along with a deformation on the fixed area where the heat flux was developed. A reduction in deformation was noticed with a variation in porosity of the UHTC material. The study also identified that porous UHTCs possess excellent thermal shock resistance owing to the release of thermal shock via the existing pores in the material [67]. Temperature sensitive interior components can be developed for hypersonic flight applications. Dense UHTCs can be employed for thermal protection at the leading edges of hypersonic flights, while porous UHTCs can be employed for developing thermally insulated interfaces for their interior components. Designing suitable hypersonic vehicles require the modification of their thermodynamic properties over a range of temperature from 253 to 2773 K. A material point method can be employed for numerical modelling for analysing the temperature dependence of properties of materials with consisting of damage and in the absence of damage. The model involves the significance of micro buckling for estimating the stiffness and thermal conductivity of the UHTC material [68]. The ABAQUS software can be employed for simulating the ultra-high-temperature thermal field of loaded aircraft moving at ultra-high speed [69].

Machine learning (ML) algorithm has been employed for predicting Young's modulus, flexural strength and fracture toughness for various processing parameters, mixture selections as well as testing parameters. An accurately trained ML model can predict mechanical properties of UHTC materials properly. ML studies have shown that the prediction performance of the ML algorithms for the Young's modulus is superior when compared to that for flexural strength and fracture toughness [70]. A three-dimensional thermomechanical phase field model (PFM) was developed for analysing the thermal shock-induced fracture by considering the dependence of properties of material on temperature. This model is completely different from other PFMs due to the fact that it can remove the unexpected damage evolution by introducing a fracture energy threshold, which is completely dependent on temperature. Thus, the PFM study shows that the tensile part of the strain energy is dominant over the thermal shock-induced cracks in UHTCs [71].

8 Applications of UHTCs

In the aerospace applications, UHTCs play a prominent role in developing the thermal protection systems. It can be employed for various other applications including transpiration cooling and other high entropy applications. Some interesting recent applications of UHTCs are summarised in the following subsections.

8.1 Oxidation Protective UHTC Coatings

Carbon–carbon (C–C) composites are useful materials for hypersonic flight vehicles; however, they undergo oxidation in the presence of air at temperature above 773 K. They require excellent heat protection system to overcome aerothermal heating under high-temperature environment. The C–C composites can be thermally protected from oxidation by employing a UHTC coating material formed of ZrB_2 and SiC. In a method employed in this direction, researchers have combined pre-treatment and processing steps to develop continuous and adherent high-temperature coatings from infiltrated preceramic polymers. The protective coatings were tested at 2873 K and were identified as extremely beneficial for resistance against oxidation in such high-temperature applications [72]. In another study, the ablation-oxidation resistance of carbon fibre (Cf)/C matrix (C)–SiC–TiC–TaC ceramic matrix composite was developed by melt infiltration of alloy into a Cf/C preform and tested for various oxidation conditions. The test conditions include an oxyacetylene flame shot of 7.5 s duration fulfilled by a radiant furnace in air at 1873 K up to 480 s. The study showed an improvement in ablation-oxidation resistance of one order of magnitude for the oxidised/ablated ceramic matrix composite when compared to the unprotected one. The CMC can be employed for various aerospace and hypersonic applications [73].

A three-layer SiC/UHTC/SiC coating was prepared for the protection of C/SiC composites for a long duration over a temperature range of 1373 K to 1773 K. A novel sintering technique was employed to densify a ZrB_2 UHTC in presence of a gaseous mixture of 70 vol% Ar and 30 vol% air. A mass loss of 0.36, 1.65 and 3.45 mg cm^{-2} was reported when the composite UHTC material is exposed to air for 114 h at 1373 K, 114 h at 1573 K and 68 h at 1773 K, respectively. The low mass loss rate arises from the beneficial properties of both ZrB_2 and SiC layers [72].

8.2 Thermal Barrier UHTC Coatings

Thermal insulation under extreme conditions is useful for carbon aerogel and are characterised by brittleness and ease of fabrication. A sol–gel polymerisation of phenolic resin and siloxane resulted in silica modified carbon aerogels (SCAs). This process is followed by pressure drying and carbonisation. The study involves an

estimation of the density of the SCA and is found to possess a high density of 0.5 g/cm^3 and a mean pore size of 33 nm. The oxidation resistance of carbon aerogels can be improved to a great extent via the transformation of siloxane to amorphous SiO_2 particles and crystalline SiC particles that can be coated on the surface of carbon nanoparticles during the carbonisation process. SCAs possess a high thermal conductivity and excellent compressive strength. They can act as an excellent thermal barrier under extremely harsh environmental conditions [74]. In a study, a novel method was proposed to improve the thickness of thermal barrier coating locally in the hotspot areas for enhancing thermal insulation and life capabilities of combustor tiles. This method involves the inclusion of a pre dent for adding an extra thickness to the thermal barrier coating. The study showed a thickness dependent temperature reduction by 13% on the addition of pre dent, which in turn provided a performance improvement of 3% [75]. A few studies have reported the development of thermal barrier UHTCs using various methods [76, 77].

9 High Entropy UHTCs

The concept of high entropy UHTCs was derived from the existence of high entropy alloys. In a high entropy alloy, there exists five or more elements in equimolar or non-equimolar concentration, which in turn make the material to possess high configurational entropy. This also helps them to form single phase solid solution with some basic crystal structures such as FCC, BCC etc. There exists a wide range of high entropy ceramic materials such as high entropy borides, carbides, silicides, fluorides, diborides etc. The high entropy diborides and carbides such as ZrB_2 , HfB_2 , ZrC , HfC and TaC represent high entropy UHTCs. The first high entropy boride was reported in 2016 and fabricated in 2018 [78, 79]. The synthesised high entropy diborides exhibit a hexagonal crystal structure and the high entropy carbides exhibit a FCC structure.

9.1 Properties of High Entropy UHTCs

The mechanical properties of high entropy UHTCs are largely dependent on the microstructure of the ceramics. The Vicker's hardness of high entropy UHTCs with high density of found to be 20–35 GPa. High entropy UHTCs can be employed for thermal barrier coating applications owing to their excellent thermal shock resistance and oxidation resistance properties. The fibre-reinforced high entropy UHTCs possess excellent mechanical properties and can be employed for various high-temperature applications. This also removes the intrinsic brittleness of bulk UHTCs. Some studies have shown that the thermal conductivity of high entropy UHTCs is lower than that of the individual metal diborides and carbides. The presence of oxygen content can also affect the thermal conductivity of high entropy UHTCs. A

Table 1 Comparison of properties of high entropy UHTCs [82]

Material	M_{exp} [GPa]	H_{exp} [GPa]
HfC	552 ± 15	31.5 ± 1.3
TaC	579 ± 20	20.6 ± 1.2
ZrC	507 ± 16	31.3 ± 1.4
NbC	585 ± 23	27.2 ± 1.7
(Hf–Ta)C	559 ± 18	32.9 ± 1.8
(Hf–Ta–Zr–Nb)C	598 ± 15	36.1 ± 1.6
Rule of mixture (HfC, TaC, ZrC, NbC)	556	27.7

Copyright 2018. Reproduced with permission from Scientific Reports

study has shown that the addition graphite can eliminate the oxygen impurity and improve the thermal conductivity of high entropy UHTCs [80].

The oxidation resistance of high entropy UHTC materials is found to be better than that of the individual diborides and carbides [78]. Due to the presence of a several elements in the high entropy ceramics, they exhibit compositional diversity, which in turn can help to improve the oxidation resistance of these materials. The addition of SiC to the high entropy UHTCs improves the oxidation resistance via the formation of an oxide layer coating for the UHTC material [81]. A comparison of experimental values of the properties such as indentation modulus (M) and hardness (H) of various high-temperature UHTCs is listed in Table 1.

9.2 *Applications of High Entropy UHTCs and Future Research Directions*

High entropy UHTCs can also exist in diverse forms such as ceramic form, coatings, thin films, fibre-reinforced composite coating form etc. The fibre-reinforced high entropy UHTC coatings possess excellent mechanical properties owing to the oxidation resistance of the high entropy UHTC material. The future research studies must focus on the high entropy UHTCs and the fibre-reinforced high entropy UHTC coatings because of their unique mechanical and thermodynamic properties. Not much studies have been done so far on the high entropy UHTCs and high entropy UHTC coatings. The studies done so far on these materials are very scarce, which in turn hinders the application of these materials under high-temperature environments.

10 Summary and Outlooks

This chapter focuses on the recent advances in UHTCs in various applications under very high-temperature environments. The borides, nitrides and carbides of various transition metals can be employed for synthesising ultra-high-temperature ceramic (UHTC) coatings and a brief overview of these materials is included in this chapter. These materials possess excessively high melting point along with excellent mechanical properties at extremely high temperature, including excellent intrinsic brittleness and hardness. The extremely poor shock resistance of bulk ceramics can be overcome to a greater extent with the application of ultra-high-temperature ceramic coatings and fibre-reinforced ultra-high-temperature ceramics. UHTC coatings are extremely useful as thermal shock absorbers, surface seals and leak minimisers. The chapter also summarises the different synthesis methods, densification methods and coating methods that can be employed for UHTCs. The solid-state powders-based and solution-based methods have been employed recently to enhance the unique properties of them. The synthesis methods face a few challenges and require highly refined approaches to synthesis high purity UHTC powders, suitable chemical synthesis reactions and proper selection of precursors delivering excellent chemical yield and less degradation. Apart from the excellent mechanical properties such as excellent elasticity, flexural strength and fracture toughness, the UHTCs must be assessed for its machinability when they are employed for hypersonic and space applications. Oxidation resistance at high-temperature environment is the most wanted property of materials especially when they are employed for various space applications. This chapter also summarised the mechanical and thermodynamic properties of UHTCs.

Recent advances show that the use of multilayers of the high-temperature ceramic protective coating reduces the oxidation of carbon-carbon (C-C) composites and protect them from aerothermal heating at temperatures above 3273 K. Hence, the mechanisms, kinetics and the end products of oxidation mechanisms help the researchers to identify the strengths and weaknesses of the UHTCs when employed for specific applications. A brief overview of the computational studies done so far on UHTCs for estimating and validating their mechanical and thermodynamical properties is also mentioned in this chapter. The atomistic computational modelling and simulation studies on the impacts of defects on the thermal and mechanical properties of UHTCs are found to be extremely useful to identify their drawbacks prior to their employment in various device configurations. In a similar way, the computational studies on UHTCs by employing thermal shock modelling tools provide useful information about their thermal shock resistance. This chapter also provides a brief overview of the applications of UHTCs along with a description of the properties and applications of the emerging high entropy UHTCs.

References

1. Belmonte, M.: Advanced ceramic materials for high temperature applications. *Adv. Eng. Mater.* **8**, 693–770 (2006). <https://doi.org/10.1002/adem.200500269>
2. Eakins, E., Jayaseelan, D.D., Lee, W.E.: Toward oxidation-resistant ZrB₂-SiC ultra high temperature ceramics. *Metall. Mater. Trans. A.* **42**, 878–887 (2011). <https://doi.org/10.1007/s11661-010-0540-8>
3. Guo, S.Q.: Densification of ZrB₂-based composites and their mechanical and physical properties: a review. *J. Eur. Ceram.* **29**, 995–1011 (2009). <https://doi.org/10.1016/j.jeurceramsoc.2008.11.008>
4. Thimmappa, S.K., Golla, B.R.: Oxidation behavior of silicon-based ceramics reinforced diboride UHTC: a review. *Silicon* **1–26** (2022). <https://doi.org/10.1007/s12633-022-01945-8>
5. Ni, D., Cheng, Y., Zhang, J., Liu, J.X., Zou, J., Chen, B., Wu, H., Li, H., Dong, S., Han, J., Zhang, X.: Advances in ultra-high temperature ceramics, composites, and coatings. *J. Adv. Ceram.* **11**, 1–56 (2022). <https://doi.org/10.1007/s40145-021-0550-6>
6. Fahrenholtz, W.G., Hilmas, G.E.: Ultra-high temperature ceramics: materials for extreme environments. *Scr. Mater.* **129**, 94–99 (2017). <https://doi.org/10.1016/j.scriptamat.2016.10.018>
7. Zhang, X., Hu, P., Han, J., Meng, S.: Ablation behavior of ZrB₂-SiC ultra high temperature ceramics under simulated atmospheric re-entry conditions. *Compos. Sci. Technol.* **68**, 1718–1726 (2008). <https://doi.org/10.1016/j.compscitech.2008.02.009>
8. Opeka, M.M., Talmy, I.G., Wuchina, E.J., Zaykoski, J.A., Causey, S.J.: Mechanical, thermal, and oxidation properties of refractory hafnium and zirconium compounds. *J. Eur. Ceram.* **19**, 2405–2414 (1999). [https://doi.org/10.1016/S0955-2219\(99\)00129-6](https://doi.org/10.1016/S0955-2219(99)00129-6)
9. Van Wie, D.M., Drewry, D.G., King, D.E., Hudson, C.M.: The hypersonic environment: required operating conditions and design challenges. *J. Mater. Sci.* **39**, 5915–5924 (2004). <https://doi.org/10.1023/B:JMSC.0000041688.68135.8b>
10. Wuchina, E., Opila, E., Opeka, M., Fahrenholtz, B., Talmy, I.: UHTCs: ultra-high temperature ceramic materials for extreme environment applications. *The Electrochem. Soc. Interface.* **16**, 30 (2007). <https://doi.org/10.1149/2.F04074IF>
11. Mao, H., Shen, F., Zhang, Y., Wang, J., Cui, K., Wang, H., Lv, T., Fu, T., Tan, T.: Microstructure and mechanical properties of carbide reinforced TiC-based ultra-high temperature ceramics: a review. *Coatings* **11**, 1444 (2021). <https://doi.org/10.3390/coatings11121444>
12. Tului, M., Lionetti, S., Pulci, G., Rocca, E., Valente, T., Marino, G.: Effects of heat treatments on oxidation resistance and mechanical properties of ultra-high temperature ceramic coatings. *Surf. Coat. Technol.* **202**, 4394–4398 (2008). <https://doi.org/10.1016/j.surfcoat.2008.04.015>
13. Tului, M., Lionetti, S., Pulci, G., Marra, F., Tirillò, J., Valente, T.: Zirconium diboride based coatings for thermal protection of re-entry vehicles: effect of MoSi₂ addition. *Surf. Coat. Technol.* **205**, 1065–1069 (2010). <https://doi.org/10.1016/j.surfcoat.2010.07.120>
14. Chamberlain, A.L., Fahrenholtz, W.G., Hilmas, G.E., Ellerby, D.T.: High-strength zirconium diboride-based ceramics. *J. Am. Ceram.* **87**, 1170–1172 (2004). <https://doi.org/10.1111/j.1551-2916.2004.01170.x>
15. Carney, C., Paul, A., Venugopal, S., Parthasarathy, T., Binner, J., Katz, A., Brown, P.: Qualitative analysis of hafnium diboride based ultra high temperature ceramics under oxyacetylene torch testing at temperatures above 2100 °C. *J. Eur. Ceram.* **34**, 1045–1051 (2014). <https://doi.org/10.1016/j.jeurceramsoc.2013.11.018>
16. Balbo, A., Sciti, D.: Spark plasma sintering and hot pressing of ZrB₂-MoSi₂ ultra-high-temperature ceramics. *Mater. Sci. Eng.: A* **475**, 108–112 (2008). <https://doi.org/10.1016/j.msea.2007.01.164>
17. Sciti, D., Guicciardi, S., Nygren, M.: Densification and mechanical behavior of HfC and HfB₂ fabricated by spark plasma sintering. *J. Am. Ceram.* **91**, 1433–1440 (2008). <https://doi.org/10.1111/j.1551-2916.2007.02248.x>
18. Shen, L., Zhao, Y., Li, Y., Wu, H., Zhu, H., Xie, Z.: Synergistic strengthening of FeCrNiCo high entropy alloys via micro-TiC and nano-SiC particles. *Mater. Tod. Commun.* **26**, 101729 (2021). <https://doi.org/10.1016/j.mtcomm.2020.101729>

19. Gholizadeh, T., Vajdi, M., Rostamzadeh, H.: A new trigeneration system for power, cooling, and freshwater production driven by a flash-binary geothermal heat source. *Renew. Energ.* **148**, 31–43 (2020). <https://doi.org/10.1016/j.renene.2019.11.154>
20. Cui, K., Zhang, Y., Fu, T., Wang, J., Zhang, X.: Toughening mechanism of mullite matrix composites: a review. *Coatings* **10**, 672 (2020). <https://doi.org/10.3390/coatings10070672>
21. Cui, K., Mao, H., Zhang, Y., Wang, J., Wang, H., Tan, T., Fu, T.: Microstructure, mechanical properties, and reinforcement mechanism of carbide toughened ZrC-based ultra-high temperature ceramics: a review. *Compos. Interfaces.* **29**, 729–748 (2022). <https://doi.org/10.1080/09276440.2021.2012409>
22. Musa, C., Licheri, R., Orrù, R., Cao, G., Balbo, A., Zanotto, F., Mercatelli, L., Sani, E.: Optical characterization of hafnium boride and hafnium carbide-based ceramics for solar energy receivers. *Sol. Energy.* **169**, 111–119 (2018). <https://doi.org/10.1016/j.solener.2018.04.036>
23. Fahrenholtz, W.G.: Thermodynamic analysis of ZrB₂–SiC oxidation: formation of a SiC-depleted region. *J. Am. Ceram.* **90**, 143–148 (2007). <https://doi.org/10.1111/j.1551-2916.2006.01329.x>
24. Fahrenholtz, W.G.: The ZrB₂ volatility diagram. *J. Am. Ceram.* **88**, 3509–3512 (2005). <https://doi.org/10.1111/j.1551-2916.2005.00599.x>
25. Zeng, Y., Wang, D., Xiong, X., Zhang, X., Withers, P.J., Sun, W., Smith, M., Bai, M., Xiao, P.: Ablation-resistant carbide Zr_{0.8}Ti_{0.2}C_{0.74}B_{0.26} for oxidizing environments up to 3000 °C. *Nat. Commun.* **8**, 15836 (2017). <https://doi.org/10.1038/ncomms15836>
26. Zhang, B., Yin, J., Zheng, J., Liu, X., Huang, Z., Dusza, J., Jiang, D.: High temperature ablation behavior of pressureless sintered Ta_{0.8}Hf_{0.2}C-based ultra-high temperature ceramics. *J. Eur. Ceram.* **40**, 1784–1789 (2020). <https://doi.org/10.1016/j.jeurceramsoc.2019.11.043>
27. Singh, A., Kuppusami, P., Khan, S., Sudha, C., Thirumurugesan, R., Ramaseshan, R., Divakar, R., Mohandas, E., Dash, S.: Influence of nitrogen flow rate on microstructural and nanomechanical properties of Zr–N thin films prepared by pulsed DC magnetron sputtering. *Appl. Surf. Sci.* **280**, 117–123 (2013). <https://doi.org/10.1016/j.apsusc.2013.04.107>
28. Yoshitake, M., Yotsuya, T.Y.T., Ogawa, S.O.S.: Effects of nitrogen pressure and RF power on the properties of reactive magnetron sputtered Zr–N films and an application to a thermistor. *Jpn. J. Appl. Phys.* **31**, 4002 (1992). <https://doi.org/10.1143/JJAP.31.4002>
29. Peters, A.B., Wang, C., Zhang, D., Hernandez, A., Nagle, D.C., Mueller, T., Spicer, J.B.: Reactive laser synthesis of ultra-high-temperature ceramics HfC, ZrC, TiC, HfN, ZrN, and TiN for additive manufacturing. *Ceram. Int.* **49**, 11204–11229 (2023). <https://doi.org/10.1016/j.ceramint.2022.11.319>
30. Buinevich, V.S., Nepapushev, A.A., Moskovskikh, D.O., Trusov, G.V., Kuskov, K.V., Vadchenko, S.G., Rogachev, A.S., Mukasyan, A.S.: Fabrication of ultra-high-temperature nonstoichiometric hafnium carbonitride via combustion synthesis and spark plasma sintering. *Ceram. Int.* **46**, 16068–16073 (2020). <https://doi.org/10.1016/j.ceramint.2020.03.158>
31. Sonber, J.K., Murthy, T.C., Subramanian, C., Hubli, R.C., Suri, A.K.: Processing methods for ultra-high temperature ceramics. In: MAX phases and ultra-high temperature ceramics for extreme environments (180–202). IGI Global (2013). <https://doi.org/10.4018/978-1-4666-4066-5.ch006>
32. Brochu, M., Gauntt, B., Zimmerly, T., Ayala, A., Loehman, R.: Fabrication of UHTCs by conversion of dynamically consolidated Zr+ B and Hf+ B powder mixtures. *J. Am. Ceram.* **91**, 2815–2822 (2008). <https://doi.org/10.1111/j.1551-2916.2008.02550.x>
33. Anselmi-Tamburini, U., Kodera, Y., Gasch, M., Unuvar, C., Munir, Z.A., Ohyanagi, M., Johnson, S.M.: Synthesis and characterization of dense ultra-high temperature thermal protection materials produced by field activation through spark plasma sintering (SPS): I. Hafnium diboride. *J. Mater. Sci.* **41**, 3097–3104 (2006). <https://doi.org/10.1007/s10853-005-2457-y>
34. Millet, P., Hwang, T.: Preparation of TiB₂ and ZrB₂. Influence of a mechano-chemical treatment on the borothermic reduction of titania and zirconia. *J. Mater. Sci.* **31**, 351–355 (1996). <https://doi.org/10.1007/BF01139151>
35. Khanra, A.K., Pathak, L.C., Godkhindi, M.M.: Carbothermal synthesis of zirconium diboride (ZrB₂) whiskers. *Adv. Appl. Ceram.* **106**, 155–160 (2007). <https://doi.org/10.1179/174367607X162019>


36. Guo, W.M., Zhang, G.J.: Reaction processes and characterization of ZrB₂ powder prepared by boro/carbothermal reduction of ZrO₂ in vacuum. *J. Am. Ceram.* **92**, 264–267 (2009). <https://doi.org/10.1111/j.1551-2916.2008.02836.x>
37. Khanra, A.K., Pathak, L.C., Mishra, S.K., Godkhindi, M.M.: Sintering of ultrafine zirconium diboride powder prepared by modified SHS technique. *Adv. Appl. Ceram.* **104**, 282–284 (2005). <https://doi.org/10.1179/174367605X52077>
38. Xie, Y., Sanders, T.H., Jr., Speyer, R.F.: Solution-based synthesis of submicrometer ZrB₂ and ZrB₂-TaB₂. *J. Am. Ceram.* **91**, 1469–1474 (2008). <https://doi.org/10.1111/j.1551-2916.2008.02288.x>
39. Devyatkin, S.V.: Electrosynthesis of zirconium boride from cryolite–alumina melts containing zirconium and boron oxides. *Russ. J. Electrochem.* **37**, 1308–1311 (2001). <https://doi.org/10.1023/A:1013295931573>
40. Su, K., Sneddon, L.G.: Polymer-precursor routes to metal borides: synthesis of titanium boride (TiB₂) and zirconium boride (ZrB₂). *Chem. Mater.* **3**, 10–12 (1991). <https://doi.org/10.1021/cm00013a005>
41. Li, F., Huang, X., Liu, J.X., Zhang, G.J.: Sol–gel derived porous ultra-high temperature ceramics. *J. Adv. Ceram.* **9**, 1–16 (2020). <https://doi.org/10.1007/s40145-019-0332-6>
42. Mashhadi, M., Khaksari, H., Safi, S.: Pressureless sintering behavior and mechanical properties of ZrB₂-SiC composites: effect of SiC content and particle size. *J. Mater. Res.* **4**, 416–422 (2015). <https://doi.org/10.1016/j.jmrt.2015.02.004>
43. Mazur, P., Grigoriev, O., Vedel, D., Melakh, L., Shepa, I.: Ultra-high temperature ceramics based on ZrB₂ obtained by pressureless sintering with addition of Cr₃C₂, Mo₂C, and WC. *J. Eur. Ceram.* **42**, 4479–4492 (2022). <https://doi.org/10.1016/j.jeurceramsoc.2022.04.043>
44. Peters, A.B., Wang, C., Zhang, D., Hernandez, A., Nagle, D.C., Mueller, T., Spicer, J.B.: Reactive laser synthesis of ultra-high-temperature ceramics HfC, ZrC, TiC, HfN, ZrN, and TiN for additive manufacturing. *Ceram. Int.* **49**, 11204–11229 (2022). <https://doi.org/10.1016/j.ceramint.2022.11.319>
45. Hu, P., Gui, K., Hong, W., Zhang, X., Dong, S.: High-performance ZrB₂-SiC-Cf composite prepared by low-temperature hot pressing using nanosized ZrB₂ powder. *J. Eur. Ceram.* **37**, 2317–2324 (2017). <https://doi.org/10.1016/j.jeurceramsoc.2017.02.008>
46. Lee, S.J., Kang, E.S., Baek, S.S., Kim, D.K.: Reactive hot pressing and oxidation behavior of HF-based ultra-high-temperature ceramics. *Surf. Rev. Lett.* **17**, 215–221 (2010). <https://doi.org/10.1142/S0218625X10013886>
47. Guillon, O., Gonzalez-Julian, J., Dargatz, B., Kessel, T., Schiering, G., Räthel, J., Herrmann, M.: Field-assisted sintering technology/spark plasma sintering: mechanisms, materials, and technology developments. *Adv. Eng. Mater.* **16**, 830–849 (2014). <https://doi.org/10.1002/adem.201300409>
48. Zhao, X., Zou, J., Ji, W., Wang, A., He, Q., Xiong, Z., Wang, W., Fu, Z.: Processing and mechanical properties of B₄C-SiCw ceramics densified by spark plasma sintering. *J. Eur. Ceram.* **42**, 2004–2014 (2022). <https://doi.org/10.1016/j.jeurceramsoc.2022.01.003>
49. Vasudevan, N., Ahamed, N.N.N., Pavithra, B., Aravindhan, A., Shanmugavel, B.P.: Effect of Ni addition on the densification of TiC: a comparative study of conventional and microwave sintering. *IJRMHM.* **87**, 105165 (2020). <https://doi.org/10.1016/j.ijrmhm.2019.105165>
50. Sharma, A., Karunakar, D.B.: Development and characterizations of ZrB₂-SiC composites sintered through microwave sintering. In: *Advances in manufacturing and industrial engineering: select proceedings of ICAPIE 2019* (pp. 815–824). Springer Singapore (2021). https://doi.org/10.1007/978-981-15-8542-5_71
51. Sun, C.N., Baldrige, T., Gupta, M.C.: Fabrication of ZrB₂-Zr cermet using laser sintering technique. *Mater. Lett.* **63**, 2529–2531 (2009). <https://doi.org/10.1016/j.matlet.2009.08.059>
52. Zhang, Y., Gai, W., Wang, H., Chen, G., Zhang, P., Li, H.: Influence of crystallite morphology on the ablative behaviors of CVD-TaC coatings prepared on C/C composites beyond 2100 °C. *Corros. Sci.* **205**, 110426 (2022). <https://doi.org/10.1016/j.corsci.2022.110426>
53. Vignoles, G.L.: Chemical vapor deposition/infiltration processes for ceramic composites. In: *Advances in Composites Manufacturing and Process Design*, pp. 147–176. Woodhead Publishing (2015). <https://doi.org/10.1016/B978-1-78242-307-2.00008-7>

54. Shappirio, J.R., Finnegan, J.J.: Synthesis and properties of some refractory transition metal diboride thin films. *Thin Solid Films* **107**, 81–87 (1983). [https://doi.org/10.1016/0040-6090\(83\)90010-X](https://doi.org/10.1016/0040-6090(83)90010-X)
55. Safavi, M.S., Walsh, F.C., Surmeneva, M.A., Surmenev, R.A., Khalil-Allafi, J.: Electrodeposited hydroxyapatite-based biocoatings: recent progress and future challenges. *Coatings* **11**, 110 (2021). <https://doi.org/10.3390/coatings11010110>
56. Kim, H.S., Kang, B.R., Choi, S.M.: Microstructure and mechanical properties of vacuum plasma sprayed HfC, TiC, and HfC/TiC ultra-high-temperature ceramic coatings. *Materials* **13**, 124 (2019). <https://doi.org/10.3390/ma13010124>
57. Ranjan, A., Islam, A., Pathak, M., Khan, M.K., Keshri, A.K.: Plasma sprayed copper coatings for improved surface and mechanical properties. *Vacuum* **168**, 108834 (2019). <https://doi.org/10.1016/j.vacuum.2019.108834>
58. Mandal, S., Chakraborty, S., Dey, P.: A study of mechanical properties and WEDM machinability of spark plasma sintered ZrB₂–B₄C ceramic composites. *Micron* **153**, 103198 (2022). <https://doi.org/10.1016/j.micron.2021.103198>
59. Jin, X., Wang, X., Liu, L., Yin, Y., Wang, H., Zhang, B., Fan, X.: Strain rate effect on the mechanical properties of ZrB₂–SiC ceramics characterized by nanoindentation. *Ceram. Int.* **48**, 10333–10338 (2022). <https://doi.org/10.1016/j.ceramint.2022.01.331>
60. Jin, X., Yang, J., Sun, Y., Li, P., Hou, C., Zhao, Y., Fan, X.: Fabrication and characterisation of high-performance joints made of ZrB₂–SiC ultra-high temperature ceramics. *J. Eur. Ceram.* **41**, 7412–7422 (2021). <https://doi.org/10.1016/j.jeurceramsoc.2021.08.018>
61. Zhang, D., Feng, J., Hu, P., Xun, L., Liu, M., Dong, S., Zhang, X.: Enhanced mechanical properties and thermal shock resistance of Cf/ZrB₂–SiC composite via an efficient slurry injection combined with vibration-assisted vacuum infiltration. *J. Eur. Ceram.* **40**, 5059–5066 (2020). <https://doi.org/10.1016/j.jeurceramsoc.2020.07.003>
62. Zhao, X., Chen, Z., Wang, H., Zhang, Z., Shao, G., Zhang, R., Fan, B., Lu, H., Xu, H., Chen, D.: The influence of additive and temperature on thermal shock resistance of ZrB₂ based composites fabricated by spark plasma sintering. *Mater. Chem. Phys.* **240**, 122061 (2020). <https://doi.org/10.1016/j.matchemphys.2019.122061>
63. Fattahi, M., Ershadi, M.N., Vajdi, M., Moghanlou, F.S., Namini, A.S., Asl, M.S.: On the simulation of spark plasma sintered TiB₂ ultra high temperature ceramics: a numerical approach. *Ceram. Int.* **46**, 14787–14795 (2020). <https://doi.org/10.1016/j.ceramint.2020.03.003>
64. Bagheri, S.M., Vajdi, M., Moghanlou, F.S., Sakkaki, M., Mohammadi, M., Shokouhimehr, M., Asl, M.S.: Numerical modeling of heat transfer during spark plasma sintering of titanium carbide. *Ceram. Int.* **46**, 7615–7624 (2020). <https://doi.org/10.1016/j.ceramint.2019.11.262>
65. Wang, A., Zhao, X., Huang, M., Zhang, Z., Xie, L.: A quantitative study of flaw/strength response in ultra-high temperature ceramics based on femtosecond laser method. *Theor. Appl. Fract. Mech.* **110**, 102775 (2020). <https://doi.org/10.1016/j.tafmec.2020.102775>
66. Emdadi, A., Watts, J., Fahrenheitz, W.G., Hilmas, G.E., Zaeem, M.A.: Predicting effective fracture toughness of ZrB₂-based ultra-high temperature ceramics by phase-field modeling. *Mater. Des.* **192**, 108713 (2020). <https://doi.org/10.1016/j.matdes.2020.108713>
67. Zuccarini, C., Ramachandran, K., Russo, S., Jayakody, Y.C., Jayaseelan, D.D.: Mathematical modeling and simulation of porosity on thermomechanical properties of UHTCs under hypersonic conditions. *IJCES.* **5**, e10168 (2023). <https://doi.org/10.1002/ces2.10168>
68. Povolny, S.J., Seidel, G.D., Tallon, C.: Numerical investigation of thermomechanical response of multiscale porous ultra-high temperature ceramics. *Ceram. Int.* **48**, 11502–11517 (2022). <https://doi.org/10.1016/j.ceramint.2022.01.006>
69. Liu, B., Wang, Y., Li, C., Tian, Z., Cheng, L.: Research on the thermal shock simulation of the super high-speed aircraft. *MAMS.* 1–8 (2022). <https://doi.org/10.1080/15376494.2022.2046218>
70. Han, T., Huang, J., Sant, G., Neithalath, N., Kumar, A.: Predicting mechanical properties of ultrahigh temperature ceramics using machine learning. *J. Am. Ceram.* **105**, 6851–6863 (2022). <https://doi.org/10.1111/jace.18636>

71. Li, D., Li, P., Li, W., Li, W., Zhou, K.: Three-dimensional phase-field modeling of temperature-dependent thermal shock-induced fracture in ceramic materials. *Eng. Fract. Mech.* **268**, 108444 (2022). <https://doi.org/10.1016/j.engfracmech.2022.108444>
72. Corral, E.L., Loehman, R.E.: Ultra-high-temperature ceramic coatings for oxidation protection of carbon-carbon composites. *J. Am. Ceram.* **91**, 1495–1502 (2008). <https://doi.org/10.1111/j.1551-2916.2008.02331.x>
73. Makurunje, P., Monteverde, F., Sigalas, I.: Self-generating oxidation protective high-temperature glass-ceramic coatings for Cf/C–SiC–TiC–TaC UHTC matrix composites. *J. Eur. Ceram.* **37**, 3227–3239 (2017). <https://doi.org/10.1016/j.jeurceramsoc.2017.03.068>
74. Wu, K., Zhou, Q., Cao, J., Qian, Z., Niu, B., Long, D.: Ultrahigh-strength carbon aerogels for high temperature thermal insulation. *J. Colloid. Interface. Sci.* **609**, 667–675 (2022). <https://doi.org/10.1016/j.jcis.2021.11.067>
75. Nagabandi, K., Pujari, A.K., Iyer, D.S.: Thermo-mechanical assessment of gas turbine combustor tile using locally varying thermal barrier coating thickness. *Appl. Therm. Eng.* **179**, 115657 (2020). <https://doi.org/10.1016/j.applthermaleng.2020.115657>
76. Zhao, K., Ye, F., Cheng, L., Zhou, J., Wei, Y., Cui, X.: Formation of ultra-high temperature ceramic hollow microspheres as promising lightweight thermal insulation materials via a molten salt-assisted template method. *ACS Appl. Mater. Interfaces.* **13**, 37388–37397 (2021). <https://doi.org/10.1021/acsami.1c09662>
77. Kumar, C.V., Kandasubramanian, B.: Advances in ablative composites of carbon based materials: a review. *Ind. Eng. Chem. Res.* **58**, 22663–22701 (2019). <https://doi.org/10.1021/acs.iecr.9b04625>
78. Gild, J., Zhang, Y., Harrington, T., Jiang, S., Hu, T., Quinn, M.C., Mellor, W.M., Zhou, N., Vecchio, K., Luo, J.: High-entropy metal diborides: a new class of high-entropy materials and a new type of ultrahigh temperature ceramics. *Sci. Rep.* **6**, 1–10 (2016). <https://doi.org/10.1038/srep37946>
79. Yan, X., Constantin, L., Lu, Y., Silvain, J.F., Nastasi, M., Cui, B.: (Hf_{0.2}Zr_{0.2}Ta_{0.2}Nb_{0.2}Ti_{0.2})C high-entropy ceramics with low thermal conductivity. *J. Am. Ceram.* **101**, 4486–4491 (2018). <https://doi.org/10.1111/jace.15779>
80. Wei, X.F., Liu, J.X., Bao, W., Qin, Y., Li, F., Liang, Y., Xu, F., Zhang, G.J.: High-entropy carbide ceramics with refined microstructure and enhanced thermal conductivity by the addition of graphite. *J. Eur. Ceram.* **41**, 4747–4754 (2021). <https://doi.org/10.1016/j.jeurceramsoc.2021.03.053>
81. Backman, L., Gild, J., Luo, J., Opila, E.J.: Part I: theoretical predictions of preferential oxidation in refractory high entropy materials. *Acta Mater.* **197**, 20–27 (2020). <https://doi.org/10.1016/j.actamat.2020.07.003>
82. Castle, E., Csanádi, T., Grasso, S., Dusza, J., Reece, M.: Processing and properties of high-entropy ultra-high temperature carbides. *Sci. Rep.* **8**, 8609 (2018). <https://doi.org/10.1038/s41598-018-26827-1>

Ultra-High-Temperature Ceramic Coatings ZrC, ZrB₂, HfC, and HfB₂



Suprabha Das , Md. Shariful Islam Sozal, Wenhao Li, and Denny John

Abstract Ultra-high-temperature ceramic coatings are a fast-developing field of study with a broad variety of applications. Due to their exceptional physical and chemical characteristics, like heat resistance, oxidation resistance, and thermal stability zirconium and hafnium-based carbide and boride coatings have gained considerable popularity. Refractory carbide coatings of zirconium and hafnium are mostly used in ultra-high-temperature applications. Zirconium carbide possesses both ceramic and metallic properties, such as a very high melting point, high hardness, and exceptional corrosion resistance. Zirconium carbide coatings are also good hydrophobic and have low interfacial contact resistance. Because of these unique qualities, hafnium carbide has a very high melting point of 3890 °C and is also chemically stable at high temperatures. Hafnium carbide forms a protective oxide layer of HfO₂ on top of it to protect the substrate against oxidation at ultra-high temperatures. HfO₂ also has a very high melting point which further protects the underlying coating and substrate. These characteristics make hafnium carbide very promising as an anti-ablation coating for ultra-high-temperature applications. The deposition of zirconium boride (ZrB₂) and hafnium boride (HfB₂) provides the substrate with thermal and mechanical protection. Mechanical and physical properties of the composites are studied to determine optimal conditions for the application of such coatings.

Keywords Ultra-high-temperature ceramic · Zirconium carbide · Hafnium carbide · Zirconium diboride · Hafnium diboride

S. Das (✉) · Md. S. I. Sozal · W. Li · D. John

Department of Mechanical and Materials Engineering, Florida International University, Miami, FL 33174, USA

e-mail: sdas014@fiu.edu

© The Author(s), under exclusive license to Springer Nature Switzerland AG 2024

441

A. Pakseresht and K. K. Amirtharaj Mosas (eds.), *Ceramic Coatings*

for High-Temperature Environments, Engineering Materials,

https://doi.org/10.1007/978-3-031-40809-0_14

1 Introduction

Ceramic coatings for ultra-high temperatures are a rapidly growing area of study with numerous uses. Zirconium- and hafnium-based carbide and boride coatings have become quite popular due to their remarkable physical and chemical properties, such as heat resistance, oxidation resistance, and thermal stability. Zirconium and hafnium refractory carbide coatings are frequently employed in ultra-high-temperature applications. They create quite dense coatings that offer excellent protection against airborne oxidation, corrosion, and ablation. They have been frequently employed to give silicon-based alloys and carbon–carbon composites a protective covering. Two carbide-based coatings and two boride-based coatings are discussed below along with their applications and challenges.

2 Zirconium Carbide Coatings

Zirconium carbide (ZrC) is a refractory ceramic material with a high melting point and excellent mechanical and thermal properties. ZrC has a cubic rock salt crystal structure and is a member of the Group IV interstitial metal carbide family, with C atoms filling the interstitial octahedral sites and Zr atoms occupying the faces' vertices and middle. The carbon/zirconium ratio in ZrC is sub-stoichiometric and the carbon vacancy ranges from 0.65 to 0.98. ZrC has a high melting temperature of 3530 °C due to the strong covalent bonding between Zr and C. Its unique properties make it a promising candidate for various high-temperature use-cases, such as gas turbines, rocket nozzles, and nuclear reactors. It is particularly useful as a structural and fission product barrier coating material [1, 2]. ZrC fibers were first made by Clifton and Johnson in 1968 [3]. This process was patented, and the reaction involved reacting carbon with Zr-oxide fibers. These ZrC fibers contained lower thermal conductivity and stability. Killin et al. studied the oxidation resistance of carbon fibers coated with ZrC in 1975 [4]. Samoilenko and Pereselentseva coated W fibers with ZrC using a flow-type quartz furnace in the same year [5, 6]. These fibers were utilized in reinforcing metal matrix composites, including alloys based on nickel and cobalt.

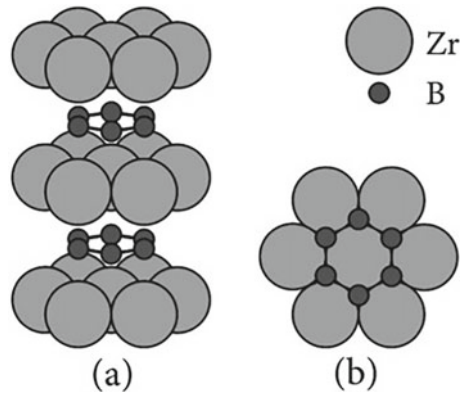
Zirconium carbide coatings are versatile materials that are employed in a range of applications because of their excellent thermal and chemical stability, high hardness, and resistance to wear and corrosion. ZrC coatings are applied to critical components in aerospace applications to shield them from high-temperature and high-stress environments [7, 8]. To increase their resistance to heat and wear, these coatings are applied to parts including turbine blades, combustion chambers, and exhaust nozzles. Due to its excellent electrical conductivity and chemical inertness, ZrC has been suggested as a potential material for sliding electrical contacts such as circuit breakers, brushes, microelectromechanical devices, and motor vehicles [9, 10]. Cutting tools are also covered in ZrC to make them harder and more resistant to

wear. To increase the performance and service life of cutting edges on instruments like drills, milling cutters, and turning tools, these coatings are used [11–13]. Biomedical implants with ZrC coatings have higher biocompatibility and wear resistance. To reduce friction, corrosion resistance, hemocompatibility of implant materials and enhance the implant's long-term performance, these coatings are used on orthopedic implants, such as hip and knee replacements [14, 15]. ZrC coatings are employed in numerous industrial applications to shield parts against abrasion, corrosion, and erosion. To increase their durability and lengthen their useful lives, these coatings are applied to parts including valves, pumps, and bearings [16, 17]. ZrC coatings are used in nuclear energy applications as well because of how well they resist radiation damage [6]. To stop corrosion and increase their endurance, these coatings are applied to fuel rods and other parts of nuclear reactors. Another unique application that Reynolds et al. reported in 1975–1976 was the vapor deposition of ZrC coatings on fuel particles which improved their irradiation behavior in a high-temperature gas-cooled nuclear reactor. The fission products were seen to be successfully held by the coatings. ZrC was chosen because of its high melting temperature decreased propensity to produce low-melting point phases, and relatively limited neutron-absorption area. In the decades that followed Reynolds' pioneering work, investigation teams in Japan have tried to advance this technology [4, 5, 13]. Although there haven't been many in-depth investigations on ZrC, its qualities—such as its high melting temperature, hardness, and corrosion and wear resistance—have made it a possible contender for a range of uses.

3 Zirconium Boride Coatings

ZrB₂ ceramics possess exceptional physical and thermal properties, including an extremely high melting point of 3245 °C, a remarkable hardness of 23 GPa, superior strength, excellent thermal conductivity of 60 W/(m K), high electrical conductivity of 1.0×10^7 S/m, outstanding resistance to ablation, and exceptional thermal shock resistance. Due to its outstanding physical and thermal properties, ZrB₂ ceramics have found widespread application in various fields, such as aerospace, metallurgy, machinery, and nuclear industry. Consequently, it has emerged as a highly promising ultra-high-temperature structural ceramic material [18–22]. However, due to the easy existence of oxygen pollution on the surface of commercial ZrB₂ powder (by amorphous B₂O₃ and crystalline ZrO₂ composition) makes it difficult to sinter and densify, so it is usually necessary to remove the oxide impurities at a lower temperature to accelerate the densification process of the material. B₂O₃ is easy to volatilize in a high-temperature vacuum environment, while the volatilization temperature of ZrO₂ is above 2000 °C. At this time, the ZrB₂ powder is coarsened, so it is necessary to add effective oxygen-scavenging additives such as compounds containing C [23, 24] or B [25, 26] with the help of chemical reaction to achieve low-temperature removal of ZrO₂, thereby effectively promoting material densification. The production of ultra-high-temperature ceramic materials with exceptional properties hinges on the

Fig. 1 Crystal structure of ZrB_2 **a** three-dimensional view and **b** top view [27]



availability of high quality, ultra-fine powders that are free from impurities. This highlights the critical role played by high-purity ultra-fine powders in the preparation of such materials. Therefore, the preparation of low-cost and high-quality ultra-high-temperature powder has become the research basis for ultra-high-temperature ceramic materials.

ZrB_2 is a metalloid compound with a hexagonal C32-type crystal structure. The outer layer of B-ions in the crystal structure of ZrB_2 contains 4 electrons, and each B-ion is linked to three other B-ions through covalent σ bonds, resulting in the formation of a hexagonal planar network structure; the extra electron forms a spatial delocalization of large π -bond structures. The bonding between B and Zr ions in ZrB_2 is primarily of an ionic nature and arises from electrostatic interactions between the oppositely charged ions. The crystal structure of ZrB_2 exhibits a two-dimensional network structure composed of alternating boron and zirconium atomic planes, as illustrated in Fig.1 [27]. The layered structure of ZrB_2 , which is similar to that of graphite, is responsible for its excellent electrical and thermal conductivity, as well as its metallic luster. The strong ionic bonding between Zr and B atoms across the boron and zirconium atomic planes, coupled with the robust B-B covalent bonding within each plane, contributes to the remarkable chemical stability, high hardness, and exceptionally high melting point of ZrB_2 [19, 28].

4 Hafnium Carbide Coatings

Refractory metal carbides, namely hafnium carbide (HfC), tantalum carbide (TaC), zirconium carbide (ZrC), and niobium carbide (NbC), have gained tremendous interest due to their prospective uses in advanced aerospace applications such as scramjet components and rockets. Among the various refractory metal carbides, hafnium carbide (HfC) got substantial significance due to its high melting point of 4163 K decreased thermal conductivity, no phase transformations, strong mechanical

stability, and excellent resistance against dry and temperature-involved oxidation and electrochemical corrosion [29–37]. In addition, because of its slower rate of recession and more passive oxidation behavior, HfC is a superior option to be used as a protective coating in high-temperature applications. It can be utilized well above 3000 °C in an inert environment and safely up to 2500 °C in an oxidizing atmosphere [30, 31, 38–40].

HfC has potential application in the thrust chambers, which are a critical component in ramjet engines, where the major structure comprises carbon-based composites. Another application involves producing structural coating on the nose cones and the main leading edge of hypersonic spacecrafts. In addition, when applied to carbon composites, it acts as a protective coating and enhance the resistance to ablation in highly combustible environments due to its perfect chemical compatibility [29, 30, 40–42].

The crystal structure of HfC_x consists of face-centered cubic (FCC) NaCl structure, where *x* varies from 0.5 to 0.98. There may be many vacancies at carbon sites depending on the value of *x*. The lattice should be more precisely described as HfC_xO_y, here, the value of *y* could be as high as 0.3 before the crystal lattice transforms into HfO₂ since HfC has a high probability of attracting oxygen into the lattice sites. As a result, before HfO₂ is formed, a sizable amount of oxygen can diffuse to HfC crystal lattice [39]. Three separate zones make up oxidized films, each with a unique oxygen diffusion constant: an outer HfO₂ layer with a monoclinic crystal structure, an intermediary HfO_{2-x}C_y layer, and a layer of residual carbides to the inner side. The intermediate layer protects the diffusion of oxygen and acts as a barrier because its oxygen diffusion constant is lower than inner residual carbide and outer HfO₂.

5 Hafnium Boride Coatings

Hafnium boride (HfB₂) belongs to the family of ultra-high-temperature ceramics (UHTCs) with desirable mechanical, thermal, and chemical properties [43–67]. This refractory ceramic material is known for high hardness (29 GPa), resistance to wear, corrosion, and oxidation and a melting temperature of 3300 °C [52, 59, 64, 65]. Hafnium boride's high stiffness, abrasion and oxidation resistance, and thermal shock resistance, combined with its high thermal conductivity (105 Wm⁻¹ K⁻¹) and high melting point, make it a highly attractive material for aerospace applications. In addition, hafnium boride is a desirable material for cutting tools because of its high hardness and resistance to wear, even when subjected to high pressures and temperatures [19, 68, 69]. Because of its desirable performance at high temperatures, this material is ideally suited for high-speed machining, a process in which the cutting edge of the tool can become very hot due to the high rate of material removal. Hafnium boride has high wear resistance because of its high hardness, which prevents it from deforming or being worn away by even the most rigorous mechanical stress. Hafnium

boride's high melting point also makes it useful for cutting tools because its mechanical qualities are not affected by high temperatures [70–72]. These tools need to be able to hold their form and sharpness even when heated to higher temperatures. Hafnium boride (HfB_2) has also garnered a lot of attention as a prospective material for use as a neutron absorber in nuclear reactors due to its high large neutron cross section of both hafnium and Boron-10. This characteristic is particularly significant in the construction of nuclear reactors since neutron absorption is required in order to control the rate of nuclear fission and prevent a nuclear meltdown from occurring. Hafnium boride is an ideal material for use in nuclear applications because, in addition to having the ability to absorb neutrons, it also possesses high thermal stability and resistance to corrosion. Because of the material's high melting point, it is capable of preserving both its structural integrity and its mechanical qualities even when subjected to temperatures that are very high, making it an ideal choice for usage in conditions that include high levels of temperature. Despite its desirable properties, hafnium boride (HfB_2) has not been widely used in applications due to the challenges associated with synthesizing thin films with the correct stoichiometry. In order for HfB_2 to be used as a tribological coating, it must be easily deposited onto relevant substrates as a thin film. Recent advancements in chemical vapor deposition (CVD) techniques have enabled the successful deposition of high quality, stoichiometric thin films of HfB_2 . For example, Jayaraman et al. successfully deposited HfB_2 thin films by CVD technique [73]. CVD is a popular technique for the deposition of thin films due to its ability to control film thickness, composition, and microstructure. In the case of HfB_2 , the CVD process involves the use of a precursor gas containing hafnium and boron ($\text{Hf}[\text{BH}_4]_4$), which is reacted with a reducing gas to form the HfB_2 thin film on the substrate surface. However, the tribological behavior of thin films is different from that of bulk samples of the same material. In addition, as-deposited thin films might experience delamination [66]. Therefore, the adhesion of the thin film on the substrate affects the tribological performance of thin film. Therefore, the thin film technology of HfB_2 is of great interest to retain the mechanical, thermal, and chemical properties.

6 Coating Techniques of Ultra-High-Temperature Ceramic Coatings

6.1 Zirconium Carbide Coatings

Zirconium carbide can be synthesized by cathodic vapor deposition, physical vapor deposition, thermal spray, laser pulse deposition, electrodeposition, reactive sputtering, and PECVD-PIP. Zirconium carbide (ZrC) coatings can be applied using various coating technologies. Some of the common coating technologies used for ZrC coatings are:

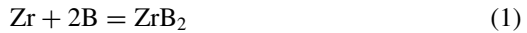
- a. **Chemical vapor deposition (CVD):** This method involves the reaction of a vapor-phase precursor with a substrate surface to form a solid coating. In the case of ZrC coatings, a Zr-containing precursor is typically used, such as zirconium tetrachloride (ZrCl₄) or Zr-alkoxide [74]. In the deposition process, various carbon sources are utilized. The compositions' sensitivity to temperature shows that zirconium and carbon formed independently. The precursor reacts with a carbon source, such as acetylene or methane, to form ZrC on the substrate surface. For example, a mixture of CH₄/C₃H₆ was used as a carbon source, H₂ was the carrier, and reduction gas was supplied together into the deposition chamber. The temperature and flow rate are varied. The factors that affect the ZrC deposition rate are that both ZrC and carbon originate from C₃H₆ precursors and have comparable deposition rate transitions. Another factor is that ZrC and pyrolytic carbon, which both derive from CH₄ precursors should have comparable deposition morphologies.
- b. **Physical vapor deposition (PVD):** This method involves the deposition of ZrC by condensation of vaporized ZrC material onto a substrate. PVD techniques commonly used for ZrC coatings include magnetron sputtering and electron beam evaporation. Arc-Physical Vapor Deposition, another name for the cathodic-arc deposition technique, was developed in the 1960s. It is a physical vapor deposition technique, in which materials are covered by electrolysis-induced vaporization of substances from targets functioning as cathodes and condensation-induced deposition on the substrate [15]. The cathode spot, which fires the ignition spots by self-extinguishing after a period of time and reigniting in certain locations, is mobile. In the event of targets with low-melting points, electromagnetic fields are also utilized to control the rates of arc movement. The interaction of the gas molecules with the cathodic arc causes their excitation, ionization, and dissociation, which results in complex films being formed. The cathodic-arc system has the significant drawback of producing a large number of coating macro-particles with poor adhesion at any given area during prolonged cathodic spots. Low reflective PVD-arc coating, multilayer coating deposition using a cathodic-arc system, and mono and layered coating deposition using a cathodic-arc evaporation approach utilizing plasma-enhanced duct equipment are some of the described cathodic-arc methods for coating ZrC.
- c. **Reactive melt infiltration:** For the fabrication of ceramic matrix composites, including zirconium carbide coatings, reactive melt infiltration is used. This procedure produces a composite material with enhanced qualities by infusing a molten metal into a preform constructed of a ceramic substance, in this case zirconium carbide. The procedure entails heating the ceramic preform above the melting point of the metal infiltrate (such as titanium or aluminum), followed by the introduction of the molten metal to the preform. A composite material with enhanced mechanical characteristics is created when the molten metal wets and fills the preforms pores. For example, graphite is used as substrate for coating and then Zr powder is placed on top of it and heated at high temperature of 2000 °C and the pressure of 200 Pa. When melting temperature is reached the Zr reacts with graphite and form Zirconium carbide coating [75].

Other techniques include electrodeposition of ZrC coatings from an aqueous or non-aqueous electrolyte containing a Zr-containing salt and a carbon source. A voltage is applied to the substrate, causing ZrC to be deposited on the surface. Thermal spray involves the deposition of ZrC coatings by spraying molten or solid feedstock particles onto a substrate using a flame, plasma, or arc jet. Common thermal spray techniques for ZrC coatings include high-velocity oxy-fuel (HVOF) and plasma spray. Overall, the choice of coating technology depends on various factors such as the desired coating properties, substrate material, and the specific application requirements.

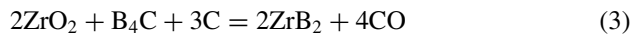
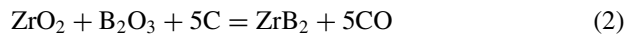
6.2 Zirconium Boride Coatings

Currently, ZrB₂ is primarily prepared using three main methods: solid-phase method, liquid-phase method, and gas-phase method.

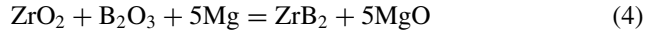
- a. **Solid-phase method:** ZrB₂ can get from the reaction of elemental Zr and B, the reaction formula is Eq. (1) shown below, the ratio of Zr/B can be strictly controlled by stoichiometric method, therefore, the reaction can get ZrB₂ powder, but the raw material is expensive [76, 77].



Eqs (2–3) shows the most commonly used ZrB₂ synthesis method, the raw materials used are cheap and easy to obtain. To obtain ZrB₂ with a higher degree of purity, it is often necessary to incorporate an excessive quantity of boron source compounds. In comparison, B₂O₃ has a lower vapor pressure than B₄C and is easier to volatilize. During the reaction process, it is more difficult to control the content, so the reaction formula (3) is better than the reaction formula (2) to prepare ZrB₂ [78, 79].



Eq (4) shows metallothermic reduction to obtain ZrB₂. Similar to the principle of carbothermal reduction reaction, replacing C with metals (Mg, Al, Ca, Si) can further reduce the carbon content in the product. The raw materials for this method to participate in the reaction are cheap and easy to obtain, and the reaction process can release a large amount of heat, so that the reaction can proceed spontaneously. The metallothermic reduction method, when combined with the self-propagating high-temperature synthesis (SHS) process, has found extensive use in the production of ZrB₂ [80, 81].



- b. **Liquid-phase method:** The sol–gel method is a frequently employed liquid-phase technique for synthesizing ZrB₂. Its essence is to use metal inorganic salt or organic salt to dissolve in a solvent to form a uniform solution, under certain conditions, alcoholysis, hydrolysis, or polycondensation of the solution containing the metal salt will be carried out to form a uniform and stable sol system, which will be aged and dried to obtain a gel, and finally, the desired powder will be obtained through high-temperature heat treatment. This process has the advantages of low temperature of synthetic powder, high chemical uniformity, high chemical purity, small particle size of synthetic powder, large specific surface area, high activity, etc. It is a common method for preparing ultra-fine powder at low temperature.

Zirconium oxychloride (ZrOC₁₂·8H₂O), boric acid, and epoxy resin were used as the sources of ZrO₂, B₂O₃, and C, respectively (the molar ratio of the substances was 1: 2: 10). The following are the detailed steps of the experiment. First, the boric acid solution is slowly dropped into the zirconium oxychloride solution, polyethylene glycol is used as a dispersant, and ammonia water is slowly added dropwise to adjust the pH value to 4 to form a binary sol. Then add the phenolic resin diluted with ethanol and stir evenly, continue to drop ammonia water to make the mixed sol-gel, dry, grind and sieve to obtain the precursor powder, put it into a high-temperature graphite resistance furnace. The powders were synthesized by calcining for 1 h in Ar gas environment at 1200–1600 °C [82]. It is also possible to use zirconium n-propoxide, boric acid, and phenolic resin as raw materials to prepare ZrB₂ powder by the same method [83]. Since most of the raw materials used in the sol-gel method are inorganic salts or alkoxides, the cost of raw materials is high, the production cycle is long, the process is complicated, involves a large number of process variables, and is easily affected and controlled by uncertain factors such as the external environment. The solvent has certain toxicity and hazards to the human body or the surrounding environment and is not suitable for large-scale production. For liquid-phase synthesis, in order to ensure the complete reduction reaction, it is necessary to add excess B source and C source. Since B and C light elements are difficult to analyze and measure, it is difficult to accurately determine the ratio of C/B/Zr, and it is difficult to obtain ZrB₂ powder with high purity.

- c. **Gas-phase method:** The gas-phase method is predominantly utilized for fabricating thin films of ZrB₂, and research in this area is relatively advanced. The ZrB₂ thin film produced using the gas-phase method can significantly enhance the mechanical properties of matrix materials, including density, hardness, wear resistance, and high-temperature strength. As a result, it holds great potential for various applications, particularly in the aerospace sector. Studies have shown that process conditions have a great influence on the formation temperature, thickness and uniformity, and microstructure of the film. Several methods are commonly employed to prepare ZrB₂ thin films, such as chemical vapor deposition (CVD),

low-pressure CVD (reaction pressure below 1000 Pa), plasma-enhanced CVD, and thermal decomposition.

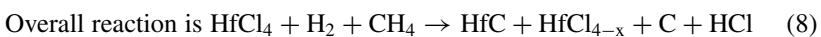
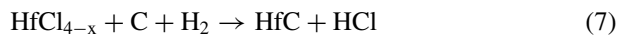
Mainly use $ZrCl_4$, BCl_3 , H_2 as raw materials, adopt chemical vapor deposition (CVD) or low-pressure CVD, and obtain ZrB_2 coating on graphite substrate under suitable reaction conditions (temperature) [84]. It is also possible to use $Zr(BH)_4$ as raw material and use thermal decomposition technology to obtain amorphous and conductive ZrB_2 coatings on Si or quartz substrates under lower temperature reaction conditions [85].

The synthesis process of this method is accompanied by the generation of HCl gas, which seriously pollutes the equipment and the atmospheric environment, and the yield is small. It can be used for laboratory research and is not suitable for industrial production.

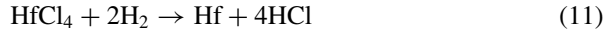
6.3 Hafnium Carbide Coatings

Hafnium carbide coatings are majorly synthesized by chemical vapor deposition, plasma spraying, magnetron sputtering and reactive melt infiltration techniques. Each of these techniques is detailed below.

- a. **Chemical Vapor Deposition (CVD):** Low-pressure CVD proves to be an efficient process to produce HfC-based protective coatings [30, 33, 36–38, 86, 87]. CVD consumes very low temperatures and pressures to yield a uniform HfC coating. HfC can be prepared from $HfCl_4-CH_4-H_2-Ar$ or $HfCl_4-C_3H_6-H_2$ system [32, 34]. In the $HfCl_4-CH_4-H_2-Ar$ system, Ar and purified H_2 are used to dilute and reduce gas, respectively. During this process, it should be ensured that there is a uniform and uninterrupted supply of $HfCl_4$ powder using a dedicated powder feeder. Constant supply ensures constant vaporization of $HfCl_4$ powder carried to the reaction chamber with Ar, H_2 , and CH_4 , at a temperature of 1600 °C. Following are the thermodynamic relationship involved in producing coatings from $HfCl_4-CH_4-H_2-Ar$ system.



In case of $HfCl_4-C_3H_6-H_2$ system [32],



- b. **Reactive Melt Infiltration:** Reactive melt infiltration (RMI) is an efficient process for incorporating hafnium-based carbides into carbon composite preform. A ceramic matrix is achieved when the infiltrated metal undergoes chemical reaction with the carbon composite preforms. The capillarity reaction between the metal melt and the pores in the preform is the critical driving force of the RMI process. RMI is frequently utilized to manufacture ceramic matrix composite reinforced with carbon fiber because of its quick production time and affordable cost. In addition, RMI can be used for creating carbide coating on carbon-carbon substrates by manipulating the melt infiltration depth. The process starts with small pieces of 50Hf-10Zr-40Si alloy ingot. The metal alloy pieces and porous carbon-carbon composite forms were placed in a graphite crucible. The graphite crucible is subjected to heating in a carbon tube furnace at a temperature of 1600 °C, 1700 °C, and 1900 °C, respectively, with a vacuum degree of 10⁻² Pa and isothermal holding at the respective temperatures for 30 min. Post-treatment, the composite preform is subjected to furnace cooling. After the process, the ceramic matrix with HfC coating is produced using RMI process [31].
- c. **Magnetron Sputtering:** Another approach for creating HfC and HfC/SiC multi-layer coatings is sputtering. Sputtering is superior to the CVD method in a number of ways. It uses a low temperature for deposition. It is an easy and adaptable technique for making thin coatings. Adjusting the deposition conditions in this process makes it possible to customize the film's qualities. It is ideally suited to the creation of multilayer coating systems [37, 38, 88].
- d. **Plasma Spraying:** Plasma spray deposition is one of the most scalable and important thermal spray techniques which can be used for consolidating refractory metal carbides. In plasma spray deposition, a plasma plume is produced by ionizing the process gases. Plasma spraying involves radio frequency, and plasma arcs, which generate a temperature as high as 13,726 °C, thereby very high thermal energy is achieved for consolidating high melting point refractory carbides. Argon, helium, and nitrogen are commonly employed for plasma spray deposition for consolidating coatings [31, 86, 87]. Here, the HfC powders are taken as the precursor for depositing coating. Particle velocity for feed-stock particles introduced into the gas stream can range from 0.02 to 0.50 m/s depending on the powder size. Plasma spraying can efficiently generate coatings with high density and minimum porosity, high densities, and strong interfacial

strengths. Plasma spraying can be used to melt ultra-high-temperature ceramic materials due to the ability to achieve higher temperatures. As a result, numerous researchers have employed plasma spraying to deposit HfC coatings. Researchers have generally reported plasma-sprayed coating microstructures with a combination of partial oxidation, a mixture of unmelted and melted splats, and porosity while depositing HfC coatings.

6.4 Hafnium Boride Coatings

- a. **Materials Preparation:** HfB₂ can be synthesized by the chemical and reduction routes. The chemical route involves the use of boron and transition metal-containing precursors to synthesize HfB₂. A nano-sized powder of HfB₂ can be synthesized using the hydrothermal reaction of HfCl₄ and NaBH₄ [89, 90]. This method is advantageous as it significantly reduces the power consumption required for the reaction to occur. On the other hand, the reduction route can be further divided into two types: carbothermal reduction and borothermal reduction [90, 91]. In the carbothermal reaction, a reducing environment is required, which is achieved by introducing a carbon source. This carbon source facilitates the reaction between hafnium and boron oxide, leading to the formation of HfB₂. The carbothermal reaction is widely used for HfB₂ synthesis due to its simplicity and cost-effectiveness. However, this process can produce contaminants, such as metal carbides and oxides that can affect the properties of the resulting material. In contrast, borothermal reduction utilizes Hf and B powders as precursor materials to produce HfB₂. Studies have shown that borothermal reduction at 1600 °C can produce HfB₂ particles with sizes ranging from 1 to 1.5 μm [90, 92]. However, controlling the particle size of HfB₂ is critical in achieving optimal performance in various applications. For instance, a smaller particle size of 0.8 μm was achieved in another study by eliminating B₂O₃ at 1100 °C through an additional washing step since B₂O₃ is known to promote HfB₂ coarsening, leading to larger particle sizes [93]. Another modified borocarbothermal reduction method using surplus B₄C and C successfully produced HfB₂ with particle sizes less than 1 μm. Smaller particle sizes help to improve the mechanical properties and sinterability of HfB₂, making it suitable for advanced applications [93–95].
- b. **Coating Technology:** Numerous studies have demonstrated the successful synthesis of films and coatings based on hafnium boride. Physical vapor deposition (PVD) and chemical vapor deposition (CVD) methods have been used to produce HfB₂ films, which can be several micrometers thick [50, 73, 94]. PVD methods involve the deposition of boride-based materials from a vapor phase, while CVD involves the chemical reaction of precursor gases on a substrate. Although both PVD and CVD have been used to produce boride-based films and coatings, there are some limitations. CVD has been found to have limited use due to the environmentally hazardous nature of some of the reactions involved

and the high reactivity and toxicity of borohydrides. In contrast, PVD has gained increasing attention in recent years due to its ease of use, cost-effectiveness, and ability to produce high-quality boride-based films and coatings. Boride-carbide multiphase coatings, such as ZrB₂-SiC composite coatings, have received significant attention due to their exceptional properties, such as high ablation and oxidation resistance [50]. While boride-carbide coatings have shown remarkable performance in various applications, the addition of HfB₂ can further enhance their protective properties. Specifically, the addition of HfB₂ can increase the ablation resistance of these coatings. This is particularly significant in applications, where high temperatures, extreme pressures, and harsh environments are present. Furthermore, the incorporation of HfB₂ can improve the longevity and protection ability of these coatings. The excellent properties of HfB₂ make it an ideal candidate for use in protective coatings for various applications.

7 Characterization and Microstructure of Ultra-High-Temperature Ceramic Coatings

7.1 Zirconium Carbide Coatings

The composition of ZrC coatings deposited is characterized by using XRD or EDS. XRD can be utilized to ascertain the coating's phase composition and spot any alterations in the crystal structure that might take place while it is being coated. It can give any details on the material's crystal structure, lattice characteristics, and crystal plane orientation. The fact that XRD is a non-destructive method of coating analysis for ZrC is one of its key benefits. In order to fully understand how the coating performs, it is also possible to examine its thickness and homogeneity. C/Zr can be determined by simple comparison of the peak strengths of carbon and zirconium (Fig. 2) [74]. The ZrC coating's surface morphology can be observed using a scanning electron microscope (SEM), which can provide details about the size and shape of the grains as well as any surface flaws like cracks or vacancies. The performance of the coating can be enhanced, and the coating process can be optimized using this information. SEM can also be used to examine the coating's grain structure in addition to surface morphology. The strength and toughness of the coating are influenced by the grain structure, which plays a significant role in determining the mechanical properties of the coating. Finally, SEM can be utilized to examine the ZrC coating's chemical makeup. SEM can be combined with energy-dispersive X-ray spectroscopy (EDS) to determine the coating's elemental composition and any contaminants. A typical SEM micrograph of the cross section of ZrC coating is shown in Fig. 3 [74]. The film is uniform. The thickness of the films can be directly measured by SEM.

Fig. 2 XRD of zirconium carbide coating synthesized using CVD [74]

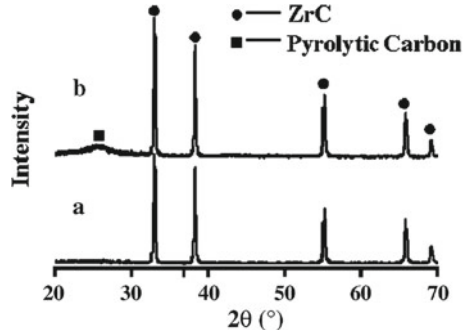
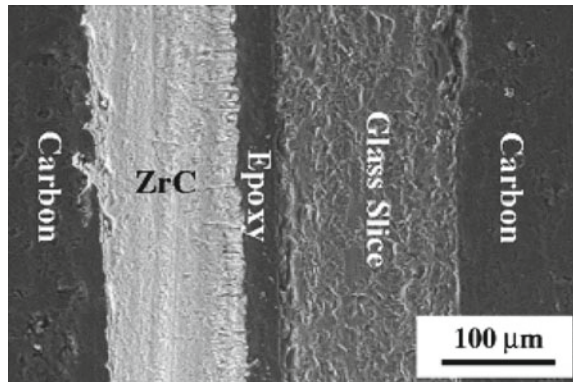


Fig. 3 SEM of zirconium carbide coating synthesized using CVD [74]



7.2 Zirconium Boride Coatings

Figure 4 shows the XRD spectrum of ZrB_2 . Although the two layers are laser sintered in an inert gas to prevent oxidation, a small amount of ZrO_2 peaks still appear in the final finished material. This is because ZrB_2 is a rare and metastable phase [96]. This also reflects the difficulty of preparing pure phase ZrB_2 materials from other aspect.

7.3 Hafnium Carbide Coatings

The XRD spectra of the CVD consolidated HfC coatings are presented in Figure 5. All coatings had just HfC diffraction peaks visible, which supports the production of pristine HfC coatings. Crystallization of HfC phases is manifested as sharp and narrower diffraction peaks. Strong (200) peak and a number of lesser peaks are displayed in Figure 5. These peaks (at $2\theta=33.4^\circ$, 38.8° , 56° , 66.8° , 70.2° , and 83.2°) were attributed to the HfC planes (111), (200), (220), (311), and 222. The different

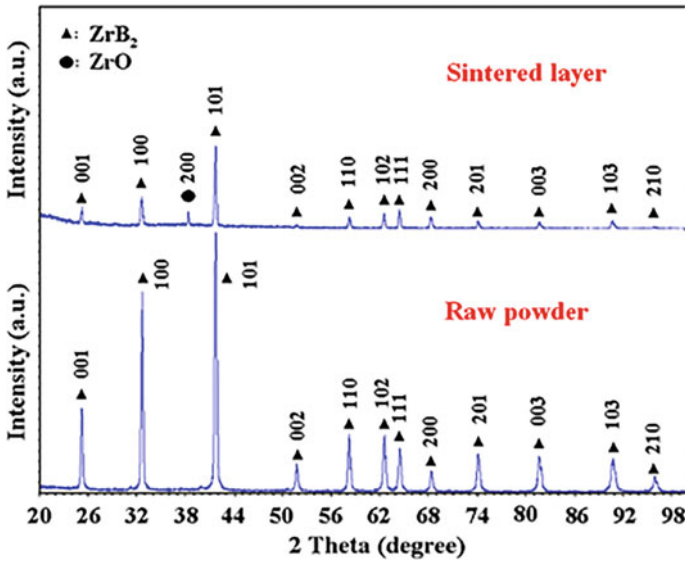
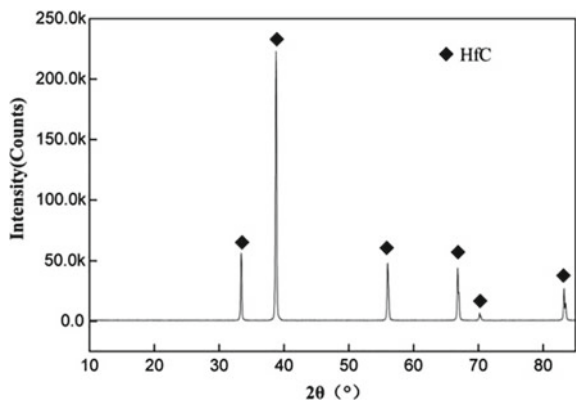


Fig. 4 XRD patterns of extracted ZrB₂ particles [96]

growth orientations of the HfC crystals are indicated by the difference in the diffraction peak intensities of the HfC coatings [31, 97]. Apart from this, the coatings prepared by atmospheric plasma spraying, which consist of temperatures beyond 2000°C have oxide peaks of hafnium [39].

The coatings of HfC prepared by CVD and plasma spraying proves promising with their dense nature. The CVD coating has no penetrable cracks or holes and demonstrated well-interconnected fine columnar grains [30, 98]. However, the coatings made by plasma spraying had a surface with higher surface roughness consisting of both fully melted and unmelted particles with some pinholes. In addition, the coating

Fig. 5 XRD patterns of extracted HfC particles [31]



surface is characterized by microcracks due to the tensile residual stresses generated during rapid solidification by cooling.

7.4 Hafnium Boride Coatings

The crystal structure of HfB_2 is hexagonal with a space group of P6/mmm. The lattice parameters for HfB_2 are $a = 3.139 \text{ \AA}$ and $c = 3.473 \text{ \AA}$. The Hf atoms are arranged in a hexagonal close-packed structure, while the boron atoms are arranged in a triangular lattice (attached reference). The density, young's modulus, bulk modulus, hardness of HfB_2 is 11.212 g/cm^3 , 480 GPa, 212 GPa, 28 GPa, respectively [19].

8 Properties of Ultra-High-Temperature Ceramic Coating

8.1 Zirconium Carbide Coatings

- a. **Grain morphology and Orientation:** The variables utilized during synthesis have an impact on a number of variables, including composition, morphology, crystalline structure, and preferential orientation, which all affect the quality of coatings. The grain shape and texture are directly influenced by the chemical content of coatings. Columnar morphology was seen when creating ZrC coatings using CVD at $1300 \text{ }^\circ\text{C}$, while equiaxed growth was seen around $1400 \text{ }^\circ\text{C}$. In a different work, ZrC columnar grains with a (220) preferred orientation were created using the chemical vapor decomposition approach at a deposition temperature of $1345 \text{ }^\circ\text{C}$. Higher hardness values and smallest particle sizes were produced at reduced deposition temperatures. In CVD-produced ZrC coatings, the grain size decreased as the C content rose. It is advantageous for ZrC coatings to have a dense and finely grained structure since it will enhance their mechanical and thermal qualities. The coating's grains typically have well-defined and uncontaminated grain boundaries, range in size from a few nanometers to several microns, and are equiaxed. These characteristics add to the coating's hardness and toughness. Furthermore, the grain shape can affect the coating's electrical conductivity and corrosion resistance. Thus, the thermal, mechanical, and electrical properties of ZrC coatings are greatly influenced by the grain shape. The mechanical characteristics of ZrC coatings, such as their wear and crack resistance, are greatly influenced by the direction of the grains, which is another critical element [1, 2].
- b. **Oxidation Property:** With a melting point of $3420 \text{ }^\circ\text{C}$ and strong thermal conductivity, ZrC is one of the ultra-high-temperature ceramics and is regarded as an ideal choice in the aerospace industry, where it is used as a protective coating. ZrO_2 , which has a melting point of $2677 \text{ }^\circ\text{C}$, can produce a dense layer that

will effectively slow down the migration of oxidation toward the substrate and prevent additional exposure. Researchers have focused on developing ZrC coatings with improved oxidation resistance properties. These coatings can protect the underlying ZrC material from oxidation and extend the lifetime of the material in high-temperature environments. The thickness, microstructure, and composition of ZrC coatings, as well as the temperature, time, and environmental composition, all affect how resistant they are to oxidation [15, 99]. Due to their ability to function as a physical barrier between the underlying ZrC material and the oxidizing environment, thicker coatings typically offer superior protection against oxidation. Moreover, a dense and homogeneous microstructure might lessen the chance of oxidation by preventing the diffusion of oxygen through the coating. ZrC coatings with different thicknesses when deposited on graphite substrates using chemical vapor deposition (CVD) and tested for their oxidation resistance properties showed that the thickest coating (20 μm) provided the best oxidation resistance, with minimal weight gain after exposure to air at 1000 °C for 10 h. The coatings' thermal diffusivities proportionally increased with temperature. Large crystalline grains assisted in enhancing their thermal diffusivities. ZrO₂ works as a thermal barrier layer, preventing heat from attacking reaching the ZrC coating underneath. The as-sprayed ZrC coatings' structure and morphology have a significant impact on the structure of the resulting ZrO₂ layer. The underlying reactions during oxidation are $\text{ZrC} + (3/2)\text{O}_2 \rightarrow \text{ZrO}_2 + \text{CO}$. However even after ZrC coating had been applied to the surface, the substrate has been observed to be severely degraded after exposure to a CH₄ combustion gas environment. ZrC can be oxidized to produce porous ZrO₂ and CO. These substances oxidize quickly, enabling the oxidation of whole specimens in a short amount of time. Moreover, the oxidation of the composites will be accelerated by the water vapor created by the processes in the combustion atmosphere. According to some reports, adding LaB₆ can increase ZrC's oxidation resistance to 1500 °C. ZrB₂ is created when the LaB₆ and ZrC interact. ZrC's resistance to oxidation in static air is enhanced by ZrB₂. The La-containing phase helps to improve oxidation resistance by increasing the density of oxide scale during oxidation 5.

- c. **Hardness:** Because of its exceptional hardness and wear resistance, zirconium carbide (ZrC) has gained substantial interest for its potential as a wear-resistant coatings for cutting tools. The performance of a coating in wear- and abrasive-prone settings is significantly influenced by its hardness. Coatings made of ZrC have a high hardness of 25 to 30 GPa. The zirconium and carbon atoms in the coating form a potent covalent bond that accounts for the coating's high hardness. Many techniques, such as adopting a layered coating structure or carefully including other materials into the coating, can increase the hardness of ZrC coatings even more. For instance, the ZrC coating's hardness and substrate adherence can both be improved by adding silicon to the coating. As ZrC coatings have a higher level of hardness and a low coefficient of friction, they also have good wear resistance. In some wear applications, they have been proven to perform better than other hard coatings like titanium nitride (TiN) and chromium nitride (CrN).

8.2 Zirconium Boride Coatings

- a. **High-Temperature Oxidation Testing:** In order to study the isothermal oxidation behavior of the comparative coated sample (ZrB_2/SiC) and pristine sample (C/SiC). Oxidation tests were carried out on the above two samples in an electric furnace at 1973 K for 2 h. The samples after the oxidation test were weighed with a high-sensitivity electronic balance. Using a three-point bending test for evaluating the flexural strength of composite materials [74]. When compared to pristine C/SiC coatings, the addition of ZrB_2 to SiC coatings can significantly decrease the extent of degradation that occurs in oxidizing environments. Specifically, the ZrB_2/SiC sample has a lower weight loss ratio (5.19% lower than C/SiC coating's 29.2%), and a higher flexural strength retention rate (37.4% higher than C/SiC coating's 6.74). Consequently, the ZrB_2/SiC coating is capable of providing long-lasting protection to C/SiC composites under high-temperature conditions (e.g., up to 1973 K) [74].
- b. **Ablation Testing:** To evaluate the ablation resistance of the coating, a test sample was subjected to an oxyacetylene flame with a temperature of roughly 2800 °C. The linear ablation rate was determined by comparing the thickness of the central area of the sample before and after ablation, while the mass ablation rate was obtained by measuring the difference in mass of the sample before and after ablation. The ZrB_2 content in the samples varied from 0 to 20%. With an increase in the ZrB_2 content, the ablation resistance of the composites exhibited an upward trend. Notably, both the mass and linear ablation rates decreased by more than 90% when the ZrB_2 content was raised to 20 wt%, providing convincing evidence that the incorporation of a ZrB_2 coating is capable of significantly enhancing the ablation resistance of the material.

The surface microstructure SEM images of the composite material that underwent a 60-second ablation process are presented in Figure 6a–d. Figure 6a shows that when there is no ZrB_2 coating, large particles and cavities appear on the material surface. As the amount of ZrB_2 increases, the ZrO_2 layer generated on the surface becomes denser gradually. The ZrO_2 layer formed after burning at high temperature can effectively isolate oxygen and improve the ablation resistance of the material [74].

8.3 Hafnium Carbide Coatings

- a. **High-Temperature Oxidation Testing:** The HfC coatings are majorly applied on the carbon composites; therefore, the oxidation capability of HfC coating is studied at 2000 °C for 20 s by using a laser [100, 101]. Since carbon starts to deteriorate at temperatures above 400 °C, the mass of the non-coated carbon composite samples decreased by about 1.5% for every 10 s. However, the mass

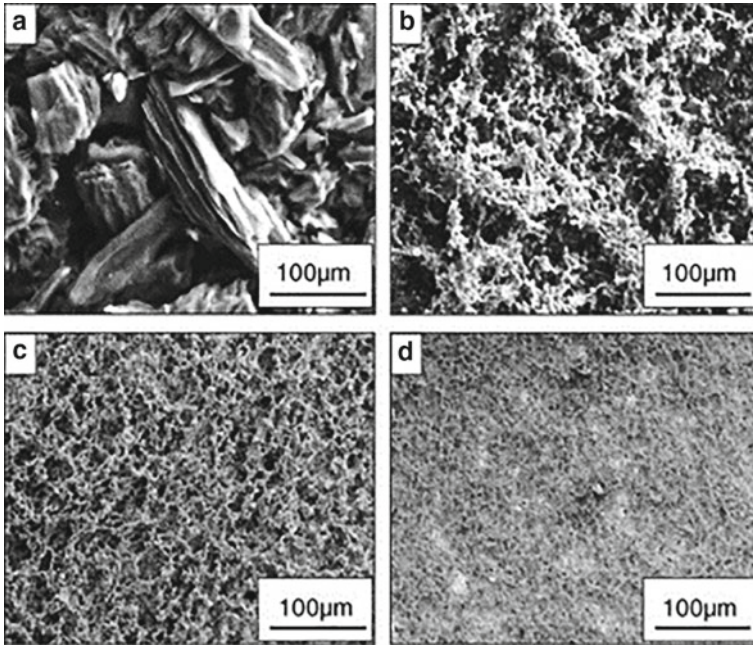


Fig. 6 SEM images of composite surfaces ablated for 60 s **a** 0% ZrB₂, **b** 5% ZrB₂, **c** 10% ZrB₂, **d** 20% ZrB₂ [74]

of the HfC deposited samples decreased at the rate of about 0.2% per 10 s, 7 times slower than the pace at which the uncoated carbon composites' weight decreased. At a low temperature (400–500 °C), HfC oxidizes, forming HfO₂. The different phases the product underwent following oxidation caused the mass reduction rates of HfC-coated as well as non-coated carbon composite samples to differ. Carbon dioxide is created when carbon oxidizes and then exits as a gas. HfC does, however, oxidize to generate HfO₂, which is still solid at 2000 °C. As a result, during laser oxidation, a solid HfO₂ layer produced on the carbon composites restricted underlying carbon from oxidizing and evaporating. The HfC coatings served as an oxidation barrier for restricting carbon composites from oxidizing.

- b. Mechanical Properties:** The Young's modulus and the microhardness of deposited with CVD with different hydrogen concentrations showed apparent variation as the concentration of hydrogen increased. This is due to the change in particles stacked to fine and coarse columnar grains during CVD as hydrogen concentration increases. The hardness obtained was in the range of 17.7 to 19.7 GPa, and the elastic modulus was in the range of 286.5 to 279.5 GPa [86]. The hardness value of the HfC coating deposited by plasma spray is 16.19 GPa [35, 40].

- c. **Ablation Testing:** The ablation experiments were conducted with the help of an oxyacetylene torch on HfC-coated carbon composite to investigate the enhancement in ablation resistance. The pristine carbon composite demonstrated rapid deterioration, which means it will undergo severe ablation under thermal exposure from the oxyacetylene torch. On the other hand, HfC-coated carbon-carbon composite samples showed excellent ablation resistance. To quantify the ablation resistance, the mass and linear ablation rates were 0.6 mg/s and 0.59 mg/s, respectively. The substrate couldn't be effectively ablated thanks to the HfC layer. In all ablation zones, the HfC covering oxidizes predominantly due to its reactivity with CO_2 gas. The evaporation of the Hf oxides and the oxidation of the hafnium carbide during the exposure consumed significant amounts of heat, providing carbon composites with efficient protection [35, 37, 87, 98].

8.4 Hafnium Boride Coatings

Thin film of HfB_2 provides excellent oxidation resistance at elevated temperatures. When HfB_2 is exposed to an oxidizing environment, such as air, it reacts with oxygen to produce HfO_2 and B_2O_3 . The formation of a glassy B_2O_3 film during the oxidation process plays a crucial role in blocking the diffusion of oxygen and heat into the coating [19]. The oxidation resistance of coating materials depends on various factors, including composition, preparation method, thermal expansion coefficient, and oxidizing conditions such as temperature, oxygen partial pressure, and gas flow rate. The oxidation temperature is a critical factor to consider because a stable glassy B_2O_3 film can exist up to a certain temperature limit, below approximately 1000 °C. At this temperature range, the glassy B_2O_3 film acts as a barrier to oxygen diffusion. However, as the temperature increases, the rates of volatilization of B_2O_3 also increase, making it challenging for the glassy B_2O_3 to cover the surface effectively at intermediate temperatures, approximately 1000–1800 °C. At high temperatures, above 1800 °C, a porous and non-protective HfO_2 layer remains as there is hardly any glassy B_2O_3 . Past studies have explored various ways to enhance the oxidation protection of HfB_2 . One approach that has shown significant promise involves adding silicide to HfB_2 . This method creates and stabilizes an outer layer of borosilicate glass, which acts as a barrier to oxygen diffusion at high temperatures, around 1700 °C. By doing so, the oxidation resistance of HfB_2 is significantly improved. The properties of hafnium boride are closely related to the strength of its bonds, which can be divided into B–B and Hf–B bonds. The type and strength of these bonds dictate the material's properties. In HfB_2 , B–B and Hf–B bonds [19, 90].

9 Challenges in Coating Technology

The development of ZrC coatings with improved oxidation resistance qualities has been the main focus of research, and new synthesis methods and composites have also been considered [22]. These coatings can prolong the life of the material in high-temperature conditions and prevent the underlying ZrC substance from oxidation. ZrB₂ material has good oxidation resistance under the condition of lower than 1100 °C, but under high-temperature condition, ZrB₂ material will be seriously degraded, which seriously affects its application under high temperature condition. Therefore, people's research on ZrB₂ materials has shifted from single-phase materials to composite materials. It is expected that ZrB₂, whether as the main crystal phase or the second phase, can complement each other with other materials while giving full play to its own advantages, so as to obtain comprehensive composite materials with excellent performance. Despite its potential, directly prepared ZrB₂–SiC coatings often exhibit poor compactness, uneven element distribution, and weak adhesion to the substrate. To address these issues, researchers have developed techniques such as powder modification and doping to significantly enhance the performance of ZrB₂–SiC coatings. When dealing with processes such as plasma spray, a higher amount of heat is consumed for consolidating the HfC coating together with rapid cooling [102]. This can lead to residual stress build-up and crack formation in the coating [36, 102]. Another challenge is to match the coefficient of thermal expansion of HfC with the substrate material; if not properly designed can result in the delamination of the coating [36, 102]. Process parameter optimization is also a critical factor that can result in many unmelted particles and porosity, which can act as weakening sites during adverse environments [42]. Hafnium boride is a material with incredible potential, as it offers unique properties that make it highly attractive for use in various industries. Its exceptional mechanical, thermal, and chemical properties make it an ideal material for high-temperature applications, such as cutting tools, aerospace components, and nuclear reactors. Its high hardness, wear resistance, corrosion resistance, and high melting point make it a material that can withstand harsh conditions and provide long-lasting performance. The synthesis of HfB₂ is challenging, but recent advancements in CVD techniques have enabled the successful deposition of high quality, stoichiometric thin films of HfB₂. While HfB₂ has already found applications in various industries, further research is needed to optimize its properties and applications. Researchers must focus on developing cost-effective synthesis methods that minimize the production of contaminants that may affect the material's properties. Additionally, further research is needed to optimize the particle size and adhesion of thin films to improve their tribological performance. The potential applications of HfB₂ are numerous and exciting. For example, HfB₂ can be used in hypersonic vehicles, where its high melting point and thermal conductivity make it an ideal material for leading edges and nose cones. It can also be used in jet engines, where its wear and corrosion resistance can help extend the life of components, reducing maintenance costs. Furthermore, HfB₂'s properties make it suitable for use in cutting tools, such as drills and saws, where its high hardness and

wear resistance can increase cutting speed and tool life. In addition to its applications in traditional industries, HfB₂ has the potential to revolutionize various cutting-edge technologies. For instance, HfB₂ can be used in energy storage devices/renewable energy sectors where its high conductivity can improve performance [103, 104]. In conclusion, HfB₂ is a material with immense potential and exciting possibilities. Its unique properties and potential applications make it an excellent subject for further research and development. With the continued advancement of synthesis techniques and an increasing understanding of its properties, HfB₂ has the potential to revolutionize various industries [105–107].

10 Conclusion and Future Work

Ultra-high-temperature ceramics have excellent comprehensive properties, have broad development prospects, and can be widely used in the field of aviation industry. HfC coating has excellent properties that can be used to protect the underlying material. High-temperature resistance, ablation resistance, and higher hardness make it a suitable choice for protecting carbon composites and other structural components in aerospace industries. Although the current research on coatings has achieved certain results, judging from the current research status, there is still room for improvement in the preparation, modification, and structural design.

- (1) Optimization of the preparation method: It is difficult for the current preparation methods to completely solve the problems of high porosity, cracks and other defects in the coating, and some preparation technologies have high costs, long cycle times, and great environmental pollution [108, 109]. Therefore, it is urgent to improve the existing preparation technology to obtain coatings with dense and uniform structure, excellent performance, and low cost.
- (2) Material modification: Material modification of coating is still the main development direction in the future. The selection of doping substances with appropriate forms is the direction of modification. For example, the use of different morphological doped phases, such as nanoparticles and fibers will effectively improve the thermal/mechanical properties of the coating.
- (3) Structural design: In order to meet the increasingly complex and extreme high-temperature application requirements, through multilayer coating design and reasonable material selection, multi-functional integration such as ablation resistance and heat insulation is realized.

References

1. Ul-Hamid, A.: Microstructure, properties and applications of Zr-carbide, Zr-nitride and Zr-carbonitride coatings: a review. *Mater. Adv.* **1**, 1012–1037 (2020). <https://doi.org/10.1039/d0ma00233j>
2. Ul-Hamid, A.: The effect of deposition conditions on the properties of Zr-carbide, Zr-nitride and Zr-carbonitride coatings—a review. *Mater. Adv.* **1**, 988–1011 (2020). <https://doi.org/10.1039/d0ma00232a>
3. Materials, O.F.: *Methods and properties* **2**, 911–913 (1969)
4. Samoilenko, V.G., Pereselentseva, L.N.: Deposition of zirconium carbide coatings acting as diffusion barriers in composites consisting of a metallic matrix and refractory metal fibers. *Sov. Powder Metall. Met. Ceram.* **14**, 725–728 (1975). <https://doi.org/10.1007/BF00800241>
5. Brückner, J., Mäntylä, T.: Reactive magnetron sputtering of zirconium carbide films using Ar–CH₄ gas mixtures. *Surf. Coatings Technol.* **59**, 166–170 (1993). [https://doi.org/10.1016/0257-8972\(93\)90077-2](https://doi.org/10.1016/0257-8972(93)90077-2)
6. Reynolds, G.H., Janvier, J.C., Kaae, J.L., Morlevat, J.P.: Irradiation behavior of experimental fuel particles containing chemically vapor deposited zirconium carbide coatings. *J. Nucl. Mater. Nucl. Mater.* **62**, 9–16 (1976). [https://doi.org/10.1016/0022-3115\(76\)90279-8](https://doi.org/10.1016/0022-3115(76)90279-8)
7. Sasaki, M., Kozukue, Y., Hashimoto, K., Takayama, K., Nakamura, I., Takano, I., Sawada, Y.: Properties of carbon films with a dose of titanium or zirconium prepared by magnetron sputtering. *Surf. Coatings Technol.* **196**, 236–240 (2005). <https://doi.org/10.1016/j.surfcoat.2004.08.085>
8. Kao, W.H.: Optimized a-C coatings by doping with zirconium for tribological properties and machining performance. *Diam. Relat. Mater. Relat. Mater.* **16**, 1896–1904 (2007). <https://doi.org/10.1016/j.diamond.2007.07.006>
9. Ferro, D., Rau, J.V., Rossi Albertini, V., Generosi, A., Teghil, R., Barinov, S.M.: Pulsed laser deposited hard TiC, ZrC, HfC and TaC films on titanium: hardness and an energy-dispersive X-ray diffraction study. *Surf. Coatings Technol.* **202**, 1455–1461 (2008). <https://doi.org/10.1016/j.surfcoat.2007.06.060>
10. Zheng, Y.F., Liu, X.L., Zhang, H.F.: Properties of Zr–ZrC–ZrC/DLC gradient films on TiNi alloy by the PIID technique combined with PECVD. *Surf. Coatings Technol.* **202**, 3011–3016 (2008). <https://doi.org/10.1016/j.surfcoat.2007.11.004>
11. Kuhn, M., Gold, P.W., Loos, J.: Wear and friction characteristics of PVD-coated roller bearings. *Surf. Coatings Technol.* **177–178**, 469–476 (2004). [https://doi.org/10.1016/S0257-8972\(03\)00914-9](https://doi.org/10.1016/S0257-8972(03)00914-9)
12. Varacalle, D.J., Lundberg, L.B., Herman, H., Bancke, G., Riggs, W.L.: Vacuum plasma sprayed zirconium carbide coatings. *Surf. Coat. Technol.* **68–69**, 86–91 (1994). [https://doi.org/10.1016/0257-8972\(94\)90143-0](https://doi.org/10.1016/0257-8972(94)90143-0)
13. Chen, C.S., Liu, C.P., Tsao, C.Y.A.: Influence of growth temperature on microstructure and mechanical properties of nanocrystalline zirconium carbide films. *Thin Solid Films* **479**, 130–136 (2005). <https://doi.org/10.1016/j.tsf.2004.11.196>
14. Floroian, L., Craciun, D., Socol, G., Dorcioman, G., Socol, M., Badea, M., Craciun, V.: Titanium implants’ surface functionalization by pulsed laser deposition of TiN, ZrC and ZrN hard films. *Appl. Surf. Sci.* **417**, 175–182 (2017). <https://doi.org/10.1016/j.apsusc.2017.03.068>
15. Hu, C., Ge, X., Niu, Y., Li, H., Huang, L., Zheng, X., Sun, J.: Influence of Oxidation Behavior of Feedstock on Microstructure and Ablation Resistance of Plasma-Sprayed Zirconium Carbide Coating. *J. Therm. Spray Technol.* **24**, 1302–1311 (2015). <https://doi.org/10.1007/s11666-015-0307-2>
16. Duerig, T., Pelton, A., Sto, D., Furuya, Y., Shimada, H., Sun, L., Huang, W.M., Ding, Z., Zhao, Y., Wang, C.C., Purnawali, H., Tang, C.: Stimulus-responsive shape memory materials: a review. *Mater. Des.* **33**, 21–28 (2012)

17. Ding, M.H., Zhang, H.S., Zhang, C., Jin, X.: Characterization of ZrC coatings deposited on biomedical 316L stainless steel by magnetron sputtering method. *Surf. Coat. Technol.* **224**, 34–41 (2013). <https://doi.org/10.1016/j.surfcoat.2013.02.047>
18. Bird, M.W., Aune, R.P., Yu, F., Becher, P.F., White, K.W.: Creep behavior of a zirconium diboride-silicon carbide composite. *J. Eur. Ceram. Soc.* **33**, 2407–2420 (2013). <https://doi.org/10.1016/j.jeurceramsoc.2013.03.022>
19. Fahrenholtz, W.G., Hilmas, G.E., Talmy, I.G., Zaykoski, J.A.: Refractory diborides of zirconium and hafnium. *J. Am. Ceram. Soc.* **90**, 1347–1364 (2007). <https://doi.org/10.1111/j.1551-2916.2007.01583.x>
20. Neuman, E.W., Hilmas, G.E., Fahrenholtz, W.G.: Strength of zirconium diboride to 2300 °C. *J. Am. Ceram. Soc.* **96**, 47–50 (2013). <https://doi.org/10.1111/jace.12114>
21. Neuman, E.W., Hilmas, G.E., Fahrenholtz, W.G.: Mechanical behavior of zirconium diboride-silicon carbide ceramics at elevated temperature in air. *J. Eur. Ceram. Soc.* **33**, 2889–2899 (2013). <https://doi.org/10.1016/j.jeurceramsoc.2013.05.003>
22. Zhang, S., Wang, S., Zhu, Y., Chen, Z.: Fabrication of ZrB₂-ZrC-based composites by reactive melt infiltration at relative low temperature. *Scr. Mater.* **65**, 139–142 (2011). <https://doi.org/10.1016/j.scriptamat.2011.03.033>
23. Zhang, S.C., Hilmas, G.E., Fahrenholtz, W.G.: Pressureless densification of zirconium diboride with boron carbide additions. *J. Am. Ceram. Soc.* **89**, 1544–1550 (2006). <https://doi.org/10.1111/j.1551-2916.2006.00949.x>
24. Zhu, S., Fahrenholtz, W.G., Hilmas, G.E., Zhang, S.C.: Pressureless sintering of zirconium diboride using boron carbide and carbon additions. *J. Am. Ceram. Soc.* **90**, 3660–3663 (2007). <https://doi.org/10.1111/j.1551-2916.2007.01936.x>
25. Zhu, S., Fahrenholtz, W.G., Hilmas, G.E., Zhang, S.C.: Pressureless sintering of carbon-coated zirconium diboride powders. *Mater. Sci. Eng. A* **459**, 167–171 (2007). <https://doi.org/10.1016/j.msea.2007.02.116>
26. Guo, W.M., Zhang, G.J., Yang, Z.G.: Pressureless sintering of zirconium diboride ceramics with boron additive. *J. Am. Ceram. Soc.* **95**, 2470–2473 (2012). <https://doi.org/10.1111/j.1551-2916.2012.05307.x>
27. Asl, M.S., Nayebi, B., Ahmadi, Z., Zamharir, M.J., Shokouhimehr, M.: Effects of carbon additives on the properties of ZrB₂-based composites: a review. *Ceram. Int.* **44**, 7334–7348 (2018). <https://doi.org/10.1016/j.ceramint.2018.01.214>
28. Chakraborty, S., Das, P.K., Ghosh, D.: Spark plasma sintering and structural properties of ZrB₂ based ceramics: a review. *Rev. Adv. Mater. Sci.* **44**, 182–193 (2016)
29. Ren, J., Zhang, Y., Zhang, J., Fu, Y., Tian, S.: Effects of HfC nanowire amount on the microstructure and ablation resistance of CVD-HfC coating. *Ceram. Int.* **44**, 11340–11349 (2018). <https://doi.org/10.1016/j.ceramint.2018.03.183>
30. Verdon, C., Szwedek, O., Jacques, S., Allemand, A., Le Petitcorps, Y.: Hafnium and silicon carbide multilayer coatings for the protection of carbon composites. *Surf. Coatings Technol.* **230**, 124–129 (2013). <https://doi.org/10.1016/j.surfcoat.2013.06.022>
31. Mohammad, F.Z., Lawson, K.J., Nicholls, J.R.: Influence of processing parameters on deposition rate and crystal structure of reactively sputtered HfC. *Surf. Eng.* **23**, 183–186 (2007). <https://doi.org/10.1179/174329406X126753>
32. Kim, D., Han, J., Park, C., Lee, H.G., Park, J.Y., Kim, W.J.: Chemical vapor deposition of dense hafnium carbide from HfCl₄-C₃H₆-H₂ System for the protection of carbon fibers. *Adv. Eng. Mater.* **21**, 1–7 (2019). <https://doi.org/10.1002/adem.201800730>
33. Wang, Y.L., Xiong, X., Li, G.D., Zhao, X.J., Chen, Z.K., Sun, W., Wang, Z.S.: Effect of gas composition on the microstructure and growth behavior of HfC coatings prepared by LPCVD. *Solid State Sci.* **20**, 86–91 (2013). <https://doi.org/10.1016/j.solidstatesciences.2013.02.011>
34. Ren, J., Zhang, Y., Fu, Y., Zhang, P., Tian, S., Zhang, L.: Effects of the second phase on the microstructure and ablation resistance of HfC coating on C/C composites. *Surf. Coat. Technol.* **344**, 250–258 (2018). <https://doi.org/10.1016/j.surfcoat.2018.03.023>
35. Xu, Y., Pan, X., Huang, S., Xu, X., Niu, Y., Zhong, X., Zheng, X.: Effect of solid oxidation products on the ablation mechanisms of ZrC and HfC based coatings above 2000 °C. *J. Mater. Res. Technol.* **22**, 1900–1910 (2023). <https://doi.org/10.1016/j.jmrt.2022.12.039>

36. Zhang, J., Zhang, Y., Fu, Y., Zhang, T., Zhu, X.: Preparation and ablation behavior of HfC–SiC co-deposited coatings with different proportions. *Corros. Sci.* **192**, 109853 (2021). <https://doi.org/10.1016/j.corsci.2021.109853>
37. Yang, Y., Li, K., Li, H.: Ablation behavior of HfC coating prepared by supersonic plasma spraying for SiC-coated C/C composites. *Adv. Compos. Lett.* **24**, 113–118 (2015). <https://doi.org/10.1177/096369351502400503>
38. Kim, H.S., Kang, B.R.: Plasma Sprayed HfC, TiC, and HfC/TiC Ultra-high-temperature ceramic coatings. *Materials* (Basel). (2020)
39. Wang, Y., Li, Z., Xiong, X., Li, X., Chen, Z., Sun, W.: Action mechanism of hydrogen gas on deposition of HfC coating using HfCl₄–CH₄–H₂–Ar system. *Appl. Surf. Sci.* **390**, 903–908 (2016). <https://doi.org/10.1016/j.apsusc.2016.08.169>
40. Wang, Y.J., Li, H.J., Fu, Q.G., Wu, H., Yao, D.J., Wei, B.B.: Ablative property of HfC-based multilayer coating for C/C composites under oxy-acetylene torch. *Appl. Surf. Sci.* **257**, 4760–4763 (2011). <https://doi.org/10.1016/j.apsusc.2010.11.020>
41. Verdon, C., Szwedek, O., Allemand, A., Jacques, S., Le Petitcorps, Y., David, P.: High temperature oxidation of two- and three-dimensional hafnium carbide and silicon carbide coatings. *J. Eur. Ceram. Soc.* **34**, 879–887 (2014). <https://doi.org/10.1016/j.jeurceramsoc.2013.10.019>
42. Glechner, T., Hudak, O.E., Wojcik, T., Haager, L., Bohrn, F., Hutter, H., Hunold, O., Ramm, J., Koložvári, S., Pitthan, E., Primetzhofer, D., Riedl, H.: Influence of the non-metal species on the oxidation kinetics of Hf, HfN, HfC, and HfB₂ coatings. *Mater. Des.* **211**, 110136 (2021). <https://doi.org/10.1016/j.matdes.2021.110136>
43. Perkins, C.L., Singh, R., Trenary, M., Tanaka, T., Paderno, Y.: Surface properties of hafnium diboride (0001) as determined by X-ray photoelectron spectroscopy and scanning tunneling microscopy. *Surf. Sci.* **470**, 215–225 (2001). [https://doi.org/10.1016/S0039-6028\(00\)00862-1](https://doi.org/10.1016/S0039-6028(00)00862-1)
44. Meléndez-Martínez, J.J., Domínguez-Rodríguez, A., Monteverde, F., Melandri, C., De Portu, G.: Characterisation and high temperature mechanical properties of zirconium boride-based materials. *J. Eur. Ceram. Soc.* **22**, 2543–2549 (2002). [https://doi.org/10.1016/S0955-2219\(02\)00114-0](https://doi.org/10.1016/S0955-2219(02)00114-0)
45. Gild, J., Zhang, Y., Harrington, T., Jiang, S., Hu, T., Quinn, M.C., Mellor, W.M., Zhou, N., Vecchio, K., Luo, J.: High-entropy metal diborides: a new class of high-entropy materials and a new type of ultrahigh temperature ceramics. *Sci. Rep.* **6**, 2–11 (2016). <https://doi.org/10.1038/srep37946>
46. Zoli, L., Sciti, D.: Efficacy of a ZrB₂–SiC matrix in protecting C fibres from oxidation in novel UHTCMC materials. *Mater. Des.* **113**, 207–213 (2017). <https://doi.org/10.1016/j.matdes.2016.09.104>
47. Silvestroni, L., Kleebe, H.J., Fahrenholtz, W.G., Watts, J.: Super-strong materials for temperatures exceeding 2000 °C. *Sci. Rep.* **7**, 1–8 (2017). <https://doi.org/10.1038/srep40730>
48. Sandin, C., Talukdar, T.K., Abelson, J.R., Tawfick, S.: Bottom-up synthesis and mechanical behavior of refractory coatings made of carbon nanotube-hafnium diboride composites. *ACS Appl. Mater. Interfaces* **11**, 1487–1495 (2019). <https://doi.org/10.1021/acsami.8b18840>
49. Cahill, J.T., Turner, S., Ye, J., Shevitski, B., Aloni, S., Baumann, T.F., Zettl, A., Kuntz, J.D., Worsley, M.A.: Ultrahigh-temperature ceramic aerogels. *Chem. Mater.* **31**, 3700–3704 (2019). <https://doi.org/10.1021/acs.chemmater.9b00496>
50. Chen, S., Qiu, X., Zhang, B., Xu, J., Zhong, F., Zhu, B., Zhang, Y., Ou-Yang, J., Yang, X.: Advances in antioxidation coating materials for carbon/carbon composites. *J. Alloys Compd.* **886**, 161143 (2021). <https://doi.org/10.1016/j.jallcom.2021.161143>
51. Kane, K.A., Pint, B.A., Mitchell, D., Haynes, J.A.: Oxidation of ultrahigh temperature ceramics: kinetics, mechanisms, and applications. *J. Eur. Ceram. Soc.* **41**, 6130–6150 (2021). <https://doi.org/10.1016/j.jeurceramsoc.2021.05.055>
52. Lin, H.S., Wang, C.Y., Djouadi, M.A., Kuang, T.C., Dong, H.F.: Structural, mechanical and electronic properties of hafnium borides: a first principle study. *J. Mater. Sci.* **58**, 1139–1157 (2023). <https://doi.org/10.1007/s10853-022-08022-w>
53. Fahrenholtz, W.G., Wuchina, E.J., Lee, W.E., Zhou, Y.: Ultra-high-temperature ceramics: materials for extreme environment applications. 144–166 (2000)

54. Kunneparambil Sukumaran, A., Thampi, A.D., Sneha, E., Arif, M., Rani, S.: Effect of bovine serum albumin on the lubricant properties of rice bran oil: a biomimetic approach. *Sadhana—Acad. Proc. Eng. Sci.* **46** (2021). <https://doi.org/10.1007/s12046-021-01717-x>
55. Monteverde, F., Guicciardi, S., Bellosi, A.: Advances in microstructure and mechanical properties of zirconium diboride based ceramics. *Mater. Sci. Eng. A* **346**, 310–319 (2003). [https://doi.org/10.1016/S0921-5093\(02\)00520-8](https://doi.org/10.1016/S0921-5093(02)00520-8)
56. Lou, L., Rodrigues de Oliveira, N., Sahani, R., Sukumaran, A.K., John, D., Agarwal, A.: Localized nanoindentation paradigm for revealing sutured tissue interface mechanics and integrity. *ACS Appl. Bio Mater.* (2023). <https://doi.org/10.1021/acsabm.2c01091>
57. Jensen, J.A., Gozum, J.E., Pollina, D.M., Girolami, G.S.: *Films* University of Illinois, pp. 1643–1644 (1988)
58. Wayda, A.L., Schneemeyer, L.F., Opila, R.L.: Low-temperature deposition of zirconium and hafnium boride films by thermal decomposition of the metal borohydrides ($M[BH_4]_4$). *Appl. Phys. Lett.* **53**, 361–363 (1988). <https://doi.org/10.1063/1.100603>
59. Opeka, M.M., Talmy, I.G., Wuchina, E.J., Zaykoski, J.A., Causey, S.J.: Mechanical, thermal, and oxidation properties of refractory hafnium and zirconium Compounds. *J. Eur. Ceram. Soc.* **19**, 2405–2414 (1999). [https://doi.org/10.1016/s0955-2219\(99\)00129-6](https://doi.org/10.1016/s0955-2219(99)00129-6)
60. Belyansky, M., Trenary, M.: Structure of heteroepitaxial thin films of hafnium diboride grown on a Hf(0001) surface as determined by scanning tunneling microscopy. *J. Phys. Chem. B* **104**, 11835–11836 (2000). <https://doi.org/10.1021/jp002559r>
61. Loehman, R., Corral, E., Dumm, H.P., Kotula, P., Tandon, R.: Sandia report ultra-high-temperature ceramics for hypersonic vehicle applications. *Mater. Charact.* (2006)
62. Chatterjee, A., Jayaraman, S., Gerbi, J.E., Kumar, N., Abelson, J.R., Bellon, P., Polycarpou, A.A., Chevalier, J.P.: Tribological behavior of hafnium diboride thin films. *Surf. Coatings Technol.* **201**, 4317–4322 (2006). <https://doi.org/10.1016/j.surfcoat.2006.08.086>
63. Chamberlain, A.L., Fahrenholtz, W.G., Hilmas, G.E.: High-strength zirconium diboride-based ceramics. **1172**, 1170–1172 (2004)
64. Li, H., Yao, D., Fu, Q., Liu, L., Zhang, Y., Yao, X., Wang, Y., Li, H.: Anti-oxidation and ablation properties of carbon/carbon composites infiltrated by hafnium boride. *Carbon NY*. **52**, 418–426 (2013). <https://doi.org/10.1016/j.carbon.2012.09.053>
65. Zapata-Solvas, E., Jayaseelan, D.D., Lin, H.T., Brown, P., Lee, W.E.: Mechanical properties of ZrB_2 - and HfB_2 -based ultra-high temperature ceramics fabricated by spark plasma sintering. *J. Eur. Ceram. Soc.* **33**, 1373–1386 (2013). <https://doi.org/10.1016/j.jeurceramsoc.2012.12.009>
66. Lee, J., Polychronopoulou, K., Cloud, A.N., Abelson, J.R., Polycarpou, A.A.: Shear strength measurements of hafnium diboride thin solid films. *Wear* **318**, 168–176 (2014). <https://doi.org/10.1016/j.wear.2014.06.017>
67. Chowdhury, S., Polychronopoulou, K., Cloud, A., Abelson, J.R., Polycarpou, A.A.: Nanomechanical and nanotribological behaviors of hafnium boride thin films. *Thin Solid Films* **595**, 84–91 (2015). <https://doi.org/10.1016/j.tsf.2015.10.030>
68. Belyansky, M., Trenary, M.: Heteroepitaxy of hafnium diboride on a hafnium (0001) single crystal surface. *Chem. Mater.* **9**, 403–405 (1997). <https://doi.org/10.1021/cm9604423>
69. Moghanlou, F.S., Vajdi, M., Sha, J., Motallebzadeh, A., Shokouhimehr, M., Asl, M.S.: A numerical approach to the heat transfer in monolithic and SiC reinforced HfB_2 , ZrB_2 and TiB_2 ceramic cutting tools. *Ceram. Int.* **45**, 15892–15897 (2019). <https://doi.org/10.1016/j.ceramint.2019.05.095>
70. Simeone, D., Hablot, O., Micalet, V., Bellon, P., Serruys, Y.: Contribution of recoil atoms to irradiation damage in absorber materials. *J. Nucl. Mater. Nucl. Mater.* **246**, 206–214 (1997). [https://doi.org/10.1016/S0022-3115\(97\)00092-5](https://doi.org/10.1016/S0022-3115(97)00092-5)
71. Nasserri, M.M.: The behavior of HfB_2 at neutron irradiation: a simulation study. *Radiat. Eff. Defects Solids. Eff. Defects Solids* **171**, 252–258 (2016). <https://doi.org/10.1080/10420150.2016.1179305>
72. Bacca, N., Zhang, C., Paul, T., Sukumaran, A.K., John, D., Rengifo, S., Park, C., Chu, S.H., Mazurkivich, M., Scott, W., Agarwal, A.: Tribological and neutron radiation properties of boron nitride nanotubes reinforced titanium composites under lunar environment. *J. Mater. Res.* **37**, 4582–4593 (2022). <https://doi.org/10.1557/s43578-022-00708-w>

73. Yang, Y., Jayaraman, S., Kim, D.Y., Girolami, G.S., Abelson, J.R.: CVD growth kinetics of HfB₂ thin films from the single-source precursor Hf(BH₄)₄. *Chem. Mater.* **18**, 5088–5096 (2006). <https://doi.org/10.1021/cm0605421>
74. Wang, Y., Liu, Q., Liu, J., Zhang, L., Cheng, L.: Deposition mechanism for chemical vapor deposition of zirconium carbide coatings. *J. Am. Ceram. Soc.* **91**, 1249–1252 (2008). <https://doi.org/10.1111/j.1551-2916.2007.02253.x>
75. Yang, X., Su, Z.A., Huang, Q.Z., Chai, L.Y., Zhong, P., Xue, L.: A zirconium carbide coating on graphite prepared by reactive melt infiltration. *J. Cent. South Univ.* **21**, 472–476 (2014). <https://doi.org/10.1007/s11771-014-1962-z>
76. Chamberlain, A.L., Fahrenholtz, W.G., Hilmas, G.E.: Reactive hot pressing of zirconium diboride. *J. Eur. Ceram. Soc.* **29**, 3401–3408 (2009). <https://doi.org/10.1016/j.jeurceramsoc.2009.07.006>
77. Çamurlu, H.E., Maglia, F.: Preparation of nano-size ZrB₂ powder by self-propagating high-temperature synthesis. *J. Eur. Ceram. Soc.* **29**, 1501–1506 (2009). <https://doi.org/10.1016/j.jeurceramsoc.2008.09.006>
78. Mishra, S.K., Pathak, L.C.: Effect of carbon and titanium carbide on sintering behaviour of zirconium diboride. *J. Alloys Compd.* **465**, 547–555 (2008). <https://doi.org/10.1016/j.jallcom.2007.11.004>
79. Khanra, A.K., Pathak, L.C., Godkhindi, M.M.: Carbothermal synthesis of zirconium diboride (ZrB₂) whiskers. *Adv. Appl. Ceram.* **106**, 155–160 (2007). <https://doi.org/10.1179/174367607X162019>
80. Nishiyama, K., Nakamura, T., Utsumi, S., Sakai, H., Abe, M.: Preparation of ultrafine boride powders by metallothermic reduction method. *J. Phys. Conf. Ser.* **176**, 2–10 (2009). <https://doi.org/10.1088/1742-6596/176/1/012043>
81. Setoudeh, N., Welham, N.J.: Formation of zirconium diboride (ZrB₂) by room temperature mechanochemical reaction between ZrO₂, B₂O₃ and Mg. *J. Alloys Compd.* **420**, 225–228 (2006). <https://doi.org/10.1016/j.jallcom.2005.07.083>
82. Yan, Y., Huang, Z., Dong, S., Jiang, D.: New route to synthesize ultra-fine zirconium diboride powders using inorganic-organic hybrid precursors. *J. Am. Ceram. Soc.* **89**, 3585–3588 (2006). <https://doi.org/10.1111/j.1551-2916.2006.01269.x>
83. Xie, Y., Sanders, T.H., Speyer, R.F.: Solution-based synthesis of submicrometer ZrB₂ and ZrB₂-TaB₂. *J. Am. Ceram. Soc.* **91**, 1469–1474 (2008). <https://doi.org/10.1111/j.1551-2916.2008.02288.x>
84. Wang, P., Li, S., Geng, X., Zhang, J., Meng, F., Zhou, L., Sun, H., Li, X., Wen, G., Wei, C.: Microstructure, surface stress and surface temperature response of ZrB₂-SiC based coatings. *J. Alloys Compd.* **843**, 156084 (2020). <https://doi.org/10.1016/j.jallcom.2020.156084>
85. Pierson, J.F., Belmonte, T., Czerwiec, T., Hertz, D., Michel, H.: Low temperature ZrB₂ remote plasma enhanced chemical vapor deposition. *Thin Solid Films* **359**, 68–76 (2000). [https://doi.org/10.1016/S0040-6090\(99\)00721-X](https://doi.org/10.1016/S0040-6090(99)00721-X)
86. Yoo, H.I., Kim, H.S., Hong, B.G., Sihm, I.C., Lim, K.H., Lim, B.J., Moon, S.Y.: Hafnium carbide protective layer coatings on carbon/carbon composites deposited with a vacuum plasma spray coating method. *J. Eur. Ceram. Soc.* **36**, 1581–1587 (2016). <https://doi.org/10.1016/j.jeurceramsoc.2016.01.032>
87. Yang, Y., Li, K., Zhao, Z., Li, H.: Ablation resistance of HfC-SiC coating prepared by supersonic atmospheric plasma spraying for SiC-coated C/C composites. *Ceram. Int.* **42**, 4768–4774 (2016). <https://doi.org/10.1016/j.ceramint.2015.11.161>
88. Yoo, Y.W., Nam, U.H., Kim, Y., Lee, H.I., Park, J.K., Byon, E.: Hafnium carbide coatings deposited by supersonic vacuum plasma spraying for ultra-high-temperature oxidation barrier on carbon composites. *Appl. Sci. Converg. Technol.* **30**, 21–24 (2021). <https://doi.org/10.5757/ASCT.2021.30.1.21>
89. Chen, L., Gu, Y., Shi, L., Yang, Z., Ma, J., Qian, Y.: Synthesis and oxidation of nanocrystalline HfB₂. *J. Alloys Compd.* **368**, 353–356 (2004). <https://doi.org/10.1016/j.jallcom.2003.08.086>
90. Venugopal, S.: Synthesis and Processing of Sub-micron Hafnium Diboride Powders and Carbon Fibre-hafnium Diboride Composites. Ph.D. thesis, Loughborough University (2013)

91. Ni, D.W., Zhang, G.J., Kan, Y.M., Wang, P.L.: Synthesis of monodispersed fine hafnium boride powders using carbo/borothermal reduction of hafnium dioxide. *J. Am. Ceram. Soc.* **91**, 2709–2712 (2008). <https://doi.org/10.1111/j.1551-2916.2008.02466.x>
92. Zhang, G.J., Guo, W.M., Ni, D.W., Kan, Y.M.: Ultrahigh temperature ceramics (UHTCs) based on ZrB₂ and HfB₂ systems: powder synthesis, densification and mechanical properties. *J. Phys. Conf. Ser.* **176** (2009). <https://doi.org/10.1088/1742-6596/176/1/012041>
93. Guo, W.M., Yang, Z.G., Zhang, G.J.: Synthesis of submicrometer HfB₂ powder and its densification. *Mater. Lett.* **83**, 52–55 (2012). <https://doi.org/10.1016/j.matlet.2012.06.012>
94. Das, S., Dubois, D., Sozal, M.S.I., Emirov, Y., Jafarizadeh, B., Wang, C., Drozd, V., Durygin, A., Cheng, Z.: Synthesis and flash sintering of zirconium nitride powder. *J. Am. Ceram. Soc.* **105**, 3925–3936 (2022). <https://doi.org/10.1111/jace.18421>
95. Sozal, M.S.I., Tang, W., Das, S., Li, W., Durygin, A., Drozd, V., Zhang, C., Jafarizadeh, B., Wang, C., Agarwal, A., Ding, D., Cheng, Z.: electrical, thermal, and H₂O and CO₂ poisoning behaviors of PrNi_{0.5}Co_{0.5}O_{3-δ} electrode for intermediate temperature protonic ceramic electrochemical cells. *Int. J. Hydrogen Energy.* **47**, 21817–21827 (2022). <https://doi.org/10.1016/j.ijhydene.2022.05.011>
96. Sun, C.N., Gupta, M.C.: Laser sintering of ZrB₂. *J. Am. Ceram. Soc.* **91**, 1729–1731 (2008). <https://doi.org/10.1111/j.1551-2916.2008.02369.x>
97. Wang, Y.L., Xiong, X., Li, G.D., Zhang, H.B., Chen, Z.K., Sun, W., Zhao, X.J.: Microstructure and ablation behavior of hafnium carbide coating for carbon/carbon composites. *Surf. Coatings Technol.* **206**, 2825–2832 (2012). <https://doi.org/10.1016/j.surfcoat.2011.12.001>
98. Li, W., Meng, J., Liu, P., Du, H., Zhang, K., Ma, F., Liu, X., Chen, X.: Fabrication and characterization of HfC/SiC nanomultilayered films with enhanced mechanical properties. *Vacuum* **128**, 230–233 (2016). <https://doi.org/10.1016/j.vacuum.2016.04.002>
99. Zhao, L., Jia, D., Duan, X., Yang, Z., Zhou, Y.: Improved oxidation resistance of zirconium carbide at 1500 °C by lanthanum hexaboride additions. *J. Am. Ceram. Soc.* **94**, 3648–3650 (2011). <https://doi.org/10.1111/j.1551-2916.2011.04830.x>
100. Jinoop, A.N., Denny, J., Paul, C.P., Ganesh Kumar, J., Bindra, K.S.: Effect of post heat-treatment on the microstructure and mechanical properties of hastelloy-X structures manufactured by laser based directed energy deposition. *J. Alloys Compd.* **797**, 399–412 (2019). <https://doi.org/10.1016/j.jallcom.2019.05.050>
101. Denny, J., Jinoop, A.N., Paul, C.P., Singh, R., Bindra, K.S.: Fatigue crack propagation behaviour of inconel 718 structures built using directed energy deposition based laser additive manufacturing. *Mater. Lett.* **276**, 128241 (2020). <https://doi.org/10.1016/j.matlet.2020.128241>
102. Hans, K., Latha, S., Bera, P., Barshilia, H.C.: Hafnium carbide based solar absorber coatings with high spectral selectivity. *Sol. Energy Mater. Sol. Cells* **185**, 1–7 (2018). <https://doi.org/10.1016/j.solmat.2018.05.005>
103. Islam, W., Mourshed, M., Masud, M.H., Sozal, S.I., Sabur, S.: Bin: Prospects of non-edible neem (*Azadirachta indica*) oil in Bangladesh: performance and emission evaluation in a direct injection diesel engine. *Int. J. Ambient Energy* **40**, 525–536 (2019). <https://doi.org/10.1080/01430750.2017.1421578>
104. Gao, J., Yang, Y., Ren, Y., Zhu, W., Li, J., Liu, Y., Dai, L., Wang, L., He, Z.: A novel hafnium boride catalyst for vanadium redox flow battery. *Ionics (Kiel)*. **28**, 4273–4282 (2022). <https://doi.org/10.1007/s11581-022-04656-7>
105. Chowdhury, A.H., Jafarizadeh, B., Pala, N., Wang, C.: Wearable capacitive pressure sensor for contact and non-contact sensing and pulse waveform monitoring. *Molecules* **27**, 1–14 (2022). <https://doi.org/10.3390/molecules27206872>
106. Jafarizadeh, B., Chowdhury, A.H., Khakpour, I., Pala, N., Wang, C.: Design rules for a wearable micro-fabricated piezo-resistive pressure sensor. *Micromachines*. **13**, (2022). <https://doi.org/10.3390/mi13060838>
107. Chowdhury, A.H., Khakpour, I., Jafarizadeh, B., Pala, N., Wang, C.: A facile fabrication of porous and breathable dielectric film for capacitive pressure sensor. *Proceedings IEEE Sensors. 2020-Oct, 2–5* (2020). <https://doi.org/10.1109/SENSOR547125.2020.9278604>

108. Gangwani, P., Perez-Pons, A., Bhardwaj, T., Upadhyay, H., Joshi, S., Lagos, L.: Securing environmental IoT data using masked authentication messaging protocol in a DAG-based blockchain: IOTA tangle. *Futur. Internet.* **13**, 312 (2021). <https://doi.org/10.3390/fi13120312>
109. Gangwani, P., Soni, J., Upadhyay, H., Joshi, S.: A deep learning approach for modeling of geothermal energy prediction. *Int. J. Comput. Sci. Inf. Secur.* **18**, 62–65 (2020)

High-Temperature W/ZrC Composite Coatings



Aliasghar Najafzadehkhoee, Maryam Vakhshouri, Pavol Hvizdoš,
and Dušan Galusek

Abstract Owing to their outstanding strength, resistance to thermal shock and ablation, high thermal stability, and good thermal expansion, composites of tungsten with zirconium carbide (W/ZrC) have attracted great attention for high-temperature applications. Various techniques can be used for the production of W/ZrC composites, including hot-pressing, spark plasma sintering, in-situ reaction sintering, and displacive compensation of porosity. Both hot-pressing and spark plasma sintering are typically used for preparing small-sized samples with simple geometry. Both in-situ reactive sintering and reactive infiltration methods are well-suited to produce refractory metal/ carbide composites. The reactive infiltration method benefits from a thorough infiltration step because of the good wettability of WC by low-melting metallic liquid of Zr_2Cu in a preform to produce a near net-shaped W/ZrC composite. The reaction of zirconium carbide with oxygen can enhance oxidation resistance through the formation of ZrO_2 layer which can be melted at a higher temperature (2677 °C), covering the surface to avoid further oxidation of substrates. Several methods have been reported to deposit the composite on complex-shaped substrates. The results showed good adhesion between coating and graphite substrates as well as a considerable increase in mechanical properties resulting from the formation of solid solution in composites. In this chapter, an attempt has been made to review the preparation of WC preforms which are mainly based on the polymerization of low-toxic methacrylamide and gelation of non-toxic sodium alginate to prepare porous preforms with complex geometries and summarize the preparation methods of W/ZrC composites using reactive sintering and infiltration methods, focusing on microstructures, mechanical properties, and progress in coating applications.

A. Najafzadehkhoee (✉) · D. Galusek
Joint Glass Centre of the IIC SAS, TNUAD, and FChPT STU, FunGlass, Študentská 2, 91150
Trenčín, Slovak Republic
e-mail: ali.najafzadeh@tuni.sk

M. Vakhshouri · D. Galusek
FunGlass, Alexander Dubček University of Trenčín, Študentská 2, 91150 Trenčín, Slovak
Republic

P. Hvizdoš
Institute of Materials Research, Slovak Academy of Sciences, Košice 04001, Slovak Republic

Keywords Coatings · High-temperature applications · W/ZrC composite

List of Abbreviations

ANOVA	Analysis of variance
APS	Ammonium persulfate
BSE	Backscattered electron
CVD	Chemical vapor deposition
DCP	Displacive compensation of porosity
HP	Hot pressing
MAM	Methacrylamide
MBAM	N,N'-Methylene bisacrylamide
ORN	Oak Ridge National Laboratory
RMs	Refractory metals
SAD	Selected area diffraction
SEM	Scanning electron microscopy
SPS	Spark Plasma Sintering
TEM	Transmission electron microscopy
TEMED	N,N,N,N'-Tetramethylethylenediamine
TIG	Tungsten inert gas
W	Tungsten
WC	Tungsten carbide
ZrC	Zirconium carbide

1 Introduction

Composites of refractory metals (RMs) with transition metal refractory carbides are extensively utilized for ultra-high-temperature applications because of their high fracture toughness, high hardness, good flexural strength, high thermal stability, and resistance to thermal shock and ablation [1]. Zirconium carbide (ZrC) shows good compatibility with tungsten (W), and therefore, the flexural strength of monolithic tungsten and fracture toughness of zirconium carbide can be improved at elevated temperatures [2]. Tungsten-zirconium carbide composites are usually fabricated using sintering methods such as hot-pressing (HP), spark plasma sintering (SPS), in-situ reactive sintering, and displacive compensation of porosity (DCP) [1, 3–7]. Large and/or complex-shaped parts cannot be produced using HP and SPS, which, in addition, require also costly machining [7]. Highly dense tungsten and carbide zirconium composites can be obtained using displacive compensation of porosity proposed by Dickerson et al. [8], composed of two steps; preparation of preforms and reactive melt infiltration of a low-melting alloy (Zr_2Cu) in WC preforms, resulting

in energy-saving and lower production cost than those formed by hot-pressing and spark plasma sintering. Moreover, due to the good wettability of tungsten carbide preforms by molten Zr_2Cu , the molten alloy can easily infiltrate into an open-porous preform at ambient pressure [9]. Gel-casting processes based on low-toxic and non-toxic polymers exhibit a complex-shaped possibility during the fabrication process to prepare open-porous preforms [10]. From several studies on the stabilization of three-dimensional network structures, only a relatively small fraction relates to the preparation of porous structures using gel-casting based on low-toxic and non-toxic polymers, with even fewer that have considered high-density carbides such as tungsten carbide (15.8 g cm^{-3}) [11] which is 4–5 times of alumina (3.96 g cm^{-3}) and silicon carbide (3.22 g cm^{-3}) densities [12–16].

This chapter emphasizes the preparation of tungsten carbide preforms and how they are applied to fabricate W/ZrC composites using reactive sintering and infiltration methods for coating applications at ultra-high temperatures. The preparation of WC preforms based on the polymerization of low-toxic methacrylamide and gelation of non-toxic sodium alginate and the rheological behavior of WC slurries are considered in Sect. 2. Following the preparation of preforms, the fabrication of W/ZrC composites, in-situ reactive sintering, and infiltration of a molten alloy into porous preforms is dealt with in Sect. 3, including optimization of reactive infiltration parameters. Recent research results in the application of W/ZrC coatings against oxidation are introduced in Sect. 4. Finally, the mechanical characterization and ablation resistance of the composites are concluded in Sect. 5.

2 Fabrication of Preforms

Porous ceramics with homogenous microstructures have been utilized in various industrial applications such as thermal insulators, catalysis, hot gas filtration, and filtration of molten alloys [11, 17–19]. Macro-porous ceramics are fabricated by different methods, for instance, direct foaming, sol-gel, freeze casting, replica, polymeric sponge, and gel-casting routes [20, 21]. Controlling pore size and distribution is very challenging in direct foaming methods [19]. However, the applications of replica and polymeric sponges are restricted due to incompatibility with some ceramic materials and the considerable cost to fabricate complex-shaped templates [22]. The gel-casting method was first developed by Omatete and Janney [10] at Oak Ridge National Laboratory (ORNL) based on the polymerization of monomers to form 3D structures of ceramics. To prevent neural toxicity associated with the use of acrylamide monomers, the process of fabricating foam ceramics has been modified to incorporate non-toxic and low-toxicity monomers [23]. This section focuses on the fabrication of tungsten carbide foams through low-toxic and non-toxic gel-casting routes which are used in the infiltration step to prepare W/ZrC composites.

2.1 Gel-Casting Based on Low-Toxic Polymers

Commercial tungsten carbide (99.9%, Eurotungstene Metal Powders Co., France) consisting of agglomerates of primary particles was used in the process (Fig. 1). Methacrylamide (MAM), a water-soluble monomer, can be co-polymerised by N,N'-Methylene bisacrylamide (MBAM). Furthermore, using a free radical-releasing initiator and catalyst, namely ammonium persulfate (APS) and N,N,N,N'-Tetramethylethylenediamine (TEMED). Figure 2 shows the flow chart of gel-casting based on low-toxic monomers. First, a high solids content slurry (up to 35 vol.%) is prepared by dissolving methacrylamide (MAM) and N,N'-methylene bisacrylamide (MBAM) in deionized water, followed by the addition of tungsten carbide powder to the solution.

Afterward, the dispersant (ammonium citrate), ammonium persulfate (APS), and catalyst are gradually added into the suspension. The final slurry is left to solidify within the mold. The preforms are dried at 700 °C with a 2 °C min⁻¹ heating rate and then, pre-sintered at 1450 °C. The details of the preparation procedure are described elsewhere [18].

It has been reported that the optimum amount of dispersant and maximum solid content to obtain flowable slurry were about 0.2 wt.% and 35 vol.% of WC powder, respectively [18, 24]. Yoghobizadeh et al. [24] investigated parameters influencing the flexural strength of WC green bodies and they found that the ratio between monomers was a critical factor for uniform gelation. They showed that inhomogeneous polymerization can occur by either decreasing the ratio of monomers or increasing the excessive cross-linkers, resulting in the formation of cracks in the

Fig. 1 SEM image of WC powder

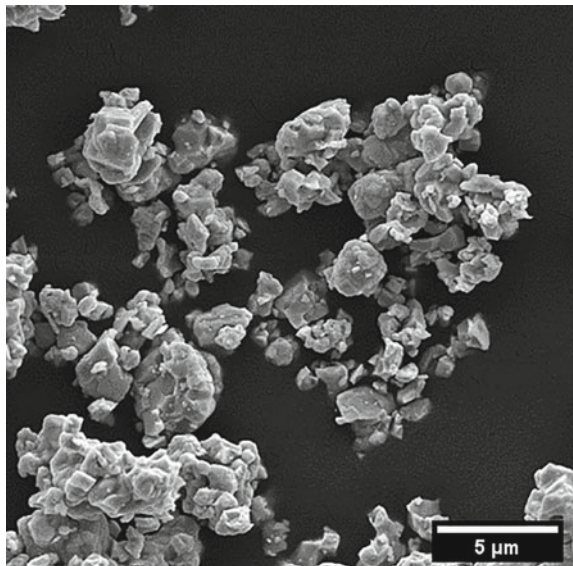
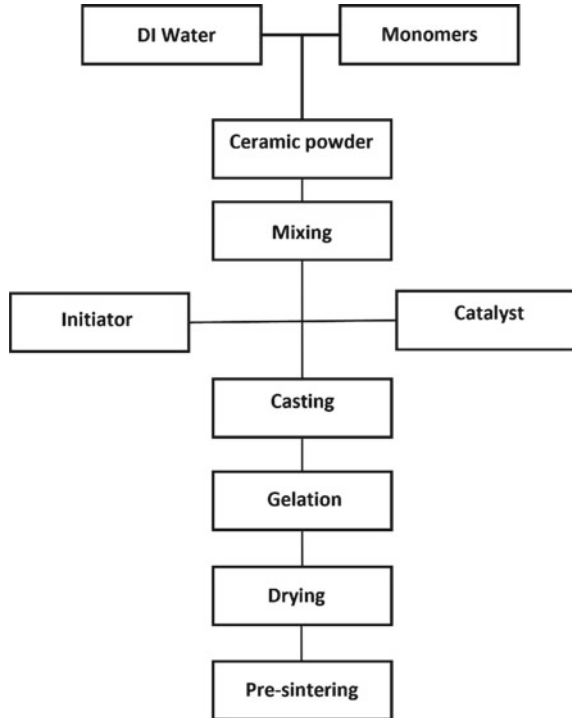


Fig. 2 Flow diagram of gel-casting using low-toxic monomer

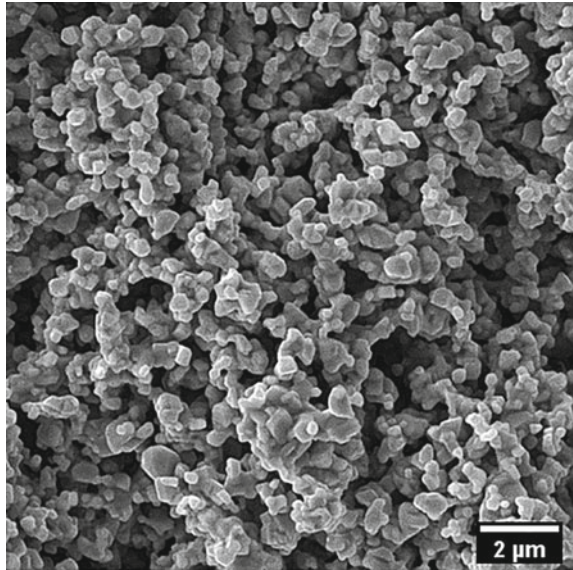


network after the drying process, thus causing to decrease in the flexural strength of green bodies. When the ratio of MAM to MBAM was 4:1, the flexural strength reached its maximum value (≈ 4 MPa) [24]. Figure 3 shows the preform pre-sintered at 1450°C with a relatively homogenous distribution of small pores. The pre-sintering temperature was sufficient to fuse WC particles and to form a strong skeleton to sustain the infiltration process [6].

2.2 Non-toxic Polymer-Based Gel-Casting

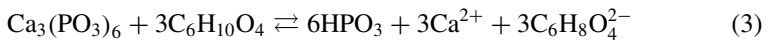
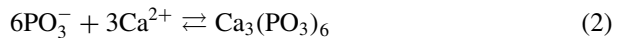
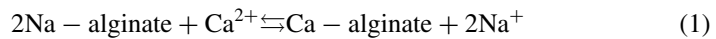
Sodium alginate, a natural polysaccharide, is often employed in gel-casting due to its gelation properties in the presence of bivalent cations like calcium. Many researchers studied the gel-casting process using non-toxic polymers to form low-density ceramic preforms such as Al_2O_3 and SiC [25, 26] while stabilization of high-density ceramic powder such as WC powder within a three-dimensional network remains challenging [11]. Figure 4 illustrates a flow chart of the non-toxic polymer-based gel-casting process. A sodium alginate solution is first mixed with ceramic powders and then, chelator $(\text{NaPO}_3)_6$, solidifier agent $(\text{Ca}_3(\text{PO}_4)_2)$, and dispersant are added to the

Fig. 3 SEM image of the pre-sintered body



solution. Finally, hexanedioic acid ($C_6H_{10}O_4$) as an initiator is introduced to the slurry.

The gelation occurs by decomposition of the complex and substitution of Na^+ with Ca^{2+} , according to Eqs. (1–3) [11, 26, 27].



The strength of green bodies can be attributed to the strength of cross-links depending on the calcium salt to chelator ratio as reported previously [11, 28]. The results revealed that the maximum value of bending strength was approximately 3.3 MPa. This is achieved by increasing the solidifier agent to chelator ratio. The strength of samples is then adequate for handling purposes although the value is lower than those achieved with the use of low-toxic polymer [11].

Following ambient drying, the green bodies are subjected to a pre-sintering process for further treatment. The microstructure of the sample pre-sintered at 1450 °C for 4 h is shown in Fig. 5. The porous microstructure with well-distributed pores is obtained after burnout and pre-sintering.

Fig. 4 Flow chart of gel-casting using non-toxic monomer

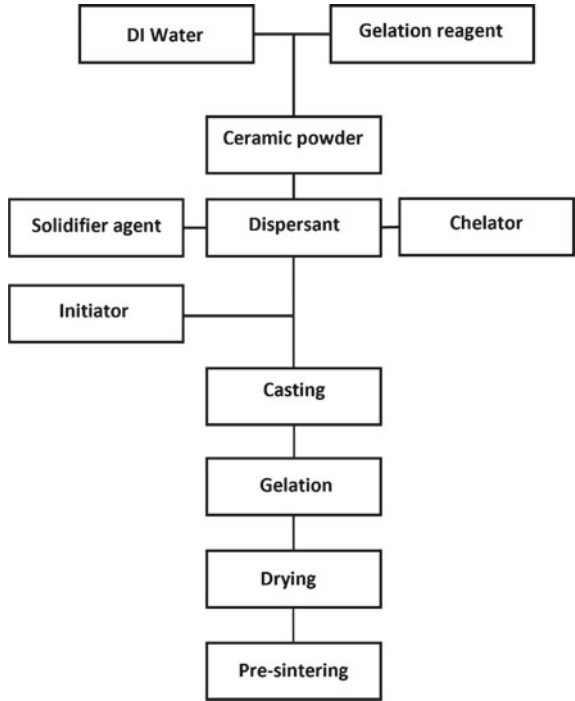
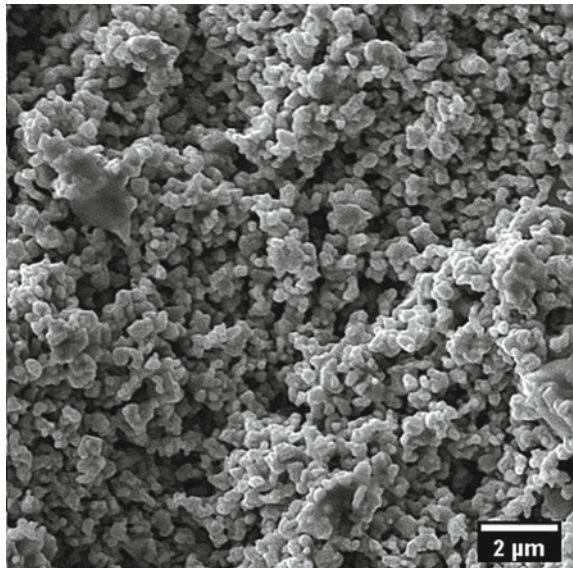


Fig. 5 Microstructure of sample sintered at 1450 °C for 4 h



2.3 Rheological Behavior of WC Slurry

Ceramic materials show complex behavior influenced by temperature, particle size, and solid content [29]. Rheological studies involve the flow ability of materials to prepare a slurry with desirable characteristics such as low viscosity and high solid loading [29, 30]. Dispersants are commonly used to increase solid loading and to obtain a more uniform distribution of particles in a slurry [28]. The impact of solid loading and different dispersants on viscosity and stabilization of WC slurries using gel-casting based on non-toxic and low-toxic polymers was analyzed [24, 28]. Compared to the gel-casting based on a non-toxic system, slurries with a relatively higher solids content and subsequently, lower shrinkage after pre-sintering can be achieved in the low-toxic system [18]. It should be noted that the solid content used in sodium alginate gel-casting can have a considerable effect on the properties of final dense ceramics; however, the strength of porous bodies needs to be high enough for the infiltration process, hence, it is essential to provide optimum conditions for uniform polymerization, high solid loading and suitable viscosity of WC slurries [10, 11, 21, 25–28, 31].

2.3.1 Viscosity Optimization in Non-toxic and Low-toxic Systems

Viscosity plays a crucial role in the gel-casting process to fabricate ceramic parts with complex shapes. The viscosity of slurries can be adjusted by solid loading, monomer concentration, and molecular weight of polymers. The viscosity needs to be high enough for the slurry to flow quickly and easily into molds and form a defect-free part [32].

The effect of different amounts of dispersant up to 0.5 wt.% on the viscosity of WC slurries in both low-toxic and non-toxic systems was investigated [24, 28]. The viscosity of WC slurries decreased by increasing the dispersant amount up to 0.35 wt.% in both non-toxic and low-toxic systems which improves wetting by the fluid and deagglomerate particles. It has been reported that slurries can attain the optimum viscosity by adding ≈ 0.25 wt.% of WC powders [18, 24, 28]. In general, the viscosity of slurries increases by increasing solids content which is attributed to the friction and intermolecular interactions among particles in liquids [29, 30]. The viscosity of the WC slurries up to 35 vol% solids content in the non-toxic and low-toxic systems was studied and the results indicated the same shear thinning behavior for WC slurries up to 30 vol.% of the WC powder [24, 28]. Higher solid contents (up to 35 vol.%) of WC are possible in low-toxic systems. The viscosity of slurries containing 30 vol.% WC was higher than 1 Pa.s at the shear rate of 100 s^{-1} in the non-toxic system, which is not suitable for the casting process. The optimum solid loading is up to 25 vol.% in the non-toxic and 33 vol.% WC powder in the low-toxic system [24, 28]. However, the maximum content of ceramic powders can be restricted by their density. For example, maximum solid loadings of ≈ 50 vol.% were reported for Al_2O_3 , SiC, and B_4C [25, 33, 34]. It should be noted that only porous preforms

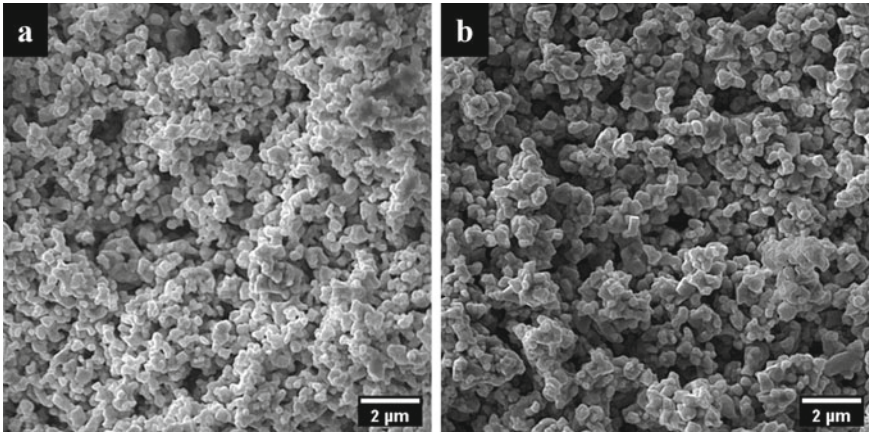


Fig. 6 SEM micrographs of pre-sintered samples prepared using **a** non-toxic sodium alginate and **b** low-toxic methacrylamide

with sufficient green strength (≈ 3 MPa) can be considered for further infiltration process; moreover, increasing the solids load prevents the shrinkage and cracks after the pre-sintering process [28, 32]. Figure 6 shows porous microstructures with well-distributed and fine pores prepared using gel-casting in both non-toxic (Fig. 6a) and low-toxic systems (Fig. 6b).

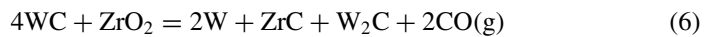
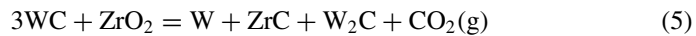
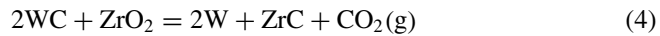
3 W/ZrC Composites

Great attention has been paid to W/ZrC composites over the past few decades due to their outstanding properties concerning their high strength, good fracture toughness, resistance to oxidation, and thermal stability. The production of W/ZrC composites has undergone significant evolution, with different methods used to fabricate them. W/ZrC composites can be produced using various methods such as hot-pressing, spark plasma sintering (SPS), in-situ reaction sintering, and displacive compensation of porosity (DCP) [1, 4, 6, 18]. For hot-pressing and spark plasma sintering, elemental ZrC and W powders are mixed and subjected to heat and pressure simultaneously; both methods are developed for the preparation of small-sized samples with simple geometry [7]. However, pressure-less in-situ sintering at high temperatures and reactive infiltration-based methods are more suitable for producing W/ZrC composites. Dense W/ZrC composites can be synthesized using pressure-less in-situ sintering where ZrO_2 and WC powders are mixed in specific volume fractions and sintered at higher temperatures (>2000 °C), while the reactive infiltration-based method offers the advantage of producing dense ceramics at 1200–1300 °C and ambient pressure. In this section, an attempt has been made to review in-situ reaction

sintering and DCP or reactive infiltration method to fabricate W/ZrC composites with a special focus on their final microstructures.

3.1 *In-situ Reactive Sintering*

In this process, starting powders are mixed and then heated to a high temperature to form dense and complex-shaped ceramics [1, 18, 35]. First, a solution containing monomers (MAM and MBAM) is prepared and then ZrO₂ and WC mixed and milled with carbon black are added to the solution. The obtained green body is subjected to overnight drying at 80 °C followed by calcination at 500 °C for 1h [18]. WC and ZrO₂ with different molar ratios can react to form ZrC and W phases, according to the following equations (Eqs. 4–6) [35].

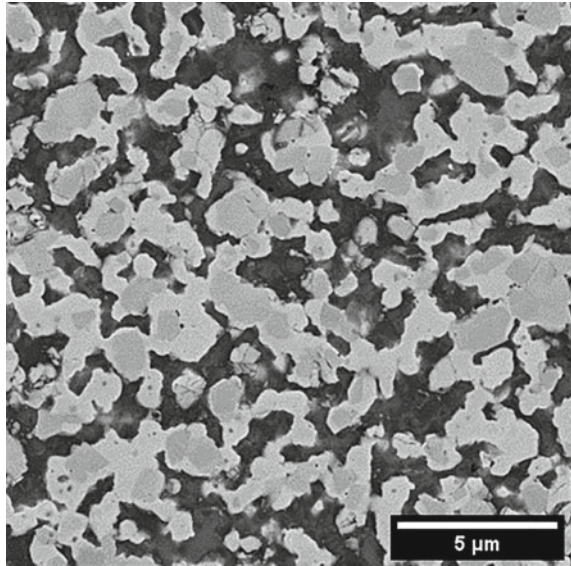


In a study conducted by Khakzadi et al. [18], the thermodynamics of reactions were evaluated using HSC Chemistry [36]. The Gibbs free energy of reactions was calculated, and the analyses indicated that the reactions may start at temperatures above 1500 °C, depending on the molar ratio between tungsten carbide and zirconium oxide. The reactions were found to be completed at approximately 2000 °C when the optimal ratio was 3:1 (WC to ZrO₂) [18]. Figure 7 shows SEM micrographs of the W/ZrC fabricated using the reactive sintering method. The final microstructure consists of a fairly homogenous distribution of tungsten (bright phase) and ZrC (dark phase). It is essential to use a relatively high temperature to complete the reactions. However, the final properties of W/ZrC composites are influenced by changing molar proportions of tungsten carbide and zirconium oxide [1, 18].

3.2 *Reactive Infiltration-Based Method*

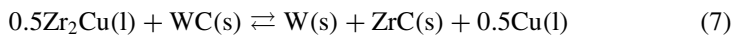
The reactive infiltration method or displacive compensation method (DCP) is a process in which a reactive alloy with a low-melting point is infiltrated into a porous preform to fabricate composite materials with improved properties [6, 37]. Compared to the in-situ reactive sintering, the formation of composites is possible at a modest temperature [6, 28]. The green bodies produced using the gel-casting process are pre-sintered and then, infiltrated by placing Zr₂Cu on the top of sintered preforms to prepare W/ZrC composites.

Fig. 7 SEM micrograph of W/ZrC composite fabricated using in-situ reactive sintering



3.2.1 Infiltration Parameters and Optimization

WC preforms obtained through gel-casting were infiltrated with molten Zr_2Cu to produce W/ZrC composites, according to Eq. (7) [1].



Various parameters including infiltration temperature and holding time influence the final properties of infiltrated composites. The infiltration temperatures of 1150, 1250, and 1350 °C and holding times of 0.5, 2, and 3.5 h are considered, with the constant 2:1 molar ratio of Zr_2Cu/WC [38]. The Taguchi design of experiments method was used to design and evaluate a series of experiments. The analysis of variance (ANOVA) results indicated that the temperature was more effective in the infiltration process, while longer holding time did not have a considerable impact on the formation of tungsten and zirconium carbide phases [38, 39].

Figure 8 shows backscattered electron (BSE) images of W/WC/ZrC composites consisting of a grey core (WC) surrounded by a brighter phase (WC) in the ZrC matrix. A homogenous distribution of tungsten, zirconium, and carbon is documented in Fig. 9. The results revealed that unreacted WC remained in the infiltrated composite at 1150 °C, and reaction kinetics could be increased by decreasing the viscosity of the melt at higher temperatures and shorter holding times e.g., 1350 °C and 0.5 h [1, 6, 9, 38]. Figure 10 shows the transmission electron microscopy (TEM) micrographs taken from the preform infiltrated at 1350 °C with a holding time of 0.5 h. The dark phase is distinguished as tungsten, whereas the grey area is comprised of zirconium carbide grains. The selected area diffraction (SAD) patterns of the W/ZrC composites

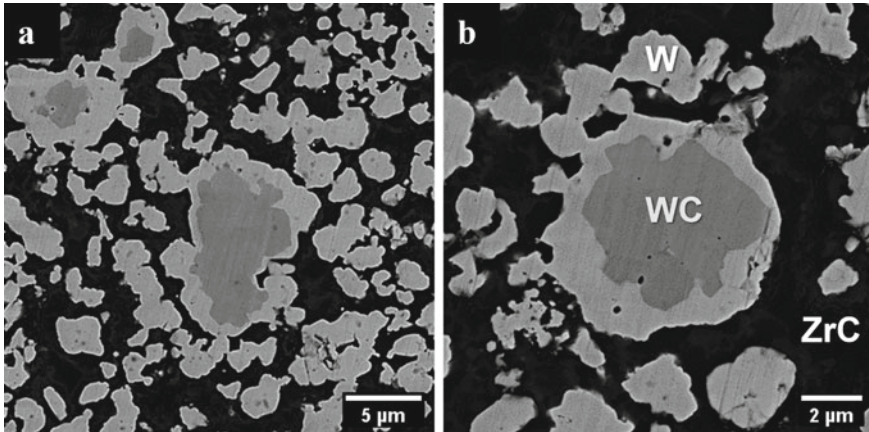


Fig. 8 **a** Backscattered SEM images of the infiltrated composites at 1150 °C–0.5 h and **b** with higher magnification

demonstrate the presence of pure tungsten and zirconium carbide phases shown in Fig. 10a. The volume fraction of the phases formed in composites is a crucial factor that determines their ultimate properties. In the DCP method, the W/ZrC composites were composed of 32–45 vol.% W and 54–68 vol.% ZrC [6, 39]. The optimum conditions of the infiltration of WC preforms by molten Zr_2Cu were reported to be 1350 °C for 0.5 h [38]. To tune the volume fraction of the formed phases affecting the final properties, the addition of ZrC powder up to 3 vol.% in the preforms was studied [37]. Section 4 discusses how the phases affect not only the mechanical properties but also the resistance to ablation in tungsten/zirconium carbide composites.

4 W-ZrC Coating

Due to their thermal stability, good resistance to thermal shock, oxidation, and ablation, W/ZrC composites show great potential as a coating material for high-temperature applications [8, 37, 38]. In particular, W/ZrC composites can be utilized to prevent the rapid oxidation of carbon-based composites above 450 °C [40]. Several efforts have been made to use stable coatings such as refractory transition metal carbides, oxides, and borides to protect carbon-based composites [41, 42]. Among these, ZrC is a material of choice with a high melting point and good ablation resistance. ZrC can protect substrates by forming a dense and adhesive ZrO_2 layer at high temperatures [41]. The application of pure ZrC coating is restricted due to its volume expansion, resulting in crack formation after ablation [43]. Since the melting temperature of ZrO_2 (approximately 2677 °C) is lower than that of pure W (about 3422 °C), it is possible for ZrO_2 to melt and coat the surface when exposed to ultra-high temperatures [1]. Various coating processes such as pack cementation technology, plasma

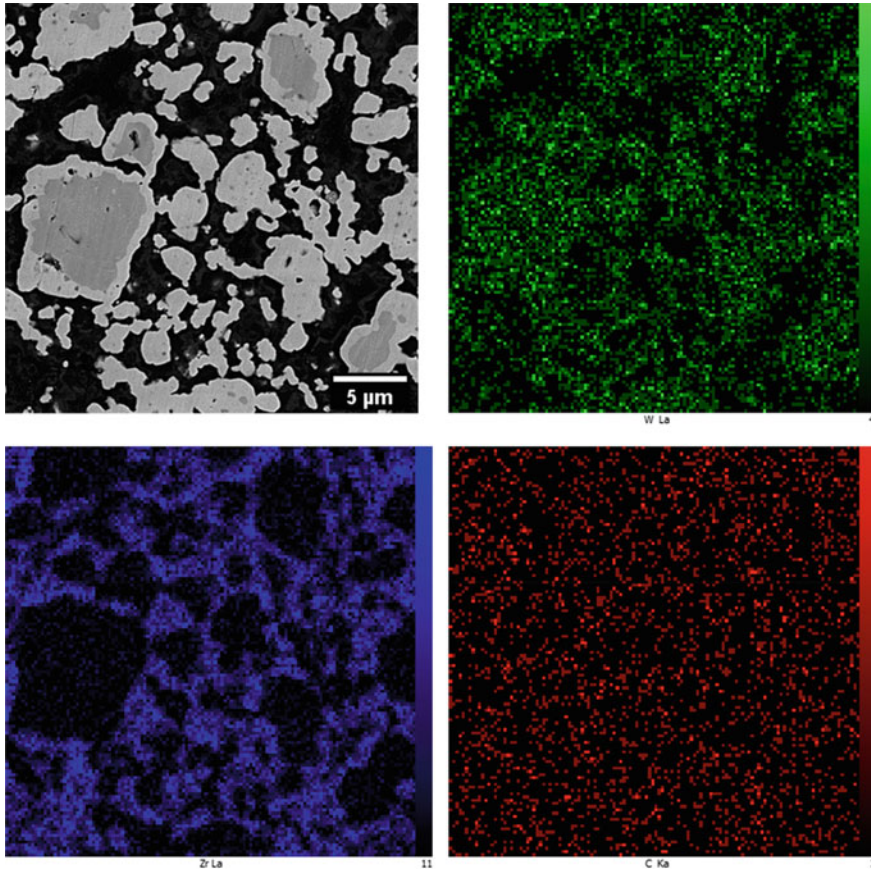


Fig. 9 Backscattered SEM micrograph of the infiltrated composite ($T = 1150\text{ }^{\circ}\text{C}$, $t = 0.5\text{ h}$) with corresponding elemental maps for W, Zr, and C

spraying, chemical vapor deposition (CVD), and laser-assisted coating process can be used [40]. Although some of the methods such as CVD can be utilized for thick protective layers and complex-shaped parts, the application is limited because of the micro-cavities or micro-cracks formed under the service conditions [44]. Recently, a tungsten inert gas (TIG) process was employed to prepare an anti-ablation layer on graphite in which the thickness can be tuned by changing heat supply, arc flow, and electrode displacement speed [40]. Compared to the laser-aided coating method, the rate of deposition in the TIG welding process is higher, resulting in energy-saving and lower production costs [40]. Wen et al. [45] fabricated dense and uniform ZrC coatings on the graphite substrates using the TIG cladding technology, significantly improving the ablation resistance. The method consists of three stages: preparation of a slurry containing ceramic powders, painting the slurry on a substrate (thickness $\approx 1\text{ mm}$), and formation of the coating using an electric arc of TIG. Several

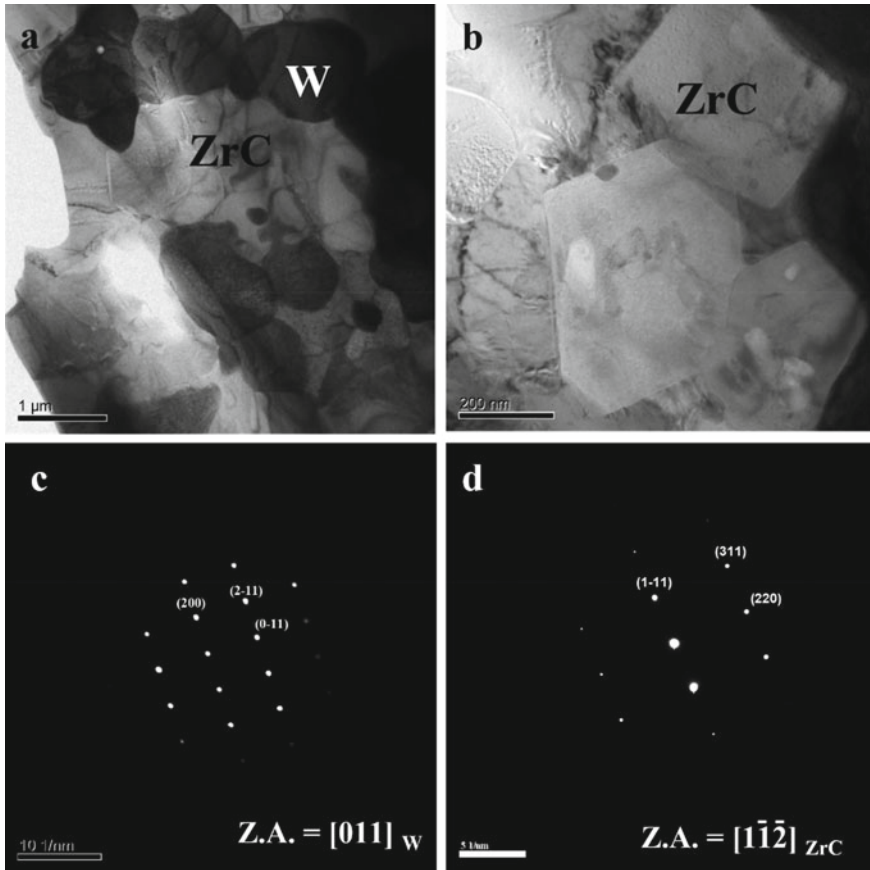


Fig. 10 **a** TEM images of the infiltrated composite ($T = 1350\text{ }^{\circ}\text{C}$ for 0.5 h), **b** high-magnification view of the bright area in **a**, and **c** and **d**. Selected diffraction patterns of tungsten and zirconium carbide in **a**, respectively

parameters such as current, voltage, cladding speed, and argon flow affecting the final properties of the coating increase the flexibility of the method to apply coatings of various compositions on large-scale structures [45]. Golestani et al. [40] examined the use of the TIG cladding method to deposit W/ZrC composites onto a graphite substrate. They also studied thermodynamics and kinetics of the formation of tungsten/zirconium carbide composites from a slurry containing tungsten carbide and zirconium oxide. Based on the previously published works on in-situ reactive sintering, a molar ratio of 3:1 was selected [18]. An aqueous solution containing 2 wt.% of sugar glue was mixed with the homogenous slurry and then, applied on a graphite substrate. Afterward, the layer was dried at $200\text{ }^{\circ}\text{C}$ for 12 h [40]. The electric arc ($\approx 3000\text{ }^{\circ}\text{C}$) causes a decrease in the viscosity of coating materials; a

molten pool can be formed in a short time due to the melting point of ZrO_2 (2677 °C), increasing diffusion rate and facilitating strong bonding at the interface [45].

4.1 Properties

4.1.1 Mechanical Properties

The mechanical properties of W/ZrC composites are linked to the volume fraction of both W and ZrC phases [6, 8]. Increasing the volume fraction of the zirconium carbide phase from 54.8 vol.% to 68.2 vol.% has been shown to enhance the flexural strength of W/ZrC composites from 429 ± 5 MPa to 460 ± 5 MPa, while reducing the displacement at the fracture point from 0.140 to 0.096 mm [6]. The average flexural strength of W/ZrC composites produced through the reactive infiltration method is lower than those prepared using reactive sintering methods, possibly due to the lower W content [37]. Moreover, the Vickers hardness of W/ZrC composites was reported in the range of 7.5 ± 0.4 to 9.5 ± 0.3 GPa depending on the final amounts of phases. The amount of ZrC is determined by the fraction of open porosity in the preforms prepared using both non-toxic and low-toxic gel-casting processes. To complete the displacive reaction during the infiltration (Eq. 7), an open porosity \approx of 50% is sufficient [38]. Beyond the limit of porosity, some residual phases such as Cu and W_2C can remain, which deteriorates the mechanical properties [1, 6]. Figure 11 shows the fracture surfaces of the infiltrated W/ZrC composites using two preforms containing 50 and 60 vol.% of open porosity. The fracture modes are characterized by both cleavage fracture (11a) and dimple rupture (11b), depending on the content of the W phase. The fracture mode can be changed from cleavage at a lower content of W (32 vol.%) to dimple rupture at a higher content of W phase (45 vol.%) [6]. Zhao et al. [2] observed $Zr_xCu_yC_z$ particles in the microstructure: they implied that cracks are deflected by the particles resulting in enhanced fracture toughness of W/ZrC composites. The cracks are usually characterized by their zigzag path in the ZrC phase [2, 6, 37, 38]. The results indicate that the cracks initiate in zirconium carbide phases and then propagate in more ductile regions. The bonding strength of grain boundaries is significantly influenced by the infiltration temperature [6].

4.1.2 Ablation Resistance

W/ZrC composites are extensively utilized in ultra-high-temperature applications because of their ability to resist erosion or removal of material due to high-temperature exposure to gas or plasma. The high melting point of W and the excellent thermal stability of ZrC make these composites highly resistant to ablation [8]. The linear and mass ablation rates of the infiltrated W/ZrC composites were determined by measuring the changes in dimensions and weight before and after exposure to a flame at a temperature of ≈ 3000 °C for 60 s [3]. The average linear and mass

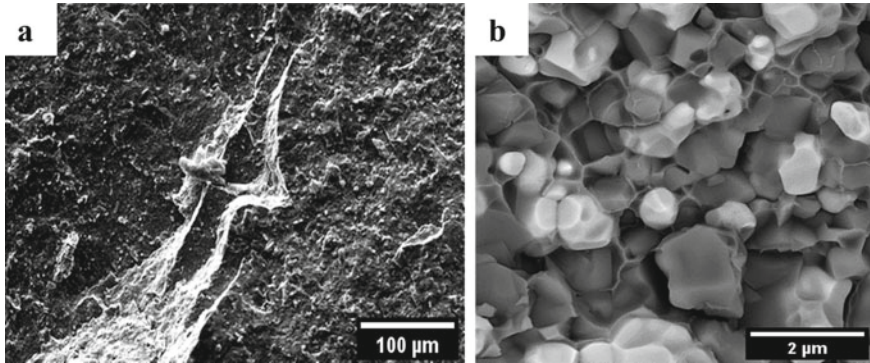


Fig. 11 SEM fractographs of W/ZrC composites prepared at 1350 °C for 0.5 h with **a** 32 vol% W and **b** 45 vol.% W

ablation rates were reported to be $3.6 \pm 0.5 \mu\text{m/s}$ and $2.1 \pm 0.1 \text{ mg/s}$, respectively [6]. However, the presence of ZrC in the composite improves its ablation resistance resulting from the formation of a protective layer that prevents the oxidation and erosion of the underlying W matrix [38]. Figure 12 shows representative SEM images of the ablated surfaces of W/ZrC composites. The ablated surface with a thickness of 55 μm (Fig. 12a) is covered by a mixture of WO_3 and ZrO_2 (Fig. 12b). Although the mismatch of thermal expansion coefficients among ZrO_2 , WO_3 , and the substrate caused micro-cracks in oxide layers (Fig. 12c), the substrate itself was crack-free [6, 37, 38]. In addition, the phase transformation of ZrO_2 during the cooling can result in crack formation in the oxide layers [6]. The study of the effect of airflow on the microstructure (Fig. 12d) revealed that the substrate cannot be protected by the porous WO_3 . On the contrary, the dense ZrO_2 layer improved the resistance of the composites against ablation [2, 6, 38]. Previous studies investigated incorporation of a ZrC nanopowder into WC preforms to enhance the amount of ZrC phase in the resulting composites. However, the findings indicate that the addition of the ZrC nanopowder does not substantially improve the resistance of WC to ablation [37].

5 Summary

W/ZrC composites can be successfully fabricated using reactive infiltration of Zr_2Cu in WC preforms at modest temperatures. The fabrication process of WC preforms has a considerable effect on the properties of final composites. Microporous WC preforms with homogenous pore distribution are produced using the gel-casting process based on low-toxic and non-toxic polymers. However, W/ZrC composites can be prepared using in-situ reactive sintering at higher temperatures. The tungsten inert gas (TIG) is one of the promising processes to apply W/ZrC composites on different substrates with an enhanced bonding interface. The volume fractions of the ZrC phase and

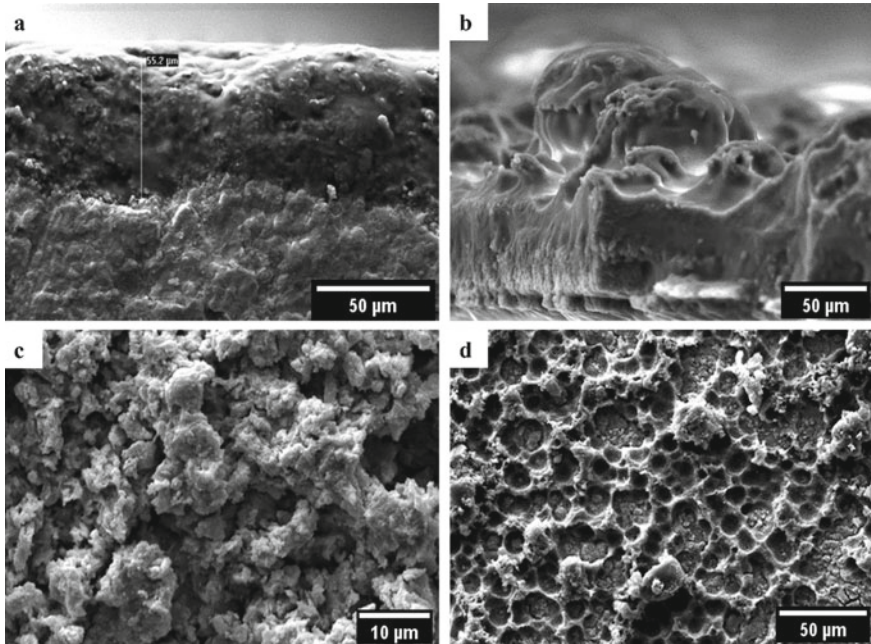


Fig. 12 SEM micrographs of the composite ablated at 3000 °C, **a** vertical view, **b** oxide layers, and direct exposure zones including **c** pores and cracks and **d** effect of airflow

residual porosity within the composites are the determining factors for their flexural strength and hardness. The formation of a dense ZrO_2 layer improves the ablation resistance significantly.

6 Future Scope

The potential future directions for W-ZrC composites at elevated temperatures and their applications in reducing the oxidation of carbon-based composites can be summarized as follows:

- **Optimization of WC Preforms:** Further research can focus on optimizing the fabrication process of WC preforms to enhance the properties of the final composites. This can involve exploring different techniques and parameters to achieve microporous WC preforms with a homogenous pore distribution, as well as investigating the use of alternative materials or additives to improve the overall quality of the preforms.
- **Development of fabrication techniques:** While in-situ reactive sintering and reactive infiltration have been mentioned as methods to prepare W/ZrC composites, there is room for exploring and developing other advanced techniques.

Researchers can investigate novel approaches such as additive manufacturing (e.g., 3D printing) or hybrid methods combining different processes to achieve composites with improved microstructural control and tailored properties.

- **Enhanced bonding interface:** The tungsten inert gas (TIG) process has shown promise for applying W/ZrC composites on different substrates. Future efforts can focus on optimizing the TIG process parameters and exploring alternative bonding techniques to further enhance the bonding interface between the composite and substrate. This can lead to improved mechanical properties and better integration of W/ZrC composites into various applications.
- **Tailoring volume fractions and porosity:** The volume fractions of the ZrC phase and residual porosity have been identified as critical factors influencing the flexural strength and hardness of W/ZrC composites. Future research can investigate the effects of these parameters on the composite's properties and explore methods to precisely control and tailor them. This can involve advanced processing techniques, optimization of precursor compositions, or additional phases to achieve desired performance.
- **Ablation resistance:** The formation of a dense ZrO₂ layer has been found to significantly improve the ablation resistance of W/ZrC composites. Future studies can focus on understanding the mechanisms behind this improvement and further enhancing the ablation resistance through the development of novel protective coatings, advanced processing techniques, or the incorporation of other reinforcing materials. This can expand the range of applications for W/ZrC composites in high-temperature environments where ablation resistance is crucial.

Acknowledgements This research work has been supported by the Research Agency of the Ministry of Education, Science, Research and Sport of the Slovak Republic, by the project: Advancement and support of R&D for “Centre for diagnostics and quality testing of materials” in the domains of the RIS3 SK specialization, Acronym: CEDITEK II., ITMS2014+ code 313011W442.

References

1. Dickerson, M.B., Snyder, R.L., Sandhage, K.H.: Dense, near net-shaped, carbide/refractory metal composites at modest temperatures by the displacive compensation of porosity (DCP) method. *J. Am. Ceram. Soc.* **85**, 730–732 (2002). <https://doi.org/10.1111/J.1151-2916.2002.TB00164.X>
2. Zhao, Y.W., Wang, Y.J., Chen, L., Zhou, Y., Song, G.M., Li, J.P.: Microstructure and mechanical properties of ZrCW matrix composite prepared by reactive infiltration at 1300 °C. *Int. J. Refract. Metals Hard Mater.* **37**, 40–44 (2013). <https://doi.org/10.1016/J.IJRMHM.2012.10.014>
3. Song, G.M., Wang, Y.J., Zhou, Y.: Elevated temperature ablation resistance and thermophysical properties of tungsten matrix composites reinforced with ZrC particles. *J. Mater. Sci.* **36**, 4625–4631 (2001). <https://doi.org/10.1023/A:1017989913219/METRICS>
4. Roosta, M., Baharvandi, H.: The comparison of W/Cu and W/ZrC composites fabricated through hot-press. *Int. J. Refract. Metals Hard Mater.* **28**, 587–592 (2010). <https://doi.org/10.1016/J.IJRMHM.2010.04.006>

5. Zhang, S.C., Hilmas, G.E., Fahrenholtz, W.G.: Zirconium carbide-tungsten cermets prepared by in situ reaction sintering. *J. Am. Ceram. Soc.* **90**, 2296–2296 (2007). <https://doi.org/10.1111/J.1551-2916.2007.01883.X>
6. Najafzadeh Khoei, A.A., Habibolahzadeh, A., Qods, F., Baharvandi, H.: Microstructure and properties of DCP-derived W-ZrC composite using nontoxic sodium alginate to fabricate WC preform. *J. Mater. Eng. Perform.* **24**, 1641–1648 (2015). <https://doi.org/10.1007/s11665-015-1427-z>
7. Mudanyi, R.K., Cramer, C.L., Elliott, A.M., Kumar, D.: Effect of W and C addition on the microstructure and phase composition of W-ZrC composites prepared by using Zr2Cu alloy and variant reactant compositions. *Open Ceramics.* **12** (2022). <https://doi.org/10.1016/J.OCE RAM.2022.100305>
8. Dickerson, M.B., Wurm, P.J., Schorr, J.R., Huffman, W.P., Wapner, P.G., Sandhage, K.H.: Near net-shape, ultra-high melting, recession-resistant ZrC/W-based rocket nozzle liners via the displacive compensation of porosity (DCP) method. *J. Mater. Sci.* **39**, 6005–6015 (2004). <https://doi.org/10.1023/B:JMASC.0000041697.67626.46/METRICS>
9. Zhao, Y., Wang, Y., Zhou, Y., Shen, P.: Reactive wetting and infiltration of polycrystalline WC by molten Zr2Cu alloy. *Scr. Mater.* **64**, 229–232 (2011). <https://doi.org/10.1016/J.SCRIPT AMAT.2010.10.018>
10. Omatete, O.O., Janney, M.A., Nunn, S.D.: Gelcasting: from laboratory development toward industrial production. *J. Eur. Ceram. Soc.* **17**, 407–413 (1997). [https://doi.org/10.1016/S0955-2219\(96\)00147-1](https://doi.org/10.1016/S0955-2219(96)00147-1)
11. Najafzadeh Khoei, A.A., Habibolahzadeh, A., Qods, F., Baharvandi, H.: Fabrication of tungsten carbide foam through gel-casting process using nontoxic sodium alginate. *Int. J. Refract. Metals Hard Mater.* **43**, 115–120 (2014). <https://doi.org/10.1016/j.ijrmhm.2013.11.011>
12. Mouazer, R., Thijs, I., Mullens, S., Luyten, J.: SiC foams produced by gelcasting: synthesis and characterization. *Adv. Eng. Mater.* **6**, 340–343 (2004). <https://doi.org/10.1002/ADEM.200400009>
13. Jin, Y., Zhang, B., Ye, F., Zhang, H., Zhong, Z., Liu, Q., Zhang, Z.: Development of ethylene glycol-based gelcasting for the preparation of highly porous SiC ceramics. *Ceram. Int.* **46**, 7896–7902 (2020). <https://doi.org/10.1016/J.CERAMINT.2019.12.009>
14. Zhang, T., Zhang, Z., Zhang, J., Jiang, D., Lin, Q.: Preparation of SiC ceramics by aqueous gelcasting and pressureless sintering. *Mater. Sci. Eng. A* **443**, 257–261 (2007). <https://doi.org/10.1016/J.MSEA.2006.08.047>
15. Xie, R., Zhang, D., Zhang, X., Zhou, K., Button, T.W.: Gelcasting of alumina ceramics with improved green strength. *Ceram. Int.* **38**, 6923–6926 (2012). <https://doi.org/10.1016/J.CERAMINT.2012.05.027>
16. Prabhakaran, K., Pavithran, C.: Gelcasting of alumina using urea-formaldehyde II. Gelation. *Ceram. Form., Ceram Int.* **26**, 67–71 (2000). [https://doi.org/10.1016/S0272-8842\(99\)00020-6](https://doi.org/10.1016/S0272-8842(99)00020-6)
17. Studart, A.R., Gonzenbach, U.T., Tervoort, E., Gauckler, L.J.: Processing routes to macroporous ceramics: a review. *J. Am. Ceram. Soc.* **89**, 1771–1789 (2006). <https://doi.org/10.1111/J.1551-2916.2006.01044.X>
18. Askari, S.R., Khakzadi, M., Shahpasandi, A., Najafzadehkhoei, A.: Fabrication of W-ZrC nanocomposite through reaction sintering using relatively low-toxic methacrylamide-based system. *Compos. Commun.* **13**, 156–161 (2019). <https://doi.org/10.1016/j.coco.2019.04.009>
19. Finhana, I.C., Machado, V.V.S., Santos, T., Borges, O.H., Salvini, V.R., Pandolfelli, V.C.: Direct foaming of macroporous ceramics containing colloidal alumina. *Ceram. Int.* **47**, 15237–15244 (2021). <https://doi.org/10.1016/J.CERAMINT.2021.02.086>
20. Deng, X., Wang, J., Huang, Z., Zhao, W., Li, F., Zhang, H.: Research progress in preparation of porous ceramics. *InterCeram: Int. Ceram. Rev.* **64**, 100–103 (2015). <https://doi.org/10.1007/BF03401108/METRICS>
21. Montanaro, L., Coppola, B., Palmero, P., Tulliani, J.M.: A review on aqueous gelcasting: a versatile and low-toxic technique to shape ceramics. *Ceram. Int.* **45**, 9653–9673 (2019). <https://doi.org/10.1016/J.CERAMINT.2018.12.079>

22. Eom, J.H., Kim, Y.W., Raju, S.: Processing and properties of macroporous silicon carbide ceramics: a review. *J. Asian Ceram. Soc.* **1**, 220–242 (2013). <https://doi.org/10.1016/J.JAS CER.2013.07.003>
23. Binner, J.G.P.: Production and properties of low density engineering ceramic foams. *Br. Ceram. Trans.* **96**, 247–249 (1997)
24. Yaghibizadeh, O., Baharvandi, H., Alizadeh, A.: Investigation of effect of acrylate gel maker parameters on properties of WC preforms for the production of W-ZrC composite. *Int. J. Refract. Metals Hard Mater.* **45**, 130–136 (2014). <https://doi.org/10.1016/J.IJRMHM.2014.04.007>
25. Wang, X., Xie, Z.P., Huang, Y., Cheng, Y.B.: Gelcasting of silicon carbide based on gelation of sodium alginate. *Ceram. Int.* **28**, 865–871 (2002). [https://doi.org/10.1016/S0272-8842\(02\)00066-4](https://doi.org/10.1016/S0272-8842(02)00066-4)
26. Akhondi, H., Taheri-Nassaj, E., Sarpoolaky, H., Taavoni-Gilan, A.: Gelcasting of alumina nanopowders based on gelation of sodium alginate. *Ceram. Int.* **35**, 1033–1037 (2009). <https://doi.org/10.1016/J.CERAMINT.2008.04.023>
27. Yang, J., Yu, J., Huang, Y.: Recent developments in gelcasting of ceramics. *J. Eur. Ceram. Soc.* **31**, 2569–2591 (2011). <https://doi.org/10.1016/J.JEURCERAMSOC.2010.12.035>
28. Najafzadeh Khoe, A.A., Habibolahzadeh, A., Qods, F., Baharvandi, H.: Study on rheological behavior of WC slurry in gel-casting process and reactive infiltration of produced foam by molten Zr2Cu alloy. *Int. J. Refract Metals Hard Mater.* **46**, 30–34 (2014). <https://doi.org/10.1016/j.ijrmhm.2014.05.006>
29. Schilling, C.H., Li, C., Tomasik, P., Kim, J.C.: The rheology of alumina suspensions: influence of polysaccharides. *J. Eur. Ceram. Soc.* **22**, 923–931 (2002). [https://doi.org/10.1016/S0955-2219\(01\)00394-6](https://doi.org/10.1016/S0955-2219(01)00394-6)
30. Vitali, S., Giorgini, L.: Overview of the rheological behaviour of ceramic slurries, (n.d.). <https://doi.org/10.5937/fmet1901042V>
31. Yu, Z., Huang, Y., Wang, C.A., Ouyang, S.: A novel gel tape casting process based on gelation of sodium alginate. *Ceram. Int.* **30**, 503–507 (2004). <https://doi.org/10.1016/J.CERAMINT.2003.08.003>
32. Trunec, M., Stastny, P., Kastyl, J.: Defect-free drying of large fine-particle zirconia compacts prepared by gelcasting method. *J. Eur. Ceram. Soc.* **42**, 7180–7186 (2022). <https://doi.org/10.1016/J.JEURCERAMSOC.2022.08.011>
33. Li, X., Jiang, D., Zhang, J., Lin, Q., Chen, Z., Huang, Z.: The dispersion of boron carbide powder in aqueous media. *J. Eur. Ceram. Soc.* **33**, 1655–1663 (2013). <https://doi.org/10.1016/J.JEURCERAMSOC.2013.02.001>
34. Dong, B., Wang, L., Min, Z., Wang, Q., Yin, C., Jia, T., Wang, Y., Zheng, X., Wang, F., Abadikhah, H., Xu, X., Zhang, Y., Wang, G.: Fabrication of novel porous Al₂O₃ substrates by combining emulsion templating and gel-tape-casting methods. *Ceram. Int.* **48**, 7320–7324 (2022). <https://doi.org/10.1016/J.CERAMINT.2021.11.205>
35. Kim, J.H., Zhe, G., Lim, J., Park, C., Kang, S.: Thermodynamic stability of in situ W-ZrC and W-Zr(CN) composites. *J. Alloys Compd.* **647**, 1048–1053 (2015). <https://doi.org/10.1016/J.JALLCOM.2015.06.117>
36. Oishi, T., Hirata, A., Ishida, H., Ono, K.: Outokumpu HSC chemistry for windows, chemical reaction and equilibrium software with extensive thermochemical. *Database* **64**, 662–668 (1994). https://doi.org/10.2320/JINSTMET1952.64.8_662
37. Najafzadehkhoe, A., Habibolahzadeh, A., Qods, F., Vakhshouri, M., Polkowski, W., Hvizdos, P., Galusek, D., Sk, A.N.: Effect of ZrC nanopowder addition in WC preforms on microstructure and properties of W-ZrC composites prepared by the displacive compensation of porosity (DCP) method. *J. Aust. Ceram. Soc.* **57**, 515–523 (2021). <https://doi.org/10.1007/s41779-020-00538-1/Published>
38. Najafzadehkhoe, A., Habibolahzadeh, A., Qods, F., Hvizdos, P.: A Taguchi approach to the influence of infiltration parameters on microstructure and properties of W-ZrC composites prepared by the displacive compensation of porosity (DCP) method. *Compos. Commun.* **20** (2020). <https://doi.org/10.1016/j.coco.2020.05.002>

39. Adabi, M., Amadeh, A.: Effect of infiltration parameters on composition of W-ZrC composites produced by displacive compensation of porosity (DCP) method. *Int. J. Refract. Metals Hard Mater.* **29**, 31–37 (2011). <https://doi.org/10.1016/J.IJRMHM.2010.06.009>
40. Golestani Fard, M.A., Baharvandi, H.: Development of W-ZrC composite coating on graphite by a TIG-aided surface cladding process. *Ceram. Int.* **47**, 27958–27971 (2021). <https://doi.org/10.1016/j.ceramint.2021.06.227>
41. Windhorst, T., Blount, G.: Carbon–carbon composites: a summary of recent developments and applications. *Mater. Des.* **18**, 11–15 (1997). [https://doi.org/10.1016/S0261-3069\(97\)00024-1](https://doi.org/10.1016/S0261-3069(97)00024-1)
42. Lee, Y.J., Joo, H.J.: Ablation characteristics of carbon fiber reinforced carbon (CFRC) composites in the presence of silicon carbide (SiC) coating. *Surf. Coat. Technol.* **180–181**, 286–289 (2004). <https://doi.org/10.1016/j.surfcoat.2003.10.071>
43. Li, Y., Liu, Y., Guo, C., Chen, Y., Liang, J., Zhang, J., Zhang, J., Guo, L.: Ablation resistance of ZrC-based composite coating with multi-layer structure for carbon/carbon composites above 2200 °C. *Corros. Sci. Sci.* **207**, 110600 (2022). <https://doi.org/10.1016/J.CORSCI.2022.110600>
44. Yang, X., Huang, Q., Su, Z., Chang, X., Chai, L., Liu, C., Xue, L., Huang, D.: Resistance to oxidation and ablation of SiC coating on graphite prepared by chemical vapor reaction. *Corros. Sci. Sci.* **75**, 16–27 (2013). <https://doi.org/10.1016/J.CORSCI.2013.05.009>
45. Wen, G., Sui, S.H., Song, L., Wang, X.Y., Xia, L.: Formation of ZrC ablation protective coatings on carbon material by tungsten inert gas cladding technique. *Corros. Sci. Sci.* **52**, 3018–3022 (2010). <https://doi.org/10.1016/J.CORSCI.2010.05.015>